Les Rencontres de Physique de la Vallée d'Aoste

Results and Perspectives in Particle Physics

edited by M. Greco

La Thuile, Aosta Valley *March 1st - 7th, 2009*

ISTITUTO NAZIONALE DI FISICA NUCLEARE
Laboratori Nazionali di Frascati

Les Rencontres de Physique de la Vallée d'Aoste

Results and Perspectives in Particle Physics

FRASCATI PHYSICS SERIES

Series Editor
Danilo Babusci

Technical Editor
Marcella Missiroli

Volume L - Special Issue

Jointly published by:

Istituto Nazionale di Fisica Nucleare - Laboratori Nazionali di Frascati
Divisione Ricerca - SIS - Ufficio Pubblicazioni
P.O. Box 13, I-00044 Frascati (Roma) Italy
`sis.publications@lnf.infn.it`

Società Italiana di Fisica
Via Saragozza 12, I-40123 Bologna, Italy
`http://www.sif.it`

FRASCATI PHYSICS SERIES

Les Rencontres de Physique de la Vallée d'Aoste
RESULTS AND PERSPECTIVES IN PARTICLE PHYSICS

ISBN: 978-88-7438-053-4

Printed in Italy by Compositori Industrie Grafiche
Via Stalingrado 97/2
40128 Bologna

FRASCATI PHYSICS SERIES

Volume L

Les Rencontres de Physique de la Vallée d'Aoste

Results and Perspectives in Particle Physics

Editor
Mario Greco

La Thuile, Aosta Valley, March 1st - 7th, 2009

Conference Organizers

Giorgio Bellettini	Pisa
Giorgio Chiarelli	Pisa
Mario Greco	Roma Tre
Gino Isidori	Laboratori Nazionali di Frascati

Chairpersons

Giorgio Bellettini	Pisa
Matteo Cacciari	Paris VI
Antonio Capone	Roma
Giorgio Chiarelli	Pisa
Alvaro De Rujula	Cern
Alexander Dolgov	Ferrara
Mario Greco	Roma Tre
Gino Isidori	Frascati
Jacobo Konigsberg	Gainesville, Florida
Sandra Leone	Pisa
Ida Peruzzi	Perugia

Preface

The 2009 Rencontres de Physique de la Vallée d'Aoste were held at the Planibel Hotel of La Thuile, Aosta Valley, on March 1st - 7th, with the twenty-third edition of "Results and Perspectives in Particle Physics".

The physics programme included various topics in particle physics, also in connection with present and future experimental facilities, as cosmology and astrophysics, neutrino physics, CP violation and rare decays, electroweak and hadron physics with e^+e^- and hadron colliders, heavy flavours, search for new physics and prospects at future facilities.

The Session on "Physics and Society" included special colloquia on "LHC status and the CERN plans", "Overview and Challenges of the ITER project" and "Innovative energy sources". We are very grateful to Lyn Evans, Norbert Holtkamp and Charles Forsberg for their participation and contribution.

Giorgio Bellettini, Giorgio Chiarelli, Gino Isidori and I would like to warmly thank the session chairpersons and the speakers for their contribution to the success of the meeting.

The regional government of the Aosta Valley, in particular through the Minister of Public Education and Culture, Laurent Vierin, has been very pleased to offer its financial support and hospitality to the Rencontres of La Thuile. Also on behalf of the participants, representatives of some major Laboratories and Institutes in the world, we would like to thank all the Regional Authorities. Special thanks are also due to Bruno Baschiera, local coordinator of the Rencontres.

We are grateful to the President of INFN, Roberto Petronzio, the Directors of INFN Laboratori Nazionali di Frascati, Mario Calvetti, and INFN Sezione di Pisa, Giovanni Batignani, for the support in the organization of the Rencontres. We would like to thank also Lucia Lilli, Claudia Tofani and Paolo Villani for their help in both planning and running the meeting. We are also grateful to Alessandra Miletto for her valuable

contribution to the local organization of the meeting. The excellent assistance provided by Giovanni Nicoletti and Mauro Giannini made it possible to set up the computer link to the international network.

Finally we would like to thank the Mayor Gilberto Roullet and the local authorities of La Thuile and the "Azienda di Promozione Turistica del Monte Bianco" for their warm hospitality, and the Planibel Hotel staff for providing us with an enjoyable atmosphere.

November 2009

Mario Greco

CONTENTS

SESSION VI - ELECTROWEAK AND TOP PHYSICS

SESSION VII - HIGGS SEARCHES

SESSION VIII - SEARCHING FOR NEW PHYSICS

SESSION IX - PHYSICS AND SOCIETY

SESSION X - PERSPECTIVES

SESSION I - COSMOLOGY AND ASTROPHYSICS

IL NUOVO CIMENTO Vol. 32 C, N. 5-6 Settembre-Dicembre 2009
DOI 10.1393/ncc/i2010-10517-1

Colloquia: LaThuile09

Cosmic rays studies with the PAMELA space experiment

R. Sparvoli(1)(2), O. Adriani(3)(4), G. C. Barbarino(5)(6), G. A. Bazilevskaya(7), R. Bellotti(8)(9), M. Boezio(10), E. A. Bogomolov(11), L. Bonechi(3)(3), M. Bongi(4), V. Bonvicini(10), S. Bottai(4), A. Bruno(8)(9), F. Cafagna(9), D. Campana(6), P. Carlson(12), M. Casolino(2), G. Castellini(13), M. P. De Pascale(1)(2), C. De Santis(1)(2), N. De Simone(1)(2), V. Di Felice(1)(2), A. M. Galper(14), L. Grishantseva(14), P. Hofverberg(12), S. V. Koldashov(14), S. Y. Krutkov(11), A. N. Kvashnin(7), A. Leonov(14), V. Malvezzi(2), L. Marcelli(2), W. Menn(15), V. V. Mikhailov(14), E. Mocchiutti(10), G. Osteria(6), P. Papini(4), M. Pearce(12)(16), P. Picozza(1)(2), M. Ricci(17), S. B. Ricciarini(4), M. Simon(15), P. Spillantini(3)(4), Y. I. Stozhkov(7), A. Vacchi(10), E. Vannuccini(4), G. Vasilyev(11), S. A. Voronov(14), Y. T. Yurkin(14), G. Zampa(10), N. Zampa(10) and V. G. Zverev(14)

(1) *Dipartimento di Fisica, Università di Roma "Tor Vergata" - Via della Ricerca Scientifica 1 I-00133 Rome, Italy*
(2) *INFN, Sezione di Roma "Tor Vergata" - Via della Ricerca Scientifica 1 I-00133 Rome, Italy*
(3) *Dipartimento di Fisica, Università di Firenze - Via Sansone 1 I-50019 Sesto Fiorentino (Firenze), Italy*
(4) *INFN, Sezione di Firenze - Via Sansone 1, I-50019 Sesto Fiorentino (Firenze), Italy*
(5) *Dipartimento di Fisica, Università di Napoli "Federico II" - Via Cintia I-80126 Napoli, Italy*
(6) *INFN, Sezione di Napoli - Via Cintia, I-80126 Napoli, Italy*
(7) *Lebedev Physical Institute - Leninsky Prospekt 53, RU-119991 Moscow, Russia*
(8) *Dipartimento di Fisica, Università di Bari - Via Amendola 173, I-70126 Bari, Italy*
(9) *INFN, Sezione di Bari - Via Amendola 173, I-70126 Bari, Italy*
(10) *INFN, Sezione di Trieste - Padriciano 99, I-34012 Trieste, Italy*
(11) *Ioffe Physical Technical Institute - Polytekhnicheskaya 26 RU-194021 St Petersburg, Russia*
(12) *Department of Physics, KTH, AlbaNova University Centre SE-10691 Stockholm, Sweden*
(13) *IFAC - Via Madonna del Piano 10, I-50019 Sesto Fiorentino (Firenze), Italy*
(14) *Moscow Engineering and Physics Institute - Kashirskoe Shosse 31 RU-11540 Moscow, Russia*
(15) *Universität Siegen - D-57068 Siegen, Germany*
(16) *The Oskar Klein Centre for Cosmoparticle Physics, AlbaNova University Centre SE-10691 Stockholm, Sweden*
(17) *INFN, Laboratori Nazionali di Frascati - Via Enrico Fermi 40, I-00044 Frascati, Italy*

(ricevuto il 10 Novembre 2009; pubblicato online il 7 Gennaio 2010)

Summary. — The instrument PAMELA, in orbit since June 15th, 2006 on board the Russian satellite Resurs DK1, is delivering to ground 16 Gigabytes of data per day. The apparatus is designed to study charged particles in the cosmic radiation, with a particular focus on antiparticles as a possible signature of dark matter annihilation in the galactic halo; the combination of a magnetic spectrometer and different detectors—indeed—allows antiparticles to be reliably identified from a large background of other charged particles. New results on the antiproton-to-proton and positron-to-all-electron ratios over a wide energy range (1–100 GeV) have been recently released by the PAMELA Collaboration, and will be summarized in this paper. While the antiproton-to-proton ratio does not show particular differences from an antiparticle standard secondary production, in the positron-to-all-electron ratio an enhancement is clearly seen at energies above 10 GeV. Possible interpretations of this effect will be briefly discussed.

PACS 95.55.Vj – Neutrino, muon, pion, and other elementary particle detectors; cosmic ray detectors.
PACS 98.80.Cq – Particle-theory and field-theory models of the early Universe (including cosmic pancakes, cosmic strings, chaotic phenomena, inflationary universe, etc.).
PACS 11.10.Kk – Field theories in dimensions other than four.
PACS 12.60.Jv – Supersymmetric models.

1. – Introduction

The study of antimatter and antiparticle content in cosmic rays is a unique tool to investigate several physics and astrophysical phenomena. The idea of performing cosmic antiprotons and positrons measurements to probe unconventional particle physics and astrophysics scenarios has a long history and moved the cosmologists for several decades. The first historical discovery of antiprotons on the top of the atmosphere dates back to the balloon-borne experiments performed by Robert Golden and Edward Bogomolov in 1979 [1, 2]. They measured a rate of antiprotons much higher than expected from interactions of cosmic rays with the interstellar matter. Many theoretical ideas were developed to interpret these results as an evidence of the existence of large domains of antimatter, of evaporation by the Hawking process of primordial black holes produced very early in the hot Big Bang in the quantum gravity era, of annihilation of exotic particles.

The search of antimatter is strictly connected with the baryon-antibaryon asymmetry in the Universe. If we postulate the existence of primordial antimatter, antihelium would be the most likely form to be detected in cosmic rays, likewise in matter primordial nucleosynthesis. In addition, the detection of antinuclei with $Z > 2$ in cosmic rays would provide direct evidence of the existence of antistellar nucleosyntesis. Moreover, several authors [3, 4] suggest that small bubbles with very high baryonic asymmetry could have been produced by the presence of stochastic or dynamical violation of CP.

New cosmological observations are giving us a coherent picture of a Universe dominated by dark matter and dark energy. There are increasingly convincing evidences that non-baryonic dark matter is the building block of all structures in the Universe. It is now well known that the energy budget of the Universe is shared among baryonic

matter (4%), dark matter (23%) and dark energy (73%). The nature of the dark matter is still unknown. The favourite candidates for the non-baryonic component are neutral weakly interacting massive particles (WIMP's) with a mass in the range between 10's of GeV to TeV. They would naturally appear as one of the thermal leftovers from the early Universe and their presence is predicted in several classes of extension of the Standard Model of particle physics. The most studied WIMP is the *neutralino*, combination of supersymmetric partners of the neutral gauge bosons of the Standard Model. Neutralinos are Majorana fermions and will annihilate with each other in the halo, resulting in the symmetric production of particles and antiparticles, the latter providing an observable signature. Another interesting candidate, among the many proposed, is the Kaluza-Klein lightest particle in the Universal Extra Dimension framework.

The search and identification of such possible sources are some of the major challenges in cosmic rays studies. However, these contributions are mixed with a huge background produced in the interaction of cosmic rays with the interstellar matter (ISM), so that they will appear as a distortion of antiproton, positron and gamma energy spectra due to this secondary production. Many balloon-borne experiments followed the pioneer ones, performed principally by the WiZard, BESS and HEAT Collaborations. Although the first historical results were not confirmed later, the way for a wide research for primary antimatter and dark matter signals in the cosmic rays was open. In 1998, on board the Space Shuttle, the AMS-01 Collaboration performed the first antimatter experiment outside the atmosphere. In June 2006 the satellite experiment PAMELA was launched in orbit by a Soyuz-U rocket from the Bajkonur cosmodrome in Kazakhstan.

2. – Instrument description

PAMELA [5], a Payload for Matter-Antimatter Exploration and Light Nuclei Astrophysics, is an experiment conceived for searching antimatter and dark matter signals in space. It is conducted by an international collaboration constituted of several INFN Divisions and Italian Universities, three Russian institutions (MEPhI and FIAN Lebedev in Moscow and IOFFE in St. Petersburg), the University of Siegen in Germany and the Royal Technical Institute in Stockholm, Sweden. The mission is performed within the framework of the RIM (Russian Italian Missions) Program, that took the heritage of the WiZard program.

The scheme of the PAMELA instrument is shown in fig. 1. PAMELA is built around a 0.43 T permanent magnet spectrometer, equipped with six planes of double-sided silicon detectors, 300 μm thick each, that allows the sign, absolute value of charge and rigidity of traversing charged particles to be determined. The resolution in the bending side is 4 μm and the MDR is 800 GV. Spillover effects limit the upper detectable antiparticle momentum to 190 GeV/c and to 270 GeV/c for antiprotons and positrons, respectively.

The discrimination between the hadronic and electromagnetic components is assured by two detectors, an imaging calorimeter and a neutron counter. The calorimeter is composed of 44 ministrip silicon layers, 380 μm thick each, placed alternatively in x and y directions and interleaved with 22 tungsten planes, for a depth of 16.3 radiation lengths and 0.6 interaction lengths. Tests with e^- and p CERN beams for wide energy intervals, as precise MonteCarlo simulations, verified a separation capability of the order of 10^5 in the e^-/p ratio and an energy resolution for electrons of 5.5% in the interval between 10 and 300 GeV. The neutron detector is composed of 36 ^{3}He counters displaced in two planes and inserted in 1 cm thick polystyrene. It counts neutrons in the showers induced in the calorimeter by hadrons or electrons. The different number of neutrons produced

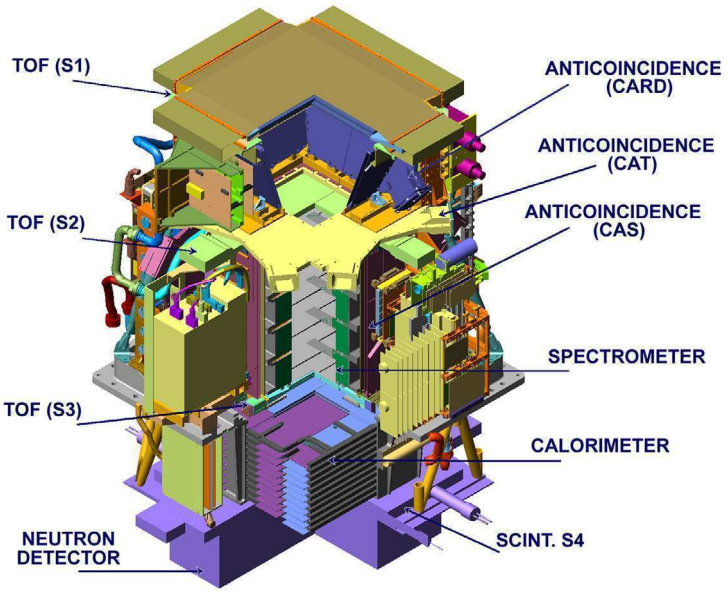

Fig. 1. – The PAMELA instrument: a schematic overview of the apparatus.

in hadronic or electromagnetic showers gives a supplementary tool in the discrimination between protons and positrons.

A set of 3 pairs of stripped plastic scintillators gives the trigger of the events and provides identification of particles coming from the bottom. Moreover, multiple $\mathrm{d}E/\mathrm{d}x$ measurements determine the module of the particle electrical charge. The spectrometer is surrounded by a plastic scintillator veto shield and the volume between the upper two time-of-flight planes is bounded by an additional plastic scintillator anticoincidence system. A plastic scintillator mounted beneath the calorimeter aids in the identification of high-energy electrons. The geometry factor of the instrument is 21.5 $\mathrm{cm}^2\mathrm{sr}$ and the total weight is 470 kg.

The apparatus, inserted in a pressurized container, was installed on board the Russian Resurs DK1 satellite (mass: 7.6 tons, height: 7.4 m), mainly devoted to Earth observation. The satellite was launched on June 15th 2006 and put in a quasi-polar (inclination 70°) low-earth elliptical orbit at an altitude ranging between 350 and 610 km.

The performance in flight of the PAMELA instrument enables searches for dark matter annihilation, antihelium (primordial antimatter) and new matter in the Universe (strangelets?). Other scientific objectives are the study of the cosmic ray production and propagation in our galaxy by precise measurements of the absolute fluxes of primary and secondary light nuclei, the monitoring of solar activity and cosmic rays solar modulation, the investigation of the interaction processes of cosmic rays with the Earth's magnetosphere, the search for high-energy electrons in order to discover local sources.

3. – Results and interpretation

Since July 2006 PAMELA instrument has been daily transmitting 16 Gigabytes of data by the satellite telemetry to the Ground Segment placed in Moscow at the NTsOMZ

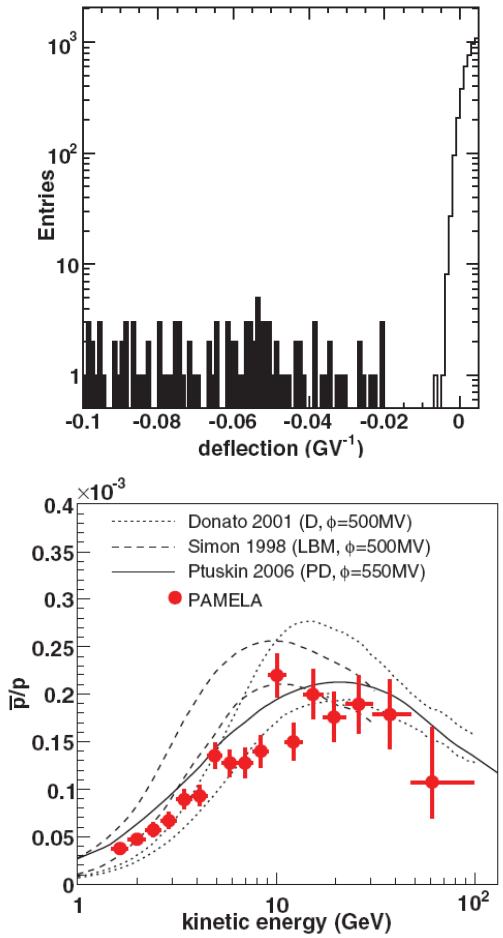

Fig. 2. – Top: the deflection reconstructed by the track fitting procedure for negatively and positively charged down-going particles. The shaded histogram corresponds to the selected antiprotons. Bottom: the antiproton-to-proton flux ratio published by PAMELA [6] compared with theoretical calculations for a pure secondary production of antiprotons [7-9].

institute. The results presented here are based on the data-set collected between July 2006 and February 2008. More than 10^9 triggers were accumulated during a total acquisition time of approximately 500 days.

Antiprotons identification was based on the determination of the rigidity by the spectrometer and the properties of the energy deposit and interaction topology in the calorimeter. The separation between negatively charged particles and spillover is shown in fig. 2, top. The calorimeter was used to reject electrons. The antiproton-to-proton flux ratio [6] measured by the PAMELA experiment is shown in fig. 2, bottom, compared with theoretical calculations assuming pure secondary production of antiprotons during the propagation of cosmic rays in the galaxy. The PAMELA data are in excellent agreement with recent results from other experiments, as shown in fig. 3. The ratio increases smoothly from about 2×10^{-5} at a kinetic energy of about 1 GeV and levels off

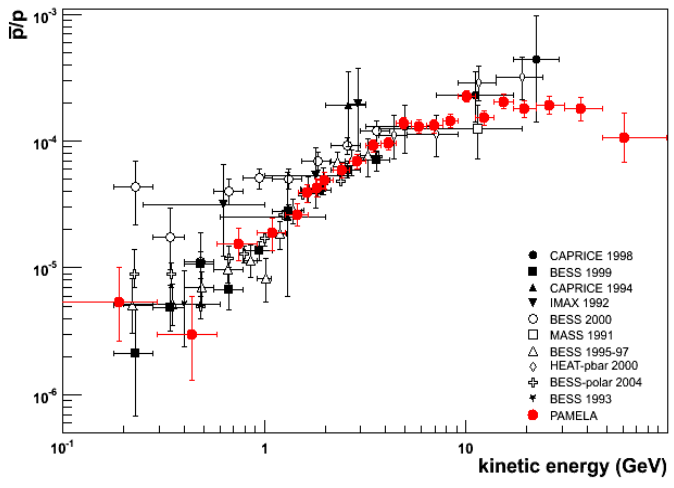

Fig. 3. – PAMELA antiproton-to-proton flux ratio compared with previous measurements [10-16].

at about 1×10^{-4} for energies above 10 GeV. The data do not present the features or structures expected from exotic sources, so they place strong limits to dark matter annihilation models. Moreover, they set tight constraints on parameters relevant for secondary production calculations, *e.g.*, the normalization and the index of the diffusion coefficient, the Alfven speed, and contribution of a hypothetical "fresh" local cosmic-ray component.

Positrons and electrons data need a very careful analysis, carried out by PAMELA using the most performing available instrumental and statistical tools, because the possibility of misidentification of protons as positrons. In fact, the proton-to-positron ratio increases from about 10^3 at 1 GeV to approximately 10^4 at 100 GeV. Particle identification was based on the matching between the momentum measured by the tracker and the total energy measured in the calorimeter, the starting point and the lateral and longitudinal profiles of the shower produced by particles in the PAMELA calorimeter, and the neutron detector response. This analysis technique has been tested at the proton and electron beams at CERN for different energies, by Monte Carlo simulations and by flight data.

The positron-to-all-electron ratio [17] measured by the PAMELA experiment is given in fig. 4. The calculation, shown in the same figure for pure secondary production of positrons during the propagation of cosmic rays in the Galaxy without reacceleration processes, proves that the positron fraction is expected to fall as a smooth function of increasing energy if secondary production dominates. In the figure PAMELA data are compared with other recent experimental data.

The data cover the energy range 1.5–100 GeV, with 151.672 electrons and 9.430 positrons identified. Two features are clearly visible. At low energies, below 5 GeV, the PAMELA results are systematically lower than data collected during the 1990's, while at high energies, above 10 GeV, they show a positron fraction increasing significantly with energy. Between 5 GeV and 10 GeV, the PAMELA positron fraction is compatible with other measurements.

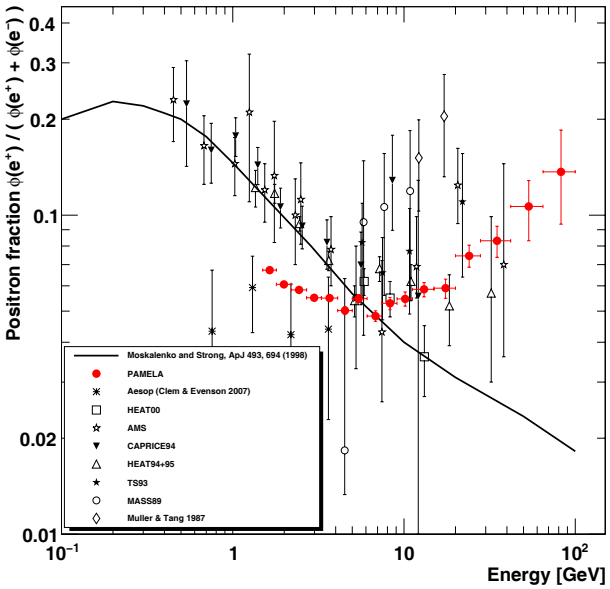

Fig. 4. – PAMELA positron fraction with a theoretical model. The solid line shows a calculation by Moskalenko and Strong [18] for pure secondary positron production during the propagation of cosmic rays in the galaxy. The positron fraction measured by the PAMELA experiment is compared with other recent experimental data [19-26].

This intriguing excess of positrons in the range 10–100 GeV has led to many speculations about its origin, as annihilation of dark matter, decaying dark matter, decaying of lightest superparticle dark matter, cosmic strings, young pulsars, a few nearby SNR.

A rise in the positron fraction at high energy has been postulated for the annihilation of dark matter particles in the galactic halo [27]. The most problematic theoretical challenge posed by the PAMELA results is the asymmetry between leptonic (positron fraction) and hadronic (antiproton-proton ratio), difficult to explain in the framework in which the neutralino is the dominant dark matter component (fig. 5). In this case suitable explanation requires a very high mass ($M = 10$ TeV, fig. 6) neutralino which is unlikely in the context of allow energy supersymmetry breaking model. Better explanations are obtained in terms of leptonic annihilation channel for a wide range of the WIMP mass (fig. 7). It is important to say, however, that all explanations in terms of dark matter annihilation request a boost factor for the annihilation standard rate ranging between 10^2 to 10^4.

Another explanation relates to a contribution from nearby and young pulsars, objects well known as particle accelerators [27]. Primary electrons are accelerated in the magnetosphere of pulsars in the polar cup and in the outer gap along the magnetic field lines emitting gamma-rays by synchrotron radiation, gammas that in the presence of pulsar gigantic magnetic field can evolve in positrons and electrons pairs. These, escaping into the interstellar medium, give a further contribution to the electron and positron components (as an example, fig. 8).

Main uncertainties in these calculations are connected to an incomplete knowledge of the primary cosmic-ray nuclei and primary electron spectra, of the interaction

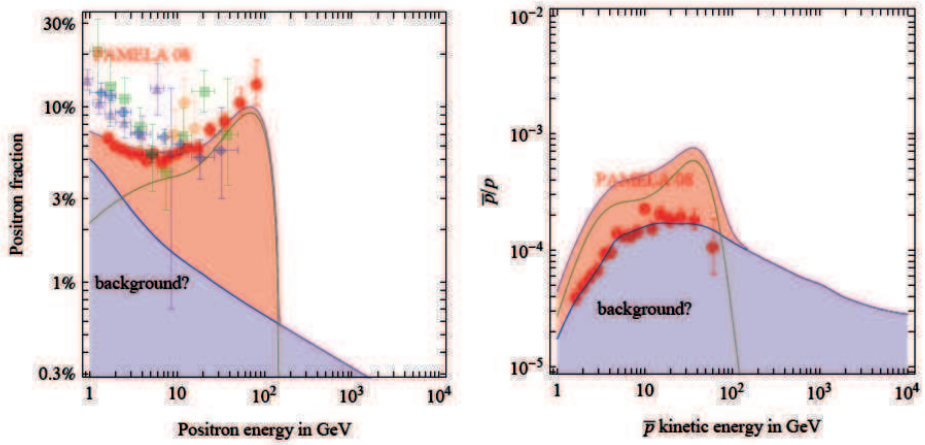

Fig. 5. – Example of fits of e^+ (left) and $\bar{p}$ (right) data, for a $M_{\mathrm{WIMP}} \approx 150\,\mathrm{GeV}$ and W^+W^- dominant annihilation channel [28].

cross-sections and the cosmic-ray propagation in the galaxy. Despite all these approximations, contributions from standard secondary production to explain this anomalous increasing of the ratio would demand high modifications in the current knowledge of the electrons, protons and helium spectra [30], although some papers report an explanation of this increasing in terms of few nearby SNR [31] or of secondary production taking place in the same region where cosmic rays are being accelerated [32]. However, to distinguish among the different hypotheses a better knowledge of the standard production of electrons and positrons is required as well of the mechanisms of their acceleration and transport in the galaxy. PAMELA is performing accurate measurements of the absolute fluxes of electrons, positrons, protons and light nuclei, that will constrain tightly the secondary production models.

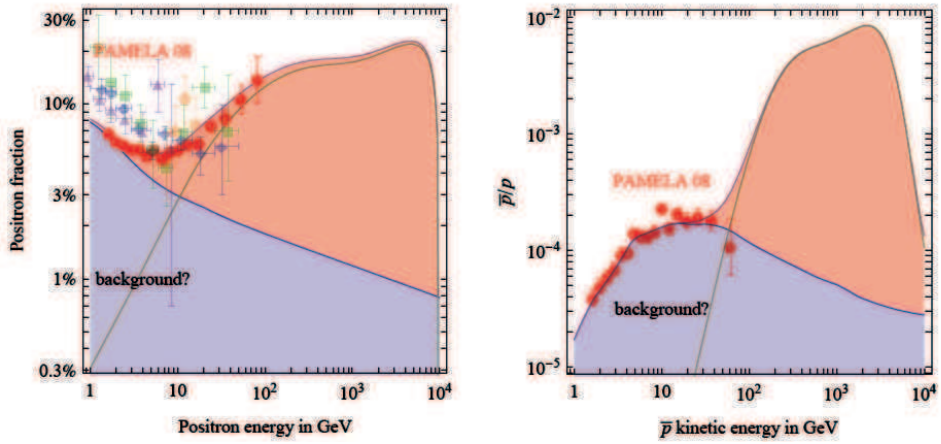

Fig. 6. – Example of fits of e^+ (left) and $\bar{p}$ (right) data, for a $M_{\mathrm{WIMP}} \approx 10\,\mathrm{TeV}$ and W^+W^- dominant annihilation channel [28].

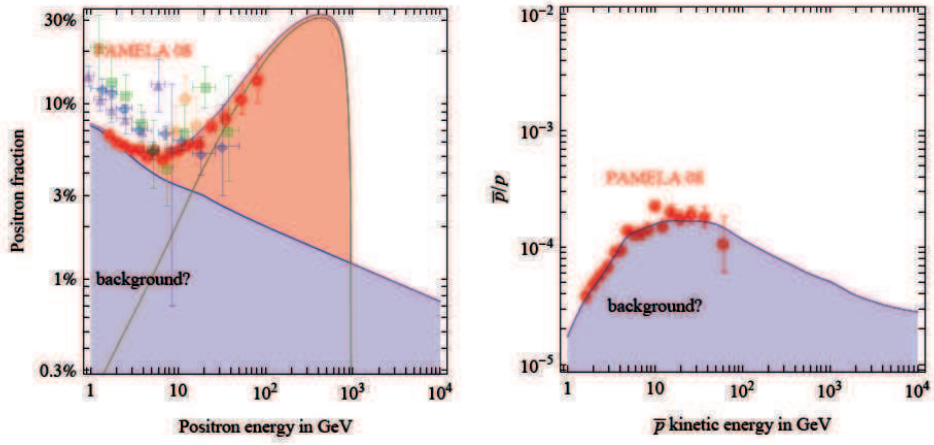

Fig. 7. – Examples of fits of e^+ (left) and $\bar{p}$ (right) data, for a $M_{\mathrm{WIMP}} \approx 1\,\mathrm{TeV}$ and $\mu^+\mu^-$ dominant annihilation channel [28].

Concerning the lower energy part of the spectrum, a disagreement between our data and the previous measurements is evident. This difference is interpreted as a consequence of time- and charge-dependent solar modulation effects. The energy spectra of cosmic rays are modified by the solar wind within the solar system, mainly at energy lower than 10 GeV. These solar modulation effects depend on the cosmic rays sign of charge and on the positive and negative phase of the Sun and it is due to gradient, curvature and drift effects. These mostly affect low-mass particles as positrons and electrons and are more important in the phase of low solar activity. The older results were obtained during the previous positive polarity of the solar cycle, when the mechanical rotation axis of the Sun and the Sun magnetic dipole had the same versus and positive charges

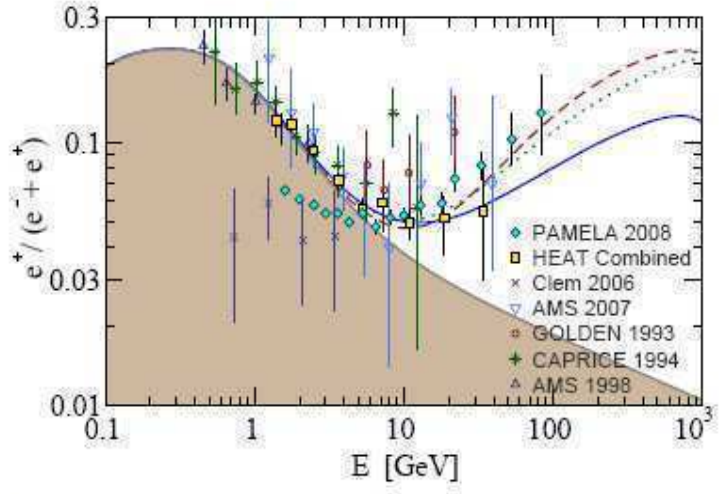

Fig. 8. – Contributions of e^- and e^+ from Geminga assuming different distance, age and energetics of the pulsar [29].

underwent a lower solar modulation. A balloon-borne experiment which flew in June 2006 has also observed a suppressed positron fraction at low energies, but with larger statistical uncertainties [26].

4. – Conclusions

Results from the analysis of the data collected and transmitted to ground from the PAMELA instrument in the first one and half year of operation show very interesting features in the positron-to-all-electron fraction. At energy above 10 GeV, an increase in the ratio, compared as expected from the standard secondary production, is generally interpreted in terms of positron primary sources, as dark matter annihilation or nearby pulsars contributions. Explanations in terms of nearby SNR or non-standard processes in the secondary positrons production are also reported. Solar modulation largely affects the low part of the spectrum, giving new information on the solar activity during the negative phase of the Sun. The antiproton-to-proton spectrum appears in agreement with the standard secondary production, in the collision between high-energy cosmic rays and interstellar matter.

REFERENCES

[1] Golden R. L. *et al.*, *Phys. Rev. Lett.*, **43** (1979) 1196.
[2] Bogomolov E. *et al.*, *XX Int. Cosmic Ray Conf.*, **2** (Moscow, 1987) 72.
[3] Bambi C. and Dolgov A. D., *Nucl. Phys. B*, **784** (2007) 132.
[4] Dolgov A. D., hep-ph/0806.4554.
[5] Picozza P. *et al.*, *Astropart. Phys.*, **27** (2007) 296.
[6] Adriani O. *et al.*, *Phys. Rev. Lett.*, **102** (2009) 051101.
[7] Simon M., Molnar A. and Roesler S., *Astrophys. J.*, **499** (1998) 250.
[8] Donato F. *et al.*, *Astrophys. J.*, **563** (2001) 172.
[9] Ptuskin V. S. *et al.*, *Astrophys. J.*, **642** (2006) 902.
[10] Boezio M. *et al.*, *Astrophys. J.*, **561** (2001) 787.
[11] Beach A. S. *et al.*, *Phys. Rev. Lett.*, **87** (2001) 271101.
[12] Hof M. *et al.*, *Astrophys. J. Lett.*, **467** (1996) 33.
[13] Mitchell J. *et al.*, *Phys. Rev. Lett.*, **76** (1996) 3057.
[14] Boezio M. *et al.*, *Astrophys. J.*, **487** (1997) 415.
[15] Asaoka Y. *et al.*, *Phys. Rev. Lett.*, **88** (2002) 051101.
[16] Hams T. *et al.*, *Proc. 30th Int. Cosmic Ray Conference* (Merida, 2006).
[17] Adriani O. *et al.*, *Nature*, **458** (2009) 697.
[18] Moskalenko I. V. and Strong A. W., *Astrophys. J.*, **493** (1998) 694.
[19] Gast H., Olzem J. and Schael S., *Proc. XLIst Rencontres de Moriond* (2006) 421.
[20] Müller D. and Tang K. K., *Astrophys. J.*, **312** (1987) 183.
[21] Golden R. L. *et al.*, *Astrophys. J.*, **436** (1994) 769.
[22] Barwick S. W. *et al.*, *Astrophys. J.*, **482** (1997) L191.
[23] Boezio M. *et al.*, *Astrophys. J.*, **532** (2000) 653.
[24] Alcaraz J. *et al.*, *Phys. Lett. B*, **484** (2000) 10.
[25] Beatty J. J. *et al.*, *Phys. Rev. Lett.*, **93** (2004) 241102.
[26] Clem J. and Evenson P., *Proc. 30th ICRC* (Merida, 2007).
[27] Profumo S., astro-ph 0812.4457 (2008) and references therein.
[28] Cirelli M. *et al.*, *Nucl. Phys. B*, **813** (2009) 1.
[29] Yüksel H. *et al.*, *Phys. Rev. Lett.*, **103** (2009) 051101.
[30] Serpico P., *Phys. Rev. D*, **79** (2009) 021302.
[31] Shaviv N. J. *et al.*, *Phys. Rev. Lett.*, **103** (2009) 111302.
[32] Blasi P., *Phys. Rev. Lett.*, **103** (2009) 051104.

IL NUOVO CIMENTO Vol. 32 C, N. 5-6 Settembre-Dicembre 2009
DOI 10.1393/ncc/i2009-10511-8

Colloquia: LaThuile09

Observations of high-energy gamma-rays with the *Fermi* Observatory

N. Giglietto on behalf of the *Fermi*-LAT Collaboration
Dipartimento Interateneo di Fisica di Bari and INFN, Sezione di Bari - Bari, Italy

(ricevuto il 10 Novembre 2009; pubblicato online il 21 Dicembre 2009)

Summary. — The *Fermi* Gamma-Ray Space Telescope is a satellite-based observatory that explores the gamma-ray sky in a wide energy range from a few keV to more than 300 GeV, allowing the investigation of many fields of gamma-ray astrophysics. Fermi will open a new and important window on a wide variety of phenomena, including black holes and active galactic nuclei, gamma-ray bursts, the origin of cosmic rays and supernova remnants and searches for hypothetical new phenomena such as supersymmetric dark matter annihilations. The primary instrument is the Large Area Telescope (LAT), which measures gamma-ray flux and spectra from 20 MeV to $>$ 300 GeV and is a successor to the highly successful EGRET experiment on CGRO. The LAT has better angular resolution, greater effective area, wider field of view and broader energy coverage than any previous experiment in this energy range. The detectors were integrated with the spacecraft in December 2006 and Fermi has been launched on June, 11 2008 from Kennedy Space Flight Centre (NASA). In an early phase of the operations, a series of calibrations and performance measurements and monitoring were performed and the first sky images were collected. This paper will present a short review of the Fermi observatory physics and the first sky images collected during the first 6 months of the science phase of the mission.

PACS 95.85.Pw – γ-ray.
PACS 97.60.Gb – Pulsars.
PACS 98.54.Cm – Active and peculiar galaxies and related systems.
PACS 98.70.Sa – Cosmic rays.

1. – Introduction

Fermi was successfully launched from Cape Canaveral on the 11th of June 2008. It is currently in an almost circular orbit around the Earth at an altitude of 565 km having an inclination of 25.6° and an orbital period of 96 minutes. After an initial period of engineering data taking and on-orbit calibration [1], the observatory was put into a sky-survey mode. The observatory has two instruments onboard, the Large Area Telescope [2, 3] (LAT), a pair-conversion gamma-ray detector and tracker and a Gamma

TABLE I. – *Summary of Large Area Telescope Instrument parameters and estimated performance.*

Parameter	Value or range
Energy range	20 MeV–300 GeV
Effective area at normal incidence	
(peak typically is in the 1–10 GeV range)	$9500\,\mathrm{cm}^2$
Energy resolution (equivalent Gaussian 1σ):	
100 MeV–1 GeV (on axis)	9%–15%
1 GeV–10 GeV (on axis)	8%–9%
10 GeV–300 GeV (on-axis)	8.5%–18%
> 10 GeV ($> 60^\circ$ incidence)	$\leq 6\%$
Single photon angular resolution (space angle)	
on-axis, 68% containment radius:	
> 10 GeV	$\leq 0.15^\circ$
1 GeV	0.6°
100 MeV	3.5°
Field of View (FoV)	2.4 sr
Timing accuracy	$< 10\,\mu$s
Event readout time (dead time)	$26.5\,\mu$s

Ray Burst Monitor (GBM), dedicated to the detection of gamma-ray bursts. The instruments on *Fermi* jointly provide coverage over the energy range from a few keV to several hundreds of GeV. With respect to previous gamma-ray missions, *Fermi*-LAT has a very large field of view that allows monitoring 20% of the sky at any instant and a very wide energy range from 20 MeV to > 300 GeV.

2. – The Large Area Telescope

The Large Area Telescope has good angular resolution for source localization and multi-wavelength studies, high sensitivity over a broad field-of-view to monitor variability and detect transients, good calorimetry over an extended energy band to study spectral breaks and cut-offs, and good calibration and stability for absolute, long-term flux measurement. The LAT measures the tracks of the electron (e^-) and positron (e^+) that result when an incident γ-ray undergoes pair-conversion, preferentially in a thin, high-Z foil, and measures the energy of the subsequent electromagnetic shower that develops in the telescope's calorimeter. Table I summarizes the scientific performance capabilities of the LAT [2]. To take full advantage of the LAT's large FoV, the primary observing mode of *Fermi* is the so-called "scanning" mode in which the normal to the front of the instrument (z-axis) on alternate orbits is pointed to $+35^\circ$ above and below the orbital plane on alternate orbits. In this way, after 2 orbits, about 3 hours for *Fermi*'s orbit, the sky exposure is almost uniform. For particularly interesting targets of opportunity, the observatory can be inertially pointed. Details of the LAT design and performance are presented in [2].

3. – Fermi physics opportunities

Since *Fermi*-LAT scans the entire sky in few hours, a dramatic change of the catalog of high-energy gamma-ray sources and an increment by an order of magnitude of the number of point sources is underway. Additionally, the timing resolution for variable phenomena (gamma-ray burst, pulsars, AGNs...) and the spatial localization of known sources are being greatly improved. The scientific objectives that *Fermi*-LAT will address include:

1) resolving the high-energy gamma-ray sky and determining the nature of the unidentified gamma-ray sources seen by EGRET and the origin of the apparently isotropic diffuse emission;

2) understanding the mechanisms of particle acceleration in celestial sources, including active galactic nuclei, pulsars, and supernovae remnants;

3) studying the high-energy behavior of gamma-ray bursts and transients;

4) using high-energy gamma-rays to probe the early universe to $z \geq 6$;

5) probing the nature of dark matter.

Fermi-LAT should help us determine how much energy extreme astrophysical sources produce, and therefore tell us about the acceleration mechanisms that produce such high-energy particles.

4. – Fermi first 6 month results

The first two months of data taking were mainly dedicated to calibrations and alignments [2]. Therefore the first results are related to the discovery of new sources and to the measurements of known objects, with the intent to verify both the pointing and the observatory features. Since Vela is the brightest source in the GeV sky, we have used this pulsar to verify spatial and temporal alignments of the *Fermi* observatory. During Launch and Early Orbit operations (L&EO), *Fermi* targeted Vela pulsar for several pointed observations added to the data taking in survey mode, and as a result established the position of Vela in gamma-rays within $0.5'$ of the the radio pulsar position [4]. *Fermi* timing validation and verification has been obtained using data collected during first period of data taking and using the known radio ephemeris measurements to verify the absolute timing of photons observed by *Fermi*, after correcting photon arrival time to the Solar System barycenter [5]. At the end of the on-orbit calibrations [1], the observatory was put into a sky-survey mode, and here we summarize most relevant results observed in the first 6 months. The EGRET era left us some unresolved problems that FERMI has started to explore:

– the nature and characteristics of GRBs;

– the identification of the unresolved sources, *i.e.* not associated to known sources from other catalogues;

– the problem of the GeV excess;

– the number of γ-ray pulsars and the γ-ray emission mechanisms.

5. – Gamma Ray Burst studies

The two instruments on *Fermi* will also provide us with the complete high-energy spectra of gamma-ray bursts, from a few keV to hundreds of GeV. These bright and distant flashes of gamma-rays, which take place at a rate of about one per day, briefly shine as the most luminous objects in the universe—yet the total energy released and their energy range has yet to be measured. The standard picture that has emerged of GRB physics is that an initial fireball powers a collimated, super-relativistic blast wave with initial Lorentz factor $\sim 10^2$–10^3. Prompt γ-ray and X-ray emission from this "central engine" may continue for few $\times 10^3$ s. Then external shocks arising from interaction of the ejecta with the circumstellar environment at lower Lorentz factors give rise to afterglows in the X-ray and lower-energy bands that are detected for hours to months. The physical details—primary energy source and energy transport, degree of blast wave collimation, and emission mechanisms—remain for debate [6]. GBM and LAT onboard *Fermi* Observatory together, record GRBs over a broad energy range spanning about 7 decades of gamma-ray energy. During the first 6 months, *Fermi* has detected several GRBs, mostly on GBM detector and others with joint observations between GBM and LAT. In September 2008, Fermi observed the exceptionally luminous GRB 080916C [7], with the largest apparent energy release yet measured. The high-energy gamma-rays are observed to start later and persist longer than the lower energy photons. A simple spectral form fits the entire GRB spectrum, providing strong constraints on emission models. The known distance of the burst enables placing lower limits on the bulk Lorentz factor of the outflow and costraints on the quantum gravity mass. The increasing number of detections of GRBs by the LAT will help constrain many uncertainties in these areas.

6. – Galactic sources

Pulsars are fast-rotating magnetic neutron stars that probably emit beams of radio waves from their poles. Taking into account radio observations, the gamma-ray energy distributions from these ultra-dense objects will tell us about the geometry of the magnetic fields present and about the location of the acceleration sites. Since the large magnetic field of a pulsar can cause gamma-ray photons to convert into e^+-e^- pairs, *Fermi*-LAT may allow us to study a process in quantum electrodynamics that is not observable anywhere else. Gamma-rays may also tell us about far high-energy particle-acceleration mechanisms more powerful than anything seen on Earth. Observations of supernova remnants suggest that particles can be accelerated to enormous energies by shocks produced as the blast from an exploding star ploughs into the interstellar medium. While the existence of such shocks is well established, the way in which particles are accelerated to extreme relativistic energies is not fully understood. Most of the Galactic point sources identified by EGRET were pulsars. There were five young radio pulsars detected with high significance, along with the radio-quiet pulsar Geminga and one likely millisecond pulsar [8]. A number of other pulsars had lower significance pulse detections and many of the bright, unidentified γ-ray sources are coincident with known radio pulsars. Surrounding young pulsars are bright non-thermal pulsar wind nebulae (PWNe). Rotation-induced electric fields in charge-depleted regions of pulsar magnetospheres ("gaps") accelerate charges to ten's of TeV and produce non-thermal emission across the electromagnetic spectrum. The coherent radio emission, through which most pulsars are discovered, is however a side-show, representing a tiny fraction

of the spin-down power. In contrast the $\sim$ GeV peak in the pulsed power can represent as much as 20–30% of the total spin-down. Many central questions remain unanswered about the pulsar emission. A basic issue is whether the high-energy emission arises near the surface, close to the classical radio emission ("polar cap" model [9]) or at a significant fraction of the light cylinder distance ("outer gap" models [10, 11]). In addition to geometrical (beam-shape) differences, the two scenarios predict that different physics dominates the pair production. Near the surface $\gamma + B \rightarrow e^+ + e^-$ is important, while in the outer magnetosphere $\gamma + \gamma \rightarrow e^+ + e^-$ dominates; these result in substantially different predictions for the high-energy pulsar spectrum. *Fermi* observations on the most intense pulsar, *i.e.* Vela, let us to conclude [4] that at least for this object, the emission seen is more compatible with outer gap [10, 11] rather than polar cap emission [9]. Moreover *Fermi* discovered several radio-quiet gamma-ray only pulsars. The first one discovered was CTA1 [12] but during these first months, the total sample includes a dozen of objects in this category. Moreover we identify several candidates as millisecond pulsars [13-15].

7. – Active Galactic Nuclei

One of the major scientific goals of the *Fermi* is to provide new data about γ-ray activity of AGNs. Rapidly varying fluxes and large luminosities of extragalactic γ-ray sources are best explained if the γ-rays are emitted from collimated jets of charged particles moving at relativistic speeds [16, 17]. *Fermi*-LAT observations [18] will help determine how these particles are accelerated, where the gamma-rays are emitted, what the energy and power budgets of the supermassive black-hole engines are, what this says for the fueling and growth of black holes, and the reasons for the differences between radio-loud and radio-quiet AGNs, and FSRQs and BL Lac objects. These are just a few of the questions that γ-ray AGN studies with the *Fermi*-LAT are helping to answer [19, 20]. Source variability is one of the most impressive features that *Fermi* has observed in the first months of observations. Most of the variable sources are AGNs. Some of these were particularly intense, in particular on 4 September 2008, a strong gamma-ray emission was detected from PKS 1454–354 with flux peaking on the time scale of a few hours then decaying on the time scale of days [21].

8. – Diffuse emission

The diffuse emission of the Milky Way is an intense celestial signal that dominates the γ-ray sky. The diffuse emission traces energetic particle interactions in the ISM, primarily protons and electrons, thus providing information about cosmic-ray spectra and intensities in distant locations [22]. This information is important for studies of cosmic-ray acceleration and propagation in the Galaxy [23]. Gamma-rays can be used to trace the interstellar gas independently of other astronomical methods, *e.g.*, the relation of molecular H_2 gas to the CO molecule [24] and hydrogen overlooked by other methods [25]. The diffuse emission may also contain signatures of new physics, such as dark matter, or may be used to put restrictions on the parameter space of supersymmetrical particle models and on cosmological models. The Galactic diffuse emission also must be modeled in detail in order to determine the Galactic and extragalactic γ-ray backgrounds and hence to build a reliable source catalog. Accounting for the diffuse emission requires first a calculation of the cosmic-ray (CR) spectra throughout the Galaxy [26, 27]. A realistic calculation that solves the transport equations for CR species must include gas

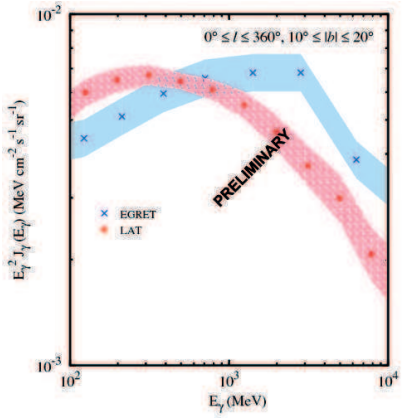

Fig. 1. – (Colour on-line) LAT spectrum averaged over all Galactic longitudes and latitude range $10^\circ \leq |b| \leq 20^\circ$. Also shown are the EGRET data for the same region of the sky. Data points: LAT, red dots; EGRET blue crosses. Systematic uncertainties: LAT red hatched regions, EGRET blue regions.

and source distributions, interstellar radiation field (ISRF), nuclear and particle cross-sections and nuclear reaction network, γ-ray production processes, and energy losses. Finally, the spectrum and spatial distribution of the diffuse γ-rays are the products of CR particle interactions with matter and the ISRF. One of the critical issues for diffuse emission remaining from the EGRET era is the so-called "GeV excess". This puzzling excess emission above 1 GeV relative to that expected [22, 26] has shown up in all models that are tuned to be consistent with directly measured cosmic-ray nucleon and electron spectra [28]. The excess has shown up in all directions, not only in the Galactic plane. The origin of the excess is intensively debated in the literature since its discovery by [22]. The excess can be the result of an error in the determination of the EGRET effective area or energy response or could be the result of yet unknown physics (see [23]). Recent studies of the EGRET data have concluded that the EGRET sensitivity above 1 GeV has been overestimated [29] or underestimated [30] or imply different cosmic-ray energy spectra in other parts of the Galaxy compared to the local values [28, 31]. If these possibilities are eliminated with high confidence, then it may be possible to attribute the excess to exotic processes, *e.g.*, dark matter annihilation products [32].

We have started a preliminary analysis of the diffuse emission using middle-latitude regions respect to the Galactic plane [33]. These regions contain a significant Galactic diffuse emission, but at the same time fewer point-like sources, respect to direct usage of central Galactic plane regions. To select events from this region a $10^\circ \leq |b| \leq 20^\circ$ selection has been applied on data. Figure 1 shows the spectrum of diffuse emission seen by *Fermi* and a comparison with EGRET data [34] and a model of the diffuse component (see [33] for more details). The EGRET data, available from the CGRO science support centre, were processed following the procedure in [28]. The LAT systematic error is $10\% \leq 100$ MeV, 5% at $10^{2.75}$ MeV, 20% for $E \geq 10$ GeV (and linearly interpolated in $\log E$ between those points). Therefore the first months of LAT science data shown in fig. 1 do not confirm the GeV excess seen by EGRET in the latitude range $10^\circ \leq |b| \leq 20^\circ$. The spectral shape is reasonably explained with a cosmic-ray propagation model.

9. – High-energy electron observations

The on-board filter [2] is configured to accept all events that deposit at least 20 GeV in the calorimeter(CAL); thus we ensure that the rare high-energy events, including electrons, are available for thorough analysis on the ground. We developed [35] a dedicated event selection for high-energy electrons that provides a large geometry factor with a residual hadron contamination less than 20% at the highest energy. As for the analysis developed for extracting LAT photon data [2], the electron selection essentially relies on the LAT capability to discriminate EM and hadronic showers based on their longitudinal and lateral development, as measured by both the TKR and CAL detectors. The background rejection power for photon science is optimized up to 300 GeV. The electron selection criteria are instead tuned in the multi-100 GeV range, where the much steeper electron spectrum requires an overall hadron rejection power of $1 : 10^4$. Events considered for the electron analysis are required to fail the ACD vetoes developed to select photon events [2]. This removes the vast majority of the potential gamma-ray contamination. The overall gamma contamination in the final electron sample is estimated as always less than 2%. *Fermi* measurements of the electron spectrum [35] do not confirm balloon observations [36] of electron excessess on the expected spectrum due to cosmic-ray propagation in our Galaxy. These new observations together with the recent observation of positron excess [37] make the complex problem of electron and positron production puzzling and these observations may put some constraints about possible dark matter signals in these channels or suggest nearby astrophysical sources as the most reasonable candidates for their production.

10. – Conclusions

The first *Fermi*-LAT results confirm the excellent quality of the instrument and confirm the capability of the observatory to start a new gamma-ray era. Among the first observations Fermi has observed several GRB, detected new pulsars, in particular several radio-quiet gamma-ray only pulsars and a new class of milli-seconds pulsars, several AGNs are monitored, the Moon and Sun emissions were detected [38,39]. Moreover, first observations of the diffuse Galactic emission from intermediate latitude regions do not confirm the previously observed by EGRET "GeV excess" and some more recent observations on the electron spectrum observed by *Fermi* [35] may complete the picture of the cosmic-ray propagation in the galaxy. During the first year of data taking therefore we expect an impressive improvement in the knowledge of all the physics topics previously indicated and a substantial increment of known sources.

* * *

The *Fermi* LAT Collaboration acknowledges the generous support of a number of agencies and institutes that have supported the *Fermi* LAT Collaboration. These include the National Aeronautics and Space Administration and the Department of Energy in the United States, the Commissariat à l'Energie Atomique and the Centre National de la Recherche Scientifique/Institut National de Physique Nucléaire et de Physique des Particules in France, the Agenzia Spaziale Italiana and the Istituto Nazionale di Fisica Nucleare in Italy, the Ministry of Education, Culture, Sports, Science and Technology (MEXT), High Energy Accelerator Research Organization (KEK) and Japan Aerospace Exploration Agency (JAXA) in Japan, and the K. A. Wallenberg Foundation and the Swedish National Space Board in Sweden.

REFERENCES

[1] Abdo A. *et al.*, *Astropart. Phys.*, **32** (2009) 193 arXiv:0904.2226.
[2] Atwood W. B. *et al.*, *Astrophys. J.*, **697** (2009) 1071, arXiv:0902.1089v1.
[3] Atwood W. B. *et al.*, *Astropart. Phys.*, **28** (2007) 422.
[4] Abdo A. A. *et al.*, *Astrophys. J.*, **696** (2009) 1084.
[5] Smith D. A. *et al.*, *Astron. Astrophys.*, **492** (2008) 923.
[6] Zhang B. and Mészáros P., *Int. J. Mod. Phys. A*, **19** (2004) 238.
[7] Abdo A. A. *et al.*, *Science*, **323** (2009) 1688.
[8] Thompson D. J., *Proc. of High-Energy Gamma-ray Astronomy Symposium*, edited by Aharonian F. A. and Völk H. J. (New York, AIP), *AIP Conf. Proc.*, **558** (2001) 103.
[9] Daugherty J. K. and Harding A. K., *Astrophys. J.*, **458** (1996) 278.
[10] Cheng K. S., Ho C. and Ruderman M., *Astrophys. J.*, **300** (1986) 500.
[11] Romani R. W., *Astrophys. J.*, **470** (1996) 469.
[12] Abdo A. A. *et al.*, *Science*, **322** (2008) 1218.
[13] Abdo A. A. *et al.*, *Astrophys. J.*, **699** (2009) 1171 doi:10.1088/004-637X/699/2/1171, arXiv:0904.4377.
[14] Abdo A. A., *Science*, **325** (2009) 840 doi:10.1126/science.1175558.
[15] Abdo A. A. *et al.*, *Science*, **325** (2009) 848 doi:10.1126/science.1176113.
[16] Blandford R. D. and Rees M. J., in *BL Lac Objects*, edited by Wolfe A. M., pp. 328–341 (1978).
[17] Maraschi L., Ghisellini G. and Celotti A., *Astrophys. J. Lett.*, **397** (1992) L5.
[18] Tosti G. *et al.*, *Atel* 1628 (2008); Foschini L. *et al.*, *Atel* 1784 (2008).
[19] Abdo A. A., *Astrophys. J.*, **700** (2009) 597 doi:1088/004-637X/700/1/597.
[20] Thompson D. J. *et al.*, *J. Geophys. Res.*, **102** (1997) 14735.
[21] Abdo A. A. *et al.*, *Astrophys. J.*, **697** (2009) 934, arXiv:0903.1713v1.
[22] Hunter S. D. *et al.*, *Astrophys. J.*, **481** (1997) 205.
[23] Moskalenko I. V. and Strong A. W., in *Proc. Int. Conf. on Astrophysical Sources of High Energy Particles and Radiation (2005)*, edited by Bulik T. *et al.* (AIP, NY), *AIP Conf. Proc.*, **801** (2005) 57.
[24] Strong A. W., Moskalenko I. V., Reimer O., Digel S. and Diehl R., *Astron. Astrophys.*, **422** (2004) L47.
[25] Grenier I. A., Casandjian J.-M. and Terrier R., *Science*, **307** (2005) 1292.
[26] Strong A. W., Moskalenko I. V. and Reimer O., *Astrophys. J.*, **537** (2000) 763.
[27] Moskalenko I. V. and Strong A., *Adv. Space Res.*, **27** (2001) 717; see `http://galprop.stanford.edu`.
[28] Strong A. W., Moskalenko I. V. and Reimer O., *Astrophys. J.*, **613** (2004) 962.
[29] Stecker F., Hunter S. D. and Kniffen D. A., *Astropart. Phys.*, **29** (2008) 25.
[30] Baughman B. M., Atwood W. B., Johnson R. P., Porter T. A. and Ziegler M., in *Proc. 30th Int. Cosmic Ray Conf. (2007)*, edited by Caballero R. *et al.*, Vol. **2** (OG part 1) (Universidad Nacional Autonoma de Mexico, Mexico City, Mexico) 2008, pp. 525-528.
[31] Porter T. A., Moskalenko I. V., Strong A. W., Orlando E. and Bouchet L., *Astrophys. J.*, **682** (2008) 400.
[32] de Boer W. *et al.*, *Phys. Rev. Lett.*, **95** (2005) 209001.
[33] Abdo A. A. *et al.*, to be published in *Phys. Rev. Lett.*, arXiv 0912.0973; see also Johannesson G., *Proceedings 44th Rencontres de Moriond* (2009).
[34] Esposito J. A. *et al.*, *Astrophys. J. Suppl.*, **123** (1999) 203.
[35] Abdo A. A., *Phys. Rev. Lett.*, **102** (2009) 181101.
[36] See Isbert Joachim, *Rencontres de Moriond EW 2009 Proceedings* and Chang J. *et al.*, *Nature*, **456** (2008) 362.
[37] Mocchiuti E. *et al.*, these proceedings; Adriani O. *et al.*, *Nature*, **458** (2009) 607, arXiv:0810.4995.
[38] Giglietto N., *AIP Conf. Proc.*, **1112** (2009) 238.
[39] Brigida M., *44th Rencontres de Moriond Proceedings (2009).*

IL NUOVO CIMENTO Vol. 32 C, N. 5-6 Settembre-Dicembre 2009
DOI 10.1393/ncc/i2009-10510-9

Colloquia: LaThuile09

Very-high-energy gamma astrophysics

A. De Angelis

Dipartimento di Fisica, Università di Udine - via delle Scienze 208, I-33100 Udine, Italy
INFN and INAF, Sezione di Trieste - Trieste, Italy
LIP/IST - Lisboa, Portugal

(ricevuto il 10 Novembre 2009; pubblicato online il 21 Dicembre 2009)

Summary. — High-energy photons are a powerful probe for astrophysics and for fundamental physics under extreme conditions. During the recent years, our knowledge of the most violent phenomena in the Universe has impressively progressed thanks to the advent of new detectors for very-high-energy γ-rays. Ground-based detectors like the Cherenkov telescopes (H.E.S.S. and MAGIC in particular) recently discovered more than 70 new very-high-energy sources. This article reviews the present status of very-high-energy gamma astrophysics, with emphasis on the results related to fundamental physics and on the experimental developments.

PACS 95.55.Vj – Neutrino, muon, pion, and other elementary particle detectors; cosmic ray detectors.
PACS 95.85.Pw – Gamma-ray.
PACS 96.50.S- – Cosmic rays.

1. – Introduction

The definition of very-high energy (VHE) photons is somehow arbitrary; conventionally we start the VHE region from an energy of 30 GeV (see [1], also for a more comprehensive review on the subject).

The source of high-energy photons from astrophysical objects is mainly gravitational energy released by collapses towards a central massive object. Typically 0.1% to 1% of the energy is emitted in the form of γ-rays. The typical energy (E) spectrum is a power-law $E^{-\Gamma}$; the *spectral index* Γ at the emitter is, according to current models, between 1.5 and 3. The accreting object can be for example a supermassive black hole in the inner part of a galaxy (Active Galactic Nucleus, or AGN), possibly a hypernova in early stage (Gamma-Ray Burst, GRB), a supernova, a binary system.

In addition, one could have characteristic photon signals also from annihilation/decay of heavy particles. In particular, the self-annihilation of a heavy WIMP χ (a candidate dark matter particle) can generate photons. The γ-ray flux from the annihilation of dark

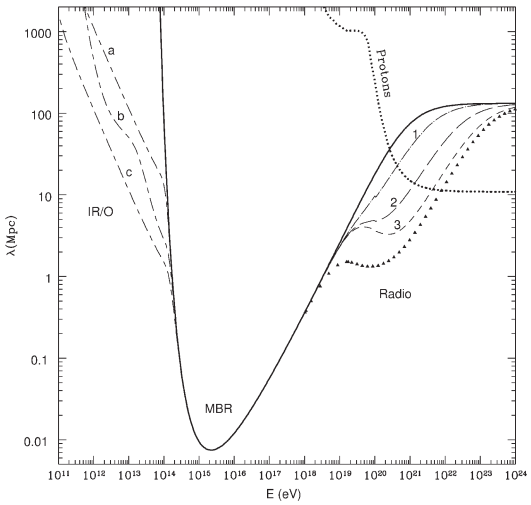

Fig. 1. – Mean free path as a function of the photon energy [2].

matter particles of mass $m_{\rm DM}$ can be expressed as the product of a factor related to the annihilation cross-section times a factor related to density:

$$\frac{\mathrm{d}N}{\mathrm{d}E} = \frac{1}{4\pi} \underbrace{\frac{\langle\sigma v\rangle}{m_{\rm DM}^2}\frac{\mathrm{d}N_\gamma}{\mathrm{d}E}}_{\text{particle physics}} \times \underbrace{\int_{\Delta\Omega\text{-l.o.s.}} \mathrm{d}l(\Omega)\rho_{\rm DM}^2}_{\text{astrophysics}}. \tag{1}$$

The particle physics factor contains $\langle\sigma v\rangle$, the velocity-weighted annihilation cross-section (there is indeed a possible component from cosmology in v), and $\mathrm{d}N_\gamma/\mathrm{d}E$, the differential γ-ray spectrum summed over the final states with their corresponding branching ratios. The astrophysical part corresponds to the squared density of the dark matter distribution integrated over the line of sight (l.o.s.) in the observed solid angle.

Finally, some gamma-ray emission could originate in decays of exotic particles of very large mass possibly produced in the early Universe. Such long-lived heavy particles are predicted in many models (*e.g.*, technicolor models or the R-parity–violating SUSY model), and the energy distribution of particles coming from their decay should be radically different from what predicted by the standard emission models from astrophysical sources [3].

2. – Propagation of γ-rays

Electron-positron (e^-e^+) pair production in the interaction of beam photons off extragalactic background photons is a source of opacity of the Universe to γ-rays (fig. 1).

The dominant process for the absorption is the pair-creation process $\gamma+\gamma_{\rm background} \to e^+ + e^-$, for which the cross-section is described by the Bethe-Heitler formula [4]:

$$\sigma(E,\epsilon) \simeq 1.25\cdot 10^{-25}(1-\beta^2)\cdot\left[2\beta(\beta^2-2)+(3-\beta^4)\ln\left(\frac{1+\beta}{1-\beta}\right)\right]\mathrm{cm}^2, \tag{2}$$

where $\beta = \sqrt{1 - \frac{(m_e c^2)^2}{E\,\epsilon}}$, m_e being the value of the electron mass, E is the energy of the (hard) incident photon and ϵ is the energy of the (soft) background photon. Notice that only QED, relativity and cosmology arguments are involved in the previous formula.

The cross-section in eq. (2) is maximized when $\epsilon \simeq \frac{500\,\mathrm{GeV}}{E}$ eV. Hence if $E = 1\,\mathrm{TeV}$ the interaction cross-section is maximal when $\epsilon \simeq 0.5\,\mathrm{eV}$ (corresponding to a near-infrared soft photon). In general, for very-high-energy photons the $\gamma\gamma \to e^+ + e^-$ interaction becomes important with optical/infrared photons, whereas the interaction with the cosmic microwave background becomes dominant at $E \sim 1\,\mathrm{PeV}$. Therefore, the background component relevant for interaction with VHE photons is the optical/infrared background radiation. This is called the extragalactic background light (EBL) [5].

The EBL consists of the sum of starlights emitted by galaxies throughout their whole cosmic history, plus possible additional contributions, like, *e.g.*, light from hypothetical first stars that formed before galaxies were assembled. Therefore, in principle the EBL contains important information both the evolution of baryonic components of galaxies and the structure of the Universe in the pre-galactic era.

The attenuation suffered by observed VHE spectra can thus be used to derive constraints on the EBL density [6].

3. – Detection techniques

The detection of high-energy photons is complicated by the absorption by the atmosphere, and by the faintness of the signal, in particular when compared to the corresponding charged particles of similar energy.

3˙1. *Atmospheric transparency and processes of interaction.* – Photons above the ultraviolet (UV) region are shielded by the Earth's atmosphere.

Photons interact with matter mostly due to the Compton mechanism and to the photoelectric effect at energies up to about 20 MeV, while e^+e^- pair production dominates above about 20 MeV. Above about 50 GeV the production of atmospheric showers bevomes sizeable, dominated by the pair production and the bremsstrahlung mechanisms: an energetic photon scatters on an atmospheric nucleus and produces a pair, which emits secondary photons via bremsstrahlung; such photons produce in turn an e^+e^- pair, and so on, giving rise to a shower of charged particles and photons. The process is described, *e.g.*, in [7, 8].

At sea level the thickness of the atmosphere corresponds to about 28 radiation lengths. This means that only satellite-based detectors can detect primary X/γ-rays. Since the fluxes of high-energy photons are low and decrease rapidly with increasing energy, VHE and UHE gammas can be detected only from the atmospheric showers they produce, *i.e.* by means of ground-based detectors; such detectors should be placed at high altitudes, where atmospheric dimming is lower.

Ground-based VHE telescopes such as MILAGRO, ARGO, CANGAROO, H.E.S.S., MAGIC and VERITAS detect the secondary particles of the atmospheric showers produced by primary photons and cosmic rays of energy higher than the primaries observed by satellites.

There are two main classes of ground-based HE gamma detectors: the Extensive Air Shower arrays (EAS) and the Cherenkov telescopes.

The EAS detectors, such as MILAGRO and ARGO, are made by a large array of detectors sensitive to charged secondary particles generated by the atmospheric showers. They have high duty cycle and a large Field of View (FoV), but a low sensitivity. Since

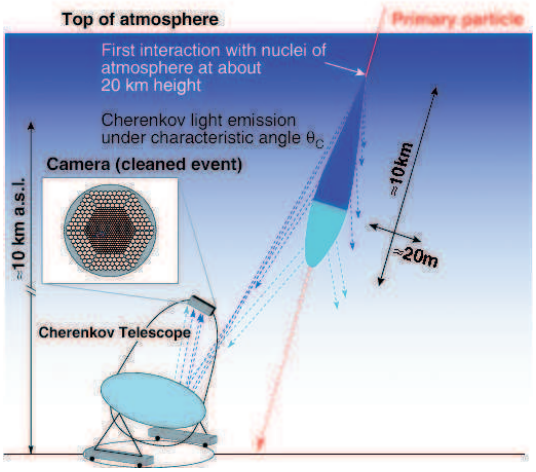

Fig. 2. – The observational technique adopted by the Imaging Atmospheric Cherenkov Telescopes (IACTs) [9].

the maximum of a photon-initiated shower at 1 TeV typically occurs at 8 km a.s.l., the energy threshold of such detectors is rather large.

Imaging Atmospheric Cherenkov Telescopes (IACTs), such as CANGAROO, H.E.S.S., MAGIC and VERITAS, detect the Cherenkov photons produced in air by charged, locally superluminal particles in atmospheric showers. They have a low duty cycle and a small FoV, but they have a high sensitivity and a low energy threshold.

The observational technique used by IACTs is to project the Cherenkov light collected by a large optical reflecting surface onto a camera made by an array of photomultiplies in the focal plane of the reflector (see fig. 2). The camera has a typical diameter of about 1 m, which corresponds to a FoV of $5^o \times 5^o$.

In the GeV-TeV region the background from charged particles is three orders of magnitude larger than the signal. Hadronic showers, however, have a different topology with respect to electromagnetic showers, being larger and more subject to fluctuations. One can thus select showers induced by gamma-rays.

Systems of more than one Cherenkov telescope provide a better background rejection, and a better angular and energy resolution than a single telescope.

The main characteristics of the main IACTs are summarized in table I.

4. – The emerging VHE gamma-ray sky

Thanks mostly to Cherenkov telescopes, a large amount of VHE sources has been detected and identified (see fig. 3). When this review has been written (April 2009), more than 80 VHE sources had been detected (only 4 were known in 2004), acting as cosmic particle accelerators. About two thirds are galactic, and one third is extragalactic.

Large part of the currently known galactic TeV sources remain unidentified. This is in part due to the difficulty of identifying extended sources with no clear sub-structure. Nonetheless, several methods of identification have been successfully applied and the situation is much more favourable than that in the GeV band where only one galactic

TABLE I. – *Main characteristics of currently operating IACTs. The energy threshold given is the approximate trigger-level threshold for observations close to zenith. The approximate sensitivity is expressed as the minimum flux (as a percentage of that of the Crab Nebula:* $\approx 2 \times 10^{-11}$ *photons* $\mathrm{cm}^{-2}\ \mathrm{s}^{-1}$ *above* 1 TeV*) of a point-like source detectable at the* 5σ *significance level in a* 50 *hour observation.*

Instrument	Lat. (°)	Long. (°)	Alt. (m)	Tels.	Tel. Area (m^2)	Total A. (m^2)	FoV (°)	Thresh. (TeV)	Sensitivity (% Crab)	Sp. res. (°)
H.E.S.S.	-23	16	1800	4	107	428	5	0.1	0.7	0.05
VERITAS	32	-111	1275	4	106	424	3.5	0.1	0.7	0.06
MAGIC	29	18	2225	2	236	472	3.5	0.05	0.8	0.07
CANGAROO-III	-31	137	160	3	57.3	172	4	0.4	15	0.1

source class (pulsars) has been unambiguously identified. The new results by the Fermi telescope will tell.

Whatever the details, the detection of photons with $E \gtrsim 100\,\mathrm{TeV}$ from supernova remnants is a proof of the acceleration of primary particles in supernova shocks to energies well above 10^{14} eV. This is getting close to the knee of the cosmic-ray spectrum; this fact might signal the high-energy end of the galactic cosmic-ray distribution. Circumstantial evidence supports a hadronic origin for at least part of the VHE emission.

Very recently, the MAGIC Collaboration has reported on the detection of the Crab pulsar at VHE [11].

Some of the observations are particularly relevant for fundamental physics.

4˙1. *The search for products of DM annihilations.* – An observation of the Galactic Centre and of several satellites of the Milky Way gave at present no result.

4˙2. *Study of the propagation from large distances.* – About 30 AGN have been detected as VHE sources by the time this review is written (April 2009). The AGN observed at VHE are uniformly distributed in the high galactic latitude sky. Measured spectral indices are plotted *versus* redshift in fig. 4.

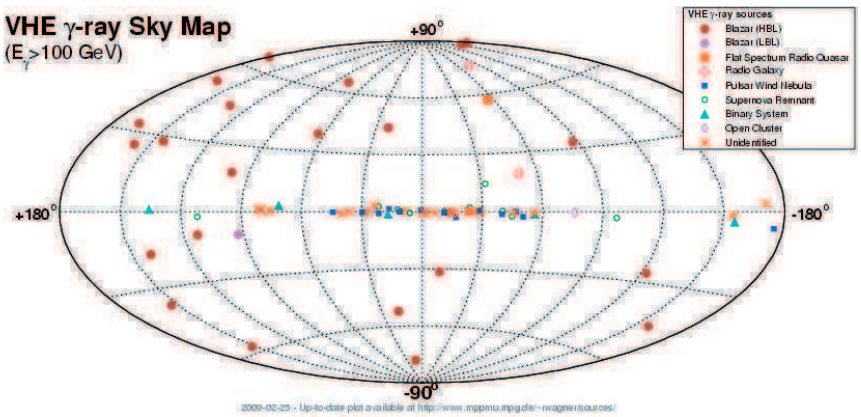

Fig. 3. – Known sources in the VHE sky in April 2009 [10].

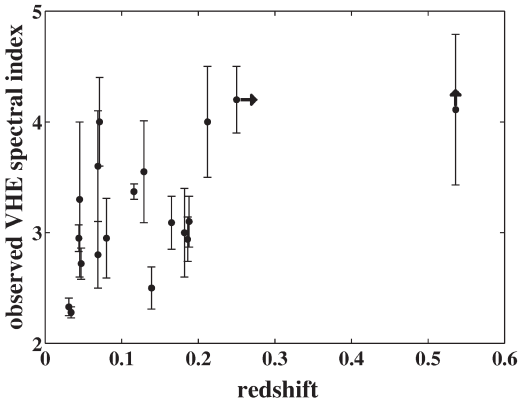

Fig. 4. – Observed spectral indexes for AGN in the VHE region.

Currently, the most distant established VHE source is 3C 279 [12], with $z = 0.536$.

The TeV spectra of blazars can be used as probes of the EBL. The TeV photons emitted by a blazar interact with the EBL photons and are likely absorbed via pair production. Whatever its intrinsic shape at emission, after traveling through the EBL-filled space, a blazar spectrum will reach the observer distorted by absorption. The strength of the absorption is measured by the optical depth $\tau(E, z)$ for the attenuation between the blazar, located at a distance redshift z, and the Earth [13]. Based on the inferred attenuation of blazar VHE emission by the EBL, and in particular on the detection of the distant ($z = 0.536$) quasar 3C 279, the transparency of the Universe at VHE γ-rays is deduced to be maximal, at the level implied by the known cosmic evolution of the stellar populations of galaxies.

Other interactions than the one just described might change our picture of the attenuation of γ-rays, and they are presently subject of thorough studies, since the present data on the absorption of photons are hardly compatible with the pure QED picture. For example, γ-rays might interact with (possibly quintessential) very light axion-like particles, which might change the absorption length [14, 15]. In particular, in the DARMA model [15], such contribution might enhance the photon flux via a regeneration mechanism. Such an interaction would be mediated by the (intergalactic) magnetic fields. A similar mechanism invokes the conversion of photons into axion-like particles at the emission source [16].

Finally, mechanisms in which the absorption is changed through violation of the Lorentz invariance as in ref. [17] are also under test; such models are particularly appealing within scenarios inspired to quantum gravity [18].

4˙3. *Studies related to flares.* – The known TeV blazars are variable in flux in all wavebands. Blazar variability, both in flux and spectrum, has been observed at VHE frequencies down to minute timescales. For Mkn 501, a rapid flare occurred on the night of July 10th, 2005, showing a doubling time as short as about 2 minutes and a delay of about 3 minutes as a function of energy of the emitted photons.

The H.E.S.S. observations of PKS 2155-304 (located at $z = 0.116$), showed a very fast flux variability: on the night of July 28th, 2006 it had a peak flux about 50 times its average flux (and about 15 times the Crab flux), and rapidly doubled it in four successive

episodes (in 67 ± 50 s, 116 ± 50 s, 173 ± 50 s, and 178 ± 50 s, respectively). It is amazing the fact that the Schwarzschild radii of the black holes powering such AGNs are two orders of magnitude larger.

The variability of the AGN in the VHE region provides information about possible violations of the Lorentz invariance (LIV). The velocity of light can be parametrized as [18]

$$V = c\left[1 + \xi\left(\frac{E}{E_{s1}}\right) + \ldots\right], \tag{3}$$

where the ξ's are parameters of order unity which can be positive or negative. At first order photons of different energies emitted at the same time are detected with a time delay $\Delta t \simeq \xi \frac{E}{E_{s1}} \frac{z}{H_0} = \xi \frac{E}{E_{QG}} \frac{L}{c}$. The MAGIC data about Mkn 501 [19] showed at 2σ a correlation between the arrival time of photons and their energy. Higher energy photons arrive later, at a rate of (0.030 ± 0.012) s/GeV. If interpreted as LIV at linear order, this yields, according to eq. (3), to $(s1/\xi) \sim M_P/30$, where $M_P \simeq 1.2 \times 10^{19}$ GeV is the Planck mass.

H.E.S.S. observations of PKS 2155 [20] evidenced no effect, allowing to set a lower limit $(s1/\xi) > 0.04\ M_P$.

In the observation of the GRB080916C [21] at a photometric redshift of 4.35 ± 0.15 the Fermi experiment has observed a correlation between the energy and the time of arrival of photons; in particular the most energetic photon, at $E = 13.2^{+0.70}_{-1.52}$ GeV, has arrived at 16.54 seconds after the primary burst. If we consider the time delay of (0.030 ± 0.012) s/GeV at $z = 0.034$ and we extrapolate it through

$$\Delta t = \frac{1}{H_0} \frac{E}{E_{s1}} \int_0^z \mathrm{d}\zeta \frac{(1+\zeta)}{\sqrt{\Omega_m (1+\zeta)^3 + \Omega_\Lambda}}, \tag{4}$$

we obtain, using a standard $\Omega_m = 0.27$, $\Omega_\Lambda = 0.73$, $h = 0.71$ cosmology, $\Delta t = (50 \pm 20)$ s.

5. – The future

A second MAGIC telescope, at a distance of 85 m from the first one, started operating in April 2009. With this new telescope, MAGIC enters in phase 2 (MAGIC 2). The H.E.S.S. Collaboration has started the construction of a large telescope, which will be inaugurated in 2010. This will lead the instrument into its phase 2 (H.E.S.S. 2). With its diameter of 28 m, the new telescope, located in the middle of the four existing telescopes, and it should decrease the trigger threshold to some 20 GeV.

Longer-term projects for ground telescopes are under discussion; one in particular, the Cherenkov Telescope Array (CTA), has a huge European involvement. The CTA facility is meant to explore the sky in the energy range from 10 GeV to 100 TeV and it is designed to combine guaranteed science with significant discovery potential.

The CTA is a cornerstone towards a multi-messenger exploration of the Universe. In the most ambitious and expensive scheme, for which the cost foreseen is of the order of 100–150 million euros, it should allow mapping the Universe in that energy range with a sensitivity of 0.001 Crab.

6. – Conclusions

High-energy photons are a powerful probe of fundamental physics under extreme conditions, since they are produced in the highest energy phenomena, they often travel through large distances, and their interactions display large boosts towards the center of mass.

Observation of X- and γ-rays gives an exciting view of the HE universe thanks to satellite-based telescopes (AGILE, GLAST) and to ground-based detectors like the Cherenkov telescopes, which discovered more than 70 new VHE sources in the last five years and are going on this way. This large population of VHE-γ-ray sources, which are often unknown sources, poses questions on the transparency of the Universe at these energy ranges; this might indicate the existence of new physics.

The progress achieved with the latest generation of Cherenkov telescopes is comparable with the one drawn by EGRET with respect to the previous γ-ray satellite detectors.

This exciting scenario gives handles for the study of new mechanisms about the VHE-γ-ray origin and propagation, and many astrophysical constraints are feeding the theories.

The exploration of the VHE sources has just started and in the next three years (2010/2012) a factor of 2 improvement in the TeV range will be can be expected by MAGIC 2, H.E.S.S. 2, and VERITAS.

REFERENCES

[1] De Angelis A., Mansutti O. and Persic M., *Riv. Nuovo Cimento*, **31**, no. 4 (2008) 187.
[2] Coppi P. and Aharonian F. A., *Astrophys. J.*, **487** (1997) L9.
[3] *GLAST Science Brochure (March 2001)*, `http://glast.gsfc.nasa.gov/science`.
[4] Heitler W., *The Quantum Theory of Radiation* (Oxford University Press, Oxford) 1960.
[5] Gould R. J. and Schréder G. P., *Phys. Rev.*, **155** (1967) 1408.
[6] Stecker F. W., *Int. Astron. Union Symp.*, **204** (2001) 135.
[7] Rossi B. and Greisen K., *Rev. Mod. Phys.*, **13** (1941) 240.
[8] Nishimura J. and Kamata K., *Prog. Theor. Phys.*, **7** (1952) 185; Greisen K., *Rev. Mod. Phys.*, **13** (1960) 240.
[9] Wagner R. M., Ph.D. thesis, Technische Universität München, MPP-2006-245 (2006).
[10] `http://www.mppmu.mpg.de/~rwagner/sources/`.
[11] Albert J. *et al.* (MAGIC), *Science*, **322** (2008) 1221.
[12] Albert J. *et al.* (MAGIC), *Science*, **320** (2008) 1752.
[13] Fazio G. G. and Stecker F. W., *Nature*, **226** (1970) 135.
[14] De Angelis A., Mansutti O. and Roncadelli M., *Phys. Lett. B*, **659** (2008) 847.
[15] De Angelis A., Roncadelli M. and Mansutti O., *Phys. Rev. D*, **76** (2007) 121301.
[16] Simet M., Hooper D. and Serpico P., *Phys. Rev. D*, **77** (2008) 063001.
[17] Kifune T., *Astrophys. J.*, **518** (1999) L21.
[18] Amelino-Camelia G. *et al.*, *Nature*, **393** (1998) 763.
[19] Albert J. *et al.* (MAGIC), *Phys. Lett. B*, **668** (2008) 253.
[20] Aharonian F. A. *et al.* (HESS), *Astron. Astrophys.*, **442** (2005) 895.
[21] Abdo A. *et al.* (Fermi), *Science*, **323** (2009) 36.

SESSION II - ASTROPARTICLE AND NEUTRINO PHYSICS

IL NUOVO CIMENTO Vol. 32 C, N. 5-6 Settembre-Dicembre 2009
DOI 10.1393/ncc/i2010-10522-4

Colloquia: LaThuile09

Study of the High Energy Cosmic Rays with the Pierre Auger Observatory

I. Lhenry-Yvon for Pierre Auger Collaboration
Institut de Physique Nucléaire d'Orsay, Université Paris 11, CNRS-IN2P3 - Orsay, France

(ricevuto il 10 Novembre 2009; pubblicato online il 15 Gennaio 2010)

Summary. — The Pierre Auger Southern Observatory, a hybrid detector for the study of ultrahigh energy cosmic rays (UHECRs), has now been operating for more than five years and has reached completion. This contribution describes the present status and performance of the Observatory, showing the advantages provided by the combined use of two different detection techniques. Selected results are presented with the emphasis given to the measurement of energy spectrum, arrival directions at the highest energies and search for photons as primary particles.

PACS 96.50.sb – Composition, energy spectra and interactions.
PACS 98.70.Sa – Cosmic rays (including sources, origin, acceleration, and interactions).
PACS 95.85.Ry – Neutrino, muon, pion, and other elementary particles; cosmic rays.

1. – Introduction

The origin of cosmic rays, and in particular at energies near 10^{20} eV, is a puzzling mystery. Cosmic rays with energies exceeding 10^{20} eV have been observed for more than 40 years (see, *e.g.* [1]) but due to their low flux only some ten events of such high energies could be detected up to recently. There are no generally accepted source candidates known to be able to produce particles of such extreme energies. Moreover, there should be a steeping in the energy spectrum near 10^{20} eV due to the interaction of cosmic rays with the microwave background radiation (CMB), due to the so-called GZK effect [2]. The non-observation of this effect in the data of the AGASA experiment [3] has motivated an enormous number of theoretical and phenomenological models trying to explain the absence of the GZK-effect and has stimulated the field as a whole.

Until very recently the experimental situation was very unclear, mainly because of a lack of statistics. At these extreme energies the flux of cosmic rays is very low, less than 1 particle per km^2 per century for cosmic rays above 10^{20} eV. Due to this, UHECRs can only be observed indirectly through the extensive air showers (EAS) they induce when colliding with a nucleus in the atmosphere, with the difficulty that the interpretation

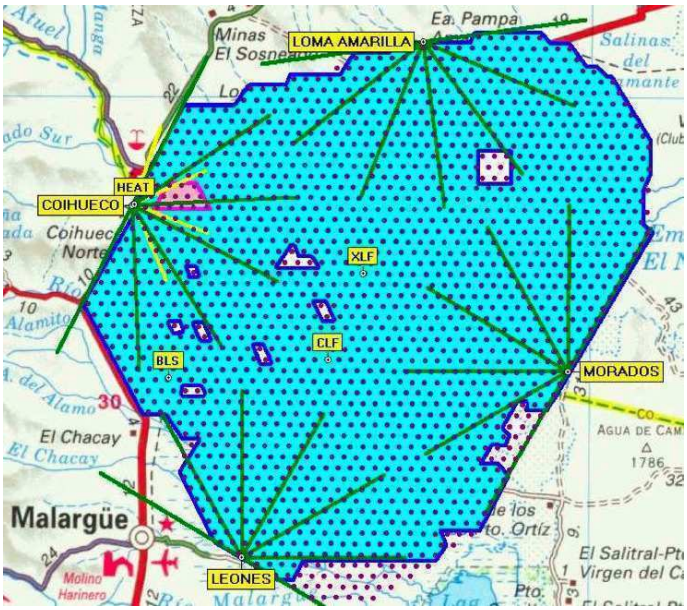

Fig. 1. – Actual deployment status of the array. Tanks within the shaded area are in operation.

of the observed EAS relies on models of hadronic interaction at energies that have not been still reached in man-made experiments. Some of the difficulties encountered in the interpretation of EAS are also believed to stem from the two different techniques with which cosmic rays were observed in past experiments, namely arrays of particle detectors spread over a large area in the case of (for instance) the AGASA experiment [3], and telescopes that collect the light produced by the fluorescence of the nitrogen molecules in the atmosphere excited by the passage of the charged particles in the shower in the case of the HiRes experiment [4].

The Pierre Auger observatory is dedicated to the high-statistics study of the high energy cosmic rays above $3 \cdot 10^{18}$ eV. It uses a hybrid design, coupling a surface array to fluorescence telescopes, the two techniques used by the two controversial experiments quoted above, which gathered most of the high energy events. It thus provides a powerful tool to probe the shape of the cosmic rays spectrum, to analyse directions and to try to measure composition. The southern site, near the town of Malargue in the Argentinian pampa, has already reached completion, and has been continuously taking data since 2004. After a description of the detector and a summary of its performance, a selection of the most recent results will be presented.

2. – Design and performance of the Pierre Auger Observatory

The Surface Detector (SD) of the Pierre Auger Observatory is composed of more than 1600 Water Cherenkov Detectors (WCD) extending over an area of 3000 km^2 with 1500 m spacing between detectors [5]. The construction was completed in June 2008. Figure 1 shows the current status of the array.

A water Cherenkov station consists of a cylindrical tank of 1.2 m average height and 10 m^2 area, containing 12 tons of purified water. Each station is an independent unit

with low-power electronics, and a GPS and radio communication systems, all powered by a solar panel and two batteries. The Cherenkov light emitted by the particles entering a tank is reflected and diffused in its inner walls and collected by three 9-inches hemispherical photomultipliers. The corresponding signals are digitized by Flash Analog Digital Converters (FADC) in time slots of 25 ns, resulting in a FADC trace. The signal collected in a tank is calculated integrating in time the FADC trace, and is calibrated in units of Vertical Equivalent Muons (VEM) corresponding to the signal produced by vertical muons crossing the tank through its center. SD stations are calibrated on line every few minutes using atmospheric muons.

The SD is overlooked by four FD sites, each holding six fluorescence telescopes. All 24 fluorescence telescopes are in place and taking data. They detect the ultraviolet fluorescence light excited by the extensive air showers. Each telescope uses Schmidt optics to image a portion of the sky of $30 \times 30°$. The UV light is focused by spherical mirrors of $3\,\mathrm{m}^2$ of area on to a camera of 440 hexagonal photomultipliers each with a field of view of 1.5° diameter. They record the longitudinal shower development and thus provide a calorimetric measurement of the primary energy with little dependence on hadronic interaction models.

The Pierre Auger Observatory is the first large aperture instrument to routinely employ the so-called hybrid technique. About 13% of the operating time, the fluorescence light emitted by a shower and the timing and signal information from at least one SD is simultaneously recorded. This unique hybrid combination has enormous advantages which stem from the fact that one can simultaneously measure several shower observables with two different techniques.

3. – The energy spectrum of UHECRs

The hybrid nature of the Pierre Auger Observatory and the huge collecting area of the SD allows the energy spectrum of UHECRs to be measured with unprecedented accuracy and statistics. The hybrid events, which are air showers detected by both instruments, are very precisely measured and provide the energy calibration tool. The surface array, with its near 100% duty cycle, gives the large sample used here. Only "vertical" events, *i.e.* events with zenith angles 60° are used. For more inclined showers, due to different physical characteristics, a different analysis is applied [6].

The comparison of the shower energy, measured using fluorescence, with the SD energy estimator or a subset of high-quality hybrid events is used to calibrate the energy scale for the array. For so-called vertical events, the parameter chosen as SD energy estimator is called $S(1000)$, the signal at a distance of 1000 m from the core. The distribution of particles in the shower at the ground level is sampled at different distances from the core, and a fit to a Lateral Distribution Function (LDF) allows to determine $S(1000)$ [7]. $S(1000)$ has been shown to be rather insensitive to shower-to-shower fluctuations, nor does it require accurate knowledge of the shape of the LDF [8]. For a fixed cosmic ray (CR) energy, $S(1000)$ depends on the zenith angle of the event due to the attenuation of the shower particles in the atmosphere and other geometrical effects. Under the assumption of anisotropic flux of primary CRs, showers generated by primary particles of the same energy will arrive at the detector with the same frequency regardless of the zenith angle (assuming 100% efficiency). Hence, selecting showers arriving with a fixed intensity (energy) as a function of $S(1000)$, under different zenith angles, allows the measurement of the attenuation of $S(1000)$ with θ. This is the classical constant integral intensity cut method (CIC) [9]. This serves to convert $S(1000)$ at any given θ

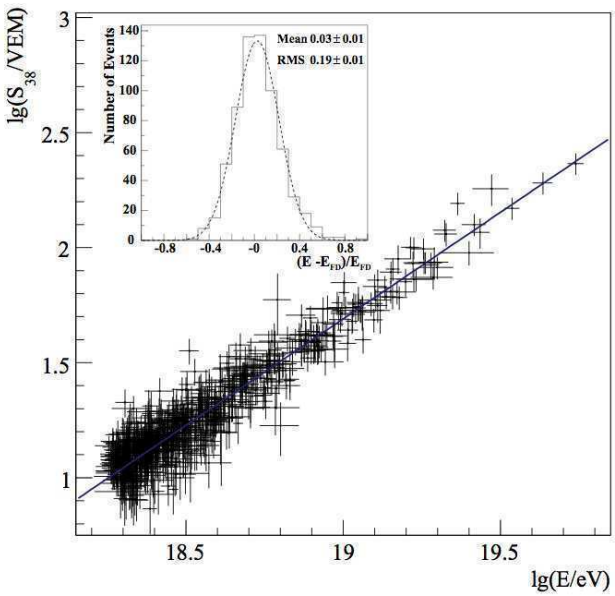

Fig. 2. – Correlation between $\log(S_{38})$ and $\log(E_{\rm FD})$ for the 661 hybrid events used in the fit. The full line is the best fit to the data. The fractional difference between the FD and SD energies is shown in the inset.

to $S(1000)$ at $\theta = 38$ (S_{38}) which is used as energy estimator. The angle of 38° minimises uncertainties, as this is the median zenith angle of the showers of interest. The calibration curve relating S_{38} and shower energy as obtained with FD data ($E_{\rm FD}$) in hybrid events is shown in fig. 2, and it is used to find the energies of the bulk of the events in which there are only SD measurements.

The systematic uncertainty due to the calibration procedure is 7% at 10^{19} eV and 15% at 10^{20} eV. The systematic uncertainties on the energy scale $E_{\rm FD}$ sum up to 22% [10]. The largest uncertainties are given by the absolute fluorescence yield (14%) [11], the absolute calibration of the fluorescence telescopes (9%) and the uncertainty due to the reconstruction method of the longitudinal shower profile (10%). The uncertainty due to the water vapour quenching on the fluorescence yield (5%) is taken into account as described in [12]. Additionally, the wavelength-dependent response of the fluorescence telescopes (3%), the uncertainties on measurements of the molecular optical depth (1%), on the measurements of the aerosol optical depth (7%) and on multiple scattering models (1%) are included in the overall systematic uncertainty. The non-detected energy (due to the contributions of muons and neutrinos) correction contributes 4% to the total systematic uncertainty of 22% [13].

To build the spectrum, candidate showers are selected on the basis of the topology and time compatibility of the triggered detectors. The SD with the highest signal must be enclosed within an active hexagon, in which all six surrounding detectors were operational at the time of the event. Thus, it is guaranteed that the shower core is contained in the array. Applying this condition, the maximum statistical uncertainty in the reconstructed $S(1000)$ due to event sampling by the array is $\simeq 3\%$ [14]. The trigger efficiency is greater than 99% for energies above about $3 \cdot 10^{18}$ eV [15]. The exposure is calculated

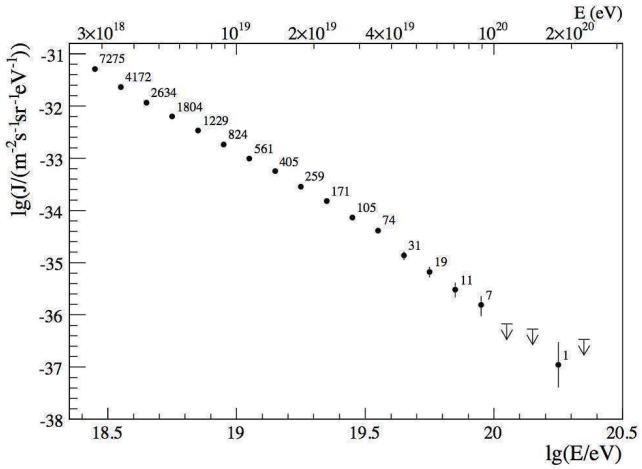

Fig. 3. – Energy spectrum derived from surface detector data calibrated with fluorescence measurements. Vertical error bars represent the statistical uncertainty only. The number of events in each bin is also given. A 22% systematic uncertainty in the absolute energy scale comes from the FD energy estimate.

by integrating the number of active detector stations of the surface array over time. Detailed monitoring information of the status of each surface detector station is stored every second and the exposure is determined with an uncertainty of 3%.

The surface detector is able to operate with an almost 100% duty cycle and collected the largest data set of ultra-high energy cosmic rays (UHECR) already during the construction phase. The spectrum corresponding to an exposure of $7000\,\mathrm{km}^2$ is shown in fig. 3, together with the event numbers of the underlying raw distribution [16].

The hypothesis that the cosmic ray spectrum continues with a constant slope above $4 \cdot 10^{19}\,\mathrm{eV}$ is rejected with a significance greater than 6 standard deviations, consistently with the prediction by Greisen and by Zatsepin and Kuzmin.

4. – Arrival directions of UHECRs

Using data collected between 1 January, 2004 and 31 August, 2007, the Pierre Auger Observatory has reported evidence of anisotropy in the arrival directions of CR with energies exceeding $\simeq 60\,\mathrm{EeV}$ [17]. The arrival directions were correlated with the positions of nearby objects from the 12th edition of the catalog of quasars and active galactic nuclei (AGN) by Véron-Cetty and Véron (VCV catalog) [18]. This catalog is not an unbiased statistical sample, since it is neither homogeneous nor statistically complete. This is not an obstacle to demonstrating the existence of anisotropy if CR arrive preferentially close to the positions of nearby objects in this sample. The nature of the catalog, however, limits the ability of the correlation method to identify the actual sources of cosmic rays. The observed correlation identifies neither individual sources nor a specific class of astrophysical sites of origin. It provides clues to the extragalactic origin of the CR with the highest energies and suggests that the suppression of the flux is due to interaction with the cosmic background radiation.

The parameters of the test were chosen by an exploratory scan using events prior to 27 May 2006. The scan searched for a correlation of CR with objects in the VCV catalog

with redshift less than $z_{\max}$ at an angular scale $\phi_{\max}$ and energy threshold $E_{\rm th}$. The scan was implemented to find a minimum of the probability P that k or more out of a total N events from an isotropic flux are correlated by chance with the selected objects at the chosen angular scale. The minimum of P value was found for the parameters $z_{\max} = 0.018$, $\phi_{\max} = 3.1^\circ$, and $E_{\rm th} = 56\,\text{EeV}$. The probability that an individual event from an isotropic flux arrives within the fraction of the sky prescribed by these parameters by chance is 0.21. The test was applied to data collected between 27 May 2006 and 31 August 2007. In this independent data, there were 13 events with energy above 56 EeV, of which 8 have arrival direction closer than 3.1° from the position of AGN less than 75 Mpc away, with 2.7 expected in average. The probability that this configuration would occur by chance is 1.7×10^{-3}. This correlation has a less than 1% probability to occur by chance if the arrival directions are isotropically distributed. Since the analysis reported in [17], the evidence for anisotropy has not strengthened [19].

Nevertheless, we have demonstrated the anisotropy of the arrival directions of the highest energy cosmic rays and their extragalactic origin. Our observations are consistent with the hypothesis that the rapid decrease of CR flux above 60 EeV, shown in sect. **1**, is due to the GZK effect. Additional data are needed to make further progress in the quest to identify the sites of ultrahigh energy CR origin.

5. – Limit on photon fraction in cosmic rays

Primary photons can experimentally be well separated from primary hadrons as they penetrate deeper into the atmosphere, particularly at energies above 10^{18} eV. Their shower development is also much less affected by uncertainties of hadronic interaction models due to the dominant electromagnetic shower component. At the highest energies the LPM effect further delays the shower development in the atmosphere (moreover increasing shower to shower fluctuations), whereas the pre-showering effect in the Earth magnetic field causes a more hadron like behavior (see [20] for a review on photon showers). Primary photons are of interest for several reasons: top-down models, originally proposed to explain the apparent absence of the GZK effect in AGASA data, predict a substantial photon flux at high energies [20]. In the presence of the GZK effect, UHE photons can also derive from the GZK process $p + \gamma_{\rm CMB} \to p + \pi^0 \to p + \gamma\gamma$ and provide relevant information about the sources and propagation. Moreover, they can be used to obtain input to fundamental physics and EHE astronomy.

The SD collects large statistics and has some observables sensitive to composition. Monte Carlo predictions of these SD observables have been compared with those in nucleonic showers and have shown this sensitivity [21]. Based on these simulations, no photon candidates were identified in SD data implying that 2%, 5% and 31% of UHECRs are photons above 10^{19}, $2 \cdot 10^{19}$ and $4 \cdot 10^{19}$ eV, respectively.

Experimentally, photon showers can be identified with the FD by their longitudinal shower profile, most importantly by $X_{\max}$, the depth in the atmosphere at which the number of electrons in a shower reaches a maximum. $X_{\max}$ is measured with data from the FD of the Pierre Auger Observatory with an accuracy of less than $20\,\text{g}\,\text{cm}^{-2}$ if suitable cuts are made. Data on $X_{\max}$ can be used to discriminate between photonic and nucleonic UHE primaries. Due to the much lower multiplicity in particle production in an electromagnetic cascade, the $X_{\max}$ of a photon-induced EAS is typically greater than that of a nucleonic-induced shower.

In ref. [22] $X_{\max}$ was used to place an upper limit of 16% on the photon fraction above 10 EeV. The hybrid detector is fully efficient for shower above 1 EeV and it allows

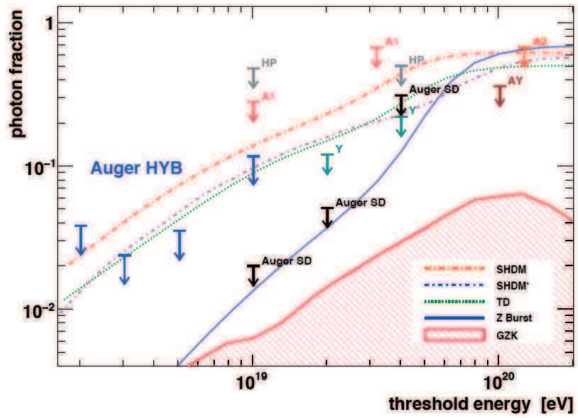

Fig. 4. – (Colour on-line) Upper limits on the photon fraction in the integral cosmic-ray flux for different experiments: AGASA (A1, A2) [24], AGASA-Yakutsk (AY) [25], Yakutsk (Y) [26], Haverah Park (HP) [27,28]. In black the limits from the Auger surface detector (Auger SD) [21] and in blue the limits above 2, 3, 5, and 10 EeV derived in this work (Auger HYB). The shaded region shows the expected GZK photon fraction as derived in [29]. Lines indicate predictions from top-down models, see [20].

thus composition study at lower energy than with the SD alone. Recently, the work was updated with more statistics and extended to data below 10 EeV. New upper limits of 3.8%, 2.4%, 3.5% and 11.7% on the fraction of photons above 2, 3, 5 and 10 EeV are obtained [23].

The derived upper limits are shown in fig. 4 along with previous experimental limits and model predictions (see ref. [20] for a review and references).

These limits improve significantly upon bounds from previous experiments and put strong constraints on certain models of the origin of cosmic rays. Current top-down models such as the super-heavy dark matter scenario do not appear to provide an adequate explanation of the UHE cosmic rays. In bottom-up models of acceleration of nuclear primaries in astrophysical sources, the expected photon fluxes are typically well below the current bounds [30].

6. – Conclusion

The Pierre Auger Observatory is the first large-scale UHECR detector to exploit the power of the hybrid technique, opening up a new era in experimental UHECR physics. The Observatory has been operating for more than 5 years and has now reached completion. Shower energies are determined in a way that minimises the dependence on models of hadronic interaction and composition. The energy spectrum of UHECRs above EeV energies was measured with vertical events. A steepening above $4 \cdot 10^{19}$ eV consistent with the GZK effect is apparent. Data from both FD and SD have been used to put stringent limits on the photon fraction in the UHECR flux. The sky has been shown to be anisotropic in UHECRs and their sources extragalactic.

* * *

I would like to thank all organisers of “Les Rencontres de Physique de la Vallée d’Aoste” for the invitation to give this talk.

REFERENCES

[1] Nagano M. and Watson A., *Rev. Mod. Phys*, **72** (2000) 689.
[2] Greisen K., *Phys. Rev. Lett.*, **16** (1966) 748; Zatsepin G. T. and Kuzmin V. A., *Sov. Phys. JETP Lett. (Engl. Transl.)*, **4** (1966) 78.
[3] Takeda M. *et al.*, *Astropart. Phys.*, **19** (2003) 447.
[4] Abu-Zayyad *et al.*, *Astropart. Phys.*, **23** (2005) 157.
[5] The Pierre Auger Collaboration, *Nucl. Instrum. Methods A*, **523** (2004) 50.
[6] Facal San Luis B. *et al.*, *Proceedings of the 30th ICRC, Merida, Mexico* (2007).
[7] Bauleo P. *et al.*, *Proceedings of the 29th ICRC, Pune, India* (2005).
[8] Hillas M., *Proceedings of the 12th International Conference on CR's*, **3** (1971).
[9] Hersil J. *et al.*, *Phys. Rev. Lett.*, **6** (1961) 245.
[10] Di Giulio C. for the Pierre Auger Collaboration, *Proceedings of the 31th ICRC, Lodz, Poland* (2009), `http://fr.arxiv.org/abs/0906.2347v1` (6).
[11] Nagano M., Kobayakawa K., Sakaki N. and Ando K., *Astropart. Phys.*, **22** (2004) 235.
[12] Ben-Zvi B. for the Pierre Auger Collaboration, *Proceedings of the 31th ICRC, Lodz, Poland* (2009), `http://fr.arxiv.org/abs/0906.2189v1` (14).
[13] Dawson B. *et al.*, *Proceedings of the 30th ICRC, Merida, Mexico* (2007) 4425.
[14] Ghia P. *et al.*, *Proceedings of 29th ICRC*, **7** (2006) 167.
[15] Allard D. *et al.*, *Proceedings of the 29th ICRC, Pune, India* (2005); The Pierre Auger Collaboration, to be published in *Nucl. Instrum. Methods*.
[16] The Pierre Auger Collaboration, *Phys. Rev. Lett.*, **2008** (2007) 061101.
[17] The Pierre Auger Collaboration, *Science*, **318** (2007) 938; *Astropart. Phys.*, **29** (2008) 188.
[18] Véron-Cetty M.-P. and Véron P., *Astron. Astrophys.*, **455** (2006) 773.
[19] Hague D. for the Pierre Auger Collaboration, *Proceedings of the 31th ICRC, Lodz, Poland* (2009), `http://fr.arxiv.org/abs/0906.2347v1` (6).
[20] Risse M. and Homola P., *Mod. Phys. Lett. A*, **22** (2007) 749.
[21] The Pierre Auger Collaboration, *Astropart. Phys.*, **29** (2008) 243.
[22] The Pierre Auger Collaboration, *Astropart. Phys.*, **27** (2007) 155.
[23] The Pierre Auger Collaboration, *Astropart. Phys.*, **31** (2009) 399.
[24] Shinozaki K. *et al.*, *Astrophys. J.*, **571** (2002) L117.
[25] Rubtsov G. *et al.*, *Phys. Rev. D*, **73** (2006) 063009.
[26] Glushkov A. V., *JETP Lett. 85*, **85** (2007) 163.
[27] Ave K. *et al.*, *Phys. Rev. Lett.*, **85** (2000) 2244.
[28] Ave K. *et al.*, *Phys. Rev. D*, **65** (2002) 063007.
[29] Gelmini G. *et al.*, astro-ph/0506128.
[30] Semikoz D., *Proceedings of the 30th ICRC, Merida, Mexico* (2007).

IL NUOVO CIMENTO Vol. 32 C, N. 5-6 Settembre-Dicembre 2009
DOI 10.1393/ncc/i2010-10519-y

Colloquia: LaThuile09

Measurement of ^{7}Be and ^{8}B solar neutrinos with BOREXINO

S. Zavatarelli[1](*), G. Bellini[2], J. Benziger[3], S. Bonetti[2], M. Buizza-Avanzini[2], B. Caccianiga[2], L. Cadonati[4], F. Calaprice[5], C. Carraro[1], A. Chavarria[5], F. Dalnoki-Veress[5], D. D'Angelo[2], S. Davini[1], H. de Kerret[6], A. Derbin[7], A. Etenko[8], K. Fomenko[9], D. Franco[2], C. Galbiati[5], S. Gazzana[10], M. Giammarchi[2], M. Goeger-Neff[11], A. Goretti[5], S. Hardy[12], Aldo Ianni[10], Andrea Ianni[5], M. Joyce[12], V. Kobychev[13], G. Korga[10], D. Kryn[6], M. Laubenstein[10], M. Leung[5], T. Lewke[11], E. Litninovich[8], B. Loer[5], P. Lombardi[2], L. Ludhova[2], I. Machulin[8], S. Manecki[12], W. Maneschg[14], G. Manuzio[1], F. Masetti[15], K. McCarty[5], Q. Meindl[11], E. Meroni[2], L. Miramonti[2], M. Misiaszek[16], D. Montanari[10], V. Muratova[7], L. Oberauer[11], M. Obolensky[6], F. Ortica[15], M. Pallavicini[1], L. Papp[10], L. Perasso[2], S. Perasso[1], A. Pocar[5], R. S. Raghavan[12], G. Ranucci[2], A. Razeto[10], P. Risso[1], A. Romani[15], D. Rountree[12], A. Sabelnikov[8], R. Saldanha[5], C. Salvo[1], S. Schonert[14], H. Simgen[14], M. Skorokhvatov[8], O. Smirnov[9], A. Sotnikov[9], S. Sukhotin[8], Y. Suvorov[2], R. Tartaglia[10], G. Testera[1], D. Vignaud[6], R. B. Vogelaar[12], F. von Feilitzsch[11], M. Wojcik[16], M. Wurm[11], O. Zaimidoroga[9] and G. Zuzel[14]

([1]) *Dipartimento di Fisica, Università di Genova and INFN, Sezione di Genova I-16146 Genova, Italy*
([2]) *Dipartimento di Fisica, Università di Milano and INFN, Sezione di Milano I-20133 Milano, Italy*
([3]) *Department of Chemical Engineering, Princeton University - NJ 08544-5263, USA*
([4]) *Physics Department, University of Massachussets - Amherst, AM01003, USA*
([5]) *Department of Physics, Princeton University - Princeton, NJ 08544-0708, USA*
([6]) *Astroparticule et Cosmologie APC - 75205 Paris cedex 13, France*
([7]) *St. Petersburg Nuclear Physics Institute - Gatchina, Russia*
([8]) *RRC Kurchatov Institute - Kurchatov Sq. 1, 123182 Moscow, Russia*
([9]) *JINR - Joliot Curie str. 6, 141980 Dubna (Moscow Region), Russia*
([10]) *Laboratori Nazionali del Gran Sasso - I-67010 Assergi (AQ), Italy*
([11]) *Technische Universität München - D-85747 Garching, Germany*
([12]) *Physics Department, Virginia Polytechnic Institute and State University Blacksburg, VA 24061-0435, USA*
([13]) *Institute for Nuclear Research - MSP 03680 Kiev, Ukraine*
([14]) *Max-Planck-Institut für Kernphysik - D-69029 Heidelberg, Germany*
([15]) *Dipartimento di Chimica, Università di Perugia and INFN, Sezione di Perugia I-06123 Perugia, Italy*
([16]) *Institute of Physics, Jagellonian University - PL-30059 Krakow, Poland*

(ricevuto il 10 Novembre 2009; pubblicato online l'8 Gennaio 2010)

(*) Contribution presented by S. Zavatarelli. E-mail: zavatare@ge.infn.it

Summary. — Borexino is a real-time liquid-scintillator detector for low-energy neutrino spectroscopy located at the Gran Sasso National Laboratories (Italy). Thanks to the unprecedented radiopurity of the target mass it is providing the first direct and simultaneous measurement of the solar neutrino survival probability in both vacuum-dominated (^{7}Be ν) and matter-enhanced regions (^{8}B ν) by a single experiment. The measured interaction rates for both the ^{7}Be and ^{8}B solar neutrinos are in fair agreement with the SSM predictions in case of the LMA-MSW oscillation solution and a further confirmation of the LMA scenario is provided by the absence of a day-night asymmetry in the ^{7}Be signal. These experimental results allow to improve the upper limit on the neutrino effective magnetic moment. Calibration campaigns aiming to reduce the systematical errors on fiducial volume definition and detector energy response are presently in progress.

PACS 95.55.Vj – Neutrino, muon, pion, and other elementary particle detectors; cosmic ray detectors.
PACS 29.40.Mc – Scintillation detectors.

1. – Introduction

The Sun is an intense source of electron neutrinos, produced in nuclear reactions of the p-p chain and of the CNO cycle. They provide a unique probe for studying both the nuclear fusion reactions that power the Sun and the fundamental properties of neutrinos. They have been studied for 30 years by means of radiochemical and water Cherenkov detectors and brought to the discovery of the ν flavour oscillations. The range of the parameters describing the oscillation phenomenon has been constrained using the data coming from solar and reactor neutrinos experiments to the so-called LMA (Large Mixing Angle) region of the plane θ_{12} Δm^2_{12} ($\tan^2(2\theta_{12}) = 0.47^{+0.06}_{-0.05}$ and $\Delta m^2_{12} = 7.59^{+0.21}_{-0.21} \cdot 10^{-5}\,\mathrm{eV}^2$ [1]). Matter effects in the Sun play a crucial role too (MSW effect). A central feature of the MSW-LMA solution is the prediction that neutrino oscillations are dominated by vacuum oscillations at low energies ($< 1\,\mathrm{MeV}$) and by resonant matter-enhanced oscillations, taking place in the Sun's core, at higher energies ($> 5\,\mathrm{MeV}$). A measure of the survival probability as a function of the ν energy is very important to confirm the MSW-LMA solution or to exploit possible traces of non-standard neutrino-matter interactions or non-standard neutrinos properties (mass varying ν) [2]. The relevance of the measurements of the various solar neutrinos components is then twofold: from one side they can increase the confidence in the oscillation scenario and from the other side, assuming the knowledge of the oscillation parameters, they could provide a measurement of the absolute solar neutrino fluxes, helping for example in the scientific debate between high- and low-metallicity solar models [3].

Among existing experiments on solar neutrinos SNO and Super-K measure the solar neutrinos fluxes with high threshold (5 MeV) because of the low Cherenkov light yield and the high intrinsic backgrounds so they are only sensitive to ^{8}B neutrinos. Radiochimical detectors did not measure the ν energy.

Borexino has opened a new chapter in the experimental history of solar ν making feasible the solar ν's spectroscopy in real time down to 200 keV. This was possible by employing a liquid-scintillator technique which has several advantages: the light yield is a factor 50 higher than the Cherenkov one and the very low solubility to ions and metal

impurities makes it possible to reach unprecented levels of radiopurity. Solar neutrinos are detected in Borexino through their elastic scattering on electrons in the scintillator. Electron neutrinos (ν_e) interact through charged and neutral currents and in the energy range of interest they have a cross-section 5 times larger than ν_μ and ν_τ, which interact only via neutral current. The electrons scattered by neutrinos are detected by means of the scintillation light retaining the information on the energy while information on the direction of the scattered electron is lost. Electron-like events induced by solar neutrinos interaction cannot be distinguished, on an event-by-event basis, from electrons or gammas due to radioactive decays so a strong effort has been devoted to the containment and comprehension of the background. The design of Borexino is based on the principle of graded shielding, with the inner core scintillator at the center of a set of concentric shells of increasing radiopurity. All components were screened and selected for low radioactivity and the scintillator and buffer were purified on site at the time of filling. The purification strategy relies on filtration, multistage distillation and nitrogen sparging. The present work reports, after a brief detector description, the main goals reached in the so-called Borexino phase I data taking period (May 2007-Oct 2008), namely the measurement of ^{7}Be solar neutrinos fluxes and D/N asimmetry, the ^{8}B solar neutrinos fluxes and the best current limits on the ν magnetic moment. Calibrations campaigns and next goals are also described.

2. – The detector

The Borexino detector is located at the Gran Sasso National Laboratories (LNGS) in central Italy, at a depth of 3800 m.w.e. The active mass consists of 278 tons of pseudocumene (PC) doped with 1.5 g/l of PPO. The scintillator is contained in a thin (125 μm) nylon vessel and is surrounded by two concentric PC buffers doped with DMP, a scintillation light quencher. The scintillator and buffers are contained in a Stainless Steel Sphere (SSS) with a diameter of 13.7 m. The SSS is enclosed in a water tank (WT), containing 2100 tons of ultrapure water as an additional shield. The scintillation light is detected via 2212 8″ photomultiplier tubes uniformely distributed on the inner surface of the SSS. Additional 208 8″ PMTs instrument the WT and detect the Cherenkov light radiated by muons in the water shield, serving as a muon veto. A detailed description of the detector can be found in [4]. Key features of the scintillator are the high light yield (500 p.e./MeV) and the fast time response that allows to reconstruct the events position by means of a time flight technique. An event is recorded when at least 25 PMT pulses occur within a time window of 99 ns (the corresponding energy threshold is about 40 keV). When a trigger occurs, a 16 μs gate is opened and time and charge of each PMT is collected. The offline software identifies the shape and the length of each scintillation pulse and reconstructs the position and energy of the each deposit. Pulse shape analysis is performed to identify various classes of events, among which eletronic noise, pile up events, muons, α and β particles.

3. – Radiopurity and background levels

Besides reducing external background, the key requirement for measuring low-energy ν with Borexino is an extreme radiopurity of the scintillator itself. During 15 years of dedicated R&D studies, the Borexino Collaboration developed a purification strategy which proved to be effective in removing the most dangerous contaminants. In particular ^{40}K contamination was found to be below $3 \cdot 10^{-18}$ g/g (90% CL) while the contamination

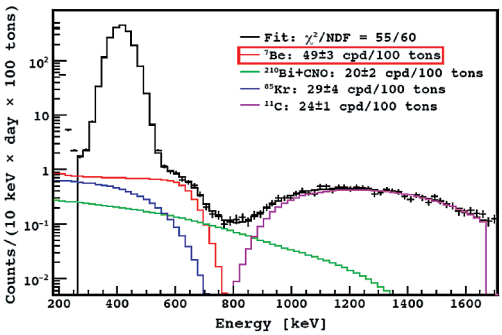

Fig. 1. – The Borexino energy spectrum obtained after applying the described analysis cuts (see text). Results of fitting procedure are also shown.

due to ^{238}U and ^{232}Th was reduced to the unprecented levels of $(1.6 \pm 0.1) \cdot 10^{-17}$ g/g and $(5 \pm 1) \cdot 10^{-18}$ g/g. By far the most important source of background is ^{14}C, a β emitter with 156 keV endpoint, which is naturally present in an organic liquid scintillator. Its isotopic ratio is evaluated to be $^{14}\mathrm{C}/^{12}\mathrm{C} = (2.7 \pm 0.6) \cdot 10^{-18}$, perfectly suited to the planned analysis threshold of 200 keV. Other important background is the 5.3 MeV α emitter ^{210}Po. The ionization quenching of the scintillator reduced the visible energy by a factor 13 and moves the α peak in the energy range of the ^{7}Be signal. Its contamination at the beginning of data taking was about 80 counts/day/ton, decreasing afterwards with time with the expected mean life of 200 days. This background could be statistically subtracted by use of a pulse-shape discrimination made possible by the PC-based scintillator. The most annoying background for the ^{7}Be ν analysis is ^{85}Kr, an air-borne contaminant, emitting electrons with 687 keV endpoint and a rate of the same order of the ^{7}Be signal. The ^{85}Kr content in the scintillator was probed through the rare decay sequence $^{85}\mathrm{Kr} \to {}^{85m}\mathrm{Rb} + e^+ + \nu_e$, $^{85m}\mathrm{Rb} \to {}^{85}\mathrm{Rb} + \gamma$ ($\tau = 1.5\,\mu$s, $BR = 0.43\%$) that offers a delayed coincidence tag and it is evaluated to be (28 ± 7) counts/day/ton. The large error is due to low statistics. At energies above 800 keV the dominant background is cosmogenically produced ^{11}C (β^+ decay, $Q = 1.98$ MeV). It is observed at an average rate of 25 counts/(day 100 tons), which is the range of prediction of the previous studies though slightly higher [5, 6].

4. – The ^{7}Be signal: fluxes and day/night asymmetry

The basic signature for the monoenergetic 0.862 MeV ^{7}Be ν is the Compton like edge of the recoil electrons at 665 keV as shown in fig. 1. Events have been selected by means of the following cuts:

- Only 1 cluster events are accepted: the event must have a unique reconstructed cluster in the gate time window (16 μs) in order to reject pile-up and fast coincident events ($\epsilon \approx 100\%$).
- Muon and muon daughters are rejected: events associated with Cherenkov light in the water tank detector are identified as cosmic muon and rejected. A 2 ms veto is applied after each muon crossing the detector to remove afterpulses and muon-induced neutrons ($\tau \approx 250\,\mu$s); the measured muon rate in Borexino is $(0.055 \pm 0.002)\,\mathrm{s}^{-1}$ and the dead time introduced by this cut is negligible.

– Space and time correlated events are rejected: events occurring withing 2 ms at the same place ($\Delta R < 1.5$ m) are removed; the Rn daughters occurring before the ^{214}Bi-^{214}Po delayed coincidences are eliminated by vetoing events up to three hours before a coincidence. The total loss of fiducial exposure due to this cuts is 0.7%.

– Fiducial volume cut: to remove external backgrounds only events reconstructed in the innermost 100 tons are accepted. Another volumetric cut $|z| < 1.8$ m was applied in order to cut out the regions close to the poles with very different detectors response resulting in a nominal fiducial mass of 78.5 t.

In fig. 1 the measured spectrum in 192 days is a shown as obtained by applying the previous cuts. The most noticeable peak, around 400 keV, is the one due to the ^{210}Po α decay, while at energies above 800 keV the beta spectrum of ^{11}C is clearly visible.

The ^{7}Be signal rate in Borexino is obtained fitting the energy spectrum by a superposition of the spectra due to solar neutrinos and to the not taggable backgrounds. Two procedures were adopted: one of them includes the ^{210}Po α peak while in the second one a further pulse shape discrimination is applied to data and the α-like events are statistically subtracted. The two results are perfectly compatible [7] and they give the value of the ^{7}Be neutrinos interaction rate of $(49 \pm 3 \pm 4)$ ev/(day 100t) after 192 days of live time. According to the Standard Solar Model with high metallicity [8, 3] the expected signal for non-oscillated solar ^{7}Be ν is (74 ± 4), which is reduced to (48 ± 4) ev/(day 100t) according to the MSW-LMA oscillation parameters. The ν_e survival probability at the ^{7}Be ν energy corresponding to our results is $P_{ee} = (0.56 \pm 0.10)$ and the non-oscillation hypothesis ($P_{ee} = 1$) can be rejected at 4 σ CL. Therefore Borexino on the one hand confirms the MSW-LMA ν oscillation scenario and, on the other hand, provides the first direct P_{ee} measurement in the low-energy vacuum regime.

A preliminary analysis of the day and night spectra provides a further confirmation of the prediction of the MSW-LMA model through the absence of a significant day-night asymmetry in the ^{7}Be flux. Data corresponding to a total live time of 422.12 days with 212.87 days and 209.25 nights have been analysed. The day-night asymmetry A_{dn} is defined as $A_{dn} = (C_n - C_d)/(C_n + C_d)$ where C_n and C_d are the counts during day and night time and it includes the contributions both of the signal and of the background. Considering the statistical precision of the ^{7}Be flux determination in the day and night periods we get for the contribution of the signal alone in the ^{7}Be energy window $A^{\nu}{}_{dn} = (0.02 \pm 0.04)_{\mathrm{stat}}$ [9], compatible with zero.

A huge experimental and analysis effort is now in progress to reduce the errors associated to the measurement of the ^{7}Be signal rate. Among the not taggable backgrounds, the most important source of uncertainty in the ^{7}Be flux determination is the ^{85}Kr content. This contamination can be measured through a very rare branch which gives a β/γ fast coincidence. At the time of our last published results [7] only 8 β/γ coincidences were selected in 192 days of live time and the contamination value was taken as a free parameter in the fitting procedure because of the too large statistical uncertainty. Now after one year of live time, the uncertainty has been reduced by 50% and the amount of contamination is contrained to (28 ± 7) counts/(days 100t) so it can be fixed in the fitting procedure. Presently the possibility to reduce the ^{85}Kr contamination throught a scintillator purification is under study. In particular, ^{85}Kr is a noble gas and the experience gained with CTF, the 4 tons prototype of Borexino [10], showed than nitrogen sparging is particularly effective to remove this background. A ^{7}Be rate measurement with a few percent accuracy requires also a strong reduction of systematical errors: the

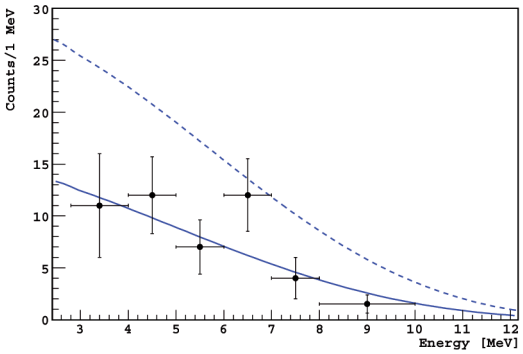

Fig. 2. – Energy spectrum of the events surviving all cuts applied in the ^{8}B ν analysis. The expected electron recoil spectrum due to oscillated (not oscillated) ^{8}B ν interaction and determined from solar model [8] with high metallicity is represented by the solid (dashed) line.

main contributions are coming from the imperfect knowledge of the fiducial volume and of the detector energy response (each of them is giving a contribution to the systematical error of 6%). We are presently reducing these uncertainties through the detector calibration: two calibration campaigns have been already completed, others are scheduled for the next months and the results are under analysis.

5. – The ^{8}B neutrinos fluxes and the survival probability in the vacuum-matter oscillation transition

The extreme radiopurity of Borexino, combined with the efficient software rejection of cosmogenic background allows to investigate the recoiled electron spectrum induced by ^{8}B solar ν, down to the energy threshold of 2.8 MeV. This value is mainly due to the presence at lower energies of a large background coming from penetrating γ-rays emitted by ^{208}Tl decay in the PMT's material. So far Borexino is the first experiment providing the real-time measurement of ^{8}B ν below 5 MeV. The major background sources at the energy above 2.8 MeV are muons, gammas from the neutron capture, radon emanation from the nylon vessel, short-lived ($t < 2$ s) and long-lived ($t > 2$ s, ^{10}C) cosmogenic isotopes and bulk ^{208}Tl contamination. In addition to the already discussed cuts, a stronger cosmogenic cut is applied by vetoing the overall detector for 5 s after a crossing muon; ^{10}C candidates are removed by the triple coincidence with the parent muon and the neutron capture on protons and the ^{208}Tl contamination due to the internal radioactivity is evaluated by measuring the delayed coincidence of its branching competitor ^{212}Bi-^{212}Po in the ^{232}Th chain and statistically subtracted. Energy spectrum of events surviving all cuts is shown in fig. 2 after statistical ^{208}Tl subtraction. The number of selected events is (48 ± 8) in 245.9 days of live time and they correspond to a rate of ^{8}B solar ν interactions (above 2.8 MeV) of $(0.26 \pm 0.04_{\rm stat} \pm 0.02_{\rm sys})$ counts/(day 100 tons) [11]. The equivalent ν_e flux survival probability, assuming the Standard Solar Model [8], is (0.35 ± 0.10) at the effective energy of 8.6 MeV. So the non-oscillation model is excluded at 4.2σ CL. Borexino is the first experiment able to simultaneously measure solar ν fluxes both in vacuum-dominated (^{7}Be ν) and matter-enhanced regions (^{8}B ν). The obtained results for P_{ee} are shown in fig. 3 and compared with expectation due to MSW-LMA theory [7]. The agreement is fair. In the case ^{8}B neutrinos fluxes an improvement in the precision

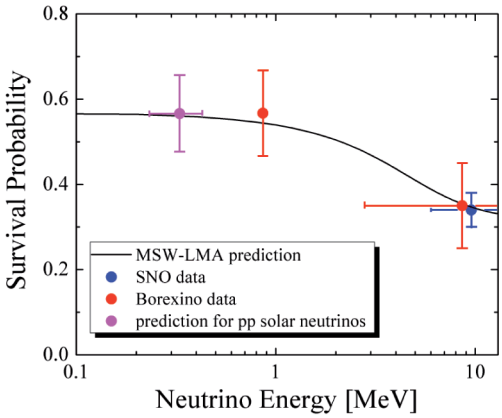

Fig. 3. – ^{7}Be and ^{8}B electron neutrino survival probability as measured by Borexino compared to previous measurements and MSW-LMA predictions.

of the measurement requires an increase of the time of measure and of the fiducial mass, besides a better definition of the fiducial volume mass and of the energy response of the detector.

6. – Neutrino effective magnetic moment

In a case of a non-null ν magnetic moment, the ν scattering cross-section off electrons is modified by the addition of an electromagnetic term, $\mathrm{d}\sigma/\mathrm{d}T_{\mathrm{em}} = \mu_\nu^2 \pi \alpha_{\mathrm{em}}^2 / m_e^2 [1/T - 1/E_\nu]$ where E_ν is the ν energy and T is the electron kinetic energy. The shape of the solar ν spectrum is sensitive to the possible presence of a non-null magnetic moment, and the sensitivity is enhanced at low energy since $\mathrm{d}\sigma/\mathrm{d}T_{\mathrm{em}}$ is proportional to $1/T$. By analysing the α subtracted energy spectrum we obtain an upper limit of $5.4 \cdot 10^{-11} \mu_B$ (90% CL) [7] which is currently the best experimental limit.

7. – Detector calibrations

Two calibration campaigns have been already completed, others are scheduled for the next months. The goal is to reduce the systematical uncertainties in the ^{7}Be and ^{8}B signal at a level of few percent. Radioactive sources have been inserted in the inner vessel center and along the vertical axis (first calibration campaign) and in more than 100 positions on and off vertical axis (second calibration campaign). An Am-Be source and several gamma sources have been used for the energy calibration while a source made by a quartz sphere filled by scintillator loaded with radon and ^{14}C was used to study the position reconstruction as a function of the event energy and of the event type (α, β and γ) and to map the relative changes of the reconstructed energy at various positions. The true position can be determined within 1 cm accuracy through the use of a red light laser (mounted on the source support) monitored by a system of CCD cameras. The position is then compared with the one reconstructed by means of time-of-flight technique from the scintillation light induced by radioactive dacays and detected by the PMT's. Particular care has been devoted to the design of the source insertion system, to the choice of its material and to the definition of the insertion procedure in order to

minimize the risk of introduction of any radioactive contaminants in the detector that would spoil the unprecented performances of Borexino. The calibration results are under analysis.

8. – Future perspectives

Borexino has provided the first real time measurements of the ^{7}Be and the lowest threshold ^{8}B neutrinos fluxes. A preliminary result about the ^{7}Be signal day/night asymmetry has also been provided. Calibrations campaigns are presently in progress and together with eventual purifications open the way to very precise ^{7}Be ν signal rate measurements (at the level of few percent) and to an improvement in the precision of the ^{8}B signal. Given the exceptional, unprecented purity levels achieved in Borexino, a broad investigation of the solar ν spectrum is prospectively possible in the future. A feasibility of pep, CNO and possibly pp solar neutrinos measurement is extensively studied. The study of geoneutrinos is also promising due to the fact that Borexino is located far away from any of the European reactors. A set of candidates has been already collected but requires statistics in order to get evidence for a signal at the 3σ level. Finally Borexino has joined the SNEWS community since February 2009 and it is now ready to detect supernova events.

REFERENCES

[1] Suzuki A., talk at the *Neutrino Telescopes 2009 Conference*.
[2] Barger *et al.*, *Phys. Rev. Lett.*, **95** (2005) 211802; Frieland A. *et al.*, *Phys. Lett. B*, **594** (2004) 347.
[3] Gravesse N. and Sauval A. G., *Space Sci. Rev.*, **85** (1998) 161; Asplund M., Gravesse N. and Sauval A. G., *Nucl. Phys. A*, **777** (2006) 1; Pena-Garay C., talk at the *Neutrino Telescopes 2007 Conference*.
[4] Alimonti G. *et al.* (Borexino Collaboration), *Nucl. Instrum. Methods A*, **600** (2009) 568.
[5] Hagner T. *et al.*, *Astropart. Phys.*, **14** (2000) 33.
[6] Back H. *et al.* (Borexino Collaboration), *Phys. Rev. C*, **74** (2006) 045805.
[7] Arpesella C. *et al.* (Borexino Collaboration), *Phys. Rev. Lett.*, **101** (2008) 091302.
[8] Bahcall J. N., Serenelli A. M. and Basu S., *Astrophys. J. Suppl.*, **165** (2006) 400.
[9] Testera G. *et al.* (Borexino Collaboration), talk at the *Neutrino Telescopes 2009 Conference*.
[10] Alimonti G. *et al.* (Borexino Collaboration), *Nucl. Instrum. Methods A*, **406** (1998) 411.
[11] Bellini G. *et al.* (Borexino Collaboration), arXiv:0808.2868(2008).

IL NUOVO CIMENTO Vol. 32 C, N. 5-6 Settembre-Dicembre 2009
DOI 10.1393/ncc/i2009-10509-2

Colloquia: LaThuile09

WIMP hunting with the Cryogenic Dark Matter Search

J. Filippini for the CDMS Collaboration

Division of Physics, Mathematics, and Astronomy, California Institute of Technology 1200 E. California Blvd., MC-367-17, Pasadena, CA 91125, USA

(ricevuto il 10 Novembre 2009; pubblicato online il 21 Dicembre 2009)

Summary. — The Cryogenic Dark Matter Search (CDMS) seeks to directly detect the scattering of weakly interacting massive particle (WIMP) dark matter in an array of cryogenic particle detectors at Soudan Underground Laboratory. CDMS uses simultaneous measurements of ionization and phonons to discriminate between nuclear and electron recoils on an event-by-event basis. The most recent run of CDMS at Soudan accumulated 397.8 (53.5) kg-days of Ge (Si) exposure and observed no candidate events, setting the strongest limit to date on spin-independent WIMP-nucleon interactions at WIMP masses $\gtrsim 44\,\mathrm{GeV}/c^2$. CDMS also sets competitive upper limits on various axion-like models. A data set $\sim 2.5\times$ larger is currently under analysis, and prototype detectors for the larger-scale SuperCDMS experiment are currently acquiring data at Soudan.

PACS 95.35.+d – Dark matter (stellar, interstellar, galactic, and cosmological).
PACS 14.80.Ly – Supersymmetric partners of known particles.

1. – Dark matter and its detection

In the decades since Fritz Zwicky's observations of anomalous galaxy cluster motions in the 1930s [1], astronomers and physicists have accumulated a vast array of evidence that the bulk of the universe's matter is in some "dark" form, thus far detected only through its gravitational influence. The visible objects we see through our telescopes are now thought to be imbedded within far more massive dark matter formations, and it is these which dominate the evolution of large-scale structure in our universe.

Though there is now broad consensus on the amount of dark matter present in the universe, very little is known about its composition. There is now overwhelming evidence that it is primarily non-baryonic in nature, however, as supported by observations of light element abundances [2] and the microwave background [3]. Whatever the constituent particles of dark matter are, they must be stable (or at least have a lifetime long compared to the present age of the universe), non-relativistic during the epoch of structure formation, and have limited interactions with other matter. Determining the nature of this dark matter remains one of the most pressing questions of modern cosmology.

Among the innumerable dark matter candidates proposed over the years, weakly interacting massive particles (WIMPs) are among the most promising. A WIMP is a hypothetical stable particle with mass $1\,\mathrm{GeV} \lesssim M_\chi c^2 \lesssim 10\,\mathrm{TeV}$ and coupling strengths characteristic of the weak interactions. The strength of the WIMP hypothesis comes from a confluence between cosmology and particle physics: the thermal relic density of such a particle can naturally match the observed dark matter abundance, and many extensions to the Standard Model of particle physics independently predict new stable particles at the weak scale. Examples of WIMPs include the lightest neutralino in many supersymmetric models, the lightest Kaluza-Klein particle in models with additional spatial dimensions, and the lightest T-odd particle in some Little Higgs theories.

If WIMPs constitute the universe's dark matter, they should occasionally scatter elastically upon atomic nuclei as the Earth passes through the Milky Way's dark matter halo. Such scattering events may be observable in sufficiently sensitive particle detectors, a strategy known as "direct detection" [4]. For $60\,\mathrm{GeV}/c^2$ WIMPs incident on a Ge target at galactic velocities ($\sim 0.001c$), we expect an exponential spectrum of nuclear recoils with energy depositions of $\sim 30\,\mathrm{keV}$. Even in clean, heavily shielded environments, however, the rate of background events far exceeds that expected from WIMP interactions (no more than a few scattering events per year in each kilogram of target material). Detecting these events thus presents an enormous experimental challenge, demanding very low energy thresholds and exquisite control over cosmogenic and radiogenic backgrounds.

2. – The Cryogenic Dark Matter Search

The Cryogenic Dark Matter Search (CDMS) is currently the world's most sensitive experiment for the direct detection of WIMP dark matter. CDMS operates an array of cryogenic particle detectors at the Soudan Underground Laboratory in northern Minnesota, USA. These detectors use a simultaneous measurement of ionization and athermal (out-of-equilibrium) phonons to distinguish nuclear recoils (WIMPs and neutrons) from electron recoils (most backgrounds) on an event-by-event basis. CDMS uses this immense discrimination power to operate in a "zero-background" regime: we seek to maintain an expected background of $\lesssim 1$ event, so that no background subtraction is necessary and even a handful WIMP-candidate events would constitute a significant signal.

2˙1. *ZIP detectors.* – The central component of the CDMS experiment is an array of thirty Z-sensitive Ionization and Phonon (ZIP) detectors [5]. Each ZIP is a disk of high-purity crystalline Ge or Si, 7.6 cm in diameter and 1 cm thick. The thirty ZIPs at Soudan are arranged into five stacks of six detectors, maintained at 40 mK to reduce thermal noise. Figure 1 illustrates a representative ZIP detector and a view of the five detector stacks installed at Soudan.

The top flat face of each detector is photolithographically patterned with four phonon sensors, each composed of 1036 tungsten transition-edge sensors (TESs) [6] wired in parallel. Energetic phonons reaching the crystal surface break Cooper pairs in superconducting aluminum fins surrounding each TES. The resulting quasiparticles diffuse across the fins and heat the TES, producing a change in resistance which is detected by a SQUID ammeter. Due to rapid response time of the TESs ($\tau_{\mathrm{rise}} \sim 5\mu\mathrm{s}$), the shapes and amplitudes of the four phonon pulses record the characteristics of the initial wave of phonons, which carries information about the event's position and total deposited energy.

Each detector's bottom face is patterned with an aluminum grid to form two ionization electrodes: an inner primary electrode and a surrounding guard ring. These electrodes

Fig. 1. – Left: a CDMS II ZIP detector in its Cu housing. The phonon sensor photolithography is visible on the top detector surface. Right: the CDMS icebox configuration in this data run, showing the tops of the five detector stacks and associated cold hardware.

are biased to $-3\,\mathrm{V}$ (for Ge; $-4\,\mathrm{V}$ for Si) with respect to the phonon sensor array to produce an electric field within the crystal. Electrons and holes generated by particle interactions drift to the surfaces under the influence of this field, producing image currents in the electrodes which are detected by a JFET charge amplifier. The inner electrode defines the detector's fiducial volume; any event depositing significant energy in the outer electrode is rejected from WIMP-search analysis.

CDMS's primary background rejection comes from ionization yield, defined as the ratio of an event's ionization signal to its total deposited energy. Fast, lightweight projectiles (*e.g.*, recoiling electrons from electromagnetic backgrounds) passing through a crystal lattice transfer a larger fraction of their energy into the production of electron-hole pairs than do slow, heavy projectiles (*e.g.*, recoiling nuclei from WIMP or neutron interactions). The left panel of fig. 2 illustrates the power of this discrimination technique

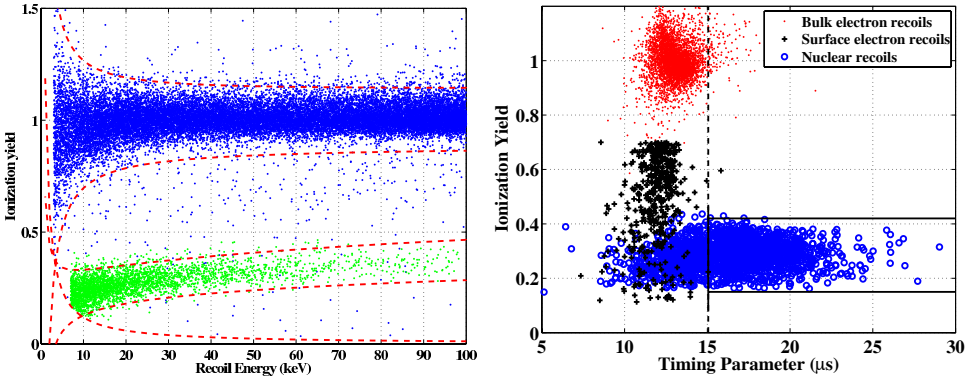

Fig. 2. – (Colour on-line) Left: ionization yield *vs.* recoil energy for particle events from *in situ* calibrations with radioactive sources. Blue (dark) points indicate electron recoils from a ^{133}Ba source, green (light) points indicate neutrons from a ^{252}Cf source. Dashed lines delineate approximate boundaries of the electron and nuclear recoil populations, as well as the ionization energy threshold. Right: ionization yield *vs.* a composite phonon pulse timing parameter, plotted for calibration data from a Ge ZIP. The solid line indicates the approximate signal region.

using data from *in situ* calibrations with radioactive sources. A cut in ionization yield alone reduces the electron recoil background by a factor of $> 10^4$ while maintaining $> 90\%$ acceptance of nuclear recoils.

Interactions within $\sim 10\,\mu$m of a detector surface (*e.g.*, from electrons or low-energy photons) may exhibit incomplete charge collection and reduced ionization yield. These surface events are identified by the faster arrival of their phonons, an effect thought to arise from changes in the phonon spectrum from phonon interactions at the metal electrodes. In this analysis we place cuts on a composite timing parameter, the sum of the rise time of the largest phonon pulse and the difference in start times between that pulse and the ionization signal. The right panel of fig. 2 illustrates the combined scheme for background rejection. Phonon pulse timing cuts reduce the surface event background by a factor of ~ 200, for overall discrimination of $> 10^6$ against electron recoil events.

2˙2. *The Soudan installation.* – CDMS is currently located at Soudan Underground Laboratory, on the 27th level of a historic iron mine in northern Minnesota, USA. The laboratory is protected by a rock overburden equivalent to 2090 meters of water, which reduces the flux of cosmic ray muons by a factor of $\sim 5 \times 10^4$ from that at the surface. The detectors are housed within the "icebox," a $\sim 1\,\mathrm{m}^3$ cold volume maintained at 40 mK by an Oxford dilution refrigerator. Further cooling power at 4 K is provided by a Gifford-McMahon cryocooler. The icebox is composed of several layers of low-activity OFHC copper; other materials near the detectors are similarly chosen to be low in radioactivity. The area surrounding these cans is purged with low-activity aged air to reduce radon plateout near the copper. The icebox is surrounded by a passive shield consisting of 50 cm of polyethylene and 22.5 cm of lead, the inner 4.5 cm of which is ancient, low-activity lead. This passive shield is encased within an active shield of forty scintillator panels to tag cosmic ray muons and their associated particle showers. The entire arrangement is located within an RF-shielded room for protection from electromagnetic interference.

3. – WIMP-search analysis

3˙1. *Data set.* – CDMS's most recent result [7] is based upon the first two exposures of CDMS at Soudan with its full complement of thirty ZIP detectors (19 Ge and 11 Si). The first run acquired data from October 21, 2006, through March 20, 2007. After a brief period of cryogenic maintenance, the second data run proceeded from April 20 through July 16, 2007. WIMP-search acquisitions were interspersed with regular calibration runs with ^{133}Ba and ^{252}Cf sources; the former yielded 28 million electron-recoil events between 10–100 keV (30× the number of comparable events in the WIMP-search background), the latter more than 10^5 nuclear recoils with which to calibrate response to nuclear recoils. Data quality and uniformity was monitored continuously through a series of automated consistency checks and visual inspections. After excluding periods of inconsistent data quality and poor detector performance, these data sets yielded a total of 397.8 (53.5) kg-days of Ge (Si) exposure.

3˙2. *WIMP candidate selection.* – In order to limit bias in the cut-setting process, the analysis of this data set was carried out blindly. A region of parameter space in the WIMP-search data covering the signal region was masked until all WIMP-selection cuts were defined. All criteria for WIMP identification were set and characterized using calibration data and the unmasked portion of the WIMP-search data. Only when all criteria were finalized did we unmask the signal region and observe the number of candidate events.

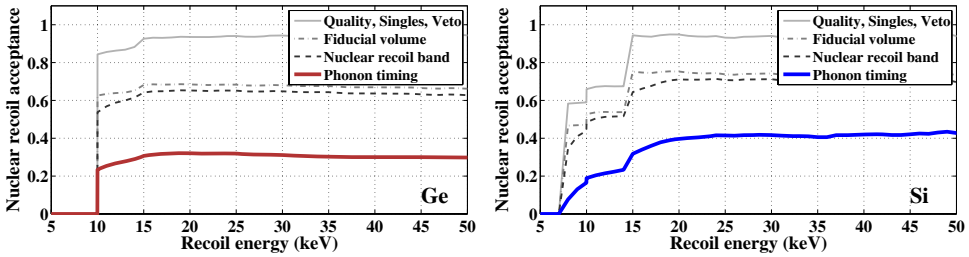

Fig. 3. – Combined nuclear recoil acceptances as functions of energy for Ge (left) and Si (right) ZIPs. Curves represent total acceptances after applying the indicated cut and all those preceding it in the caption.

After removing periods of poor data quality and poorly reconstructed events, we demand that a WIMP candidate satisfy the following major conditions:

1) *Multiplicity*: Significant energy deposited in one and only one detector, and none in the surrounding scintillator panels.
2) *Fiducial volume*: No significant ionization energy deposited in the outer electrode.
3) *Ionization yield*: Each event's ionization yield must be consistent with that of neutrons at the 95% level.
4) *Phonon timing*: Each event's phonon timing parameter must exceed a detector-dependent threshold, chosen to exclude surface events.

Figure 3 illustrates the efficiency (fractional signal acceptance) of these cuts as a function of energy. In this analysis we only consider events with recoil energy between 10–100 keV for the Ge detectors (7–100 keV for Si), with slightly higher thresholds imposed on some detectors with poorer noise performance.

4. – Expected backgrounds

4˙1. *Nuclear recoils*. – The rate of neutrons from cosmogenic muons has been calculated using the GEANT4 and FLUKA Monte Carlo packages, accounting for the effects of the shielding and analysis cuts and calibrated against the rate of muons observed in the scintillator panels. Based upon these simulations, the cosmogenic neutron background for this analysis is expected to be < 0.1 events. This prediction is lower than some previous estimates (*e.g.* [8]), primarily due to an improved estimate of the scintillator shield's ability to tag particle showers even when the initial muon is not detected.

Neutrons may also be produced by (α, n) and spontaneous fission processes caused by uranium and thorium contaminants in the surrounding shielding materials. Similar processes also occur in the surrounding rock, but the polyethylene shield renders their contributions negligible. Based upon current estimates and upper limits on these contaminants, we expect < 0.1 background events in this analysis from radiogenic neutrons. Improved upper limits on contamination are expected to reduce this estimate.

4˙2. *Electron recoils*. – The expected background from surface electron recoils (predominantly from the radon chain) was estimated based upon the performance of the phonon timing cut on WIMP-search events just outside of the signal region.

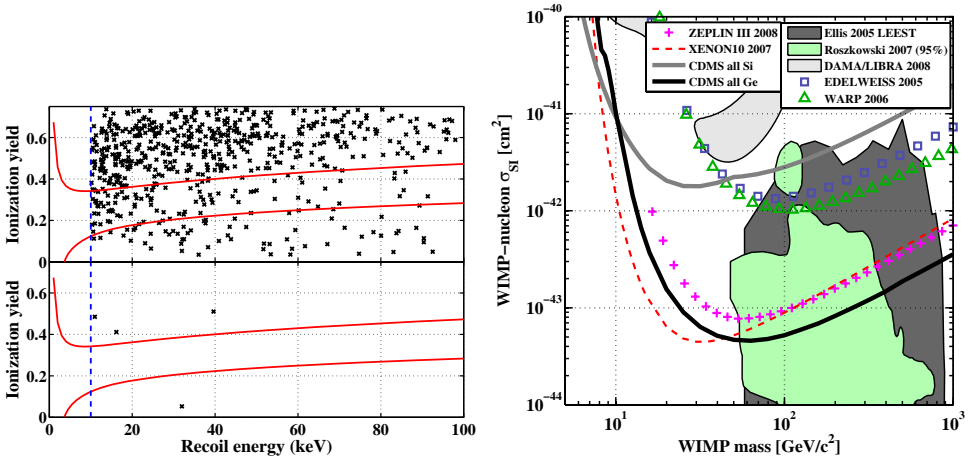

Fig. 4. – Left: distribution of low-yield events in the Ge detectors before (top) and after (bottom) application of the phonon timing cut. Solid lines indicate the ionization yield acceptance region, while the dashed line is the energy threshold of this analysis. Right: limits on spin-independent WIMP-nucleon interactions from CDMS at Soudan, alongside other recent experimental results [10-13]. Also shown for comparison are regions from representative predictions from constrained supersymmetric models [14,15] and one interpretation [16] of the DAMA/LIBRA signal claim [17].

Details of the low-statistics Bayesian estimator used are described in [9]. We expect $0.6^{+0.5}_{-0.3}(\text{stat.})^{+0.3}_{-0.2}(\text{syst.})$ electron recoil background events in Ge in this analysis, $1.1^{+0.9}_{-0.6}(\text{stat.}) \pm 0.1(\text{syst.})$ in Si.

5. – WIMP-search results

The WIMP-search data from the Ge detectors were unmasked on February 4, 2008; no WIMP candidate events were observed. The left panel of fig. 4 illustrates the low-yield events observed in the Ge detectors before (top) and after (bottom) application of the phonon timing cut. The Si detectors were unmasked on December 3, 2008; again, no candidate events were observed.

The right panel of fig. 4 illustrates the combined results from this analysis and all previous CDMS data from Soudan, interpreted as upper limits on the spin-independent (scalar) WIMP-nucleon scattering cross-section (σ_{SI}). Also shown for comparison are results from several other leading experiments, as well as predictions from recent studies of supersymmetric parameter space. The combined CDMS Ge data set requires $\sigma_{SI} < 4.6 \times 10^{-44}\,\text{cm}^2$ (46 zeptobarns) at 90% confidence for a WIMP of mass $60\,\text{GeV}/c^2$. This limit is 3.4× stronger than that from the previous CDMS data sets [18, 19], and the strongest upper limit yet set above $\sim 44\,\text{GeV}/c^2$. These data can also be interpreted as limits on spin-dependent (axial) WIMP-neutron interactions (not shown), but no new parameter space is excluded.

6. – Searches for axion-like particles

In addition to the WIMP-search analysis described above, other rare-event searches can benefit from the low background rate and excellent energy resolution of the CDMS data set (left panel of fig. 5). We have recently completed two analyses of these data

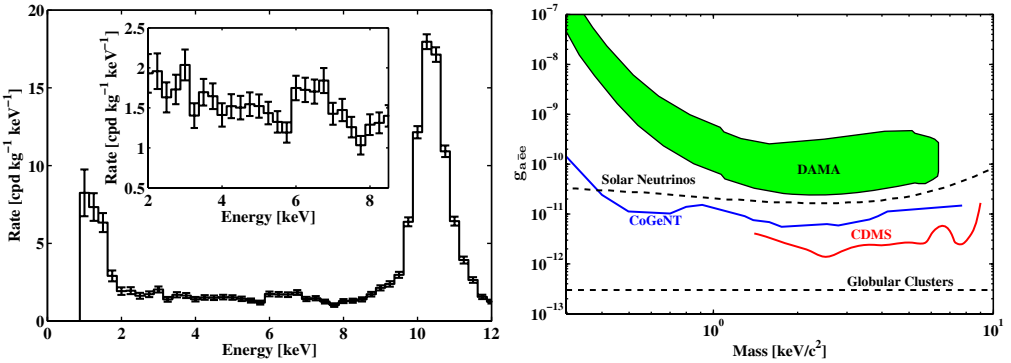

Fig. 5. – Left: rate of low-energy electron-recoils in all CDMS Ge detectors, after correcting for detection efficiency. The prominent spectral lines at left and right are known X-rays from neutron activation of Ge. The inset shows a closer view of the region from 2–8.5 keV. Right: upper limits on the axio-electric coupling of a galactic dark matter particle from CDMS, CoGeNT, and various astrophysical searches. Also shown is one interpretation of the DAMA annual modulation signal.

to search for axion-like particles [20] which deposit electromagnetic energy through conversion to photons or electron-positron pairs. CDMS sets an upper limit on an axion-like component of the galactic halo that is comparable to interpretations of the DAMA/LIBRA annual modulation signal (right panel of fig. 5). CDMS also sets interesting limits on axion-like particles produced in the Sun, based upon a novel analysis incorporating our knowledge of the absolute orientations of each detector's crystal axes.

7. – The future of CDMS

The CDMS Collaboration is currently analyzing further data from this detector array, acquired at Soudan between July 2007 and September 2008. This new data set is expected to represent an increase in sensitivity of $\sim 2.5\times$ over current limits. New results with these data are expected in summer 2009.

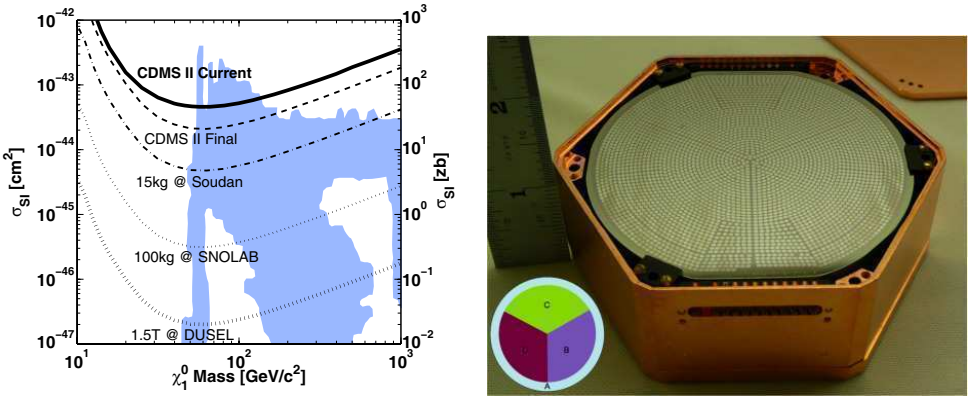

Fig. 6. – Left: projected sensitivities of proposed extensions to CDMS, assuming continued "zero-background" operation. Shaded region represents a scan of CMSSM models [22]. Right: prototype SuperCDMS ZIP. The new phonon sensor patterning is visible on the top surface and shown schematically in the inset.

Development is also underway toward larger-scale WIMP-search experiments using CDMS technology (left panel of fig. 6). The right panel of fig. 6 illustrates a next-generation ZIP detector for SuperCDMS, an upgrade of the Soudan installation to 15 kg of Ge target mass. These detectors are 2.5× thicker than current ZIPs, a change that limits the costs of fabrication and the rate of surface events in each unit of target mass. These ZIPs also incorporate improvements in phonon sensor design to increase sensitivity and simplify event position reconstruction. We are also developing technology for a 1 ton Ge experiment at the upcoming Deep Underground Science and Engineering Laboratory (DUSEL) at Homestake. Technologies under consideration include large-diameter substrates made from dislocation-free Ge, interleaved ionization electrodes [21], and multiplexed phonon sensors based upon kinetic inductance.

* * *

JF thanks the organizers for an enjoyable and informative conference. The CDMS Collaboration is supported in part by the National Science Foundation, the Department of Energy, the Swiss National Foundation, and NSERC Canada. JF is supported by a Moore Postdoctoral Fellowship in Experimental Physics.

REFERENCES

[1] Zwicky F., *Helv. Phys. Acta*, **6** (1933) 110.
[2] Olive K. A., Steigman G. and Walker T. P., *Phys. Rep.*, **333** (2000) 389.
[3] Komatsu E. *et al.*, *Astrophys. J. Suppl. S.*, **180** (2009) 330.
[4] Gaitskell R. J., *Annu. Rev. Nucl. Part. Sci.*, **54** (2004) 315.
[5] Akerib D. S. *et al.* (CDMS Collaboration), *Phys. Rev. D*, **72** (2005) 052009.
[6] Irwin K. D. and Hilton G. C., *Transition-Edge Sensors*, in *Cryogenic Particle Detection*, edited by Enss C. (Springer-Verlag, Berlin) 2005, pp. 63-149.
[7] Ahmed Z. *et al.* (CDMS Collaboration), *Phys. Rev. Lett.*, **102** (2009) 011301.
[8] Mei D. and Hime A., *Phys. Rev. D*, **73** (2006) 053004.
[9] Filippini J., Ph.D. Dissertation, University of California, Berkeley (2008).
[10] Sanglard V. *et al.* (EDELWEISS Collaboration), *Phys. Rev. D*, **71** (2005) 122002.
[11] Benetti P. *et al.* (WARP Collaboration), *Astropart. Phys.*, **28** (2008) 495.
[12] Lebedenko V. N. *et al.* (ZEPLIN III Collaboration), *Phys. Rev. D*, **80** (2009) 052010.
[13] Angle J. *et al.* (XENON10 Collaboration), *Phys. Rev. Lett.*, **100** (2008) 091301.
[14] Ellis J. R. *et al.*, *Phys. Rev. D*, **71** (2005) 095007.
[15] Roszkowski L. *et al.*, *JHEP*, **07** (2007) 075.
[16] Savage C. *et al.*, *JCAP*, **0904** (2009) 010.
[17] Bernabei *et al.* (DAMA/LIBRA Collaboration), *Eur. Phys. J. C*, **56** (2008) 333.
[18] Akerib D. S. *et al.* (CDMS Collaboration), *Phys. Rev. Lett.*, **93** (2004) 211301.
[19] Akerib D. S. *et al.* (CDMS Collaboration), *Phys. Rev. Lett.*, **96** (2006) 011302.
[20] Ahmed Z. *et al.* (CDMS Collaboration), *Phys. Rev. Lett.*, **103** (2009) 141802.
[21] Brink P. L. *et al.*, *Nucl. Instrum. Methods A*, **559** (2006) 414.
[22] Baltz E. A. and Gondolo P., *JHEP*, **10** (2004) 052.

IL NUOVO CIMENTO Vol. 32 C, N. 5-6 Settembre-Dicembre 2009
DOI 10.1393/ncc/i2010-10539-7

Colloquia: LaThuile09

Neutrino magnetic moment and neutrino energy quantization in rotating media

I. Balantsev([1]), Yu. Popov([2]) and A. Studenikin([1])

([1]) *Department of Theoretical Physics, Moscow State University - Moscow, Russia*
([2]) *Skobeltsyn Institute of Nuclear Physics, Moscow State University - Moscow, Russia*

(ricevuto il 10 Novembre 2009; pubblicato online il 18 Gennaio 2010)

Summary. — After a brief discussion on neutrino electromagnetic properties, we consider the problem of neutrino energy spectra in different media. It is shown that in two particular cases (*i.e.*, neutrino propagation in a) transversally moving with increasing speed medium and b) rotating medium) neutrino energies are quantized. These phenomena can be important for astrophysical applications, for instance, for physics of rotating neutron stars.

PACS 12.20.-m – Quantum electrodynamics.
PACS 13.15.+g – Neutrino interactions.

1. – Introduction—neutrino electromagnetic properties

Initially the problem considered in this paper has originated from the studies of neutrino electromagnetic properties and related items. There is no doubt that the recent experimental and theoretical studies of flavour conversion in solar, atmospheric, reactor and accelerator neutrino fluxes give strong evidence of nonzero neutrino mass. A massive neutrino can have nontrivial electromagnetic properties [1]. A recent review on neutrino electromagnetic properties can be found in [2]. The present situation in the domain is characterized by the fact that in spite of reasonable efforts in studies of neutrino electromagnetic properties, there is no any experimental confirmation in favour of neutrino electromagnetic characteristics being nonvanishing. However, it is very plausible to assume that a neutrino may have nonzero electromagnetic properties. In particular, it seems very reasonable that a neutrino has a nonvanishing magnetic moment [2, 3].

Neutrino magnetic moment interaction effects. If a neutrino has nontrivial electromagnetic properties, notably nonvanishing magnetic (or electric) transition dipole moments or nonzero millicharge and charge radius, then a direct neutrino coupling to photons becomes possible and several processes exist important for applications [4]. A set of typical and most important neutrino electromagnetic processes involving the direct neutrino couplings with photons is: 1) a neutrino radiative decay $\nu_1 \to \nu_2 + \gamma$, neutrino

Cherenkov radiation in external environment (plasma and/or electromagnetic fields), 2) photon (plasmon) decay to a neutrino-antineutrino pair in plasma $\gamma \to \nu\bar{\nu}$, 3) neutrino scattering off electrons (or nuclei), 4) neutrino spin (spin-flavor) precession in magnetic field. Another very important phenomenon is the resonant amplification of the neutrino spin-flavour oscillations in matter that was first considered in [5].

Note a new mechanism of electromagnetic radiation produced by a neutrino moving in matter and originated due to neutrino magnetic moment [6-8]. It was termed the spin light of neutrino in matter ($SL\nu$) [6]. Although the $SL\nu$ was considered first within quasiclassical approach, it was clear that this is a quantum phenomenon by its nature. The quantum theory of this radiation has been elaborated [7] (see also [8]) within development [9, 10] of a quite powerful method that implies the use of the exact solutions of the modified Dirac equation for the neutrino wave function in matter. For elaboration of the quantum theory of the $SL\nu$ one has to find the solution of the quantum equation for the neutrino wave function and for the neutrino energy spectrum in medium.

2. – Quantum equation for neutrino in medium

The modified Dirac equation for the neutrino wave function exactly accounting for the neutrino interaction with matter [7]:

$$\left\{ i\gamma_\mu \partial^\mu - \frac{1}{2}\gamma_\mu(1+\gamma_5) f^\mu - m \right\} \Psi(x) = 0. \tag{1}$$

This is the most general form of the equation for the neutrino wave function in which the effective potential $V_\mu = \frac{1}{2}(1+\gamma_5) f_\mu$ includes both the neutral and charged current interactions of neutrino with the background particles and which can also account for effects of matter motion and polarization. It should be mentioned that other modifications of the Dirac equation were previously used in [11] for studies of the neutrino dispersion relations, neutrino mass generation and neutrino oscillations in the presence of matter.

In the case of matter composed of electrons, neutrons, and protons and for the neutrino interaction with background particles given by the standard model supplied with the singlet right-handed neutrino one has

$$f^\mu = \sqrt{2} G_F \sum_{f=e,p,n} j_f^\mu q_f^{(1)} + \lambda_f^\mu q_f^{(2)}, \tag{2}$$

where

$$q_f^{(1)} = \left(I_{3L}^{(f)} - 2Q^{(f)} \sin^2\theta_W + \delta_{ef} \right), \qquad q_f^{(2)} = -\left(I_{3L}^{(f)} + \delta_{ef} \right), \tag{3}$$

$$\delta_{ef} = \begin{cases} 1 & \text{for } f = e, \\ 0 & \text{for } f = n, p. \end{cases}$$

Here $I_{3L}^{(f)}$ and $Q^{(f)}$ are, respectively, the values of the isospin third components and the electric charges of matter particles ($f = e, n, p$). The corresponding currents j_f^μ and

polarization vectors λ_f^μ are

$$j_f^\mu = (n_f, n_f \mathbf{v}_f), \qquad \lambda_f^\mu = \left(n_f(\boldsymbol{\zeta}_f \mathbf{v}_f), n_f \boldsymbol{\zeta}_f \sqrt{1 - v_f^2} + \frac{n_f \mathbf{v}_f (\boldsymbol{\zeta}_f \mathbf{v}_f)}{1 + \sqrt{1 - v_f^2}} \right), \tag{4}$$

where θ_W is the Weinberg angle. In the above formulas (4), n_f, $\mathbf{v}_f$ and $\boldsymbol{\zeta}_f$ ($0 \leq |\boldsymbol{\zeta}_f|^2 \leq 1$) stand, respectively, for the invariant number densities, average speeds and polarization vectors of the matter components.

In the case of matter at rest it is possible to solve the modified Dirac equation for different types of neutrinos moving in matter of different composition, as is shown in [7]. The energy spectrum of different neutrinos moving in matter is given by

$$E_\varepsilon = \varepsilon \eta \sqrt{\mathbf{p}^2 \left(1 - s\alpha \frac{m}{p}\right)^2 + m^2} + \alpha m. \tag{5}$$

In the general case of matter composed of electrons, neutrons and protons the matter density parameter α for different neutrino species is

$$\alpha_{\nu_e, \nu_\mu, \nu_\tau} = \frac{1}{2\sqrt{2}} \frac{G_F}{m} (n_e(4 \sin^2 \theta_W + \varrho) + n_p(1 - 4 \sin^2 \theta_W) - n_n), \tag{6}$$

where $\varrho = 1$ for the electron neutrino and $\varrho = -1$ for the muon and tau neutrinos.

The value $\eta = \mathrm{sign}(1 - s\alpha \frac{m}{p})$ in (5) provides a proper behavior of the wave function in the hypothetical massless case. The values $s = \pm 1$ specify the two neutrino helicity states, ν_+ and ν_-. The quantity $\varepsilon = \pm 1$ splits the solutions into the two branches that in the limit of the vanishing matter density, $\alpha \to 0$, reproduce the positive- and negative-frequency solutions, respectively.

In the next two sections we apply the developed method of exact solutions to two particular cases when neutrino is propagating a medium transversally moving with increasing speed [12, 9] and in a rotating medium of constant density. In both cases the obtained energy spectrum of the neutrino is quantized like the energy spectrum of an electron is quantized in a constant magnetic field.

3. – Neutrino quantum states in a medium transversally moving with increasing speed

First we consider a neutrino propagating in a medium composed of neutrons that move perpendicular to the neutrino path with linearly increasing speed. This can be regarded as the first approach to modelling of neutrino propagation inside a rotating neutron star [12, 9]. The corresponding modified Dirac equation for the neutrino wave function is given by (1) with the matter potential accounting for rotation,

$$f^\mu = -G(n, n\mathbf{v}), \qquad \mathbf{v} = (\omega y, 0, 0), \tag{7}$$

where $G = \frac{G_F}{\sqrt{2}}$. Here ω is the angular frequency of matter rotation around the OZ axis, it also is supposed that the neutrino propagates along the OY axis. For the neutrino

wave function components $\psi(x)$ we get from the modified Dirac equation (1), a set of equations([1]),

$$
\begin{aligned}
(8) \qquad [i(\partial_0 - \partial_3) + Gn]\psi_1 + [-(i\partial_1 + \partial_2) + Gn\omega y]\psi_2 &= m\psi_3,\\
[(-i\partial_1 + \partial_2) + Gn\omega y]\,\psi_1 + [i(\partial_0 + \partial_3) + Gn]\psi_2 &= m\psi_4,\\
i(\partial_0 + \partial_3)\psi_3 + (i\partial_1 + \partial_2)\psi_4 &= m\psi_1,\\
(i\partial_1 - \partial_2)\psi_3 + i(\partial_0 - \partial_3)\psi_4 &= m\psi_2.
\end{aligned}
$$

In a general case, it is not a trivial task to find solutions of this set of equations.

The problem is reasonably simplified in the limit of a very small neutrino mass, *i.e.* when the neutrino mass can be ignored in the left-hand side of (8) with respect to the kinetic and interaction terms in the right-hand sides of these equations. In this case two pairs of the neutrino wave function components decouple one from each other and four equations (8) split into the two independent sets of two equations, that couple together the neutrino wave function components in pairs, (ψ_1, ψ_2) and (ψ_3, ψ_4).

The second pair of eqs. (8) does not contain a matter term and is attributed to the sterile right-handed chiral neutrino state, ψ_R. The corresponding solution can be taken in the plain-wave form

$$
(9) \qquad \psi_R \sim L^{-\frac{3}{2}} \exp[i(-p_0 t + p_1 x + p_2 y + p_3 z)]\psi,
$$

where p_μ is the neutrino momentum. Then for the components ψ_3 and ψ_4 we obtain from (8) the following equations:

$$
\begin{aligned}
(10) \qquad (p_0 - p_3)\psi_3 - (p_1 - ip_2)\psi_4 &= 0,\\
-(p_1 + ip_2)\psi_3 + (p_0 + p_3)\psi_4 &= 0.
\end{aligned}
$$

Finally, from (10) for the sterile right-handed neutrino we get

$$
(11) \qquad \psi_R = \frac{\mathrm{e}^{-ipx}}{L^{3/2}\sqrt{2p_0(p_0 - p_3)}} \begin{pmatrix} 0 \\ 0 \\ -p_1 + ip_2 \\ p_3 - p_0 \end{pmatrix},
$$

where $px = p_\mu x^\mu$, $p_\mu = (p_0, p_1, p_2, p_3)$ and $x_\mu = (t, x, y, z)$. This solution, as it should do, has the vacuum dispersion relation.

In the neutrino mass vanishing limit the first pair of eqs. (8) corresponds to the active left-handed neutrino. The form of these equations is similar to the corresponding equations for a charged particle (*e.g.*, an electron) moving in a constant magnetic field B given by the potential $\boldsymbol{A} = (By, 0, 0)$ (see, for instance, [13]). To display the analogy, we note that in our case the matter current component $n\boldsymbol{v}$ plays the role of the vector potential $\boldsymbol{A}$. The existed analogy between an electron dynamics in an external electromagnetic field and a neutrino dynamics in background matter is discussed in [9].

([1]) The chiral representation for Dirac matrices is used.

The solution of the first pair of eqs. (8) can be taken in the form

$$\psi_L \sim \frac{1}{L}\exp[i(-p_0 t + p_1 x + p_3 z)]\psi(y), \tag{12}$$

and for the components ψ_1 and ψ_2 of the neutrino wave function we obtain from (8) the following equations:

$$\begin{aligned}(p_0 + p_3 + Gn)\psi_1 - \sqrt{\rho}\left(\frac{\partial}{\partial\eta} - \eta\right)\psi_2 = 0,\\ \sqrt{\rho}\left(\frac{\partial}{\partial\eta} + \eta\right)\psi_1 + (p_0 - p_3 + Gn)\psi_2 = 0,\end{aligned} \tag{13}$$

where

$$\eta = \sqrt{\rho}\left(x_2 + \frac{p_1}{\rho}\right), \quad \rho = Gn\omega. \tag{14}$$

For the wave function we finally get

$$\psi_L = \frac{\rho^{\frac{1}{4}}\mathrm{e}^{-ip_0 t + ip_1 x + ip_3 z}}{L\sqrt{(p_0 - p_3 + Gn)^2 + 2\rho N}}\begin{pmatrix}(p_0 - p_3 + Gn)u_N(\eta)\\ -\sqrt{2\rho N}u_{N-1}(\eta)\\ 0\\ 0\end{pmatrix}, \tag{15}$$

where $u_N(\eta)$ are Hermite functions of order N. For the energy of the active left-handed neutrino we get

$$p_0 = \sqrt{p_3^2 + 2\rho N} - Gn, \quad N = 0, 1, 2, \ldots . \tag{16}$$

The energy depends on the neutrino momentum component p_3 along the rotation axis of matter and the quantum number N that determines the magnitude of the neutrino momentum in the orthogonal plane. For description of antineutrinos one has to consider the "negative sign" energy eigeinvalues (see similar discussion in sect. **2**). Thus, the energy of an electron antineutrino in the rotating matter composed of neutrons is given by

$$\tilde{p}_0 = \sqrt{p_3^2 + 2\rho N} + Gn, \quad N = 0, 1, 2, \ldots . \tag{17}$$

Obviously, generalization for different other neutrino flavours and matter composition is just straightforward (see (4) and (6)).

Thus, it is shown [12] that the transversal motion of an active neutrino and antineutrino is quantized in moving matter very much like an electron energy is quantized in a constant magnetic field that corresponds to the relativistic form of the Landau energy levels (see [13]).

4. – Neutrino energy in a rotating medium

Now we consider a more consistent model of a neutrino motion in a rotating matter. For this case we choose the effective matter potential in (1) in the following form:

$$f^\mu = -G(n, n\mathbf{v}), \qquad \mathbf{v} = (-\omega y, \omega x, 0). \tag{18}$$

Contrary to the case considered in the previous section, eq. (1) with the potential (18) describes the case when a neutrino is moving in a rotating medium. It is shown below how eq. (1) with (18) can be solved and the corresponding neutrino energy spectrum is obtained.

The solution of eq. (1) with (18) can be sought in the form

$$\psi(t,x,y,z) = \mathrm{e}^{-ip_0 t + ip_3 z} \begin{pmatrix} \psi_1(x,y) \\ \psi_2(x,y) \\ \psi_3(x,y) \\ \psi_4(x,y) \end{pmatrix}. \tag{19}$$

Substituting (19) into (1) with (18) and using the explicit form of the Dirac matrices in the chiral representation, we arrive at a system of linear equations for the neutrino wave function components:

$$\begin{aligned} -(p_0+p_3+Gn)\psi_1 + i\left\{\left(\frac{\partial}{\partial x} - i\frac{\partial}{\partial y}\right) + Gn\omega(x-iy)\right\}\psi_2 &= -m\psi_3, \\ i\left\{\left(\frac{\partial}{\partial x} + i\frac{\partial}{\partial y}\right) - Gn\omega(x+iy)\right\}\psi_1 + (p_3-p_0-Gn)\psi_2 &= -m\psi_4, \\ (p_0-p_3)\psi_3 + i\left(\frac{\partial}{\partial x} - i\frac{\partial}{\partial y}\right)\psi_4 &= m\psi_1, \\ +i\left(\frac{\partial}{\partial x} + i\frac{\partial}{\partial y}\right)\psi_3 + (p_0+p_3)\psi_4 &= m\psi_2. \end{aligned} \tag{20}$$

In the polar coordinates $x + iy = r\mathrm{e}^{i\phi}$, $x - iy = r\mathrm{e}^{-i\phi}$ one has

$$\frac{\partial}{\partial x} + i\frac{\partial}{\partial y} = \mathrm{e}^{i\phi}\left(\frac{\partial}{\partial r} + \frac{i}{r}\frac{\partial}{\partial \phi}\right), \qquad \frac{\partial}{\partial x} - i\frac{\partial}{\partial y} = \mathrm{e}^{-i\phi}\left(\frac{\partial}{\partial r} - \frac{i}{r}\frac{\partial}{\partial \phi}\right), \tag{21}$$

and the system of eqs. (20) transforms to

$$\begin{aligned} -(p_0+p_3+Gn)\psi_1 + i\mathrm{e}^{-i\phi}\left\{\frac{\partial}{\partial r} - \frac{i}{r}\frac{\partial}{\partial \phi} + \rho r\right\}\psi_2 &= -m\psi_3, \\ i\mathrm{e}^{i\phi}\left\{\frac{\partial}{\partial r} + \frac{i}{r}\frac{\partial}{\partial \phi} - \rho r\right\}\psi_1 + (p_3-p_0-Gn)\psi_2 &= -m\psi_4, \\ (p_0-p_3)\psi_3 + i\mathrm{e}^{-i\phi}\left(\frac{\partial}{\partial r} - \frac{i}{r}\frac{\partial}{\partial \phi}\right)\psi_4 &= m\psi_1, \\ +i\mathrm{e}^{i\phi}\left(\frac{\partial}{\partial r} + \frac{i}{r}\frac{\partial}{\partial \phi}\right)\psi_3 + (p_0+p_3)\psi_4 &= m\psi_2. \end{aligned} \tag{22}$$

It is possible to show that the operator of the total momentum $J_z = L_z + S_z$, where $L_z = -i\frac{\partial}{\partial\phi}$, $S_z = \frac{1}{2}\sigma_3$, commutes with the corresponding Hamiltonian of the considered system. Therefore the solutions can be taken in the form

$$\begin{pmatrix}\psi_1\\ \psi_2\\ \psi_3\\ \psi_4\end{pmatrix} = \begin{pmatrix}i\chi_1(r)e^{i(l-1)\phi}\\ \chi_2(r)e^{il\phi}\\ i\chi_3(r)e^{i(l-1)\phi}\\ \chi_4(r)e^{il\phi}\end{pmatrix}, \tag{23}$$

that are the eigenvectors for the total momentum operator J_z with the corresponding eigenvalues $l - \frac{1}{2}$. After substitution of (23) the system (22) can be rewritten in the following form:

$$\begin{aligned}
-(p_0 + p_3 + Gn)\chi_1 + \left\{\frac{\mathrm{d}}{\mathrm{d}r} + \frac{l}{r} + \rho r\right\}\chi_2 &= -m\chi_3,\\
\left\{\frac{\mathrm{d}}{\mathrm{d}r} - \frac{l-1}{r} - \rho r\right\}\chi_1 + (p_0 - p_3 + Gn)\chi_2 &= m\chi_4,\\
(p_0 - p_3)\chi_3 + \left(\frac{\mathrm{d}}{\mathrm{d}r} + \frac{l}{r}\right)\chi_4 &= m\chi_1,\\
\left(\frac{\mathrm{d}}{\mathrm{d}r} - \frac{l-1}{r}\right)\chi_3 - (p_0 + p_3)\chi_4 &= -m\chi_2.
\end{aligned} \tag{24}$$

For further consideration it is convenient to introduce the rising and decreasing operators

$$R^+ = \frac{\mathrm{d}}{\mathrm{d}r} - \frac{l-1}{r} - \rho r, \qquad R^- = \frac{\mathrm{d}}{\mathrm{d}r} + \frac{l}{r} + \rho r. \tag{25}$$

After application of the decreasing R^- and increasing R^+ operators to the second and first equations of (22) correspondingly, one gets

$$\begin{aligned}
R^-R^+\chi_1 + ((p_0 + Gn)^2 - p_3^2 - m^2)\chi_1 &= m(Gn\chi_3 + \rho r\chi_4),\\
R^+R^-\chi_2 + ((p_0 + Gn)^2 - p_3^2 - m^2)\chi_2 &= m(Gn\chi_4 + \rho r\chi_3).
\end{aligned} \tag{26}$$

Note that the system (24), as well as the system (8), can be solved exactly in the limit of vanishing neutrino mass $m \to 0$. In order to find the nonzero-mass correction to the energy spectrum of a neutrino in a bound state in matter, the neutrino square integrable wave function should be found. Therefore, in analogy with the zero-mass case we take $\chi_3 = \chi_4 = 0$ in the lowest order of perturbation series expansion. Thus we arrive at the system

$$\begin{aligned}
R^-R^+\chi_1 + ((p_0 + Gn)^2 - p_3^2 - m^2)\chi_1 &= 0,\\
R^+R^-\chi_2 + ((p_0 + Gn)^2 - p_3^2 - m^2)\chi_2 &= 0.
\end{aligned} \tag{27}$$

The solution of (27) can be written in the form

$$\begin{pmatrix}\chi_1\\ \chi_2\end{pmatrix} = \begin{pmatrix}C_1\mathcal{L}_s^{l-1}(\rho r^2)\\ C_2\mathcal{L}_s^{l}(\rho r^2)\end{pmatrix}, \tag{28}$$

where $\mathcal{L}_s^l$ are the Laguerre functions [13]. After substitution of (28) into (27) and taking into account the properties of the increasing and decreasing rising operators,

$$R^+\mathcal{L}_s^{l-1}(\rho r^2) = -2\sqrt{\rho(s+l)}\,\mathcal{L}_s^l(\rho r^2), \qquad R^-\mathcal{L}_s^l(\rho r^2) = 2\sqrt{\rho(s+l)}\,\mathcal{L}_s^{l-1}(\rho r^2), \tag{29}$$

we get from (27) the equation for the neutrino energy spectrum in matter:

$$m^2 + p_3^2 + 4(s+l)\rho - (p_0 + Gn)^2 = 0. \tag{30}$$

Solving this equation we get for the neutrino energies

$$p_0 = \pm\sqrt{m^2 + p_3^2 + 4N\rho} - Gn, \quad N = 0, 1, 2, \ldots, \tag{31}$$

where the quantum number $N = s + l$ is introduced. As usually, two signs in the solution correspond to the neutrino and antineutrino energies, correspondingly,

$$p_0 = \sqrt{m^2 + p_3^2 + 4N\rho} - Gn, \qquad \tilde{p}_0 = \sqrt{m^2 + p_3^2 + 4N\rho} + Gn. \tag{32}$$

From the obtained energy spectrum it is just straightforward that the transversal motion momentum of an antineutrino is given by

$$\tilde{p}_\perp = 2\sqrt{NG\omega}. \tag{33}$$

The quantum number N determines also the radius of the quasiclassical orbit in matter (it is supposed that $N \gg 1$ and $p_3 = 0$),

$$R = \sqrt{\frac{N}{Gn\omega}}. \tag{34}$$

It follows that antineutrinos can have bound orbits inside a rotating star. To make an estimation of magnitudes, let us consider a model of a rotating neutron star with radius $R_{NS} = 10\,\mathrm{km}$, matter density $n = 10^{37}\,\mathrm{cm}^{-3}$ and angular frequency $\omega = 2\pi \times 10^3\,\mathrm{s}^{-1}$. For this set of parameters, the radius of an orbit is less than the typical star radius R_{NS} if the quantum number $N \leq N_{\max} = 10^{10}$. Therefore, antineutrinos that occupy orbits with $N \leq 10^{10}$ can be bounded inside the star. The scale of the bounded antineutrinos energy estimated by (32) is of the order $\tilde{p}_0 \sim 1\,\mathrm{eV}$. It should be underlined that within the quasiclassical approach the neutrino binding on circular orbits is due to an effective force that is orthogonal to the particle speed. Note that there is another mechanism of neutrinos binding inside a neutron star when the effect is produced by a gradient of the matter density (see the last paper in [11]). A discussion on the "matter-induced Lorentz force" that can be introduced in order to explain a neutrino motion on quasiclassical circular orbits can be found in [9].

We argue that the effect of a neutrino energy quantization can have important consequences for physics of rotating neutron stars.

* * *

One of the authors (AS) thanks G. Bellettini, G. Chiarelli, M. Greco and G. Isidori for the kind invitation to participate in the XXIII Rencontres de Physique

de La Vallée D'Aoste on Results and Perspectives in Particle Physics and also thanks all the organizers for their hospitality in La Thuile. The authors are also thankful to A. Grigoriev for fruitful discussions.

REFERENCES

[1] Marciano W. J. and Sanda A. I., *Phys. Lett. B*, **67** (1977) 303; Lee B. W. and Shrock R. E., *Phys. Rev. D*, **16** (1977) 1444; Fujikawa K. and Shrock R. E., *Phys. Rev. Lett.*, **45** (1980) 963.
[2] Giunti C. and Studenikin A., hep-ph/0812.3646 preprint (2008).
[3] Studenikin A., *Nucl. Phys. B (Proc. Suppl.)*, **188** (2009) 220.
[4] Raffelt G., *Phys. Rev. Lett.*, **64** (1990) 2856; *Stars as Laboratories for Fundamental Physics*, in *Univ. of Chicago Press*, edited by Schellinger P., Thomas G. and Tryneski J. (Chicago, USA) 1996; Raffelt G., *Phys. Rep.*, **320** (1999) 319; Haft M., Raffelt G. and Wiess A., *Astrophys. J.*, **425** (1994) 222.
[5] Lim C. and Marciano W., *Phys. Rev. D*, **37** (1988) 1368; Akhmedov E., *Phys. Lett.*, **213** (1988) 64.
[6] Lobanov A. and Studenikin A., *Phys. Lett. B*, **564** (2003) 27; **601** (2004) 171; Dvornikov M., Grigoriev A. and Studenikin A., *Int. J. Mod. Phys. D*, **14** (2005) 309.
[7] Studenikin A. and Ternov A., *Phys. Lett. B*, **608** (2005) 107, hep-ph/0410297, hep-ph/0410296; Grigoriev A., Studenikin A. and Ternov A., *Phys. Lett. B*, **622** (2005) 199, hep-ph/0502231; *Gravit. Cosmol.*, **11** (2005) 132; *Phys. Atom. Nucl.*, **69** (2006) 1940.
[8] Lobanov A., *Dokl. Phys.*, **50** (2005) 286; *Phys. Lett. B*, **619** (2005) 136.
[9] Studenikin A., *J. Phys. A: Math. Theor.*, **41** (2008) 164047.
[10] Studenikin A., *J. Phys. A: Math. Gen.*, **39** (2006) 6769; Grigoriev A., Studenikin A. and Ternov A., *Phys. Atom. Nucl.*, **72** (2009) 718.
[11] Mannheim P., *Phys. Rev. D*, **37** (1988) 1935; Nötzold D. and Raffelt G., *Nucl. Phys. B*, **307** (1988) 924; Nieves J., *Phys. Rev. D*, **40** (1989) 866; Chang L. N. and Zia R. K., *Phys. Rev. D*, **38** (1988) 1669; Pantaleone J., *Phys. Lett. B*, **268** (1991) 227; Pantaleone J., *Phys. Rev. D*, **46** (1992) 510; Kiers K. and Weiss N., *Phys. Rev. D*, **56** (1997) 5776; Kiers K. and Tytgat M., *Phys. Rev. D*, **57** (1998) 5970; Oraevsky V., Semikoz V. and Smorodinsky Ya., *Phys. Lett. B*, **277** (1989) 255; Haxton W. and Zhang W.-M., *Phys. Rev. D*, **43** (1991) 2484; Loeb A., *Phys. Rev. Lett.*, **64** (1990) 115.
[12] Grigoriev A., Savochkin A. and Studenikin A., *Russ. Phys. J.*, **50** (2007) 845.
[13] Sokolov A. A and Ternov I. M, *Synchrotron Radiation* (Pergamon Press, Oxford, UK) 1968.

IL NUOVO CIMENTO Vol. 32 C, N. 5-6 Settembre-Dicembre 2009
DOI 10.1393/ncc/i2010-10538-8

Colloquia: LaThuile09

Recent results from the OPERA experiment

F. Di Capua on behalf of the OPERA Collaboration
INFN, Sezione di Napoli - Napoli, Italy

(ricevuto il 10 Novembre 2009; pubblicato online il 18 Gennaio 2010)

Summary. — Several experiments carried out in the last decades with atmospheric and accelerator neutrinos, as well as with solar and reactor neutrinos, contributed to our present understanding of neutrino mixing (see, *e.g.*, Strumia and Vissani [arXiv:hep-ph/0606054] for a review). The OPERA experiment aims at measuring the first detection of neutrino oscillation in appearance mode through the detection of ν_τ in an almost pure ν_μ beam produced at CERN SPS (CNGS), 730 km far from the detector. The ν_τ appearance signal is detected through the measurement of the decay daughter particles of the τ lepton produced in CC ν_τ interactions. Since the short-lived τ particle has, at the energy of the beam, an average decay length of about ~ 1 mm, a micrometric detection resolution is needed. Runs with CNGS neutrinos were succesfully carried out in 2007 and 2008 with the detector fully operational with its related facilities for the emulsion handling and analysis. After a brief description of the beam and of the experimental setup we report on the collection, reconstruction and analysis procedures of first samples of neutrino interaction events.

PACS 13.15.+g – Neutrino interactions.
PACS 14.60.Lm – Ordinary neutrinos (ν_e, ν_μ, ν_τ).
PACS 29.40.Rg – Nuclear emulsions.

1. – Introduction

Evidence for neutrino oscillations have been unambiguously observed by several experiments [1], by using atmospheric and accelerator neutrinos, as well as with solar and reactor neutrinos. However, as far as the atmospheric neutrino sector is concerned, despite the fact that there are many experimental indications supporting the $\nu_\mu \to \nu_\tau$ solution, a direct evidence of the ν_τ appearance is still missing.

OPERA [2] uses the long-baseline ($L = 730$ km) CNGS neutrino beam [3] from CERN to LNGS. The beam is designed to provide $4.5 \cdot 10^{19}$ proton-on-target/year (p.o.t./y) with a running time of 200 days per year. The beam parameters have been optimized in order to maximize the number of ν_τ charged current interactions in the OPERA detector. The average neutrino energy is $\langle E \rangle = 17$ GeV with a small contamination of $\overline{\nu}_\mu$ (4.0%) and of ν_e, $\overline{\nu}_e$ (less than 1%).

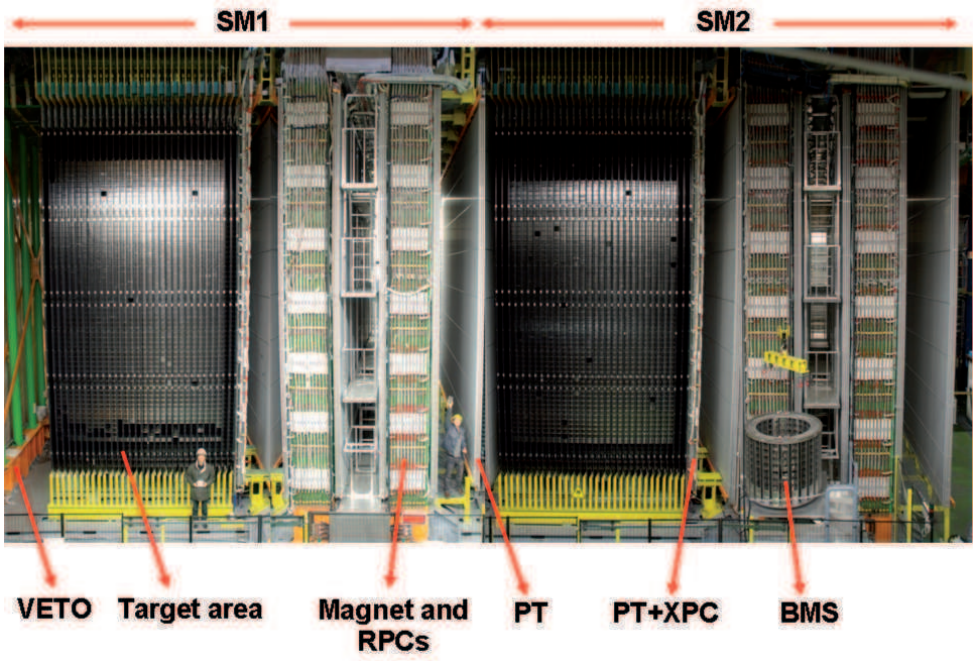

Fig. 1. – View of the OPERA detector; the neutrino beam enters from the left. The upper horizontal lines indicate the position of the two identical supermodules (SM1 and SM2). The "target area" is made of walls filled with ECC bricks interleaved with planes of plastic scintillators (TT). Arrows show the position of the VETO planes, the drift tubes (PT) pulled alongside the XPC, the magnets and the RPC installed between the magnet iron slabs. The Brick Manipulator System (BMS) is also visible. See [2] for more details.

In 5 years of data taking, OPERA is able to observe 10 to 15 ν_τ events after oscillation at full mixing in the range $2.5 \times 10^{-3} < \Delta m^2 < 3 \times 10^{-3}\,\mathrm{eV}^2$, with a total background of 0.75 events.

2. – The OPERA detector

The detection of the short-lived τ lepton ($c\tau = 87.11\,\mu\mathrm{m}$) produced in the charged-current (CC) interaction of a ν_τ is mandatory. This sets two conflicting requirements: a large target mass to collect enough statistics and an extremely high spatial accuracy to observe the short-lived τ lepton.

The τ is identified by the detection of its characteristic decay topologies either in one prong (electron, muon or hadron) or in three-prongs; its short track is measured with a large mass target made of 1 mm thick lead plates (target mass and absorber material) interspaced with thin nuclear emulsion films (high-accuracy tracking devices). This detector is historically called Emulsion Cloud Chamber (ECC).

The OPERA apparatus (fig. 1) consists of 2 identical parts called *super-modules* (SMs). Each super-module consists of a target section of about 625 tons made of emulsion/lead bricks, of a scintillator strips tracker detector (TT) and of a muon spectrometer. TT planes serve as trigger devices and allow selecting the brick containing a neutrino

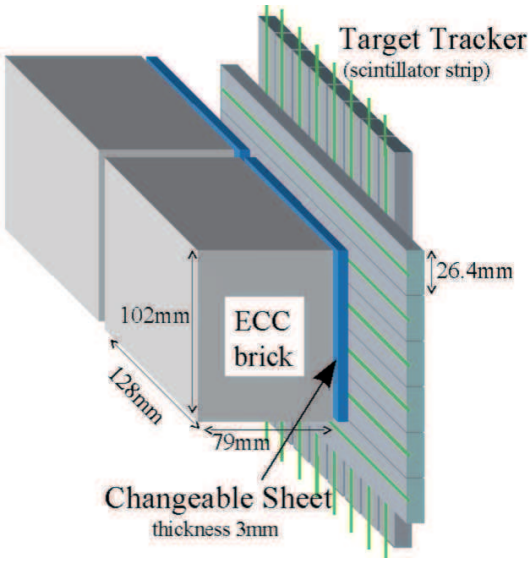

Fig. 2. – Schematic view of two bricks with their Changeable Sheets and target tracker planes.

interaction. The muon spectrometer at the downstream end of each SM, allows measuring charge and momentum of penetrating tracks. A large size anti-coincidence detector (VETO), made of two glass RPC planes mounted in front of the first target, allows to reject charged particles originating from outside the target fiducial region coming from neutrino interactions in the surrounding rock material.

Each target section is a sequence of vertical steel containers (walls) hosting the bricks, interleaved with double-layered plastic scintillator strips planes as Target Trackers (TT). Each brick wall contains $\sim$ 2900 bricks for a total of 150000 bricks in the whole apparatus.

A target brick consists of 56 lead plates of 1 mm thickness interleaved with 57 emulsion films [4]. The transverse dimensions of a brick are $12.8 \times 10.2\,\mathrm{cm}^2$ and the thickness along the beam z direction is 7.9 cm (about 10 radiation lengths). The weight is 8.3 kg.

An OPERA film has 2 emulsion layers (each 44 μm thick) on both sides of a transparent triacetylcellulose base (205 μm thick). The total thickness is $293 \pm 5\,\mu$m. The large amount of emulsion films used, translated in surface, covers 100,000 m^2.

In order to reduce the emulsion scanning load the use of Changeable Sheets (CS) film interfaces [5], successfully applied in the CHORUS experiment [6], was extended to OPERA. Tightly packed doublets of emulsion films are glued to the downstream face of each brick and can be removed without opening the brick. The global layout of brick, CS and TT is schematically shown in fig. 2.

The scanning of emulsion films is performed with two different types of automatic microscopes: the European Scanning System (ESS) [7, 8] and the Japanese S-UTS [9]. Microscope systems have comparable performances ensuring a scanning speed two order of magnitude greater than that of the systems used in past experiments, and a spatial and angular resolution of the order of $\sim 1\,\mu$m and 1 mrad, respectively.

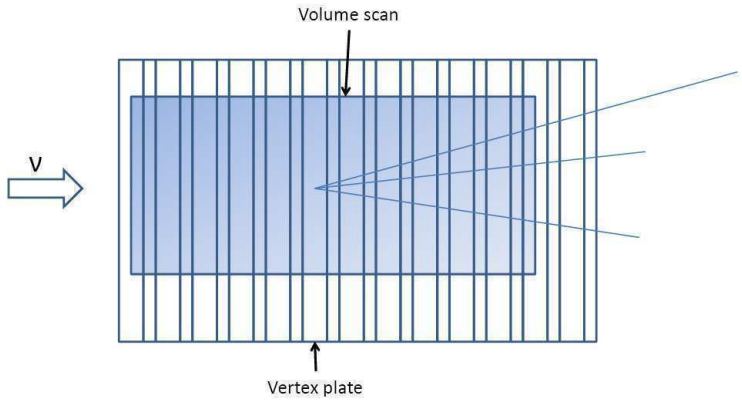

Fig. 3. – Schematic view of the volume scan performed around the stopping point of the track.

3. – Event analysis chain

We describe in the following the breakdown of the different steps carried out to analyze neutrino interaction events from the identification of the "fired" brick up to the detailed kinematical analysis of the vertex in the emulsion films.

Once a trigger in the electronic detectors is selected to be compatible with an interaction inside a brick, electronic detector data are processed by a software reconstruction program that selects the brick with the highest probability to contain the neutrino interaction vertex. This brick is removed from the target wall by the BMS and exposed to X-rays for film-to-film alignment. There are two independent X-ray exposures: the first one ensures a common reference system to the CS film doublet and the most downstream film of the brick (frontal exposure); the second one produces thick lateral marks on the brick edges, used for film to film alignment inside the brick.

After the first X-ray exposure the CS doublet is detached from the brick and developed underground, while the brick is kept in a box made of 5 cm thick iron shielding to reduce the radioactivity background. The scanning of the CS is done in two laboratories hosting a farm of microscopes (Scanning Stations), one at LNGS and the other in Nagoya. CS films are analyzed with a procedure called "general scanning" that looks for tracks in all the available angular range (typically ± 400 mrad around the perpendicular to the film) in an area of about 50 cm^2 around the TT prediction. The residuals with respect to the TT prediction, are of the order of about 1 cm in position and 20 mrad in angle.

If the CS scanning detects tracks compatible with those reconstructed in the electronic detectors the second X-ray exposure (lateral marking) is performed and the brick is brought to the surface laboratory. It is exposed to cosmic rays for about 24 hours in a dedicated pit in order to select high-energy cosmic muons to provide straight tracks for a sub-micrometric film-to-film alignment. The brick emulsion films are then developed and dispatched to the various scanning laboratories in Europe and Japan.

All tracks measured in the CS are sought in the most downstream films of the brick and followed back until they are not found in three consecutive films. The stopping point is considered as the signature either for a primary or a secondary vertex. The existence of the vertex is then confirmed by scanning a volume with a transverse size of 1 cm^2 for 11 films in total, upstream and downstream of the stopping point (see fig. 3).

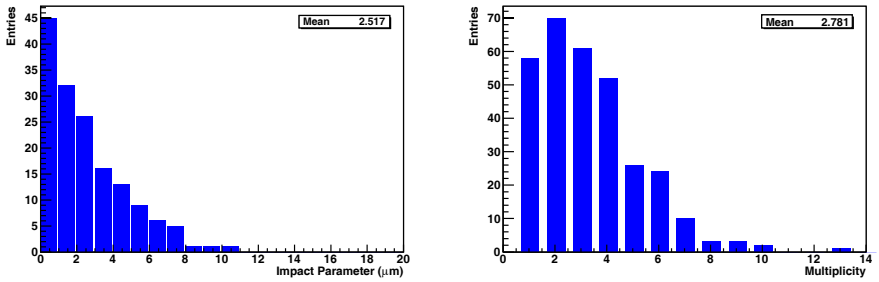

Fig. 4. – Left panel: impact parameter distribution of the muon track in CC events with respect to the reconstructed vertices. Right panel: charged track multiplicity distribution of the events.

The track impact parameter distribution of the muon in CC events with respect to the reconstructed vertex position and the event track multiplicity distribution are shown in fig. 4. As expected, the impact parameter distribution is peaked at zero and has a mean value of 2.5 μm. The multiplicity distribution shows the anticipated enhancements for even track numbers due to the preferred interaction of neutrinos with neutrons.

4. – First results and decay topologies

After a short commissioning run in 2006 the CNGS operation started on September 2007 at rather low intensity. The first event inside the OPERA target was observed on October 3rd. Unfortunately, due to a fault of the CNGS facility, the physics run lasted only a few days. During this run 8.2×10^{17} protons on target (p.o.t.) were accumulated: this corresponds to about ~ 3.6 effective nominal days of running. With such an integrated intensity 32 neutrino interactions in the bricks and 3 in the scintillator material of the target tracker were expected; we actually observed 38 events on time with the arrival of the beam at Gran Sasso.

A much longer run took place in 2008 when 1.782×10^{19} protons were delivered on the CNGS target with a mean value of $\sim 2 \times 10^{13}$ protons per extraction. OPERA collected 10100 events on time and among them about 1700 interactions in the target region. At the time of the conference 315 neutrino interactions were located and their topology was fully reconstructed: among them 270 were CC events while 45 were NC events.

Among these events secondary decay topologies are expected, mainly due to charm production. The detection of these events have a great importance in OPERA. Since charm decays exhibit the same topology as τ decays, measuring the charm-like event reconstruction efficiency provides an important cross-check of the τ event reconstruction capability. On the other hand, charm events are a potential source of background, in particular if the muon at the primary vertex is not identified (see fig. 5). Therefore, searching for charm-decays in events with the primary muon correctly identified provides a direct measurement of this background.

The event in fig. 6 has high track multiplicity at the primary vertex and one of the scan-back track shows a kink topology. The measured decay angle is 204 mrad and the flight length of the decaying particle is 3247 μm. The decay occurred in the third lead plate downstream of the interaction plate. No large angle tracks are produced at the decay vertex. The daughter momentum, measured by using the Multiple Coulomb

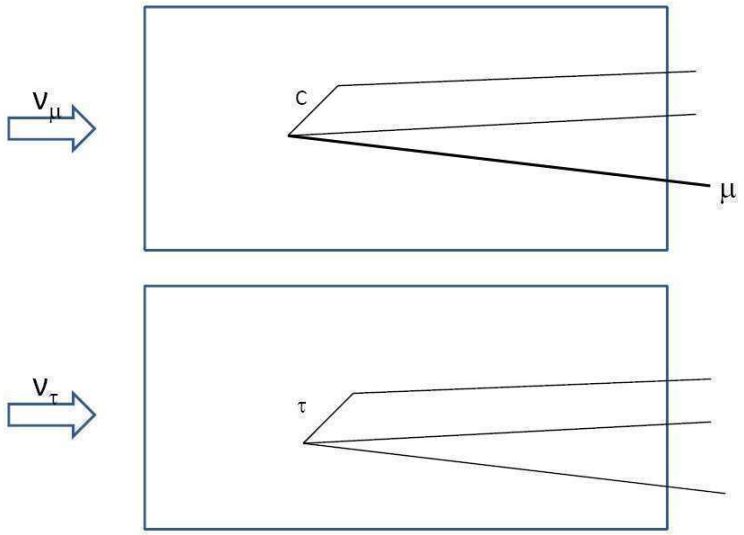

Fig. 5. – Schematic view of the charm and tau decay topologies.

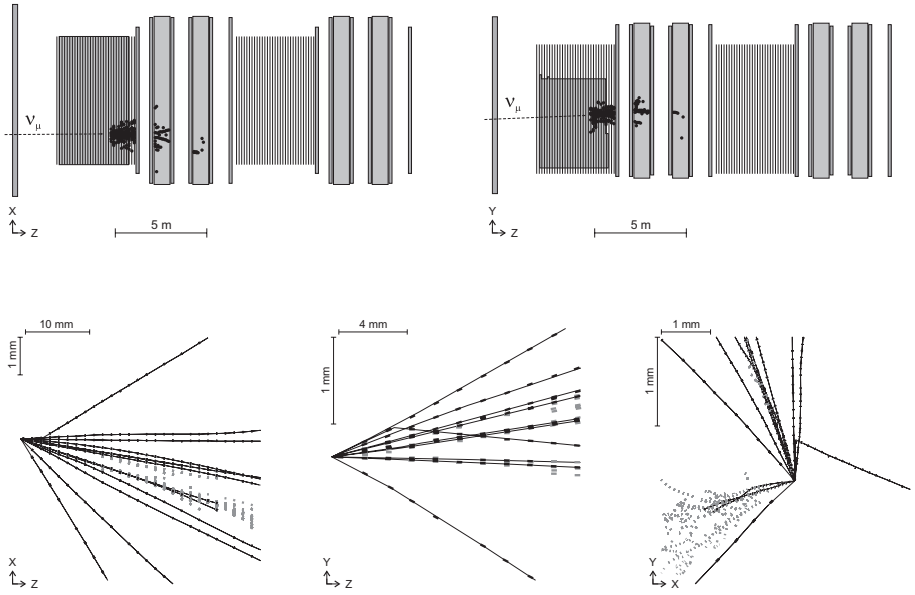

Fig. 6. – Online display of the OPERA electronic detector of a ν_μ charged-current interaction with a charm-like topology (top panel). The emulsion reconstruction is shown in the bottom panels where the charm-like topology is seen as a track with a kink: top view (bottom left), side view (bottom center), frontal view (bottom right). The dots visible in the lower panel are due to an electromagnetic shower.

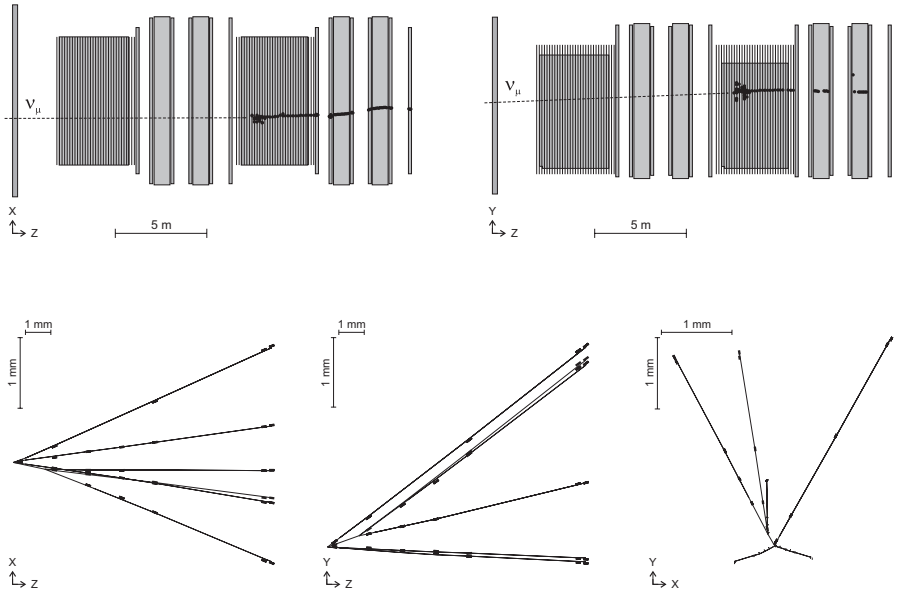

Fig. 7. – Online display of the OPERA electronic detector of a ν_μ charged-current interaction with a charm-like topology (top panel). The emulsion reconstruction is shown in the bottom panels where the charm-like topology is seen as a three-prongs secondary vertex: top view (bottom left), side view (bottom center), frontal view (bottom right).

Scattering technique [10] is $3.9^{+1.7}_{-0.9}\,\mathrm{GeV}/c$ at the 90% CL. Therefore, at the 90% CL the transverse momentum ranges between $610\,\mathrm{MeV}/c$ and $1140\,\mathrm{MeV}/c$. The daughter particle being a hadron, we computed the probability that a hadron interaction mimics a hadronic charm decay. According to the FLUKA Monte Carlo [11] the probability that a hadron interaction mimics a charm-decay with transverse momentum larger than $610\,\mathrm{MeV}/c$ is only 4×10^{-4}.

A second charm-like topology is shown in fig. 7. A 4-prong primary vertex is observed originating at a depth of about $30\,\mu$m in the upstream lead plate. The charmed hadron track points to a 3-prong decay vertex located at a distance of $1150\,\mu$m from the primary vertex ($200\,\mu$m inside the lead). The interaction occurs downstream in the brick and the tracks only cross four emulsion films and the CS doublet (the two most downstream hits in the figure). The muon track and the charm candidate track lie in a back-to-back configuration ($\Delta\phi \simeq 150°$). The momenta of the daughter tracks have also been measured by extracting the downstream brick and using the Multiple Coulomb Scattering technique. The measured values are $p_1 = 2.4^{+1.3}_{-0.6}$, $p_2 = 1.3^{+0.4}_{-0.3}$ and $p_3 = 1.2^{+1.7}_{-0.4}\,\mathrm{GeV}/c$ (transverse momenta of about 610, 90 and 340 MeV/c, total momentum: $4.8^{+2.2}_{-0.8}\,\mathrm{GeV}/c$), at the 90% CL. The probability of a decay in flight of a K is about 10^{-3}. The probability of a hadron interaction has been evaluated using FLUKA and amounts to 10^{-6}. Assuming a $D \to K\pi\pi$ decay, an invariant mass of $1.1^{+0.2}_{-0.1}\,\mathrm{GeV}/c^2$ is obtained. On the other hand, assuming a $D_s \to KK\pi$ decay an invariant mass of $1.5^{+0.4}_{-0.1}\,\mathrm{GeV}/c^2$ is derived. In the latter case the invariant mass is consistent with the mass of a charmed hadron while in the first case the consistency is marginal.

5. – Conclusions and outlook

In the 2008 run OPERA detected about 1700 neutrinos interacting in the targets, consistently with the value expected from the CNGS integrated intensity. At the time of the La Thuille Conference 315 interactions were located in the bricks: 45 NC and 270 CC interactions. The Scanning Stations and the scanning laboratories of the Collaboration are completing the analysis of the bricks.

A new physics run was started in June 2009 and completed in November 2009: a total integrated intensity of 3.5×10^{19} protons on target has been delivered, 3700 neutrino interactions in the target have been collected. With such statistics we expect to observe the first τ event candidates.

REFERENCES

[1] Strumia A. and Vissani F., *Neutrino masses and mixings and...*, arXiv:hep-ph/0606054.
[2] Acquafredda R. *et al.* (OPERA Collaboration), *JINST*, **4** (2009) P04018.
[3] CNGS project: `http://proj-cngs.web.cern.ch/proj-cngs/`.
[4] Nakamura T. *et al.*, *Nucl. Instrum. Methods A*, **556** (2006) 80.
[5] Anokhina A. *et al.* (OPERA Collaboration), *JINST*, **3** (2008) P07005.
[6] Eskut E. *et al.* (CHORUS Collaboration), *Nucl. Instrum. Methods A*, **401** (1997) 7.
[7] Rosa G. *et al.*, *Nucl. Instrum. Methods A*, **394** (1997) 357; Armenise N. *et al.*, *Nucl. Instrum. Methods A*, **551** (2005) 261; De Serio M. *et al.*, *Nucl. Instrum. Methods A*, **554** (2005) 247; Arrabito L. *et al.*, *Nucl. Instrum. Methods A*, **568** (2006) 578; Kreslo I. *et al.*, *JINST*, **3** (2008) P04006.
[8] Arrabito L. *et al.*, *JINST*, **2** (2007) P05004.
[9] Aoki S. *et al.*, *Nucl. Instrum. Methods B*, **51** (1990) 466; Nakano T., PhD Thesis, University of Nagoya (1997); Nakano T. (CHORUS Collaboration), *International Europhysics Conference on High-Energy Physics (HEP 2001), Budapest, Hungary, 12-18 July 2001.*
[10] De Serio M. *et al.*, *Nucl. Instrum. Methods A*, **512** (2003) 539; Kodama K. *et al.*, *Nucl. Instrum. Methods A*, **574** (2007) 192.
[11] For details on the FLUKA Monte Carlo we refer to `http://www.fluka.org`.

IL NUOVO CIMENTO Vol. 32 C, N. 5-6 Settembre-Dicembre 2009
DOI 10.1393/ncc/i2010-10525-1

Colloquia: LaThuile09

New results from MiniBooNE: A search for electron antineutrino appearance at $\sim 1\,\mathrm{eV}^2$

G. Karagiorgi for the MiniBooNE Collaboration
Massachusetts Institute of Technology - Cambridge, MA 02139, USA

(ricevuto il 10 Novembre 2009; pubblicato online il 15 Gennaio 2010)

Summary. — These proceedings summarize the first MiniBooNE electron antineutrino appearance search results, corresponding to a data sample collected for 3.39×10^{20} protons on target (POT). The search serves as a direct test of the LSND oscillation signature, and provides complementary information which can be used in studies addressing the MiniBooNE neutrino-mode low-energy excess.

PACS 14.60.Lm – Ordinary neutrinos.
PACS 14.60.Pq – Neutrino mass and mixing.
PACS 14.60.St – Non-standard-model neutrinos, right-handed neutrinos, etc.

1. – The MiniBooNE and LSND anomalies

The MiniBooNE experiment has performed a search for $\bar{\nu}_\mu \to \bar{\nu}_e$ oscillations at large Δm^2 [1], an oscillation signature that had been observed by the LSND experiment, with 3.8σ significance [2]. This oscillation interpretation relies on the existence of a fourth, sterile neutrino mass eigenstate, with $\Delta m^2 \sim 0.1$–$100\,\mathrm{eV}^2$. Mixing via this fourth mass eigenstate can lead to a small probability amplitude for $\bar{\nu}_\mu \to \bar{\nu}_e$ and $\nu_\mu \to \nu_e$ oscillations at $L[\mathrm{m}]/E[\mathrm{MeV}] \sim 1$. MiniBooNE has previously searched for this type of oscillation using a neutrino beam [3], and, under the assumption of CPT conservation, has excluded the LSND interpretation 98% confidence level (CL) [3]. At the same time, the search revealed an excess of ν_e events at low energy [4], which is inconsistent with the LSND excess under the a single sterile neutrino oscillation hypothesis; however, extensions of this model [5] offer the possibility of reconsiling the MiniBooNE neutrino results with the LSND antineutrino result. These models involve large CP violation which leads to different probabilities for $\nu_\mu \to \nu_e$ as opposed to $\bar{\nu}_\mu \to \bar{\nu}_e$ oscillations. Other models [6] have also been suggested as explanations, some of which offer predictions for antineutrino running at MiniBooNE. In order to provide another handle on the low-energy excess, MiniBooNE was approved in 2007 for extended antineutrino running [7], which also enabled MiniBooNE to perform a direct test of the LSND oscillation interpretation, using antineutrinos.

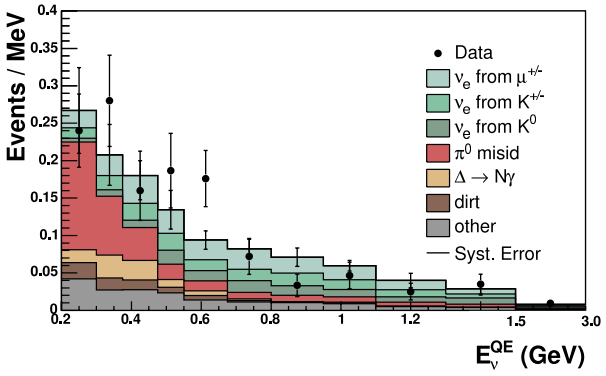

Fig. 1. – Monte Carlo background prediction and observed data as a function of reconstructed neutrino energy for the present antineutrino data sample corresponding to 3.39×10^{20} POT.

2. – The MiniBooNE electron antineutrino appearance search

The MiniBooNE experiment uses 8 GeV protons incident on a beryllium target in order to produce mesons which subsequently decay to generate the neutrino beam. A magnetic field is used at the target to focus positively charged mesons in the forward direction, and defocus negatively charged mesons, to produce a neutrino beam. Reversing the polarity of the magnetic field allows MiniBooNE to switch from a neutrino to an antineutrino beam. The flux [8] consists primarily of $\bar{\nu}_\mu$ and ν_μ. The low ν_e and $\bar{\nu}_e$ content of the beam minimizes the background to the oscillation search, ensuring sensitivity to small-amplitude (of order 10^{-3}) oscillations. The $\bar{\nu}_\mu$ flux has a mean energy of ~ 600 MeV. The MiniBooNE detector [9] is located at $L = 541$ m from the proton target. This establishes an L/E similar to LSND, and therefore sensitivity to $\Delta m^2 \sim 1\,\mathrm{eV}^2$. The detector is a spherical tank, 12 meters in diameter, filled with mineral oil and lined with photomultiplier tubes (PMTs). The particle detection and identification method relies on the detection of Cherenkov and scintillation light emitted by outgoing charged particles which are produced in neutrino interactions.

The antineutrino oscillation analysis [1] employs the same analysis chain that was implemented in neutrino mode [4]. The analysis relies on differentiation between a majority of $\bar{\nu}_\mu$ charged-current quasi-elastic (CCQE) events, and $\bar{\nu}_e$ CCQE events, which are the signal. A track-based event reconstruction is implemented, which uses PMT hit topology and timing to identify electron-like or muon-like Cherenkov rings from the corresponding CCQE interactions. The $\bar{\nu}_e$ and $\bar{\nu}_\mu$ CCQE spectra are fitted simultaneously as a function of reconstructed antineutrino energy, E_ν^{QE}, and the oscillation parameters Δm^2 and $\sin^2 2\theta$ are extracted. The $\bar{\nu}_\mu$ CCQE prediction is used in the fit in order to provide a constraint to the $\bar{\nu}_e$ CCQE prediction, as both spectra are correlated through flux and cross-section systematics.

The $\bar{\nu}_e$ CCQE background prediction, for 3.39×10^{20} POT, is shown in fig. 1. The background is dominated at low energy by mis-identified $\bar{\nu}_\mu$ events, such as neutral-current (NC) π^0 interactions. That is because MiniBooNE cannot differentiate between a single photon or a single electron produced in the detector. At high energy, the dominant background is CCQE interactions of intrinsic $\bar{\nu}_e$ from the beam, produced in K and $\pi \rightarrow \mu$ decays. The sensitivity to $\bar{\nu}_\mu \rightarrow \bar{\nu}_e$ oscillations is shown in fig. 2. The MiniBooNE

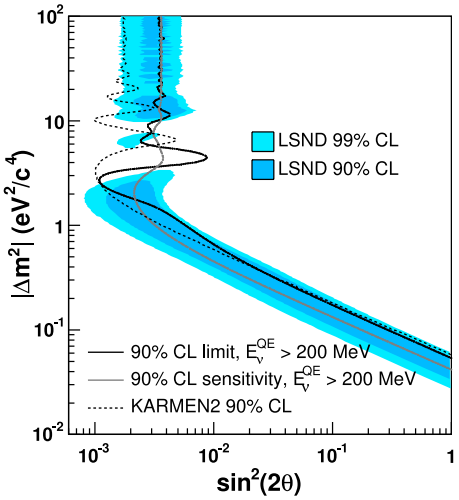

Fig. 2. – The antineutrino sensitivity and limit to LSND-allowed $\bar{\nu}_\mu \to \bar{\nu}_e$ oscillations, from fits to $200 < E_\nu^{QE} < 3000$ MeV. The MiniBooNE antineutrino dataset corresponds to 3.39×10^{20} POT. Also shown is the limit from KARMEN [10].

sensitivity provides substantial coverage of the lower Δm^2 region allowed at 90% CL by a joint analysis of LSND and KARMEN [10] data [1].

3. – Results

The reconstructed energy spectrum of $\bar{\nu}_e$ CCQE data is shown in fig. 1, overlaid on the predicted $\bar{\nu}_e$ CCQE background. At energies above 475 MeV, the data agree with the background prediction within systematic and statistical uncertainties. The 475–675 MeV energy region shows a 2.8σ data fluctuation above background prediction. This fluctuation forces the MiniBooNE limit, shown in fig. 2, to be significantly worse than the sensitivity at lower Δm^2. The MiniBooNE best oscillation fit corresponds to ($\Delta m^2 = 4.4\,\mathrm{eV}^2$, $\sin^2 2\theta = 0.004$).

Interestingly, the low-energy region (200–475 MeV) shows no evidence of an excess. In this range, MiniBooNE observes 61 events, compared to a background expectation of 61.5 ± 11.7 (sys+stat) events. Table I shows the probability (from a two-parameter fit to the data) that each of the following hypotheses explains the observed number of low-energy neutrino and antineutrino events: 1) Same σ: Same NC cross-section for neutrinos and antineutrinos. 2) π^0 scaled: Scaled to the number of NC π^0 events. 3) POT scaled: Scaled to number of POT. 4) BKGD scaled: Scaled to the total number of background events. 5) CC scaled: Scaled to the number of CC events. 6) Kaon scaled: Scaled to the number of low-energy K events. 7) Neutrino scaled: Scaled to the number of neutrino events. The same σ, POT scaled, and Kaon scaled hypotheses are disfavored as explanations of the MiniBooNE low-energy excess. The most preferred model is that where the low-energy excess is contributed from only neutrinos in the beam.

TABLE I. – *The χ^2-probability that each hypothesis explains the observed number of low-energy neutrino and antineutrino events, assuming only statistical, fully correlated systematic, and fully uncorrelated systematic errors. A proper treatment of systematic correlations is in progress.*

Hypothesis	stat.-only	stat. and correlated sys.	stat. and uncorrelated sys.
Same σ	0.1%	0.1%	6.7%
π^0 scaled	3.6%	6.4%	21.5%
POT scaled	0.0%	0.0%	1.8%
BKGD scaled	2.7%	4.7%	19.2%
CC scaled	2.9%	5.2%	19.9%
Kaon scaled	0.1%	0.1%	5.9%
ν scaled	38.4%	51.4%	58.0%

4. – Conclusion

MiniBooNE has performed a blind analysis for $\bar{\nu}_\mu \to \bar{\nu}_e$ oscillations. The $\bar{\nu}_e$ data is found in agreement with the background prediction as a function of E_ν^{QE}. No strong evidence for oscillations in antineutrino mode has been found, given the current statistics. Interestingly, there is no evidence of significant excess at low energy in antineutrino mode. This has already placed constraints to various suggested low-energy excess interpretations. MiniBooNE is currently collecting more antineutrino data, for a total of 5.0×10^{20} POT, and has been approved for further running, to collect a total of $10. \times 10^{20}$ POT. This will improve sensitivity to oscillations, and allow further investigation of the neutrino-mode low-energy excess. Additional information will be provided by the NuMI-beam neutrinos detected at MiniBooNE [11].

REFERENCES

[1] AGUILAR-AREVALO A. A. *et al.*, preprint arXiv:0904.1958 [hep-ex].
[2] ATHANASSOPOULOS C. *et al.*, *Phys. Rev. Lett.*, **75** (1995) 2650; **77** (1996) 3082; **81** (1998) 1774; AGUILAR-AREVALO A. A. *et al.*, *Phys. Rev. D*, **64** (2001) 112007.
[3] AGUILAR-AREVALO A. A. *et al.*, *Phys. Rev. Lett.*, **98** (2007) 231801.
[4] AGUILAR-AREVALO A. A. *et al.*, *Phys. Rev. Lett.*, **102** (2009) 101802.
[5] SOREL M. *et al.*, *Phys. Rev. D*, **70** (2004) 073004; MALTONI M. and SCHWETZ T., *Phys. Rev. D*, **76** (2007) 093005; KARAGIORGI G., *AIP Conf. Proc.*, **981** (2008) 210.
[6] HARVEY J. A. *et al.*, *Phys. Rev. Lett.*, **99** (2007) 261601; *Phys. Rev. D*, **77** (2008) 085017; PAS H. *et al.*, *Phys. Rev. D*, **72** (2005) 095017; GOLDMAN T. *et al.*, *Phys. Rev. D*, **75** (2007) 091301; NELSON A. E. and WALSH J., *Phys. Rev. D*, **77** (2008) 033001; KOSTELECKY V. A. and MEWES M., *Phys. Rev. D*, **69** (2004) 016005; KATORI T. *et al.*, *Phys. Rev. D*, **74** (2006) 105009; GIUNTI C. and LAVEDER M., *Phys. Rev. D*, **77** (2008) 093002.
[7] AGUILAR-AREVALO A. A. *et al.*, *Addendum to the MiniBooNE Run Plan: MiniBooNE Physics in 2006* (2006).
[8] AGUILAR-AREVALO A. A. *et al.*, *Phys. Rev. D*, **79** (2009) 072002.
[9] AGUILAR-AREVALO A. A. *et al.*, *Nucl. Instrum. Methods A*, **599** (2009) 28.
[10] ARMBRUSTER B. *et al.*, *Phys. Rev. D*, **65** (2002) 112001.
[11] ADAMSON P. *et al.*, *Phys. Rev. Lett.*, **102** (2008) 211801.

IL NUOVO CIMENTO Vol. 32 C, N. 5-6 Settembre-Dicembre 2009
DOI 10.1393/ncc/i2010-10544-x

Colloquia: LaThuile09

Search for neutrino charged current coherent pion production in SciBooNE

K. Hiraide(*) for the SciBooNE Collaboration
Department of Physics, Kyoto University - Kyoto 606-8502, Japan

(ricevuto il 10 Novembre 2009; pubblicato online il 20 Gennaio 2010)

Summary. — SciBooNE is a neutrino experiment measuring the neutrino cross-sections on carbon in the one GeV region. We have performed a search for charged current coherent pion production from muon neutrinos scattering on carbon, $\nu_\mu {}^{12}\mathrm{C} \to \mu^{-12}\mathrm{C}\pi^+$. No evidence for coherent pion production is observed. We set 90% confidence level upper limits on the cross-section ratio of charged current coherent pion production to the total charged current cross-section at 0.67×10^{-2} at mean neutrino energy 1.1 GeV and 1.36×10^{-2} at mean neutrino energy 2.2 GeV.

PACS 13.15.+g – Neutrino interactions.
PACS 13.60.Le – Meson production.
PACS 25.30.Pt – Neutrino-induced reactions.
PACS 95.55.Vj – Neutrino, muon, pion, and other elementary particle detectors; cosmic ray detectors.

1. – Introduction

Evidences of neutrino oscillation have been observed by several experiments over the last decade, and neutrino oscillation physics has entered the era of precision measurements. In the second generation accelerator neutrino oscillation experiments, precise knowledge of neutrino cross-sections with nuclei are important to achieve the best sensitivity. However, the typical accuracy of neutrino-nucleus cross-sections in the one GeV region, which is relevant to many future experiments, is 20% with our current knowledge. Among several neutrino interaction channels, neutrino interactions producing single pion form significant backgrounds for neutrino oscillation studies with a few-GeV neutrino beam, and thus understanding those processes is essential. It has been known for years that neutrinos can produce pions by interacting coherently with the nucleons forming the target nucleus. Both charged current (CC) and neutral current (NC) coherent modes

(*) Present address: Kamioka Observatory, Institute for Cosmic Ray Research, University of Tokyo, Gifu 506-1205, Japan.

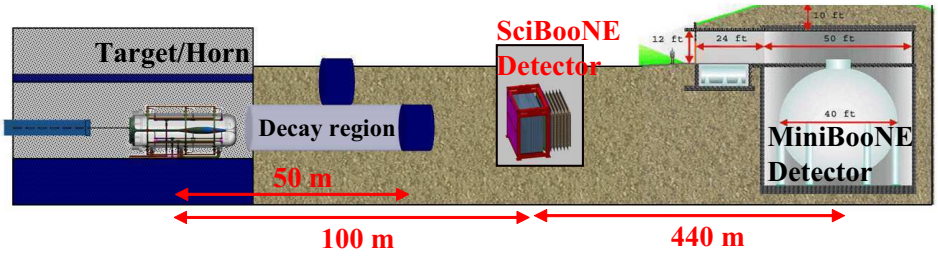

Fig. 1. – Schematic drawing of the experimental setup of SciBooNE.

are possible, $\nu_\mu A \to \mu^- A\pi^+$ and $\nu_\mu A \to \nu_\mu A\pi^0$, where A is a nucleus. The outgoing lepton and pion tend to go in the forward direction in the lab frame, and no nuclear breakup occurs. Recent results on coherent pion production have induced interest of the neutrino physics community. The non-existence of charged current coherent pion production in a 1.3 GeV wide-band neutrino beam has been reported by K2K [1], while there exist charged current coherent pion production positive results at higher neutrino energies. On the one hand, evidence for NC coherent pion production in the similar neutrino energy has been recently reported by MiniBooNE [2].

The SciBooNE experiment [3] is designed to measure the neutrino cross sections on carbon in the one GeV region. In this paper, we report the first measurement of charged current coherent pion production on carbon by neutrinos in the SciBooNE experiment, which was recently published in ref. [4].

2. – The SciBooNE experiment

Figure 1 shows a schematic drawing of the experimental setup of SciBooNE. The experiment uses the Booster Neutrino Beam (BNB) at Fermilab. The primary proton beam, with kinetic energy 8 GeV, is extracted to strike a 71 cm long, 1 cm diameter beryllium target. Each beam spill consists of 81 bunches of protons, containing typically 4×10^{12} protons in a total spill duration of 1.6 μs. The target sits at the upstream end of a magnetic focusing horn that is pulsed with approximately 170 kA to focus the mesons, primarily π^+, produced by the p-Be interactions. In a 50 m long decay pipe following the horn, π^+ decay and produce neutrinos, before the mesons encounter an absorber. The flux is dominated by muon neutrinos (93% of total), with small contributions from muon antineutrinos (6.4%), and electron neutrinos and antineutrinos (0.6% in total). The flux-averaged mean neutrino energy is 0.7 GeV. When the horn polarity is reversed, π^- are focused and hence a predominantly antineutrino beam is created.

The SciBooNE detector is located 100 m downstream from the neutrino production target. The detector complex consists of three sub-detectors: a fully active fine-grained scintillator tracking detector (SciBar), an electromagnetic calorimeter (EC) and a muon range detector (MRD). The SciBar detector consists of 14336 extruded plastic scintillator strips, each $1.3 \times 2.5 \times 300\,\mathrm{cm}^3$. The scintillators are arranged vertically and horizontally to construct a $3 \times 3 \times 1.7\,\mathrm{m}^3$ volume with a total mass of 15 tons. Each strip is read out by a wavelength-shifting fiber attached to a 64-channel multi-anode PMT. Charge and timing information from each MA-PMT is recorded by custom electronics. The minimum length of a reconstructed track is 8 cm which corresponds to a proton with momentum of 450 MeV/c. The EC is installed downstream of SciBar, and consists of

32 vertical and 32 horizontal modules made of scintillating fibers embedded in lead foils. Each module has dimensions of $4.0 \times 8.2 \times 262\,\mathrm{cm}^3$, and is read out by two $1''$ PMTs on both ends. The EC has a thickness of $11X_0$ along the beam direction to measure π^0 emitted from neutrino interactions and the intrinsic ν_e contamination. The energy resolution is $14\%/\sqrt{E(\mathrm{GeV})}$. The MRD is located downstream of the EC in order to measure the momentum of muons up to $1.2\,\mathrm{GeV}/c$ with range. It consists of 12 layers of $2''$-thick iron plates sandwiched between layers of 6 mm-thick plastic scintillator planes. The cross-sectional area of each plate is $305 \times 274\,\mathrm{cm}^2$. The horizontal and vertical scintillator planes are arranged alternately, and the total number of scintillators is 362.

The experiment took both neutrino and antineutrino data from June 2007 until August 2008. In total, 2.64×10^{20} POT were delivered to the beryllium target during the SciBooNE data run. After beam and detector quality cuts, 2.52×10^{20} POT are usable for physics analyses; 0.99×10^{20} POT for neutrino data and 1.53×10^{20} POT for antineutrino data. Results from the full neutrino data sample are presented in this paper.

3. – Event selection

The experimental signature of charged current coherent pion production is the existence of two and only two tracks originating from a common vertex, both consistent with minimum ionizing particles (a muon and a charged pion).

To identify charged current events, we search for tracks in SciBar matching with a track or hits in the MRD. Such a track is defined as a SciBar-MRD matched track. The most energetic SciBar-MRD matched track in any event is considered as the muon candidate. The matching criteria impose a muon momentum threshold of $350\,\mathrm{MeV}/c$. The neutrino interaction vertex is reconstructed as the upstream edge of the muon candidate. We select events whose vertices are in the SciBar fiducial volume, $2.6\,\mathrm{m} \times 2.6\,\mathrm{m} \times 1.55\,\mathrm{m}$, a total mass of 10.6 tons. Finally, event timing is required to be within $2\,\mu$s beam timing window. The cosmic-ray background contamination in the beam timing window is only 0.5%, estimated using a beam-off timing window. Approximately 30000 events are selected as our standard charged current sample, which is called SciBar-MRD matched sample. According to the MC simulation, the selection efficiency and purity of true ν_μ charged current events are 27.9% and 92.8%, respectively. Two subsamples of the SciBar-MRD matched sample are further defined: the MRD stopped sample and the MRD penetrated sample. Events with the muon stopping in the MRD are classified as MRD stopped events. Events with the muon exiting from the downstream end of the MRD are defined as the MRD penetrated sample, in which we can measure only a part of the muon momentum. The average neutrino beam energy for true charged current events in the MRD stopped and MRD penetrated samples is 1.0 GeV and 2.0 GeV, respectively, enabling a measurement of charged current coherent pion production at two different mean neutrino energies.

Once the muon candidate and the neutrino interaction vertex are reconstructed, we search for other tracks originating from the vertex. Most events are reconstructed as either one track or two track events. The two-track sample is further divided based on particle identification. The particle identification variable, Muon Confidence Level (MuCL) is related to the probability that a particle is a minimum ionizing particle based on the energy deposition. The probability of misidentification is estimated to be 1.1% for muons and 12% for protons. We first require that the MuCL of the SciBar-MRD matched track is greater than 0.05 to reject events with a proton penetrating into the MRD. Then the second track in the event is classified as a pion-like or a proton-like track

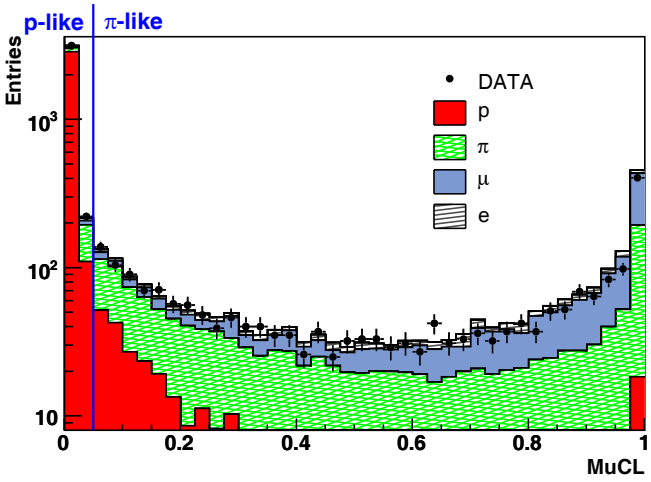

Fig. 2. – MuCL of the second track for two-track events in the MRD stopped sample.

with the same MuCL threshold. Figure 2 shows the contributions to the second track from true proton, pion, muon, and electron tracks as predicted by the MC simulation.

In a charged current resonant pion event, $\nu p \rightarrow \mu^- p \pi^+$, the proton is often not reconstructed due to its low energy, and such an event is therefore identified as a two-track $\mu + \pi$ event. To separate charged current coherent pion events from charged current resonant pion events, additional protons with momentum below the tracking threshold are instead detected by their large energy deposition around the vertex, so-called vertex activity. Figure 3 shows the maximum energy for $\mu + \pi$ events in the MRD stopped sample. A peak around 6 MeV corresponds to the energy deposited in the strip containing

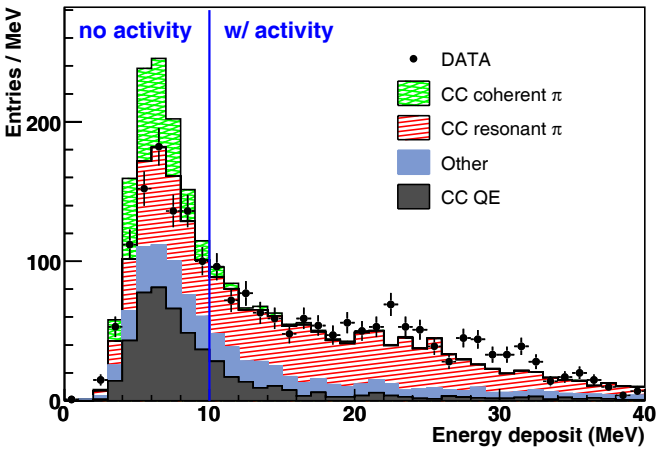

Fig. 3. – Maximum deposited energy in a strip around the vertex for the $\mu + \pi$ events in the MRD stopped sample.

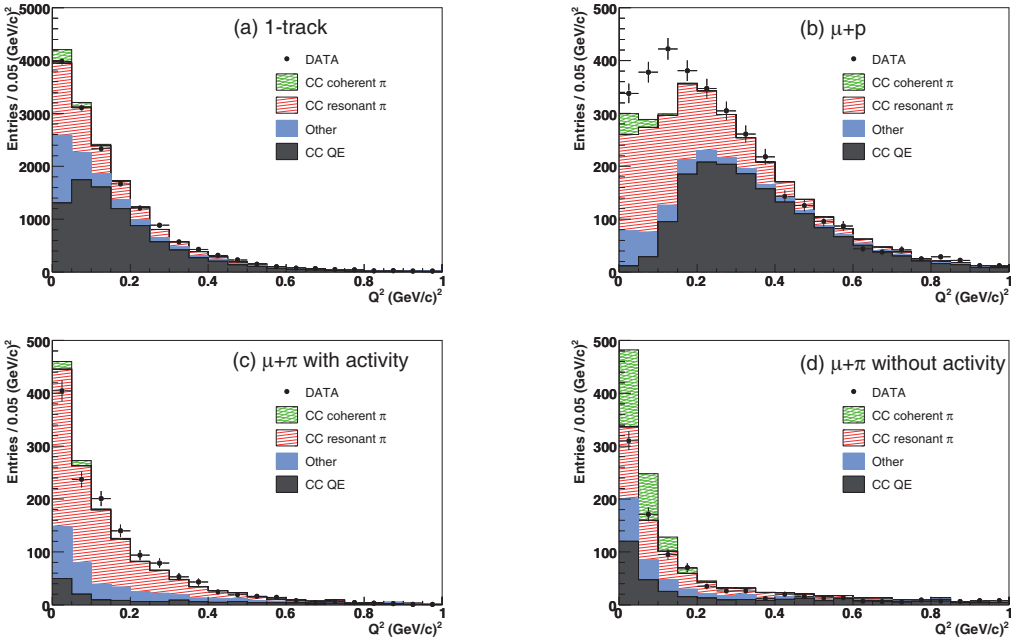

Fig. 4. – Reconstructed Q^2 after fitting for (a) the one track, (b) $\mu + p$, (c) $\mu + \pi$ with activity, and (d) $\mu + \pi$ without activity samples.

the vertex by two minimum ionizing particles, and a high-energy tail is mainly due to the low-energy proton. Events with energy deposition greater than 10 MeV are considered to have activity at the vertex.

Four sub-samples, the one-track events, $\mu+p$ events, $\mu+\pi$ events with vertex activity, and $\mu+\pi$ events without vertex activity are used for constraining systematic uncertainties in the simulation. The MC distributions of the square of the four-momentum transfer (Q^2) are fitted to the distributions of the four aforementioned data samples. The reconstructed Q^2 is calculated as

$$Q^2_{\rm rec} = 2E^{\rm rec}_\nu (E_\mu - p_\mu \cos\theta_\mu) - m^2_\mu, \tag{1}$$

where $E^{\rm rec}_\nu$ is the reconstructed neutrino energy calculated by assuming charged current quasi-elastic (CC-QE) kinematics,

$$E^{\rm rec}_\nu = \frac{1}{2}\frac{(m^2_p - m^2_\mu) - (m_n - V)^2 + 2E_\mu(m_n - V)}{(m_n - V) - E_\mu + p_\mu \cos\theta_\mu} \tag{2}$$

where m_p and m_n are the mass of proton and neutron, respectively, and V is the nuclear potential, which is set to 27 MeV. The fitting is described in detail in ref. [4]. Figure 4 shows the reconstructed Q^2 distributions after the fitting.

Charged current coherent pion candidates are extracted from the $\mu + \pi$ events which do not have vertex activity. The sample still contains CC-QE events in which a proton

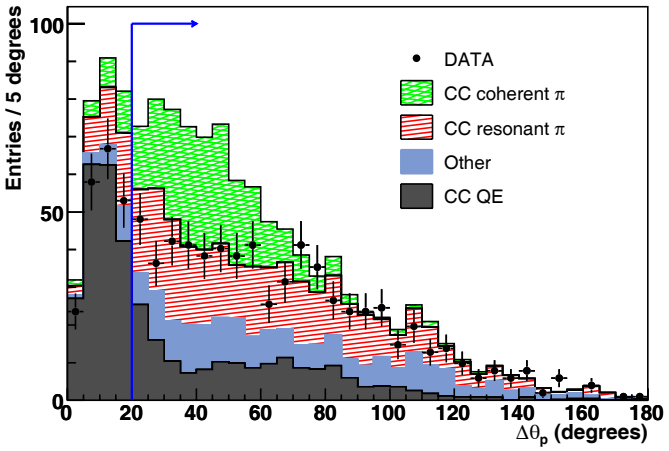

Fig. 5. – $\Delta\theta_p$ for the $\mu + \pi$ events in the MRD stopped sample.

is misidentified as a minimum ionizing track. We reduce this background by using kinematic information in the event. Since the CC-QE interaction is a two-body interaction, one can predict the proton direction from the measured muon momentum and muon angle. For each two-track event, we define an angle called $\Delta\theta_p$ as the angle between the expected proton track and the observed second track directions. Figure 5 shows the $\Delta\theta_p$ distribution for $\mu+\pi$ events in the MRD stopped sample. Events with $\Delta\theta_p$ larger than 20 degrees are selected. With this selection, 48% of charged current quasi-elastic events in the $\mu+\pi$ sample are rejected, while 91% of charged current coherent pion events pass the cut according to the MC simulation. Further selections are applied in order to separate charged current coherent pion events from charged current resonant pion events which are the dominant backgrounds for this analysis. Figure 6 shows the angular distribution of pion candidates with respect to the beam direction. In the case of charged current coherent pion events, both the muon and pion tracks are directed forward, and therefore events in which the track angle of the pion candidate with respect to the beam direction is less than 90 degrees are selected.

Figure 7 (left) shows reconstructed Q^2 for the $\mu + \pi$ events in the MRD stopped sample after the pion track direction cut. Although a CC-QE interaction is assumed, the Q^2 of charged current coherent pion events is reconstructed with a resolution of 0.016 $(\mathrm{GeV}/c)^2$ and a shift of -0.024 $(\mathrm{GeV}/c)^2$ according to the MC simulation. Finally, events with reconstructed Q^2 less than 0.1 $(\mathrm{GeV}/c)^2$ are selected. In the signal region, 247 charged current coherent pion candidates are observed, while the expected number of background events is 228 ± 12. The error comes from the errors on the fitting parameters. The selection efficiency for the signal is estimated to be 10.4%. The mean neutrino beam energy for true charged current coherent pion events in the sample is estimated to be 1.1 GeV after accounting for the effects of the selection efficiency.

The same selection is applied to the MRD penetrated sample to extract charged current coherent pion candidates at higher energy. Figure 7 (right) shows reconstructed Q^2 for the MRD penetrated charged current coherent pion sample. In the signal region, 57 charged current coherent pion candidates are observed, while the expected number of

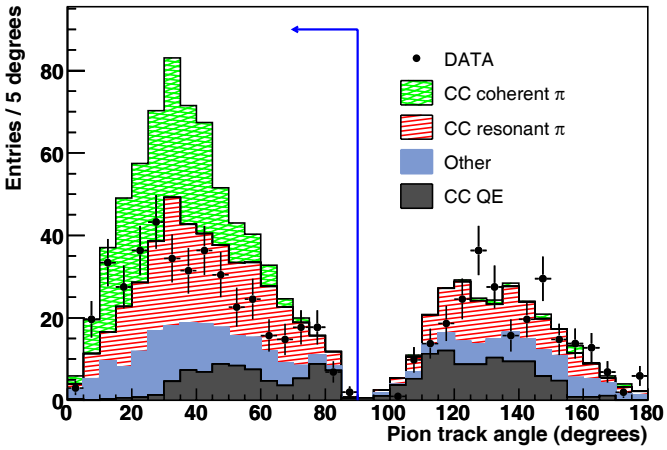

Fig. 6. – Track angle of the pion candidate with respect to the beam direction for the $\mu + \pi$ events after the charged current quasi-elastic rejection.

background events is 40 ± 2.2. The selection efficiency for the signal is estimated to be 3.1%. The mean neutrino beam energy for true charged current coherent pion events in the sample is estimated to be 2.2 GeV.

4. – σ (CC coherent π)/σ (CC) cross-section ratio

We measure the cross-section ratios of charged current coherent pion production to total charged current interaction with two distinct data samples. With the MRD stopped sample, the ratio of the charged current coherent pion production to total charged current cross-sections is measured to be $(0.16 \pm 0.17(\text{stat})^{+0.30}_{-0.27}(\text{sys})) \times 10^{-2}$. The result is consistent with the nonexistence of charged current coherent pion production, and hence we set an upper limit on the cross-section ratio by using the likelihood distribution ($\mathcal{L}$) which is convolved with the systematic error. We calculate the 90% confidence level (CL)

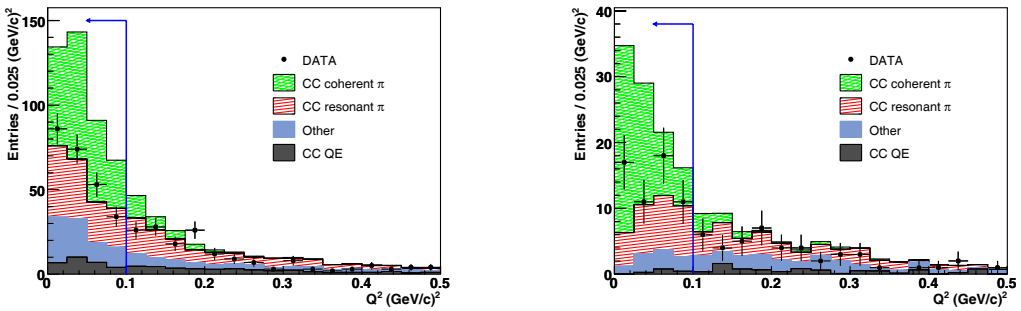

Fig. 7. – Reconstructed Q^2 for the MRD stopped charged current coherent pion sample (left), and the MRD penetrated charged current coherent pion sample (right).

upper limit (UL) using the relation $\int_0^{UL} \mathcal{L}\mathrm{d}x / \int_0^{\infty} \mathcal{L}\mathrm{d}x = 0.9$ to be

$$\sigma(\text{CC coherent } \pi)/\sigma(\text{CC}) < 0.67 \times 10^{-2} \tag{3}$$

at a mean neutrino energy of 1.1 GeV.

With the MRD penetrated sample, the cross-section ratio is measured to be $(0.68 \pm 0.32(\text{stat})^{+0.39}_{-0.25}(\text{sys})) \times 10^{-2}$. No significant evidence for charged current coherent pion production is observed, and hence we set an upper limit on the cross-section ratio at 90% CL:

$$\sigma(\text{CC coherent } \pi)/\sigma(\text{CC}) < 1.36 \times 10^{-2} \tag{4}$$

at a mean neutrino energy of 2.2 GeV.

According to the Rein-Sehgal model [5, 6] implemented in our simulation, the cross-section ratio of charged current coherent pion production to total charged current interactions is expected to be 2.04×10^{-2}. Our limits correspond to 33% and 67% of the prediction at 1.1 GeV and 2.2 GeV, respectively. Our results are consistent with the K2K result [1]: σ (CC coherentπ)$/\sigma$(CC) $< 0.60 \times 10^{-2}$ at 90% CL measured in a 1.3 GeV wideband neutrino beam.

5. – Conclusions

In summary, we have searched for muon neutrino charged current coherent pion production on carbon in the few-GeV region using the full SciBooNE neutrino data set of 0.99×10^{20} POT. No evidence of charged current coherent pion production is found, and hence we set 90% CL upper limits on the cross-section ratio of charged current coherent pion production to total charged current cross-sections at 0.67×10^{-2} and 1.36×10^{-2}, at mean neutrino energies of 1.1 GeV and 2.2 GeV, respectively.

* * *

The SciBooNE Collaboration gratefully acknowledges support from various grants, contracts and fellowships from the MEXT (Japan), the INFN (Italy), the Ministry of Education and Science and CSIC (Spain), the STFC (UK), and the DOE and NSF (USA). The author is grateful to the Japan Society for the Promotion of Science for support.

REFERENCES

[1] Hasegawa M. *et al.* (K2K Collaboration), *Phys. Rev. Lett.*, **95** (2005) 252301 [arXiv:hep-ex/0506008].
[2] Aguilar-Arevalo A. A. *et al.* (MiniBooNE Collaboration), *Phys. Lett. B*, **664** (2008) 41 [arXiv:0803.3423 [hep-ex]].
[3] Aguilar-Arevalo A. A. *et al.* (SciBooNE Collaboration), arXiv:hep-ex/0601022.
[4] Hiraide K. *et al.* (SciBooNE Collaboration), *Phys. Rev. D*, **78** (2008) 112004 [arXiv:0811.0369 (hep-ex)].
[5] Rein D. and Sehgal L. M., *Nucl. Phys. B*, **223** (1983) 29.
[6] Rein D. and Sehgal L. M., *Phys. Lett. B*, **657** (2007) 207 [arXiv:hep-ph/0606185].

IL NUOVO CIMENTO Vol. 32 C, N. 5-6 Settembre-Dicembre 2009
DOI 10.1393/ncc/i2010-10520-6

Colloquia: LaThuile09

The GSI time anomaly: Facts and fiction

C. Giunti
INFN, Sezione di Torino - Via P. Giuria 1, I–10125 Torino, Italy

(ricevuto il 10 Novembre 2009; pubblicato online il 7 Gennaio 2010)

Summary. — The claims that the GSI time anomaly is due to the mixing of neutrinos in the final state of the observed electron capture decays of hydrogen-like heavy ions are refuted with the help of an analogy with a double-slit experiment. It is a consequence of causality. It is shown that the GSI time anomaly may be caused by quantum beats due to the existence of two coherent energy levels of the decaying ion with an extremely small energy splitting (about 6×10^{-16} eV) and relative probabilities having a ratio of about 1/99.

PACS 14.60.Pq – Neutrino mass and mixing.
PACS 78.47.jm – Quantum beats.

A GSI experiment [1] observed an anomalous oscillatory time modulation of the electron capture decays

$$^{140}\mathrm{Pr}^{58+} \to {}^{140}\mathrm{Ce}^{58+} + \nu_e \,, \tag{1}$$

$$^{142}\mathrm{Pm}^{60+} \to {}^{142}\mathrm{Nd}^{60+} + \nu_e \,. \tag{2}$$

The hydrogen-like ions $^{140}\mathrm{Pr}^{58+}$ and $^{142}\mathrm{Pm}^{60+}$ were produced by fragmentation of a beam of ^{152}Sm with 500–600 MeV energy per nucleon on a ^{9}Be target and stored in the ESR cooler-storage ring where they circulated with a frequency of about 2 MHz and were monitored by Schottky Mass Spectrometry. The electron capture data are fitted by an oscillatory decay rate with a period $T \simeq 7$ s and an amplitude $A \simeq 0.2$ [1].

It has been proposed [1-4] that the GSI anomaly is due to the interference of the massive neutrinos which compose the final electron neutrino state,

$$|\nu_e\rangle = \cos\vartheta|\nu_1\rangle + \sin\vartheta|\nu_2\rangle \,, \tag{3}$$

where ϑ is the solar mixing angle (see refs. [5-10]).

In order to assess the viability of this explanation of the GSI anomaly, it is necessary to understand that interference is the result of the superposition of two or more waves [11]. If the waves come from the same source, interference can occur if the waves evolve different phases by propagating through different paths. Therefore, interference occurs after wave

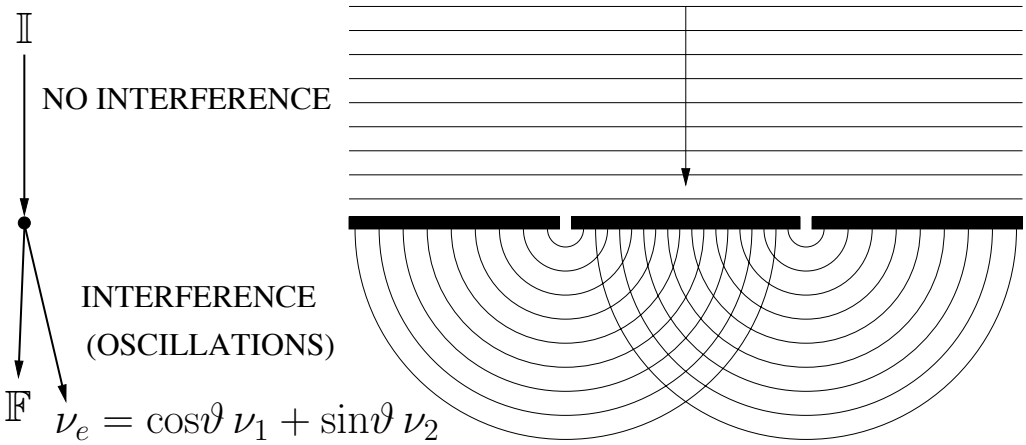

Fig. 1. – Analogy between the electron capture decay process (4) and a double-slit interference experiment.

propagation, not at the wave source. In the case of the GSI experiment, there cannot be any interference effect of ν_1 and ν_2 in the electron-capture decays (1) and (2), which are the sources of ν_1 and ν_2.

Let us illustrate these remarks through an analogy with the well-known double-slit interference experiment with classical or quantum waves depicted in fig. 1. In a double-slit experiment an incoming-plane-wave packet hits a barrier with two tiny holes, generating two outgoing-spherical-wave packets which propagate on the other side of the barrier. The two outgoing waves are coherent, since they are created with the same initial phase in the two holes. Hence, the intensity after the barrier, which is proportional to the squared modulus of the sum of the two outgoing waves, exhibits interference effects. The interference depends on the different path lengths of the two outgoing spherical waves after the barrier.

For the analogy with the double-slit experiment, let us write schematically an electron-capture decay process of the type in eqs. (1) and (2) as

$$\mathbb{I} \to \mathbb{F} + \nu_e \,. \tag{4}$$

Taking into account the neutrino mixing in eq. (3), we have two different decay channels:

$$\mathbb{I} \to \mathbb{F} + \nu_1 \,, \qquad \mathbb{I} \to \mathbb{F} + \nu_2 \,. \tag{5}$$

The initial state in the two decay channels is the same. In our analogy with the double-slit experiment, the initial state $\mathbb{I}$ is analogous to the incoming-wave packet. The two final states $\mathbb{F} + \nu_1$ and $\mathbb{F} + \nu_2$ are analogous to the two outgoing-wave packets. Different weights of ν_1 and ν_2 production due to $\vartheta \neq \pi/4$ correspond to different sizes of the two holes in the barrier.

In the analogy, the decay rate of $\mathbb{I}$ corresponds to the fraction of intensity of the incoming wave which crosses the barrier, which depends only on the sizes of the holes. It does not depend on the interference effect which occurs after the wave has passed through

the barrier. In a similar way, the decay rate of $\mathbb{I}$ cannot depend on the interference of ν_1 and ν_2 which occurs after the decay has happened.

Of course, flavor neutrino oscillations caused by the interference of ν_1 and ν_2 can occur after the decay of $\mathbb{I}$, in analogy with the occurrence of interference of the outgoing waves in the double-slit experiment, regardless of the fact that the decay rate is the incoherent sum of the rates of production of ν_1 and ν_2 and the fraction of intensity of the incoming wave which crosses the barrier is the incoherent sum of the fractions of intensity of the incoming wave which passes through the two holes.

The above argument is a simple consequence of causality: the interference of ν_1 and ν_2 occurring after the decay cannot affect the decay rate.

Causality is explicitly violated in ref. [2], where the decaying ion is described by a wave packet, but it is claimed that there is a selection of the momenta of the ion caused by a final neutrino momentum splitting due to the mass difference of ν_1 and ν_2. This selection violates causality. In the double-slit analogy, the properties of the outgoing wave packets are determined by the properties of the incoming wave packet, not vice versa. In a correct treatment, all the momentum distribution of the wave packet of the ion contributes to the decay, generating appropriate neutrino wave packets.

The authors of refs. [3,4] use a different approach: they calculate the decay rate with the final neutrino state

$$|\nu\rangle = \sum_{k=1}^{3} |\nu_k\rangle \,. \tag{6}$$

This state is different from the standard electron neutrino state, which is given by

$$|\nu_e\rangle = \sum_{k=1}^{3} U_{ek}^{*} \, |\nu_k\rangle \,, \tag{7}$$

where U is the mixing matrix (in the two-neutrino mixing approximation of eq. (3), $U_{e1} = \cos\vartheta$, $U_{e2} = \sin\vartheta$, and $U_{e3} = 0$). It is not even properly normalized to describe one particle ($\langle\nu|\nu\rangle = 3$). Moreover, it leads to a decay rate which is different from the standard decay rate, given by the incoherent sum of the rates of decay into the different massive neutrinos final states weighted by the corresponding element of the mixing matrix [12-16]. The decay rate is given by the integral over the phase space of the decay probability

$$P_{\mathbb{I}\to\mathbb{F}+\nu} = |\langle \nu, \mathbb{F}|\mathsf{S}|\mathbb{I}\rangle|^2 = \left| \sum_{k=1}^{3} \langle \nu_k, \mathbb{F}|\mathsf{S}|\mathbb{I}\rangle \right|^2 \,, \tag{8}$$

where S is the S-matrix operator. Considering the S-matrix operator at first order in perturbation theory,

$$\mathsf{S} = 1 - i \int \mathrm{d}^4x \, \mathcal{H}_W(x) \,, \tag{9}$$

with the effective four-fermion interaction Hamiltonian

$$\mathcal{H}_W(x) = \frac{G_F}{\sqrt{2}} \cos\theta_{\rm C}\, \overline{\nu_e}(x)\gamma_\rho(1-\gamma^5)e(x)\, \overline{n}(x)\gamma^\rho(1-g_A\gamma^5)p(x)$$
$$= \frac{G_F}{\sqrt{2}} \cos\theta_{\rm C} \sum_{k=1}^{3} U^*_{ek}\overline{\nu_k}(x)\gamma_\rho(1-\gamma^5)e(x)\, \overline{n}(x)\gamma^\rho(1-g_A\gamma^5)p(x)\,, \tag{10}$$

where $\theta_{\rm C}$ is the Cabibbo angle, one can write the matrix elements in eq. (8) as

$$\langle \nu_k, \mathbb{F}|\mathsf{S}|\mathbb{I}\rangle = U^*_{ek}\mathcal{M}_k\,, \tag{11}$$

with

$$\mathcal{M}_k = \frac{G_F}{\sqrt{2}} \cos\theta_{\rm C}\, \langle \nu_k, \mathbb{F}|\overline{\nu_k}(x)\gamma_\rho(1-\gamma^5)e(x)\, \overline{n}(x)\gamma^\rho(1-g_A\gamma^5)p(x)|\mathbb{I}\rangle\,. \tag{12}$$

Therefore, the decay probability is given by

$$P_{\mathbb{I}\to\mathbb{F}+\nu} = \left| \sum_{k=1}^{3} U^*_{ek}\mathcal{M}_k \right|^2 . \tag{13}$$

This decay probability is different from the standard one [12-16], which is obtained by summing incoherently over the probabilities of decay into the different massive neutrinos final states weighted by the corresponding element of the mixing matrix:

$$P = \sum_{k=1}^{3} |U_{ek}|^2\, |\mathcal{M}_k|^2\,. \tag{14}$$

The analogy with the double-slit experiment and the causality argument discussed above support the correctness of the standard decay probability P. Another argument against the decay probability $P_{\mathbb{I}\to\mathbb{F}+\nu}$ is that in the limit of massless neutrinos it does not reduce to the decay probability in the Standard Model,

$$P_{\rm SM} = |\mathcal{M}_{\rm SM}|^2\,, \tag{15}$$

with

$$\mathcal{M}_{\rm SM} = \frac{G_F}{\sqrt{2}} \cos\theta_{\rm C}\, \langle \mathbb{F}, \nu_e^{\rm SM}|\overline{\nu_e^{\rm SM}}(x)\gamma_\rho(1-\gamma^5)e(x)\, \overline{n}(x)\gamma^\rho(1-g_A\gamma^5)p(x)|\mathbb{I}\rangle\,, \tag{16}$$

where $\nu_e^{\rm SM}$ is the SM massless electron neutrino. Indeed, for the matrix elements $\mathcal{M}_k$ we have

$$\mathcal{M}_k \xrightarrow[m_k\to 0]{} \mathcal{M}_{\rm SM}\,, \tag{17}$$

leading to

$$P_{\mathbb{I}\to\mathbb{F}+\nu} \xrightarrow[m_k\to 0]{} |\mathcal{M}_{\rm SM}|^2 \left|\sum_{k=1}^{3} U_{ek}^*\right|^2 . \tag{18}$$

This is different from the SM decay probability in eq. (15). Notice that the contribution of the elements of the mixing matrix should disappear automatically in the limit $m_k \to 0$. In fact, even in the SM one can define the three massless flavors neutrinos ν_e, ν_μ, ν_τ as arbitrary unitary linear combinations of three massless neutrinos ν_1, ν_2, ν_3. However, all physical quantities are independent of such an arbitrary transformation.

We conclude that the state in eq. (6) does not describe the neutrino emitted in an electron-capture decay process of the type in eq. (4) and refs. [3,4] are flawed.

The correct normalized state ($\langle\nu_e|\nu_e\rangle = 1$) which describes the electron neutrino emitted in an electron-capture decay processes of the type in eq. (4) is [9,17]

$$\begin{aligned} |\nu_e\rangle &= \left(\sum_j |\langle\nu_j, \mathbb{F}|\mathsf{S}|\mathbb{I}\rangle|^2\right)^{-1/2} \sum_{k=1}^{3} |\nu_k\rangle \, \langle\nu_k, \mathbb{F}|\mathsf{S}|\mathbb{I}\rangle \\ &= \left(\sum_j |U_{ej}|^2 |\mathcal{M}_j|^2\right)^{-1/2} \sum_{k=1}^{3} U_{ek}^* \mathcal{M}_k \, |\nu_k\rangle \, . \end{aligned} \tag{19}$$

In experiments which are not sensitive to the differences of the neutrino masses, as neutrino oscillation experiments, we can approximate $\mathcal{M}_k \simeq \overline{\mathcal{M}}$ and the state (19) reduces to the standard electron neutrino state in eq. (7) (apart for an irrelevant phase $\overline{\mathcal{M}}/|\overline{\mathcal{M}}|$).

With the electron neutrino state in eq. (19), the decay probability is given by

$$P_{\mathbb{I}\to\mathbb{F}+\nu_e} = |\langle\nu_e, \mathbb{F}|\mathsf{S}|\mathbb{I}\rangle|^2 = \sum_{k=1}^{3} |\langle\nu_k, \mathbb{F}|\mathsf{S}|\mathbb{I}\rangle|^2 = \sum_{k=1}^{3} |U_{ek}|^2 \, |\mathcal{M}_k|^2 \, . \tag{20}$$

This is the correct standard result in eq. (14): the decay probability is given by the incoherent sum over the probabilities of decay into different massive neutrinos weighted by the corresponding element of the mixing matrix.

Using eq. (17) and the unitarity of the mixing matrix, one can also easily check that $P_{\mathbb{I}\to\mathbb{F}+\nu_e}$ reduces to $P_{\rm SM}$ in eq. (15) in the massless neutrino limit.

Although the GSI time anomaly cannot be due to effects of neutrino mixing in the final state of the electron capture process, it can be due to interference effects in the initial state. In fact, there could be an interference between two coherent energy states of the decaying ion which produces quantum beats (see, for example, ref. [18]). Also in this case we can draw an analogy with a double-slit experiment. However, we must change the setup, considering the double-slit experiment with two coherent sources of waves depicted in fig. 2. The two coherent sources are produced by an incoming-plane-wave packet hitting a first barrier with two tiny holes. The two coherent outgoing waves interfere in the space between the first and the second barrier. The interference at the holes in the second barrier induces a modulation of the intensity which crosses the barrier.

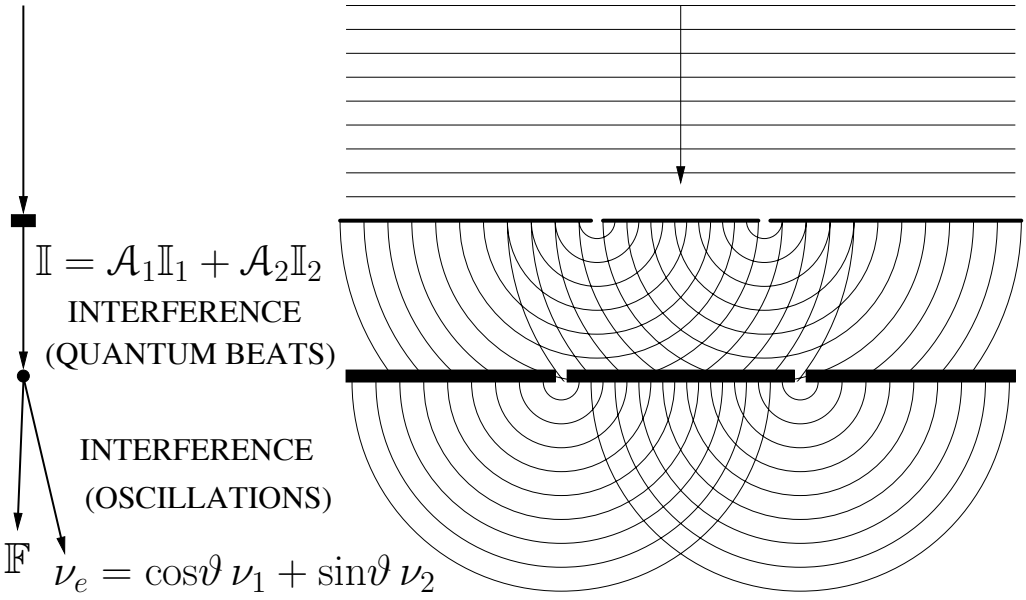

Fig. 2. – Analogy between quantum beats in the electron-capture decay process (4) and a double-slit interference experiment with two coherent sources.

The role of causality is clear: the interference effect is due to the different phases of the two coherent incoming waves at the holes in the second barrier, which have developed during the propagation of the two waves along different path lengths between the two barriers. Analogously, quantum beats in the GSI experiment can be due to interference of two coherent energy states of the decaying ion which develop different phases before the decay. The two coherent energy states could be produced in the creation process of the ion, which in GSI occurs through fragmentation of a beam of heavier ions on a target [1], as illustrated in fig. 2. Alternatively, the two coherent energy states could be due to interactions of the decaying ion in the storage ring.

The quantum-mechanical description of quantum beats is rather simple. If the two energy states of the decaying ion $\mathbb{I}_1$ and $\mathbb{I}_2$ are produced at the time $t = 0$ with amplitudes $\mathcal{A}_1$ and $\mathcal{A}_2$ (with $|\mathcal{A}_1|^2 + |\mathcal{A}_2|^2 = 1$), we have

$$|\mathbb{I}(t=0)\rangle = \mathcal{A}_1\,|\mathbb{I}_1\rangle + \mathcal{A}_2\,|\mathbb{I}_2\rangle\,. \tag{21}$$

Assuming, for simplicity, that the two states with energies E_1 and E_2 have the same decay rate Γ, at the time t we have

$$|\mathbb{I}(t)\rangle = \left(\mathcal{A}_1\,e^{-iE_1t}\,|\mathbb{I}_1\rangle + \mathcal{A}_2\,e^{-iE_2t}\,|\mathbb{I}_2\rangle\right)e^{-\Gamma t/2}\,. \tag{22}$$

The probability of electron capture at the time t is given by

$$\begin{aligned} P_{\mathrm{EC}}(t) &= |\langle\nu_e, \mathbb{F}|\mathsf{S}|\mathbb{I}(t)\rangle|^2 \\ &= \left[1 + A\,\cos(\Delta E t + \varphi)\right]\overline{P}_{\mathrm{EC}}\,e^{-\Gamma t}\,, \end{aligned} \tag{23}$$

where S is the S-matrix operator, $A \equiv 2|\mathcal{A}_1||\mathcal{A}_2|$, $\Delta E \equiv E_2 - E_1$,

$$\overline{P}_{\mathrm{EC}} = |\langle \nu_e, \mathbb{F}|\mathsf{S}|\mathbb{I}_1\rangle|^2 = |\langle \nu_e, \mathbb{F}|\mathsf{S}|\mathbb{I}_2\rangle|^2 \,, \tag{24}$$

and φ is a constant phase which takes into account possible phase differences of $\mathcal{A}_1$ and $\mathcal{A}_2$ and of $\langle \nu_e, \mathbb{F}|\mathsf{S}|\mathbb{I}_1\rangle$ and $\langle \nu_e, \mathbb{F}|\mathsf{S}|\mathbb{I}_2\rangle$.

The fit of GSI data presented in ref. [1] gave

$$\Delta E(^{140}\mathrm{Pr}^{58+}) = (5.86 \pm 0.07) \times 10^{-16}\,\mathrm{eV}\,, \qquad A(^{140}\mathrm{Pr}^{58+}) = 0.18 \pm 0.03\,, \tag{25}$$

$$\Delta E(^{142}\mathrm{Pm}^{60+}) = (5.82 \pm 0.18) \times 10^{-16}\,\mathrm{eV}\,, \qquad A(^{142}\mathrm{Pm}^{60+}) = 0.23 \pm 0.04\,. \tag{26}$$

Therefore, the energy splitting is extremely small and the oscillation amplitude A is significantly smaller than one.

The authors of ref. [1] noted that the splitting of the two hyperfine $1s$ energy levels of the electron is many order of magnitude too large (and the contribution to the decay of one of the two states is suppressed by angular momentum conservation). It is difficult to find a mechanism which produces a smaller energy splitting. Furthermore, since the amplitude $A \simeq 0.2$ of the interference is rather small, it is necessary to find a mechanism which generates coherently the states $\mathbb{I}_1$ and $\mathbb{I}_2$ with probabilities $|\mathcal{A}_1|^2$ and $|\mathcal{A}_2|^2$ having a ratio of about 1/99!

An important question is if the coherence of $\mathbb{I}_1$ and $\mathbb{I}_2$ is preserved during the decay time. Since the measuring apparatus monitors the ions through elastic electromagnetic interactions with a frequency of the order of the revolution frequency in the ESR storage ring, about 2 MHz, the coherence can be preserved only if the interaction with the measuring apparatus does not distinguish between the two states. In this case the interaction is coherent, *i.e.* the two states suffer the same phase shift. Since the energy splitting ΔE is extremely small, I think that coherence is maintained for a long time if $\mathbb{I}_1$ and $\mathbb{I}_2$ have the same electromagnetic properties.

In conclusion, I have shown that the GSI time anomaly cannot be due to neutrino mixing in the final state of the observed electron-capture decays of the hydrogen-like $^{140}\mathrm{Pr}^{58+}$ and $^{142}\mathrm{Pm}^{60+}$ ions. The argument has been clarified through an analogy with a double-slit experiment, emphasizing that it is a consequence of causality [11]. I have explained the reasons why the claim in refs. [2-4] that the GSI time anomaly is due to the mixing of neutrinos in the final state of the electron-capture process is incorrect (see also refs. [19,20]). I have also shown that the GSI time anomaly may be due to quantum beats due to the existence of two coherent energy levels of the decaying ion. However, since the required energy splitting is extremely small (about 6×10^{-16} eV) and the two energy levels must be produced with relative probabilities having a ratio of about 1/99, it is very difficult to find an appropriate mechanism.

REFERENCES

[1] Litvinov Y. A. *et al.*, *Phys. Lett. B*, **664** (2008) 162, arXiv:0801.2079.
[2] Lipkin H. J., arXiv:0805.0435.
[3] Ivanov A. N., Reda R. and Kienle P., arXiv:0801.2121.
[4] Faber M., arXiv:0801.3262.
[5] Bilenky S. M., Giunti C. and Grimus W., *Prog. Part. Nucl. Phys.*, **43** (1999) 1, arXiv:hep-ph/9812360.

[6] Gonzalez-Garcia M. and Nir Y., *Rev. Mod. Phys.*, **75** (2003) 345, arXiv:hep-ph/0202058.
[7] Maltoni M. *et al.*, *New J. Phys.*, **6** (2004) 122, arXiv:hep-ph/0405172.
[8] Strumia A. and Vissani F., arXiv:hep-ph/0606054.
[9] Giunti C. and Kim C. W., *Fundamentals of Neutrino Physics and Astrophysics* (Oxford University Press) 2007.
[10] Gonzalez-Garcia M. C. and Maltoni M., *Phys. Rep.*, **460** (2007) 1, arXiv:0704.1800.
[11] Giunti C., *Phys. Lett. B*, **665** (2008) 92, arXiv:0805.0431.
[12] Shrock R. E., *Phys. Lett. B*, **96** (1980) 159.
[13] McKellar B. H. J., *Phys. Lett. B*, **97** (1980) 93.
[14] Kobzarev I. Y. *et al.*, *Sov. J. Nucl. Phys.*, **32** (1980) 823.
[15] Shrock R. E., *Phys. Rev. D*, **24** (1981) 1232.
[16] Shrock R. E., *Phys. Rev. D*, **24** (1981) 1275.
[17] Giunti C., *J. Phys. G: Nucl. Part. Phys.*, **34** (2007) R93, arXiv:hep-ph/0608070.
[18] Carter R. and Huber J., *Chem. Soc. Rev.*, **29** (2000) 305.
[19] Burkhardt H. *et al.*, arXiv:0804.1099.
[20] Kienert H. *et al.*, *J. Phys. Conf. Ser.*, **136** (2008) 022049, arXiv:0808.2389, *Proceedings of Neutrino 2008, 26-31 May 2008, Christchurch, New Zealand*, see `http://www2.phys.canterbury.ac.nz/ jaa53/`.

IL NUOVO CIMENTO Vol. 32 C, N. 5-6 Settembre-Dicembre 2009
DOI 10.1393/ncc/i2009-10516-3

Colloquia: LaThuile09

Status of neutrino masses and mixing in 2009

G. Altarelli

Dipartimento di Fisica "E. Amaldi", Università di Roma Tre and INFN
Sezione di Roma Tre - I-00146 Rome, Italy
CERN, Department of Physics, Theory Unit - CH–1211 Geneva 23, Switzerland

(ricevuto il 10 Novembre 2009; pubblicato online il 4 Gennaio 2010)

Summary. — We present a very concise summary of the status of our knowledge and understanding of neutrino masses and mixing.

PACS 11.30.-j – Symmetry and conservation laws.
PACS 12.10.-g – Unified field theories and models.
PACS 12.60.-i – Models beyond the standard model.
PACS 13.15.+g – Neutrino interactions.

1. – Experimental data

That neutrinos have a mass has been established by experiments on neutrino oscillations that measure differences of squared masses and mixing angles [1]. Two distinct oscillation frequencies have been at first measured in solar and atmospheric neutrino oscillations and later confirmed by experiments on Earth, like KamLAND and K2K. A signal corresponding to a third mass difference was claimed by the LSND experiment but not confirmed by KARMEN and recently by MiniBooNE. Two well-separated differences need at least three neutrino mass eigenstates involved in oscillations. Conversely the three known neutrino species can be sufficient. At least two ν's must be massive while, in principle, the third one could still be massless. In the following we will assume the simplest picture with three active neutrinos (CPT invariance and no sterile neutrinos). The mass eigenstates involved in solar oscillations are m_1 and m_2 and, by definition, $|m_2| > |m_1|$, so that $\Delta m^2_{\rm sun} = |m_2|^2 - |m_1|^2 > 0$. The atmospheric neutrino oscillations involve m_3: $\Delta m^2_{\rm atm} = |\Delta m^2_{31}|$ with $\Delta m^2_{31} = |m_3|^2 - |m_1|^2$ either positive (normal hierarchy) or negative (inverse hierarchy). The present data are compatible with both cases. The degenerate spectrum occurs when the average absolute value of the masses is much larger than all mass squared differences: $|m_i|^2 \gg \Delta m^2_{hk}$. With the standard set of notations and definitions [1] the present data are summarised in table I.

Oscillation experiments only measure differences of squared masses and do not provide information about the absolute neutrino mass scale. Limits on that are obtained [1]

TABLE I. – *Fit to neutrino oscillation data.*

	ref. [2]	ref. [3]
$(\Delta m^2_{\rm sun})$ $(10^{-5}\,{\rm eV}^2)$	$7.67^{+0.16}_{-0.19}$	$7.65^{+0.23}_{-0.20}$
$\Delta m^2_{\rm atm}$ $(10^{-3}\,{\rm eV}^2)$	$2.39^{+0.11}_{-0.08}$	$2.40^{+0.12}_{-0.11}$
$\sin^2\theta_{12}$	$0.312^{+0.019}_{-0.018}$	$0.304^{+0.022}_{-0.016}$
$\sin^2\theta_{23}$	$0.466^{+0.073}_{-0.058}$	$0.50^{+0.07}_{-0.06}$
$\sin^2\theta_{13}$	0.016 ± 0.010	$0.010^{+0.016}_{-0.011}$

from the endpoint of the tritium beta-decay spectrum, from cosmology and from neutrinoless double-beta decay ($0\nu\beta\beta$). From tritium we have an absolute upper limit of 2.2 eV (at 95% CL) on the mass of electron antineutrino, which, combined with the observed oscillation frequencies under the assumption of three *CPT*-invariant light neutrinos, represents also an upper bound on the masses of the other active neutrinos. Complementary information on the sum of neutrino masses is also provided by the Galaxy power spectrum combined with measurements of the cosmic microwave background anisotropies. According to recent analyses of the most reliable data [4] $\sum_i |m_i| < 0.60$–$0.75\,{\rm eV}$ (at 95% CL) depending on the retained data (the numbers for the sum have to be divided by 3 in order to obtain a limit on the mass of each neutrino). The discovery of $0\nu\beta\beta$ decay would be very important because it would establish lepton number violation and the Majorana nature of ν's, and provide direct information on the absolute scale of neutrino masses. As already mentioned the present limit from $0\nu\beta\beta$ (with large ambiguities from nuclear matrix elements) is about $|m_{ee}| < (0.3$–$0.8)\,{\rm eV}$ [4] (see eq. (3)).

2. – Majorana neutrinos and the see-saw mechanism

Given that neutrino masses are certainly extremely small, it is really difficult from the theory point of view to avoid the conclusion that the lepton number L conservation is probably violated and that ν's are Majorana fermions. In this case the smallness of neutrino masses can be naturally explained as inversely proportional to the very large scale where L is violated, of order the grand unification scale $M_{\rm GUT}$ or maybe, for the lightest among them, the Planck scale $M_{\rm Pl}$. If neutrinos are Majorana particles, their masses arise from the generic dimension-five non-renormalizable operator of the form

$$O_5 = \frac{(Hl)_i^T \lambda_{ij} (Hl)_j}{M} + {\rm h.c.}, \tag{1}$$

with H being the ordinary Higgs doublet, l_i the $SU(2)$ lepton doublets, λ a matrix in flavour space, M a large scale of mass and a charge conjugation matrix C between the lepton fields is understood.

Neutrino masses generated by O_5 are of the order $m_\nu \approx v^2/M$ for $\lambda_{ij} \approx O(1)$, where $v \sim O(100\,{\rm GeV})$ is the vacuum expectation value of the ordinary Higgs. A particular realization leading to comparable masses is the see-saw mechanism [5], where M derives from the exchange of heavy neutral objects of weak isospin 0 or 1. In the simplest case the exchanged particle is the ν_R and the resulting neutrino mass matrix reads (1st-type

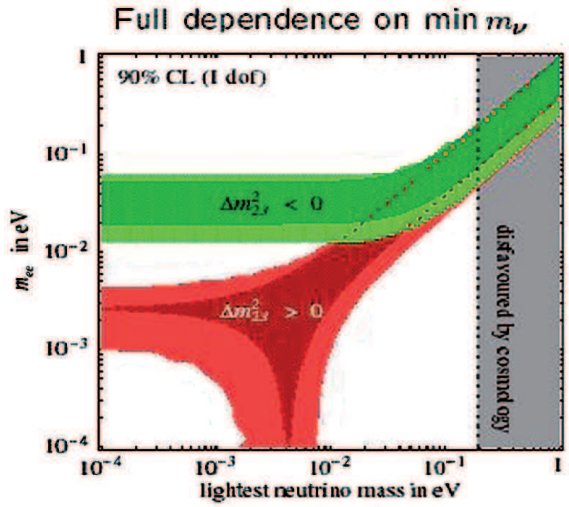

Fig. 1. – A plot [6] of m_{ee} in eV, the quantity measured in neutrinoless double-beta decay, given in eq. (3), *versus* the lightest neutrino mass m_1, also in eV. The upper (lower) band is for inverse (normal) hierarchy.

see-saw):

$$m_\nu = m_D^T M^{-1} m_D. \tag{2}$$

As one can see, the light neutrino masses are quadratic in the Dirac masses and inversely proportional to the large Majorana mass. For $m_\nu \approx \sqrt{\Delta m^2_{atm}} \approx 0.05\,\text{eV}$ and $m_\nu \approx m_D^2/M$ with $m_D \approx v \approx 200\,\text{GeV}$, we find $M \approx 10^{15}\,\text{GeV}$ which indeed is an impressive indication that the scale for lepton number violation is close to M_{GUT}. Thus probably neutrino masses are a probe into the physics near M_{GUT}. This argument, in my opinion, strongly discourages models where neutrino masses are generated near the weak scale and are suppressed by some special mechanism.

3. – Importance of neutrinoless double-beta decay

Oscillation experiments cannot distinguish between Dirac and Majorana neutrinos. The detection of neutrinoless double-beta decay would provide direct evidence of L non-conservation, and the Majorana nature of neutrinos. It would also offer a way to possibly disentangle the 3 cases of degenerate-, normal- or inverse-hierachy neutrino spectrum. The quantity which is bound by experiments on $0\nu\beta\beta$ is the 11 entry of the ν mass matrix, which in general, from $m_\nu = U^* m_{\text{diag}} U^\dagger$, is given by

$$|m_{ee}| = |(1 - s^2_{13})\,(m_1 c^2_{12} + m_2 s^2_{12}) + m_3 e^{2i\phi} s^2_{13}|, \tag{3}$$

where $m_{1,2}$ are complex masses (including Majorana phases) while m_3 can be taken as real and positive and ϕ is the U_{PMNS} phase measurable from CP violation in oscillation experiments. Starting from this general formula it is simple to derive the bounds for degenerate, inverse-hierarchy or normal-hierarchy mass patterns shown in fig. 1.

In the next few years a new generation of experiments will reach a larger sensitivity on $0\nu\beta\beta$ by about an order of magnitude. If these experiments should observe a signal this would indicate that the inverse hierarchy is realized, if not, then the normal-hierarchy case remains a possibility.

4. – Baryogenesis via leptogenesis from heavy ν^c decay

In the Universe we observe an apparent excess of baryons over antibaryons. It is appealing that one can explain the observed baryon asymmetry by dynamical evolution (baryogenesis) starting from an initial state of the Universe with zero baryon number. For baryogenesis one needs the three famous Sakharov conditions: B violation, CP violation and no thermal equilibrium. In the history of the Universe these necessary requirements have possibly occurred at different epochs. Note however that the asymmetry generated by one epoch could be erased at following epochs if not protected by some dynamical reason. In principle these conditions could be verified in the SM at the electroweak phase transition. B is violated by instantons when kT is of the order of the weak scale (but $B - L$ is conserved), CP is violated by the CKM phase and sufficiently marked out-of-equilibrium conditions could be realized during the electroweak phase transition. So the conditions for baryogenesis at the weak scale in the SM superficially appear to be present. However, a more quantitative analysis [7] shows that baryogenesis is not possible in the SM because there is not enough CP violation and the phase transition is not sufficiently strong first order, unless the Higgs mass is below a bound which by now is excluded by LEP. In SUSY extensions of the SM, in particular in the MSSM, there are additional sources of CP violation and the bound on m_H is modified but also this possibility has by now become at best marginal after the results from LEP2.

If baryogenesis at the weak scale is excluded by the data it can occur at or just below the GUT scale, after inflation. But only that part with $|B - L| > 0$ would survive and not be erased at the weak scale by instanton effects. Thus baryogenesis at $kT \sim 10^{10}$–10^{15} GeV needs $B - L$ violation and this is also needed to allow m_ν if neutrinos are Majorana particles. The two effects could be related if baryogenesis arises from leptogenesis then converted into baryogenesis by instantons [8]. The decays of heavy Majorana neutrinos (the heavy eigenstates of the see-saw mechanism) happen with violation of lepton number L, hence also of $B - L$ and can well involve a sufficient amount of CP violation. Recent results on neutrino masses are compatible with this elegant possibility. Thus the case of baryogenesis through leptogenesis has been boosted by the recent results on neutrinos.

5. – Models of neutrino mixing

After KamLAND, SNO and the upper limits on the absolute value of neutrino masses not too much hierarchy in the spectrum of neutrinos is indicated by experiments:

$$r = \Delta m^2_{\rm sol}/\Delta m^2_{\rm atm} \sim 1/30. \tag{4}$$

Precisely $r = 0.032^{+0.006}_{-0.005}$ at 3σ's [2, 3]. Thus, for a hierarchical spectrum, $m_2/m_3 \sim \sqrt{r} \sim 0.2$, which is comparable to the Cabibbo angle $\lambda_C \sim 0.22$ or $\sqrt{m_\mu/m_\tau} \sim 0.24$. This suggests that the same hierarchy parameter (raised to powers with $o(1)$ exponents) may apply for quark, charged lepton and neutrino mass matrices. This in turn indicates that, in the absence of some special dynamical reason, we do not expect quantities like θ_{13}

or the deviation of θ_{23} from its maximal value to be too small. Indeed it would be very important to know how small the mixing angle θ_{13} is and how close to maximal θ_{23} is.

We see from table I [2,3] that within measurement errors the observed neutrino mixing matrix is compatible with the so-called Tri-Bimaximal (TB) form [9]. The best measured neutrino mixing angle θ_{12} is just about 1σ below the TB value $\tan^2\theta_{12} = 1/2$, while the maximal value for θ_{23} is well inside the 1-σ interval and θ_{13} is still compatible with zero (see table I).

The TB mixing matrix (in a particular phase convention) is given by

$$U_{\rm TB} = \begin{pmatrix} \sqrt{\frac{2}{3}} & \frac{1}{\sqrt{3}} & 0 \\ -\frac{1}{\sqrt{6}} & \frac{1}{\sqrt{3}} & -\frac{1}{\sqrt{2}} \\ -\frac{1}{\sqrt{6}} & \frac{1}{\sqrt{3}} & \frac{1}{\sqrt{2}} \end{pmatrix}. \tag{5}$$

The TB mixing matrix suggests that mixing angles are independent of mass ratios (while for quark mixings relations like $\lambda_C^2 \sim m_d/m_s$ are typical). In fact in the basis where charged lepton masses are diagonal, the effective neutrino mass matrix in the TB case is given by $m_\nu = U_{\rm TB}\,{\rm diag}(m_1, m_2, m_3)U_{\rm TB}^T$:

$$m_\nu = \left[\frac{m_3}{2}M_3 + \frac{m_2}{3}M_2 + \frac{m_1}{6}M_1\right], \tag{6}$$

where

$$M_3 = \begin{pmatrix} 0 & 0 & 0 \\ 0 & 1 & -1 \\ 0 & -1 & 1 \end{pmatrix}, \qquad M_2 = \begin{pmatrix} 1 & 1 & 1 \\ 1 & 1 & 1 \\ 1 & 1 & 1 \end{pmatrix}, \qquad M_1 = \begin{pmatrix} 4 & -2 & -2 \\ -2 & 1 & 1 \\ -2 & 1 & 1 \end{pmatrix}. \tag{7}$$

The eigenvalues of m_ν are m_1, m_2, m_3 with eigenvectors $(-2,1,1)/\sqrt{6}$, $(1,1,1)/\sqrt{3}$ and $(0,1,-1)/\sqrt{2}$, respectively. The expression in eq. (6) can be reproduced in models with sequential dominance or with form dominance, discussed by S. King and collaborators [10].

As we see the most general neutrino mass matrix corresponding to TB mixing, in the basis of diagonal charged leptons, is of the form

$$m = \begin{pmatrix} x & y & y \\ y & x+v & y-v \\ y & y-v & x+v \end{pmatrix}. \tag{8}$$

This is a symmetric, 2-3 symmetric matrix with $a_{11} + a_{12} = a_{22} + a_{23}$.

Thus, one possibility is that one takes this coincidence seriously and considers models where TB mixing is a good first approximation. In a series of papers [11-17] it has been pointed out that a broken flavour symmetry based on the discrete group A_4 appears to be particularly suitable to reproduce this specific mixing pattern in Leading Order (LO). Other solutions based on alternative discrete or continuous flavour groups have also been

considered [18-20], but the A_4 models have a very economical and attractive structure, *e.g.*, in terms of group representations and of field content.

We recall that A_4, the group of even permutations of 4 objects, can be generated by the two elements S and T obeying the relations (a "presentation" of the group)

$$S^2 = (ST)^3 = T^3 = 1. \tag{9}$$

The 12 elements of A_4 are obtained as: 1, S, T, ST, TS, T^2, ST^2, STS, TST, T^2S, TST^2, T^2ST. The inequivalent irreducible representations of A_4 are 1, $1'$, $1''$ and 3. It is immediate to see that one-dimensional unitary representations are given by

$$\begin{aligned} &1 \quad S = 1, \quad T = 1, \\ &1' \quad S = 1, \quad T = e^{i4\pi/3} \equiv \omega^2, \\ &1'' \quad S = 1, \quad T = e^{i2\pi/3} \equiv \omega. \end{aligned} \tag{10}$$

The three-dimensional unitary representation, in a basis where the element T is diagonal, is given by

$$T = \begin{pmatrix} 1 & 0 & 0 \\ 0 & \omega^2 & 0 \\ 0 & 0 & \omega \end{pmatrix}, \qquad S = \frac{1}{3}\begin{pmatrix} -1 & 2 & 2 \\ 2 & -1 & 2 \\ 2 & 2 & -1 \end{pmatrix}. \tag{11}$$

Note that the generic mass matrix for TB mixing in eq. (8) can be specified as the most general matrix that is invariant under μ-τ symmetry, implemented by the unitary matrix $A_{\mu\tau}$:

$$A_{\mu\tau} = \begin{pmatrix} 1 & 0 & 0 \\ 0 & 0 & 1 \\ 0 & 1 & 0 \end{pmatrix} \tag{12}$$

and under the S transformation:

$$m = SmS, \quad m = A_{\mu\tau} m A_{\mu\tau}, \tag{13}$$

where S is given in eq. (11). This observation plays a role in leading to A_4 as a candidate group for TB mixing, because S is a matrix of A_4 (but $A_{\mu\tau}$ is not and μ-τ symmetry has to be separately implemented).

The flavour symmetry is broken by two triplets φ_S and φ_T and by singlets ξ. All these fields are gauge singlets. The fields φ_T, φ_S and ξ develop a VEV along the directions

$$\langle \varphi_T \rangle = (v_T, 0, 0), \qquad \langle \varphi_S \rangle = (v_S, v_S, v_S), \qquad \langle \xi \rangle = u. \tag{14}$$

A crucial part of all serious A_4 models is the dynamical generation of this alignment in a natural way. In most of the models A_4 is accompanied by additional flavour symmetries, either discrete like Z_N or continuous like $U(1)$, which are necessary to eliminate unwanted couplings, to ensure the needed vacuum alignment and to reproduce the observed mass hierarchies. In the leading approximation A_4 models lead to exact TB mixing. Given the set of flavour symmetries and having specified the field content, the non-leading

corrections to the TB mixing arising from higher-dimensional effective operators can be evaluated in a well-defined expansion. In the absence of specific dynamical tricks, in a generic model, all the three mixing angles receive corrections of the same order of magnitude. Since the experimentally allowed departures of θ_{12} from the TB value $\sin^2\theta_{12} = 1/3$ are small, at most of $\mathcal{O}(\lambda_C^2)$, with λ_C the Cabibbo angle, it follows that both θ_{13} and the deviation of θ_{23} from the maximal value are expected in these models to also be at most of $\mathcal{O}(\lambda_C^2)$ (note that λ_C is a convenient hierarchy parameter not only for quarks but also in the charged-lepton sector with $m_\mu/m_\tau \sim 0.06 \sim \lambda_C^2$ and $m_e/m_\mu \sim 0.005 \sim \lambda_C^{3-4}$). A value of $\theta_{13} \sim \mathcal{O}(\lambda_C^2)$ is within the sensitivity of the experiments which are now in preparation and will take data in the near future.

6. – A_4, quarks and GUTs

Much attention has been devoted to the question whether models with TB mixing in the neutrino sector can be suitably extended to also successfully describe the observed pattern of quark mixings and masses and whether this more complete framework can be made compatible with (supersymmetric (SUSY)) $SU(5)$ or $SO(10)$ grand unification. Early attempts of extending models based on A_4 to quarks [21,13] and to construct grand-unified versions [22] have not been satisfactory, *e.g.*, do not offer natural mechanisms for mass hierarchies and/or for the vacuum alignment. A direct extension of the A_4 model to quarks leads to the identity matrix for V_{CKM} in the lowest approximation, which at first looks promising. But the corrections to it turn out to be strongly constrained by the leptonic sector, because lepton mixings are nearly TB, and, in the simplest models, are proven to be too small to accommodate the observed quark mixing angles [13]. Also, the quark classification adopted in these models is not compatible with A_4 commuting with $SU(5)$ (in ref. [23] an A_4 model compatible with the Pati-Salam group $SU(4) \times SU(2)_L \times SU(2)_R$ has been presented). Due to this, larger discrete groups have been considered for the description of quarks and for grand-unified versions with approximate TB mixing in the lepton sector. A particularly appealing set of models is based on the discrete group T', the double covering group of A_4 [24]. In ref. [25] a viable description was obtained, *i.e.* in the leptonic sector the predictions of the A_4 model are reproduced, while the T' symmetry plays an essential role for reproducing the pattern of quark mixing. But, again, the classification adopted in this model is not compatible with grand unification. Unified models based on the discrete groups T' [26], S_4 [27] and $\Delta(27)$ [28] have been discussed. Several models using the smallest non-Abelian symmetry S_3 (which is isomorphic to D_3) can also be found in the recent literature [29].

As a result, the group A_4 was considered by most authors to be unsuitable to also describe quarks and to lead to a grand unified description. We have recently shown [15] that this negative attitude is not justified and that it is actually possible to construct a viable model based on A_4 which leads to a grand unified theory (GUT) of quarks and leptons with TB mixing for leptons. At the same time our model offers an example of an extra-dimensional GUT in which a description of all fermion masses and mixings is attempted. The model is natural, since most of the small parameters in the observed pattern of masses and mixings as well as the necessary vacuum alignment are justified by the symmetries of the model. The formulation of $SU(5)$ in extra dimensions has the usual advantages of avoiding large Higgs representations to break $SU(5)$ and of solving the doublet-triplet splitting problem. A see-saw realization in terms of an A_4 triplet of right-handed neutrinos ν_R ensures the correct ratio of light neutrino masses with respect to the GUT scale. In our model extra-dimensional effects directly contribute to determine

the flavour pattern, in that the two lightest tenplets T_1 and T_2 are in the bulk (with a doubling T_i and T_i', $i = 1, 2$ to ensure the correct zero-mode spectrum), whereas the pentaplets F and T_3 are on the brane. The hierarchy of quark and charged-lepton masses and of quark mixings is determined by a combination of extra dimensional suppression factors for the first two generations and of the $U(1)$ charges, while the neutrino mixing angles derive from A_4. The choice of the transformation properties of the two Higgses H_5 and $H_{\bar{5}}$ is also crucial. They are chosen to transform as two different A_4 singlets 1 and $1'$. As a consequence, mass terms for the Higgs colour triplets are not directly allowed at all orders and their masses are introduced by orbifolding, *à la* Kawamura [30]. Finally, in this model, proton decay is dominated by gauge vector boson exchange giving rise to dimension-six operators. Given the relatively large theoretical uncertainties, the decay rate is within the present experimental limits. In conclusion, the model is shown to be directly compatible with approximate TB mixing for leptons as well as with a realistic pattern of fermion masses and of quark mixings in a SUSY $SU(5)$ framework.

7. – Bimaximal mixing and S_4

Alternatively one can assume that the agreement of TB mixing with the data is accidental. Indeed there are many models that fit the data and yet TB mixing does not play a role in their architecture. For example, in ref. [31] there is a list of Grand Unified $SO(10)$ models with fits to the neutrino mixing angles that show good agreement with the data although most of them have no relation with TB mixing. Similarly for models based on $SU(5) \otimes U(1)$ [1]. Another class of examples is found in ref. [32]. However, in most cases, for this type of models different mixing angles could also be accommodated by simply varying the fitted values of the parameters. Assuming that the agreement of TB mixing with the data is accidental, we observe that the present data do not exclude a larger value for θ_{13}, $\theta_{13} \sim \mathcal{O}(\lambda_C)$, than generally implied by models with approximate TB mixing. In fact, two recent analyses of the available data lead to $\sin^2\theta_{13} = 0.016 \pm 0.010$ at 1σ [2] and $\sin^2\theta_{13} = 0.010^{+0.016}_{-0.011}$ at 1σ [3], which are compatible with both options. If experimentally it is found that θ_{13} is near its present upper bound, this could be interpreted as an indication that the agreement with the TB mixing is accidental. Then a scheme where instead the Bimaximal (BM) mixing is the correct first approximation could be relevant. The BM mixing matrix is given by

$$U_{\rm BM} = \begin{pmatrix} \frac{1}{\sqrt{2}} & -\frac{1}{\sqrt{2}} & 0 \\ \frac{1}{2} & \frac{1}{2} & -\frac{1}{\sqrt{2}} \\ \frac{1}{2} & \frac{1}{2} & \frac{1}{\sqrt{2}} \end{pmatrix}. \tag{15}$$

In the BM scheme $\tan^2\theta_{12} = 1$, to be compared with the latest experimental determination: $\tan^2\theta_{12} = 0.45 \pm 0.04$ (at 1σ) [2, 3], so that a rather large non-leading correction is needed such that $\tan^2\theta_{12}$ is modified by terms of $\mathcal{O}(\lambda_C)$. This is in line with the well-known empirical observation that $\theta_{12} + \lambda_C \sim \pi/4$, a relation known as quark-lepton complementarity [33], or similarly $\theta_{12} + \sqrt{m_\mu/m_\tau} \sim \pi/4$. No compelling model leading, without parameter fixing, to the exact complementarity relation has been produced so far. Probably the exact complementarity relation is to be replaced with something like

$\theta_{12} + \mathcal{O}(\lambda_C) \sim \pi/4$ or $\theta_{12} + \mathcal{O}(m_\mu/m_\tau) \sim \pi/4$ (which we could call "weak" complementarity), as in models where the large ν mixings arise from the diagonalisation of charged leptons. Along this line of thought, we have used the expertise acquired with non-Abelian finite flavour groups to construct a model [34] based on the permutation group S_4 which naturally leads to the BM mixing at LO. We have adopted a supersymmetric formulation of the model in 4 space-time dimensions. The complete flavour group is $S_4 \times Z_4 \times U(1)_{FN}$. At LO, the charged leptons are diagonal and hierarchical and the light neutrino mass matrix, after see-saw, leads to the exact BM mixing. The model is built in such a way that the dominant corrections to the BM mixing, from higher-dimensional operators in the superpotential, only arise from the charged-lepton sector and naturally inherit λ_C as the relevant expansion parameter. As a result the mixing angles deviate from the BM values by terms of $\mathcal{O}(\lambda_C)$ (at most), and weak complementarity holds. A crucial feature of the model is that only θ_{12} and θ_{13} are corrected by terms of $\mathcal{O}(\lambda_C)$ while θ_{23} is unchanged at this order (which is essential to make the model agree with the present data).

8. – Conclusion

In the last decade we have learnt a lot about neutrino masses and mixings. A list of important conclusions have been reached. Neutrinos are not all massless but their masses are very small. Probably masses are small because neutrinos are Majorana particles with masses inversely proportional to the large scale M of lepton number violation. It is quite remarkable that M is empirically not far from M_{GUT}, so that neutrino masses fit well in the SUSY GUT picture. Also out of equilibrium decays with CP and L violation of heavy RH neutrinos can produce a $B-L$ asymmetry, then converted near the weak scale by instantons into an amount of B asymmetry compatible with observations (baryogenesis via leptogenesis) [8]. It has been established that neutrinos are not a significant component of dark matter in the Universe. We have also understood there is no contradiction between large neutrino mixings and small quark mixings, even in the context of GUTs.

This is a very impressive list of achievements. Coming to a detailed analysis of neutrino masses and mixings a very long collection of models have been formulated over the years. With continuous improvement of the data and more precise values of the mixing angles most of the models have been discarded by experiment. By now, besides the detailed knowledge of the entries of the V_{CKM} matrix we also have a reasonable determination of the neutrino mixing matrix U_{PMNS}. It is remarkable that neutrino and quark mixings have such a different qualitative pattern. One could have imagined that neutrinos would bring a decisive boost towards the formulation of a comprehensive understanding of fermion masses and mixings. In reality it is frustrating that no real illumination was sparked on the problem of flavour. We can reproduce in many different ways the observations but we have not yet been able to single out a unique and convincing baseline for the understanding of fermion masses and mixings. In spite of many interesting ideas and the formulation of many elegant models the mysteries of the flavour structure of the three generations of fermions have not been much unveiled.

* * *

I thank the Organizers of Les Rencontres, in particular my colleague at Roma Tre Mario Greco, for their kind invitation.

REFERENCES

[1] Altarelli G. and Feruglio F., *New J. Phys.*, **6** (2004) 106 [arXiv:hep-ph/0405048].

[2] Fogli G. L., Lisi E., Marrone A., Palazzo A. and Rotunno A. M., *Phys. Rev. Lett.*, **101** (2008) 141801 [arXiv:0806.2649 [hep-ph]]; Fogli G. L., Lisi E., Marrone A., Palazzo A. and Rotunno A. M., arXiv:0809.2936 [hep-ph].

[3] Schwetz T., Tortola M. and Valle J. W. F., *New J. Phys.*, **10** (2008) 113011. [arXiv:0808.2016 [hep-ph]]; Maltoni M. and Schwetz T., arXiv:0812.3161 [hep-ph].

[4] Fogli G. L. *et al.*, arXiv:0805.2517 [hep-ph].

[5] Minkowski P., *Phys. Lett. B*, **67** (1977) 421; Yanagida T., in *Proceedings of the Workshop on Unified Theory and Baryon Number in the Universe*, KEK, *March 1979*; Glashow S. L., in *"Quarks and Leptons", Cargèse*, edited by Lévy M. *et al.* (Plenum, New York) 1980, p. 707; Gell-Mann M., Ramond P. and Slansky R., in *Supergravity* (Stony Brook) 1979; Mohapatra R. N. and Senjanovic G., *Phys. Rev. Lett.*, **44** (1980) 912.

[6] Feruglio F., Strumia A. and Vissani F., *Nucl. Phys. B*, **637** (2002) 345; *Addendum: Nucl. Phys. B*, **659** (2003) 359 [arXiv:hep-ph/0201291].

[7] For a review see for example: Trodden M., *Rev. Mod. Phys.*, **71** (1999) 1463.

[8] For a review see for example: Buchmuller W., Peccei R. D. and Yanagida T., *Annu. Rev. Nucl. Part. Sci.*, **55** (2005) 311 [arXiv:hep-ph/0502169].

[9] Harrison P. F., Perkins D. H. and Scott W. G., *Phys. Lett. B*, **530** (2002) 167 [arXiv:hep-ph/0202074]; Harrison P. F. and Scott W. G., *Phys. Lett. B*, **535** (2002) 163 [arXiv:hep-ph/0203209]; *Phys. Lett. B*, **547** (2002) 219 [arXiv:hep-ph/0210197]; *Phys. Lett. B*, **557** (2003) 76 [arXiv:hep-ph/0302025]; arXiv:hep-ph/0402006; arXiv:hep-ph/0403278; Xing Z. z., *Phys. Lett. B*, **533** (2002) 85 [arXiv:hep-ph/0204049].

[10] King S. F., [arXiv:0904.3255[hep-ph]].

[11] Ma E. and Rajasekaran G., *Phys. Rev. D*, **64** (2001) 113012 [arXiv:hep-ph/0106291]; Ma E., *Mod. Phys. Lett. A*, **17** (2002) 627 [arXiv:hep-ph/0203238]; Babu K. S., Ma E. and Valle J. W. F., *Phys. Lett. B*, **552** (2003) 207 [arXiv:hep-ph/0206292]; Hirsch M., Romao J. C., Skadhauge S., Valle J. W. F. and Villanova del Moral A., arXiv:hep-ph/0312244; *Phys. Rev. D*, **69** (2004) 093006 [arXiv:hep-ph/0312265]; Ma E., *Phys. Rev. D*, **70** (2004) 031901; *Phys. Rev. D*, **70** (2004) 031901 [arXiv:hep-ph/0404199]; *New J. Phys.*, **6** (2004) 104 [arXiv:hep-ph/0405152], arXiv:hep-ph/0409075; Chen S. L., Frigerio M. and Ma E., *Nucl. Phys. B*, **724** (2005) 423 [arXiv:hep-ph/0504181]; Ma E., *Phys. Rev. D*, **72** (2005) 037301 [arXiv:hep-ph/0505209]; Hirsch M., Villanova del Moral A., Valle J. W. F. and Ma E., *Phys. Rev. D*, **72** (2005) 091301; 119904(E) [arXiv:hep-ph/0507148]; Babu K. S. and He X. G., arXiv:hep-ph/0507217; Ma E., *Mod. Phys. Lett. A*, **20** (2005) 2601 [arXiv:hep-ph/0508099]; Zee A., *Phys. Lett. B*, **630** (2005) 58 [arXiv:hep-ph/0508278]; Ma E., *Phys. Rev. D*, **73** (2006) 057304 [arXiv:hep-ph/0511133]; He X. G., Keum Y. Y. and Volkas R. R., *JHEP*, **0604** (2006) 039 [arXiv:hep-ph/0601001]; Adhikary B., Brahmachari B., Ghosal A., Ma E. and Parida M. K., *Phys. Lett. B*, **638** (2006) 345 [arXiv:hep-ph/0603059]; Ma E., *Mod. Phys. Lett. A*, **21** (2006) 2931 [arXiv:hep-ph/0607190]; *Mod. Phys. Lett. A*, **22** (2007) 101 [arXiv:hep-ph/0610342]; Lavoura L. and Kuhbock H., *Mod. Phys. Lett. A*, **22** (2007) 181 [arXiv:hep-ph/0610050]; King S. F. and Malinsky M., *Phys. Lett. B*, **645** (2007) 351 [arXiv:hep-ph/0610250]; Morisi S., Picariello M. and Torrente-Lujan E., *Phys. Rev. D*, **75** (2007) 075015 [arXiv:hep-ph/0702034]; Hirsch M., Joshipura A. S., Kaneko S. and Valle J. W. F., *Phys. Rev. Lett.*, **99** (2007) 151802 [arXiv:hep-ph/0703046]; Yin F., *Phys. Rev. D*, **75** (2007) 073010 [arXiv:0704.3827 [hep-ph]]; Bazzocchi F., Kaneko S. and Morisi S., *JHEP*, **0803** (2008) 063 [arXiv:0707.3032 [hep-ph]]; Bazzocchi F., Morisi S. and Picariello M., *Phys. Lett. B*, **659** (2008) 628 [arXiv:0710.2928 [hep-ph]]; Honda M. and Tanimoto M., *Prog. Theor. Phys.*, **119** (2008) 583 [arXiv:0801.0181 [hep-ph]]; Brahmachari B., Choubey S. and Mitra M., *Phys. Rev. D*, **77** (2008) 073008; 119901(E) [arXiv:0801.3554 [hep-ph]]; Bazzocchi F., Morisi S., Picariello M. and Torrente-Lujan E., *J. Phys. G*, **36** (2009) 015002 [arXiv:0802.1693 [hep-ph]];

Adhikary B. and Ghosal A., *Phys. Rev. D*, **78** (2008) 073007 [arXiv:0803.3582 [hep-ph]]; Hirsch M., Morisi S. and Valle J. W. F., *Phys. Rev. D*, **78** (2008) 093007 [arXiv:0804.1521 [hep-ph]]; Frampton P. H. and Matsuzaki S., arXiv:0806.4592 [hep-ph]; Csaki C., Delaunay C., Grojean C. and Grossman Y., arXiv:0806.0356 [hep-ph]; Feruglio F., Hagedorn C., Lin Y. and Merlo L., arXiv:0807.3160 [hep-ph]; Bazzocchi F., Frigerio M. and Morisi S., arXiv:0809.3573 [hep-ph]; Grimus W. and Lavoura L., arXiv:0811.4766 [hep-ph]; Morisi S., arXiv:0901.1080 [hep-ph]; Ciafaloni P., Picariello M., Torrente-Lujan E. and Urbano A., arXiv:0901.2236 [hep-ph]; Chen M. C. and King S. F., arXiv:0903.0125 [hep-ph].

[12] Altarelli G. and Feruglio F., *Nucl. Phys. B*, **720** (2005) 64 [arXiv:hep-ph/0504165].

[13] Altarelli G. and Feruglio F., *Nucl. Phys. B*, **741** (2006) 215 [arXiv:hep-ph/0512103].

[14] Altarelli G., Feruglio F. and Lin Y., *Nucl. Phys. B*, **775** (2007) 31 [arXiv:hep-ph/0610165].

[15] Altarelli G., Feruglio F. and Hagedorn C., *JHEP*, **0803** (2008) 052 [arXiv:0802.0090 [hep-ph]].

[16] Lin Y., *Nucl. Phys. B*, **813** (2009) 91 [arXiv:0804.2867 [hep-ph]]; arXiv:0903.0831 [hep-ph].

[17] Altarelli G. and Meloni D., arXiv:0905.0620[hep-ph].

[18] King S. F., *JHEP*, **0508** (2005) 105 [arXiv:hep-ph/0506297]; de Medeiros Varzielas I. and Ross G. G., arXiv:hep-ph/0507176. de Medeiros Varzielas I., King S. F. and Ross G. G., *Phys. Lett. B*, **644** (2007) 153 [arXiv:hep-ph/0512313]; de Medeiros Varzielas I., King S. F. and Ross G. G., *Phys. Lett. B*, **648** (2007) 201 [arXiv:hep-ph/0607045]; King S. F. and Malinsky M., *JHEP*, **0611** (2006) 071 [arXiv:hep-ph/0608021]; Antusch S., King S. F. and Malinsky M., *JHEP*, **0806** (2008) 068 [arXiv:0708.1282 [hep-ph]].

[19] For other approaches to the tri-bimaximal mixing see: Matias J. and Burgess C. P., *JHEP*, **0509** (2005) 052 [arXiv:hep-ph/0508156]; Luo S. and Xing Z. z., arXiv:hep-ph/0509065; Grimus W. and Lavoura L., arXiv:hep-ph/0509239; Caravaglios F. and Morisi S., arXiv:hep-ph/0510321; de Medeiros Varzielas I., King S. F. and Ross G. G., *Phys. Lett. B*, **648** (2007) 201 [arXiv:hep-ph/0607045]; Feruglio F., Hagedorn C., Lin Y. and Merlo L., *Nucl. Phys. B*, **775** (2007) 120 [arXiv:hep-ph/0702194]; Chen M. C. and Mahanthappa K. T., *Phys. Lett. B*, **652** (2007) 34 [arXiv:0705.0714 [hep-ph]]; Frampton P. H. and Kephart T. W., *JHEP*, **0709** (2007) 110 [arXiv:0706.1186 [hep-ph]]; Ding G. J., arXiv:0803.2278 [hep-ph]; He Zhang, *Phys. Lett. B*, **655** (2007) 132; Bazzocchi F. and Morisi S., arXiv:0811.0345 [hep-ph]; de Medeiros Varzielas I., Ross G. G. and Serna M., arXiv:0811.2226 [hep-ph]; Frampton P. H. and Matsuzaki S., arXiv:0902.1140 [hep-ph].

[20] Bazzocchi F., Merlo L. and Morisi S., arXiv:0901.2086 [hep-ph]; arXiv:0902.2849 [hep-ph].

[21] Ma E., *Mod. Phys. Lett. A*, **17** (2002) 627 [arXiv:hep-ph/0203238].

[22] Ma E., *Mod. Phys. Lett. A*, **20** (2005) 2767 [arXiv:hep-ph/0506036]; **21** (2006) 2931 [arXiv:hep-ph/0607190]; Ma E., Sawanaka H. and Tanimoto M., *Phys. Lett. B*, **641** (2006) 301 [arXiv:hep-ph/0606103]; Morisi S., Picariello M. and Torrente-Lujan E., *Phys. Rev. D*, **75** (2007) 075015 [arXiv:hep-ph/0702034]; Grimus W. and Kuhbock H., arXiv:0710.1585 [hep-ph].

[23] King S. F. and Malinsky M., *Phys. Lett. B*, **645** (2007) 351 [arXiv:hep-ph/0610250].

[24] Frampton P. H. and Kephart T. W., *Int. J. Mod. Phys. A*, **10** (1995) 4689 [arXiv:hep-ph/9409330]; Aranda A., Carone C. D. and Lebed R. F., *Phys. Lett. B*, **474** (2000) 170 [arXiv:hep-ph/9910392]; *Phys. Rev. D*, **62** (2000) 016009 [arXiv:hep-ph/0002044]; Carr P. D. and Frampton P. H., arXiv:hep-ph/0701034; Frampton P. H. and Kephart T. W., *JHEP*, **0709** (2007) 110 [arXiv:0706.1186 [hep-ph]]; Aranda A., *Phys. Rev. D*, **76** (2007) 111301 [arXiv:0707.3661 [hep-ph]].

[25] Feruglio F., Hagedorn C., Lin Y. and Merlo L., *Nucl. Phys. B*, **775** (2007) 120 [arXiv:hep-ph/0702194].

[26] Chen M. C. and Mahanthappa K. T., *Phys. Lett. B*, **652** (2007) 34 [arXiv:0705.0714 [hep-ph]].

[27] Lee D. G. and Mohapatra R. N., *Phys. Lett. B*, **329** (1994) 463 [arXiv:hep-ph/9403201]; Mohapatra R. N., Parida M. K. and Rajasekaran G., *Phys. Rev. D*, **69** (2004) 053007 [arXiv:hep-ph/0301234]; Hagedorn C., Lindner M. and Mohapatra R. N., *JHEP*, **0606** (2006) 042 [arXiv:hep-ph/0602244]; Cai Y. and Yu H. B., *Phys. Rev. D*, **74** (2006) 115005 [arXiv:hep-ph/0608022].

[28] de Medeiros Varzielas I., King S. F. and Ross G. G., *Phys. Lett. B*, **648** (2007) 201 [arXiv:hep-ph/0607045].

[29] Dermisek R. and Raby S., *Phys. Lett. B*, **622** (2005) 327 [arXiv:hep-ph/0507045]; Morisi S. and Picariello M., *Int. J. Theor. Phys.*, **45** (2006) 1267 [arXiv:hep-ph/0505113]; Picariello M., arXiv:hep-ph/0611189; Caravaglios F. and Morisi S., arXiv:hep-ph/0510321; Morisi S., arXiv:hep-ph/0604106; Caravaglios F. and Morisi S., arXiv:hep-ph/0503234; Haba N. and Yoshioka K., *Nucl. Phys. B*, **739** (2006) 254 [arXiv:hep-ph/0511108]; Tanimoto M. and Yanagida T., *Phys. Lett. B*, **633** (2006) 567 [arXiv:hep-ph/0511336]; Koide Y., *Eur. Phys. J. C*, **48** (2006) 223 [arXiv:hep-ph/0508301]; Mohapatra R. N., Nasri S. and Yu H. B., *Phys. Lett. B*, **636** (2006) 114 [arXiv:hep-ph/0603020]; Mohapatra R. N., Nasri S. and Yu H. B., *Phys. Lett. B*, **639** (2006) 318 [arXiv:hep-ph/0605020]; Kubo J., Mondragon A., Mondragon M. and Rodriguez-Jauregui E., *Prog. Theor. Phys.*, **109** (2003) 795; **114** (2005) 287(E) [arXiv:hep-ph/0302196]; Kubo J., *Phys. Lett. B*, **578** (2004) 156; **619** (2005) 387(E) [arXiv:hep-ph/0309167]; Grimus W. and Lavoura L., *JHEP*, **0601** (2006) 018 [arXiv:hep-ph/0509239]; Teshima T., *Phys. Rev. D*, **73** (2006) 045019 [arXiv:hep-ph/0509094]; Kaneko S., Sawanaka H., Shingai T., Tanimoto M. and Yoshioka K., *Prog. Theor. Phys.*, **117** (2007) 161 [arXiv:hep-ph/0609220]; Koide Y., *Phys. Rev. D*, **73** (2006) 057901 [arXiv:hep-ph/0509214]; Koide Y., *Eur. Phys. J. C*, **50** (2007) 809 [arXiv:hep-ph/0612058]; Chen C. Y. and Wolfenstein L., arXiv:0709.3767 [hep-ph]; Chen S. L., Frigerio M. and Ma E., *Phys. Rev. D*, **70** (2004) 073008; 079905(E) [arXiv:hep-ph/0404084]; Lavoura L. and Ma E., *Mod. Phys. Lett. A*, **20** (2005) 1217 [arXiv:hep-ph/0502181]; Feruglio F. and Lin Y., arXiv:0712.1528 [hep-ph].

[30] Witten E., *Nucl. Phys. B*, **258** (1985) 75; Kawamura Y., *Prog. Theor. Phys.*, **105** (2001) 999 [arXiv:hep-ph/0012125]; Faraggi A. E., *Phys. Lett. B*, **520** (2001) 337 [arXiv:hep-ph/0107094] and references therein.

[31] Albright C. H. and Rodejohann W., *Phys. Lett. B*, **665** (2008) 378 arXiv: 0804.4581[hep-ph].

[32] Plentinger F. and Seidl G., arXiv:0803.2889[hep-ph].

[33] Raidal M., *Phys. Rev. Lett.*, **93** (2004) 161801 [arXiv:hep-ph/0404046]; Minakata H. and Smirnov A. Y., *Phys. Rev. D*, **70** (2004) 073009 [arXiv:hep-ph/0405088]; Minakata H., arXiv:hep-ph/0505262; Frampton P. H. and Mohapatra R. N., *JHEP*, **0501** (2005) 025, hep-ph/0407139; Ferrandis J. and Pakvasa S., *Phys. Rev. D*, **71** (2005) 033004, hep-ph/0412038; Kang S. K., Kim C. S. and Lee J., arXiv:hep-ph/0501029; Altarelli G., Feruglio F. and Masina I., *Nucl. Phys. B*, **689** (2004) 157 [arXiv:hep-ph/0402155]; Li N. and Ma B. Q., hep-ph/0501226; Cheung K., Kang S. K., Kim C. S. and Lee J., hep-ph/0503122; Xing Z. z., hep-ph/0503200; Datta A., Everett L. and Ramond P., arXiv:hep-ph/0503222; Ohlsson T., arXiv:hep-ph/0506094; Antusch S., King S. F. and Mohapatra R. N., arXiv:hep-ph/0504007; Lindner M., Schmidt M. A. and Smirnov A. Y., arXiv:hep-ph/0505067; King S. F., *JHEP*, **0508** (2005) 105 [arXiv:hep-ph/0506297]; Dighe A., Goswami S. and Roy P., *Phys. Rev. D*, **73** (2006) 07130 [arXiv:hep-ph/0602062]; Chauhan B. C., Picariello M., Pulido J. and Torrente-Lujan E., *Eur. Phys. J. C*, **50** (2007) 573 [arXiv:hep-ph/0605032]; Schmidt M. A. and Smirnov A. Yu., *Phys. Rev. D*, **74** (2006) 113003 [arXiv:hep-ph/0607232]; Hochmuth K. A. and Rodejohann W., *Phys. Rev. D*, **75** (2007) 073001 [arXiv:hep-ph/0607103]; Plentinger F., Seidl G. and Winter W., *Nucl. Phys. B*, **791** (2008) 60 [arXiv: hep-ph/0612169]; *Phys. Rev. D*, **76** (2007) 113003 [arXiv:0707.2379 [hep-ph]].

[34] Altarelli G., Feruglio F. and Merlo L., [arXiv:0903.1940[hep-ph]].

SESSION III - QCD PHYSICS/HADRONIC INTERACTIONS

Jan Kašpar	Soft physics at the LHC with TOTEM
Niccolò Moggi	Study of soft QCD at the Tevatron
Michael Begel	Study of hard QCD at the Tevatron
Simona Giovannella	Hadronic physics with KLOE
Einan Gardi	Infrared singularities in QCD amplitudes
Daniel Traynor	QCD studies at HERA
Francesco Hautmann	Production of jets at forward rapidities in hadronic collisions

IL NUOVO CIMENTO Vol. 32 C, N. 5-6 Settembre-Dicembre 2009
DOI 10.1393/ncc/i2010-10543-y

Colloquia: LaThuile09

Soft physics at the LHC with TOTEM

J. Kašpar on behalf of the TOTEM Collaboration

CERN - Geneva, Switzerland
Institute of Physics of the AS CR - Prague, Czech Republic

(ricevuto il 10 Novembre 2009; pubblicato online il 20 Gennaio 2010)

Summary. — The TOTEM experiment at CERN's Large Hadron Collider is dedicated to forward hadronic phenomena. The tree pillars of its physics programme are: an accurate measurement of the total pp cross-section, a measurement of elastic scattering in a wide kinematic range and a wide study of diffractive processes. TOTEM plans to run at all LHC optics conditions with special emphasis on the high β^* optics runs that enables TOTEM to make measurements of the total cross-section using the luminosity-independent method. A key element of this method is the extrapolation to $t = 0\,\mathrm{GeV}^2$ of the differential elastic cross-section. An adequate parametrization of the differential elastic cross-section and a treatment of the Coulomb part is presented and applied to the two high β^* optics, 1535 and 90 m. The expected precision on the total cross-section measurement for the two optics is about 5% and about 1%, respectively. The TOTEM physics in the early LHC runs will include measurement of high-$|t|$ elastic scattering and high-mass diffraction and studies of the forward charged particle multiplicy.

PACS 13.85.-t – Hadron-induced high- and super-high-energy interactions (energy $> 10\,\mathrm{GeV}$).
PACS 29.40.-n – Radiation detectors.

1. – Introduction

The TOTEM experiment [1-3] is dedicated to forward hadronic phenomena. The tree pillars of its physics programme are: an accurate measurement of the total pp cross-section, a measurement of elastic scattering in a wide kinematic range and studies of diffractive processes.

The programme is touching one of the least explored and understood areas of hadronic physics. This fact can be well demonstrated by fig. 1. The left plot shows several model predictions for elastic differential cross-sections which differ by several orders of magnitude at large $|t|$ (four-momentum transfer squared). The right figure compiles data on the total pp cross-section. Due to large uncertainties of cosmic ray experiments and conflicting Tevatron data [4, 5], this data set can hardly favor any of the proposed theoretical descriptions over another. TOTEM shall shed some light onto those open

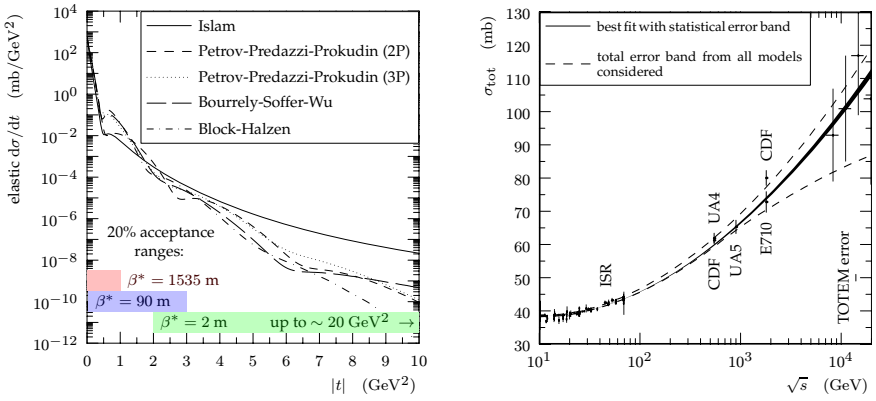

Fig. 1. – Left: predictions of the elastic differential cross-section at a center-of-mass energy of 14 TeV by several phenomenological models. Acceptance bands for the main optics (see sect. **2**) are shown at the bottom. Right: a compilation of available data for the total pp cross-section with a fit by the COMPETE Collaboration [6]. The anticipated ultimate precision (1%) is shown in the bottom right corner.

questions by providing precise measurements—see for instance the anticipated error bar for the total cross-section in fig. 1.

The challenging programme brings special requirements for the detector apparatus. In particular, *large pseudorapidity coverage*—to detect most fragments from inelastic collisions and excellent *acceptance for surviving forward protons*. To accomplish this task, TOTEM comprises three subdetectors: the inelastic telescopes T1 and T2 and a system of Roman Pots (RP) for proton detection. This design results in a unique apparatus with an excellent pseudorapidity coverage, see fig. 2 (a). The acceptance of the RPs can be further varied by using different optics, as will be discussed in the next

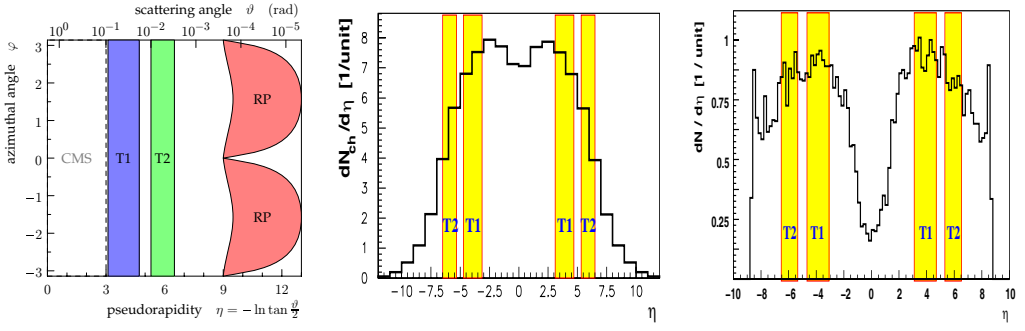

(a) (b) (c)

Fig. 2. – (a) The coverage of the three subsystems of TOTEM. The shown acceptance of the RPs refers to the $\beta^* = 1535\,\mathrm{m}$ optics. For the other optics, the acceptance is shifted to lower pseudorapidity values, which narrows the gap between the RPs and T2. (b) and (c) Pseudorapidity distributions of the charged particle multiplicity for non-diffractive (b) and single diffractive (c) inelastic collisions at the energy of 14 TeV. The main objective is to register most events—and that is achieved with this design, even if some particles are missed.

section. The placement of telescopes T1 and T2 has been optimized to maximize the inelastic trigger efficiency (see figs. 2 (b) and (c)), which is of crucial importance for the total cross-section measurement (discussed in sect. **3**). For details on instrumentation see [1, 2].

2. – Running scenarios

The forward protons, before being registered by the RP system, will pass through the lattice of the LHC magnets, and thus the observed hit pattern will depend on the accelerator settings (beam optics). In this way, the optics defines the acceptance and the resolution of the proton kinematics reconstruction (for details see chapter 6 in [2]). Besides the optics, the beam collision parameters (such as luminosity) can be optimized for certain physics measurements. TOTEM plans to use the following three running scenarios.

1) $\beta^* = 1535\,\mathrm{m}$ with $\mathcal{L} \approx (10^{28}\text{–}10^{29})\,\mathrm{cm}^{-2}\,\mathrm{s}^{-1}$. This is the ultimate optics for low-$|t|$ elastic scattering and precise (1% error) total cross-section measurement. The precision is made possible by very good angular resolution $\sigma(\vartheta) \approx 0.3\,\mu\mathrm{rad}$ (mainly due to the beam divergence). The momentum-loss ($\xi \equiv \Delta p/p$) resolution is $\sigma(\xi) \approx (2\text{–}10) \cdot 10^{-3}$ for this optics.

2) $\beta^* = 90\,\mathrm{m}$ with $\mathcal{L} \approx 10^{30}\,\mathrm{cm}^{-2}\,\mathrm{s}^{-1}$ is a universal optics allowing for measurement of elastic scattering (medium $|t|$ range), total cross-section (5% uncertainty) and also for diffraction studies. The angular and momentum-loss resolutions are $\sigma(\vartheta) \approx 1.7\,\mu\mathrm{rad}$ and $\sigma(\xi) \approx (6\text{–}15) \cdot 10^{-3}$.

3) $\beta^* = (0.5\text{–}3)\,\mathrm{m}$ (standard optics for the general purpose experiments) are suited for high-$|t|$ elastic scattering and various diffractive measurements. The relatively low cross-sections of these processes require high luminosities $\mathcal{L} \approx (10^{32}\text{–}10^{33})\,\mathrm{cm}^{-2}\,\mathrm{s}^{-1}$. The angular and momentum-loss resolutions are $\sigma(\vartheta) \approx 15\,\mu\mathrm{rad}$ and $\sigma(\xi) \approx (1\text{–}6) \cdot 10^{-3}$.

See fig. 3 for a comparison of proton acceptances for the above optics. Figure 1 left shows that all the three scenarios are needed to measure elastic scattering in the wide $|t|$ range.

All the scenarios mentioned have been conceived for the nominal LHC energy of 14 TeV. However, as it is planned in October 2009, the LHC will start up at a reduced energy of 7 TeV. But one may still assume that the main characteristics of the discussed scenarios will remain unchanged. The beginning of the LHC operation is scheduled for $\beta^* \approx 2\,\mathrm{m}$ runs. TOTEM plans for this period are presented in sect. **4**. Then, TOTEM intends to request the 90 m optics as soon as possible. This optics is relatively easy to get (it does not require a special injection as the $\beta^* = 1535\,\mathrm{m}$ one) and still allows for measurements throughout the entire physics programme—note (*e.g.*, in fig. 3) that all ξ's are seen through a broad $|t|$ range. Moreover the $|t|$ range is shifted by nearly two orders down in comparison to the low β^* optics and therefore corresponding cross-sections are much higher.

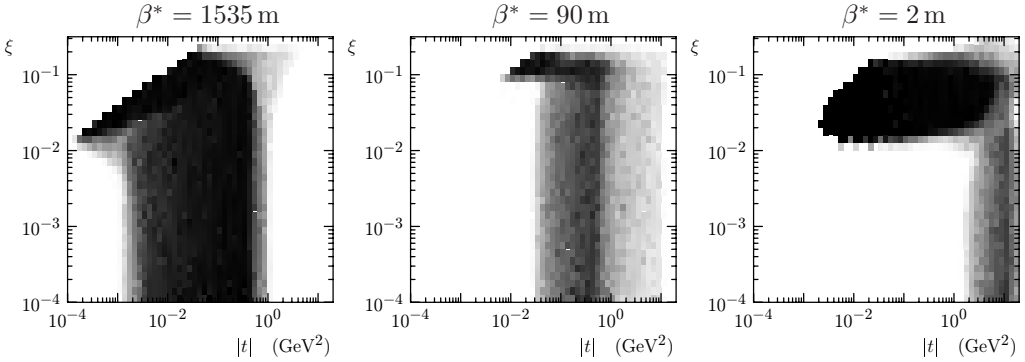

Fig. 3. – A comparison of RP acceptances for several optics at the center-of-mass energy of 14 TeV. Black color represents full acceptance while white zero acceptance. Note that the acceptance for elastic events can be read at the bottom horizontal axis ($\xi \to 0$).

3. – Measurement of the total cross-section

TOTEM intends to measure the total cross-section by the *luminosity-independent method*. It is based on the Optical Theorem:

$$\sigma_{\mathrm{tot}}(s) \propto \Im T^H(s, t=0), \tag{1}$$

relating the total cross-section σ_{tot} to the hadronic([1]) component of the elastic scattering amplitude $T^H(s,t)$. When it is complemented by common definitions for luminosity $\mathcal{L}$ and rates N

$$\varrho = \left.\frac{\Re T^H}{\Im T^H}\right|_{t=0}, \qquad \frac{\mathrm{d}\sigma}{\mathrm{d}t} \propto |T^H|^2, \qquad \mathrm{d}N = \mathcal{L}\mathrm{d}\sigma, \qquad N_{\mathrm{tot}} = N_{\mathrm{el}} + N_{\mathrm{inel}}, \tag{2}$$

one can obtain relations for the total cross-section and luminosity:

$$\sigma_{\mathrm{tot}} = \frac{1}{1+\varrho^2}\,\frac{\mathrm{d}N/\mathrm{d}t|_{t=0}}{N_{\mathrm{el}} + N_{\mathrm{inel}}}\,, \qquad \mathcal{L} = (1+\varrho^2)\,\frac{(N_{\mathrm{el}} + N_{\mathrm{inel}})^2}{\mathrm{d}N/\mathrm{d}t|_{t=0}}\,. \tag{3}$$

Here, $\mathrm{d}N/\mathrm{d}t|_{t=0}$ stands for elastic rate in the Optical Point (*i.e.* $t = 0$), which is to be obtained by an extrapolation procedure discussed in subsect. **3**˙1. N_{el} is the total elastic rate, which will be measured by the RPs and adjusted, again, by the extrapolation procedure. N_{inel} represents the total inelastic rate measured by the telescopes T1 and T2 (for more details see sect. 2.2 in [7]).

The ϱ quantity can only be determined by an analysis of the Coulomb-hadronic interference (see below in subsect. **3**˙1) and there is only a small $|t|$ window, where these effects are significant enough. Moreover, for the energy of 14 TeV this region is found around $t = 1 \cdot 10^{-3}\,\mathrm{GeV}^2$ which is on the very edge of TOTEM's acceptance. Therefore TOTEM might not be able to determine the ρ value at the nominal LHC energy, unless

([1]) There is obviously a second component due to the Coulomb scattering. Their interference is briefly discussed in subsect. **3**˙1.

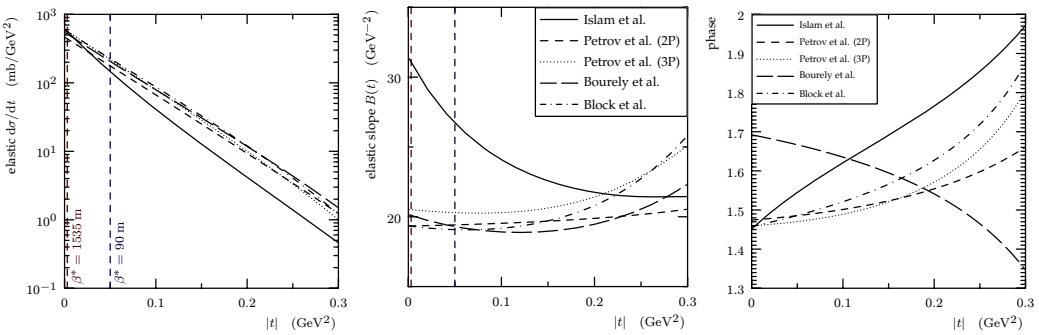

(a) (b) (c)

Fig. 4. – Model predictions for $E = 14\,\text{TeV}$ in a low-$|t|$ region. (a) Predictions for the elastic differential cross-section. (b) Predictions for the elastic slope $B(s,t) = \frac{\mathrm{d}}{\mathrm{d}t} \log \frac{\mathrm{d}\sigma}{\mathrm{d}t}$. (c) Predictions for the hadronic phase.

allowed to insert the RPs closer than the standard 10 beam-σ distance (which would push the acceptance to lower $|t|$). For reduced energies, the prospects are much brighter as the interference region shifts towards higher $|t|$ values. Even if TOTEM was unable to resolve ρ, its value could be taken from external predictions (*e.g.* [6]). Note that expected ρ values are small ≈ 0.14 and since ρ enters formulae (3) only via $1 + \varrho^2$, the influence of any uncertainty is small [2, 7].

3˙1. *Extrapolation to $t = 0$.* – The value $\mathrm{d}\sigma/\mathrm{d}t|_0$ is, indeed, not accessible experimentally and thus an extrapolation from a higher-$|t|$ region must be applied. A necessary condition for any successful extrapolation is a suitable parameterization. Looking at fig. 4, showing several model predictions in a low-$|t|$ region, one can observe an *almost* exponential decrease of the elastic cross-section up to $|t| \leq 0.25\,\text{GeV}^2$. This is further supported by the *almost* constant differential slope $B(s,t)$ in the quoted range([2]). The plot (c) hints that the phase of hadronic amplitudes can be described by a polynomial of a low degree. These arguments suggest that the following parameterization is adequate:

$$T^H(s,t) = e^{M(t)} e^{iP(t)}, \qquad \frac{\mathrm{d}\sigma}{\mathrm{d}t} = |T^{C+H}(s,t)|^2, \quad \text{with } M, P \text{ polynomials for a fixed } s. \tag{4}$$

T^{C+H} stands for the scattering amplitude of the combined Coulomb and hadronic forces and will be discussed below. The questions to be answered are: what is the optimal fit range and what is the optimal degree of the polynomials. It is obvious that if too many free parameters are introduced, they cannot be resolved with confidence. This is mainly a problem for the phase polynomial $P(t)$ since any phase information can only be resolved from a narrow Coulomb interference window, as discussed above. The optimal values shall give good results for most of the models considered; in this way the procedure can be regarded as model independent.

([2]) The model of Islam *et al.* is an exception which would be easily recognized (*e.g.*, in large-$|t|$ elastic scattering) and a different strategy would be applied.

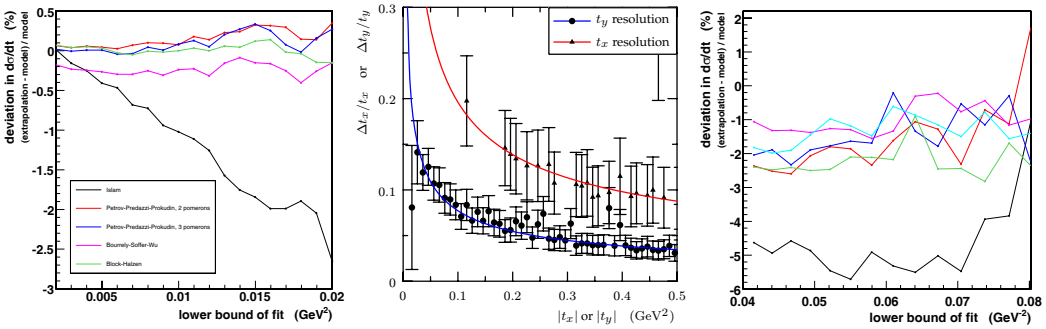

(a) (b) (c)

Fig. 5. – (a) The extrapolation deviation as a function of fit's lower bound for the $\beta^* = 1535\,\mathrm{m}$ optics. (b) Comparison of t_x and t_y resolutions for the $\beta^* = 90\,\mathrm{m}$ optics. (c) The extrapolation deviation for the 90 m optics. All plots are based on *preliminary* simulation/reconstruction data.

So far, only the hadronic contribution T^H to the elastic scattering has been discussed. It is clear that the Coulomb interaction will play a role and therefore must be taken into account. At the time being, there are two approaches to calculate scattering amplitudes T^{C+H} for the combined interaction: the *traditional* (*à la* West-Yennie [8]) and the *eikonal* (see, *e.g.*, Kundrát-Lokajíček [9]). The traditional approach is based on rather constraining assumptions on the form of the hadronic amplitude, and furthermore it has recently been shown internally inconsistent [10].

As mentioned in sect. **2**, TOTEM plans to measure the total cross-section with two optics: $\beta^* = 1535\,\mathrm{m}$ and 90 m. The lowest measurable $|t|$ values differ quite considerably (see fig. 2 right and vertical marks in fig. 4) and therefore the extrapolation strategies differ as well.

For the 1535 m optics, the Coulomb interference effects play a role and thus an interference formula must be applied (the eikonal one has been used in this study). The following configuration has been found optimal: quadratic $B(t)$ and constant phase with upper bound $|t| = 4 \cdot 10^{-2}\,\mathrm{GeV}^2$. Preliminary results are shown in fig. 5 (a). One can see that most models lie within a band $\pm 0.2\%$ (except for the model of Islam *et al.*—see footnote 2).

As for what concerns the 90 m optics, the Coulomb effects are negligible and therefore the phase parameterization becomes irrelevant([3]). On the other hand, the horizontal t component t_x can be resolved with a limited resolution only—see fig. 5 (b). Since $t = t_x + t_y$, the considerable uncertainties propagate to the full t distribution. A number of solutions might be suggested.

1) Use the t-distribution (*i.e.* $\mathrm{d}\sigma/\mathrm{d}t$) despite large uncertainties.
2) Using azimuthal symmetry, one can "transform" a t_y-distribution in a t-distribution:

$$\frac{\mathrm{d}\sigma}{\mathrm{d}t_y} = \frac{\mathrm{d}\sigma}{\mathrm{d}t_x} \quad \Rightarrow \quad \frac{\mathrm{d}\sigma}{\mathrm{d}t}(t) \propto \int_t^0 \mathrm{d}u\, \frac{\mathrm{d}\sigma}{\mathrm{d}t_y}(u)\, \frac{\mathrm{d}\sigma}{\mathrm{d}t_y}(t-u).$$

([3]) The T^{C+H} coincides with T^H and the phase factor $\exp[iP(t)]$ cancels out when differential cross-section is calculated according to eq. (4).

However, since low-$|t_y|$ information is missing (out of acceptance), an extrapolation step would be needed just for this transformation.

3) "Transform" a t-parameterization in a t_y-parameterization and fit it directly through t_y data:

$$t_y = t \sin^2\varphi, \text{ with } \varphi \text{ uniformly distributed}$$
$$\Rightarrow \quad \frac{\mathrm{d}\sigma}{\mathrm{d}t_y}(t_y) = \frac{2}{\pi}\int_0^{\pi/2} \frac{\mathrm{d}\varphi}{\sin^2\varphi}\,\frac{\mathrm{d}\sigma}{\mathrm{d}t}\left(\frac{t_y}{\sin^2\varphi}\right).$$

Considering a parameterization of type eq. (4), one can derive an approximate formula:

$$\frac{\mathrm{d}\sigma}{\mathrm{d}t} = e^{a+bt+ct^2+\dots} \quad \Rightarrow \quad \frac{\mathrm{d}\sigma}{\mathrm{d}t_y}(t_y) \approx \frac{1}{\sqrt{\pi}}\,\frac{e^{a+bt_y+ct_y^2+\dots}}{\sqrt{|b\,t_y|}},$$

which can be justified provided the non-linear terms in the exponent $(ct^2, \dots)$ do not give an essential contribution—which is the case, see fig. 4.

Eventually, the third approach has been chosen and a cubic polynomial with an upper bound of $|t| = 0.25\,\mathrm{GeV}^2$ has been found optimal. Preliminary results are plotted in fig. 5 (c). Most models fall in a band between -1% and -3% (Islam's model being again an exception—see footnote 2). The overall offset of -2% is a consequence of the beam divergence and can be corrected in the data analysis.

3˙2. *Inelastic rate.* – The inelastic rate N_{inel} (in eq. (3)) is to be measured by the forward trackers T1 and T2. In order to maximize the detection efficiency a number of trigger strategies is foreseen, see, *e.g.*, sect. 2.2 in [7]. The dominant contribution of trigger losses is expected to arise from low-mass single or double diffractive events. To correct for this deficiency, an extrapolation procedure has been established (details can be found in sect. 6.2.2 in [2]).

4. – Early measurements

As of October 2009, the LHC schedule counts on first physics collisions at the center-of-mass energy of $\sqrt{s} = 7\,\mathrm{TeV}$ and $\beta^* \sim 2\,\mathrm{m}$. The expected RP acceptance and resolution for this scenario are similar to the nominal energy case, see sect. **2**. That means ξ acceptance $0.02 < \xi < 0.18$ and resolution $\sigma(\xi) < 6 \cdot 10^{-3}$, elastic acceptance $2 < |t| < 20\,\mathrm{GeV}^2$ and resolution $\sigma(t) \approx 0.2/\sqrt{|t|}$. These parameters are suitable for the physics studies listed below.

– The vertical RPs will measure *high* $|t|$ *elastic scattering.*

– Given the range where ξ can be determined by (horizontal) RPs, TOTEM will measure spectra of *high-mass diffractive processes.* For single diffraction,the mass spectrum $\mathrm{d}\sigma^{\mathrm{SD}}/\mathrm{d}M$ could be measured for masses $1\,\mathrm{TeV} < M < 3\,\mathrm{TeV}$. For double pomeron exchange([4]) the distribution $\mathrm{d}\sigma^{\mathrm{DPE}}/\mathrm{d}M$ will be available for masses

([4]) Here, the term "double pomeron exchange" is used as a synonym to central diffraction.

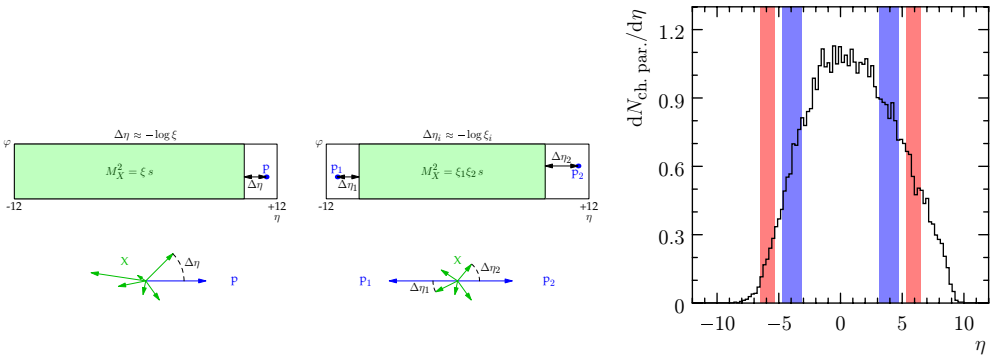

(a) (b) (c)

Fig. 6. – (a) and (b) Characteristic event structures of high-mass single diffraction (a) and double pomeron exchange (b). The boxes in the upper part present pseudorapidity *vs.* azimuthal angle charts. The diagrams in the bottom show momenta of particles in sample events, together with rapidity gaps $\Delta\eta$ between outgoing protons p and edges of the diffractive system X. (c) Pseudorapidity distribution of charged particles produced in single diffractive events with ξ range compatible with the RP acceptance in the LHC start-up scenario. In this simulation, only intact protons with negative pseudorapidity have been considered. The shaded vertical bands represent the coverage of the telescopes T1 (blue) and T2 (red).

$0.14\,\mathrm{TeV} < M < 1.3\,\mathrm{TeV}$. See fig. 6 (a) and (b) for typical event topologies for these processes.

The value of ξ can be alternatively determined by the telescopes T1 and T2. When an edge of a rapidity gap is detected in the telescopes (see the bands around $\eta \approx -5$ in fig. 6 (c)), the gap size $\Delta\eta$ can be related to the momentum loss by $\Delta\eta \approx -\log\xi$. In this way, the accessible mass regions can be extended to lower values.

– The telescopes T1 and T2 alone can be used for studies of *forward charged particle multiplicities*.

REFERENCES

[1] TOTEM: Technical Design Report, CERN-LHCC-2004-002 (2004); addendum CERN-LHCC-2004-020.
[2] Anelli G. *et al.* (TOTEM Collaboration), *JINST*, **3** (2008) S08007.
[3] Latino G. (TOTEM Collaboration), *The TOTEM Experiment at LHC, 22nd Les Rencontres de Physique de la Vallee d'Aoste, Aosta Valley, Italy (2008).*
[4] Abe F. *et al.* (CDF Collaboration), *Phys. Rev. D*, **50** (1994) 5550.
[5] Amos N. A. *et al.* (E710 Collaboration), *Phys. Rev. Lett.*, **68** (1992) 2433.
[6] Cudell J. R. *et al.* (COMPETE Collaboration), *Phys. Rev. Lett.*, **89** (2002) 201801.
[7] Deile M. (TOTEM Collaboration), *Total cross-section measurement and diffractive physics with TOTEM, 12th International Conference on Elastic and Diffractive Scattering, Hamburg (2007).*
[8] West G. B. and Yennie D. R., *Phys. Rev.*, **172** (1968) 1413.
[9] Kundrát V. and M. Lokajíček, *Z. Phys. C*, **63** (1994) 619.
[10] Kundrát V., Lokajíček M. and Vrkoč I., *Phys. Lett. B*, **656** (2007) 182.

IL NUOVO CIMENTO Vol. 32 C, N. 5-6 Settembre-Dicembre 2009
DOI 10.1393/ncc/i2009-10515-4

Colloquia: LaThuile09

Study of soft QCD at the Tevatron

N. Moggi on behalf of the CDF and D0 Collaborations

Istituto Nazionale Fisica Nucleare - Bologna, Italy

(ricevuto il 10 Novembre 2009; pubblicato online il 4 Gennaio 2010)

Summary. — Measurements of particle production and inclusive differential cross-sections in inelastic pp collisions are reported together with studies of the underlying event in various event topologies. A comparison with Monte Carlo model predictions at the hadron level is performed. The aim is to provide data that can be used to improve QCD models of minimum-bias production and of the underlying event.

PACS 13.85.Hd – Inelastic scattering: many-particle final states.
PACS 13.85.Qk – Inclusive production with identified leptons, photons, or other nonhadronic particles.

1. – Introduction

At the energy of the Tevatron Collider "soft" non-perturbative hadron interactions represent the largest part of the inelastic cross-section. A minimum-bias (MB) trigger is usually employed to collect samples of soft collisions, but such a trigger is actually meant to collect events from all possible inelastic interactions proportionally to their natural production rate. Therefore MB physics offers a chance for studying both the theoretically poorly understood softer phenomena and the interplay between the soft and the hard (perturbative) interactions [1].

The observables that are experimentally accessible in the MB final state represent a complicated mixture of different physics effects. The available Monte Carlo models may be tuned to give an acceptable description of single observables, but are unable to describe simultaneously the entire set. In order to simulate accurately a minimum-bias sample, it is necessary not only a model of the "ordinary" QCD 2-to-2 parton scattering process both in the perturbative (hard) and in the non-perturbative (soft) regime; also the knowledge of the correct mixture of soft and hard collisions and a reliable description of all softer components of the interaction are necessary [2]. Such softer components may be recognized as the remains of the hard scattering not associated with the hard process ("beam-beam remnants", BBR) and as other 2-to-2 parton-parton scatterings other than

the hard one ("multiple parton interactions", MPI)([1]). Is is customary to define the sum of BBR + MPI final state particles as "underlying event". The understanding of the underlying event is especially important for precision measurements of many high-p_T observables where it forms an unavoidable background (see, *e.g.* [3]). This is especially true in high luminosity environments such as at the Large Hadron Collider [4].

Here three distinct but correlated and complementary studies will be described. The first addresses the features of inelastic inclusive particle production, the second addresses the description of the "underlying event", and the third investigates specifically the modeling of MPI.

2. – MB studies

This analysis [5] is based on an integrated luminosity of $506\,\mathrm{pb}^{-1}$ collected with the CDF II detector [6] at $\sqrt{s} = 1.96\,\mathrm{TeV}$ during the first Tevatron stores in Run II. Two systems of gas Cherenkov counters (CLC) [7], covering the pseudorapidity forward regions $3.7 < |\eta| < 4.7$, are used to determine the luminosity. The MB trigger is implemented by requiring a coincidence in time of signals in both forward and backward CLC modules. The sample collected consists of inelastic central interactions with a small contamination of diffractive events. The average instantaneous luminosity is about $20 \times 10^{30}\,\mathrm{cm}^{-2}\mathrm{s}^{-1}$.

All data presented is corrected for the trigger and vertex efficiency, undetected pile-up and event selection acceptance. The background of diffractive interactions is subtracted. Primary charged particles are measured in the region of $|\eta| < 1$ and $p_T > 0.4\,\mathrm{GeV}/c$, and are corrected for the tracking efficiency, contamination of secondary particles and mis-identified tracks.

A set of simulated Monte Carlo (MC) events about twice the size of the data sample was generated with PYTHIA [8] "Tune A" [9]. To model the mixture of hard and soft interactions, PYTHIA introduces a p_T^0 cut-off parameter that regulates the divergence of the 2-to-2 parton-parton perturbative cross-section at low momenta. This parameter is used also to regulate the additional parton-parton scatterings that may occur in the same collision [10]. Thus, fixing the amount of multiple-parton interactions (*i.e.*, setting the p_T cut-off) allows the hard 2-to-2 parton-parton scattering to be extended all the way down to $p_T(hard) = 0$ without hitting a divergence. The amount of hard scattering in simulated MB events is, therefore, related to the activity of the so-called underlying event in the hard scattering processes. The final state, likewise, is subject to several effects such as the treatments of the beam remnants and color (re)connection effects.

2˙1. *Single-particle p_T spectrum.* – The differential single-particle invariant p_T differential cross-section $\mathrm{d}^3\sigma/p_T\Delta\phi\Delta y\mathrm{d}p_T$ is shown in fig. 1. This measurement was last published by the CDF [11] for 1800 GeV data. The new measurement extends the p_T spectrum from 10 to over $100\,\mathrm{GeV}/c$ and is about 4% higher in cross-section. The tail of the distribution is at least three orders of magnitude higher than what could be expected by extrapolating to high p_T the function that fits the 1800 GeV data. In order to fit the whole spectrum, we introduced a more complex parametrization:

$$f = A\left(\frac{p_0}{p_T + p_0}\right)^n + B\left(\frac{1}{p_T}\right)^s. \tag{1}$$

([1]) Secondary parton-parton collisions may also have large momentum transfer but at the Tevatron energy such rare events may be neglected in the MB sample.

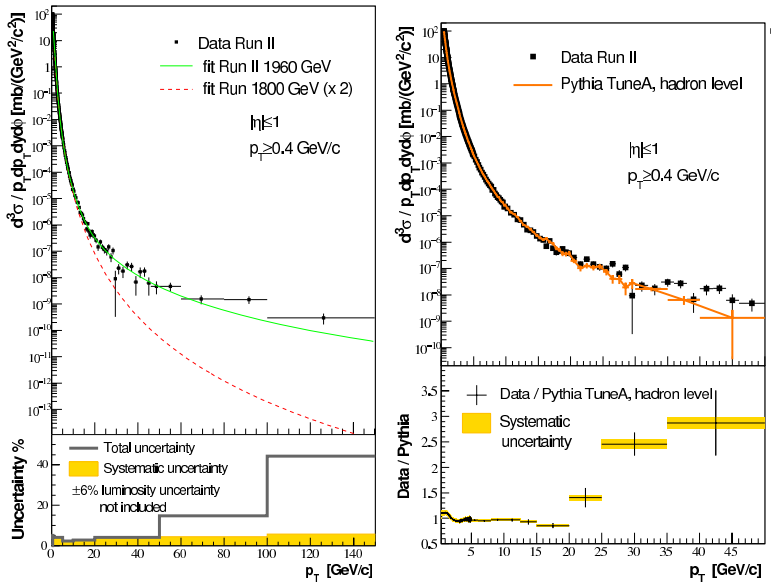

Fig. 1. – Left: the track p_T differential cross-section with statistical uncertainty is shown. All particle tracks are assumed to be pions. A fit to the functional form used in the 1800 GeV analysis is also shown (dashed line). The fit with the more complex function (eq. (1)) is shown as a continuous line. In the plot at the bottom, the systematic and the total uncertainties are shown. Right: comparison with PYTHIA Tune A simulation at the hadron level. The ratio of data over prediction is shown in the lower plot. Note that these distributions are cut off at 50 GeV/c since PYTHIA does not produce particles at all beyond that value.

Figure 1 (right) shows a comparison with PYTHIA simulation at hadron level. The data show a larger cross-section than simulation at high p_T starting from about 20 GeV/c. The MC generator does not produce any particles at all beyond 50 GeV/c.

2˙2. *Event* $\sum E_T$ *cross-section.* – The differential cross-section $\mathrm{d}^3\sigma/(\Delta\phi\Delta\eta\mathrm{d}\sum(E_T))$ for $|\eta| < 1$ is shown in fig. 2. The event average transverse energy sum is $\sum E_T = 10.4 \pm 0.2(\mathrm{stat.}) \pm 0.7(\mathrm{syst.})$ GeV. This kind of measurement is new to the field, and represents a first attempt at describing the full final state including neutral particles. In this regard, it is complementary to the charged particle measurement in describing the global features of the inelastic $p\bar{p}$ cross-section. The PYTHIA simulation does not closely reproduce the data over the whole $\sum E_T$ spectrum. In particular the peak of the MC distribution is slightly shifted to higher energies with respect to the data.

3. – UE studies

It is possible to take advantage of the topological structure of hadron collisions to study the underlying event. The goal is a systematic study of final-state observables that may be used to tune and improve QCD Monte Carlo models of the underlying event. Three event topologies have been used. In the "leading jet" events a single jet is required in $|\eta| < 2$ [12]. The particles arising from BBR and MPI may hardly be experimentally separated from those originated by the initial- and final-state gluon radiation (ISR, FSR).

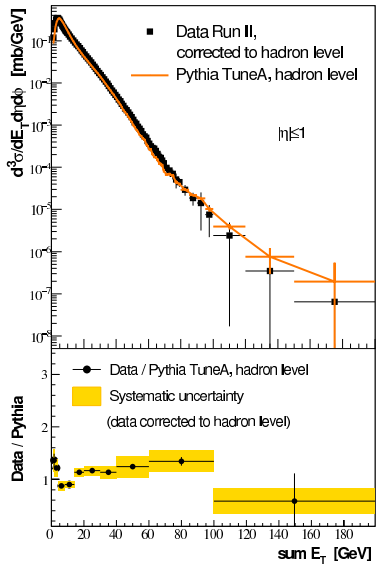

Fig. 2. – The differential $\sum E_T$ cross-section in $|\eta| < 1$ compared to a PYTHIA prediction at the hadron level. The ratio of data to PYTHIA Tune A is shown in the lower plot.

Drell-Yan lepton pair production is a unique event topology for UE studies since there is no final-state gluon radiation [13].

The result data presented here are collected by the CDF II experiment. Charged particles are measured in $|\eta| < 1$ and $p_T > 0.5\,\mathrm{GeV}/c$ and are corrected to particle level. Tracking efficiency and effects of pile-up are corrected for. Jet data are based on a sample of about $2.2\,\mathrm{fb}^{-1}$ collected with various jet triggers. Jets are reconstructed using the MidPoint cone based algorithm with cone size of 0.7 and $f_{\mathrm{merge}} = 0.75$. They are required to lie in $|\eta| < 2$ and the measure of their transverse energy E_T is corrected for the calorimeter response and acceptance [14]. Drell-Yan data are based on a sample of about $2.7\,\mathrm{fb}^{-1}$ collected with a lepton (electron or muon) trigger. These events are selectd by requiring two leptons of opposite charge ($e^{\pm}$ or $\mu^{\pm}$) with $p_T > 20\,\mathrm{GeV}/c$, $|\eta| < 1$, and invariant mass of the pair in the range $70 < |M_{\mathrm{pair}}| < 110\,\mathrm{GeV}$ with $|\eta_{\mathrm{pair}}| < 6$. They are often referred to as "Z-boson" events.

In all cases, the direction of the leading jet (or of the Z-boson) is used to define four regions in η-ϕ space. The "toward" region is defined to be in $|\Delta\phi| < 60°$ where $\Delta\phi = \phi - \phi_{\mathrm{jet}}$ is the relative azimuthal angle between a charged particle and the direction of the leading jet (or Z-boson); the "away" region in $|\Delta\phi| > 120$; the regions in $60° < \Delta\phi < 120°$ and $60° < -\Delta\phi < 120°$ are called "transverse" (fig. 3).

In high-p_T jet production the "forward" and "away" regions receive large energy and particle contributions from the jets, while the "transverse" regions, orthogonal to the plane of the hard 2-to-2 scattering, are more sensitive to the UE. A "MAX" and "MIN" transverse region are defined to be, respectively, the one containing the largest (smallest) number of charged particles or scalar p_T sum of particles. It is expected that "transMAX" will pick up the hardest ISR/FSR contribution, while the contribution from the UE will be the same for both. Therefore the "transMIN" will be more sensitive to the UE. In Drell-Yan production the forward region, after excluding the two leptons, is very similar

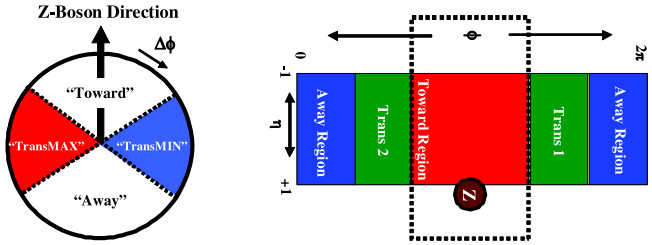

Fig. 3. – The "away", "toward" and "transverse" regions in ϕ (left) and η (right).

to the "transMIN" region that is less likely to receive contributions from ISR. With low p_T Z-bosons, essentially everything other than the final lepton pair is the underlying event. Large-p_T bosons generate additional gluons via bremsstrahlung, resulting in multi-parton final states fragmenting into hadrons and forming away-side jets, but in the "toward" and "transverse" regions only the underlying event remains (fig. 4).

Since the regions observed have different η-ϕ areas, some observables are built as densities of number of charged particles ($\mathrm{d}N/\mathrm{d}\eta\mathrm{d}\phi$) or of scalar p_T sum of particles ($\mathrm{d}p_T/\mathrm{d}\eta\mathrm{d}\phi$) by dividing by the area. Also other observables are studied, like the average ($\langle p_T \rangle$) and the maximum p_T of charged particles. All are analyzed as a function of the p_T of the leading jet or of the Z-boson.

Many observables have been studied in all event topologies and compared to a variety of MC models. Only few can be shown here, but it is important that MC generators be tuned on a wide range of observables and topologies. PYTHIA Tune A is compared to the leading-jet sample and Tune AW to the Drell-Yan sample. The two tunes differ only in that Tune AW fits also the Z-boson p_T distribution [15] as well as the underlying event. Other PYTHIA tunes, for example the one used by the ATLAS Collaboration, have also been considered. Details of these tunes may be found in [4] and references therein. The HERWIG Monte Carlo generator [16] does not provide any multiple parton-parton interaction mechanism, but an *ad hoc* MPI generator called JIMMY [17] may be added to improve the agreement with the underlying event observables. Details on the relative tunes may be found in [13].

From fig. 5 it is clear that HERWIG, without MPI, does not produce enough activity in the transverse regions for either process. Disagreement is stronger in Drell-Yan than

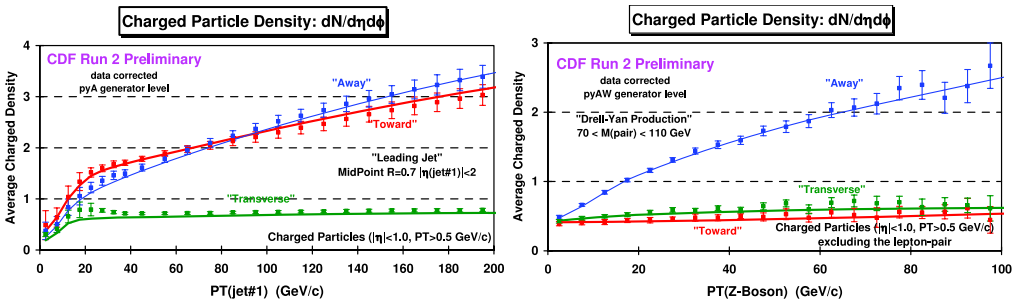

Fig. 4. – The "away", "toward" and "transverse" regions for leading-jet (left) and Drell-Yan (right) events.

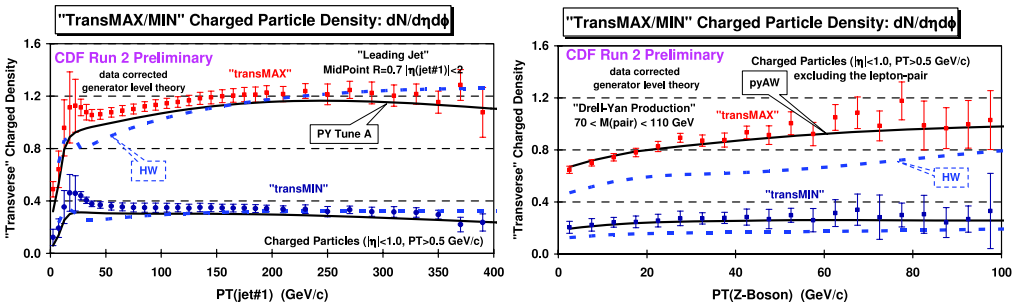

Fig. 5. – The "transMAX" and "transMIN" regions for leading-jet (left) and Drell-Yan (right) events. A comparison with PYTHIA Tune A (AW) and HERWIG is shown.

in leading-jet event because the lack of MPI becomes more evident in the absence of FSR. The $\langle p_T \rangle$ plots (not shown here) show that in HERWIG the charged-particle p_T distributions for both processes are also too soft.

In fig. 6 the "toward" and "transMIN" regions are compared. The particle densities are larger in the former than in the latter, a feature which is well described by PYTHIA but not by HERWIG that produces too few particles. When adding MPI (JIMMY) the particle density becomes too large. All MC models considered fit well the sum p_T density $\mathrm{d}p_T/\mathrm{d}\eta\mathrm{d}\phi$ in these regions.

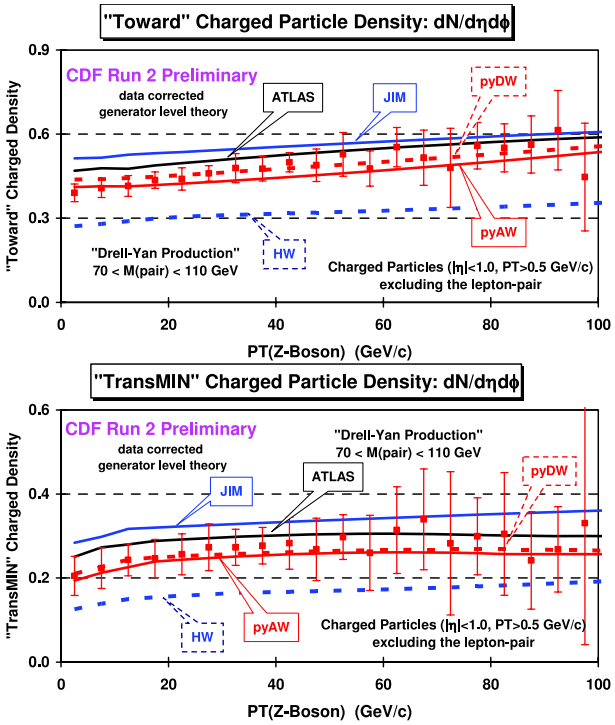

Fig. 6. – The "toward" and "transMIN" regions charged-particle densities in Drell-Yan events compared to PYTHIA and HERWIG.

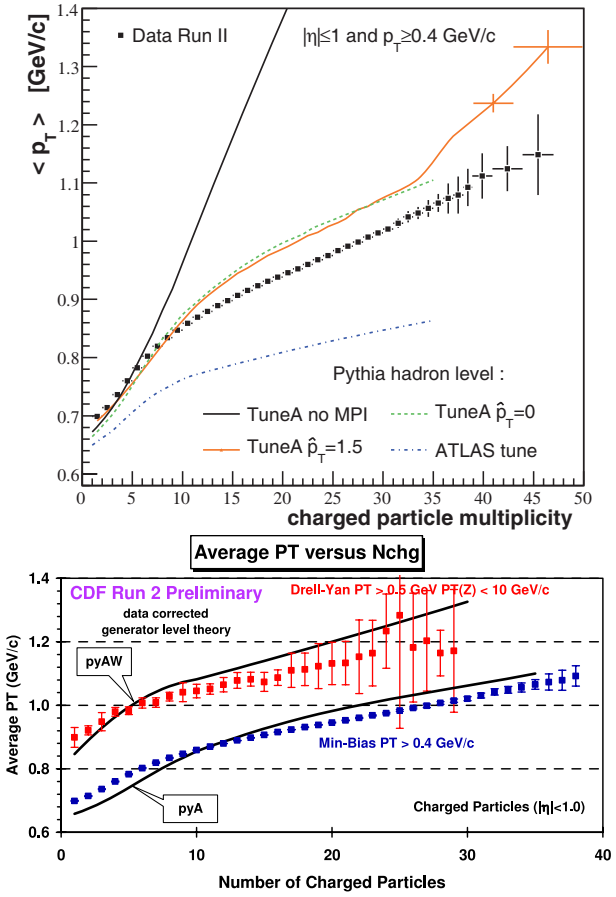

Fig. 7. – Upper: the dependence of the average charged-particle p_T on the event multiplicity is shown for the MB sample. A comparison with various PYTHIA tunes at the hadron level is shown. Tune A with $\hat{p}_{T0} = 0\,\mathrm{GeV}/c$ is very similar to $\hat{p}_{T0} = 1.5\,\mathrm{GeV}/c$. The same tuning with no multiple parton interactions allowed ("no MPI") yields an average p_T much higher than data for multiplicities greater than about 5. The ATLAS tune yields too low an average p_T over the whole multiplicity range. The uncertainties shown are only statistical. Lower: the average charged-particle p_T *versus* the multiplicity of charged particles in MB and Drell-Yan events compared to PYTHIA Tune A and Tune AW.

4. – Dependence of $\langle p_T \rangle$ with N_{ch}

The rate of change of the average charged-particle momentum $\langle p_T \rangle$ *versus* the charged-particle multiplicity N_{ch} is one of the variables most sensitive to the combination of the various physical effects present in MB collisions, and is also the most poorly reproduced by the available MC generators [1]. It may be seen as a measure of the amount of hard-*versus*-soft processes, but it is also sensitive to the modeling of the multiple-parton interactions (MPI) [18]. If only two processes contribute to the MB final state, one soft, and one hard (the hard 2-to-2 parton-parton scattering), then demanding large N_{ch} would preferentially select the hard process and lead to a high $\langle p_T \rangle$. However, we see from fig. 7 (Tune A *no MPI*) that with these two processes alone, the average p_T increases much too rapidly. MPI provide another mechanism for producing large

multiplicities that are harder than the beam-beam remnants, but not as hard as the primary 2-to-2 hard scattering. By introducing this mechanism, PYTHIA in the Tune A configuration gives a fairly good description of the correlation.

PYTHIA Tune AW also reproduces fairly well the same correlation in Drell-Yan events, while HERWIG (not shown here) rises too sharply due to the lack of MPI.

It is interesting to compare the MB data to a softer Drell-Yan subsample selected for having a p_T of the Z-boson $< 10\,\mathrm{GeV}/c$. This selection suppresses the high-p_T away side jet so that the higher particle multiplicities may be originated by MPI and ISR only. There is no *a priori* reason for the two samples to agree. However, they are remarkably similar and described fairly well by PYTHIA Tune A and Tune AW, respectively. This suggests that MPI are playing a similar role in both these processes.

5. – Conclusions

A set of precision measurements of the MB and UE was provided and compared to the available MC models. The MB sample shows no sign of discontinuity in the transition from soft to hard interactions. All data analysed favor models with multiple parton-parton interactions. PYTHIA may be tuned to reproduce the MB inclusive distributions and the features underlying event both in jet and Drell-Yan samples.

The behavior of the average charged-particle p_T *versus* the charged-particle multiplicity turns out to be an important observable sensible to the mixing of soft and hard processes and to the modeling of MPI. No available model correctly reproduces this correlation among particles in the final state. The distribution is found to be remarkably similar in MB and in low-p_T Drell-Yan events.

The results presented will lead to a better understanding of soft-hadron interactions and to more precise high-p_T measurements at the Tevatron and at the Large Hadron Collider.

REFERENCES

[1] ACOSTA D. *et al.*, *Phys. Rev. D*, **65** (2002) 072005.
[2] FIELD R., *AIP Conf. Proc.*, **928** (2007) 91.
[3] FIELD R., *Moscow 2006, ICHEP* (2007) 581.
[4] MORAES A., BUTTAR C. and DAWSON I., *Eur. Phys. J. C*, **50** (2007) 435.
[5] AALTONEN T. *et al.*, *Phys. Rev. D*, **79** (2009) 112005.
[6] ACOSTA D. *et al.*, *Phys. Rev. D*, **71** (2005) 032001; 052003; ABULENCIA D. *et al.*, *J. Phys. G Nucl. Part. Phys.*, **34** (2007) 2457.
[7] ACOSTA D. *et al.*, *Nucl. Instrum. Methods A*, **494** (2002) 57.
[8] SJOSTRAND T. *et al.*, *Comput. Phys. Commun.*, **135** (2001) 238.
[9] SJOSTRAND T., MRENNA S. and SKANDS P., *JHEP*, **026** (2006) 0605; ACOSTA D. *et al.*, *Phys. Rev. D*, **70** (2004) 072002.
[10] SJOSTRAND T. and SKANDS P., *Eur. Phys. J. C*, **39** (2005) 129.
[11] ABE F. *et al.*, *Phys. Rev. Lett.*, **61** (1988) 1819.
[12] AFFOLDER T. *et al.*, *Phys. Rev. D*, **65** (2002) 092002.
[13] FIELD R. and KAR D., CDF internal report 9567, to be submitted to *Phys. Rev. D*.
[14] BHATTI A. *et al.*, *Nucl. Instrum. Methods A*, **566** (2006) 375.
[15] ABE F. *et al.*, *Phys. Rev. Lett.*, **67** (1991) 2937.
[16] MARCHESINI G. and WEBBER B. R., *Nucl. Phys. B*, **310** (1988) 461; CATANI S., MARCHESINI G. and WEBBER B. R., *Nucl. Phys. B*, **349** (1991) 635.
[17] BUTTERWORTH J. M., FORSHAW J. R. and SEYMOUR M. H., *Z. Phys. C*, **7** (1996) 637.
[18] SKANDS P. and WICKE D., *Eur. Phys. J. C*, **52** (2007) 133.

IL NUOVO CIMENTO Vol. 32 C, N. 5-6 Settembre-Dicembre 2009
DOI 10.1393/ncc/i2010-10531-3

Colloquia: LaThuile09

Study of hard QCD at the Tevatron

M. Begel for the D0 and CDF Collaborations
Brookhaven National Laboratory - Upton, NY 11973, USA

(ricevuto il 10 Novembre 2009; pubblicato online il 18 Gennaio 2010)

Summary. — Recent measurements of photon, jet, and boson+jet production from the CDF and D0 Collaborations are presented. NLO pQCD describes most of the results except for the shapes of inclusive isolated photon and γ+jet differential cross-section measurements. Calculations involving matrix elements matched to parton showers agree with the data except at low p_T. Limits on several exotic models are set based on dijet distributions.

PACS 13.85.Qk – Inclusive production with identified leptons, photons, or other nonhadronic particles.
PACS 13.87.-a – Jets in large-Q^2 scattering.

Large-p_T processes in hadronic interactions originate in the hard scattering of partons. Measurements of boson and jet production test next-to-leading–order (NLO) perturbative QCD (pQCD) calculations and constrain parton distribution functions (PDF) [1,2]. Jet production is also sensitive to the presence of new physical phenomena including quark compositeness, large extra-dimensions, and resonances that decay with jets in the final state. Measurements of the production of vector bosons with associated jets test NLO pQCD as well as models used to describe backgrounds to other processes such as $t\bar{t}$, single top quark production, and searches for the Higgs boson and new physical phenomena.

Direct photons are produced primarily through $q\bar{q}$ annihilation ($q\bar{q} \to \gamma g$) and quark-gluon Compton-like scattering ($qg \to \gamma q$). Direct photons were therefore considered an important sample for extracting information about the gluon PDF. Unfortunately, direct photons have been excluded from global PDF fits for most of the past decade due to differences between NLO pQCD and many experimental results [3]. The inclusive isolated-photon cross-sections from D0 [4] and CDF [5] are presented in fig. 1 as a function of photon p_T. Overlayed on the data are the results from the NLO pQCD calculation JETPHOX [6]. While the prediction agrees with the data within uncertainties, the shape is different. This is similar to the shape seen in previous measurements from D0 and CDF as well as from many other direct photon experiments [3]. The differences between theory and data are more obvious in comparisons of theory with the measurements of photon+jet production from D0 [7] shown in fig. 2. Here, as in the inclusive photon measurements, NLO pQCD [6] basically agrees with data within uncertainties

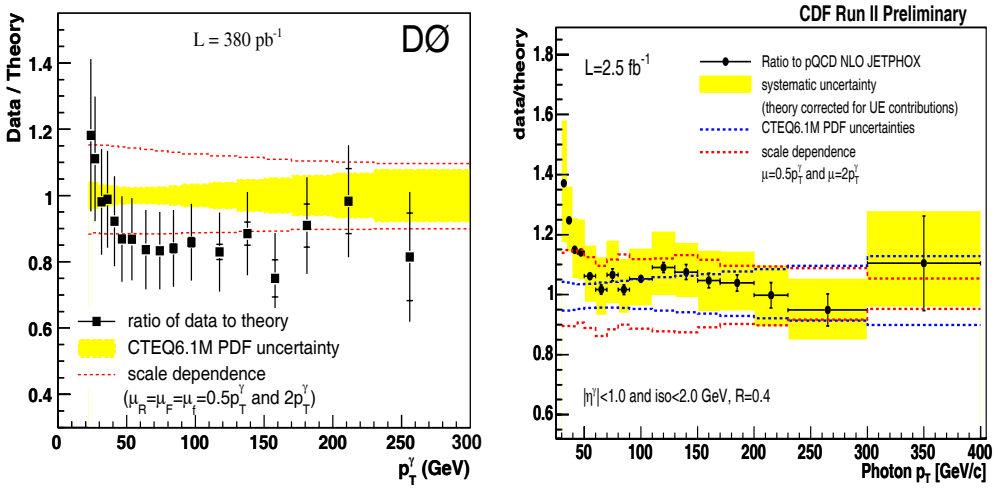

Fig. 1. – Ratio of data to NLO pQCD for the inclusive production of isolated photons.

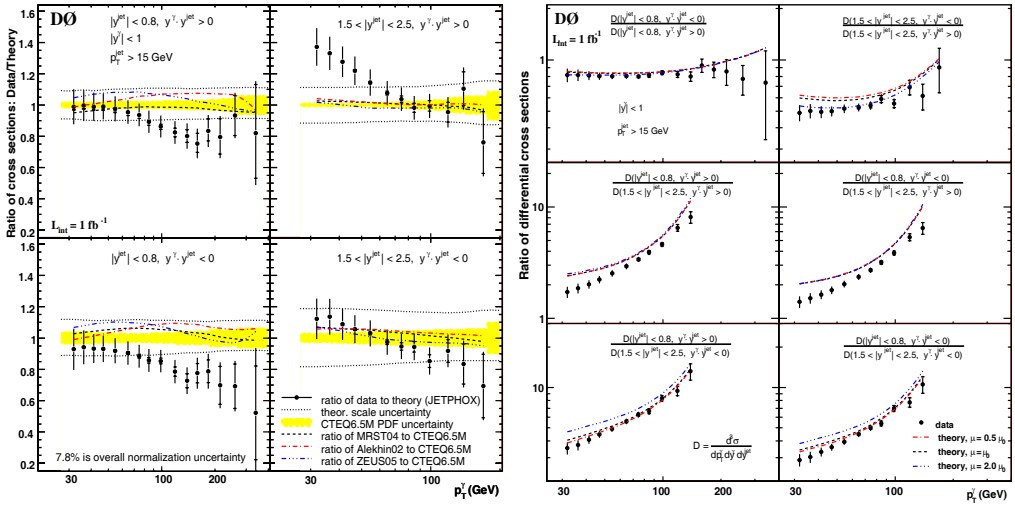

Fig. 2. – Production of γ+jet events as a function of p_T^γ from D0. Left: ratio of data-to-theory for four rapidity regions. Right: comparison of theory to data for ratios of rapidity regions.

though the discrepancies in the data-to-theory shapes in fig. 2 (left) are similar to those in fig. 1 and other photon measurements [3]. The γ+jet cross-sections were measured in four regions that combined the central-rapidity photons with both central- and forward-rapidity jets. Many systematic uncertainties cancel in ratios of one region to another in both data and theory. These comparisons are shown in fig. 2 (right). NLO pQCD clearly disagrees with the measurements for several of the ratios of one region to another.

Jet production is also dependent on the gluon PDF and jet data have supplanted photons in the global PDF fits [1, 2]. CDF and D0 have recently published precision measurements of the inclusive jet cross-section as a function of p_T in multiple rapidity

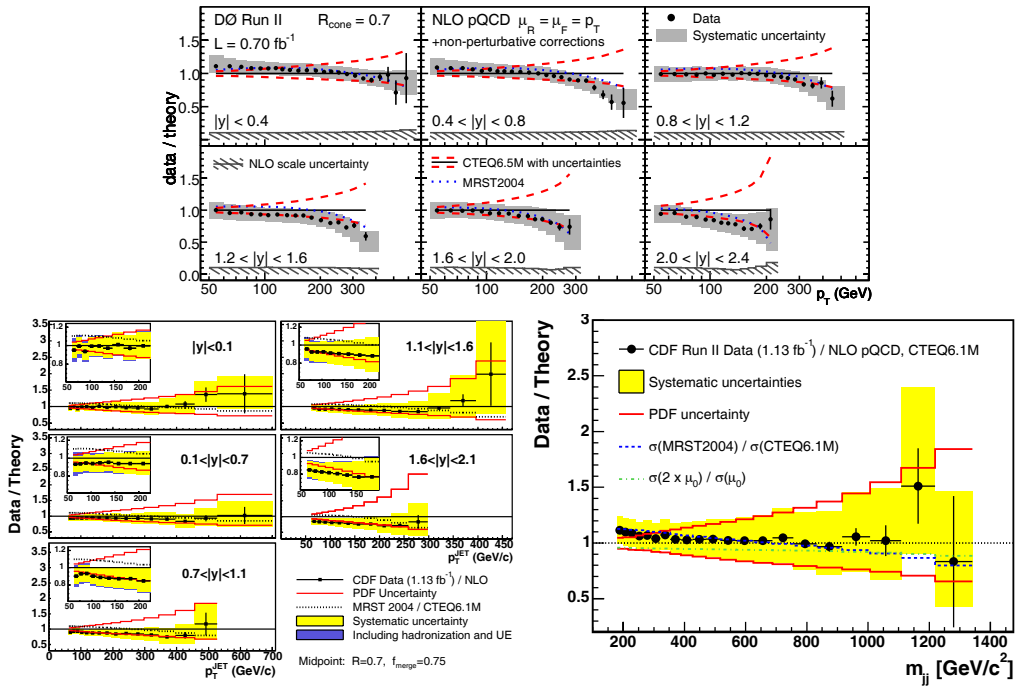

Fig. 3. – Ratio of data to NLO pQCD for inclusive jet (top and lower left) and dijet production (lower right).

bins [8,9]. Ratios of the data to the NLO pQCD calculation (NLOJET++ [10] calculated with FASTNLO [11]) are shown in fig. 3. NLO pQCD agrees very well with the data. Uncertainties from recent CTEQ PDF [2] are shown in fig. 3 as the lines. The data systematic uncertainties, shown by the shaded bands and dominated by the energy scale calibration, are smaller than the PDF uncertainties for inclusive jet production. These data have already significantly impacted the current round of global PDF fits [1].

CDF has also measured the differential cross-section for dijet production as a function of the dijet mass [12]. As shown in fig. 3 (lower right), the NLO pQCD calculation [10,11] agrees with the data. No significant evidence of a dijet mass resonance was observed, so exclusion limits were placed on a variety of exotic models including the production of W' and Z' bosons as shown in fig. 4 (left). Angular distributions are also sensitive to the presence of new physical phenomena. D0 has compared the shapes of the $\chi_{\rm dijet} = \exp|y_1 - y_2|$ distribution binned as a function of the dijet mass [13]. This is compared with NLO pQCD in fig. 4 (right) and with several additional models including one for quark compositeness and two for extra dimensions. The standard model expectation agrees with the data and so limits were placed on the potential new physics.

Z+jet events are produced through diagrams analogous to those for direct photon production except that the hard scale, Q^2, is dominated by the mass of the Z boson. Characteristics of Z+jet events therefore provide useful tests of NLO pQCD, particularly for the emission of multiple jets. Additionally, since Z+jet events form an important background in studies of $t\bar{t}$ production and in searches for the Higgs boson or for new physical phenomena, it is also useful to compare Z+jet events to models such as

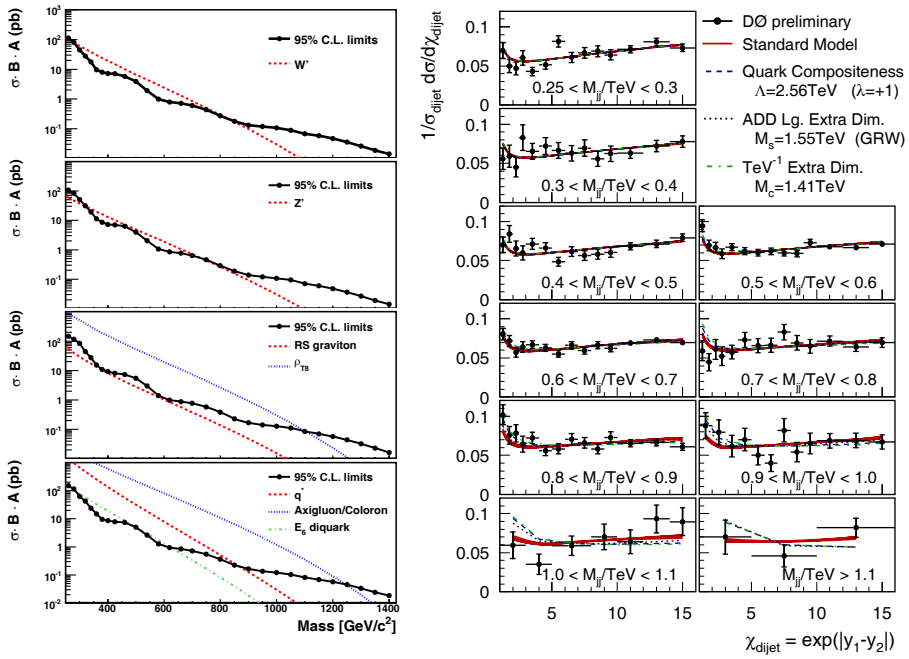

Fig. 4. – Left: exclusion limits for resonant production in the dijet decay channel. Right: angular distribution, $\chi_{\rm dijet} = \exp|y_1 - y_2|$, binned as a function of dijet mass. Overlayed are comparisons with NLO pQCD and several new physics models.

ALPGEN [14] or SHERPA [15] that match tree-level matrix elements with parton shower Monte Carlo (MEPS) [16]. Differential cross-section measurements have recently been published by the CDF and D0 Collaborations [17,18] as shown in fig. 5. The NLO pQCD calculation (MCFM [19]) reproduces the jet multiplicity and the p_T and rapidity spectra of both the Z-boson and the jets. ALPGEN and SHERPA do not compare as well with data, particularly at low p_T.

W+jet events also provide useful tests of NLO pQCD calculations and MEPS models. The higher statistics in W+jet events compared to Z+jet events is particularly useful for detailed comparisons at higher jet multiplicities or with the properties of dijets in events containing at least two jets. These are shown for CDF data [20] in fig. 6. NLO pQCD [19] compares well with the jet multiplicity and p_T distributions (fig. 6 (top-left and right)), however, the MEPS calculations (SMPR [21] and ALPGEN which is denoted as MLM) do not compare as favorably in the low p_T regime. ALPGEN does generally reproduce the characteristics of the leading two jets in W+jets events that have at least two jets. This is shown in fig. 6 (left-center and left-bottom) which display the dijet mass and angular separation ($\Delta R = \sqrt{(\Delta\phi)^2 + (\Delta\eta)^2}$). This indicates that ALPGEN provides a reasonable mix of gluon-splitting (peak at low ΔR) and uncorrelated diagrams (peak near π).

D0 and CDF have also explored the production of vector bosons with associated heavy-flavor jets. Both collaborations have recently published measurements of $W + c$ jet production which probes the strange content of the proton [22, 23]. Results from NLO pQCD calculations agree with these measurements. CDF measured the $W + c$ cross-section as $9.8 \pm 2.8^{+1.4}_{-1.8} \pm 0.6\,\text{pb}$ compared to an NLO pQCD expecta-

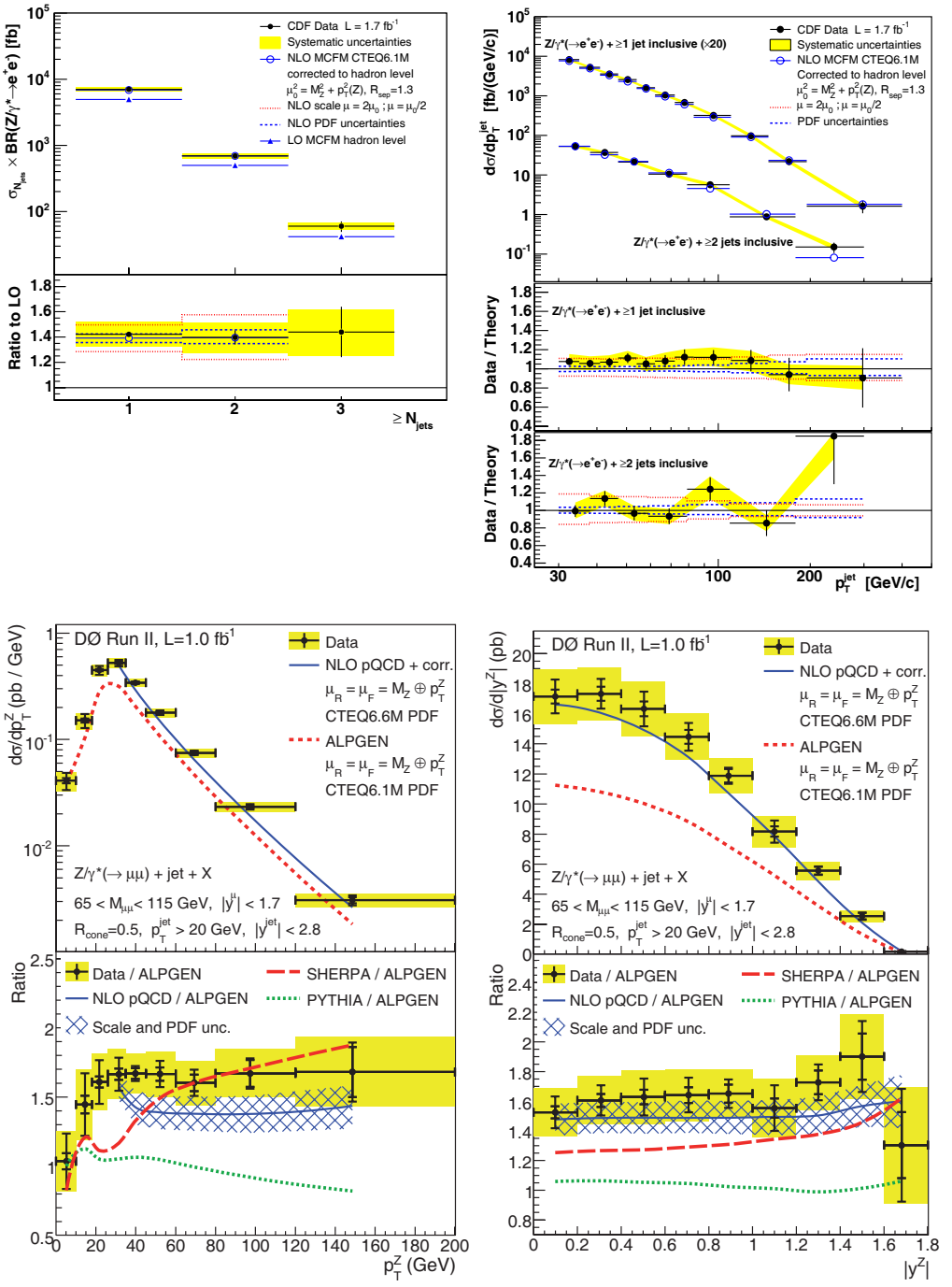

Fig. 5. – Differential cross-sections for Z+jets production. Upper left: jet multiplicity; upper right: jet p_T; lower left: Z p_T; lower right: Z rapidity.

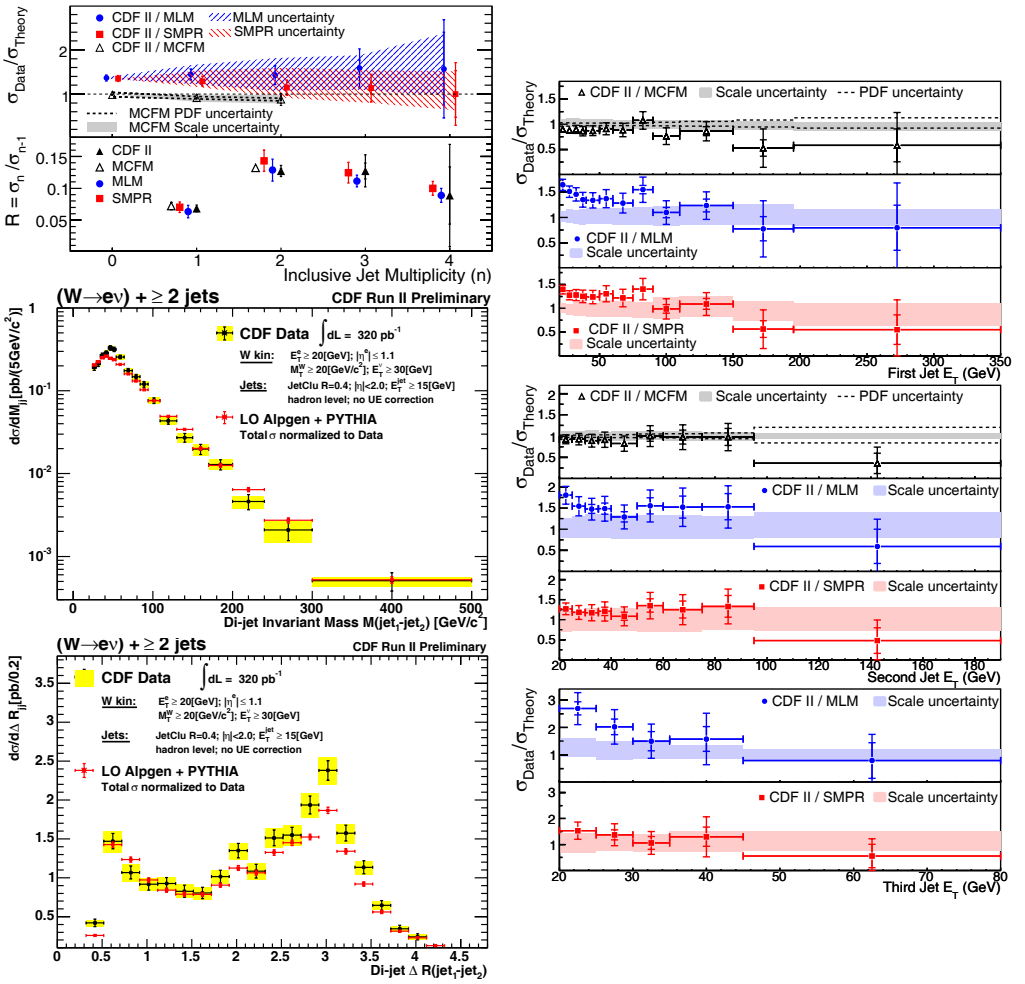

Fig. 6. – Ratio of data-to-theory for W+jets production as a function of jet multiplicity (upper left) and jet p_T (right). Differential distributions in the mass and angular separation between the jets in W+dijet events are displayed in the center left and lower left.

tion of $11^{+1.4}_{-3.0}$ pb [19] while D0 measured the ratio with respect to W+jet production of $0.074 \pm 0.019^{+0.012}_{-0.014}$ compared to 0.044 ± 0.003 from ALPGEN.

D0 has recently published the differential cross-section for the production of a direct photon with associated c and b jets [24]. These measurements are shown in ratio with NLO pQCD expectations in fig. 7 (left). Theoretical expectations agree with the $\gamma + b$ jet data, but disagree at high p_T for $\gamma + c$ jet. The uncertainties are large, but this is suggestive of an intrinsic charm component in the proton. The b content of the proton can also be probed by $Z+b$ jet events [25,26]. Differential cross-sections from CDF are shown in fig. 7 (right) binned in the p_T of the Z boson and in the jet p_T. Theoretical expectations roughly agree with the data; PYTHIA provides the best description of the data. Both collaborations have published ratios of the $Z+b$ jet to Z+jet cross-sections; NLO pQCD is slightly higher than the measurement. CDF reports $(2.11 \pm 0.33 \pm 0.34)\%$ compared

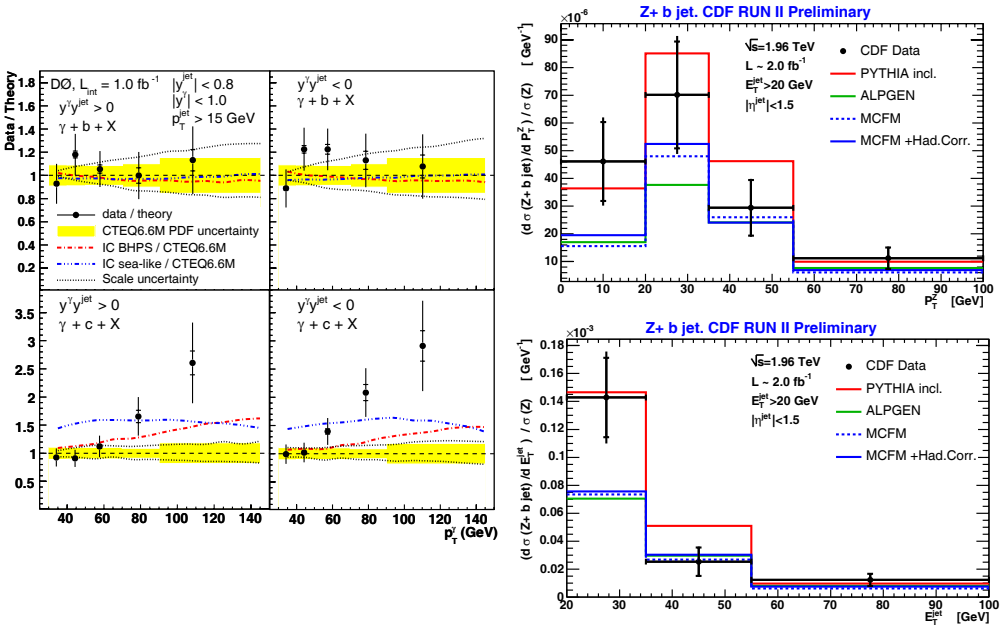

Fig. 7. – Left: ratio of data to NLO pQCD for $\gamma + b$ jet (upper) and $\gamma + c$ jet (lower) production. Right: differential cross-section for the production of $Z + b$ jet as a function of the Z p_T (upper) and jet p_T (lower).

to NLO pQCD [19] at $(1.77 \pm 0.27)\%$ while D0 reports $(2.3 \pm 0.4^{+0.2}_{-0.8})\%$ compared to $(1.8 \pm 0.4)\%$. CDF has also measured the production of b-jets in association with a W boson [27]. The b jets are typically produced through a gluon splitting diagram: $g \to b\bar{b}$. CDF measures a cross-section of $2.74 \pm 0.27 \pm 0.42$ pb compared to the expectation from ALPGEN of 0.78 pb—a significant difference.

Recent Tevatron results on boson and jet production were presented. Differences between results from NLO pQCD [6] and the measured inclusive isolated photon cross-sections [4,5] were similar to those seen with other photon experiments [3]. The disagreement was larger with the γ+jet measurement [7]. NLO pQCD [10,11] agreed very well with both the inclusive jet [7,8] and dijet [12] differential cross-sections. Limits on several exotic models were set based on the dijet mass and χ_{dijet} [13] distributions. NLO pQCD also reproduced the characteristics of Z+jet [17,18] and W+jet events [20]; matrix-element plus parton shower Monte Carlo performed less favorably [14, 15, 21]. NLO pQCD [19] reproduced the $W + c$ jet production [22,23] and $\gamma + b$ jet p_T distributions [24], but did not compare as favorably with the $\gamma + c$ jet [24] or $Z + b$ jet [25,26] measurements.

REFERENCES

[1] Martin A. D. *et al.*, arXiv:0901.0002 [hep-ph].
[2] Tung W. K. *et al.*, *JHEP*, **0702** (2007) 053; Pumplin J. *et al.*, *Phys. Rev. D*, **65** (2001) 014013.
[3] Apanasevich L. *et al.*, *Phys. Rev. D*, **59** (1999) 074007. For a different viewpoint, see Aurenche P. *et al.*, *Phys. Rev. D*, **73** (2006) 094007.

[4] Abazov V. M. *et al.* (D0 Collaboration), *Phys. Lett. B*, **639** (2006) 151; **658** (2008) 285(E).
[5] http://www-cdf.fnal.gov/physics/new/qcd/inclpho08/web.html.
[6] Aurenche P. *et al.*, *Nucl. Phys. B*, **297** (1988) 661; Aversa F. *et al.*, *Nucl. Phys. B*, **327** (1989) 105; Catani S. *et al.*, *JHEP*, **0205** (2002) 028.
[7] Abazov V. M. *et al.* (D0 Collaboration), *Phys. Lett. B*, **666** (2008) 435.
[8] Aaltonen T. *et al.* (CDF Collaboration), *Phys. Rev. D*, **78** (2008) 052006.
[9] Abazov V. M. *et al.* (D0 Collaboration), *Phys. Rev. Lett.*, **101** (2008) 062001.
[10] Nagy Z., *Phys. Rev. D*, **68** (2003) 094002.
[11] Kluge T., Rabbertz K. and Wobisch M., hep-ph/0609285.
[12] Aaltonen T. *et al.* (CDF Collaboration), arXiv:0812.4036 [hep-ex].
[13] Abazov V. M. *et al.* (D0 Collaboration), D0 note 5733-CONF (2008).
[14] Mangano M. *et al.*, *JHEP*, **0307** (2003) 001.
[15] Gleisberg T. *et al.*, *JHEP*, **0402** (2004) 056.
[16] Hoche S. *et al.*, hep-ph/0602031.
[17] Aaltonen T. *et al.* (CDF Collaboration), *Phys. Rev. Lett.*, **100** (2008) 102001.
[18] Abazov V. M. *et al.* (D0 Collaboration), *Phys. Lett. B*, **669** (2008) 278.
[19] Campbell J. and Ellis R. K., *Phys. Rev. D*, **65** (2002) 113007.
[20] Aaltonen T. *et al.* (CDF Collaboration), *Phys. Rev. D*, **77** (2008) 011108(R).
[21] Mrenna S. and Richardson P., *JHEP*, **0405** (2004) 040.
[22] Abazov V. M. *et al.* (D0 Collaboration), *Phys. Lett. B*, **666** (2008) 23.
[23] Aaltonen T. *et al.* (CDF Collaboration), *Phys. Rev. Lett.*, **100** (2008) 091803.
[24] Abazov V. M. *et al.* (D0 Collaboration), *Phys. Rev. Lett.*, **102** (2009) 192002.
[25] Abazov V. M. *et al.* (D0 Collaboration), *Phys. Rev. Lett.*, **94** (2005) 161801.
[26] Aaltonen T. *et al.* (CDF Collaboration), arXiv:0812.4458 [hep-ex].
[27] Aaltonen T. *et al.* (CDF Collaboration), CDF note 9321 (2008).

IL NUOVO CIMENTO Vol. 32 C, N. 5-6 Settembre-Dicembre 2009
DOI 10.1393/ncc/i2010-10524-2

Colloquia: LaThuile09

Hadronic physics with KLOE

F. Ambrosino(3)(4), A. Antonelli(1), M. Antonelli(1), F. Archilli(8)(9), P. Beltrame(2), G. Bencivenni(1), S. Bertolucci(1), C. Bini(6)(7), C. Bloise(1), S. Bocchetta(10)(11), F. Bossi(1), P. Branchini(11), G. Capon(1), T. Capussela(1), F. Ceradini(10)(11), P. Ciambrone(1), E. De Lucia(1), A. De Santis(6)(7), P. De Simone(1), G. De Zorzi(6)(7), A. Denig(2), A. Di Domenico(6)(7), C. Di Donato(4), B. Di Micco(10)(11), M. Dreucci(1), G. Felici(1), S. Fiore(6)(7), P. Franzini(6)(7), C. Gatti(1), P. Gauzzi(6)(7), S. Giovannella(1)(*), E. Graziani(11), G. Lanfranchi(1), J. Lee-Franzini(1)(12), M. Martini(1)(5), P. Massarotti(3)(4), S. Meola(3)(4), S. Miscetti(1), M. Moulson(1), S. Müller(2), F. Murtas(1), M. Napolitano(3)(4), F. Nguyen(10)(11), M. Palutan(1), E. Pasqualucci(7), A. Passeri(11), V. Patera(1)(5), P. Santangelo(1), B. Sciascia(1), T. Spadaro(1), M. Testa(6)(7), L. Tortora(11), P. Valente(7), G. Venanzoni(1), R. Versaci(1)(5) and G. Xu(1)(13)

(1) *Laboratori Nazionali di Frascati dell'INFN - Frascati, Italy*

(2) *Institut für Kernphysik, Johannes Gutenberg Universität - Mainz, Germany*

(3) *Dipartimento di Scienze Fisiche dell'Università "Federico II" - Napoli, Italy*

(4) *INFN, Sezione di Napoli - Napoli, Italy*

(5) *Dipartimento di Energetica dell'Università "La Sapienza" - Rome, Italy*

(6) *Dipartimento di Fisica dell'Università "La Sapienza" - Rome, Italy*

(7) *INFN, Sezione di Roma - Rome, Italy*

(8) *Dipartimento di Fisica dell'Università "Tor Vergata" - Rome, Italy*

(9) *INFN, Sezione di Roma Tor Vergata - Rome, Italy*

(10) *Dipartimento di Fisica dell'Università "Roma Tre" - Rome, Italy*

(11) *INFN, Sezione di Roma Tre - Rome, Italy*

(12) *Physics Department, State University of New York at Stony Brook Stony Brook, NY, USA*

(13) *Institute of High Energy Physics of Academica Sinica - Beijing, China*

(ricevuto il 10 Novembre 2009; pubblicato online il 15 Gennaio 2010)

(*) E-mail: simona.giovannella@lnf.infn.it

Summary. — The KLOE experiment has collected 2.5 fb^{-1} of e^+e^- collisions at the ϕ peak and about 300 pb^{-1} in the center-of-mass energy region 1000–1030 MeV. Data taken on peak are used to study the properties of light scalar and pseudoscalar mesons, produced through ϕ radiative decays, and to precisely measure the pion form factor using Initial State Radiation events. Energy scan data are used to measure the cross-section of the process $e^+e^- \to \omega\pi^0$ as a function of the center-of-mass energy and to perform a preliminary study of the reaction $e^+e^- \to e^+e^-\pi^0\pi^0$.

PACS 13.66.Bc – Hadron production in e^+e^- interactions.

1. – Introduction

The high statistics collected by the KLOE experiment provides precise measurements of fundamental properties and dynamics of light mesons, thus offering an important testing ground for non-perturbative QCD and Standard Model tests. At the same time, studies on the meson internal structure gives important information to the long-lasting debates on the existence of exotic particles.

2. – Light scalar mesons

The still unresolved structure of these states is studied either through electric dipole transitions such as $\phi \to a_0(980)\gamma$, looking at the mass spectrum of the scalar meson decay products, or with the search for processes like $\phi \to [a_0(980) + f_0(980)]\gamma \to K\bar{K}\gamma$ and $\gamma\gamma \to \sigma(600) \to \pi\pi$.

2˙1. $\phi \to a_0(980)\gamma \to \eta\pi^0\gamma$. – Two independent analyses using $\eta \to \gamma\gamma$ or $\eta \to \pi^+\pi^-\pi^0$ decays are performed from a sample of 410 pb^{-1} [1]. Both analyses share the requirement of five photons from the interaction point. Two tracks of opposite charge pointing to the interaction region are also required for the second channel. At the end of the analysis, after applying kinematical cuts to reduce background contamination, the fully neutral channel has a larger number of signal events $(13,269 \pm 192)$ and higher background contamination ($\sim 50\%$) while for the $\eta \to \pi^+\pi^-\pi^0$ both quantities are reduced by a factor 3.6. The absence of a major source of interfering background allows to obtain the branching fraction directly from event counting for both channels:

$$BR(\phi \to \eta\pi^0\gamma) = 7.01 \pm 10_{\text{stat}} \pm 20_{\text{syst}} \qquad (\eta \to \gamma\gamma), \tag{1}$$

$$BR(\phi \to \eta\pi^0\gamma) = 7.12 \pm 13_{\text{stat}} \pm 22_{\text{syst}} \qquad (\eta \to \pi^+\pi^-\pi^0). \tag{2}$$

The two samples lead to consistent branching ratio values, thus a combined fit of the two spectra is performed. The couplings, fitted according to the Kaon Loop [2] and the No Structure [3] models, point to a sizeable $s\bar{s}$ content of the $a_0(980)$.

2˙2. *Search for* $\phi \to K\bar{K}\gamma$. – In this process, never been observed, the $K\bar{K}$ system has scalar quantum numbers, therefore it is expected to proceed through the $\phi \to [a_0(980) + f_0(980)]\gamma \to K\bar{K}\gamma$ decay chain.

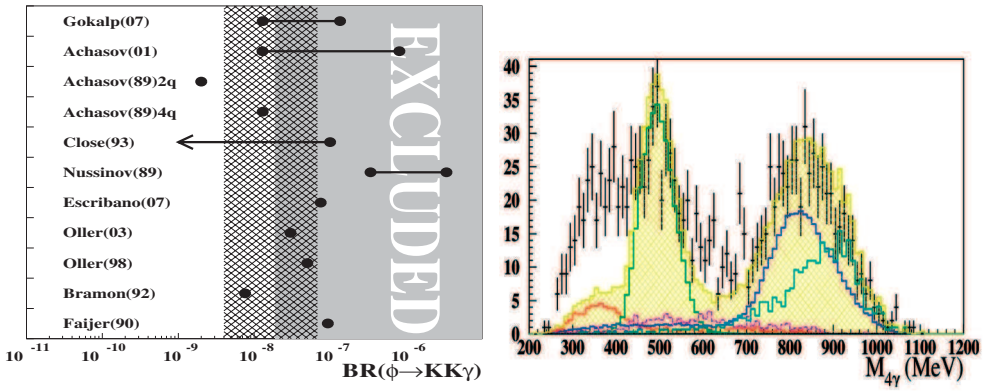

Fig. 1. – Left: excluded region at 90% CL for $BR(\phi \to K\bar{K}\gamma)$, compared with theoretical estimates and with KLOE predictions from $\phi \to f_0(980)\gamma \to \pi\pi\gamma$ and $\phi \to a_0(980)\gamma \to \eta\pi\gamma$ (hatched). Right: fit to $M_{4\gamma}$ with ϕ decays and e^+e^- annihilation processes for data taken at 1 GeV.

The selected channel for this search is $\phi \to K_S K_S \gamma \to \pi^+\pi^-\pi^+\pi^-\gamma$. The main backgrounds are the resonant $e^+e^- \to \phi\gamma \to K_S K_L \gamma$ and the continuum $e^+e^- \to \pi^+\pi^-\pi^+\pi^-\gamma$ processes. Monte Carlo (MC) signal has been simulated according to phase space and radiative decay dynamics. Selection cuts have been optimized on MC.

From an integrated luminosity of $2.2\,\mathrm{fb}^{-1}$, 5 candidate events are found in data, while 3.2 ± 0.7 events are expected from MC [4]. This leads to $BR(\phi \to K\bar{K}\gamma) < 1.9 \times 10^{-8}$ at the 90% CL. Figure 1, left, compares this measurement with the predictions of various theoretical models. Some of them are excluded. The present upper limit is consistent with the $BR(\phi \to K\bar{K}\gamma)$ prediction computed with $f_0(980)$ and $a_0(980)$ couplings measured by KLOE [5, 6, 1].

2˙3. *Search for* $\gamma\gamma \to \sigma(600) \to \pi^0\pi^0$. – While there is a long debate on the observation of the $\sigma(600)$ as a bound $\pi^+\pi^-$ state, there is no direct evidence for the $\sigma(600) \to \pi^0\pi^0$ decay. At DAΦNE, the detection of the process $e^+e^- \to e^+e^-\pi^0\pi^0$ implies the intermediate process $\gamma\gamma$ to a scalar meson state. From a sample of $11\,\mathrm{pb}^{-1}$ of data taken at $\sqrt{s} = 1\,\mathrm{GeV}$, the feasibility study of the $\pi^0\pi^0 \to 4\gamma$'s invariant mass ($M_{4\gamma}$) spectrum, without tagging e^+ or e^- in the final state, is performed. Preliminary results show an excess of events in the $M_{4\gamma}$ region below 400 MeV, where the contribution from the $\sigma(600)$ is expected, that is not explained by ϕ decays or e^+e^- annihilation processes. This preliminary work is encouraging and motivates the analysis extension to the whole sample of $240\,\mathrm{pb}^{-1}$ collected by KLOE at $\sqrt{s} = 1\,\mathrm{GeV}$.

3. – The $\eta \to \pi^+\pi^-e^+e^-$ decay

The $\eta \to \pi^+\pi^-e^+e^-$ decay allows to probe the structure of the η meson [7], to compare the predictions of the branching ratio value based on Vector Meson Dominance model and Chiral Perturbation Theory [8-11] and to study CP violation beyond the prediction of the Standard Model by measuring the angular asymmetry between pions and electrons decay planes [12].

The analysis has been performed on $1733\,\mathrm{pb}^{-1}$ [13]. The events are required to have at least four tracks coming from a cylinder around the Interaction Point. A cluster not

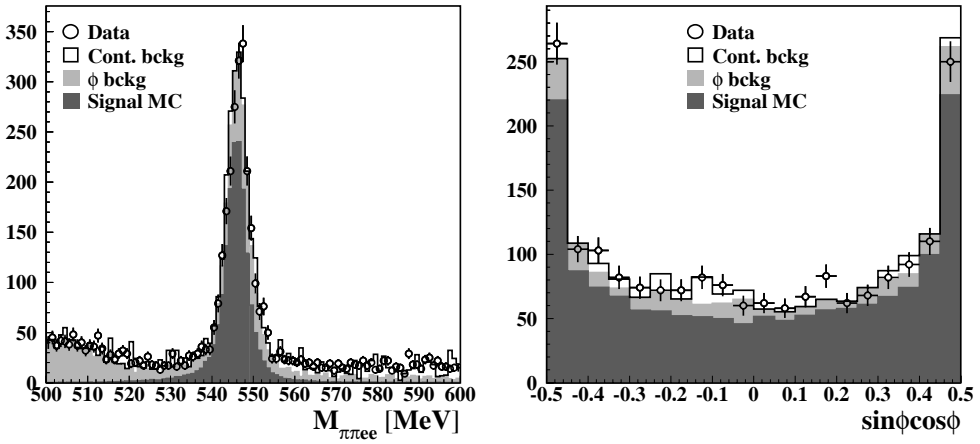

Fig. 2. – Left: fit to the invariant mass of the four selected tracks. Right: distribution of the $\sin\phi\cos\phi$ variable in the signal region. Dots: data. The black histogram is the expected distribution, *i.e.* signal MC (dark grey), ϕ background (light grey) and background in the continuum (white).

associated to any track, having time compatible with the photon time of flight, energy of at least 250 MeV and in the polar-angle range (23°–157°), is also required.

Background sources can be grouped into ϕ-decays and events in the continuum. The former is mainly due to $\phi \to \pi^+\pi^-\pi^0$ events (with π^0 Dalitz decay) and to $\phi \to \eta\gamma$ events either with $\eta \to \pi^+\pi^-\pi^0$ (with π^0 Dalitz decay) or with $\eta \to \pi^+\pi^-\gamma$ (with photon conversion on the beam pipe). The latter comes mainly from $e^+e^- \to e^+e^-(\gamma)$ events. Because of poor MC statistics, they have been studied using off-peak data taken at $\sqrt{s} = 1\,\text{GeV}$, where ϕ decays are negligible. Backgrounds are reduced applying cuts on track momenta and reconstructing the invariant mass and the distance of the candidate electron pairs on the beam pipe to remove photon conversions.

Background contribution is evaluated performing a fit on the sidebands of the $\pi^+\pi^-e^+e^-$ invariant mass after the cuts on track momenta with background shapes. The output of the fit ($P(\chi^2) = 0.35$) is shown in the left panel of fig. 2. For the signal estimate we limit ourselves to the region $[535, 555]\,\text{MeV}$ and perform the event counting after background subtraction. The resulting value obtained for the branching ratio is

$$BR(\eta \to \pi^+\pi^-e^+e^-\gamma) = (26.8 \pm 0.9_{\text{stat}} \pm 0.7_{\text{syst}}) \times 10^{-5}. \tag{3}$$

The decay plane asymmetry is calculated starting from the momenta of the four particles and is expressed as a function of the angle ϕ between the pion and the electron planes in the η rest frame. The value obtained is

$$\mathcal{A}_\phi = (-0.6 \pm 2.5_{\text{stat}} \pm 1.8_{\text{syst}}) \times 10^{-2}, \tag{4}$$

which is the first measurement of this asymmetry. The distribution of the $\sin\phi\cos\phi$ variable is shown in the right panel of fig. 2.

TABLE I. – *Fit results for the evaluation of the η' gluonium content. In the first column, only the first two parameters are left free.*

Parameter	KLOE published	KLOE update	KLOE update (no glue)
$Z^2_{\eta'}$	0.14 ± 0.04	0.12 ± 0.04	0 (fixed)
φ_P	$(39.7 \pm 0.7)^\circ$	$(40.4 \pm 0.6)^\circ$	$(41.4 \pm 0.5)^\circ$
Z_{NS}	0.91 ± 0.05	0.94 ± 0.03	0.93 ± 0.02
Z_S	0.89 ± 0.07	0.83 ± 0.05	0.82 ± 0.05
φ_V	3.2°	$(3.32 \pm 0.09)^\circ$	$(3.34 \pm 0.09)^\circ$
m_s/m	1.24 ± 0.07	1.24 ± 0.07	1.24 ± 0.07
$P(\chi^2)$	49%	20.5%	0.5%

4. – Search for gluonium in η'

The η'-meson, being almost a pure $SU(3)$ singlet, is a good candidate for a sizeable gluonium content. In this hypothesis, the η and η' wave functions can be written in terms of the u, d quark wave function ($|q\bar{q}\rangle = \frac{1}{\sqrt{2}}(|u\bar{u}\rangle + |d\bar{d}\rangle)$), the strange component ($|s\bar{s}\rangle$) and the gluonium ($|GG\rangle$) [14]:

$$|\eta'\rangle = \cos\varphi_G \sin\varphi_P \,|q\bar{q}\rangle + \cos\varphi_G \cos\varphi_P \,|s\bar{s}\rangle + \sin\varphi_G \,|GG\rangle, \tag{5}$$

$$|\eta\rangle = \cos\varphi_P \,|q\bar{q}\rangle - \sin\varphi_P \,|s\bar{s}\rangle, \tag{6}$$

where φ_P is the η-η' mixing angle and $Z^2_G = \sin^2\varphi_G$ is the gluonium fraction in the η'-meson.

From the study of $\phi \to \eta'\gamma \to \pi^+\pi^-7\gamma$'s and $\phi \to \eta\gamma \to 7\gamma$'s decays, the ratio $R_\phi = BR(\phi \to \eta'\gamma)/BR(\phi \to \eta\gamma)$ has been measured [15]: $R_\phi = (4.77 \pm 0.09_{\text{stat}} \pm 0.19_{\text{syst}}) \times 10^{-3}$. Using the approach of refs. [16,17], where the $SU(3)$ breaking is taken into account via the constituent quark mass ratio $m_s/\bar{m}$, R_ϕ can be parametrized as

$$R_\phi = \cot^2\varphi_P \cos^2\varphi_G \left(1 - \frac{m_s}{\bar{m}} \frac{C_{NS}}{C_S} \frac{\tan\varphi_V}{\sin 2\varphi_P}\right)^2 \left(\frac{p_{\eta'}}{p_\eta}\right)^3; \tag{7}$$

$p_{\eta'}$ and p_η are the momenta of the η'- and η-meson, respectively, φ_V is the ϕ-ω mixing angle and C_{NS}, C_S takes into account the vector and pseudoscalar wave function overlap. Combining our R_ϕ result with other experimental constraints and using the corresponding $SU(3)$ relations between decay modes [17, 18], we found a $3\,\sigma$ evidence for gluonium content in η' (table I, left column). Since the parameters C_{NS}, C_S, φ_V and $m_s/\bar{m}$ were taken from [16], obtained in the hypothesis of no η' gluonium content, we repeat the fit adding other $SU(3)$ relations and enlarging the number of free parameters. As shown in table I, the new result is in good agreement for all parameters, confirming the $3\,\sigma$ evidence for gluonium in η'. The quality of the fit get worse when $Z^2_{\eta'}$ is fixed to zero.

We also investigated the origin of the discrepancy between our result and the one of ref. [17], where a similar fit leads to a null gluonium content in η', even if consistent with our measurement. The key point is the use of the $\Gamma(\eta' \to \gamma\gamma)/\Gamma(\pi^0 \to \gamma\gamma)$ constraint in our approach, which significantly increases the central value of $Z^2_{\eta'}$, reducing the error.

TABLE II. – *Fit results for the* $e^+e^- \to \pi^+\pi^-\pi^0\pi^0$ *and* $e^+e^- \to \pi^0\pi^0\gamma$ *cross-sections.*

Parameter	4π channel	$\pi\pi\gamma$ channel
σ_0 (nb)	$7.89 \pm 0.06 \pm 0.07$	$0.724 \pm 0.010 \pm 0.003$
$\Re(Z)$	$0.106 \pm 0.007 \pm 0.004$	$0.011 \pm 0.015 \pm 0.006$
$\Im(Z)$	$-0.103 \pm 0.004 \pm 0.003$	$-0.154 \pm 0.007 \pm 0.004$
σ' (nb/MeV)	$0.064 \pm 0.003 \pm 0.001$	$0.0053 \pm 0.0005 \pm 0.0002$
χ^2/N_{df}, $P(\chi^2)$	4.78/13 (98%)	11.79/13 (54%)

5. – The $e^+e^- \to \omega\pi^0$ process

In the energy region of few tens of MeV around M_ϕ, the $\omega\pi^0$ production cross-section is largely dominated by the non-resonant processes $e^+e^- \to \rho/\rho'$. However, in a region closer to M_ϕ, a contribution from the OZI and G-parity–violating decay $\phi \to \omega\pi^0$ is expected. This strongly suppressed decay can be observed only through the interference pattern with the previous reaction, which shows up as a dip in the production cross-section as a function of the center-of-mass energy ($\sqrt{s}$). The interference scheme depends on the final state used in the analysis. For the $\pi^+\pi^-\pi^0\pi^0$ channel only the already mentioned processes are present while for $\pi^0\pi^0\gamma$ there are also contributions from $\phi \to f_0(980)\gamma$ and $\phi \to \rho\pi^0$ which modify the $\sqrt{s}$ behaviour.

The dependence of the cross-section on the center-of-mass energy can be parametrized in the form [19]

$$\sigma(\sqrt{s}) = \sigma_{NR}(\sqrt{s}) \cdot \left| 1 - Z \frac{M_\phi \Gamma_\phi}{D_\phi} \right|^2, \tag{8}$$

where $\sigma_{NR}(\sqrt{s})$ is the bare cross-section for the non-resonant process, Z is a complex interference parameter while M_ϕ, Γ_ϕ and D_ϕ are the mass, the width and the inverse propagator of the ϕ-meson, respectively. Since in the considered center-of-mass energy range the non-resonant cross-section increases almost linearly, we assume a simple linear dependence: $\sigma_{NR}(\sqrt{s}) = \sigma_0 + \sigma'(\sqrt{s} - M_\phi)$.

The analysis has been performed on $\sim 600\,\mathrm{pb}^{-1}$ at center-of-mass energies between 1000 and 1030 MeV [20]. For both final states used in this analysis ($\pi^+\pi^-\pi^0\pi^0$ and $\pi^0\pi^0\gamma$) data are filtered by selecting events with the expected signature. After performing a kinematic fit, which improves the energy resolution of photons, specific cuts for background rejection are applied. The measured values of visible cross-section are then fitted using as free parameters σ_0^i, $\Re(Z_i)$, $\Im(Z_i)$ and σ_i', where i is the 4π or $\pi\pi\gamma$ final state. The values for the extracted parameters are reported in table II. From them we obtain: $\Gamma(\omega \to \pi^0\gamma)/\Gamma(\omega \to \pi^+\pi^-\pi^0) = 0.0897 \pm 0.0016$. Since these two final states correspond to $\sim 98\%$ of the ω decay channels, this ratio and the sum of the existing BR measurements on the remaining rarer decays [21] are used to extract the main ω branching fractions imposing the unitarity:

$$BR(\omega \to \pi^+\pi^-\pi^0) = (90.24 \pm 0.19)\%, \tag{9}$$

$$BR(\omega \to \pi^0\gamma) = (8.09 \pm 0.14)\%, \tag{10}$$

with a correlation of -71%.

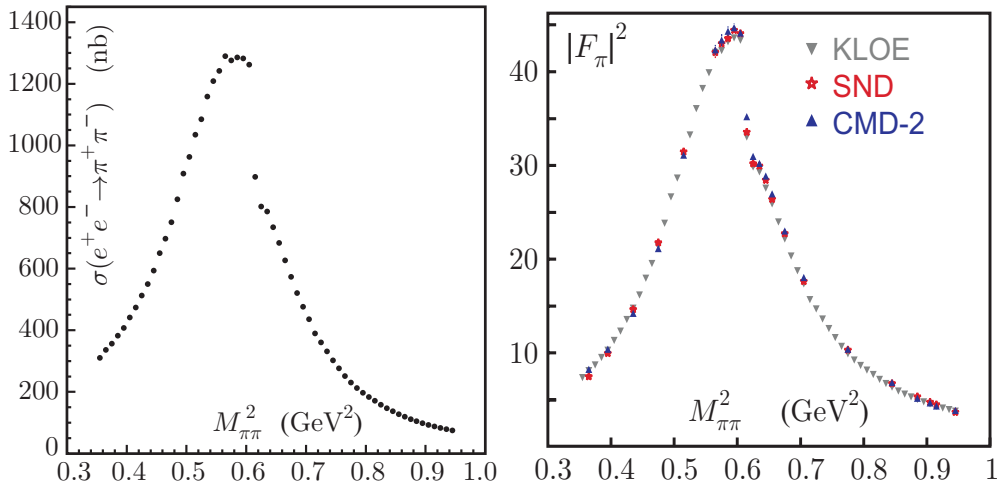

Fig. 3. – Differential cross-section for the process $e^+e^- \to \pi^+\pi^-$ (left) and comparison of the resulting pion form factor with SND and CMD-2 experiments (right).

Using the parameters obtained from the $\pi^+\pi^-\pi^0\pi^0$ analysis, the Γ_{ee} measurement from KLOE [22] for the evaluation of σ_ϕ, and our value for $BR(\omega \to \pi^+\pi^-\pi^0)$, we extract

$$BR(\phi \to \omega\pi^0) = (4.4 \pm 0.6) \times 10^{-5}, \tag{11}$$

in agreement and with better accuracy with respect to what obtained by the SND experiment $(5.2^{+1.3}_{-1.1} \times 10^{-5})$ [19].

6. – Measurement of $\sigma(e^+e^- \to \pi^+\pi^-\gamma(\gamma))$

The anomalous magnetic moment of the muon has been measured with an accuracy of 0.54 ppm [23]. The main source of uncertainty in the value predicted by the Standard Model is given by the hadronic contribution to the lowest order, a_μ^{hlo}. This quantity can be evaluated via a dispersion integral of the hadronic cross-section measurements. The pion form factor F_π, proportional to the $\sigma_{\pi\pi}$ cross-section, accounts for $\sim 70\%$ of the central value and for $\sim 60\%$ of the uncertainty in a_μ^{hlo}.

The analysis has been performed on 240 pb^{-1} of data taken at the ϕ peak, corresponding to 3.1 Million events [24]. The differential spectrum of the $\pi^+\pi^-$ invariant mass, $M_{\pi\pi}$, is measured from ISR events, $e^+e^- \to \pi^+\pi^-\gamma$, and the total cross-section $\sigma_{\pi\pi}$ is obtained using the formula [25]: $s\,\frac{\mathrm{d}\sigma_{\pi\pi\gamma}}{\mathrm{d}M^2_{\pi\pi}} = \sigma_{\pi\pi}(M^2_{\pi\pi})\; H(M^2_{\pi\pi})$, where H is the radiator function, describing the photon emission at the initial state. This formula neglects Final State Radiation (FSR) terms, which are however properly taken into account in the analysis.

The analysis requires two charged pion tracks having $50° < \theta_\pi < 130°$ and a photon emitted within a cone of $\theta_\gamma < 15°$ around the beam line. The photon is not explicitly detected and its direction is reconstructed by closing the kinematics of the event. The separation of pion and photon selection regions greatly reduces the contamination from the resonant process $e^+e^- \to \phi \to \pi^+\pi^-\pi^0$, in which the π^0 mimics the missing momentum of the photon(s) and from FSR. On the other hand, a highly energetic photon emitted at small angle forces the pions also to be at small angles

(and thus outside the selection cuts), resulting in a kinematical suppression of events with $M^2_{\pi\pi} < 0.35\,\mathrm{GeV}^2$. Residual contamination from the processes $\phi \to \pi^+\pi^-\pi^0$ and $e^+e^- \to \mu^+\mu^-\gamma$ is greatly reduced by kinematical cuts, while a particle ID estimator, based on calorimeter information and time-of-flight, is used to suppress the high rate of radiative Bhabhas.

The $\pi\pi\gamma$ differential cross-section (fig. 3 left) is obtained from the observed spectrum after subtracting the residual background events and correcting for the selection efficiency and the luminosity. The total cross-section is then extracted, taking into account next-to-leading–order ISR effects and vacuum polarisation. The cross-section inclusive of FSR is then used to determine $a_\mu^{\pi\pi}$:

$$a_\mu^{\pi\pi}(0.592 < M_{\pi\pi} < 0.975\,\mathrm{GeV}) = (387.2 \pm 3.3) \times 10^{-10}. \tag{12}$$

The total error has a negligible statistical contribution and comparable experimental systematic and theoretical calculation uncertainties (0.6% each). This result is in agreement with CMD-2 and SND values [26, 27], as shown in fig. 3 right, and confirms the current disagreement between the Standard Model prediction for a_μ and its direct measured value.

REFERENCES

[1] Ambrosino F. *et al.* (KLOE Collaboration), *Phys. Lett. B*, **681** (2009) 5.
[2] Achasov N. N. and Gubin V. V., *Phys. Rev. D*, **56** (1997) 4084.
[3] Isidori G., Maiani L., Nicolaci M. and Pacetti S., *JHEP*, **0605** (2006) 049.
[4] Ambrosino F. *et al.* (KLOE Collaboration), *Phys. Lett. B*, **679** (2009) 10.
[5] Ambrosino F. *et al.* (KLOE Collaboration), *Phys. Lett. B*, **634** (2006) 148.
[6] Ambrosino F. *et al.* (KLOE Collaboration), *Eur. Phys. J. C*, **49** (2007) 473.
[7] Landsberg L. G., *Phys. Rep.*, **128** (1985) 301.
[8] Jarlskog C. and Pilkuhn H., *Nucl. Phys. B*, **1** (1967) 264.
[9] Faessler A., Fuchs C. and Krivoruchenko M. I., *Phys. Rev. C*, **61** (2000) 035206.
[10] Picciotto C. and Richardson S., *Phys. Rev. D*, **48** (1993) 3395.
[11] Borasoy B. and Nissler R., *Eur. Phys. J. A*, **33** (2007) 95.
[12] Gao D. N., *Mod. Phys. Lett. A*, **17** (2002) 1583.
[13] Ambrosino F. *et al.* (KLOE Collaboration), *Phys. Lett. B*, **675** (2009) 283.
[14] Rosner J. L., *Phys. Rev. D*, **27** (1983) 1101.
[15] Ambrosino F. *et al.* (KLOE Collaboration), *Phys. Lett. B*, **648** (2007) 267.
[16] Bramon A., Escribano R. and Scadron M. D., *Phys. Lett. B*, **503** (2001) 271.
[17] Escribano R. and Nadal J., *JHEP*, **05** (2007) 6.
[18] Kuo E., *Phys. Rev. D*, **63** (2001) 054027.
[19] Aulchenko V. M. *et al.*, *J. Exp. Theor. Phys.*, **90** (2000) 927.
[20] Ambrosino F. *et al.* (KLOE Collaboration), *Phys. Lett. B*, **669** (2008) 223.
[21] Yao W. M. *et al.*, *J. Phys. G*, **33** (2006) 1 and 2007 partial update for 2008 edition [`http://pdg.web.cern.ch/pdg`].
[22] Ambrosino F. *et al.* (KLOE Collaboration), *Phys. Lett. B*, **608** (2005) 199.
[23] Bennett G. W. *et al.* (Muon g-2 Collaboration), *Phys. Rev. D*, **73** (2006) 072003.
[24] Ambrosino A. *et al.* (KLOE Collaboration), *Phys. Lett. B*, **670** (2009) 285.
[25] Binner S., Kühn J. H. and Melnikov K., *Phys. Lett. B*, **459** (1999) 279.
[26] Achasov M. N. *et al.* (SND Collaboration), *J. Exp. Theor. Phys.*, **103** (2006) 380.
[27] Akhmetshin R. R. *et al.* (CMD-2 Collaboration), *Phys. Lett. B*, **648** (2007) 28.

IL NUOVO CIMENTO Vol. 32 C, N. 5-6 Settembre-Dicembre 2009
DOI 10.1393/ncc/i2010-10528-x

Colloquia: LaThuile09

Infrared singularities in QCD amplitudes

E. Gardi([1]) and L. Magnea([2])

([1]) *School of Physics, The University of Edinburgh - Edinburgh EH9 3JZ, Scotland, UK*
([2]) *Dipartimento di Fisica Teorica, Università di Torino and INFN, Sezione di Torino Via P. Giuria 1, I-10125 Torino, Italy*

(ricevuto il 10 Novembre 2009; pubblicato online il 15 Gennaio 2010)

Summary. — We review recent progress in determining the infrared singularity structure of on-shell scattering amplitudes in massless gauge theories. We present a simple ansatz where soft singularities of any scattering amplitude of massless partons, to any loop order, are written as a sum over colour dipoles, governed by the cusp anomalous dimension. We explain how this formula was obtained, as the simplest solution to a newly-derived set of equations constraining the singularity structure to all orders. We emphasize the physical ideas underlying this derivation: the factorization of soft and collinear modes, the special properties of soft gluon interactions, and the notion of the cusp anomaly. Finally, we briefly discuss potential multi-loop contributions going beyond the sum-over-dipoles formula, which cannot be excluded at present.

PACS 11.15.-q – Gauge field theories.
PACS 12.38.-t – Quantum chromodynamics.
PACS 12.38.Cy – Summation of perturbation theory.

1. – The role of infrared singularities

Understanding soft and collinear singularities is essential for the application of QCD to collider physics. Indeed, cross-section calculations beyond tree level involve intricate cancellations of such singularities in the sum over final states. A detailed understanding of the singularities is therefore a prior condition to making precise predictions. Furthermore, knowing the singularities, one can resum the dominant radiative corrections to all orders, greatly improving the accuracy of the prediction.

Beyond their immediate significance to phenomenology, infrared singularities open a window into the all-order structure of perturbation theory. They admit a simple, iterative structure, which is common to all gauge theories. Understanding this structure is an important step towards understanding scattering amplitudes in gauge theories in general. As an example, recent progress in studying scattering amplitudes in the maximally supersymmetric ($\mathcal{N} = 4$) Yang-Mills theory in the planar limit [1-5], has demonstrated

that in that case the iterative structure of the amplitude persists in its finite parts. Moreover, for the first time a bridge was formed between the weak coupling expansion and the strong coupling limit. In these studies the infrared singularity structure had a key role. In particular, the cusp anomalous dimension $\gamma_K(\alpha_s)$ [6-11], which, as we shall see, governs soft singularities in any scattering amplitude, was shown to have an important role also in determining the finite parts of the amplitude. Today $\gamma_K(\alpha_s)$ is the best understood anomalous dimension, at both weak [12] and strong coupling [4, 13-15]. As shown by this example, there is a strong theoretical incentive to gain full understanding of the singularity structure of scattering amplitudes. Let us now discuss the more pragmatic motivation aiming at precision collider phenomenology.

Cross-section calculations beyond tree level. – The very fact that gauge theory amplitudes are plagued by long-distance singularities while the corresponding cross-sections are finite, makes the determination of these singularities essential. The cancellation of infrared singularities in cross-sections takes place upon summing over degenerate states, as originally shown in QED by Bloch and Nordsieck [16], and later proven in [17, 18]. Virtual gluons generate singularities in amplitudes owing to the integrations over loop momenta, which extend over regions where the gluons are soft or collinear with any of the hard partons—this puts some internal propagators on shell, leading to singularities. In contrast, real emission diagrams are finite, but singularities appear upon performing phase-space integrations over regions where the emitted partons become soft or collinear with other partons. The physical cross-section is a sum of these two contributions, which can be separately computed in dimensional regularization. Schematically, using $D = 4 - 2\epsilon$ dimensions with $\epsilon < 0$, one finds cancellations of the form

$$\underbrace{\frac{1}{\epsilon}}_{\text{virtual}} + \underbrace{(Q^2)^\epsilon \int_0^{m^2_{\text{jet}}} \frac{\mathrm{d}k^2}{(k^2)^{1+\epsilon}}}_{\text{real}} \implies \ln(m^2_{\text{jet}}/Q^2), \tag{1}$$

where Q^2 represents a hard energy scale, *e.g.*, the squared centre-of-mass energy s, while m^2_{jet} represents the phase-space limit in the integration of the radiated gluon, which depends on the observable considered, *e.g.*, a jet mass. Because of their different origin, these singularities render any calculation of scattering cross-sections beyond tree level highly non-trivial.

At the one-loop order we have a complete understanding of these singularities. This forms the basis for general subtraction algorithms, for example based on a colour dipole picture [19], rendering the phase-space integration finite. The possibility to perform such local subtraction has been invaluable to practical cross-section calculations. Present-day collider phenomenology requires computations of multi-leg processes in general kinematics, in order to allow for maximal flexibility in the application of kinematic cuts dictated by the search strategies and experimental needs. This leads to complicated phase-space integrations, which can only be done numerically. Thus, a local subtraction of the singularities—which guarantees finite integrals—is an absolute necessity. General subtraction algorithms do not exist yet at the multi-loop level and their development is of prime importance to precision computations. The first step in this direction is the determination of the singularity structure of amplitudes, the subject of the present talk.

Resummation. – Beyond fixed-order cross-section calculations, infrared singularities also provide the key to resummation of soft and collinear gluon radiation. Singular contributions cancel between real and virtual corrections, but, as shown schematically in eq. (1), a residual logarithm survives. These logarithmically enhanced corrections (Sudakov logarithms) are the dominant radiative corrections for many cross-sections. In particular, these corrections are parametrically leading when the relevant scales are far apart—for example in eq. (1) when $m^2_{\text{jet}} \ll Q^2$. Whenever the logarithm becomes as large as the inverse power of the coupling, it spoils the converges of the expansion, and corrections involving powers of $\alpha_s \ln(m^2_{\text{jet}}/Q^2)$ need to be resummed to all orders. The situation is complicated by the fact that, due to overlapping soft and collinear divergences, each order in perturbation theory can give rise to two logarithms, yielding $\alpha_s \ln^2(m^2_{\text{jet}}/Q^2)$. In this case, resummation is necessary already for $\ln(m^2_{\text{jet}}/Q^2) \sim 1/\sqrt{\alpha_s}$. Because these logarithms are all generated by the singularities in the amplitude, which always exponentiate, higher powers of the logarithms at any order in the coupling can be predicted based on the singular terms in the first few orders in the loop expansion. This is a key ingredient for resummation.

The most widely used applications of this picture are parton shower event generators, which implement Sudakov resummation with leading logarithmic accuracy, keeping complete kinematic information on the generated final state. To achieve better precision one typically resorts to a more inclusive approach. Indeed, it has been repeatedly demonstrated in a variety of applications, *e.g.*, [20-25], that precise predictions can be obtained in kinematic regions that are characterized by a large hierarchy of scales upon performing Sudakov resummation, provided one gains sufficient control of subleading logarithms and related power corrections.

The theory of Sudakov resummation is especially well developed in inclusive observables, where the hard-scattering process involves just two coloured partons [22,23,26-31]. Such processes are characterized by a single or a double hierarchy of scales. Examples of the first category include deep-inelastic structure functions at large Bjorken x [32], and Drell-Yan or Higgs production near partonic threshold, or at small transverse momentum [22, 23]. Examples of the second include event-shape distributions [20, 33], heavy-quark production [21,34], and inclusive meson decay spectra [24,25]. The Sudakov factor in processes involving two (incoming or outgoing) partons, may be written in the generic form

$$\text{Sud}(m^2, N) = \exp\left[C_i \int_0^1 \frac{\mathrm{d}r}{r} \left(\underbrace{(1-r)^{N-1}}_{\text{real}} \underbrace{-1}_{\text{virtual}} \right) R(m^2, r) \right], \tag{2}$$

where $C_i = C_F$ or C_A depending on the colour representation of the hard partons (fundamental or adjoint), and the radiator is given by

$$C_i \frac{R(m^2, r)}{r} = -\frac{1}{r} \left[\int_{r^2 m^2}^{r m^2} \frac{\mathrm{d}k^2}{k^2} \gamma_K \left(\alpha_s(k^2)\right) + 2\mathcal{B}\left(\alpha_s(r m^2)\right) - 2\mathcal{D}\left(\alpha_s(r^2 m^2)\right) \right]. \tag{3}$$

These two equations summarize, in a compact way, the form of logarithmically enhanced terms in a typical infrared-safe cross-section, to all orders in perturbation theory. This simple structure is a consequence of factorization, namely the fact that soft and jet subprocesses decouple from the hard interaction and are mutually incoherent. Equation (2)

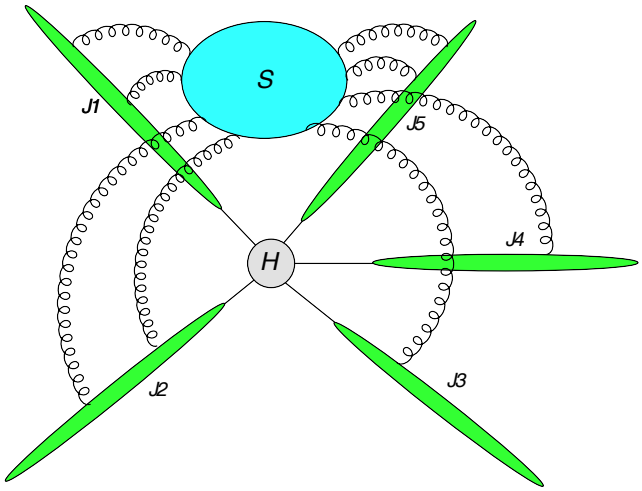

Fig. 1. – Singular configurations for a fixed-angle multiparton scattering amplitude.

incorporates the cancellation between real and virtual singularities anticipated in (1). Note that this equation is written in moment space: only then does the real emission phase-space factorise (see, however, [35]). Equation (3) describes the structure of the Sudakov exponent in terms of a few anomalous dimensions which are functions of the running coupling only. This additive structure of the exponent is in one-to-one correspondence with the phase-space origin of the various corrections: collinear logarithms, characterised by momenta of order $m^2 r$, are controlled by $\mathcal{B}(\alpha_s)$; soft (large-angle) logarithms, characterised by momenta of order $m^2 r^2$, are controlled by $\mathcal{D}(\alpha_s)$; finally, the overlap between the soft and the collinear regions is governed by the cusp anomalous dimension $\gamma_K(\alpha_s)$, which is a universal quantity, the one and only source of double logarithms.

Singularities in multileg amplitudes. – The application of Sudakov resummation to hard processes with several coloured partons is less developed, and it will become more important for LHC physics. The starting point to perform such a resummation is the analysis of the singularity structure of the corresponding scattering amplitudes (fig. 1) at fixed angles [36,37], assuming no strong hierarchy between the various kinematic invariants. *A priori*, upon considering a multileg hard process with general kinematics, one may expect a complicated singularity structure, more intricate than the simple expressions of eqs. (2) and (3). Yet, the goal remains to understand the singularities to any loop order in terms on a small set of anomalous dimensions, which are functions of the coupling only.

A further complication arises in a non-Abelian gauge theory, as soon as the amplitude involves more than three hard partons: soft-gluon interactions induce correlations between kinematic and colour degrees of freedom. Soft gluons still exponentiate, but this exponentiation now involves matrices defined in a given colour basis (see below). Resummation formulae such as eqs. (2) and (3) may only hold upon diagonalizing these matrices. The size of the matrices depends only on the colour representations of the external hard partons. *A priori*, however, at each loop order one would expect new colour correlations (as suggested by fig. 2), which would require re-diagonalizing the matrix.

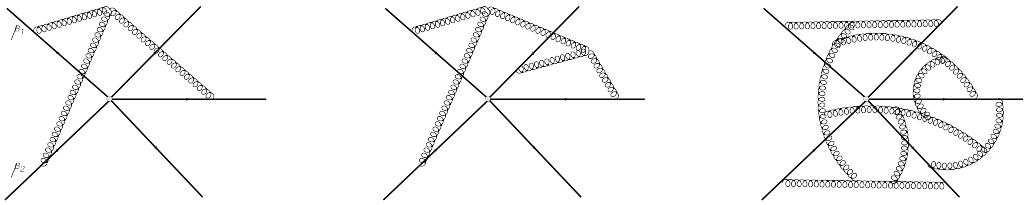

Fig. 2. – Gluon "webs" entering the soft function at 2, 3 and 8 loops, respectively.

The theoretical understanding of infrared singularities in multileg processes has recently taken a significant leap forward. The first step was taken in [38], where a two-loop calculation of the infrared singularities in multileg amplitudes was first performed. The conclusions were rather suprising at the time: the colour matrix structure of the soft anomalous dimension that controls the singularities at two loops turned out to be identical to the one at one loop. The next step was taken very recently in [39] and in parallel in [40, 41]. These papers explained the findings of [38] and proposed a formula that generalizes this result to all loops. According to this formula, no new correlations are introduced by multi-loop webs. Instead, the correlations generated by soft gluons are always described by a sum over two-body interactions between hard partons, and thus the matrix structure at any loop order is the same as at one loop. We shall present this formula in the next section. This proposal is based on a set of all-order constraints (see sects. **6** and **7**, below) that relate the singularity structure in any multileg amplitude to the cusp anomalous dimension $\gamma_K(\alpha_s)$. The derivation of these constraints is based on factorization and on the universal properties of soft-gluon interactions, which are described in sects. **3**, **4** and **5**. Importantly, in amplitudes with four legs or more the sum-over-dipoles formula is still an ansatz: although this formula is consistent with all available constraints, there may be additional contributions at three loops or beyond, which we can constrain but not exclude at present. This issue is briefly summarized in sect. **8**.

2. – The sum-over-dipoles formula

Consider a scattering amplitude $\mathcal{M}(p_i/\mu, \alpha_s(\mu^2), \epsilon)$, involving a fixed number n of hard coloured partons carrying momenta p_i, $i = 1 \dots n$, all lightlike, $p_i^2 = 0$, and any number of additional non-coloured particles. We assume that ultraviolet renormalization has been performed (μ being the renormalization scale) thus all remaining singularities are associated with long distances, and can be regularized working in $D = 4 - 2\epsilon$ dimensions, with $\epsilon < 0$. The singularities depend on all the kinematic invariants that can be formed out of the hard parton momenta, $p_i \cdot p_j$ ($n(n-1)/2$ invariants for an n-parton amplitude). We work with general kinematics and assume no special hierarchy between these invariants; they must all be large compared to $\Lambda^2_{\rm QCD}$, and their ratios are regarded as numbers of order unity. Momentum conservation is not imposed between the coloured partons, allowing for any recoil momentum to be carried by non-coloured particles in both the initial and final states. Soft and collinear factorization properties guarantee that all infrared singularities can be absorbed into an overall multiplicative factor Z: one writes formally

$$\mathcal{M}\left(p_i/\mu, \alpha_s(\mu^2), \epsilon\right) = Z\left(p_i/\mu_F, \alpha_s(\mu_F^2), \epsilon\right)\, \mathcal{H}\left(p_i/\mu, \mu/\mu_F, \alpha_s(\mu^2)\right), \tag{4}$$

where $\mathcal{H}$ is finite and can be taken to be independent of ϵ. Note that in general, the factorization scale μ_F, at which Z is defined, is distinct from the renormalization scale μ. For simplicity in the following we choose $\mu_F = \mu$. Equation (4) should be understood as a matrix multiplication in colour space: $\mathcal{H}$ is a vector in some colour basis, accounting for the hard-scattering process, including any loop corrections involving highly virtual gluons. These are necessarily finite. Z is a matrix in this space, mixing the components of the vector $\mathcal{H}$, and accounting for soft and collinear singularities. According to the ansatz of ref. [39] Z assumes the form([1])

$$Z\left(p_i/\mu, \alpha_s(\mu^2), \epsilon\right) = \exp\left[\int_0^{\mu^2} \frac{\mathrm{d}\lambda^2}{\lambda^2}\left(\frac{1}{8}\,\widehat{\gamma}_K\left(\alpha_s(\lambda^2,\epsilon)\right)\sum_{(i,j)}\ln\left(\frac{2p_i\cdot p_j\,\mathrm{e}^{\mathrm{i}\pi\lambda_{ij}}}{\lambda^2}\right)\mathrm{T}_i\cdot\mathrm{T}_j - \frac{1}{2}\sum_{i=1}^{n}\gamma_{J_i}\left(\alpha_s(\lambda^2,\epsilon)\right)\right)\right], \tag{5}$$

where the notation $\sum_{(i,j)}$ indicates a sum over all pairs of hard partons forming colour dipoles, where each pair is counted twice (i,j) and (j,i), and $\mathrm{T}_i\cdot\mathrm{T}_j \equiv \sum_a \mathrm{T}_i^{(a)}\cdot\mathrm{T}_j^{(a)}$, where T_i is a generator([2]) in the colour representation of parton i. The overall colour charge is conserved,

$$\sum_{i=1}^{n}\mathrm{T}_i^{(a)} = 0. \tag{6}$$

The same ansatz was proposed independently in ref. [40, 41].

As originally proposed in [43] (see also [44]), singularities in eq. (5) are generated exclusively through integration over the D-dimensional running coupling $\alpha_s(\lambda^2,\epsilon)$, which obeys the renormalization group equation

$$\mu\frac{\partial\alpha_s(\mu^2,\epsilon)}{\partial\mu} = \beta(\epsilon,\alpha_s) = -\,2\,\epsilon\,\alpha_s - \frac{\alpha_s^2}{2\pi}\sum_{n=0}^{\infty}b_n\left(\frac{\alpha_s}{\pi}\right)^n, \tag{7}$$

where $b_0 = (11C_A - 2n_f)/3$. It is easy to verify that the solution to this equation for small coupling and fixed, negative ϵ, is power suppressed at small scales,

$$\alpha_s(\lambda^2,\epsilon) = \left(\frac{\lambda^2}{\mu^2}\right)^{-\epsilon}\left[\alpha_s(\mu^2,\epsilon) + \mathcal{O}(\alpha_s^2)\right], \tag{8}$$

which guarantees convergence of integrals ranging from $\lambda^2 = 0$ to some fixed scale μ^2, as in eq. (5). Non-trivial higher-loop corrections enter in (5) only through higher-order

([1]) Following [42] we keep track of the unitarity phases by writing $-p_i\cdot p_j = |p_i\cdot p_j|\,\mathrm{e}^{\mathrm{i}\pi\lambda_{ij}}$, where $\lambda_{ij} = 1$ if i and j are both initial-state partons or are both final-state partons, and $\lambda_{ij} = 0$ otherwise.

([2]) $\mathrm{T}^{(a)}$ should be interpreted as follows: for a final-state quark or an initial-state antiquark: $t^a_{\alpha\beta}$; for a final-state antiquark or an initial-state quark: $-t^a_{\beta\alpha}$; for a gluon: $\mathrm{i}\,f_{cab}$.

corrections to the anomalous dimensions $\gamma_K^{(i)}(\alpha_s)$ and $\gamma_{J_i}(\alpha_s)$. The former—but not the latter—is assumed here to admit Casimir scaling, namely to depend on the colour representation of the parton i only through an overall factor given by the corresponding quadratic Casimir,

$$\gamma_K^{(i)}(\alpha_s) = C_i\,\widehat{\gamma}_K(\alpha_s); \quad C_i \equiv \mathrm{T}_i \cdot \mathrm{T}_i. \tag{9}$$

$\widehat{\gamma}_K(\alpha_s) = 2\alpha_s/\pi + \mathcal{O}(\alpha_s^2)$ is known explicitly to three-loop order based on the calculation by Moch, Vermaseren and Vogt [12, 45]. Potential contributions of higher-order Casimirs at four loops and beyond will be briefly discussed in sect. **8**.

The first term in eq. (5), which is governed by the cusp anomalous dimension $\widehat{\gamma}_K$, represents the singularities generated by the interaction of large-angle soft gluons described by the $\mathcal{S}$ function in fig. 1. This term is written as a sum over colour dipoles formed by any pair of hard partons; it correlates the kinematic dependence on the Lorentz invariant $p_i \cdot p_j$ with the corresponding product of colour generators, $\mathrm{T}_i \cdot \mathrm{T}_j$. This correlation is precisely the one present at the one-loop order. This would imply that no new correlations are generated by multi-loop webs such as the ones shown in fig. 2—a highly non-trivial statement, which was not yet tested by direct calculations beyond the two-loop level.

The second term in eq. (5) represents the interaction of collinear gluons. It is governed by the jet anomalous dimension corresponding to each of the external partons, quarks or gluons. These anomalous dimensions are defined in (26) below; they depend not only on the colour representation of these partons but also on their spin. Their values are known to three-loop order, based on the calculation of the quark and gluon form factors in refs. [46, 47]; the coefficients have been conveniently collected in Appendix A of [41].

Equation (5) may well be the exact expression for the singularities of any on-shell scattering amplitude in massless gauge theories. As already emphasized, the simplicity of this result is striking, especially when compared to the lengthy and complicated expressions one typically obtains for multi-leg amplitudes. It is also not what one would naturally expect looking at the diagrams of fig. 2. Indeed eq. (5) requires that some remarkable cancellations take place in these diagrams. It is therefore very interesting to see how eq. (5) emerged out of general considerations. This is the goal of the following sections.

3. – Eikonal approximation and rescaling invariance

The first key ingredient in deriving the constraints on the singularity structure is the universal nature of soft gluon interactions, in particular their independence from the absolute momentum scale of the hard parton to which they couple. Let us first explain the origin of this property and then analyse its consequences in the context of the factorization of an on-shell amplitude.

Consider, for example, soft-gluon radiation off a hard quark, as shown in fig. 3. We assume that after this emission the quark is on shell, so that $p^2 = m^2$ (where m^2 can vanish, but this is not necessary for the argument that follows). Applying the ordinary Feynman rules, one obviously obtains a result that depends on the radiating particle spin and momentum—the first expression in eq. (10). Considering instead the limit where

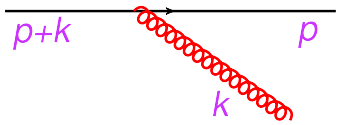

Fig. 3. – Gluon bremsstrahlung off an outgoing quark. The final-state quark is on shell, $p^2 = m^2$.

the gluon is soft ($k \to 0$) one obtains a much simpler result,

$$\bar{u}(p)\left(-\mathrm{i}g_s T^{(a)}\gamma^\mu\right)\frac{\mathrm{i}(\not{p}+\not{k}+m)}{(p+k)^2-m^2+\mathrm{i}\varepsilon} \underset{k\to 0}{\Longrightarrow} \bar{u}(p) g_s T^{(a)} \frac{p^\mu}{p\cdot k+\mathrm{i}\varepsilon}\,, \tag{10}$$

which depends only on the colour charge and direction β of the quark momentum

$$g_s T^{(a)}\frac{p^\mu}{p\cdot k+\mathrm{i}\varepsilon} = g_s T^{(a)}\frac{\beta^\mu}{\beta\cdot k+\mathrm{i}\varepsilon}\,. \tag{11}$$

Equivalently, we observe that the resulting "eikonal" Feynman rules are invariant with respect to rescaling of the quark velocity, $\beta \to \kappa\beta$, a symmetry property that will be central to our discussion in what follows. Finally, we note that the eikonal approximation is conveniently formulated by replacing the dynamical hard partons, which provide the source for the radiation, with Wilson lines along their classical trajectories,

$$\Phi_\beta(0,-\infty) = P\exp\left[\mathrm{i}g_s\int_{-\infty}^{0}\mathrm{d}\lambda\,\beta\cdot A(\lambda\beta)\right]. \tag{12}$$

Here rescaling invariance is inherent: it is realised through reparametrization of the integral along the path.

4. – Factorization

The second key element is the factorization of soft and collinear singularities in the amplitude, illustrated in fig. 1. Following [38, 48-51], we write

$$\begin{aligned}\mathcal{M}_L(p_i/\mu,\alpha_s(\mu^2),\epsilon) = \sum_K \mathcal{S}_{LK}(\beta_i\cdot\beta_j,\alpha_s(\mu^2),\epsilon)\,H_K\left(\frac{2p_i\cdot p_j}{\mu^2},\frac{(2p_i\cdot n_i)^2}{n_i^2\mu^2},\alpha_s(\mu^2)\right)\\ \times\prod_{i=1}^{n}\frac{J_i\left(\dfrac{(2p_i\cdot n_i)^2}{n_i^2\mu^2},\alpha_s(\mu^2),\epsilon\right)}{\mathcal{J}_i\left(\dfrac{2(\beta_i\cdot n_i)^2}{n_i^2},\alpha_s(\mu^2),\epsilon\right)}\,.\end{aligned} \tag{13}$$

Here the hard function H_K and the amplitude $\mathcal{M}_L$ are vectors in the space of available color configurations; the soft function $\mathcal{S}_{LK}$ is a matrix in this space, while the jet functions J_i and $\mathcal{J}_i$ do not carry any colour index. The soft matrix $\mathcal{S}$ and the jet functions J and $\mathcal{J}$ contain all soft and collinear singularities of the amplitude, while the hard functions H_K can be taken to be independent of ϵ. Each of the functions appearing in eq. (13) is separately gauge invariant and admits operator definitions that are given below.

The soft and jet functions involve semi-infinite Wilson lines, defined in (12). The "partonic jet" function (for, say, an outgoing quark with momentum p) is defined by

$$\overline{u}(p)\, J\left(\frac{(2p\cdot n)^2}{n^2\mu^2}, \alpha_s(\mu^2), \epsilon\right) = \langle p|\, \overline{\psi}(0)\, \Phi_n(0,-\infty)\, |0\rangle. \tag{14}$$

The function J represents a transition amplitude connecting the vacuum and a one-particle state. The eikonal line Φ_n simulates interactions with partons moving in different directions: the direction n^μ is arbitrary, but off the light-cone, in order to avoid spurious collinear singularities.

The factorization formula (13) also involves the eikonal approximation to the partonic jet J, which we call the "eikonal jet". It is defined by

$$\mathcal{J}\left(\frac{2(\beta\cdot n)^2}{n^2}, \alpha_s(\mu^2), \epsilon\right) = \langle 0|\, \Phi_\beta(\infty,0)\, \Phi_n(0,-\infty)\, |0\rangle, \tag{15}$$

where the velocity vector β_i of each jet is related to the corresponding momentum p_i by $p_i = \beta_i Q_0/\sqrt{2}$, with Q_0 a hard scale such that $p_i\cdot p_j/Q_0^2$ is of order one for all i, j.

Both the partonic jet (14) and the eikonal jet (15) have soft divergences, as well as collinear divergences associated to their lightlike leg; thus, they display double poles order by order in perturbation theory. The double poles are however the same, since in the soft region $\mathcal{J}$ correctly approximates J: singular contributions to the two functions differ only by hard collinear radiation.

The final ingredient in (13) is the soft matrix, which we define by taking the eikonal approximation for all gluon exchanges: since soft gluons do not resolve the details of the hard interaction nor the internal structure of the jets, they couple effectively to Wilson lines in the colour representations of the corresponding hard external partons. Such exchanges mix the colour components of the amplitude, forming a matrix in colour space. Choosing a basis of independent tensors c_L in color space, we write

$$\sum_L (c_L)_{\{\alpha_k\}} \mathcal{S}_{LK}\left(\beta_i\cdot\beta_j, \alpha_s(\mu^2), \epsilon\right) = \sum_{\{\eta_k\}} \langle 0|\, \prod_{i=1}^{n} \left[\Phi_{\beta_i}(\infty,0)_{\alpha_k,\eta_k}\right]\, |0\rangle (c_K)_{\{\eta_k\}}. \tag{16}$$

Note that in eq. (16) we keep all Wilson lines strictly on the light-cone ($p_i^2 = 0$ and thus $\beta_i^2 = 0$). Therefore, the soft matrix $\mathcal{S}_{LK}$ displays not only single poles corresponding to large-angle soft gluons, but also double poles associated with overlapping soft and collinear singularities. Recall that the jet functions J_i also include the regions of overlapping soft and collinear singularities. It is for this reason that in the factorization formula, eq. (13), we have divided each partonic jet J_i jet by $\mathcal{J}_i$, thus removing from J_i its eikonal part, which is already accounted for in $\mathcal{S}_{LK}$. One observes then that the ratios $J_i/\mathcal{J}_i$ are free of soft singularities: they contain only single collinear poles at each order in perturbation theory. Similarly, the "reduced" soft matrix

$$\overline{\mathcal{S}}_{LK}\left(\rho_{ij}, \alpha_s(\mu^2), \epsilon\right) = \frac{\mathcal{S}_{LK}\left(\beta_i\cdot\beta_j, \alpha_s(\mu^2), \epsilon\right)}{\displaystyle\prod_{i=1}^{n} \mathcal{J}_i\left(\frac{2(\beta_i\cdot n_i)^2}{n_i^2}, \alpha_s(\mu^2), \epsilon\right)}, \tag{17}$$

where

$$\rho_{ij} \equiv \frac{(\beta_i \cdot \beta_j \, \mathrm{e}^{\mathrm{i}\,\pi\lambda_{ij}})^2}{\frac{2(\beta_i \cdot n_i)^2}{n_i^2}\,\frac{2(\beta_j \cdot n_j)^2}{n_j^2}} \tag{18}$$

is free of collinear poles, and contains only infrared singularities originating from soft gluon radiation at large angles with respect to all external legs. The kinematic dependence of $\overline{\mathcal{S}}$ on ρ_{ij} will be explained below.

5. – The cusp anomaly and the jet functions

The third and final ingredient necessary for deriving the constraints on the singularities of on-shell amplitudes is the cusp anomaly. In the following we will recall the definition of the cusp anomalous dimension and explain its role in governing the kinematic dependence of Wilson-line operators. This will allow us first to understand the structure of the eikonal jet function $\mathcal{J}$ to all orders in perturbation theory, and eventually to constrain the soft function $\mathcal{S}$.

To this end, let us recall some general properties of operators that are composed of semi-infinite Wilson lines. The first observation is that all radiative corrections to such operators vanish identically in dimensional regularization, since the corresponding integrals involve no scale. This trivial result however involves cancellations between ultraviolet and infrared singularities; therefore, upon renormalization, $\mathcal{J}$ becomes non-trivial: the contribution of each graph equals minus the corresponding ultraviolet counterterm. As a consequence, using a minimal subtraction scheme, the result for $\mathcal{J}$ (or for $\mathcal{S}$) at each order in α_s is a sum of poles in ϵ, without any non-negative powers.

Let us now briefly recall the renormalization properties of Wilson loops with cusps [6-11, 52-54]. Consider first an operator

$$W\left(\gamma_{12}, \alpha_s(\mu^2), \epsilon\right) = \langle 0|\, \Phi_{n_1}(\infty, 0)\, \Phi_{n_2}(0, -\infty)\, |0\rangle, \tag{19}$$

involving two semi-infinite rays, both off the lightcone ($n_1^2,\, n_2^2 \neq 0$), which join at the origin to form a cusp with (Minkowski) angle γ_{12}, where

$$\cosh(\gamma_{12}) = \frac{(n_1 \cdot n_2)}{\sqrt{n_1^2}\,\sqrt{n_2^2}}\,. \tag{20}$$

The contour closes at infinity and it is smooth everywhere except at the origin. Reference [53] has shown that the presence of the cusp along the contour introduces an ultraviolet singularity which can be removed by a multiplicative renormalization constant, implying that

$$\frac{\mathrm{d}\ln W}{\mathrm{d}\ln\mu} \equiv -\,\Gamma_{\mathrm{cusp}}(\gamma_{12}, \alpha_s(\mu^2)) = -\,C_i\,\frac{\alpha_s(\mu^2)}{\pi}\,[\gamma_{12}\coth(\gamma_{12}) - 1] + \mathcal{O}(\alpha_s^2), \tag{21}$$

where $C_i = C_A$ or C_F depending on the representation of the Wilson lines. Considering the limit where n_1 or n_2 is near the lightcone, one finds that

$$\gamma_{12} \simeq \ln\left(\frac{2n_1 \cdot n_2}{\sqrt{n_1^2}\,\sqrt{n_2^2}}\right) \gg 1, \tag{22}$$

and

$$\frac{\mathrm{d}\ln W\left(\gamma_{12},\alpha_s(\mu^2),\epsilon\right)}{\mathrm{d}\ln\mu} = -\frac{\gamma_K^{(i)}(\alpha_s(\mu^2))}{2}\ln\left(\frac{2n_1\cdot n_2}{\sqrt{n_1^2}\sqrt{n_2^2}}\right)+\mathcal{O}(1). \tag{23}$$

It is clear that in the strictly lightlike limit, the *r.h.s.* of (23) and (21) become singular. This is a collinear singularity, appearing on top of the ultraviolet singularity already present in W owing to the cusp. Therefore, if we consider directly the renormalization of the analogue of W with one of the rays being strictly lightlike, say $n_2^2=0$ —precisely the case of $\mathcal{J}$ in eq. (15)—we expect a singular anomalous dimension. Indeed, in dimensional regularization the renormalization group equation of $\mathcal{J}$ takes the form [39]

$$\begin{aligned}\mu\frac{\mathrm{d}}{\mathrm{d}\mu}\ln\mathcal{J}_i\left(\frac{2(\beta\cdot n)^2}{n^2},\alpha_s(\mu^2),\epsilon\right) &\equiv -\gamma_{\mathcal{J}_i}\left(\frac{2(\beta\cdot n)^2}{n^2},\alpha_s(\mu^2),\epsilon\right)\\ &= \frac{1}{2}\,\delta_{\mathcal{J}_i}(\alpha_s(\mu^2)) - \frac{1}{4}\gamma_K^{(i)}(\alpha_s(\mu^2))\ln\left(\frac{2(\beta\cdot n)^2}{n^2}\right) - \frac{1}{4}\int_0^{\mu^2}\frac{\mathrm{d}\xi^2}{\xi^2}\,\gamma_K^{(i)}(\alpha_s(\xi^2,\epsilon)),\end{aligned} \tag{24}$$

where the third term is singular, $\mathcal{O}(1/\epsilon)$. Having seen the origin of this singularity in (23), it is not surprising that the dependence of $\gamma_{\mathcal{J}}$ on the kinematic variable $2(\beta\cdot n)^2/n^2$—the second term in (24)—is governed by the same anomalous dimension, $\gamma_K^{(i)}(\alpha_s)$, that governs the singularity of $\gamma_{\mathcal{J}_i}$—the third term in (24). This relation between kinematic dependence and singular terms, which we have now observed in $\gamma_{\mathcal{J}_i}$, is a general property of this class of operators which will be essential for what follows.

To understand it from a different angle, let us now have another look at eqs. (21) and (24) considering the symmetry property of the eikonal Feynman rules (10) under rescaling of the eikonal velocity vectors. Clearly eq. (21) is consistent with this symmetry: any function of γ_{12} defined in (20) would be. In contrast, in the strictly lightlike case of (24), there is no kinematic variable that could be consistent with this symmetry. $\mathcal{J}$ can only depend on $2(\beta\cdot n)^2/n^2$, as indeed can be confirmed by an explicit calculation, and therefore it breaks the rescaling symmetry: it depends explicitly on the normalization of β. Note that rescaling of the vector n_μ, which is not light-like, remains a symmetry.

Solving (24) we obtain a closed form expression for the eikonal jet [39], in terms of anomalous dimensions which depend just on the coupling,

$$\begin{aligned}\mathcal{J}_i\left(\frac{2(\beta_i\cdot n_i)^2}{n_i^2},\alpha_s(\mu^2),\epsilon\right) = \exp\Bigg[\frac{1}{2}\int_0^{\mu^2}\frac{\mathrm{d}\lambda^2}{\lambda^2}\Bigg(&\frac{1}{2}\delta_{\mathcal{J}_i}\left(\alpha_s(\lambda^2,\epsilon)\right)\\ &-\frac{1}{4}\gamma_K^{(i)}\left(\alpha_s(\lambda^2,\epsilon)\right)\ln\left(\frac{2(\beta_i\cdot n_i)^2\,\mu^2}{n_i^2\lambda^2}\right)\Bigg)\Bigg].\end{aligned} \tag{25}$$

We see that the entire kinematic dependence of $\mathcal{J}$ is associated with the breaking of the rescaling symmetry with respect to the lightlike direction β_μ; it is directly related to presence of double poles in $\mathcal{J}$, and it is governed by the cusp anomalous dimension, $\gamma_K^{(i)}(\alpha_s)$. In the following, we will show how this observation, made in [39], allowed us to constrain the kinematic dependence of the soft function $\mathcal{S}$.

Before turning to the soft function, let us quote the equivalent expression for the partonic jet J_i, which will be of use in the following. The partonic jet has an infrared singularity structure similar to the eikonal jet, however it has a *finite* ultraviolet anomalous dimension, the one we have encountered in (5),

$$\mu\frac{\mathrm{d}}{\mathrm{d}\mu}\ln J_i\left(\frac{(2p_i\cdot n_i)^2}{n_i^2\mu^2},\alpha_s(\mu^2),\epsilon\right)\equiv-\gamma_{J_i}(\alpha_s(\mu^2)). \tag{26}$$

As a consequence, the partonic jet function can be written as

$$\begin{aligned}J_i&\left(\frac{(2p_i\cdot n_i)^2}{n_i^2\mu^2},\alpha_s(\mu^2),\epsilon\right)=\\ &H_{J_i}\left(\alpha_s\left(\frac{(2p_i\cdot n_i)^2}{n_i^2}\right),\epsilon\right)\exp\left[-\frac{1}{2}\int_0^{\mu^2}\frac{\mathrm{d}\lambda^2}{\lambda^2}\gamma_{J_i}(\alpha_s(\lambda^2,\epsilon))\right.\\ &\left.+\frac{\mathrm{T}_i\cdot\mathrm{T}_i}{2}\int_0^{\frac{(2p_i\cdot n_i)^2}{n_i^2}}\frac{\mathrm{d}\lambda^2}{\lambda^2}\left(-\frac{1}{4}\widehat{\gamma}_K(\alpha_s(\lambda^2,\epsilon))\ln\left(\frac{(2p_i\cdot n_i)^2}{\lambda^2\,n_i^2}\right)+\frac{1}{2}\widehat{\delta}_{\overline{\mathcal{S}}}(\alpha_s(\lambda^2,\epsilon))\right)\right],\end{aligned} \tag{27}$$

where H_J is a finite coefficient function, independent of μ^2. Equation (27) displays the fact that in addition to the collinear singularities generated by γ_{J_i} the jet function (14) involves soft (eikonal) singularities; these are summarized by the second line of (27). Beyond the $\gamma_K^{(i)}$ terms, one finds single-pole terms governed by $\delta_{\overline{\mathcal{S}}}^{(i)}$. This function, which is defined in eqs. (4.7) and (4.9) in [39], does not depend on the spin of parton i and it has a maximally non-Abelian structure. For simplicity, we further assumed here that $\delta_{\overline{\mathcal{S}}}^{(i)}$ admits Casimir scaling, $\delta_{\overline{\mathcal{S}}}^{(i)}=\mathrm{T}_i\cdot\mathrm{T}_i\,\widehat{\delta}_{\overline{\mathcal{S}}}$, although this may not hold beyond three loops (and it would not be important in what follows). In contrast, γ_{J_i}, which governs the collinear singularities, does depend on the spin of parton i (it differs for quarks and for gluons, see Appendix A of [41]) and it is not maximally non-Abelian. As anticipated, the double poles in (25) and (27) are the same, while single poles differ.

6. – Derivation of the constraints on soft singularities

We are finally in a position to derive the promised constraints on soft singularities. We will show, in particular, that the relation established above, considering the case of the eikonal jet, between kinematic dependence of single-pole terms and the cusp anomalous dimension, generalises to soft singularities in multileg amplitudes. These singularities are described by the function $\mathcal{S}$ in (13). $\mathcal{S}$ is defined by (16) and it obeys a matrix evolution equation of the form

$$\mu\frac{\mathrm{d}}{\mathrm{d}\mu}\mathcal{S}_{IK}(\beta_i\cdot\beta_j,\alpha_s,\epsilon)=-\sum_J\Gamma^{\mathcal{S}}_{IJ}(\beta_i\cdot\beta_j,\alpha_s,\epsilon)\,\mathcal{S}_{JK}(\beta_i\cdot\beta_j,\alpha_s,\epsilon). \tag{28}$$

The soft anomalous dimension matrix $\Gamma^{\mathcal{S}}$ depends on all the kinematic invariants in the process, and it is *a priori* a very complicated object. It encapsulates the correlation between colour and kinematic degrees of freedom, which may be of increasing complexity as one considers higher-loop corrections (fig. 2).

We recall that in $\mathcal{S}$ all the Wilson lines are lightlike, $\beta_i^2 = 0$, $\forall i$. Therefore, similarly to $\mathcal{J}$, we expect this function to break the rescaling invariance with respect to each of the velocities β_i. This was already taken into account in assigning the arguments in $\mathcal{S}$ and in $\Gamma^{\mathcal{S}}$: these functions depend on the set of Lorentz invariants $\beta_i \cdot \beta_j$, and thus violate the rescaling symmetry. We will be able to constrain $\Gamma^{\mathcal{S}}$—and thus $\mathcal{S}$—because we know exactly how this symmetry is violated.

The key point is that the amplitude $\mathcal{M}$ itself cannot depend on the normalization one chooses for the velocities appearing in eikonal functions. Thus, in the factorization formula, eq. (13), this dependence must cancel out. This cancellation can only involve the eikonal functions $\mathcal{S}$ and $\mathcal{J}_i$, not the partonic jet or the hard function, which depend directly on the dimensionful kinematic variables p_i. The form of the factorization formula (13) implies in fact that the cancellation of any rescaling violation must occur within the reduced soft function $\overline{\mathcal{S}}$, defined in (17). This is intuitively clear: we saw that rescaling violation is intimately related to the presence of double poles, and that both are governed by the cusp anomalous dimension $\gamma_K^{(i)}$. The soft function $\mathcal{S}$, much like the eikonal jets, is defined with lightlike Wilson lines, thus including regions of overlapping ultraviolet and collinear singularities, which are the origin of double poles as well as rescaling violation at the single pole level. Upon dividing $\mathcal{S}$ by the product of all eikonal jets, as done in (17), these regions are removed, yielding $\overline{\mathcal{S}}$, which describes large-angle soft singularities, and is entirely free of double poles and of the associated violation of rescaling symmetry at the single pole level. Given the kinematic dependence of $\mathcal{S}$ and $\mathcal{J}_i$, and the expected recovery of the symmetry $\beta_i \to \kappa_i \beta_i$, $\forall i$, we deduce that $\overline{\mathcal{S}}$ can only depend on the variables ρ_{ij}, defined in (18).

To proceed, it is useful to consider the renormalization group equation for the reduced soft function. In analogy with (28) we have

$$\mu \frac{\mathrm{d}}{\mathrm{d}\mu} \overline{\mathcal{S}}_{IK}(\rho_{ij}, \alpha_s, \epsilon) = -\sum_J \Gamma^{\overline{\mathcal{S}}}_{IJ}(\rho_{ij}, \alpha_s)\, \overline{\mathcal{S}}_{JK}(\rho_{ij}, \alpha_s, \epsilon). \tag{29}$$

In contrast to $\Gamma^{\mathcal{S}}$, the anomalous dimension of the reduced soft function, $\Gamma^{\overline{\mathcal{S}}}$, is finite ($\overline{\mathcal{S}}$ itself has only single poles) and invariant under rescalings, as reflected in the fact that it must depend on β_i though ρ_{ij} only. Using the definition of the reduced soft function in eq. (17) we can directly relate the anomalous dimension $\Gamma^{\overline{\mathcal{S}}}$ to $\Gamma^{\mathcal{S}}$ and to the anomalous dimension of the eikonal jets, $\gamma_{\mathcal{J}_i}$ of eq. (24). We obtain

$$\begin{aligned} \Gamma^{\overline{\mathcal{S}}}_{IJ}(\rho_{ij}, \alpha_s) &= \Gamma^{\mathcal{S}}_{IJ}(\beta_i \cdot \beta_j, \alpha_s, \epsilon) - \delta_{IJ} \sum_{k=1}^{n} \gamma_{\mathcal{J}_k}\left(\frac{2(\beta_k \cdot n_k)^2}{n_k^2}, \alpha_s, \epsilon\right) \\ &= \Gamma^{\mathcal{S}}_{IJ}(\beta_i \cdot \beta_j, \alpha_s, \epsilon) - \delta_{IJ} \sum_{k=1}^{n} \Bigg[-\frac{1}{2}\delta_{\mathcal{J}_k}(\alpha_s) \\ &\quad + \frac{1}{4}\gamma_K^{(k)}(\alpha_s) \ln\left(\frac{2(\beta_k \cdot n_k)^2}{n_k^2}\right) + \frac{1}{4}\int_0^{\mu^2} \frac{\mathrm{d}\xi^2}{\xi^2} \gamma_K^{(k)}\left(\alpha_s(\xi^2, \epsilon)\right) \Bigg]. \end{aligned} \tag{30}$$

This equation implies highly non-trivial constraints on soft singularities. It tells us precisely how the double poles and the rescaling violation of the single poles in $\Gamma^{\mathcal{S}}$ cancel

out. In particular, observing that the jet terms $\gamma_{\mathcal{J}_k}$ are diagonal in colour space (they are proportional to the identity matrix), we deduce that

– off diagonal terms in $\Gamma^{\mathcal{S}}$ must be finite, and must depend only on *conformal cross ratios*,

$$\rho_{ijkl} \equiv \frac{(\beta_i \cdot \beta_j)(\beta_k \cdot \beta_l)}{(\beta_i \cdot \beta_k)(\beta_j \cdot \beta_l)} = \left(\frac{\rho_{ij}\,\rho_{kl}}{\rho_{ik}\,\rho_{jl}}\right)^{1/2} \mathrm{e}^{-\mathrm{i}\pi(\lambda_{ij}+\lambda_{kl}-\lambda_{ik}-\lambda_{jl})}, \tag{31}$$

which can be interchangeably expressed in terms of $\beta_i \cdot \beta_j$ (the arguments of $\Gamma^{\mathcal{S}}$), or in terms of ρ_{ij} (the arguments of $\Gamma^{\overline{\mathcal{S}}}$);

– diagonal terms in $\Gamma^{\mathcal{S}}$ have a singularity determined by γ_K, according to

$$\Gamma^{\mathcal{S}}_{IJ}(\beta_i \cdot \beta_j, \alpha_s, \epsilon) = \delta_{IJ} \sum_{k=1}^{n} \frac{1}{4} \int_0^{\mu^2} \frac{\mathrm{d}\xi^2}{\xi^2} \gamma_K^{(k)}\left(\alpha_s(\xi^2, \epsilon)\right) + \mathcal{O}(\epsilon^0) \tag{32}$$

and must contain finite terms depending on $\beta_i \cdot \beta_j$ in a way tailored to combine with the $(\beta_i \cdot n_i)^2/n_i^2$ dependence of the various jet functions to generate ρ_{ij}.

The constraints on the structure of the anomalous dimension $\Gamma^{\overline{\mathcal{S}}}$ can be compactly expressed by taking a logarithmic derivative of eq. (31) with respect to $(\beta_i \cdot n_i)^2/n_i^2$. On the *l.h.s* one uses the chain rule: for any function F which depends on $(\beta_i \cdot n_i)^2/n_i^2$ only through the combinations ρ_{ij} of (18), one has

$$\frac{\partial}{\partial \ln((\beta_i \cdot n_i)^2/n_i^2)} F(\rho_{ij}) = -\sum_{j \neq i} \frac{\partial}{\partial \ln \rho_{ij}} F(\rho_{ij}). \tag{33}$$

On the *r.h.s* of eq. (31), the derivative with respect to $(\beta_i \cdot n_i)^2/n_i^2$ acts only on the corresponding $\gamma_{\mathcal{J}_i}$ term. The resulting equations are

$$\sum_{j \neq i} \frac{\partial}{\partial \ln(\rho_{ij})} \Gamma^{\overline{\mathcal{S}}}_{IJ}(\rho_{ij}, \alpha_s) = \frac{1}{4}\, \gamma_K^{(i)}(\alpha_s)\, \delta_{IJ}, \quad \forall i,\, I, J. \tag{34}$$

Thus, there are n constraints for an n legged amplitude, each of which is a matrix equation (holding for each matrix element (I, J)). This set of constraints holds in any colour basis, and to all orders in perturbation theory. Its most intriguing aspect is that it correlates the kinematic dependence of the (reduced) soft matrix with its dependence on the colour degrees of freedom: the *l.h.s* in (34) is a sum of non-diagonal matrices in colour space, while the *r.h.s* is proportional to the identity matrix.

7. – Solving the equations

Given n independent equations and $n(n-1)/2$ kinematic variables it is clear at the outset that eq. (34) alone is not sufficient to uniquely fix the kinematic dependence of $\Gamma^{\overline{\mathcal{S}}}$ in the multileg case. For $n = 2, 3$ eq. (34) does have a unique solution (see sect. 4 and Appendix A in [39]). This is already an important step, extending previously known

results for the singularity structure to all loops. For $n \geq 4$ partons, however, the number of kinematic variables exceeds the number of equations, and additional constraints will be needed. Nevertheless, we will see that a minimal solution, consistent with all information known to date, naturally emerges out of eq. (34).

Considering eq. (34), we note that $\gamma_K^{(i)}$ depends implicitly on the colour representation of parton i. To solve the equations we need to make this dependence explicit. Given that $\gamma_K^{(i)}$ admits Casimir scaling (9) at least to three loops, we write

$$\gamma_K^{(i)}(\alpha_s) \equiv C_i\, \widehat{\gamma}_K(\alpha_s) + \widetilde{\gamma}_K^{(i)}, \tag{35}$$

where $\widetilde{\gamma}_K^{(i)} = \mathcal{O}(\alpha_s^4)$ accounts for possible dependence on the representation of parton i through higher-order Casimir operators. It is presently an open question([3]) whether such terms appear.

Our constraints now take the form

$$\sum_{j\neq i} \frac{\partial}{\partial \ln(\rho_{ij})}\, \Gamma^{\overline{\mathcal{S}}}(\rho_{ij}, \alpha_s) = \frac{1}{4}\left[C_i\, \widehat{\gamma}_K(\alpha_s) + \widetilde{\gamma}_K^{(i)}(\alpha_s)\right], \quad \forall i. \tag{36}$$

Using the linearity of these equations we can obviously write the general solution as a superposition of two functions

$$\Gamma^{\overline{\mathcal{S}}} = \Gamma^{\overline{\mathcal{S}}}_{\text{Q.C.}} + \Gamma^{\overline{\mathcal{S}}}_{\text{H.C.}}, \tag{37}$$

which are, respectively, solutions of the equations

$$\sum_{j\neq i} \frac{\partial}{\partial \ln(\rho_{ij})}\, \Gamma^{\overline{\mathcal{S}}}_{\text{Q.C.}}(\rho_{ij}, \alpha_s) = \frac{1}{4}\, \mathrm{T}_i \cdot \mathrm{T}_i\, \widehat{\gamma}_K(\alpha_s), \quad \forall i, \tag{38}$$

$$\sum_{j\neq i} \frac{\partial}{\partial \ln(\rho_{ij})}\, \Gamma^{\overline{\mathcal{S}}}_{\text{H.C.}}(\rho_{ij}, \alpha_s) = \frac{1}{4}\, \widetilde{\gamma}_K^{(i)}(\alpha_s), \quad \forall i. \tag{39}$$

Here Q.C. and H.C. stand for Quadratic Casimir and Higher-order Casimir, respectively. Let us now focus on determining $\Gamma^{\overline{\mathcal{S}}}_{\text{Q.C.}}$, leaving aside $\Gamma^{\overline{\mathcal{S}}}_{\text{H.C.}} = \mathcal{O}(\alpha_s^4)$, which will be briefly discussed in sect. **8**.

A solution for $\Gamma^{\overline{\mathcal{S}}}$, obeying eq. (38), is given by

$$\Gamma^{\overline{\mathcal{S}}}(\rho_{ij}, \alpha_s) = -\frac{1}{8}\, \widehat{\gamma}_K(\alpha_s) \sum_{(i,j)} \ln(\rho_{ij})\, \mathrm{T}_i \cdot \mathrm{T}_j + \frac{1}{2}\, \widehat{\delta}_{\overline{\mathcal{S}}}(\alpha_s) \sum_{i=1}^{n} \mathrm{T}_i \cdot \mathrm{T}_i, \tag{40}$$

where $\sum_{(i,j)}$ in the first term in (40) indicates a sum over all pairs of hard partons, forming a colour dipole; each dipole is counted twice in the sum. Note this term carries

([3]) An argument against Casimir scaling has been made [55, 56], based on the dependence of $\gamma_K^{(i)}$ on the representation in the strong-coupling limit at large N_c. The argument is based on a class of antisymmetric representations with k indices, where the ratio k/N_c is kept fixed when $N_c \to \infty$; in this case the strong-coupling limit of $\gamma_K^{(i)}$ does not admit Casimir scaling.

the entire dependence on kinematics, correlating it with the colour structure. In contrast, the second term is independent of kinematics and is proportional to the unit matrix in colour space. Analysis of the $n = 2$ case (the Sudakov form factor) allows to identify this function (see eqs. (4.7) and (4.9) in [39]) as the one appearing at single-pole level in the partonic jet, the last term in eq. (27).

It is easy to verify that (40) satisfies (38): taking a derivative with respect to $\ln(\rho_{ij})$, for specific partons i and j, isolates the color dipole $\mathrm{T}_i \cdot \mathrm{T}_j$; summing over j for fixed i, and enforcing colour conservation, given by eq. (6), one recovers eq. (38).

Integrating the renormalization group equation (29), with $\Gamma^{\overline{S}}$ given by eq. (40), we obtain an expression for the reduced soft function,

$$\overline{S}(\rho_{ij}, \alpha_s, \epsilon) = \exp\left[-\frac{1}{2} \int_0^{\mu^2} \frac{\mathrm{d}\lambda^2}{\lambda^2} \left(\frac{1}{2}\, \widehat{\delta}_{\overline{S}}(\alpha_s(\lambda^2, \epsilon)) \sum_{i=1}^{n} \mathrm{T}_i \cdot \mathrm{T}_i \right.\right. \\ \left.\left. -\frac{1}{8}\, \widehat{\gamma}_K(\alpha_s(\lambda^2, \epsilon)) \sum_{(i,j)} \ln(\rho_{ij})\, \mathrm{T}_i \cdot \mathrm{T}_j \right) \right]. \tag{41}$$

Substituting eq. (41) into the factorization formula, eq. (13), together with the corresponding expression for the partonic jet, eq. (27), we obtain a complete description of the singularity structure of the amplitude, eq. (5). Note that the Z factor and the hard amplitude $\mathcal{H}$ in (4) are separately independent of the auxiliary vectors n_i, as they must be. In contrast, the various elements in the factorization formula (13) do depend on these vectors. The cancellation of this dependence is non-trivial: it is guaranteed by the fact that $\overline{\mathcal{S}}$ admits the constraints of (34), and by the fact that the kinematic dependence of the singularities of the partonic jet function (27) matches the one of the eikonal jet, eq. (25). It is essential that all the single-pole terms that carry n_i dependence in the various functions are governed by the cusp anomalous dimension γ_K alone. Indeed, to obtain eq. (5), we combine terms proportional to γ_K in the soft and jet functions. In doing so we use colour conservation, $\sum_{j \neq i} \mathrm{T}_j = -\mathrm{T}_i$, as well as the relation between the kinematic variables of the various functions,

$$\underbrace{\ln\left(\frac{(2p_i \cdot n_i)^2}{n_i^2} \right)}_{J_i} + \underbrace{\ln\left(\frac{(2p_j \cdot n_j)^2}{n_j^2} \right)}_{J_j} + \underbrace{\ln\left(\frac{\left(\beta_i \cdot \beta_j\, \mathrm{e}^{\mathrm{i}\pi\lambda_{ij}}\right)^2}{\frac{2(\beta_i \cdot n_i)^2}{n_i^2} \frac{2(\beta_j \cdot n_j)^2}{n_j^2}} \right)}_{\overline{S}} = \\ 2 \ln(2p_i \cdot p_j\, \mathrm{e}^{\mathrm{i}\pi\lambda_{ij}}). \tag{42}$$

Note also that the poles associated with $\widehat{\delta}_{\overline{S}}(\alpha_s(\lambda^2, \epsilon))$ cancel out between the soft and jet functions, given by eqs. (41) and (27), respectively.

It is interesting to compare at this point our approach to that of Becher and Neubert in ref. [41]. The final expression at the amplitude level, eq. (5), is the same. The set of constraints, eq. (48) in [41], is also equivalent. The underlying factorization scheme, and consequently the arguments leading to these constraints, are however somewhat different. In particular, ref. [41] does not define jet functions using auxiliary Wilson lines (n_i in our formulation); instead, it keeps track of the jets through their mass, taking p_i slightly

off the light cone, $p_i^2 \neq 0$. In their formulation, the equivalent of eq. (42) takes the form (eq. (43) in [41])

$$\underbrace{\ln\left(\frac{-p_i^2}{\mu^2}\right)}_{J_i} + \underbrace{\ln\left(\frac{-p_j^2}{\mu^2}\right)}_{J_j} + \underbrace{\ln\left(\frac{2\,p_i\cdot p_j\,\mathrm{e}^{\mathrm{i}\pi\lambda_{ij}}\mu^2}{(-p_i^2)(-p_j^2)}\right)}_{S} = \ln\left(\frac{2p_i\cdot p_j\,\mathrm{e}^{\mathrm{i}\pi\lambda_{ij}}}{\mu^2}\right), \tag{43}$$

which is again realised owing to the fact that in each function the corresponding logarithm is governed by the cusp anomalous dimension. Recall that in our derivation the argument of the reduced soft function is dictated by rescaling invariance; in contrast, in [41] the argument of the soft function is essentially dictated by power counting, and it is not invariant with respect to rescaling.

8. – Possible contributions beyond the sum-over-dipoles formula

As already mentioned, the ansatz of (40) does not in general provide a unique solution of the available constraints. Thus eq. (5), while consistent with all existing calculations, may still be missing some large-angle soft singularities beyond a certain loop order. Such further singularities are however strongly constrained both in their functional form and in their color structure. It is worthwhile emphasizing that calculations in the large-N_c limit cannot resolve the question at hand, since planar eikonal diagrams necessarily factorize into a product of colour dipoles, those made of adjacent Wilson lines, and are therefore automatically consistent with the sum-over-dipoles formula. The analysis must therefore be done at finite N_c. Reference [39] has identified two classes of corrections that may appear, and although some progress was made, neither of the two can be excluded to all orders at present.

The first class of corrections corresponds to potential higher-order Casimir contributions. In case higher-order Casimir operators do show up in the cusp anomalous dimension at some loop order, *i.e.* $\widetilde{\gamma}_K$ in (35) does not vanish, the anomalous dimension of the reduced soft function of any amplitude will receive additional corrections. These corrections are subject to the very stringent constraints of (39). For amplitudes with two or three legs these corrections still have a dipole structure (see, *e.g.*, Appendix A in [39]), however, for amplitudes with four legs or more, non-trivial structures that couple more than two hard partons may arise.

The second class of corrections, which may be present even if γ_K admits Casimir scaling, is given by solutions of the homogeneous equation associated with eq. (38). Indeed, adding to our ansatz any function $\Delta^{\overline{S}}(\rho_{ij})$ satisfying

$$\sum_{j\neq i} \frac{\partial}{\partial \ln(\rho_{ij})} \Delta^{\overline{S}}(\rho_{ij}, \alpha_s) = 0, \quad \forall i, \tag{44}$$

one obtains a new solution of eq. (38). Equation (44) is solved by any function of the conformal invariant cross ratios defined in (31). Any such solution has the property of being invariant with respect to velocity rescalings without involving the jets. Such functions can of course be written directly in terms of the original kinematic variables $p_i \cdot p_j$ and are therefore not constrained by soft-collinear factorization.

Interesting examples for $\Delta^{\overline{\mathcal{S}}}$ in the four-parton case were proposed in [39]:

$$\sum_{j,k,l}\sum_{a,b,c} \mathrm{i}\, f_{abc}\, \mathrm{T}_j^a \mathrm{T}_k^b \mathrm{T}_l^c \ln(\rho_{ijkl}) \ln(\rho_{iklj}) \ln(\rho_{iljk}), \tag{45}$$

$$\sum_{j,k,l}\sum_{a,b,c} d_{abc}\, \mathrm{T}_j^a \mathrm{T}_k^b \mathrm{T}_l^c \ln^2(\rho_{ijkl}) \ln^2(\rho_{iklj}) \ln^2(\rho_{iljk}), \tag{46}$$

where the sum over partons is understood to exclude identical indices, and where colour conservation, $\mathrm{T}_i^d = -\mathrm{T}_j^d - \mathrm{T}_k^d - \mathrm{T}_l^d$, has been taken into account. Note that these functions are, by contruction, symmetric under the exchange of Wilson lines (Bose symmetry): this correlates colour and kinematic degrees of freedom. These functions, moreover, do not contribute in the limit where any two hard partons become collinear, and therefore they cannot be excluded using the properties of the splitting amplitude discussed in [41].

Functions of conformal-invariant cross ratios such as (45) correlate colour and kinematic degrees of freedom of four partons. They cannot arise at two loops because two-loop webs can connect at most three partons. This explains, *a posteriori*, the findings of ref. [38], which explicitly showed that there are no new correlations generated at the two-loop order beyond those of pairwise interactions([4]). Non-trivial corrections to the sum-over-dipoles formula can therefore first arise at three loops.

Unfortunately, at three loops no complete calculation is available yet. However, several important steps have been taken. First, as already emphasized in [39], three-loop corrections to this formula must satisfy eq. (44)—they must be functions of conformal invariant cross ratios, and they must vanish identically in amplitudes of less than four legs. Beyond that, it was explicitly shown that the class of three-loop diagrams containing matter loops is consistent with the sum-over-dipoles formula [63].

A further step was taken in ref. [41], where it was shown that if dependence on the kinematic variables is assumed to be single-logarithmic, there is no possible structure that could appear at three loops beyond the sum-over-dipoles formula. This argument is based on eliminating all possible structures using the factorization constraints discussed above, together with Bose symmetry, and an additional constraint on the singularity structure in the limit where two hard partons become collinear based on the properties of the splitting amplitude. It should be emphasized that the assumption of single-logarithmic kinematic dependence is crucial here, so the question of possible corrections to the sum-over-dipoles formula at three loops is still open.

As mentioned above, at four loops a new class of corrections may appear [39], induced by higher-order (quartic) Casimir contributions to the cusp anomalous dimension. Addressing this issue, ref. [41] examined again all possible structures that could appear at four loops under the assumption of single-logarithmic kinematic dependence. Also here the conclusion is that no such structure survives the constraints.

9. – Conclusions

We have reviewed recent exciting progress in determining the infrared singularities of on-shell scattering amplitudes in massless non-Abelian gauge theories. It is now firmly established [39, 41] that the cusp anomalous dimension has a central role in governing

([4]) Note that new structure does appear in the case of scattering involving heavy quarks, as shown in refs. [57-62].

soft singularities of multi-leg amplitudes with an arbitrary number of legs and for a general N_c. This role is summarized by a set of differential equations (34) constraining the kinematic dependence of the soft anomalous dimension matrix of any amplitude, to any loop order, in an arbitrary colour basis. These constraints are a direct consequence of factorization and of the special properties of soft gluon interactions with massless hard partons.

The simplest solution to this set of constraints yields a closed-form expression for the singularities of any massless scattering amplitude, eq. (5). According to this formula the correlations induced by soft gluon interactions between colour and kinematic degrees of freedom take the form of a sum over colour dipoles. No new correlations are generated by multi-loop webs (fig. 2): the colour matrix structure remains the same as at one loop, and the cusp anomalous dimension alone governs all non-collinear singularities.

We have further shown that possible corrections to this simple sum-over-dipoles formula belong to one of two categories: the ones that are generated by potential higher-order Casimir contributions to the cusp anomalous dimension, which must then satisfy eq. (39), and the ones that can be written in terms of conformal invariant cross ratios (31), solving the homogeneous equations (44). The former may contribute to any amplitude starting from four loops, while the latter can only appear in amplitudes with four or more hard partons, starting at three loops. So far all explicit calculations are consistent with the sum-over-dipoles formula, but it remains an open question whether such corrections do show up at some loop order.

* * *

We would like to thank L. Dixon, J. Maldacena, G. Korchemsky and G. Sterman for useful discussions. Work supported in part by the European Community's Marie-Curie Research Training Network "Tools and Precision Calculations for Physics Discoveries at Colliders" ("HEPTOOLS"), contract MRTN-CT-2006-035505.

REFERENCES

[1] Bern Z., Dixon L. J. and Smirnov V. A., *Phys. Rev. D*, **72** (2005) 085001, hep-th/0505205.
[2] Bern Z., Dixon L. J., Kosower D. A., Roiban R., Spradlin M., Vergu C. and Volovich A., *Phys. Rev. D*, **78** (2008) 045007, arXiv:0803.1465 [hep-th].
[3] Drummond J. M., Korchemsky G. P. and Sokatchev E., *Nucl. Phys. B*, **795** (2008) 385, arXiv:0707.0243 [hep-th]; Brandhuber A., Heslop P. and Travaglini G., *Nucl. Phys. B*, **794** (2008) 231, arXiv:0707.1153 [hep-th]; Drummond J. M., Henn J., Korchemsky G. P. and Sokatchev E., *Nucl. Phys. B*, **795** (2008) 52, arXiv:0709.2368 [hep-th]; arXiv:0712.1223 [hep-th]; *Phys. Lett. B*, **662** (2008) 456, arXiv:0712.4138 [hep-th]; *Nucl. Phys. B*, **815** (2009) 142, arXiv:0803.1466 [hep-th].
[4] Alday L. F. and Maldacena J. M., *JHEP*, **0706** (2007) 064, arXiv:0705.0303 [hep-th].
[5] Alday L. F. and Roiban R., *Phys. Rep.*, **468** (2008) 153, arXiv:0807.1889 [hep-th].
[6] Polyakov A. M., *Nucl. Phys. B*, **164** (1980) 171.
[7] Korchemsky G. P. and Radyushkin A. V., *Phys. Lett. B*, **171** (1986) 459.
[8] Ivanov S. V., Korchemsky G. P. and Radyushkin A. V., *Yad. Fiz.*, **44** (1986) 230, (*Sov. J. Nucl. Phys.*, **44** (1986) 145).
[9] Korchemsky G. P. and Radyushkin A. V., *Nucl. Phys. B*, **283** (1987) 342.
[10] Korchemsky G. P., *Phys. Lett. B*, **220** (1989) 629.
[11] Korchemsky G. P., *Mod. Phys. Lett. A*, **4** (1989) 1257.

[12] Moch S., Vermaseren J. A. M. and Vogt A., *Nucl. Phys. B*, **688** (2004) 101, hep-ph/0403192; Kotikov A. V., Lipatov L. N., Onishchenko A. I. and Velizhanin V. N., *Phys. Lett. B*, **595** (2004) 521; **632** (2006) 754 (Erratum).
[13] Beisert N. and Staudacher M., *Nucl. Phys. B*, **727** (2005) 1, hep-th/0504190.
[14] Beisert N., Eden B. and Staudacher M., *J. Stat. Mech.*, **0701** (2007) P021, hep-th/0610251.
[15] Basso B., Korchemsky G. P. and Kotanski J., *Phys. Rev. Lett.*, **100** (2008) 091601, arXiv:0708.3933 [hep-th].
[16] Bloch F. and Nordsieck A., *Phys. Rev.*, **52** (1937) 54.
[17] Kinoshita T., *J. Math. Phys.*, **3** (1962) 650.
[18] Lee T. D. and Nauenberg M., *Phys. Rev.*, **133** (1964) B1549.
[19] Catani S. and Seymour M. H., *Phys. Lett. B*, **378** (1996) 287, hep-ph/9602277.
[20] Gardi E. and Rathsman J., *Nucl. Phys. B*, **609** (2001) 123, hep-ph/0103217; *Nucl. Phys. B*, **638** (2002) 243, hep-ph/0201019.
[21] Cacciari M. and Gardi E., *Nucl. Phys. B*, **664** (2003) 299, hep-ph/0301047.
[22] Bozzi G., Catani S., de Florian D. and Grazzini M., *Nucl. Phys. B*, **791** (2008) 1, arXiv:0705.3887 [hep-ph].
[23] Ahrens V., Becher T., Neubert M. and Yang L. L., *Eur. Phys. J. C*, **62** (2009) 333 [arXiv:0809.4283 [hep-ph]].
[24] Andersen J. R. and Gardi E., *JHEP*, **0601** (2006) 097, hep-ph/0509360.
[25] Andersen J. R. and Gardi E., *JHEP*, **0701** (2007) 029, hep-ph/0609250; **0506** (2005) 030, hep-ph/0502159.
[26] Gardi E., *Inclusive distributions near kinematic thresholds*, in the *Proceedings of FRIF Workshop on First Principles Non-Perturbative QCD of Hadron Jets, LPTHE, Paris, France, 12-14 Jan 2006*, pp. E003, hep-ph/0606080.
[27] Sterman G., *Nucl. Phys. B*, **281** (1987) 310.
[28] Catani S. and Trentadue L., *Nucl. Phys. B*, **327** (1989) 323.
[29] Contopanagos H., Laenen E. and Sterman G., *Nucl. Phys. B*, **484** (1997) 303, hep-ph/9604313.
[30] Laenen E., Sterman G. and Vogelsang W., hep-ph/0010184.
[31] Gardi E. and Grunberg G., *Nucl. Phys. B*, **794** (2008) 61, arXiv:0709.2877 [hep-ph].
[32] Gardi E. and Roberts R. G., *Nucl. Phys. B*, **653** (2003) 227, hep-ph/0210429.
[33] Catani S., Trentadue L., Turnock G. and Webber B. R., *Nucl. Phys. B*, **407** (1993) 3.
[34] Kidonakis N., *Int. J. Mod. Phys. A*, **15** (2000) 1245, hep-ph/9902484.
[35] Becher T., Neubert M. and Pecjak B. D., *JHEP*, **0701** (2007) 076, hep-ph/0607228.
[36] Botts J. and Sterman G., *Nucl. Phys. B*, **325** (1989) 62.
[37] Kidonakis N. and Sterman G., *Nucl. Phys. B*, **505** (1997) 321, hep-ph/9705234.
[38] Mert Aybat S., Dixon L. J. and Sterman G., *Phys. Rev. D*, **74** (2006) 074004, hep-ph/0607309.
[39] Gardi E. and Magnea L., *JHEP*, **0903** (2009) 079, arXiv:0901.1091 [hep-ph].
[40] Becher T. and Neubert M., *Phys. Rev. Lett.*, **102** (2009) 162001 [arXiv:0901.0722 [hep-ph]].
[41] Becher T. and Neubert M., *JHEP*, **0906** (2009) 081 [arXiv:0903.1126 [hep-ph]].
[42] Catani S., *Phys. Lett. B*, **427** (1998) 161, hep-ph/9802439.
[43] Magnea L. and Sterman G., *Phys. Rev. D*, **42** (1990) 4222.
[44] Magnea L., *Nucl. Phys. B*, **593** (2001) 269, hep-ph/0006255.
[45] Vogt A., Moch S. and Vermaseren J. A. M., *Nucl. Phys. B*, **691** (2004) 129, hep-ph/0404111.
[46] Moch S., Vermaseren J. A. M. and Vogt A., *JHEP*, **0508** (2005) 049, hep-ph/0507039.
[47] Moch S., Vermaseren J. A. M. and Vogt A., *Phys. Lett. B*, **625** (2005) 245, hep-ph/0508055.
[48] Sterman G. and Tejeda-Yeomans M. E., *Phys. Lett. B*, **552** (2003) 48, hep-ph/0210130.
[49] Dixon L. J., Magnea L. and Sterman G., *JHEP*, **0808** (2008) 022, arXiv:0805.3515 [hep-ph].

[50] Sen A., *Phys. Rev. D*, **28** (1983) 860.
[51] Kidonakis N., Oderda G. and Sterman G., *Nucl. Phys. B*, **531** (1998) 365, hep-ph/9803241.
[52] Dotsenko V. S. and Vergeles S. N., *Nucl. Phys. B*, **169** (1980) 527.
[53] Brandt R. A., Neri F. and Sato M. a., *Phys. Rev. D*, **24** (1981) 879.
[54] Korchemskaya I. A. and Korchemsky G. P., *Nucl. Phys. B*, **437** (1995) 127, hep-ph/9409446.
[55] Maldacena Juan,, private communication, January 2009.
[56] Armoni A., *JHEP*, **0611** (2006) 009, hep-th/0608026.
[57] Mitov A., Sterman G. and Sung I., *Phys. Rev. D*, **79** (2009) 094015 [arXiv:0903.3241 [hep-ph]].
[58] Kidonakis N., *Phys. Rev. Lett.*, **102** (2009) 232003 [arXiv:0903.2561 [hep-ph]].
[59] Becher T. and Neubert M., *Phys. Rev. D*, **79** (2009) 125004; **80** (2009) 109901 (Erratum) [arXiv:0904.1021 [hep-ph]].
[60] Gluza J., Mitov A., Moch S. and Riemann T., *JHEP*, **0907** (2009) 001 [arXiv:0905.1137 [hep-ph]].
[61] Beneke M., Falgari P. and Schwinn C., *Nucl. Phys. B*, **828** (2010) 69 [arXiv:0907.1443 [hep-ph]].
[62] Ferroglia A., Neubert M., Pecjak B. D. and Yang L. L., *Phys. Rev. Lett.*, **103** (2009) 201601 [arXiv:0907.4791 [hep-ph]].
[63] Dixon L. J., *Phys. Rev. D*, **79** (2009) 091501 [arXiv:0901.3414 [hep-ph]].

IL NUOVO CIMENTO Vol. 32 C, N. 5-6 Settembre-Dicembre 2009
DOI 10.1393/ncc/i2010-10529-9

Colloquia: LaThuile09

QCD studies at HERA

D. Traynor(*)(**)

Queen Mary, University of London - Mile End Road, London, E1 4NS, UK

(ricevuto il 10 Novembre 2009; pubblicato online il 18 Gennaio 2010)

Summary. — This article presents a summary of recent results on QCD from HERA. Including; new neutral current and charged current measurements from H1 and ZEUS from the lowest to the highest Q^2, new combinations of both H1 and ZEUS published HERAI data and corresponding PDF fits, the first measurements of F_L, and the extraction of α_s from jet measurements.

PACS 12.38.Qk – Experimental tests.

1. – New deep inelastic scattering results from HERA

Both H1 and ZEUS have recently released new results of the inclusive ep cross-sections covering a kinematic range in Q^2 ($0.2 < Q^2 < 50000\,\mathrm{GeV}^2$) and Bjorken x ($5 \times 10^{-6} < x < 0.65$). The inclusive ep deep inelastic scattering (DIS) cross-section can be expressed in terms of the two structure functions, F_2 and F_L, as

$$\sigma_r(x, Q^2, y) = \frac{\mathrm{d}^2\sigma}{\mathrm{d}x\mathrm{d}Q^2}\frac{Q^2 x}{2\pi\alpha^2 Y_+} = F_2(x, Q^2) - \frac{y^2}{Y_+}F_L(x, Q^2),$$

where Q^2 is the virtuality of the exchanged boson, the Bjorken x is, in the rest frame of the incident proton, the fraction of the proton momentum entering the hard interaction and the inelasticity y is the fraction of the electrons energy that the virtual photon carries. Two types of DIS cross-sections are measured, neutral current which involves the exchange of a virtual photon or Z-boson ($ep \to eX$), and charged current which is mediated by the exchange of a W-boson ($ep \to \nu_e X$).

(*) On behalf of the H1 and ZEUS Collaborations.
(**) E-mail: d.traynor@qmul.ac.uk

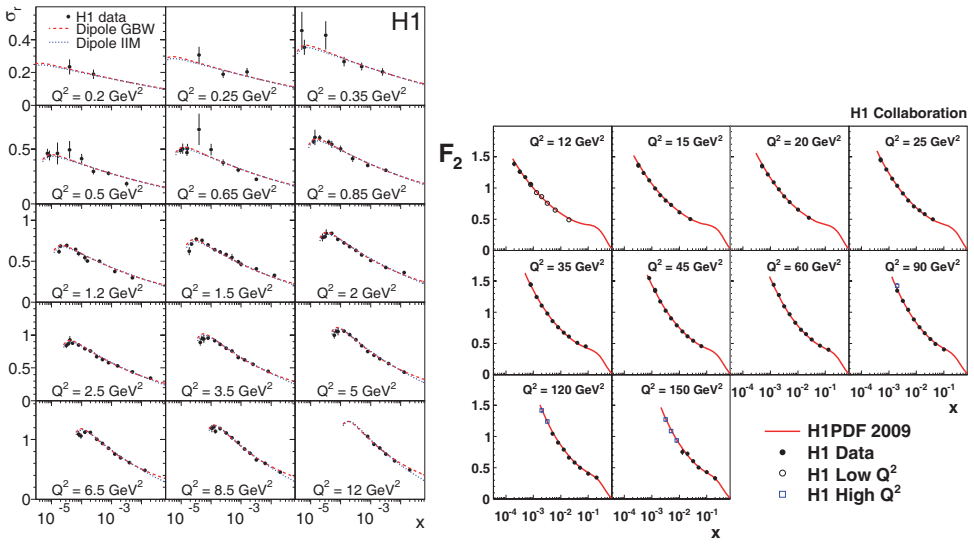

Fig. 1. – Left: reduced cross-section σ_r, from the combined low-Q^2 H1 data, as a function of x for fixed Q^2 intervals compared to the GBW and IIM models. The errors represent the statistical and systematic uncertainties added in quadrature. Right: measurement of the structure function F_2 at medium Q^2, as a function of x for fixed Q^2 intervals. The error bars represent the total measurement uncertainties. The curve represents the H12009 QCD fit.

1˙1. *Low-Q^2 neutral current.* – A measurement of the inclusive ep scattering cross-section in the region of low momentum transfers, $0.2\,\mathrm{GeV}^2 \leq Q^2 \leq 12\,\mathrm{GeV}^2$, and low Bjorken x, $5 \times 10^{-6} < x < 0.02$ has been published by H1 [1]. The result is based on two data sets collected in dedicated runs by the H1 Collaboration at HERA at beam energies of 27.6 GeV and 920 GeV for positrons and protons, respectively. A combination with data previously published by H1 leads to a cross-section measurement of a few percent, $\sim 2\%$ accuracy in a large part of the phase space. A kinematic reconstruction method exploiting radiative ep events extends the measurement to lower Q^2 and larger x.

For the region $Q^2 \simeq 1\,\mathrm{GeV}^2$, in which the transition from photoproduction to DIS takes place, the data as presented are the most precise result of the H1 Collaboration. The data have been compared to theoretical models which apply to the transition region from photoproduction to deep inelastic scattering. The Colour Dipole Model (CDM) predicts both structure functions F_2 and F_L using a single characteristic dipole scattering cross-section. In fig. 1, left, the data are compared to two versions of the CDM, the GBW model [2] and the IIM model [3], which are found to generally describe the cross-section data well.

1˙2. *Medium-Q^2 neutral current.* – A new measurement of the inclusive double differential cross-section for deep inelastic positron proton scattering in the region of small Bjorken x, $2 \times 10^{-4} \leq x \leq 0.1$, and four-momentum transfer squared, $12\,\mathrm{GeV}^2 \leq Q^2 \leq 150\,\mathrm{GeV}^2$ has been made by H1 [4] with beam energies of $E_e = 27.6\,\mathrm{GeV}$ and $E_p = 920\,\mathrm{GeV}$. A small bias in a similar previously published data set, taken at $E_p = 820\,\mathrm{GeV}$, is found and corrected. The two data sets are then combined and represent the most precise measurement in this kinematic region to date, with typical total uncertainties in the range of 1.3–2% and includes all H1 HERAI data.

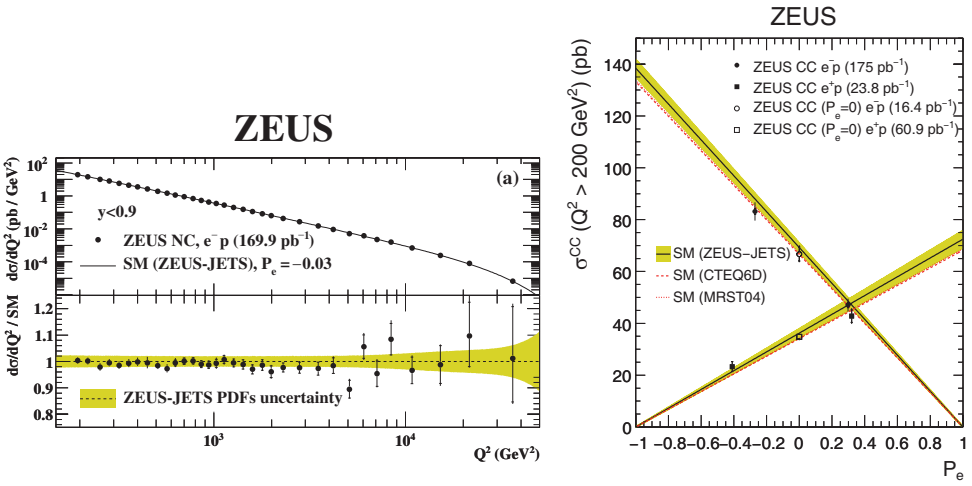

Fig. 2. – Left: the e^-p NC DIS cross-sections $\mathrm{d}\sigma/\mathrm{d}Q^2$ for $y < 0.9$ and the ratio to the SM prediction. The closed circles represent data points in which the inner error bars show the statistical uncertainty while the outer bars show the statistical and systematic uncertainties added in quadrature. The curves show the predictions of the SM evaluated using the ZEUS-JETS PDFs, the shaded band shows the uncertainties from the fit. Right: the total cross-sections for e^-p and e^+p CC DIS as a function of the longitudinal polarisation of the lepton beam. The lines show the predictions of the SM evaluated using the ZEUS-JETS, CTEQ6D and MRST04 PDFs. The shaded bands show the experimental uncertainty from the ZEUS-JETS PDF.

The kinematic range of the measurement corresponds to a wide range of inelasticity y, from 0.005 to 0.6. The data are used to determine the structure function $F_2(x, Q^2)$, which is observed to rise continuously towards low x at fixed Q^2, fig. 1, right. An NLO QCD fit to the H1 data alone, including the new medium-Q^2 data, is also shown. The fit implements a variable flavour treatment of heavy quark threshold effects. This new H1PDF 2009 fit supersedes the H1PDF 2000 previously obtained and provides a new determination of the gluon and quark densities of the proton including experimental, model, and parameterisation uncertainties.

1˙3. *High-Q^2 neutral current.* – Measurements of the neutral-current cross-sections for deep inelastic scattering in e^-p collisions at HERA with a longitudinally polarised electron beam have been published by ZEUS [5]. The single differential cross-sections $\mathrm{d}\sigma/\mathrm{d}Q^2$ (fig. 2, left), $\mathrm{d}\sigma/\mathrm{d}x$ and $\mathrm{d}\sigma/\mathrm{d}y$ and the double-differential cross-sections in Q^2 and x are measured in the kinematic region $y < 0.9$ and $Q^2 > 185\,\mathrm{GeV}^2$ for both positively and negatively polarised electron beams and for each polarisation state separately.

The measurements are based on an integrated luminosity of $169.9\,\mathrm{pb}^{-1}$ taken with the ZEUS detector in 2005 and 2006 at a centre-of-mass energy of 318 GeV. The structure functions $x\tilde{F}_3$ and $xF_3^{\gamma Z}$ were also determined by combining the e^-p results with previously measured e^+p neutral-current data. The asymmetry parameter A^- is used to demonstrate the parity-violating effects of electroweak interactions at large spacelike photon virtuality. The measurements agree well with the predictions of the standard model.

1˙4. *Charged current.* – Measurements of the cross-sections for charged-current deep inelastic scattering in ep collisions with a longitudinally polarised electron beam have

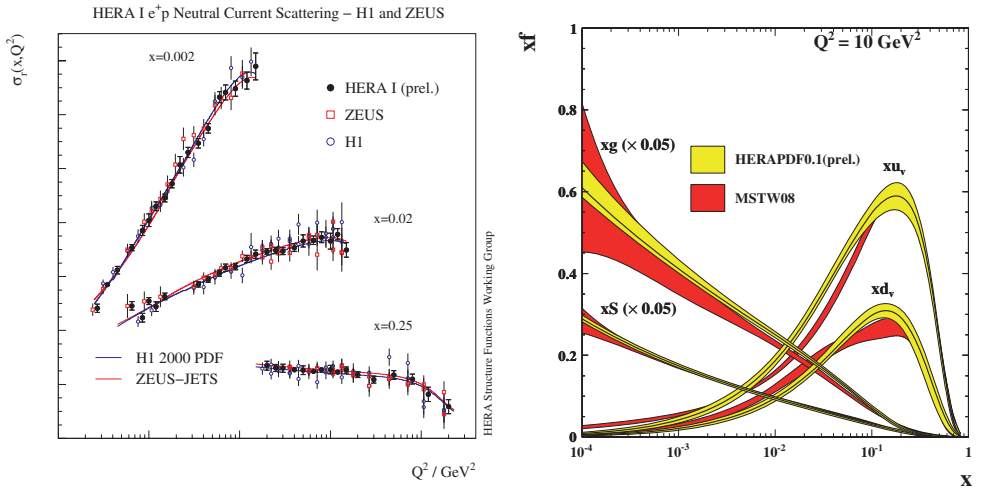

Fig. 3. – Left: deep inelastic neutral-current e^+p scattering cross-section measurements for three selected x bins as a function of Q^2. The H1(open points) and ZEUS data (open squares) are compared to the H1 and ZEUS combined data (closed points). Measurements from the individual experiments have been shifted for clarity. The error bars show the total uncertainty. The curves are NLO QCD fits as performed by H1 and ZEUS to their own data. Right: HERA PDFs at $Q^2 = 10\,\mathrm{GeV}^2$ compared to the PDFs from MSTW08 (prel.) [8].

been published by ZEUS [6]. The measurements are based on a data sample with an integrated luminosity of $175\,\mathrm{pb}^{-1}$ collected with the ZEUS detector at HERA at a centre-of-mass energy of 318 GeV. Measurements made include; the total cross-section for positively and negatively polarised electron beams, fig. 2, right, the differential cross-sections $\mathrm{d}\sigma/\mathrm{d}Q^2$, $\mathrm{d}\sigma/\mathrm{d}x$ and $\mathrm{d}\sigma/\mathrm{d}y$ for $Q^2 > 200\,\mathrm{GeV}^2$, and the double-differential cross-section $\mathrm{d}^2\sigma/\mathrm{d}x\mathrm{d}Q^2$ in the kinematic range $280 < Q^2 < 30000\,\mathrm{GeV}^2$ and $0.015 < x < 0.65$. The measured cross-sections are compared with the predictions of the standard model and overall are well described by the predictions of the standard model.

2. – HERA data combination and PDF fits

It is possible to improve the precision of the ZEUS and H1 neutral and charged current inclusive cross-sections by combining their published HERAI measurements [7]. This is possible because they are measuring the same physics in a similar kinematic region. These data have been combined using a theory-free Hessian fit in which the only assumption is that there is a true value of the cross-section, for each process, at each x and Q^2 point. Thus each experiment has been calibrated to the other. This works well because the sources of systematic uncertainty in each experiment are rather different, such that all the systematic uncertainties are re-evaluated. The resulting systematic uncertainties on each of the combined data points are significantly smaller than the statistical errors, fig. 3, left.

The combined HERAI data set provides high-precision data, with small systematic uncertainties, across a broad kinematic range such that these data can be used as the sole input for an NLO QCD PDF fit. The data at low x, $x < 0.01$, provide information on the sea and the gluon PDFs, and the high-Q^2 HERA data can be used to determine

the valence PDFs. The consistent treatment of systematic uncertainties in the combined data set ensures that experimental uncertainties on the PDFs can be calculated without need for an increased χ^2 tolerance. This results in PDFs with greatly reduced experimental uncertainties compared to the separate analyses of the ZEUS and H1 experiments. Model uncertainties, including those arising from parametrization dependence, have also been carefully considered. The resulting HERAPDFs (called HERAPDF0.1 [9]) have impressive precision compared to the global fits, fig. 3, right.

3. – Longitudinal structure function, F_L

Both H1 [10] and ZEUS [11] have recently released measurements of the longitudinal structure function, F_L. The two proton structure functions F_L and F_2 are of complementary nature. They are related to the $\gamma^* p$ interaction cross-sections of longitudinally and transversely polarised virtual photons, σ_L and σ_T, according to $F_L \propto \sigma_L$ and $F_2 \propto (\sigma_L + \sigma_T)$. Therefore the relation $0 \leq F_L \leq F_2$ holds. In the Quark Parton Model (QPM), F_2 is the sum of the quark and anti-quark x-distributions, weighted by the square of the electric quark charges, whereas the value of F_L is zero. In Quantum Chromodynamics (QCD), the longitudinal structure function differs from zero, receiving contributions from quarks and from gluons. At low x and in the Q^2 region of deep inelastic scattering the gluon contribution greatly exceeds the quark contribution. Therefore F_L is a direct measure of the gluon distribution to a very good approximation. The gluon distribution is also constrained by the scaling violations of $F_2(x, Q^2)$ as described by the DGLAP QCD evolution equations. An independent measurement of F_L at HERA, and its comparison with predictions derived from the gluon distribution extracted from the Q^2 evolution of $F_2(x, Q^2)$, thus represents a crucial test on the validity of perturbative QCD at low Bjorken x.

The measurement of F_L requires several sets of DIS cross-sections at fixed x and Q^2 but at different y. This was achieved at HERA by variations of the proton beam energy whilst keeping the lepton beam energy fixed. The measurement of $F_L(x, Q^2)$ is based on data collected with a positron beam energy of 27.5 GeV and three proton beam energies, 920, 575 and 460 GeV.

The longitudinal structure function is extracted from the measurements of the reduced cross-section as the slope of σ_r *vs.* y^2/Y_+, this procedure is illustrated in fig. 4, left. The measured F_L values agree with higher-order QCD calculations based on parton densities obtained using cross-section data previously measured at HERA, fig. 4, right.

A summary of results from H1 for F_L, averaged in x for a given Q^2, for medium and high Q^2 is shown in fig. 5.

4. – α_s from jets

Jet production in neutral-current (NC) deep inelastic scattering (DIS) at HERA provides an important testing ground for Quantum Chromodynamics (QCD). While inclusive DIS gives only indirect information on the strong coupling via scaling violations of the proton structure functions, the production of jets allows a direct measurement of α_s.

The new HERA combined $\alpha_s(M_Z)$ value is $\alpha_s(M_Z) = 0.1198 \pm 0.0019(\text{exp.}) \pm 0.0026(\text{th.})$ (HERA combined 2007), with an experimental uncertainty of 1.6% and a theoretical uncertainty of 2.2%. In addition, to study the running of the strong coupling, fits of $\alpha_s(M_Z)(\mu_R = E_T)$ for several bins of E_T and integrated over Q^2 were performed. The results are shown in fig. 6, left, compared to the pQCD evolution of $\alpha_s(M_Z)$ from

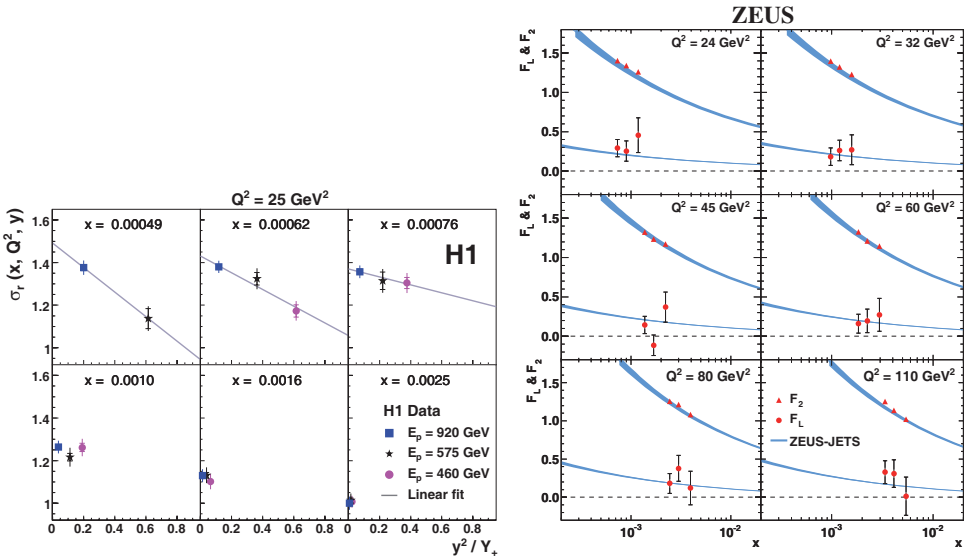

Fig. 4. – Left: the reduced inclusive DIS cross-section plotted as a function of y^2/Y_+ for six values of x at $Q^2 = 25\,\mathrm{GeV}^2$, as measured by H1. The inner error bars denote the statistical error, the full error bars include the systematic errors. The luminosity uncertainty is not included in the error bars. For the first three bins in x, corresponding to larger y, a straight line fit is shown, the slope of which determines $F_L(x, Q^2)$. Right: F_L and F_2 at 6 values of Q^2 as a function of x. The points and triangles represent the ZEUS data for F_L and F_2, respectively. The error bars on the data represent the combined statistical and systematic uncertainties. The error bars on F_2 are smaller than the symbols. A further $\pm 2.5\%$ correlated normalisation uncertainty is not included. The DGLAP predictions for F_L and F_2 using the ZEUS-JETS PDFs are also shown. The bands indicate the uncertainty in the predictions.

the HERA combined 2007 fit. As can be seen in the figure, the running of the coupling from the HERA jet data is in agreement with the prediction of pQCD.

The new HERA combined $\alpha_s(M_Z)$ value is shown in fig. 6, right, together with the values obtained by each collaboration separately, the 2004 HERA average [12], the most recent value from LEP [13] and the 2006 world average [14]. The determinations are consistent with each other and with the world average. The 2004 HERA average, which is the average of many determinations of $\alpha_s(M_Z)$ at HERA, has a very small experimental uncertainty (0.9%), but the theoretical uncertainty is large (4%), since in making that average the sources of theoretical uncertainty were conservatively assumed to be fully correlated. With the new method of combination presented here, no assumption on correlations is made, and a significant reduction on the theoretical uncertainty is achieved by combining observables for which these uncertainties are well under control. Even though the experimental uncertainty of the HERA combined 2007 value is higher than the HERA average 2004, the total uncertainty of the new combined value, 2.7%, is reduced to almost half due to the significant reduction of the theoretical uncertainty. The theory error is dominated by the missing higher orders estimated by the scale uncertainty. A comparison to the most recent value of $\alpha_s(M_Z)$ from LEP, $\alpha_s(M_Z) = 0.1211 \pm 0.0010(\mathrm{exp.}) \pm 0.0018(\mathrm{th.})$, shows that the central values are compat-

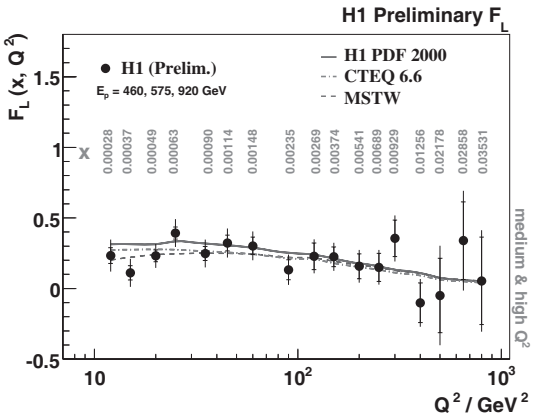

Fig. 5. – (Colour online) The longitudinal structure function F_L averaged in x at a given value of Q^2 in the full range of medium and high Q^2. The resulting x values of the averaged F_L measurements are given in the figure for each point in Q^2. The inner error bars are the statistical errors and the full error bars represent the statistical and systematic errors, added in quadrature. The correlated systematic error between the averaged F_L measurements is estimated to vary between 0.05 and 0.10 in the measured kinematics range. The solid red line represents a QCD prediction based on the H1 PDF2000 fit. The dashed line represents the MSTW and the dash-dotted line the CTEQ6.6 predictions (private communications).

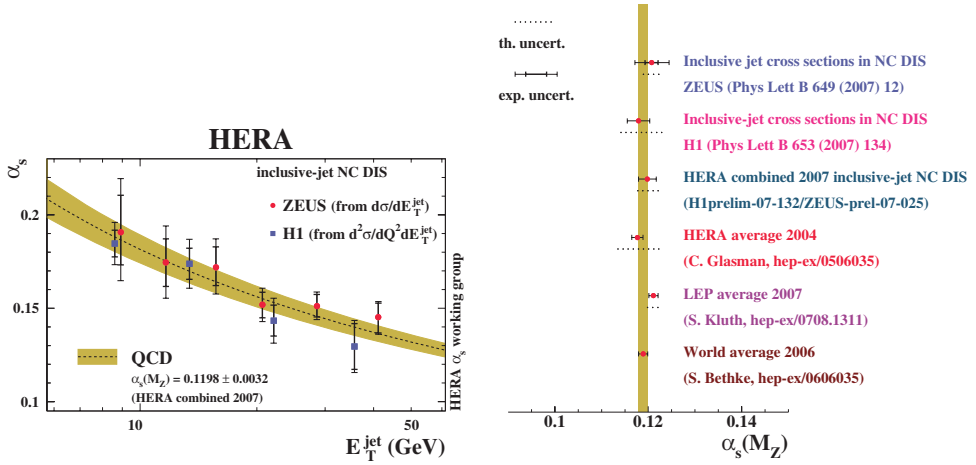

Fig. 6. – Left: results for the fitted values of $\alpha_s(E_T)$ using the inclusive jet cross-sections from H1 and ZEUS. The inner (outer) error bar denotes the experimental (total) uncertainty for each fitted value. The dashed line shows the two-loop solution of the renormalisation group equation evolving the HERA combined 2007 $\alpha_s(M_Z)$, with the band denoting the total uncertainty. Right: determinations of $\alpha_s(M_Z)$ from ZEUS and H1 together with the HERA combined 2007 $\alpha_s(M_Z)$ value. For comparison, the HERA average 2004 and the world average 2006 are also shown. The shaded band represents the uncertainty of the world average.

ible within the experimental uncertainty and that the uncertainty of the HERA combined 2007 value is very competitive with LEP, which includes an average of many precise determinations, such as that coming from τ decays.

REFERENCES

[1] Aaron F. D. *et al.* (H1 Collaboration), *Eur. Phys. J. C*, **63** (2009) 625, hep-ex/0904.0929.
[2] Golec-Biernat K. and Wüsthoff M., *Phys. Rev. D*, **59** (1999) 014017, hep-ph/9807513.
[3] Iancu E., Itakura K. and Munier S., *Phys. Lett. B*, **590** (2004) 199, hep-ph/0310338.
[4] Aaron F. D. *et al.* (H1 Collaboration), *Eur. Phys. J. C*, **64** (2009) 561, hep-ex/0904.3513.
[5] Chekanov S. *et al.* (ZEUS Collaboration), *Eur. Phys. J. C*, **62** (2009) 625, hep-ex/0901.2385.
[6] Chekanov S. *et al.* (ZEUS Collaboration), *Eur. Phys. J. C*, **61** (2009) 223, hep-ex/0812.4620v3.
[7] H1 and ZEUS Collaborations, *Proceedings of the 23rd International Symposium on Lepton and Photon Interactions at High Energy, Daegu, Korea (2007)*, `http://www-h1.desy.de/h1/www/publications/htmlsplit/H1prelim-07-007.long.html`.
[8] Thorne R., private communication.
[9] H1 and ZEUS Collaborations, *Proceedings of the 34th International Conference on High Energy Physics, Philadelphia, USA (2008)*, hep-ex/0809.4946.
[10] Aaron F. D. *et al.* (H1 Collaboration), *Phys. Lett. B*, **665** (2008) 139-146, hep-ex/0805.2809.
[11] Chekanov S. *et al.* (ZEUS Collaboration), *Phys. Lett. B*, **682** (2009) 8, DESY-09-046.
[12] Glasman C., *Proceedings of the 13th International Workshop on Deep Inelastic Scattering, Madison, USA (2005)*, hep-ex/0506035.
[13] Kluth S., in α_s *from LEP*. Talk given at *EPS07, Manchester, England (2007)*, hep-ex/0708.1311.
[14] Bethke S., *Prog. Part. Nucl. Phys.*, **58** (2007) 351.

IL NUOVO CIMENTO Vol. 32 C, N. 5-6 Settembre-Dicembre 2009
DOI 10.1393/ncc/i2010-10518-0

Colloquia: LaThuile09

Production of jets at forward rapidities in hadronic collisions

F. Hautmann

Department of Theoretical Physics, University of Oxford - Oxford OX1 3NP, UK

(ricevuto il 10 Novembre 2009; pubblicato online il 7 Gennaio 2010)

Summary. — We discuss high-$p_{\rm T}$ production processes at forward rapidities in hadron-hadron collisions, and describe recent results on using QCD high-energy factorization in forward jet production at the LHC.

PACS 12.38.-t – Quantum chromodynamics.
PACS 13.85.-t – Hadron-induced high- and super-high-energy interactions (energy $> 10\,\text{GeV}$).
PACS 13.87.-a – Jets in large-Q^2 scattering.

1. – Introduction

Experiments at the Large Hadron Collider (LHC) will explore the region of large rapidities both with general-purpose detectors and with dedicated instrumentation, including forward calorimeters and proton taggers [1-7]. The LHC forward-physics program involves a wide range of topics, from new particle discovery processes [3, 8, 9] to new aspects of strong-interaction physics [7, 10] to heavy-ion collisions [11, 12]. Owing to the large center-of-mass energy and the unprecedented experimental coverage at large rapidities, it becomes possible for the first time to investigate the forward region with high-$p_\perp$ probes.

In this article we report on studies of forward production of jets [13] based on QCD high-energy factorization at fixed transverse momentum [14]. This theoretical framework serves to take into account consistently both the higher-order logarithmic corrections in the large rapidity interval and those in the hard jet transverse energy. In sect. **2** we introduce the basic structure of jet production in the LHC forward region. In sect. **3** we consider associated parton showering effects. In sect. **4** we consider effects from the short-distance matrix elements that control the resummation of logarithmically enhanced corrections in $\sqrt{s}/E_T$, where E_T is the hard jet transverse energy. We give concluding remarks in sect. **5**.

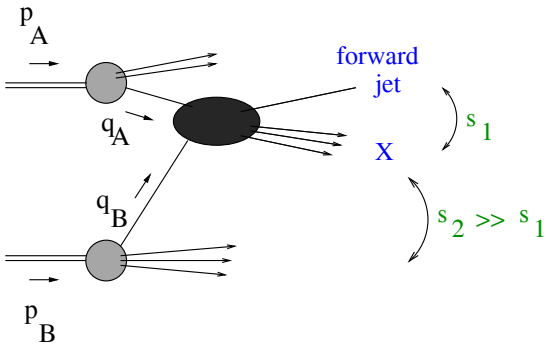

Fig. 1. – Jet production in the forward rapidity region in hadron-hadron collisions.

2. – Forward jets at the LHC

The hadroproduction of a forward jet associated with hard final state X is pictured in fig. 1. The kinematics of the process is characterized by the large ratio of sub-energies $s_2/s_1 \gg 1$ and highly asymmetric longitudinal momenta in the partonic initial state, $q_A \cdot p_B \gg q_B \cdot p_A$. At the LHC the use of forward calorimeters allows one to measure events where jet transverse momenta $p_\perp > 20\,\text{GeV}$ are produced several units of rapidity apart, $\Delta y \gtrsim 4$–6 [1, 5, 7]. Working at polar angles that are small but sufficiently far from the beam axis not to be affected by beam remnants, one measures azimuthal-plane correlations between high-$p_\perp$ events (fig. 2) widely separated in rapidity [7, 13].

The presence of multiple large-momentum scales implies that, as recognized in [15-17], reliable theoretical predictions for forward jets can only be obtained after summing logarithmic QCD corrections at high energy to all orders in α_s([1]). This motivates efforts [22-25] to construct new, improved algorithms for Monte Carlo event generators capable of describing jet production beyond the central rapidity region.

In the LHC forward kinematics, realistic phenomenology of hadronic jet final states requires taking account of both logarithms of the large rapidity interval (of high-energy type) and logarithms of the hard transverse momentum (of collinear type). The theoretical framework to resum consistently both kinds of logarithmic corrections in QCD calculations is based on high-energy factorization at fixed transverse momentum [14].

Reference [13] investigates forward jets in this framework. It presents the short-distance matrix elements needed to evaluate the factorization formula, including all partonic channels, in a fully exclusive form. On the one hand, once convoluted with the BFKL off-shell gluon Green's function according to the method of [14], these matrix elements control the summation of high-energy logarithmic corrections to the jet cross-sections. They contain contributions both to the next-to-leading-order BFKL kernel [26] and to the jet impact factors [27, 28]. On the other hand, they can be used in a shower Monte Carlo generator implementing parton-branching kernels at unintegrated level (see, *e.g.*, [29, 30] for recent works) to generate fully exclusive events.

([1]) Analogous observation applies to forward jets associated to deeply inelastic scattering [18, 19]. Indeed, measurements of forward jet cross-sections at Hera [20] have illustrated that either fixed-order next-to-leading calculations or standard shower Monte Carlos [20-22], *e.g.* PYTHIA or HERWIG, are not able to describe forward jet *ep* data.

Fig. 2. – Left: High-$p_\perp$ events in the forward and central detectors; right: azimuthal plane segmentation.

The high-energy factorized form [13, 14, 27] of the forward-jet cross-section is represented in fig. 3a. Initial-state parton configurations contributing to forward production are asymmetric, with the parton in the top subgraph being probed near the mass shell and large x, while the parton in the bottom subgraph is off-shell and small-x. The jet cross-section differential in the final-state transverse momentum Q_t and azimuthal angle φ is given schematically by [13, 14, 27]

$$\frac{\mathrm{d}\sigma}{\mathrm{d}Q_t^2\mathrm{d}\varphi} = \sum_a \int \phi_{a/A} \otimes \frac{\mathrm{d}\widehat{\sigma}}{\mathrm{d}Q_t^2\mathrm{d}\varphi} \otimes \phi_{g^*/B}, \tag{1}$$

where $\otimes$ specifies a convolution in both longitudinal and transverse momenta, $\widehat{\sigma}$ is the hard-scattering cross-section, calculable from a suitable off-shell continuation of perturbative matrix elements, $\phi_{a/A}$ is the distribution of parton a in hadron A obtained from near-collinear shower evolution, and $\phi_{g^*/B}$ is the gluon unintegrated distribution in hadron B obtained from non-collinear, transverse-momentum–dependent shower evolution.

In the next section we comment on the initial-state shower evolution. In sect. **4** we turn to hard-scattering contributions.

3. – Parton shower evolution

Parton distributions can be obtained by parton shower Monte Carlo methods via branching algorithms based on collinear evolution of the jets developing from the hard

Fig. 3. – (a) Factorized structure of the cross-section; (b) a typical contribution to the qg channel matrix element.

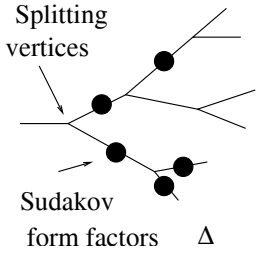

Fig. 4. – Parton branching in terms of splitting probabilities and form factors.

event [31]. The branching probability can be given in terms of two basic quantities (fig. 4), the splitting functions at the vertices of the parton cascade and the form factors to go from one vertex to the other. An important ingredient of this approach is the inclusion of soft-gluon coherence effects [31-33] through angular ordering of the emissions in the shower.

Corrections to collinear-ordered showers, however, arise in high-energy processes with multiple hard scales [7, 34, 35], as is the case with the production of jets at forward rapidities in fig. 1. In particular, new color-coherence effects set in this regime due to emissions from internal lines in the branching decay chain [7,27,36] that involve space-like partons carrying small longitudinal momentum fractions. The picture of the coherent branching is modified in this case because the emission currents become dependent on the total transverse momentum transmitted down the initial-state parton decay chain [14, 27, 34, 35, 37]. Correspondingly, one needs to work at the level of unintegrated splitting functions and partonic distributions [38,39] in order to take into account color coherence not only for large x but also for small x in the angular region (fig. 5)

$$\alpha/x > \alpha_1 > \alpha, \tag{2}$$

where the angles α for the partons radiated from the initial-state shower are taken with respect to the initial beam jet direction, and increase with increasing off-shellness.

The case of LHC forward jet production is a multiple-scale problem where coherence effects of the kind above enter, in the factorization formula (1), both the short-distance factor $\widehat{\sigma}$ and the long-distance factor ϕ. Contributions from the coherence region (2) are potentially enhanced by terms $\alpha_s^n \ln^m \sqrt{s}/p_\perp$, where $\sqrt{s}$ is the total center-of-mass energy

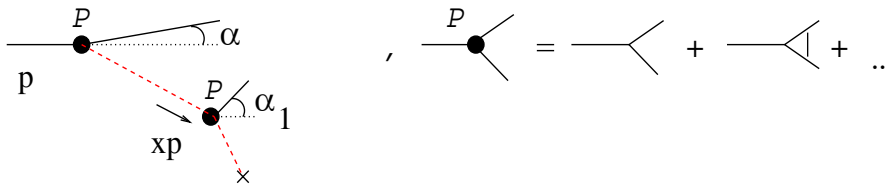

Fig. 5. – Left: coherent radiation in the space-like parton shower for $x \ll 1$; right: the unintegrated splitting function $\mathcal{P}$, including small-x virtual corrections.

and $p_\perp$ is the jet transverse momentum([2]). These contributions represent corrections to the angular ordering implemented in collinear showers and are not included at present in standard Monte Carlo generators [31]. Work to develop methods for unintegrated shower evolution, capable of including such corrections, is underway by several authors.

The proposal [29] incorporates NLO corrections to flavor non-singlet QCD evolution in an unintegrated-level Monte Carlo. The approach is based on the generalized ladder expansion of [41], which is extended to the high-energy region in [40]. This approach could in principle be applied generally, including flavor singlet evolution, and used to treat also forward hard processes.

Shower Monte Carlo generators based on small-x evolution equations, on the other hand, have typically included the unintegrated gluon distribution only [35, 37]. We observe that unintegrated quark contributions can be incorporated for sea quarks via the transverse-momentum–dependent but universal splitting kernel given in [40], which has the structure

$$\mathcal{P}_{g\to q}(z;q_\perp,k_\perp) = P^{(0)}_{qg}(z)\ \left(1+\sum_{n=1}^{\infty}\ b_n(z)(k_\perp^2/q_\perp^2)^n\right), \tag{3}$$

where $P^{(0)}$ is the DGLAP splitting function, and all coefficients b_n are known. The kernel (3) has been used for inclusive small-x calculations [42]. Its Monte Carlo implementation is relevant to take into account effects from the unintegrated quark distribution in the simulation of exclusive final states [43]. We note that quark contributions to evolution at the fully unintegrated level will also enter the treatment of the subleading high-energy corrections that are being discussed for jet production [28, 44].

Analyses of forward jet hadroproduction including parton showering effects are in progress [45].

4. – The factorizing hard cross-sections

Logarithmic corrections for large rapidity $y \sim \ln s/p_\perp^2$ are resummed to all orders in α_s via eq. (1), by convoluting (fig. 3) unintegrated distribution functions with well-prescribed short-distance matrix elements, obtained from the high-energy limit of higher-order scattering amplitudes [13, 27]. With reference to fig. 3b, in the forward production region we have $(p_4+p_6)^2 \gg (p_3+p_4)^2$ and longitudinal-momentum ordering, so that

$$p_5 \simeq (1-\xi_1)p_1, \qquad p_6 \simeq (1-\xi_2)p_2 - k_\perp, \qquad \xi_1 \gg \xi_2. \tag{4}$$

Here ξ_1 and ξ_2 are longitudinal-momentum fractions, and $k_\perp$ is the di-jet transverse momentum in the laboratory frame. It is convenient to define the rapidity-weighted average $Q_\perp = (1-\nu)p_{\perp 4} - \nu p_{\perp 3}$, with $\nu = (p_2\cdot p_4)/p_2\cdot(p_1-p_5)$. In fig. 3b eq. (1) factorizes the high-energy qg amplitude in front of the (unintegrated) distribution from the splitting in the bottom subgraph. The factorization in terms of this parton splitting distribution is valid at large y not only in the collinear region but also in the large-angle

([2]) Terms with $m > n$ are known to drop out from inclusive processes due to strong cancellations associated with coherence, so that, for instance, the anomalous dimensions γ^{ij} for space-like evolution receive at most single-logarithmic corrections at high energy [26, 40]. This need not be the case for exclusive jet distributions, where such cancellations are not present and one may expect larger enhancements.

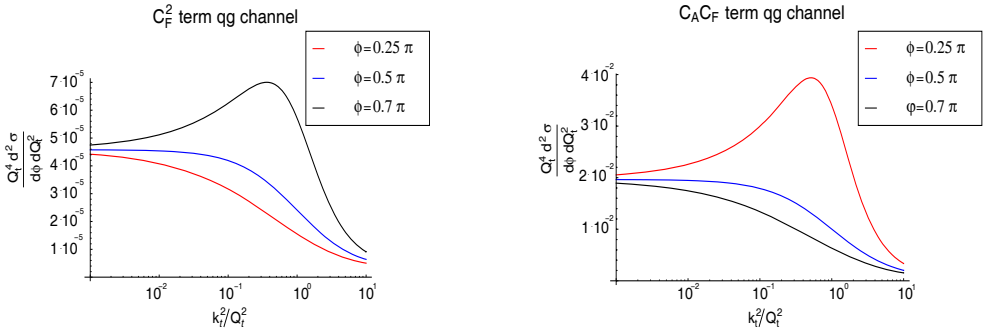

Fig. 6. – The (k_t/Q_t)-dependence of the factorizing qg hard cross-section at high energy [13]: C_F^2 term (left); $C_F C_A$ term (right).

emission region [14]. As a result the rapidity resummation is carried out consistently with perturbative high-$Q_\perp$ corrections [14, 27] at any fixed order in α_s.

The explicit expressions for the relevant high-energy amplitudes are given in [13]. Figures 6 and 7 illustrate features of the factorizing matrix elements, partially integrated over final states. We plot distributions differential in $Q_\perp$ and azimuthal angle φ ($\cos\varphi = Q_\perp \cdot k_\perp/|Q_\perp||k_\perp|$) for the case of the qg channel. Figure 6 shows the dependence on $k_\perp$, which measures the distribution of the third jet recoiling against the leading di-jet system. Figure 7 shows the energy dependence.

The region $k_\perp/Q_\perp \to 0$ in fig. 6 corresponds to the leading-order process with two back-to-back jets. The resummation of the higher-order logarithmic corrections for large $y \sim \ln s/p_\perp^2$ is precisely determined [14, 27] by integrating the u-pdfs over the $k_\perp$-distribution in fig. 6. So the results in fig. 6 illustrate quantitatively the significance of contributions with $k_\perp \simeq Q_\perp$ in the large-y region. The role of coherence from multi-gluon emission is to set the dynamical cut-off at values of $k_\perp$ of order $Q_\perp$. Non-negligible effects arise at high energy from the finite-$k_\perp$ tail. These effects are not included in collinear-branching generators (and only partially in fixed-order perturbative calculations), and become more and more important as the jets are observed at large rapidity separations. The dependence on the azimuthal angle in figs. 6 and 7 is also relevant, as forward-jet measurements will rely on azimuthal plane correlations between jets far apart in rapidity (fig. 2).

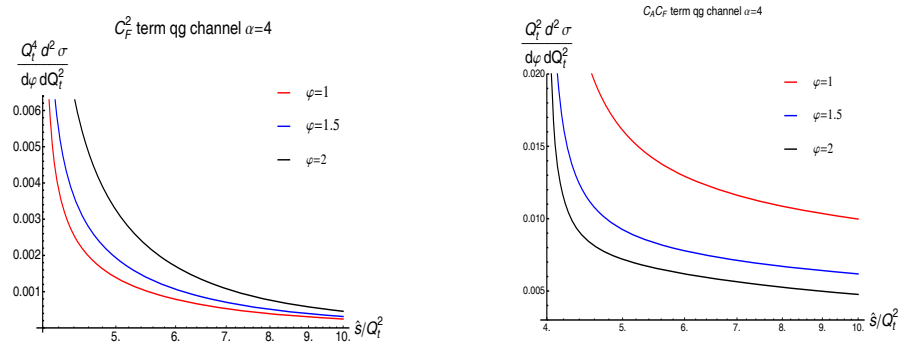

Fig. 7. – The energy dependence of the qg hard cross-section [13].

Results for all other partonic channels are given in [13]. It is worth stressing that quark and gluon contributions are of comparable size in the LHC forward kinematics [45]: realistic phenomenology requires including all channels. Note also that since the forward kinematics selects asymmetric parton momentum fractions, effects due to the $x \to 1$ endpoint behavior [46] at the fully unintegrated level may become relevant as well.

Let us finally recall that if effects of high-density parton dynamics [10,47] show up at the LHC, they will influence forward-jet event distributions. In such a case, the unintegrated formalism discussed above would likely be the natural framework to implement this dynamics at parton shower level.

5. – Conclusion

Forward + central detectors at the LHC allow jet correlations to be measured across rapidity intervals of several units, $\Delta y \gtrsim 4$–6. Such multi-jet states can be relevant to new-particle discovery processes as well as new aspects of standard model physics.

Existing sets of forward-jet data in ep collisions, much more limited than the potential LHC yield, indicate that neither conventional parton-showering Monte Carlos nor next-to-leading-order QCD calculations are capable of describing forward-jet phenomenology. Improved methods to evaluate QCD are needed to treat the multi-scale region implied by the forward kinematics.

In this article we have discussed ongoing progress, examining in particular factorization properties of multi-parton matrix elements in the forward region, and prospects to include parton-showering effects with gluon coherence not only in the collinear region but also in the large-angle emission region.

* * *

I thank M. Greco, the conference organizers and the conference staff for the kind invitation and for the nice atmosphere at the meeting. The results presented in this article have been obtained in collaboration with M. Deak, H. Jung and K. Kutak.

REFERENCES

[1] CMS Collaboration, CERN-LHCC-2006-001 (2006); CMS PAS FWD-08-001 (2008).
[2] ATLAS Collaboration, CERN-LHCC-2008-004 (2008); CERN-LHCC-2007-001 (2007).
[3] Albrow M. G. *et al.* (FP420 Collaboration), arXiv:0806.0302 [hep-ex].
[4] CMS Collaboration and TOTEM Collaboration, CERN-LHCC-2006-039/G -124 (2006).
[5] Aslanoglou X. *et al.*, CERN-CMS-NOTE-2008-022 (2008); *Eur. Phys. J. C*, **52** (2008) 495.
[6] Grothe M., arXiv:0901.0998 [hep-ex].
[7] Jung H. *et al.*, *Proceedings of the Workshop "HERA and the LHC"*, arXiv:0903.3861 [hep-ph].
[8] De Roeck A. *et al.*, *Eur. Phys. J. C*, **25** (2002) 391.
[9] Heinemeyer S. *et al.*, *Eur. Phys. J. C*, **53** (2008) 231.
[10] d'Enterria D., arXiv:0806.0883 [hep-ex]; *Eur. Phys. J. A*, **31** (2007) 816.
[11] Accardi A. *et al.*, CERN-2004-009-B, CERN-2004-009-A; hep-ph/0308248.
[12] CMS Collaboration, CERN-LHCC-2007-009 (2007).
[13] Deak M., Hautmann F., Jung H. and Kutak K., Oxford preprint OUTP-09-15-P.
[14] Catani S., Ciafaloni M. and Hautmann F., *Phys. Lett. B*, **307** (1993) 147; *Nucl. Phys. B*, **366** (1991) 135; *Phys. Lett. B*, **242** (1990) 97.

[15] Mueller A. H. and Navelet H., *Nucl. Phys. B*, **282** (1987) 727.
[16] Del Duca V., Peskin M. E. and Tang W. K., *Phys. Lett. B*, **306** (1993) 151.
[17] Stirling W. J., *Nucl. Phys. B*, **423** (1994) 56.
[18] Mueller A. H., *Nucl. Phys. B Proc. Suppl.*, **18C** (1990) 125.
[19] Tang W. K., *Phys. Lett. B*, **278** (1992) 363; Bartels J., De Roeck A. and Loewe M., *Z. Phys. C*, **54** (1992) 635; Kwiecinski J., Martin A. D. and Sutton P. J., *Phys. Rev. D*, **46** (1992) 921; Catani S., Ciafaloni M. and Hautmann F., *Nucl. Phys. B Proc. Suppl.*, **29A** (1992) 182.
[20] Knutsson A., LUNFD6-NFFL-7225-2007 (2007); Jönsson L., *AIP Conf. Proc.*, **828** (2006) 175.
[21] Webber B. R., hep-ph/9510283, in *Proceedings of the Workshop DIS95*.
[22] Ewerz C., Orr L. H., Stirling W. J. and Webber B. R., *J. Phys. G*, **26** (2000) 696; Forshaw J., Sabio Vera A. and Webber B. R., *J. Phys. G*, **25** (1999) 1511.
[23] Orr L. H. and Stirling W. J., *Phys. Lett. B*, **436** (1998) 372.
[24] Andersen J. R., Del Duca V., Frixione S., Maltoni F., Schmidt C. R. and Stirling W. J., hep-ph/0109019; Andersen J. R., Del Duca V., Frixione S., Schmidt C. R. and Stirling W. J., *JHEP*, **0102** (2001) 007.
[25] Andersen J. R., arXiv:0906.1965 [hep-ph]; Andersen J. R. and Sabio Vera A., *Phys. Lett. B*, **567** (2003) 116.
[26] Fadin V. S. and Lipatov L. N., *Phys. Lett. B*, **429** (1998) 127; Camici G. and Ciafaloni M., *Phys. Lett. B*, **430** (1998) 349.
[27] Ciafaloni M., *Phys. Lett. B*, **429** (1998) 363.
[28] Schwennsen F., hep-ph/0703198; Bartels J., Sabio Vera A. and Schwennsen F., arXiv:0709.3249, *JHEP*, **0611** (2006) 051.
[29] Jadach S. and Skrzypek M., arXiv:0905.1399 [hep-ph].
[30] Hautmann F. and Jung H., *JHEP*, **0810** (2008) 113; arXiv:0804.1746 [hep-ph].
[31] Webber B. R., CERN Academic Training Lectures (2008).
[32] Dokshitzer Yu. L., Khoze V. A., Mueller A. H. and Troian S. I., *Perturbative QCD* (Editions Frontieres, Gif-sur-Yvette) 1991.
[33] Ciafaloni M., in *Perturbative Quantum Chromodynamics*, edited by Mueller A. H. (World Scientific, Singapore) 1989.
[34] Marchesini G. and Webber B. R., *Nucl. Phys. B*, **386** (1992) 215.
[35] Andersson B. *et al.*, *Eur. Phys. J. C*, **25** (2002) 77.
[36] Andersson B., Gustafson G. and Samuelsson J., *Nucl. Phys. B*, **467** (1996) 443.
[37] Jung H., *Mod. Phys. Lett. A*, **19** (2004) 1.
[38] Collins J. C., hep-ph/0106126, in *Proceedings of the Workshop DIS01*; arXiv:0808.2665 [hep-ph], in *Proceedings of the Light Cone 2008 Workshop*.
[39] Hautmann F. and Jung H., *Nucl. Phys. Proc. Suppl.*, **184** (2008) 64 [arXiv:0712.0568 [hep-ph]]; arXiv:0808.0873 [hep-ph]; Hautmann F., *Acta Phys. Polon. B*, **40** (2009) 2139.
[40] Catani S. and Hautmann F., *Nucl. Phys. B*, **427** (1994) 475; *Phys. Lett. B*, **315** (1993) 157.
[41] Curci G., Furmanski W. and Petronzio R., *Nucl. Phys. B*, **175** (1980) 27.
[42] Ciafaloni M. and Colferai D., *JHEP*, **0509** (2005) 069; Ciafaloni M., Colferai D., Salam G. P. and Stasto A. M., *Phys. Lett. B*, **635** (2006) 320; Altarelli G., Ball R. D. and Forte S., arXiv:0802.0968 [hep-ph].
[43] Jung H. *et al.*, in preparation.
[44] Sabio Vera A. and Schwennsen F., *Nucl. Phys. B*, **776** (2007) 170; Marquet C. and Royon C., *Phys. Rev. D*, **79** (2009) 034028; Aurenche P., Basu R. and Fontannaz M., *Eur. Phys. J. C*, **57** (2008) 681; Fontannaz M., LPT-Orsay preprint (April 2009).
[45] Deak M., Hautmann F., Jung H. and Kutak K., in preparation.
[46] Hautmann F., *Phys. Lett. B*, **655** (2007) 26; arXiv:0708.1319; Collins J. C. and Hautmann F., *JHEP*, **0103** (2001) 016; *Phys. Lett. B*, **472** (2000) 129.
[47] Iancu E. and Mueller A. H., *JHEP*, **0801** (2008) 026; Iancu E., Kugeratski M. S. and Triantafyllopoulos D. N., *Nucl. Phys. A*, **808** (2008) 95; Gelis F., Lappi T. and Venugopalan R., *Int. J. Mod. Phys. E*, **16** (2007) 2595.

SESSION IV - HEAVY FLAVOUR PHYSICS

IL NUOVO CIMENTO Vol. 32 C, N. 5-6 Settembre-Dicembre 2009
DOI 10.1393/ncc/i2010-10537-9

Colloquia: LaThuile09

B_s and CP violation at the Tevatron

A. Schmidt on behalf of the CDF and DØ Collaborations
Institut für Experimentelle Kernphysik, Universität Karlsruhe - Karlsruhe, Germany

(ricevuto il 10 Novembre 2009; pubblicato online il 18 Gennaio 2010)

Summary. — The violation of the CP symmetry is an important probe for testing the Standard Model of particle physics as well as a missing piece in understanding the history of the universe. While CP violation in the B^0 and B^+ sector has been precisely measured by the B factories, the Tevatron with its two experiments CDF and DØ is still the only place to produce and study large samples of B_s^0-mesons until the startup of the LHC. This article gives an overview of recent results on CP violation in the B_s^0 sector from both Tevatron experiments.

PACS 11.30.Er – Charge conjugation, parity, time reversal, and other discrete symmetries.
PACS 14.40.Nd – Bottom mesons.

1. – The B_s-meson system

The phenomenology of B_s^0-mesons can be described in three bases of eigenstates: The *flavour eigenstates* are defined by the quark content: $|B_s^0\rangle = |\bar{b}s\rangle$, $|\bar{B}_s^0\rangle = |b\bar{s}\rangle$. Their time evolution is given by the Schrödinger equation

$$i\frac{\partial}{\partial t}\begin{pmatrix}|B_s^0\rangle\\|\bar{B}_s^0\rangle\end{pmatrix} = \left(\mathbf{M} - \frac{i}{2}\mathbf{\Gamma}\right)\begin{pmatrix}|B_s^0\rangle\\|\bar{B}_s^0\rangle\end{pmatrix} \tag{1}$$

with the Hermitian 2×2 mass and decay matrices $\mathbf{M}$ and $\mathbf{\Gamma}$. Diagonalization of this effective Hamiltonian leads to the heavy and light *mass eigenstates*:

$$|B_s^H\rangle = p\,|B_s^0\rangle - q\,|\bar{B}_s^0\rangle, \tag{2}$$

$$|B_s^L\rangle = p\,|B_s^0\rangle + q\,|\bar{B}_s^0\rangle. \tag{3}$$

The complex parameters p and q are normalized by the relation $|p|^2 + |q|^2 = 1$. Mass and width difference between the heavy- and light-mass eigenstates are defined as

$$\Delta m = m_H - m_L = 2\,|M_{12}|, \tag{4}$$

$$\Delta\Gamma = \Gamma_L - \Gamma_H = 2\,|\Gamma_{12}|\cos(\phi_s), \tag{5}$$

where ϕ_s is a complex phase between M_{12} and Γ_{12}:

$$\phi_s = \arg\left(-\frac{M_{12}}{\Gamma_{12}}\right). \tag{6}$$

The CP operator leads to the CP *eigenstates*

$$|B_s^{\text{even}}\rangle = \frac{1}{\sqrt{2}}(|B_s^0\rangle - |\bar{B}_s^0\rangle), \tag{7}$$

$$|B_s^{\text{odd}}\rangle = \frac{1}{\sqrt{2}}(|B_s^0\rangle + |\bar{B}_s^0\rangle), \tag{8}$$

where the width difference is defined as $\Delta\Gamma^{CP} = \Gamma^{\text{even}} - \Gamma^{\text{odd}}$. The relation between $\Delta\Gamma^{CP}$ and $\Delta\Gamma$ contains the phase ϕ_s:

$$\Delta\Gamma = \Delta\Gamma^{CP}\cos(\phi_s). \tag{9}$$

In case of CP conservation ($\phi_s = 0$), mass and CP eigenstates coincide. The Standard Model prediction $\phi_s = 0.004$ is very small [1]. As new physics is expected to have no influence on Γ_{12} but could contribute to M_{12} [1], the phase ϕ_s between the two elements can be significantly enhanced by new physics effects.

Δm_s is the frequency of $B_s^0 - \bar{B}_s^0$ oscillations and has already been measured by CDF [2] and DØ [3]. The $B_s^0 \to D_s D_s$ final state gives access to $\Delta\Gamma^{CP}$, while information on ϕ_s can be gained in B_s^0 decays to a flavour specific final state as well as from $B_s^0 \to J/\psi\,\phi$ decays. These measurements will be presented in the following sections.

2. – The Decay $B_s^0 \to D_s^{(*)} D_s^{(*)}$ and $\Delta\Gamma_s^{CP}$

The CKM favoured $B_s^0 \to c\bar{c}s\bar{s}$ transition is the dominant contribution of all B_s^0 decays to CP eigenstates, with the largest fraction ending in the colour allowed $D_s^{(*)} D_s^{(*)}$ final state. The $B_s^0 \to D_s D_s$ final state is purely CP even [4]. In the Shifman-Voloshin limit assuming $m_b - 2m_c \to 0$ and infinite number of colours [5], also $B_s^0 \to D_s^{(*)} D_s^{(*)}$ is dominantly CP even, neglecting small CP odd components. Therefore, the observation of that decay indicates a width difference $\Delta\Gamma_s^{CP}$, which can be obtained from the branching ratio

$$\frac{\Delta\Gamma_s^{CP}}{\Gamma_s} \approx 2 \cdot \text{Br}[B_s^0 \to D_s^{(*)} D_s^{(*)}]. \tag{10}$$

DØ published an analysis of $B_s^0 \to D_s^{(*)} D_s^{(*)}$ on $2.8\,\text{fb}^{-1}$ of data [6]. The decay was observed with 3.2σ significance and the measured branching ratio yields to

$$\Delta\Gamma_s^{CP}/\Gamma_s = 0.072 \pm 0.021(\text{stat}) \pm 0.022(\text{syst}). \tag{11}$$

The CDF analysis of $B_s^0 \to D_s D_s$ uses $360\,\text{pb}^{-1}$ of data [7]. This analysis observed the decay at 7.5σ. As the studied $D_s D_s$ final state is only one out of the final states contributing to the width difference, a limit has been set:

$$\Delta\Gamma_s^{CP}/\Gamma_s \geq 0.012 \text{ at } 95\% \text{ CL}. \tag{12}$$

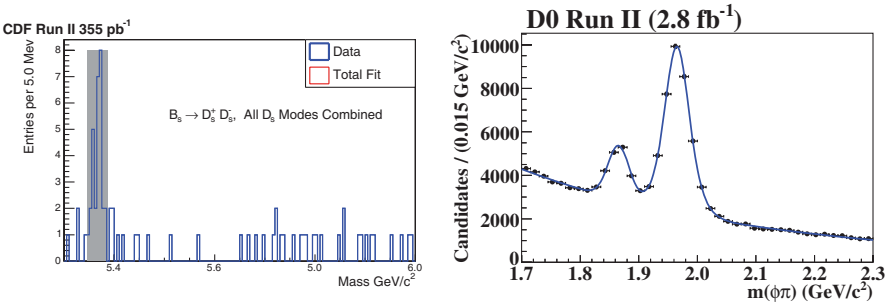

Fig. 1. – The mass spectrum observed in the CDF $B_s^0 \to D_s D_s$ analysis is shown in the left plot. In the DØ mass spectrum on the right, the peak at higher mass is from D_s and the lower peak from $D^{\pm}$ candidates.

In fig. 1, the observed mass spectra from the two experiments can be seen. Because DØ reconstructs one of the D_s candidates in a semileptonic decay missing a neutrino, the mass spectrum for the hadronically reconstructed D_s candidate is shown.

3. – CP asymmetry in semileptonic B_s^0 decays

Information on the phase ϕ_s can be gained by measuring the CP asymmetry,

$$a_{fs}^s = \frac{\Gamma_{\bar{B}_s^0 \to f} - \Gamma_{B_s^0 \to \bar{f}}}{\Gamma_{\bar{B}_s^0 \to f} + \Gamma_{B_s^0 \to \bar{f}}} = \frac{|M_{12}|}{|\Gamma_{12}|} \sin(\phi_s), \tag{13}$$

in B_s^0 decays to flavour specific final states. As this is often done in semileptonic B_s^0 decays, it is also called the *semileptonic CP asymmetry*. In these decays, $B_s^0 \to f$ and $\bar{B}_s^0 \to \bar{f}$ are allowed, while $B_s^0 \to \bar{f}$ and $\bar{B}_s^0 \to f$ can only be reached via mixing. The Standard Model expectation is $a_{fs}^s = (2.06 \pm 0.57) \cdot 10^{-5}$ [1].

The DØ collaboration performed a time-dependent a_{fs}^s analysis on $5\,\mathrm{fb}^{-1}$ [8] in the decay

$$B_s^0 \to \mu^+ D_s^- X \tag{14}$$

with subsequent decays of $D_s^- \to \phi\pi^-$, $\phi \to K^+K^-$ and $D_s^- \to K^{*0}K^-$, $K^{*0} \to K^+\pi^-$. Most of the data sample was collected with single muon triggers, although no explicit trigger requirement was made. The resulting $KK\pi$ mass spectra after a likelihood-based candidate selection can be seen in fig. 2.

The final-state b-quark flavour is known from the muon of the semileptonic decay. To obtain the initial state flavour, an opposite-side tagging algorithm was used which relies in most cases on the charge of a second muon in the event. Approximately 21% of all events are tagged.

An unbinned maximum-likelihood fit is used to extract the parameters of interest. Contributions from peaking, prompt and long-lived background are modeled in the likelihood function and their parameters are determined from the data sample. To minimize asymmetries caused by detector effects, the polarity of the magnetic field of the DØ detector was reversed regularly during data taking.

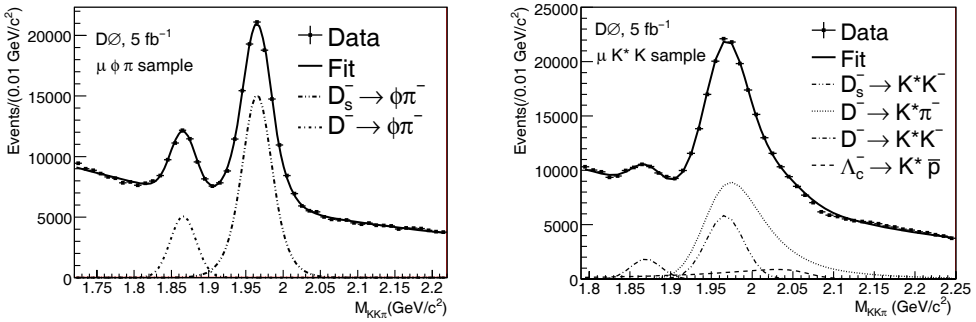

Fig. 2. – Mass distributions observed in the DØ a^s_{fs} analysis. The $D_s^- \to \phi\pi^-$ channel can be seen in the left plot, the $D_s^- \to \mu^+ K^{*0} K^-$ on the right.

The resulting measurement

$$a^s_{fs} = \left[-1.7 \pm 9.1\ (\text{stat})^{+1.2}_{-2.3}(\text{syst})\right] \cdot 10^{-3} \tag{15}$$

indicates that with increasing statistics this analysis will be close to reaching the sensitivity for constraining models of new physics.

4. – CP violation in $B^0_s \to J/\psi\ \phi$ decays

The decay $B^0_s \to J/\psi\ \phi$ is one of the most interesting probes of new physics in the entire experimental scenario. In a time dependent measurement of the CP asymmetry

$$A_{CP}(t) = \frac{\Gamma(\bar{B^0_s} \to f_{CP}) - \Gamma(B^0_s \to f_{CP})}{\Gamma(\bar{B^0_s} \to f_{CP}) + \Gamma(B^0_s \to f_{CP})} \approx \pm \sin(2\beta_s)\ \sin(\Delta m_s\ t), \tag{16}$$

it gives access to the angle $\beta_s^{J/\psi\ \phi}$ of the unitarity triangle given by the second and third column of the CKM matrix:

$$2\ \beta_s^{J/\psi\ \phi} = -\arg[(V_{tb}V^*_{ts})^2/(V_{cb}V^*_{cs})^2]. \tag{17}$$

The presence of new physics enhancing ϕ_s would affect $\beta_s^{J/\psi\ \phi}$ in the same way [9].

The $J/\psi\ \phi$ final state can be reached with and without mixing and is a mixture of CP even and odd states. In the decay of the pseudoscalar B^0_s-meson into two vector mesons J/ψ and ϕ, the $L = 0, 2$ states are CP even and the $L = 1$ state is CP odd. The sensitivity to the phase is increased by studying the time evolution of CP even and CP odd states separately, which can be distiguished by the angular distributions of their decay products. Information about mixing is gained by tagging the production flavour of the B^0_s-meson.

Both Tevatron experiments have performed flavour tagged analyses on $2.8\,\text{fb}^{-1}$ of data [10, 11]. However, they use different conventions: CDF aims for measuring $\beta_s^{J/\psi\ \phi}$, while DØ uses $\phi_s^{J/\psi\ \phi} = -2\ \beta_s^{J/\psi\ \phi}$. For easier reading, only $\beta_s^{J/\psi\ \phi}$ will be used in the

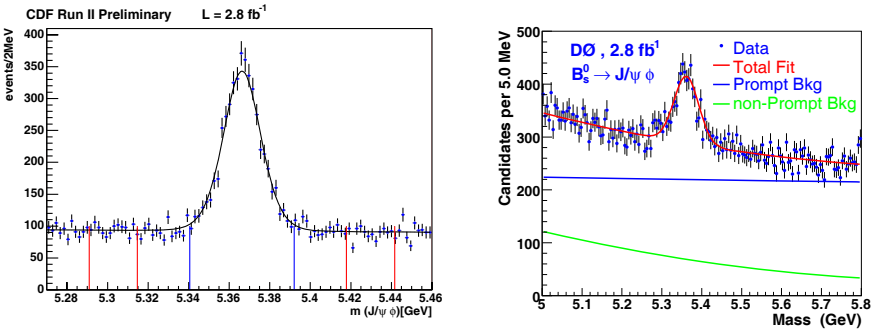

Fig. 3. – Mass distribution of the $B_s^0 \to J/\psi\ \phi$ signal sample for the CDF (left) and the DØ analysis (right).

following text. In both cases, the samples of

$$B_s^0 \to J/\psi\ \phi, \qquad J/\psi \to \mu^+\mu^-, \qquad \phi \to K^+K^- \tag{18}$$

decays have been collected with a di-muon trigger. A selection based on artificial neural networks leads to about 3200 signal events for the CDF analysis, while DØ yields approximately 2000 signal events from a cut based selection. The resulting mass spectra can be found in fig. 3.

Information about the B_s^0 production flavour can be gained from various sources. As b-quarks at the Tevatron are usually produced in form of $b\bar{b}$ pairs, there are experimental signatures of a second B-hadron (the so-called *opposite-side* B) besides the B_s^0-meson (the *same-side* B) that was reconstructed in the decay to $J/\psi\ \phi$.

Same-side tagging makes use of fragmentation tracks: As the B_s^0-meson contains an s-quark, the fragmentation partner of that s-quark must be somewhere in the vicinity. If it ends up in a charged kaon, the charge of this kaon is correlated to the B_s^0 production flavour. Opposite-side tagging evaluates the properties and decay tracks of the other B-hadron in the event. The inclusive charge of the opposite-side B decay jet, leptons from semileptonic B decays as well as kaons from the $b \to c \to s$ decay chain are the main sources of information.

In a binary decision, the chance that a random decision is correct is already 50%. Therefore, the *dilution* of a flavour tagging algorithm

$$\mathcal{D} = \frac{N_{\mathrm{RS}} - N_{\mathrm{WS}}}{N_{\mathrm{RS}} + N_{\mathrm{WS}}} \tag{19}$$

is zero if the number of correct decisions N_{RS} equals the number of incorrect decision N_{WS}. As most tagging algorithms do not provide a decision for every event, the *efficiency* ϵ gives the fraction of tagged events. The effective reduction of statistics due to flavour tagging uncertainties usually scales with $\epsilon\mathcal{D}^2$ and is called the *tagging effectiveness*.

CDF uses a same-side kaon tagging algorithm with $\epsilon\mathcal{D}^2 = 3.7\%$ for the first $1.35\,\mathrm{fb}^{-1}$ of the dataset. For the whole $2.8\,\mathrm{fb}^{-1}$, a neural network combination of opposite-side electron, muon and jet charge taggers with $\epsilon\mathcal{D}^2 = 1.8\%$ is used. DØ combined existing same-side and opposite-side tagging with a likelihood method with a tagging effectiveness $\epsilon\mathcal{D}^2 = 4.7\%$.

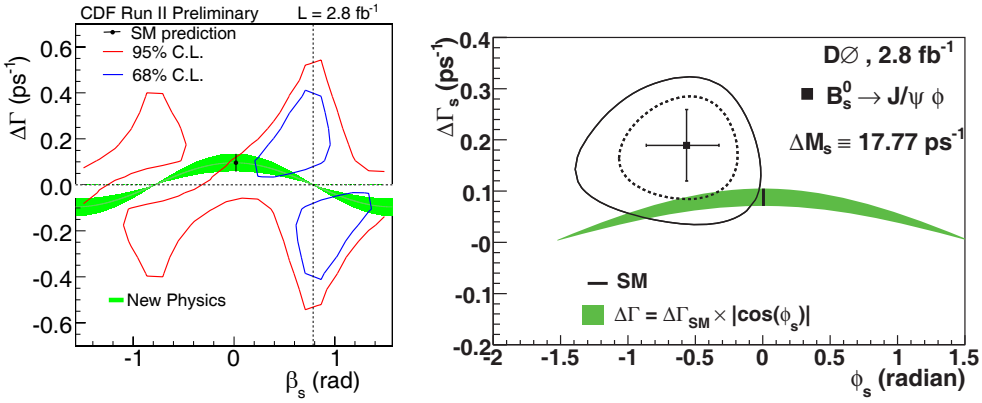

Fig. 4. – (Colour online) Confidence regions of the CDF (left) and DØ (right) $B_s^0 \to J/\psi\ \phi$ analyses.

To extract $\Delta\Gamma$ and $\beta_s^{J/\psi\ \phi}$, an unbinned maximum-likelihood fit is performed in mass, tagging information, proper decay time and angular distributions. Due to an indeterminacy of the strong phases in the three decay amplitudes of the $L = 0, 1, 2$ final states, the likelihood function shows two symmetric minima in the $(\Delta\Gamma_s, \beta_s^{J/\psi\ \phi})$-plane. Because the two minima overlap and do not have a Gaussian shape, CDF evaluates confidence regions using the Feldman Cousins method, while DØ decided to constrain the strong phases and remove one of the minima. The resulting contours can be seen in fig. 4. The green band indicates the physical region under the assumption that new physics only affects M_{12}, but not Γ_{12} [1]. Currently, the compatibility with the Standard Model point is 1.8σ for the CDF and 1.7σ for the DØ result. Both contours seem to favour a minimum in the same region of the parameter space.

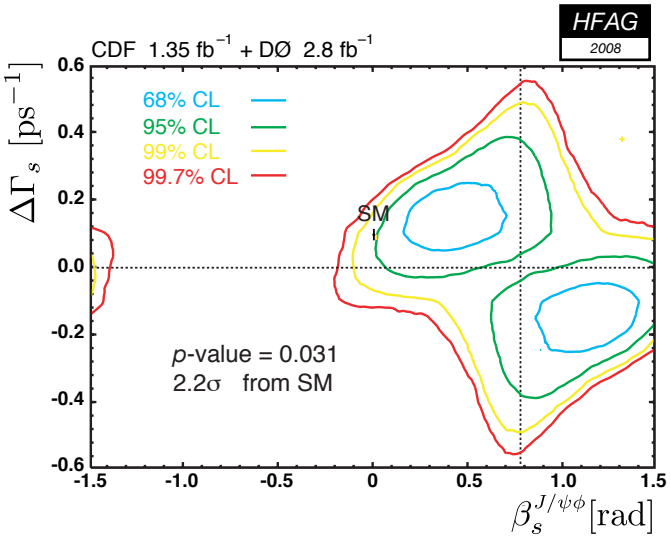

Fig. 5. – HFAG combination of the 2.8 fb^{-1} DØ analysis [11] with the 1.35 fb^{-1} CDF analysis [13].

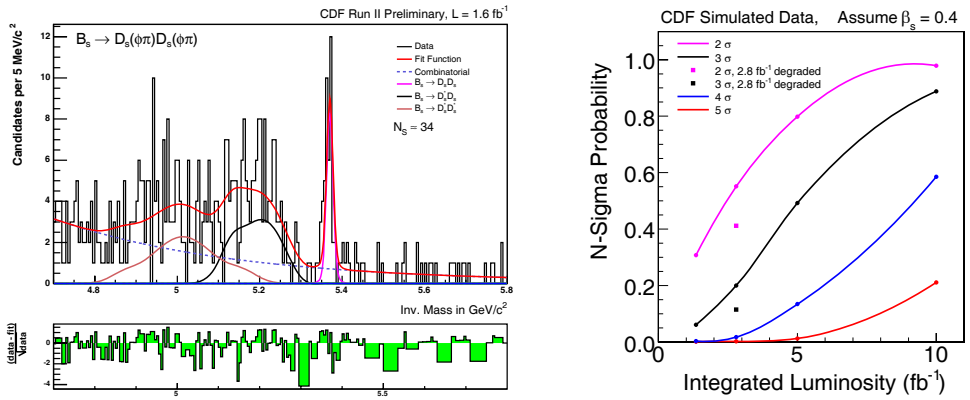

Fig. 6. – $B_s^0 \to D_s D_s$ invariant mass spectrum on $1.6\,\mathrm{fb}^{-1}$ from the update of the CDF $B_s^0 \to D_s^{(*)} D_s^{(*)}$ analysis (left) and sensitivity projection for a N-σ observation if $\beta_s = 0.4$ as a function of integrated luminosity (right).

The Heavy Flavor Averaging Group (HFAG) combined the current DØ result on $2.8\,\mathrm{fb}^{-1}$ with the previous CDF result on $1.35\,\mathrm{fb}^{-1}$ [13] using the two-dimensional profile likelihoods [12]. DØ released the strong phase constraint for that combination. The resulting contour can be seen in fig. 5. In the combined result, a discrepancy to the Standard Model prediction of 2.2σ is observed.

5. – Outlook

Each of the two Tevatron experiments has around $5\,\mathrm{fb}^{-1}$ data ready for use in the upcoming analysis updates. As the accelerator is performing very well and the initial luminosities are still being improved, even more data can be expected in the remaining time of Tevatron operations.

An updated $B_s^0 \to D_s^{(*)} D_s^{(*)}$ analysis including D_s^* states is in preparation by the CDF collaboration. A preliminary mass spectrum can be seen in fig. 6. Besides more data, other analysis improvements for $B_s^0 \to J/\psi\ \phi$ are in preparation. DØ plans to improve the selection of candidates, while improved flavour tagging has been developed at CDF. For future Tevatron results of $B_s^0 \to J/\psi\ \phi$, a combination group has been installed. Not only a combination of the two-dimensional profile likelihoods, also a simultaneous fit on the full-likelihood functions is planned. In fig. 6, a projection is shown on what could be reached with future Tevatron data. If new physics actually causes a large phase $\beta_s^{J/\psi\ \phi} = 0.4$ in B_s^0 mixing, there is a reasonable chance to observe it when combining the power of both Tevatron experiments.

REFERENCES

[1] Lenz A. and Nierste U., *JHEP*, **06** (2007) 072.
[2] Abulencia A. *et al.* (CDF Collaboration), *Phys. Rev. Lett.*, **97** (2003) 242003.
[3] D0 Collaboration, conference note 5618-CONF.
[4] Dunietz I., Fleischer R. and Nierste U., *Phys. Rev. D*, **63** (2001) 114015.
[5] Shifman M. A. and Voloshin M. B., *Sov. J. Nucl. Phys.*, **47** (1988) 511.

[6] Abazov V. M. *et al.* (D0 Collaboration), *Phys. Rev. Lett.*, **102** (2009) 091801.
[7] Aaltonen A. *et al.* (CDF Collaboration), *Phys. Rev. Lett.*, **100** (2008) 021803.
[8] Abazov V. M. *et al.* (D0 Collaboration), submitted to *Phys. Rev. Lett.*, arXiv:0904.3907v1 [hep-ex].
[9] Lenz A., *Nucl. Phys. Proc. Suppl.*, **177-178** (2008) 81.
[10] CDF Collaboration, public note 9458.
[11] Abazov V. M. *et al.* (D0 Collaboration), *Phys. Rev. Lett.*, **101** (2008) 241801.
[12] Baberio E. *et al.* (HFAG), arXiv:0808.1297v3 [hep-ex].
[13] Aaltonen T. *et al.* (CDF Collaboration), *Phys. Rev. Lett*, **100** (2008) 161802.

IL NUOVO CIMENTO Vol. 32 C, N. 5-6 Settembre-Dicembre 2009
DOI 10.1393/ncc/i2010-10541-1

Colloquia: LaThuile09

Measurements of CKM parameters at the B factories

G. Sciolla(*)

Department of Physics, Massachusetts Institute of Technology
Room 26-443, 77 Massachusetts Avenue, Cambridge MA 02139, USA

(ricevuto il 10 Novembre 2009; pubblicato online il 18 Gennaio 2010)

Summary. — In the past 10 years our knowledge of the elements of the Cabibbo-Kobayashi-Maskawa matrix has improved substantially. This article reviews some of the many contributions from the B factories to this progress, and discusses their implication in terms of understanding CP violation in the Standard Model and beyond.

PACS 11.30.Er – Charge conjugation, parity, time reversal, and other discrete symmetries.
PACS 12.15.Hh – Determination of Kobayashi-Maskawa matrix elements.
PACS 13.25.Hw – Decays of bottom mesons.

1. – The Unitarity Triangle

According to Kobayashi and Maskawa [1], CP violation in the Standard Model (SM) is due to a complex phase appearing in the quark mixing matrix, the Cabibbo-Kobayashi-Maskawa (CKM) matrix. Following Wolfenstein's notation [2], the CKM matrix can be expressed in terms of the four real parameters λ, A, ρ and η as

$$(1) \qquad \begin{pmatrix} V_{ud} & V_{us} & V_{ub} \\ V_{cd} & V_{cs} & V_{cb} \\ V_{td} & V_{ts} & V_{tb} \end{pmatrix} = \begin{pmatrix} 1-\lambda^2/2 & \lambda & A\lambda^3(\rho - i\eta) \\ -\lambda & 1-\lambda^2/2 & A\lambda^2 \\ A\lambda^3(1-\rho-i\eta) & -A\lambda^2 & 1 \end{pmatrix} + O(\lambda^4).$$

While the parameters λ and A have been precisely known for a long time, the parameters ρ and η were poorly measured until recently. The parameter η is of particular interest, because if $\eta = 0$ the Standard Model would not be able to explain CP violation. If the CKM matrix is unitary, then $V^+V = 1$. This implies six unitarity conditions that

(*) Representing the *BABAR* and Belle Collaborations; E-mail: sciolla@mit.edu

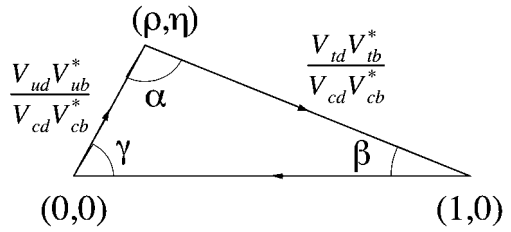

Fig. 1. – The Unitarity Triangle.

relate the nine elements of the matrix. The condition that relates the first and third columns of the matrix can be written as

$$\frac{V_{ud}V_{ub}^*}{V_{cd}V_{cb}^*} + \frac{V_{td}V_{tb}^*}{V_{cd}V_{cb}^*} + 1 = 0. \tag{2}$$

This equation represents a triangle in the complex (ρ, η)-plane with the base normalized to 1. This triangle, knows as the Unitarity Triangle (UT), is depicted in fig. 1. The angles (α, β, and γ) and sides of the triangle are defined in fig. 1.

The study of B-meson decays allows us to perform a number of measurements that set constraints in the (ρ, η)-plane. In the Standard Model all measurements must be consistent. The presence of New Physics could cause inconsistencies for some of the measurements of $\approx 10\%$. A redundant and precise set of measurements providing constraints in the (ρ, η)-plane is therefore essential to test the CKM mechanism and probe for New Physics beyond the Standard Model.

The main contributors to this physics program are the two experiments at the asymmetric B factories, *BABAR* [3] and Belle [4]. Collectively, these experiments recorded to date over one billion $B\overline{B}$ pairs in e^+e^- interactions at the $\Upsilon(4S)$ resonance. The large data set and clean experimental environment allowed the B factories to measure all sides and angles of the UT. The two Tevatron experiments, CDF and DO, add constraints from their measurement of B_s^0 mixing. In addition, several kaon experiments provide complementary information by measuring the CP-violating parameter ϵ_K in K^0 decays.

2. – CP violation in B^0 decays

The angles of the UT can be determined through the measurement of the time dependent CP asymmetry, $A_{CP}(t)$. This quantity is defined as

$$A_{CP}(t) \equiv \frac{N(\overline{B}^0(t) \to f_{CP}) - N(B^0(t) \to f_{CP})}{N(\overline{B}^0(t) \to f_{CP}) + N(B^0(t) \to f_{CP})}, \tag{3}$$

where $N(\overline{B}^0(t) \to f_{CP})$ is the number of $\overline{B}^0$ that decay into the CP-eigenstate f_{CP} after a time t.

In general, this asymmetry can be expressed as the sum of two components:

$$A_{CP}(t) = S_f \sin(\Delta m t) - C_f \cos(\Delta m t), \tag{4}$$

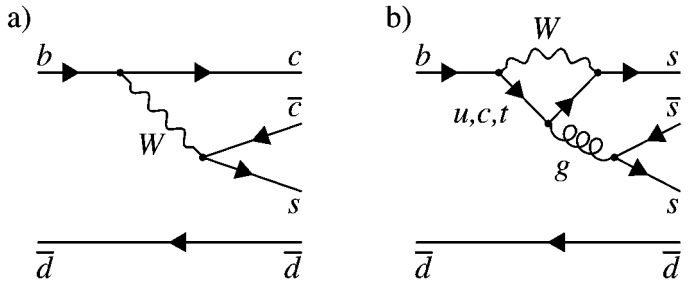

Fig. 2. – Feynman diagrams that mediate the B^0 decays used to measure the angle β: a) $B^0 \to$ charmonium $+ K^0$; b) penguin-dominated B decays.

where Δm is the difference in mass between B^0 mass eigenstates. The sine coefficient S_f is related to an angle of the UT, while the cosine coefficient C_f measures direct CP violation.

When only one diagram contributes to the final state, the cosine term in eq. (4) vanishes. As an example, for decays such as $B \to J/\psi K^0$, $S_f = -\eta_f \times \sin 2\beta$, where η_f is the CP eigenvalue of the final state, negative for charmonium $+ K_S$, and positive for charmonium $+ K_L$. It follows that

$$A_{CP}(t) = -\eta_f \sin 2\beta \sin(\Delta m t), \tag{5}$$

which shows how the angle β is measured by the amplitude of the time dependent CP asymmetry.

The measurement of $A_{CP}(t)$ utilizes decays of the $\Upsilon(4S)$ into two neutral B-mesons, of which one (B_{CP}) can be completely reconstructed into a CP eigenstate, while the decay products of the other ($B_{\rm tag}$) identify its flavor at decay time. The time t between the two B decays is determined by reconstructing the two B decay vertices. The CP asymmetry amplitudes are determined from an unbinned maximum likelihood fit to the time distributions separately for events tagged as B^0 and $\overline{B}^0$.

3. – The angle β

The most precise measurement of the angle β of the UT is obtained in the study of the decay $B^0 \to$ charmonium $+ K^0$. These decays, known as "golden modes," are dominated by a tree level diagram $b \to c\bar{c}s$ with internal W boson emission (fig. 2a). The leading penguin diagram contribution to the final state has the same weak phase as the tree diagram, and the largest term with different weak phase is a penguin diagram contribution suppressed by $O(\lambda^2)$. This makes $C_f = 0$ in eq. (4) a very good approximation.

Besides the theoretical simplicity, these modes also offer experimental advantages because of their relatively large branching fractions ($\sim 10^{-4}$) and the presence of narrow resonances in the final state, which provide a powerful rejection of combinatorial background. The CP eigenstates considered for this analysis are $J/\psi K_S$, $\psi(2S)K_S$, $\chi_{c1}K_S$, $\eta_c K_S$ and $J/\psi K_L$.

The asymmetry between the two Δt distributions, clearly visible in fig. 3 is a striking manifestation of CP violation in the B system. The same figure also displays the corresponding raw CP asymmetry with the projection of the unbinned maximum-likelihood

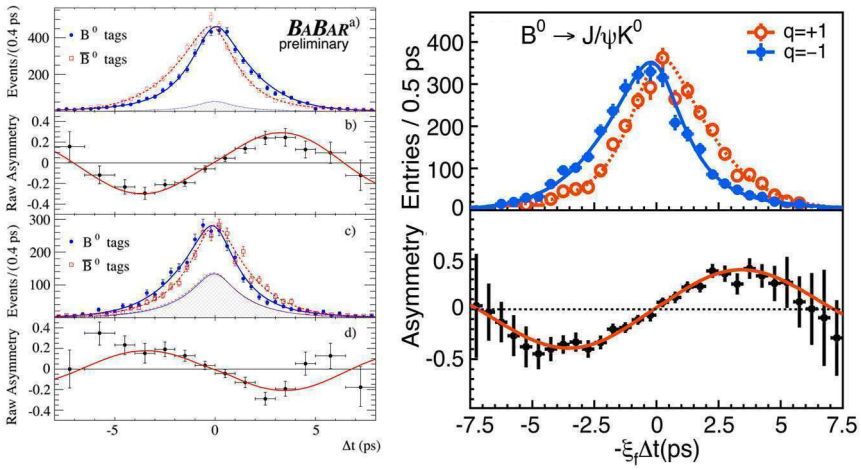

Fig. 3. – Measurements of $\sin 2\beta$ in the "golden modes" by *BABAR* (left) and Belle (right). Left plot (*BABAR*): a) time distributions for events tagged as B^0 (full dots) or $\overline{B}^0$ (open squares) in CP odd (charmonium K_S) final states; b) corresponding raw CP asymmetry with the projection of the unbinned maximum-likelihood fit superimposed; c) and d) corresponding distributions for CP even ($J/\psi K_L$) final states. Right plot (Belle): top) time distributions for events tagged as B^0 (open dots) or $\overline{B}^0$ (full dots) in charmonium K_S final states; bottom) corresponding raw CP asymmetry with the projection of the unbinned maximum-likelihood fit superimposed.

fit superimposed. The measurements from *BABAR* [5] and Belle [6] are averaged to obtain $\sin 2\beta = 0.670 \pm 0.023$ [7]. This measurement provides the strongest constraints in the (ρ, η)-plane.

An independent measurement of the angle β through the study of B decays dominated by penguin diagrams allows us to search for physics beyond the Standard Model. In the SM, final states dominated by $b \to s\bar{s}s$ or $b \to s\bar{d}d$ decays offer a clean and independent way of measuring $\sin 2\beta$ [8]. Examples of these final states are ϕK^0, $\eta' K^0$, $f_0 K^0$, $\pi^0 K^0$, ωK^0, $K^+K^-K_S$ and $K_S K_S K_S$. These decays are mediated by the gluonic penguin diagram illustrated in fig. 2b. In presence of physics beyond the Standard Model, new particles such as squarks and gluinos, could participate in the loop and affect the time dependent asymmetries [9].

A summary of the measurements of $A_{CP}(t)$ in penguin modes by the *BABAR* [10-12] and Belle [13] experiments is reported in fig. 4. Each channel as well as the average of all the penguin modes are in agreement with the value of $\sin 2\beta$ measured in the golden mode within the experimental error.

4. – The angle α

If the decay $B^0 \to \pi^+\pi^-$ were dominated by the $b \to u$ tree level diagram, the amplitude of the time-dependent CP asymmetry in this channel would be a clean measurement of the parameter $\sin 2\alpha$. Unfortunately, the analysis is complicated by sizable contributions from the gluonic $b \to d$ penguin amplitudes to this final state. As a result, the fit to the time-dependent CP asymmetry (eq. (4)) must include both the sine and the cosine terms. The coefficient of the sine term measures the parameter $\alpha_{\rm eff}$, which

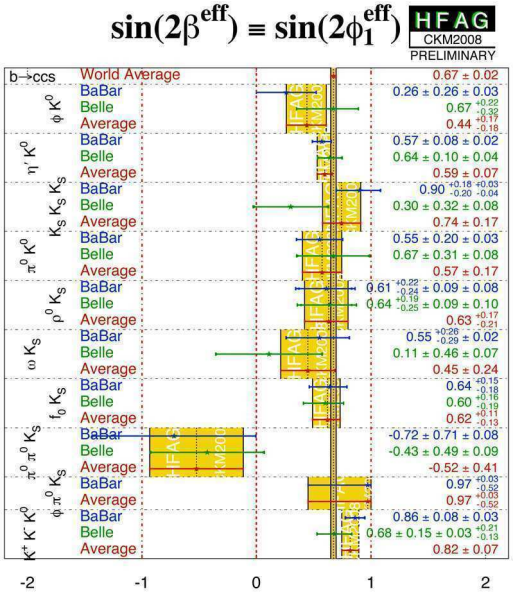

Fig. 4. – (Colour on-line) *BABAR* and Belle measurements of "sin 2β" in the penguin-dominated channels. The narrow yellow band indicates the world average of the charmonium + K^0 final states $\pm 1\sigma$.

is related to the angle α of the UT through the correction $\Delta\alpha = \alpha - \alpha_{\rm eff}$. $\Delta\alpha$ can be extracted from an analysis of the branching fractions and CP asymmetries of the full set of isospin-related $b \to u\overline{u}d$ channels [14].

A similar measurement can be performed using the decays $B \to \rho\rho$. This analysis is complicated by the fact that since the ρ is a vector meson, $\rho^+\rho^-$ final states are characterized by three possible angular-momentum states, and therefore they are expected to be an admixture of $CP = +1$ and $CP = -1$ states. However, polarization studies [15-17] indicate that this final state is almost completely longitudinally polarized, and therefore almost a pure CP eigenstate, which simplifies the analysis.

A recent measurement [17] of the branching fraction of $B^+ \to \rho^+\rho^0$ by the *BABAR* Collaboration has substantially improved our knowledge of the UT angle α. The improvement is primarily due to the increase in the measured value of $B(B^+ \to \rho^+\rho^0)$ compared to previous results. $B^+ \to \rho^+\rho^0$ determines the length of the common base of the isospin triangles for the B and $\overline{B}$ decays. The increase in the base length flattens both triangles, making the four possible solutions [14] nearly degenerate.

Additional constraints are obtained by the study of $B \to \rho\pi$ decays.

Combining all *BABAR* and Belle results, we measure $\alpha = (92^{+6.0}_{-6.5})^\circ$ [18]. This new result represents a substantial improvement over previous measurements of α.

5. – The angle γ

The angle γ is measured exploiting the interference between the decays $B^- \to D^{(*)0}K^{(*)-}$ and $B^- \to \overline{D}^{(*)0}K^{(*)-}$, where both D^0 and $\overline{D}^0$ decay to the same final state. This measurement can be performed in three different ways: utilizing decays

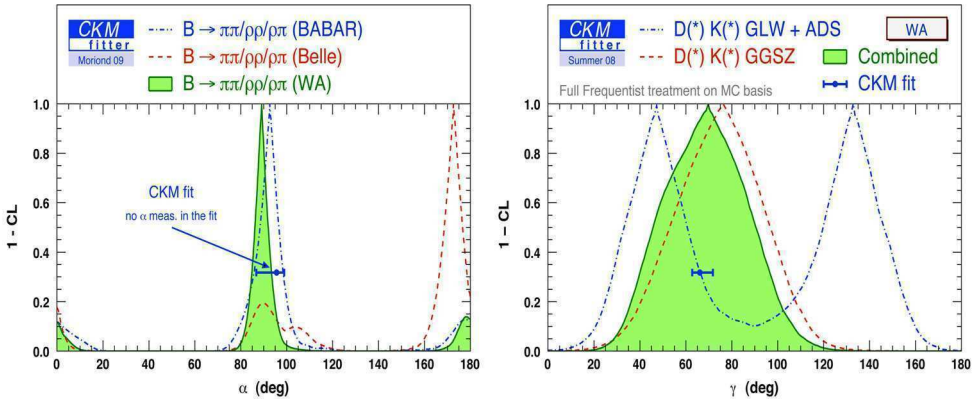

Fig. 5. – Constraints on the UT angles α (left) and γ (right) from various direct measurements compared with indirect constraints [18].

of D-mesons to CP eigenstates [19], utilizing doubly Cabibbo-suppressed decays of the $\overline{D}$-meson [20], and exploiting the interference pattern in the Dalitz plot of $D \to K_S\pi^+\pi^-$ decays [21]. Combining all results from *BABAR* and Belle, we measure $\gamma = (70^{+27}_{-29})^\circ$ [18] (see fig. 5).

6. – The left side of the Unitarity Triangle

The left side of the Unitarity Triangle is determined by the ratio of the CKM matrix elements $|V_{ub}|$ and $|V_{cb}|$. Both are measured in the study of semi-leptonic B decays. The measurement of $|V_{cb}|$ is already very precise, with errors of the order of 1–2% [7]. The determination of $|V_{ub}|$ is more challenging, mainly due to the large background coming from $b \to c\ell\nu$ decays, about 50 times more likely to occur than $b \to u\ell\nu$ transitions.

Two approaches, inclusive and exclusive, can be used to determine $|V_{ub}|$. In inclusive analyses of $B \to X_u\ell\nu$, the $b \to c\ell\nu$ background is suppressed by cutting on a number of kinematical variables. This implies that only partial rates can be directly measured, and theoretical assumptions are used to infer the total rate and extract $|V_{ub}|$. Averaging all inclusive measurements from the *BABAR*, Belle, and CLEO experiments we determine $|V_{ub}| = (3.96 \pm 0.20^{+0.20}_{-0.23}) \times 10^{-3}$ [7, 22], where the first error is experimental and the second theoretical.

In exclusive analyses, $|V_{ub}|$ is extracted from the measurement of the branching fraction $B \to \pi\ell\nu$. These analyses are usually characterized by a good signal/background ratio, but lead to measurements with larger statistical errors due to the small branching fractions of the mode studied. In addition, the theoretical errors are also larger, due to the uncertainties in the form factor calculation. Both experimental and theoretical errors are expected to decrease in the future, making this approach competitive with the inclusive method.

Further discussion on the measurement of $|V_{ub}|$ and $|V_{cb}|$ can be found in ref. [23].

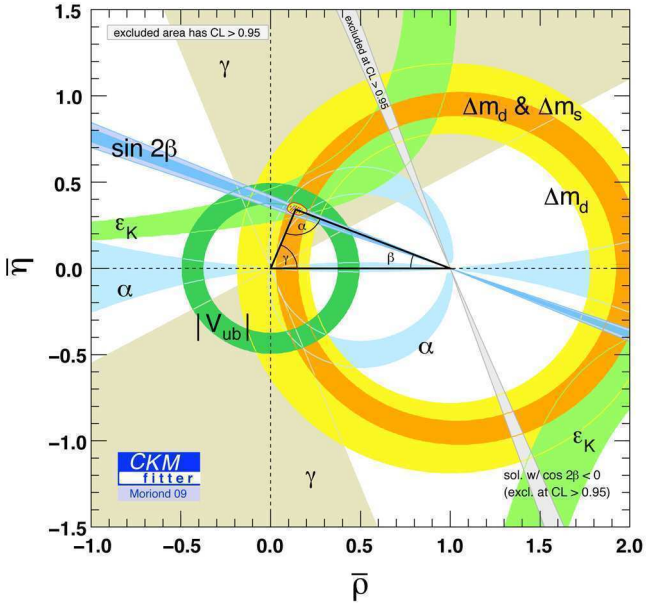

Fig. 6. – Constraints on the apex of the Unitarity Triangle resulting from all measurements.

7. – The right side of the Unitarity Triangle

The right side of the Unitarity Triangle is determined by the ratio of the CKM matrix elements $|V_{td}|$ and $|V_{ts}|$. This ratio can be determined with small ($\approx 4\%$) theoretical uncertainly from the measurement of ratio of the B_d^0 and B_s^0 mixing frequencies. Combining the measurements of Δm_s from the Tevatron [24] and world average Δm_d, we extract $|V_{td}/V_{ts}| = 0.2060 \pm 0.0007(\text{exp})^{+0.0081}_{-0.0060}(\text{theo})$ [25].

An independent determination of $|V_{td}/V_{ts}|$ can be obtained by the measuring the ratio of the branching fractions $BF(B \to \rho\gamma)/BF(B \to K^*\gamma)$. Recent measurements of the branching fractions of $B \to \rho\gamma$ from *BABAR* [26] and Belle [27] yield $|V_{td}/V_{ts}| = 0.210 \pm 0.015(\text{exp}) \pm 0.018(\text{theo})$. The comparison between the two measurements of $|V_{td}/V_{ts}|$ allows for an independent test of the Standard Model.

8. – Conclusion

Precise and redundant measurements of the sides and angles of the Unitarity Triangle provide a crucial test of CP violation in the Standard Model. The present constraints on the (ρ, η) plane are illustrated in fig. 6. The measurements of the angles β and α from the B factories provide two of the most precise constraints. The comparison shows good agreement between all measurements, as predicted by the CKM mechanism.

The accuracy of several measurements is now of the order of a few percent. This is about the level of precision needed for detecting $O(0.1)$ effects expected from New Physics. Final results from the B factories, results from new-generation flavor experiments, and progress in theory, especially lattice QCD, will be key to observing physics beyond the Standard Model in the flavor sector.

REFERENCES

[1] Kobayashi M. and Maskawa T., *Prog. Theor. Phys.*, **49** (1973) 652.
[2] Wolfenstein L., *Phys. Rev. Lett.*, **51** (1983) 1945.
[3] Aubert B. *et al.* (*BABAR* Collaboration), *Nucl. Instrum. Methods A*, **479** (2002) 1.
[4] Abashian A. *et al.* (Belle Collaboration), *Nucl. Instrum. Methods A*, **479** (2002) 117.
[5] Aubert B. *et al.* (*BABAR* Collaboration), *Phys. Rev. D*, **79** (2009) 072009.
[6] Chen K. F. *et al.* (Belle Collaboration), *Phys. Rev. Lett.*, **98** (2007) 031802.
[7] The Heavy Flavor Averaging Group, `http://www.slac.stanford.edu/xorg/hfag/`.
[8] London D. and Peccei R. D., *Phys. Lett. B*, **223** (1989) 257; Deshpande N. G. and Trampetic J., *Phys. Rev. D*, **41** (1990) 895; Fleischer R., *Z. Phys. C*, **62** (1994) 81; Deshpande N. G. and He X. G., *Phys. Lett. B*, **336** (1994) 471; Grossman Y., Ligeti Z., Nir Y. and Quinn H., *Phys. Rev. D*, **68** (2003) 015004; Gronau M. and Rosner J. L., *Phys. Lett. B*, **564** (2003) 90.
[9] Carter A. B. and Sanda A. I., *Phys. Rev. D*, **23** (1981) 1567; Bigi I. I. and Sanda A. I., *Nucl. Phys. B*, **193** (1981) 85; Fleischer R. and Mannel T., *Phys. Lett. B*, **511** (2003) 240; Grossman Y., Isidori G. and Worah M. P., *Phys. Rev. D*, **58** (1998) 057504; Grossman Y., Ligeti Z., Nir Y. and Quinn H., *Phys. Rev. D*, **68** (2003) 015004; Grossman Y. and Worah M. P., *Phys. Lett. B*, **395** (1997) 241; Fleischer R., *Int. J. Mod. Phys. A*, **12** (1997) 2459; London D. and Soni A., *Phys. Lett. B*, **407** (1997) 61.
[10] Aubert B. *et al.* (BABAR Collaboration), arXiv:0808.0700 [hep-ex]; Aubert B. *et al.* (BABAR Collaboration), *Phys. Rev. D*, **79** (2009) 052003.
[11] Aubert B. (The BABAR Collaboration), arXiv:0905.3615 [hep-ex].
[12] Aubert B. *et al.* (BABAR Collaboration), *Phys. Rev. D*, **76** (2007) 071101.
[13] Chen K. F. *et al.* (Belle Collaboration), *Phys. Rev. Lett.*, **98** (2007) 031802; Adachi I. *et al.* (Belle Collaboration), arXiv:0809.4366 [hep-ex]; Dalseno J. *et al.* (Belle Collaboration), *Phys. Rev. D*, **79** (2009) 072004; Abe K. *et al.* (Belle Collaboration), *Phys. Rev. D*, **76** (2007) 091103.
[14] Gronau M. and London D., *Phys. Rev. Lett.*, **65** (1990) 3381.
[15] Aubert B. *et al.* (BaBar Collaboration), *Phys. Rev. D*, **76** (2007) 052007.
[16] Aubert B. *et al.* (BaBar Collaboration), *Phys. Rev. D*, **78** (2008) 071104.
[17] Aubert B. *et al.* (BaBar Collaboration), arXiv:0901.3522 [hep-ex].
[18] The CKMfitter Collaboration, `http://ckmfitter.in2p3.fr/`.
[19] Gronau M. and Wyler D., *Phys. Lett. B*, **265** (1991) 172; Gronau M. and London D., *Phys. Lett. B*, **253** (1991) 483.
[20] Atwood D., Dunietz I. and Soni A., *Phys. Rev. Lett.*, **78** (1997) 3257.
[21] Giri A., Grossman Y., Soffer A. and Zupan J., *Phys. Rev. D*, **68** (2003) 054018.
[22] Gambino P., Giordano P., Ossola G. and Uraltsev N., *JHEP*, **0710** (2007) 058.
[23] Gambino P., these proceedings.
[24] Abulencia *et al.* (CDF Collaboration), *Phys. Rev. Lett.*, **97** (2006) 242003.
[25] Amsler C. *et al.* (Particle Data Group), *Phys. Lett. B*, **667** (2008) 1.
[26] Aubert B. *et al.* (BABAR Collaboration), *Phys. Rev. Lett.*, **98** (2007) 151802.
[27] Taniguchi N. *et al.* (Belle Collaboration), *Phys. Rev. Lett.*, **101** (111801) 2008; 129904 (Erratum).

IL NUOVO CIMENTO Vol. 32 C, N. 5-6 Settembre-Dicembre 2009
DOI 10.1393/ncc/i2010-10536-x

Colloquia: LaThuile09

LHCb status and early physics prospects

M. Pepe Altarelli(*) on behalf of the LHCb Collaboration
CERN, PH Department - CH-1211 Geneve 23, Switzerland

(ricevuto il 10 Novembre 2009; pubblicato online il 18 Gennaio 2010)

Summary. — LHCb is a dedicated detector for b and c physics at the LHC. I will present a concise review of the detector design and expected performance together with some first results on the commissioning of the different sub-systems based on cosmic data and particle beams delivered by the LHC during the summer of 2008. The experiment is ready to exploit first data expected from the LHC. An integrated luminosity of $\sim 0.3\,\mathrm{fb}^{-1}$, which should be collected during the first year of physics running, will already allow LHCb to perform a number of very significant mesurements with the potential of revealing New Physics effects, such as the measurement of the $\mathrm{B_s}$ mixing phase $\phi_{\mathrm{J}/\psi\,\phi}$, or the search of the decay $\mathrm{B_s^0} \to \mu^+\mu^-$ beyond the limit set by CDF and D0.

PACS 12.15.Ff – Quark and lepton masses and mixing.
PACS 12.15.Hh – Determination of Kobayashi-Maskawa matrix elements.
PACS 12.60.-i – Models beyond the standard model.
PACS 13.20.He – Decays of bottom mesons.

1. – Introduction

LHCb is a dedicated b- and c-physics precision experiment at the LHC that will search for New Physics (NP) beyond the Standard Model (SM) through the study of very rare decays of charm and beauty-flavoured hadrons and precision measurements of CP-violating observables. In the last decade, experiments at B factories have confirmed that the mechanism proposed by Kobayashi and Maskawa is the major source of CP violation observed so far. The SM description of flavour-changing processes has been confirmed in the b → d transition at the level of 10–20% accuracy. However, NP effects can still be large in b → s transitions, modifying the $\mathrm{B_s}$ mixing phase $\phi_{\mathrm{J}/\psi\,\phi}$, measured from $\mathrm{B_s^0} \to \mathrm{J}/\psi\,\phi$ decays, or in channels dominated by other loop diagrams, such as the very rare decay $\mathrm{B_s^0} \to \mu^+\mu^-$, or in $\mathrm{B_s^0} \to \phi\phi$. Therefore, the challenge of the future b experiments is to widen the range of measured decays, reaching channels that are strongly

(*) E-mail: monica.pepe.altarelli@cern.ch

suppressed in the SM and, more generally, to improve the precision of the measurements to achieve the necessary sensitivity to NP effects in loops. LHCb will extend the b-physics results from the B factories by studying decays of heavier b hadrons, such as B_s or B_c, which will be copiously produced at the LHC. It will complement the direct search of NP at the LHC by providing important information on the NP flavour structure through a dedicated detector, optimized for this kind of physics.

2. – b physics at the LHC: environment, background, general trigger issues

The LHC will be the world's most intense source of b-hadrons. In proton-proton collisions at $\sqrt{s} = 14\,\text{TeV}$, the $b\bar{b}$ cross-section is expected to be $\sim 500\,\mu\text{b}$ producing 10^{12} $b\bar{b}$ pairs in a standard (10^7 s) year of running at the LHCb operational luminosity of $2 \times 10^{32}\,\text{cm}^{-2}\,\text{s}^{-1}$. As in the case of the Tevatron, a complete spectrum of b-hadrons will be available, including B_s, B_c mesons and baryons such as Λ_b. However, less than 1% of all inelastic events contain b quarks, hence triggering is a critical issue.

At the nominal LHC design luminosity of $10^{34}\,\text{cm}^{-2}\,\text{s}^{-1}$, multiple p-p collisions within the same bunch crossing (so-called pile-up) would significantly complicate the b-production and decay-vertex reconstruction. For this reason the luminosity at LHCb will be locally controlled by appropriately focusing the beam to yield $\mathcal{L} = 2\text{–}5 \times 10^{32}\,\text{cm}^{-2}\,\text{s}^{-1}$, at which the majority of the events have a single p-p interaction. This matches well with the expected LHC conditions during the start-up phase. Furthermore, running at relatively low luminosity reduces the detector occupancy of the tracking systems and limits radiation damage effects.

The dominant production mechanism at the LHC is through gluon-gluon fusion in which the momenta of the incoming partons are strongly asymmetric in the p-p centre-of-mass frame. As a consequence, the $b\bar{b}$ pair is boosted along the direction of the higher momentum gluon, and both b-hadrons are produced in the same forward (or backward) direction in the p-p centre-of-mass frame. The detector is therefore designed as a single arm forward spectrometer covering the pseudorapidity range $1.9 < \eta < 4.9$, which ensures a high geometric efficiency for detecting all the decay particles from one b-hadron together with the decay particles from the accompanying $\bar{b}$-hadron to be used as a flavour tag. A modification to the LHC optics, displacing the interaction point by 11.25 m from the centre, has permitted maximum use to be made of the existing cavern by freeing 19.7 m for the LHCb detector components.

A detector design based on a forward spectrometer offers further advantages: b-hadrons are expected to have a hard momentum spectrum in the forward region; their average momentum is $\sim 80\,\text{GeV}/c$, corresponding to approximately 7 mm mean decay distance, which facilitates the separation between primary and decay vertices. This property, coupled to the excellent vertex resolution capabilities, allows proper time to be measured with a resolution of ~ 40 fs, which is crucial for studying CP violation and oscillations with B_s-mesons, because of their high oscillation frequency. Furthermore, the forward, open geometry allows the vertex detector to be positioned very close to the beams and facilitates detector installation and maintenance. In particular, the silicon detector sensors, housed, like Roman pots, in a secondary vacuum, are split in two halves that are retracted by ~ 30 mm from the interaction region before the LHC ring is filled, in order to allow for beam excursions during injection and ramping. They are then positioned within ~ 8 mm from the interaction region after stable beam conditions have been obtained.

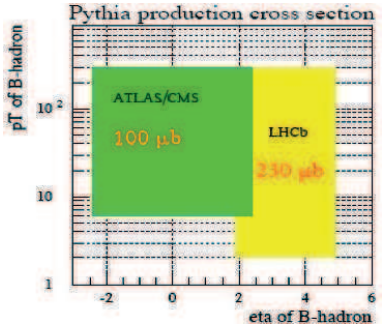

Fig. 1. – b-hadron transverse momentum as a function of the pseudorapidity η, showing the (η, p_{T}) region covered by ATLAS and CMS, compared to that covered by LHCb.

Figure 1 illustrates the LHCb acceptance in the plane (η, p_{T}) of the b-hadrons in comparison to that of ATLAS and CMS: ATLAS and CMS cover a pseudorapidity range of $|\eta| < 2.5$ and rely on high-p_{T} lepton triggers. LHCb relies on much lower p_{T} triggers, which are efficient also for purely hadronic decays. Most of the ATLAS and CMS b-physics programme will be pursued during the first few years of operation, for luminosities of order $10^{33}\,\mathrm{cm}^{-2}\,\mathrm{s}^{-1}$. Once LHC reaches its design luminosity, b physics will become exceedingly difficult for ATLAS and CMS due to the large pile-up (20 interactions per bunch crossing, on average), except for very few specific channels characterized by a simple signature, like $\mathrm{B}_{\mathrm{s}}^{0} \to \mu^{+}\mu^{-}$.

3. – Detector description and performance

The key features of the LHCb detector are:

– A versatile trigger scheme efficient for both leptonic and hadronic final states, which is able to cope with a variety of modes with small branching fractions;

– Excellent vertex and proper time resolution;

– Precise particle identification (ID), specifically for hadron (π/K) separation;

– Precise invariant mass reconstruction to efficiently reject background due to random combinations of tracks. This implies a high momentum resolution.

A schematic layout is shown in fig. 2. It consists of a vertex locator (VELO), a charge particle tracking system with a large aperture dipole magnet, aerogel and gas Ring Imaging Cherenkov counters (RICH), electromagnetic (ECAL) and hadronic (HCAL) calorimeters and a muon system. In the following, the most salient features of the LHCb detector are described in more detail. A much more complete description of the detector characteristics can be found in [1, 2].

3˙1. *Trigger*. – One of the most critical elements of LHCb is the trigger system. At the chosen LHCb nominal luminosity, taking into account the LHC bunch crossing structure, the rate of events with at least two particles in the LHCb acceptance is $\sim 10\,\mathrm{MHz}$ (instead of the nominal 40 MHz LHC crossing rate). The rate of events containing b-quarks is $\sim 100\,\mathrm{kHz}$, while the rate of events containing c quarks is much larger ($\sim 600\,\mathrm{kHz}$). However, the rate of interesting events is just a very small fraction of the total rate

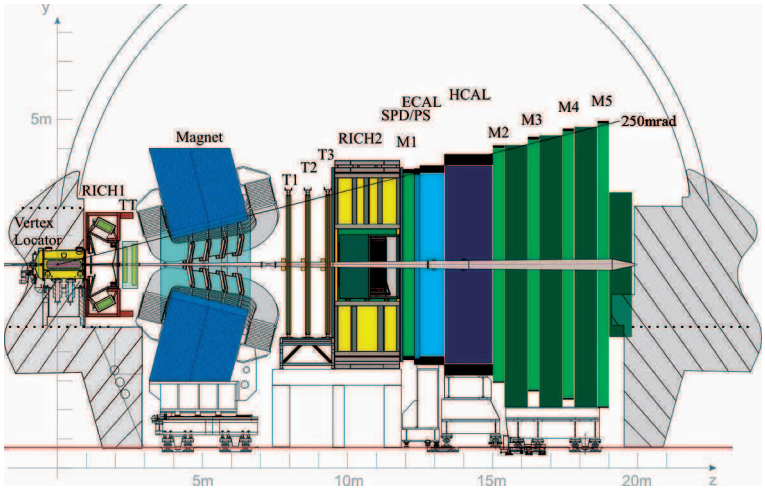

Fig. 2. – Side view of the LHCb detector showing the Vertex Locator (VELO), the dipole magnet, the two RICH detectors, the four tracking stations TT and T1-T3, the Scintillating Pad Detector (SPD), Preshower (PS), Electromagnetic (ECAL) and Hadronic (HCAL) calorimeters, and the five muon stations M1-M5.

($\sim$ Hz), due to the combined effect of branching fraction and detector acceptance, hence the need for a highly selective and efficient trigger.

The LHCb trigger exploits the fact that b-hadrons are long-lived, resulting in well-separated primary and secondary vertices, and have a relatively large mass, resulting in decay products with large p_{T}. It consists of two levels: Level0 (L0) and High Level Trigger (HLT). L0, implemented on custom electronics boards, is designed to reduce the input rate to 1 MHz at a fixed latency of 4 μs. At this rate, events are sent to a computer farm with up to $\sim$ 2000 multiprocessor boxes where several HLT software algorithms are executed. The HLT, which has access to the full detector information, reduces the rate from 1 MHz to $\sim$ 2 kHz.

L0, based on calorimeter and muon chamber information, selects muons, electrons, photons or hadrons above a given p_{T} or E_{T} threshold, typically in the range 1 to 4 GeV. The L0 hadron trigger occupies most of the bandwidth (700 kHz) and is unique within the LHC experiments. The muon triggers (single and double) select $\sim$ 200 kHz, while the rest of the bandwidth is due to the electromagnetic calorimeter triggers. Typically, the L0 efficiency is $\sim$ 50% for hadronic channels, $\sim$ 90% for muon channels and $\sim$ 70% for radiative channels, normalized to offline selected events.

The HLT algorithms are designed to be simple, to minimize systematic uncertainties, and fast. This is realized by reconstructing for each trigger only a few tracks, which are used for the final decision. The HLT comprises several paths (alleys) to confirm and progressively refine the L0 decision, followed by inclusive and exclusive selections. The choice of the alley depends on the L0 decision. The average execution time is few ms, which matches with the expected size of the CPU farm. The total trigger rate after the HLT is $\sim$ 2 kHz, a relatively high rate that also includes calibration samples to be used to understand the detector performance.

3˙2. *VELO and tracking system.* – The LHCb tracking system consists of a warm dipole magnet, which generates a magnetic field integral of $\sim$ 4 Tm, four tracking stations

and the VELO. The first tracking station located upstream of the magnet consists of four layers of silicon strip detectors. The remaining three stations downstream of the magnet are each constructed from four double layers of straw tubes in the outer region, covering most ($\sim 98\%$) of the tracker area, and silicon strips in the area closer to the beam pipe ($\sim 2\%$). However, $\sim 20\%$ of the charged particles traversing the detector go through the silicon inner tracker, due to the forward-peaked multiplicity distribution. The expected momentum resolution increases from $\delta p/p \sim 0.35\%$ for low-momentum tracks to 0.55% at the upper end of the momentum spectrum. This translates into an invariant mass resolution of $\delta M \sim 20\,\mathrm{MeV}/c^2$ for $\mathrm{B_s}$ decays into two charged tracks, such as $\mathrm{B_s^0} \to \mu^+\mu^-$, substantially better than in the general-purpose detectors at LHC.

The VELO consists of 21 stations, each made of two silicon half-disks, which measure the radial and azimuthal coordinates. The VELO has the unique feature of being located at a very close distance from the beam line (0.8 cm), inside a vacuum vessel, separated from the beam vacuum by a thin aluminum foil. This allows an impressive vertex resolution to be achieved, translating, for instance, in a proper time resolution of $\sim 36\,\mathrm{fs}$ for the decay $\mathrm{B_s^0} \to \mathrm{J}/\psi\,\phi$, *i.e.* a factor of ten smaller than the $\mathrm{B_s}$ oscillation period and a factor of two better than in the general-purpose detectors. The resolution on the impact parameter can be parameterized as $\delta IP \sim 14\,\mu\mathrm{m} + 35\,\mu\mathrm{m}/p_\mathrm{T}$.

3˙3. *Particle identification.* – Particle identification is provided by the two RICH detectors and the calorimeter and muon systems.

The RICH system is one of the crucial components of the LHCb detector. The first RICH, located upstream of the magnet, employs two radiators, $\mathrm{C_4H_{10}}$ gas and aerogel, ensuring a good separation in the momentum range from 2 to $60\,\mathrm{GeV}/c$. A second RICH in front of the calorimeters, uses a $\mathrm{CF_4}$ gas radiator and extends the momentum coverage up to $\sim 100\,\mathrm{GeV}/c$. The calorimeter system comprises a pre-shower detector consisting of 2.5 radiation length lead sheet sandwiched between two scintillator plates, a 25 radiation length lead-scintillator electromagnetic calorimeter of the shashlik type and a 5.6 interaction length iron-scintillator hadron calorimeter. The muon detector consists of five muon stations equipped with multiwire proportional chambers, with the exception of the centre of the first station, which uses triple-GEM detectors.

Electrons, photons and π^0s are identified using the calorimeter system. The average electron identification efficiency extracted from $\mathrm{J}/\psi \to \mathrm{e^+e^-}$ decays is $\sim 95\%$ for a pion misidentification rate of $\sim 0.7\%$. Muons are identified using the muon detector with an average efficiency in the acceptance extracted from $\mathrm{J}/\psi \to \mu\mu$ decays of $\sim 93\%$ for a pion misidentification rate of $\sim 1\%$. The RICH system provides good particle identification over the entire momentum range. The average efficiency for kaon identification for momenta between 2 and $100\,\mathrm{GeV}/c$ is $\epsilon(\mathrm{K} \to \mathrm{K}) \sim 95\%$, with a corresponding average pion misidentification rate $\epsilon(\pi \to \mathrm{K}) \sim 5\%$.

4. – Commissioning

During the summer of 2008 the commissioning activities converged into a fully operational detector. All sub-detectors were included under central control and data taking was extensively exercised. Although the geometry of the LHCb detector is not well suited for cosmic runs (the rate of "horizontal" cosmic events is well below 1 Hz), over one million cosmic events were recorded using muon and calorimeter cosmic triggers. These cosmic data have proved to be extremely useful to perform a coarse initial geometrical and time alignment of the larger detectors. As an example, fig. 3 shows the distributions

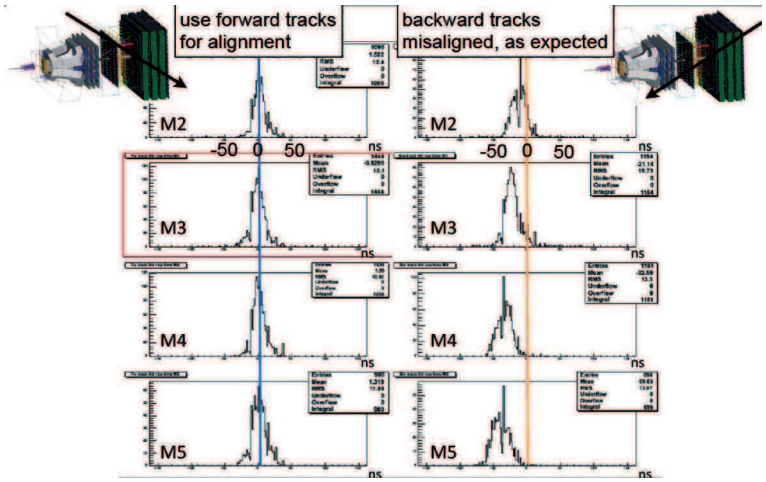

Fig. 3. – Readout time distribution with respect to reference time (in ns) for forward and backward tracks in four muon stations (M2-M5).

of the readout time, optimized for forward tracks, of four muon stations. The readout time is measured with respect to the trigger time as provided by the scintillator pad detector of the calorimeter system. The distributions are nicely centred at zero only for the forward tracks.

At the end of August 2008, the machine carried out several tests of the transfer line ("synchronization tests"). A beam of 450 GeV protons extracted from the SPS was injected into the LHC and dumped on an injection line beam stopper ("TED") located approximately 340 m downstream of LHCb. This produced a large flux of nearly parallel particles that hit the detector from the back, *i.e.* from the muon stations towards the VELO. These data were particularly useful for the time and position alignment of those sub-detectors (IT, TT and VELO) that could not make use of cosmic events, as they are either too small or too distant from the detectors providing the trigger. The initial alignment with reconstructed tracks indicated no major problems and a resolution in the expected range.

As an example, for the VELO the detector displacement was measured to be less than $\sim 10\,\mu$m with respect to the survey information. The achieved resolution was measured to match the binary resolution $\left(=\frac{\text{pitch}}{\sqrt{12}}\right)$, which is consistent with expectation, given that the large majority ($\sim 90\%$) of the used clusters are one-strip clusters. Improvements to the resolution are expected with an optimized tuning of the signal processing algorithms and of the readout time alignment. Moreover, the resolution is expected to be better for tracks at angles around 140 mrad, for which the charge sharing between adjacent strips is optimal.

5. – Early physics at LHCb

The objective of the very first running phase is to complete the commissioning of the sub-detectors and of the trigger. Large minimum bias data samples ($\sim 10^8$ per day at 2 kHz output rate) will be collected as soon as the LHC delivers p-p collisions using a simple interaction trigger based on total energy in the calorimeters. These data will provide a high-statistics and high-purity V^0 sample (K^0_S, Λ, $\overline{\Lambda}$), which can be used to probe

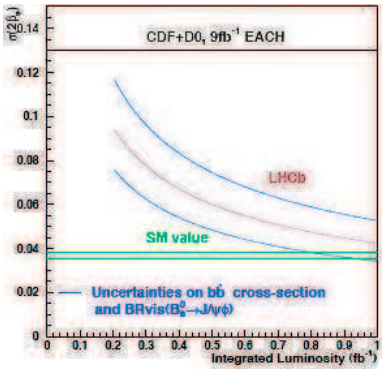

Fig. 4. – (Colour online) Statistical uncertainty on $\phi_{J/\psi\,\phi}$ *vs.* the integrated luminosity. The blue lines show the uncertainties coming from the $b\bar{b}$ cross-section and the visible branching ratio on $B_s^0 \to J/\psi\,\phi$. The green band is the SM value. The Tevatron line is the combined CDF/D0 uncertainty in 2008 scaled to $18\,\mathrm{fb}^{-1}$, as expected by the end of run 2.

the hadronization process in a rapidity range complementary to that of the other LHC detectors and in which phenomenological models tuned to Tevatron data show significant differences when extrapolated to LHC energies. Measurements will include differential cross-sections and production ratios for different strange particles as a function of rapidity and transverse momentum.

A simple, lifetime-unbiased muon trigger, requiring $p_T > 1\,\mathrm{GeV}/c$ at L0, will allow us to collect a large, clean sample of $J/\psi \to \mu\mu$ decays. With an integrated luminosity of $5\,\mathrm{pb}^{-1}$, $\sim 3\times10^6$ events are expected with a S/B of ~ 4 at $\sqrt{s} = 8\,\mathrm{TeV}$, which may be the initial LHC centre-of-mass energy. This sample can be used to extract both the prompt J/ψ and $b \to J/\psi$ production cross-sections in a region not accessible to other collider experiments. Other charmonia related measurements will also be performed, such as that of the J/ψ polarization or of the production of the exotic X, Y and Z charmonia states observed in recent years.

An integrated luminosity of 0.2–$0.3\,\mathrm{fb}^{-1}$, which should hopefully be collected during the first year of physics running, will already allow LHCb to realize a number of very significant b-physics measurements, with the potential of revealing NP effects, such as the measurement of the B_s mixing phase $\phi_{J/\psi\,\phi}$, the search of the decay $B_s^0 \to \mu^+\mu^-$ beyond the limit set by CDF and D0, or the study of the decay $B_d \to K^{*0}\mu^+\mu^-$ (for this last decay, with $0.2\,\mathrm{fb}^{-1}$ LHCb should be able to collect ~ 700 events, which is a larger sample than at all existing facilities combined).

A flavour tagged, angular analysis of the decay $B_s^0 \to J/\psi\,\phi$ allows the determination of a CP-violating phase $\phi_{J/\psi\,\phi}$. In the SM this phase is predicted to be $-2\beta_s \simeq -0.04$, where β_s is the smaller angle of the "b-s unitarity triangle". However NP could significantly modify this prediction, if new particles contribute to the B_s^0-$\overline{B_s^0}$ box diagram. In fact, the CDF and D0 Collaborations [3, 4] have reported a first measurement of the B_s mixing phase. Their combined result deviates from the SM prediction by $\sim 2.2\sigma$ with a central value for $2\beta_s$ as large as 0.77. LHCb has the capability to significantly improve the existing experimental knowledge of this phase thanks to the large signal yield ($\sim 12\,\mathrm{k}$ events for $0.2\,\mathrm{fb}^{-1}$), the excellent proper time resolution to resolve fast B_s oscillations ($\sim 40\,\mathrm{fs}$), the good flavour tagging ($\sim 6\%$), and the good control of the proper time and angular acceptance. Figure 4 shows the statistical uncertainty on the phase $\phi_{J/\psi\,\phi}$

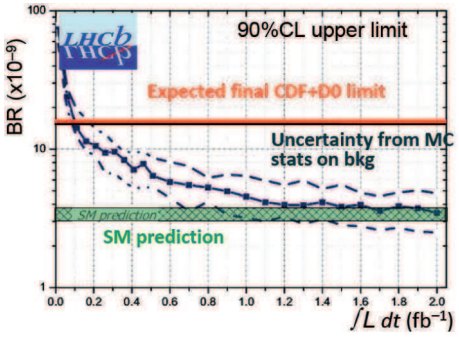

Fig. 5. – (Colour online) Expected 90% CL upper limit of $\mathrm{BR}(\mathrm{B}_\mathrm{s}^0 \to \mu^+\mu^-)$ in the absence of signal as a function of the integrated luminosity. The green band is the SM value. The Tevatron line is the combined CDF/D0 uncertainty in 2008 scaled to $18\,\mathrm{fb}^{-1}$, as expected by the end of run 2.

as a function of the integrated luminosity. As one can see, already with $0.3\,\mathrm{fb}^{-1}$, LHCb should be able to improve on the expected Tevatron limit.

The decay $\mathrm{B}_\mathrm{s}^0 \to \mu^+\mu^-$ has been identified as another very interesting potential constraint on the parameter space of models for physics beyond the SM. The BR for this decay is computed to be very small in the SM: $\mathrm{BR}(\mathrm{B}_\mathrm{s}^0 \to \mu^+\mu^-) = (3.35 \pm 0.32) \times 10^{-9}$ [5], but could be enhanced in certain NP scenarios. For example, in the MSSM, this branching ratio is known to increase as the sixth power of $\tan\beta = \nu_\mathrm{u}/\nu_\mathrm{d}$, the ratio of the two vacuum expectation values. Any improvement to this limit is therefore particularly important for models with large $\tan\beta$. The upper limit to the $\mathrm{B}_\mathrm{s}^0 \to \mu^+\mu^-$ branching ratio measured at the Tevatron is $\mathrm{BR}(\mathrm{B}_\mathrm{s}^0 \to \mu^+\mu^-) < 4.7 \times 10^{-8}$ at 90% CL [6, 7]. For this measurement, LHCb has developed an analysis based on the use of control channels to minimize the dependence on MC simulation. The main issue for this analysis is the rejection of the background, largely dominated by random combinations of two muons originating from two distinct b decays. This background can be kept under control by exploiting the excellent LHCb vertexing capabilities, and mass resolution. Figure 5 shows, as a function of the integrated luminosity, the BR value excluded at 90% CL. Already with $\sim 0.2\,\mathrm{fb}^{-1}$ LHCb should improve on the expected Tevatron limit, while a $\sim 3\sigma$ observation will require an integrated luminosity of $3\,\mathrm{fb}^{-1}$, assuming the SM value.

In subsequent years, the experiment will develop its full physics programme, and plans are to accumulate an integrated luminosity of $\sim 10\,\mathrm{fb}^{-1}$. Such a data sample will, for example, allow LHCb to improve the error on the CKM angle γ by a factor of $\sim$ five, and probe NP in rare B-meson decays with electroweak, radiative and hadronic penguin modes.

6. – Conclusions

The large $\mathrm{b\bar{b}}$ production cross-section at the LHC provides a unique opportunity to study in detail CP violation and rare b decays with the LHCb detector. In particular, production of $\mathrm{B_s}$ mesons could play a crucial role in disentangling effects originating from NP and a few observables sensitive to NP should already be accessible at the end of the 1st year of data taking. During the last year LHCb was fully installed and commissioned

using cosmic events and first LHC-induced tracks. At this point we are all eagerly waiting to exploit first data expected from the LHC in 2009/2010.

* * *

I would like to thank the Organizers of Les Rencontres for their kind invitation and my LHCb colleagues for providing the material discussed in this article, in particular Tatsuya Nakada for taking the time to read this manuscript.

REFERENCES

[1] LHCb Collaboration, *LHCb Reoptimized Detector, Design and Performance*, LHCC-2003-030 (2003).
[2] LHCb Collaboration, *The LHCb Detector at the LHC*, *JINST*, **3** (2008) S08005.
[3] CDF Collaboration, *First Flavor-Tagged determination of Bounds on Mixing-Induced CP Violation in* $B_s^0 \to J/\psi\,\phi$ *Decays*, *Phys. Rev. Lett.*, **100** (2008) 161802.
[4] D0 Collaboration, *Measurement of* B_s *mixing parameters from the flavor-tagged decay* $B_s^0 \to J/\psi\,\phi$, arXiv:0802.2255v1 [hep-ex] 2008.
[5] Blanke M., Buras. A., Guadagnoli D. and Tarantino C., arXiv:hep-ph/0604057v5 2006.
[6] CDF Collaboration, *Phys. Rev. A*, **100** (2008) 101802.
[7] D0 Collaboration, D0 note 5344-CONF (2007).

SESSION V - CP VIOLATION AND RARE DECAYS

Mario Antonelli	Precision test of the SM with K_{l2} and K_{l3} decays at KLOE
Francesca Bucci	The NA62 experiment
Marco Grassi	Status and perspectives of the $\mu^+ \to e^+\gamma$ decay search with the MEG experiment
Yuuji Unno	Rare decays and CP violation at B-factories
Peter Onyisi	Heavy-flavor physics at CLEO-c
Antonio Masiero	LFV and EDMs in SUSY with flavour symmetries

IL NUOVO CIMENTO Vol. 32 C, N. 5-6 Settembre-Dicembre 2009
DOI 10.1393/ncc/i2010-10532-2

Colloquia: LaThuile09

Precision test of the SM with K_{l2} and K_{l3} decays at KLOE

M. Antonelli

Laboratori Nazionali di Frascati dell'INFN - Via E. Fermi, 40
00044 Frascati (Rome) , Italy

(ricevuto il 10 Novembre 2009; pubblicato online il 18 Gennaio 2010)

Summary. — Kaon decay studies seeking new-physics (NP) effects in leptonic (K_{l2}) or semileptonic (K_{l3}) decays are discussed. A unitarity test of the first row of the CKM mixing matrix is obtained from the KLOE precision measurements of K_{l3} widths for $K^{\pm}$, K_L, and (unique to KLOE) K_S, complemented with the absolute branching ratio for the $K_{\mu 2}$ decay. KLOE results lead to constraints for NP models and can probe possible charged Higgs exchange contribution in SM extensions with two Higgs doublets. The main focus in the present document is set on a new measurement of $R_K = \Gamma(K_{e2})/\Gamma(K_{\mu 2})$ with an accuracy at the % level, aiming at finding evidence of deviations from the SM prediction induced by lepton-flavor violation NP effects.

PACS 13.20.Eb – Decays of K mesons.
PACS 13.66.Jn – Precision measurements in e^-e^+ interactions.

1. – Introduction

New precise measurements of $K \to l\nu_l(\gamma)$ (K_{l2}) and $K \to \pi l\nu_l(\gamma)$ (K_{l3}) decays can possibly shed light on new physics (NP). The first indication of the need of improving the present knowledge in this field was given by the 2004 version of the PDG: a deviation from unitarity of the CKM matrix was observed in the first row, amounting to more than two standard deviations [1],

$$\Delta = 1 - V_{ud}^2 - V_{us}^2 - V_{ub}^2 = 0.0043(16)_{Vud}(11)_{Vus}. \tag{1}$$

This called for new precise determinations of the V_{us} parameter of the CKM matrix, traditionally extracted from K_{l3} decays using the following expression:

$$\Gamma^i(K_{e3(\gamma),\mu 3(\gamma)}) = |V_{us}|^2 \frac{C_i^2 G_F^2 M^5}{128\pi^3} S_{\mathrm{EW}} \, |f_+^{K^0}(0)|^2 I^i_{e3,\mu 3} \, (1 + \delta^i_{e3,\mu 3}), \tag{2}$$

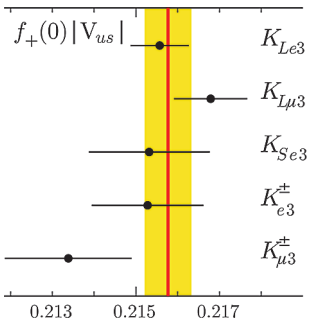

Fig. 1. – Five determinations of $f_+ \times |V_{us}|$ using the K_S lifetime (from PDG) as the only input other than KLOE measurements.

where i indexes $K^0 \to \pi^-$ and $K^+ \to \pi^0$ transitions for which $C_i^2 = 1$ and $1/2$, respectively, G_F is the Fermi constant, M is the appropriate kaon mass, and $S_{\rm EW}$ is a universal short-distance electroweak correction [2]. The δ^i term accounts for long-distance radiative corrections depending on the meson charges and lepton masses and, for $K^\pm$, for isospin-breaking effects. These corrections are presently known at the few-per-mille level [3]. The $f_+^{K^0}(0)$ form factor parametrizes the vector-current transition $K^0 \to \pi^-$ at zero momentum transfer t, while the dependence of vector and scalar form factors on t enters into the determination of the integrals $I_{e3,\,\mu3}$ of the Dalitz-plot density over the physical region.

After four years of analysis of KLOE data, we present the most comprehensive set of results from a single experiment, including BR's for K_{e3} and $K_{\mu3}$ decays for K_L [4] and $K^\pm$ [5], and the BR for $K_S \to \pi e\nu$ [6,7] (unique to KLOE); form factor slopes from analysis of K_{Le3} [8] and $K_{L\mu3}$ [9]; lifetime measurements for K_L [10] and $K^\pm$ [11]; the K^0 mass [12]. Using the K_S lifetime from PDG [13] as the only input other than KLOE measurements, we obtain five results for the product $f_+(0)|V_{us}|$ [14], as shown in fig. 1. The average of these has been obtained taking all correlations into account and it is $f_+(0) \times |V_{us}| = 0.2157(6)$. As a comparison, using data from KLOE, KTeV, NA48, and ISTRA+ experiments, the world average [15] is 0.2166(5). From the KLOE result and using $f_+(0) = 0.9644(49)$ from the UKQCD/RBC Collaboration [16], we obtain

$$|V_{us}| = 0.2237(13). \tag{3}$$

Using the world average [17] $V_{ud} = 0.97418(26)$ from $0^+ \to 0^+$ nuclear β decays, CKM unitarity can be seen to be satisfied: $\Delta = 9(8) \times 10^{-4}$.

KLOE has provided the most precise determination of the $K_{\mu2}$ BR [18], which can be linked to the ratio V_{us}/V_{ud} via the following relation [19]:

$$\frac{\Gamma(K \to \mu\nu)}{\Gamma(\pi \to \mu\nu)} = \frac{m_K \left(1 - m_\mu^2/m_K^2\right)^2}{m_\pi \left(1 - m_\mu^2/m_\pi^2\right)^2} \left|\frac{V_{us}}{V_{ud}}\right|^2 \frac{f_K^2}{f_\pi^2} C.$$

The theoretical inputs are the form-factor ratio f_K/f_π and the radiative corrections described by the factor C. We use $f_K/f_\pi = 1.189(7)$ from lattice calculations [20] and

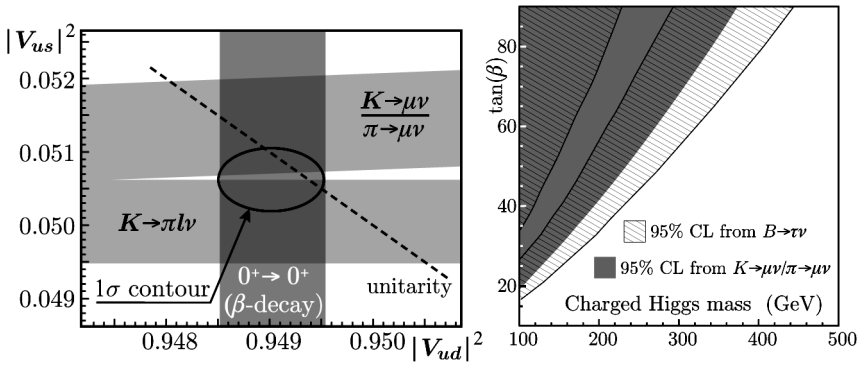

Fig. 2. – Left: the 1-σ fit result to V_{ud} and V_{us} is shown by the solid line ellipse, in agreement with the unitarity bound shown by the dashed line. Right: excluded regions from the analysis of decays $K \to \mu\nu$ (filled area) and $B \to \tau\nu$ (hatched area).

$C = 0.9930(35)$ [19], thus obtaining

$$|V_{us}/V_{ud}| = 0.2326(15). \tag{4}$$

From the KLOE results of eqs. (3) and (4), and from the world-average value of V_{ud}, a combined fit to V_{us} and V_{ud} has been done. The result is shown in left panel of fig. 2: the fit χ^2 is 2.34 for one degree of freedom (13% probability) and the results are: $|V_{us}| = 0.2249(10)$ and $|V_{ud}| = 0.97417(26)$, with a correlation of 3%. From these, not only can we now state that the CKM unitary holds to within 10^{-3}, $\Delta = 0.0004 \pm 0.0005_{Vud} \pm 0.0004_{Vus}$, but we can obtain severe constraints for many NP models.

1˙1. *Unitarity and coupling-universality tests.* – In the SM, unitarity of the weak couplings and gauge universality dictate:

$$G_{\rm F}^2\left(|V_{ud}|^2 + |V_{us}|^2\right) = G_\mu^2\ \left(V_{ub}^2 \text{ negligible}\right), \tag{5}$$

where G_μ^2 is the decay constant obtained from the measurement of the μ lifetime [21]. The above measurement of V_{us}^2 from KLOE inputs provides relevant tests for possible breaking of the CKM unitarity ($\Delta \neq 0$) and/or of the coupling universality ($G_F \neq G_\mu$). This can happen in some NP scenarios, some example of which we discuss below.

NP might lead to exotic and still unobserved μ decays contributing to the μ lifetime. The resulting total BR for μ exotic modes equals the unitarity violation Δ. Some of these modes, such as $\mu^+ \to e^+\overline{\nu}_e\nu_\mu$, are at present constrained to be less than $\sim 1\%$, so that information from unitarity improves on that from direct searches by more than a factor of 10 [22, 23].

The existence of additional heavy Z-bosons would influence unitarity at the loop level entering in muon and charged current semileptonic decays differently [24]: $\Delta = -0.01\lambda \ln[r_Z^2/(r_Z^2 - 1)]$, where $r_Z = m_{Z'}/m_W$ and λ is a model-dependent constant of order 1. In the case of $SO(10)$ grand unification, $\lambda \sim 1.9$ and a unitarity test from KLOE results yields $M_{Z'} > 750\,\text{GeV}$ at 95% of CL. In non-universal gauge interaction models, a tree-level contribution from Z' bosons appears, so that the unitarity test is sensitive to even larger masses [25].

In supersymmetric extensions of the SM (SUSY), loops affect muon and semileptonic decays differently. Unitarity can constrain SUSY up to mass scales of the order of 0.5 TeV, depending on the extent of cancellation between squark and slepton effects [26].

Measurements of K_{l2} widths can be linked to new-physics effects, too. The ratio of $K_{\mu 2}$-to-$\pi_{\mu 2}$ decay widths might accept NP contributions from charged-Higgs exchange [27, 28] in supersymmetric extensions of the SM with two Higgs doublets. In this scenario, the ratio V_{us}/V_{ud} extracted from $K_{\mu 2}$, $\pi_{\mu 2}$ should differ from that extracted from K_{l3} and superallowed Fermi transitions ("0^+"):

$$\left|\frac{V_{us}(K_{l2})V_{ud}(0^+)}{V_{us}(K_{l3})V_{ud}(\pi_{l2})}\right| = \left|1 - \frac{m_K^2(m_s - m_d)\tan^2\beta}{M_H^2 m_s(1+\epsilon_0\tan\beta)}\right|,$$

where $\tan\beta$ is the ratio of up- and down-Higgs vacuum expectation values, M_H is the charged Higgs mass, and $\epsilon_0 \sim 0.01$ [29]. The KLOE result of eq. (4) can be translated into an exclusion plot in the plane $\tan\beta$ *vs.* M_H (see right panel of fig. 2), showing that this analysis is complementary to and competitive with that [28] using the average $\mathrm{BR}(B \to \tau\nu) = 1.73(35) \times 10^{-4}$ of BaBar and Belle measurements [30].

1˙2. *Test of lepton-flavor violation.* – A significant effort has been devoted along the years to isolate signals from lepton flavor violating (LFV) transitions, which are forbidden or ultra-rare in the Standard Model (SM). The sensitivity to decays such as $\mu \to e\gamma$, $\mu \to eee$, $K_L \to \mu e(+\pi^0\text{'s})$, and others roughly improved by two orders of magnitude for each decade [31]. No signal has been observed, thus ruling out SM extensions with LFV amplitudes with mediator masses below ~ 100 TeV.

These results allowed the focus to be put on the detection of NP-LFV effects in loop amplitudes, by studying specific processes suppressed in the SM. In this field, a strong interest for a new measurement of the ratio $R_K = \Gamma(K \to e\nu)/\Gamma(K \to \mu\nu)$ has recently arisen, triggered by the work of ref. [32]. The SM prediction of R_K benefits from cancellation of hadronic uncertainties to a large extent and therefore can be calculated with high precision. Including radiative corrections, the total uncertainty is less than 0.5 per mille [33]:

$$R_K = (2.477 \pm 0.001) \times 10^{-5}. \tag{6}$$

Since the electronic channel is helicity-suppressed by the $V - A$ structure of the charged weak current, R_K can receive contributions from physics beyond the SM, for example from multi-Higgs effects inducing an effective pseudoscalar interaction. It has been shown in ref. [32] that deviations from the SM of up to few percent on R_K are quite possible in minimal supersymmetric extensions of the SM and in particular should be dominated by lepton-flavor–violating contributions with tauonic neutrinos emitted in the electron channel:

$$R_K = R_K^{\mathrm{SM}} \times \left[1 + \left(\frac{m_K^4}{m_H^4}\right)\left(\frac{m_\tau^2}{m_e^2}\right)\left|\Delta_R^{31}\right|^2 \tan^6\beta\right], \tag{7}$$

where M_H is the charged-Higgs mass, Δ_R^{31} is the effective e-τ coupling constant depending on MSSM parameters, and $\tan\beta$ is the ratio of the two vacuum expectation values. Note that the pseudoscalar constant f_K cancels in R_K^{SM}.

In order to compare with the SM prediction at this level of accuracy, one has to treat carefully the effect of radiative corrections, which contribute to nearly half the $K_{e2\gamma}$ width. In particular, the SM prediction of eq. (7) is made considering all photons emitted by the process of internal bremsstrahlung (IB) while ignoring any contribution from structure-dependent direct emission (DE). Of course both processes contribute, so in the analysis DE is considered as a background which can be distinguished from the IB width by means of a different photon energy spectrum.

Two experiments are participating in the challenge to push the error on R_K from the present 6% down to less than 1%. In 2007, KLOE and NA48/2 announced preliminary results [34] with errors ranging from 2% to 3%. Moreover, the new NA62 Collaboration collected more than 100 000 K_{e2} events in a dedicated run of the NA48 detector, aiming at reaching an accuracy of few per mille on R_K [35].

2. – Measuring R_K at KLOE

DAΦNE, the Frascati ϕ factory, is an e^+e^- collider working at $\sqrt{s} \sim m_\phi \sim 1.02\,\text{GeV}$. ϕ mesons are produced, essentially at rest, with a visible cross-section of $\sim 3.1\,\mu\text{b}$ and decay into K^+K^- pairs with a BR of $\sim 49\%$.

Kaons get a momentum of $\sim 100\,\text{MeV}/c$ which translates into a low speed, $\beta_K \sim 0.2$. K^+ and K^- decay with a mean length of $\lambda_\pm \sim 90\,\text{cm}$ and can be distinguished from their decays in flight to one of the two-body final states $\mu\nu$ or $\pi\pi^0$.

The kaon pairs from ϕ decay are produced in a pure $J^{PC} = 1^{--}$ quantum state, so that observation of a K^+ in an event signals, or tags, the presence of a K^- and vice versa; highly pure and nearly monochromatic $K^\pm$ beams can thus be obtained and exploited to achieve high precision in the measurement of absolute BR's.

The analysis of kaon decays is performed with the KLOE detector, consisting essentially of a drift chamber, DCH, surrounded by an electromagnetic calorimeter, EMC. A superconducting coil provides a 0.52 T magnetic field. The DCH [36] is a cylinder of 4 m in diameter and 3.3 m in length, which constitutes a fiducial volume for $K^\pm$ decays extending for $\sim 1\lambda_\pm$. The momentum resolution for tracks at large polar angle is $\sigma_p/p \leq 0.4\%$. The c.m. momenta reconstructed from identification of 1-prong $K^\pm \to \mu\nu, \pi\pi^0$ decay vertices in the DC peak around the expected values with a resolution of 1–1.5 MeV, thus allowing clean and efficient $K^\mp$ tagging.

The EMC is a lead/scintillating-fiber sampling calorimeter [37] consisting of a barrel and two endcaps, with good energy resolution, $\sigma_E/E \sim 5.7\%/\sqrt{E(\text{GeV})}$, and excellent time resolution, $\sigma_T = 54\,\text{ps}/\sqrt{E(\text{GeV})} \oplus 50\,\text{ps}$.

In early 2006, the KLOE experiment completed data taking, having collected $\sim 2.5\,\text{fb}^{-1}$ of integrated luminosity at the ϕ peak, corresponding to ~ 3.6 billion K^+K^- pairs. Using the present KLOE dataset, a measurement of R_K with an accuracy of about 1% has been performed.

Given the $K^\pm$ decay length of $\sim 90\,\text{cm}$, the selection of one-prong $K^\pm$ decays in the DC required to tag $K^\mp$ has an efficiency smaller than 50%. In order to keep the statistical uncertainty on the number of $K \to e\nu$ counts below 1%, a "direct search" for $K \to e\nu$ and $K \to \mu\nu$ decays is performed, without tagging. Since the wanted observable is a ratio of BR's for two channels with similar topology and kinematics, one expects to benefit from some cancellation of the uncertainties on tracking, vertexing, and kinematic identification efficiencies. Small deviations in the efficiency due to the different masses of e's and μ's will be evaluated using MC.

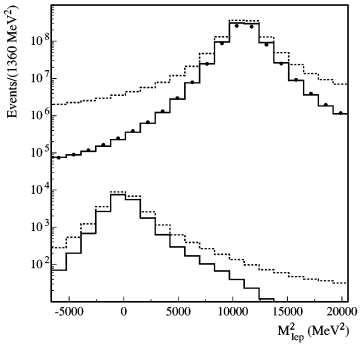

Fig. 3. – $M^2_{\rm lep}$ distribution before (dashed line) and after (solid line) quality cuts are applied.

Selection starts by requiring a kaon track decaying in a DC fiducial volume (FV) with laboratory momentum between 70 and 130 MeV, and a secondary track of relatively high momentum (above 180 MeV). The FV is defined as a cylinder parallel to the beam axis with length of 80 cm, and inner and outer radii of 40 and 150 cm, respectively. Quality cuts are applied to ensure good track fits.

A powerful kinematic variable used to distinguish $K \to e\nu$ and $K \to \mu\nu$ decays from the background is calculated from the track momenta of the kaon and the secondary particle: assuming $M_\nu = 0$, the squared mass of the secondary particle ($M^2_{\rm lep}$) is evaluated. The distribution of $M^2_{\rm lep}$ is shown in fig. 3 for MC events before and after quality cuts are applied. The selection applied is enough for clean identification of a $K \to \mu\nu$ sample, while further rejection is needed in order to identify $K \to e\nu$ events: the background, which is dominated by badly reconstructed $K \to \mu\nu$ events, is ~ 10 times more frequent than the signal in the region around M^2_e.

Information from the EMC is used to improve background rejection. To this purpose, we extrapolate the secondary track to the EMC surface and associate it to a nearby EMC cluster. For electrons, the associated cluster is close to the EMC surface and the cluster energy $E_{\rm cl}$ is a measurement of the particle momentum $p_{\rm ext}$, so that $E_{\rm cl}/p_{\rm ext}$ peaks around 1. For muons, clusters tend to be more in depth in the EMC and $E_{\rm cl}/p_{\rm ext}$ tends to be smaller than 1, since only the kinetic energy is visible in the EMC. Electron clusters can also be distinguished from μ (or π) clusters, since electrons shower and deposit their energy mainly in the first plane of EMC, while muons behave like minimum ionizing particles in the first plane and deposit a sizable fraction of their kinetic energy from the third plane onward, when they are slowed down to rest (Bragg's peak), see left panel of fig. 4. Particle identification has been therefore based on the asymmetry of energy deposits between the first and the next-to-first planes, on the spread of energy deposits on each plane, on the position of the plane with the maximum energy, and on the asymmetry of energy deposits between the last and the next-to-last planes. All pieces of information are combined with neural network (NN) trained on $K_L \to \pi\ell\nu$ data, taking into account variations of the EMC response with momentum and impact angle on the calorimeter. The distribution of the NN output, NN, for an independent $K_L \to \pi e\nu$ sample is shown in the right panel of fig. 4 for data and Monte Carlo (MC). Additional separation has been obtained using time-of-flight information.

The number of $K \to e\nu(\gamma)$ is determined with a binned likelihood fit to the two-dimensional NN *vs.* $M^2_{\rm lep}$ distribution. Distribution shapes for signal and $K_{\mu 2}$ background, other sources being negligible, are taken from MC; the normalization factors for

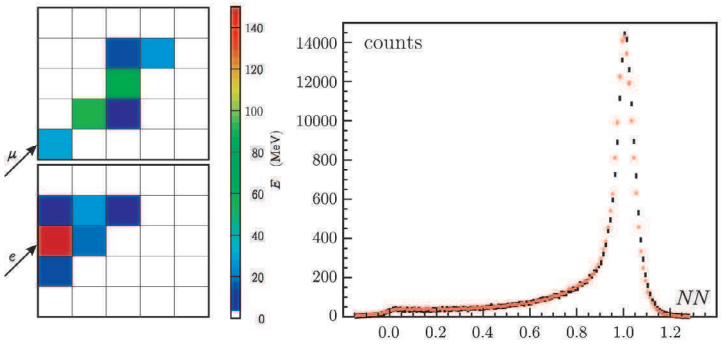

Fig. 4. – (Colour online) Left: cell distribution for 200 MeV e (top) and μ (bottom) from two selected events from $K_L \to \pi\ell\nu$. Right: distribution of NN output, NN, for electrons of a $K_L \to \pi e\nu$ sample from data (black histogram) and MC (red histogram).

the two components are the only fit parameters. In the fit region, a small fraction of $K \to e\nu(\gamma)$ events is due to the direct-emission structure-dependent component (DE): the value of this contamination, $f_{\rm SD}$, is fixed in the fit to the expectation from simulation. This assumption has been evaluated by performing a dedicated measurement of SD, which yielded as a by-product a determination of $f_{\rm SD}$ with a 4% accuracy. This implies a systematic error on K_{e2} counts of 0.2%, as obtained by repeating the fit with values of $f_{\rm SD}$ varied within its uncertainty.

In the fit region, we count 7064 ± 102 $K^+ \to e^+\nu(\gamma)$ and 6750 ± 101 $K^- \to e^-\bar{\nu}(\gamma)$ events. Figure 5 shows the sum of fit results for K^+ and K^- projected onto the $M^2_{\rm lep}$ axis in a signal- (NN > 0.98) and a background- (NN < 0.98) enhanced region.

To assess the uncertainty on the R_K measurement arising from limited knowledge of the momentum resolution, we have examined the agreement between the $M^2_{\rm lep}$ distributions for data and MC in the $K_{\mu 2}$ region. For the NN distribution, the EMC response at the cell level has been tuned by comparing data and MC samples. In order to evaluate the systematic error associated with these procedures, we studied the result variation with different fit range values, corresponding to a change for the overall K_{e2} purity from $\sim 75\%$ to $\sim 10\%$. The results are stable within statistical fluctuations. A systematic

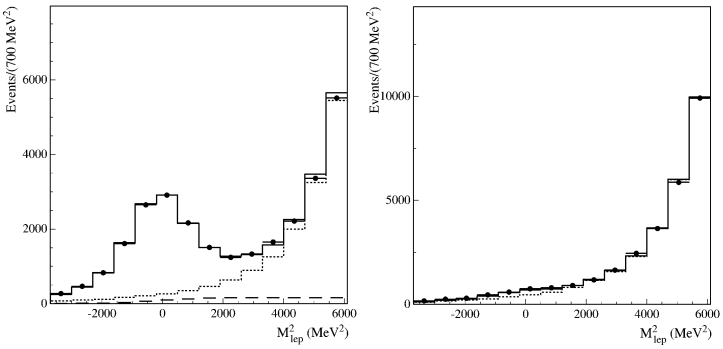

Fig. 5. – Fit projections onto the $M^2_{\rm lep}$ axis for two slices in NN output, NN > 0.98 and NN < 0.98, giving enhanced values of signal and background contributions, respectively.

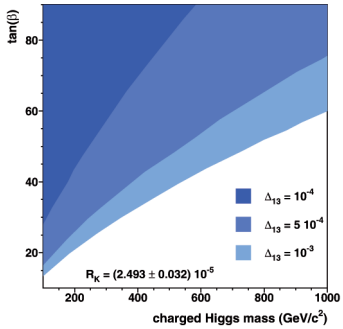

Fig. 6. – 95% CL excluded regions in the plane ($\tan\beta$, charged-Higgs mass) for $\Delta_R^{31} = 10^{-4}$, 5×10^{-3}, 10^{-3}.

uncertainty of 0.3% for R_K is derived "à la PDG" [13] by scaling the uncorrelated errors so that the reduced χ^2 value of results is 1.

The number of $K_{\mu 2}$ events in the same data set is extracted from a fit to the $M^2_{\rm lep}$ distribution. The fraction of background events under the muon peak is estimated from MC to be $< 0.1\%$. We count 2.878×10^8 (2.742×10^8) $K^+_{\mu 2}$ ($K^-_{\mu 2}$) events. Difference in K^+ and K^- counting is ascribed to K^- nuclear interactions in the material traversed.

The ratio of K_{e2} to $K_{\mu 2}$ efficiency is evaluated with MC and corrected for data-to-MC ratios using control samples. To check the corrections applied we also measured $R_3 = {\rm BR}(K_{e3})/{\rm BR}(K_{\mu 3})$, in the same data sample and by using the same methods for the evaluation of the efficiency as for the R_K analysis. We found $R_3 = 1.507(5)$ and $R_3 = 1.510(6)$, for K^+ and K^-, respectively. These are in agreement within a remarkable accuracy with the expectation [15] from world-average form-factor slope measurements, $R_3 = 1.506(3)$.

3. – R_K result and interpretation

The final result is $R_K = (2.493 \pm 0.025 \pm 0.019) \times 10^{-5}$. The 1.1% fractional statistical error has contributions from signal count fluctuation (0.85%) and background subtraction. The 0.8% systematic error has a relevant contribution (0.6%) from the statistics of the control samples used to evaluate corrections to the MC. The result does not depend on K charge: quoting olny the uncorrelated errors, $R_K(K^+) = 2.496(37)10^{-5}$ and $R_K(K^-) = 2.490(38)10^{-5}$.

The result is in agreement with SM prediction of eq. (6). Including the new KLOE result, the world average reaches an accuracy at the % level: $R_K = 2.468(25) \times 10^{-5}$. In the framework of MSSM with LFV couplings, the R_K value can be used to set constraints in the space of relevant paremeters (see eq. (7)). The regions excluded at 95% CL in the plane ($\tan\beta$, charged-Higgs mass) are shown in fig. 6 for different values of the effective LFV coupling Δ_R^{31}.

REFERENCES

[1] Particle Data Group, *Phys. Lett. B*, **592** (2004) 1.
[2] Sirlin A., *Rev. Mod. Phys.*, **50** (1978) 573; *Nucl. Phys. B*, **196** (1982) 83.
[3] Cirigliano V. *et al.*, *Eur. Phys. J. C*, **23** (2002) 121.

[4] KLOE Collaboration, *Phys. Lett. B*, **632** (2006) 43.
[5] KLOE Collaboration, *JHEP*, **0802** (2008) 098.
[6] KLOE Collaboration, *Phys. Lett. B*, **636** (2006) 173.
[7] KLOE Collaboration, *Eur. Phys. J. C*, **48** (2006) 767.
[8] KLOE Collaboration, *Phys. Lett. B*, **636** (2006) 166.
[9] KLOE Collaboration, *JHEP*, **0712** (2008) 105 and arXiv:0707.4631 (2007).
[10] KLOE Collaboration, *Phys. Lett. B*, **626** (2005) 15.
[11] KLOE Collaboration, *JHEP*, **0801** (2008) 073.
[12] KLOE Collaboration, *JHEP*, **0712** (2007) 073.
[13] Particle Data Group, *Phys. Lett. B*, **667** (2008) 1.
[14] KLOE Collaboration, *JHEP*, **0804** (2008) 059.
[15] FlaviaNet Working Group on Kaon Decays, arXiv:0801.1817.
[16] RBC/UKQCD Collaboration, arXiv:0710.5136 (2007).
[17] Towner I. S. and Hardy J. C., arXiv:0710.3181 (2007).
[18] KLOE Collaboration, *Phys. Lett. B*, **632** (2006) 76.
[19] Marciano W. J., *Phys. Rev. Lett.*, **93** (2004) 231803.
[20] HPQCD/UKQCD Collaboration, arXiv:0706.1726 (2007).
[21] MuLan Collaboration, *Phys. Rev. Lett.*, **99** (2007) 032001, arXiv:0704.1981.
[22] Review by W. J. Marciano and E. Blucher, pages 733-737 of ref. [13].
[23] Marciano W. J., *PoS KAON*, 003 (2007).
[24] Marciano W. and Sirlin A., *Phys. Rev. D*, **35** (1987) 1672.
[25] Lee K. Y., *Phys. Rev. D*, **76** (2007) 117702.
[26] Barbieri R. *et al.*, *Phys. Lett. B*, **156** (1985) 348; Hagiwara K. *et al.*, *Phys. Rev. Lett.*, **75** (1995) 3605; Kurylov A. and Ramsey-Musolf M., *Phys. Rev. Lett.*, **88** (2000) 071804.
[27] Hou W. S., *Phys. Rev. D*, **48** (1992) 2342.
[28] Isidori G. and Paradisi P., *Phys. Lett. B*, **639** (2006) 499.
[29] Isidori G. and Retico A., *JHEP*, **11** (2001) 001.
[30] Belle Collaboration, *Phys. Rev. Lett.*, **97** (2006) 251802; Babar Collaboration, *Phys. Rev. D*, **76** (2007) 052002. For Belle and Babar updates, see A. Bozek and E. Baracchini contributions in the 2009 edition of Rencontrès de Moriond EW.
[31] Landsberg L. G., *Phys. Atom. Nucl.*, **68** (2005) 1190 [arXiv:hep-ph/0410261].
[32] Masiero A., Paradisi P. and Petronzio R., *Phys. Rev. D*, **74** (2006) 011701.
[33] Cirigliano V. and Rosell I., arXiv:0707.4464 (2007).
[34] Sibidanov A. (KLOE Collaboration), arXiv:0707.4623 (2007); Fiorini L. (NA48 Collaboration), *Nucl. Phys. Proc. Suppl.*, **169** (2007) 205; Kozhuharov V. (NA48 Collaboration), *PoS KAON*, 049 (2007).
[35] See A. Winhart contribution in the 2009 edition of Rencontrès de Moriond EW.
[36] KLOE Collaboration, *Nucl. Instrum. Methods A*, **488** (2002) 51.
[37] KLOE Collaboration, *Nucl. Instrum. Methods A*, **482** (2002) 364.

IL NUOVO CIMENTO Vol. 32 C, N. 5-6 Settembre-Dicembre 2009
DOI 10.1393/ncc/i2010-10550-0

Colloquia: LaThuile09

The NA62 experiment

F. Bucci(*)

*Università di Firenze and INFN, Sezione di Firenze - Via G. Sansone 1
50019 Sesto Fiorentino (FI), Italy*

(ricevuto il 10 Novembre 2009; pubblicato online il 20 Gennaio 2010)

Summary. — We discuss the NA62 experiment which aims at the search for phenomena beyond the Standard Model (SM) by measuring the ratio $R_K = \Gamma(K^\pm \to e^\pm\nu(\gamma))/\Gamma(K^\pm \to \mu^\pm\nu(\gamma))$ and the ultra rare decay $K^+ \to \pi^+\nu\overline{\nu}$. First, we summarize the status of the R_K analysis, based on $\sim 40\%$ of the 2007-2008 NA62 data set, then, we describe the NA62 proposal to measure the branching ratio of the very rare decay $K^+ \to \pi^+\nu\overline{\nu}$ and we give an update on the status of the detectors needed to perform the measurement.

PACS 13.20.Eb – Decays of K mesons.
PACS 12.60.-i – Models beyond the standard model.

1. – Introduction

The information coming from the rare kaon decays is a key element to understand the flavor structure of possible physics beyond the SM. In this perspective, the decay modes which are interesting to measure are the leptonic decay $K \to l\nu$ (K_{l2}) and the flavor-changing neutral-current process $K \to \pi\nu\overline{\nu}$. Due to the uncertainties on non-perturbative quantities like f_K (the decay constant of K-mesons), we cannot fully exploit the leptonic decay K_{l2} in constraining new physics, in spite of the fact that it is possible to obtain non-SM contributions which exceed the high experimental precision which has been achieved on this mode. On the other hand, when considering the ratio R_K of the electronic and muonic decay modes, the hadronic uncertainties cancel to a very large extent. As a result, the SM prediction of R_K is known with excellent acccuracy [1]:

$$R_K^{\mathrm{SM}} = \left(\frac{m_e}{m_\mu}\right)^2 \left(\frac{m_K^2 - m_e^2}{m_K^2 - m_\mu^2}\right)^2 (1 + \delta R_{\mathrm{QED}}) = (2.477 \pm 0.001) \times 10^{-5},$$

(*) On behalf of NA62 Collaboration.

where $\delta R_{\rm QED} = (3.78 \pm 0.04)\%$ is a correction due to the inner bremsstrahlung (IB) part of the radiative $K_{e2\gamma}$ process. By definition, the IB part is included in R_K, while the structure-dependent (SD) part is not. The factor $(m_e/m_\mu)^2$ accounts for the helicity suppression of the $K^\pm \to e^\pm\nu$ mode.

The current PDG average, $R_K^{\rm PDG} = (2.35 \pm 0.11) \cdot 10^{-5}$, is based on the results of three experiments from the 1970's. The recent preliminary results from NA48/2 [2] and KLOE [3] experiments lead to 1% precision.

Enhancement of R_K by a few percent is quite possible in minimal supersymmetric extensions of the SM, and it is expected to be dominated by the lepton flavor-violating contributions with the emission of the tau neutrino [4]:

$$R_K^{\rm LFV} = \frac{\sum_i K \to e\nu_i}{\sum_i K \to \mu\nu_i} \cong \frac{\Gamma_{\rm SM}(K \to e\nu_e) + \Gamma(K \to e\nu_\tau)}{\Gamma_{\rm SM}(K \to \mu\nu_\mu)}, \quad i = e, \mu, \tau.$$

In the large $\tan\beta$ regime ($\tan\beta = 40$) and with a relatively heavy $H^\pm$ ($M_H = 500\,{\rm GeV}/c^2$), $R_K^{\rm LFV} \simeq R_K^{\rm SM}(1 + 0.013)$.

The unique feature of the rare decays $K \to \pi\nu\overline{\nu}$ is that their SM branching ratios can be computed to an exceptionally high degree of precision. These transitions are described, indeed, by Z^0-penguin and box diagrams mediated by $\mathcal{O}(G_F^2)$ interactions where a power-like GIM mechanism suppresses the non-perturbative effects. A related feature is that these decays are mediated by one single effective operator, whose hadronic matrix elements can be extracted from the well-measured $K \to \pi e\nu$ decay rates. The recent SM prediction reads [5]

$${\rm BR}(K^+ \to \pi^+\nu\overline{\nu}) = (0.85 \pm 0.07) \times 10^{-10}, \qquad {\rm BR}(K_L \to \pi^0\nu\overline{\nu}) = (2.76 \pm 0.40) \times 10^{-11}.$$

The precision of the theoretical predictions contrasts with the large uncertainties affecting the current experimental results [6, 7]:

$${\rm BR}(K^+ \to \pi^+\nu\overline{\nu}) = 1.73^{+1.15}_{-1.05} \times 10^{-10}, \qquad {\rm BR}(K_L^0 \to \pi^0\nu\overline{\nu}) \leq 6.7 \cdot 10^{-8}\ 90\%\,{\rm CL}.$$

The clean theoretical character of $K \to \pi\nu\overline{\nu}$ decays remains valid in all realistic extensions of the SM. As a result, precise measurements of ${\rm BR}(K \to \pi\nu\overline{\nu})$ provide unique and clean information about the flavor structure of any extension of the SM.

2. – The NA62 experiment

The NA62 experiment is a fixed target experiment at the Super Proton Syncrotron (SPS) of CERN which inherits from the experience, the infrastructure and some of the detectors of the NA48s experiments. Two phases can be distinguished for the NA62 experiment. In the first one, the aim is the R_K measurement with an accuracy better than 0.4% on data collected during 2007 and 2008. The second is the $K^+ \to \pi^+\nu\overline{\nu}$ measurement with a 10% accuracy.

3. – The R_K measurement

NA62 collected almost $160 \cdot 10^3$ K_{e2} candidates during four months of data taking in 2007 and additional two weeks in 2008. To improve the $K_{e2}/K_{\mu2}$ separation, a kaon beam with a $75\,{\rm GeV}/c$ central momentum and a narrow momentum band ($\Delta(p)/p = 2\%$)

was used. The K_{e2} decay signature consists of a single reconstructed track, thus the background in the K_{e2} sample induced by the beam halo becomes an important issue. Since the beam halo background was much higher for K^-_{e2} ($\sim 20\%$) than for K^+_{e2} ($\sim 1\%$), most of the data sample ($\sim 90\%$) was taken with K^+ beam only and about 10% with K^- beam only. K_{e2} and $K_{\mu 2}$ were collected simultaneously so that the results do not depend on the kaon flux measurement and many systematic effects cancel at first order. Detailed Monte Carlo (MC) simulations have been developed, however, they are used only to evaluate the geometric acceptance corrections and the "energetic" bremsstrahlung events for muons as discussed below. R_K is computed in bins of the reconstructed momentum of the charged track.

The following subdetectors, located downstream a vacuum decay volume, are relevant for the R_K measurement:

– A magnetic spectrometer composed of four drift chambers (DCHs) and a spectrometer magnet used to measure the momenta of the charged particles. Each chamber has four views. The resolution of the track momentum is $\sigma(p)/p = (0.47 \oplus 0.02\, p)\%$ (p in GeV/c).

– A plastic scintillator hodoscope (HOD) with good time resolution ($\sigma(t) \sim 200\,\text{ps}$) used to produce fast trigger signals.

– A liquid-krypton electromagnetic calorimeter (LKr) used for gamma detection and particle identification. It is an almost homogeneous ionization chamber with high granularity. The energy resolution is $\sigma(E)/E = (3.2/\sqrt{E} \oplus 9.0/E \oplus 0.42)\%$ (E in GeV).

3˙1. *Event selection*. – Due to the topological similarity of K_{e2} and $K_{\mu 2}$ decays, a large part of the selection conditions is common for both channels, which leads to cancellations of systematic uncertainties in R_K. We require:

– only one charged particle track reconstructed by the spectrometer within the geometrical acceptance with a momentum between 15 and 65 GeV/c and a good reconstructed vertex;

– no cluster in the LKr associated to a track with an energy $> 2\,\text{GeV}$.

To separate K_{e2} from $K_{\mu 2}$ decays, we use

– Particle identification based on the ratio of the track energy deposit in the LKr to its momentum measured by the spectrometer (E/p). Particles with E/p between 0.95 and 1.1 are identified as electron, particles with E/p less than 0.2 are identified as muon.

– Kinematical identification of K_{e2} and $K_{\mu 2}$ based on the reconstruction of the squared missing mass, $m^2_{\text{miss}} = (p_K - p_l)^2$, assuming the track to be an electron or a muon. A sufficient kinematical separation of K_{e2} and $K_{\mu 2}$ decays in the region of high lepton momentum ($p > 30\,\text{GeV}/c$) is not achievable.

3˙2. *Background*. – In very rare cases a muon can deposit over $\sim 95\%$ of its energy in the LKr calorimeter by "energetic" bremsstrahlung events, faking an electron. The probability of such an event in the NA62 experimental conditions is $\sim 3 \times 10^{-6}$. However, due to the helicity suppression of the electron channel, the background in the

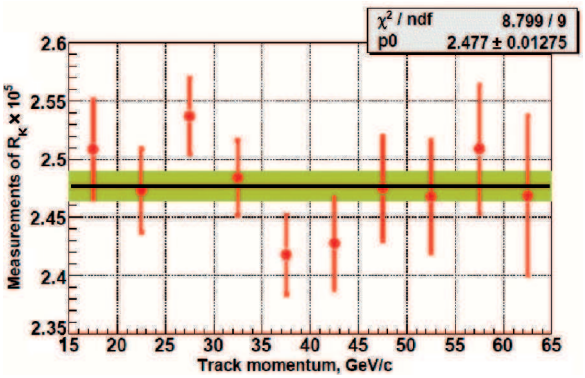

Fig. 1. – Ten independent measurements of R_K in bins of track momentum. An overall offset is applied to hide the result. Uncertainties due to $K_{e2\gamma}$ background correlated between momentum bins are excluded.

K_{e2} sample originating from the $K_{\mu 2}$ decays amounts to several percent and is one of the central issues of the analysis. We perform a direct measurement of this probability to validate in the highly energetic muon range the theoretical computation of the bremsstrahlung cross-section which is used to evaluate the $K_{\mu 2}$ background. To collect pure muon sample and avoid the electron contamination from muon decays, a lead wall was installed between the hodoscope planes during certain periods of data taking. The measured momentum dependence of the probability is in excellent agreement with the results obtained from simulation. The simulation also demonstrates that the presence of the lead wall significantly modifies the probability. The preliminary result for the background contamination is $(8.07 \pm 0.21)\%$. The uncertainty is due to the limited size of the data sample used to validate the MC simulation with the lead wall setup. Analysis with additional muon samples collected in 2008 is expected to improve the precision of the estimation.

By definition, another background source for the K_{e2} decay is the SD radiative $K_{e2\gamma}$ decay. In this case the background contamination is evaluated by using MC simulation and the uncertainty is due to the limited experimental and theoretical knowledge of the process. Fortunately, the relevant $K_{e2\gamma}$ kinematic region is accessible for a model-independent branching ratio measurement. Such a measurement, based on the NA62 2007 data sample, has started and is expected to improve the corresponding systematic uncertainty on R_K.

The background contamination in the K_{e2} sample induced by beam halo muons decaying to electrons kinematically and geometrically compatible to a K_{e2} decay is directly measured with the 2007 K^- only sample to be $(1.23 \pm 0.07)\%$. An additional K^- only sample collected in 2008, which is half the size of the 2007 one, will allow a further improvement of the uncertainty. Beam halo contamination in the $K_{\mu 2}$ sample is measured to be 0.14% with the same technique as for the K_{e2} decay. Other minor background contributions to the $K^\pm \to e^\pm \nu$ decay ($\sim 0.1\%$) are due to $K^+ \to \pi^0 e^+ \nu$ and $K^+ \to \pi^+ \pi^0$ decays.

3˙3. *Analysis summary and prospects.* – The independent measurements of R_K in track momentum bins performed on $\sim 40\%$ of the whole data sample are presented in fig. 1 with an overall offset artificially applied to set the result of the fit to the SM expectation. The

TABLE I. – *Summary of the main uncertainties on the R_K measurement.*

Source	$\delta R_K/R_K$
Statistical	0.43%
$K_{\mu 2}$	0.25%
K_{e2}	0.32%
Beam halo	0.10%
Total	$\sim 0.60\%$

stability of R_K over momentum bins points to a good control over the main systematic effects. The statistical and the systematic uncertainties are listed in table I. The whole data sample of $160 \cdot 10^3$ K_{e2} candidates will allow pushing the statistical uncertainty below the 0.3% level and the ultimate precision of the measurement is expected to reach 0.4%, as declared in the proposal [8].

4. – The $K^+ \to \pi^+ \nu\overline{\nu}$ measurement

The NA62 Collaboration has proposed [9] to measure the branching ratio of the very rare decay $K^+ \to \pi^+ \nu\overline{\nu}$. The aim is to observe $\sim$ 100 signal events in two years of data taking with a background-to-signal ratio smaller than 10%. To have a larger signal acceptance (10%), we propose to study the reaction in flight.

4˙1. *Kinematics and backgrounds.* – The signature of the $K^+ \to \pi^+ \nu\overline{\nu}$ event is only one track in the final state and anything else. The main background sources are the $K^+ \to \mu^+ \nu$ (63.5%) and the $K^+ \to \pi^+ \pi^0$ (20.9%) decays.

Background events rejection relies on:

– precise timing to associate the outgoing π^+ to the correct incoming K^+,

– kinematic rejection of backgrounds induced by two- and three-body kaon decays,

– μ and γ veto,

– particle identification (K^+/π^+ and π^+/μ^+).

4˙2. *Detector layout.* – The detector layout is shown in fig. 2. A 75 GeV/c unseparated hadron beam with an instantaneous rate of $\sim$ 800 MHz and a kaon fraction of $\sim$ 6% enters the decay tank. Particle identification of the beam particles is provided by a differential Čerenkov counter (CEDAR). The timing, tracking and momentum measurement of the beam particles is provided by silicon micro-pixel detectors (GTK) placed in a four-dipole magnetic achromat. The decay tank is surrounded by twelve stations of photon anti-counters (ANTI) and the decay particles are tracked by four stations of straw tubes (STRAWs) operating in vacuum to reduce the multiple scattering effects. The π/μ separation up to 35 GeV/c is provided by a ring imaging Čerenkov detector (RICH). The NA48 liquid-krypton calorimeter (LKr) is used as a photon veto in the forward region and a muon veto detector (MUV) provides fast muon rejection. The sensitivity of the experiment is limited by the rate that can be handled by the GTK detectors.

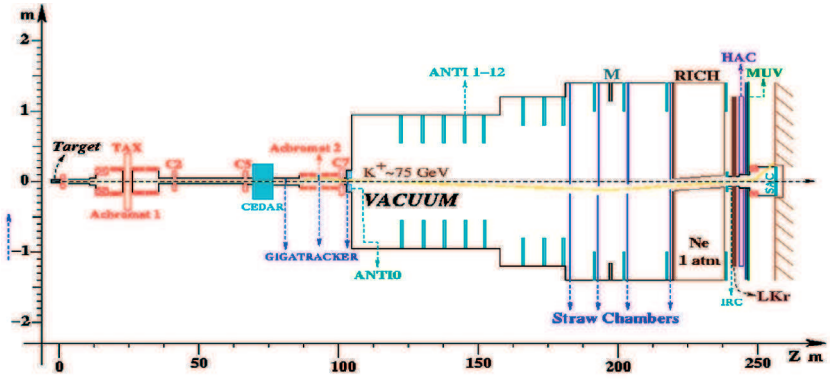

Fig. 2. – The NA62 detector layout.

4·3. *Experimental requirements.* – To allow the association with the decay particle without too many ambiguities introduced by accidental tracks, the GTK must provide a time resolution of $\sim 200\,\text{ps}$ per station, while the crossing time of the decay pion must be measured by the RICH with a resolution of $\sim 100\,\text{ps}$.

We define the missing squared mass $m^2_{\text{miss}} = (p_K - p_\pi)^2$ on the assumption that the charged decay product is a pion. About 92% of the total background is kinematically constrained and can be rejected by applying a cut on m^2_{miss}. By assuming a 10% signal acceptance, a background-to-signal ratio smaller than 10% requires a resolution on $m^2_{\text{miss}} \sim 10^{-3}\,\text{GeV}^2/c^4$, which implies stringent requirements on the GTK and STRAWs performances ($\sigma \sim 100\,\mu\text{m}$). The remaining 8% of background spams across the signal regions. In this case, rejection relies only on γ, μ veto and particle identification.

We need a muon rejection with an inefficiency below 10^{-7} and a 10^{-8} inefficiency in vetoing the π^0. A muon rejection factor of 10^{-5} can be achieved exploiting the different penetration probability through matter of muons and pions. A further $5 \cdot 10^{-3}$ suppression factor can be provided by the RICH. As far as the π^0 veto is concerned, by limiting the highest range of the π^+ to $35\,\text{GeV}/c$ one ensures that, for the potentially dangerous backgrounds originating from the $K^+ \to \pi^+\pi^0$ decay, at least 40 GeV of electromagnetic energy is deposited in hermetic calorimeters so that the π^0 can hardly be missed. According to our estimates, based on data accumulated in NA48 and test beams and simulation the photon detection efficiency satisfies the experiment specifications for the π^0 rejection.

4·4. *Status of the experiment.* – The GKT will be made of three silicon pixel stations placed along the beam line. The sensor technology is based on p-in-n. Each station covers an area of $60 \times 27\,\text{mm}^2$ with the area split into $300 \times 300\,\mu\text{m}^2$ pixels $200\,\mu\text{m}$ thick. Important R&D studies are underway concerning sensors, bump-bonding, cooling and read-out chips [10].

STRAWs will operate in vacuum to minimize the multiple scattering of the outgoing pion. The STRAW tracker will contain four chambers. Each chamber will have four views (x, y, u, v). The straw wall will be $36\,\mu\text{m}$ metalised Mylar. The baseline for the detector gas is a mixture of CO_2 (80%), Isobutan C_4H_{10} (10%) and CF_4 (10%). A prototype of the STRAW tracker was operated in a vacuum tank in 2007 and 2008 at the CERN SPS. The achieved position resolution is in line with the expectations.

TABLE II. – *Signal and background events expected in one year of* NA62 *data taking.*

Decay mode	Events/year
Signal (flux 4.8×10^{12})	55
$K^+ \to \pi^+\pi^0$	2.4
$K^+ \to \mu^+\nu$	1.2
$K^+ \to e^+\pi^+\pi^-\nu$	≤ 1.6
Other 3-track decays	≤ 0.8
$K^+ \to \pi^+\pi^0\gamma$	1.1
$K^+ \to \mu^+\nu\gamma$	0.4
$K^+ \to 1^+(\mu^+)\pi^0\nu$, others	—
Total expected background	≤ 7.5

The RICH will be composed by a cylindrical vessel 18 m long with a diameter of ~ 4 m filled with neon at atmospheric pressure. Tests performed with a full length RICH prototype have measured a 50 μrad angle resolution and a 65 ps time resolution [11], which satisfies completely the experimental requirements. Additional tests are foreseen to validate the π/μ separation.

The photon veto system must be fully hermetic in an angular range from 0 to 50 mrad. It will be composed by the ANTIs, the NA48 LKr calorimeter and two forward calorimeters (IRC and SAC). The ANTIs will be made of lead glass blocks recovered from the OPAL electromagnetic calorimeter and arranged into 12 stations surrounding the decay vacuum. A 25 blocks prototype has been tested at BTF in Frascati with a 471 MeV electron beam. An energy resolution $\sigma(E)/E = 9.7\%$ and a cluster time resolution $\sigma(t) = 560$ ps have been measured. An additional test with μ and K has been performed at CERN in October 2008. Extensive measurements of the photon detection capability of the NA48 LKr were performed using a sample of $K^+ \to \pi^+\pi^0$ collected by NA48. The inefficiency to detect high-energy photons ($E > 10$ GeV) was found to be less than 10^{-5}.

4˙5. *Perspectives*. – The sensitivity of the experiment was evaluated by Monte Carlo simulation. The number of expected signal and background events for one year of data taking is shown in table II. We expect to measure the branching ratio of $K^+ \to \pi^+\nu\overline{\nu}$ with a 10% accuracy in two years of data taking.

5. – Conclusions

The R_K analysis on a partial data sample ($\sim 40\%$) is well advanced and aims at a preliminary result with $\sim 0.7\%$ accuracy. The analysis demonstrates that the overall uncertainty of 0.4%, as declared in the proposal, is within reach.

The experiment to measure the branching ratio of $K^+ \to \pi^+\nu\overline{\nu}$ has been approved by the CERN SPSC and Research Board. The R&D program is close to the end and the construction has already started. The construction should take about two and a half years and the first data taking is expected to take place in 2012.

REFERENCES

[1] Cirigliano V. and Rosell I., *Phys. Rev. Lett.*, **99** (2007) 231801.
[2] Fiorini L., *PoS (HEP2005)* 288 (2005); Kozhuharov V., *PoS (KAON)* 049 (2007).
[3] Antonelli M., these proceedings.
[4] Masiero A., Paradisi P. and Petronzio R., *Phys. Rev. D*, **74** (2006) 011701.
[5] Brod J., to be published in the *Proceedings of the CKM Workshop 2008*.
[6] Artamonov A. V. *et al.* (E949 Collaboration), *Phys. Rev. Lett.*, **101** (2008) 191802 [arXiv:0808.2459].
[7] Ahn J. K. *et al.* (E391a Collaboration), *Phys. Rev. Lett.*, **100** (2008) 201802 [arXiv:0712.4164].
[8] NA48/2 and P-326 Status Report, CERN-SPSC-2006-033.
[9] Anelli G. *et al.* (P326 Collaboration), Proposal to measure the rare decay $K^+ \to \pi^+ \nu\overline{\nu}$ at the CERN SPE, CERN-SPSC-2005-013 and CERN-SPSC-P-326 (2005).
[10] Fiorini M. *et al.*, *Nucl. Instrum. Methods A*, **572** (2007) 290.
[11] Anzivino G. *et al.*, *Nucl. Instrum. Methods A*, **593** (2008) 314.

IL NUOVO CIMENTO Vol. 32 C, N. 5-6 Settembre-Dicembre 2009
DOI 10.1393/ncc/i2010-10527-y

Colloquia: LaThuile09

Status and perspectives of the $\mu^+ \to e^+\gamma$ decay search with the MEG experiment

M. Grassi on behalf of the MEG Collaboration
INFN, Sezione di Pisa - Largo Bruno Pontecorvo 3, 56127 Pisa, Italy

(ricevuto il 10 Novembre 2009; pubblicato online il 15 Gennaio 2010)

Summary. — The MEG experiment aims at evidence of new physics beyond the Standard Model by searching for charged lepton flavour violation with the $\mu^+ \to e^+\gamma$ decay. This experiment will improve the present experimental limit by two orders of magnitude in the upcoming three years. Novel detectors were developed for this measurement as well as multiple and redundant calibration methods which are mandatory to constantly monitor the performances of the apparatus. The status of the MEG experiment is reviewed and the future perspectives are discussed.

PACS 11.30.Hv – Flavor symmetries.
PACS 13.35.Bv – Decays of muons.
PACS 14.60.Ef – Muons.

1. – Introduction

The $\mu^+ \to e^+\gamma$ decay is forbidden in the Standard Model of electroweak interactions because of the assumed symmetry of lepton flavour conservation. Though it has never been observed, with a current upper limit on the branching ratio of 1.2×10^{-11} set by the MEGA experiment [1], it is believed to take place at a certain level in any viable extension of the Standard Model [2, 3]. There is a wide class of models, namely Grand-Unified Supersymmetric theories, which predict $\mu^+ \to e^+\gamma$ decay to exist with a branching ratio in the range 10^{-14}–10^{-11}.

The MEG experiment will search for this lepton flavour violating decay with a sensitivity of $\approx 10^{-13}$ on the branching ratio. The discovery of this decay would be the first direct evidence of new physics beyond the Standard Model, while the absence of the signal in this range would pose important constraints for the development of new theories.

2. – Signal and background

The $\mu^+ \to e^+\gamma$ decay is characterized by a two-body final state, with the positron and photon being coincident in time and emitted back-to-back in the rest frame of the muon, each with an energy equal to half that of the muon mass.

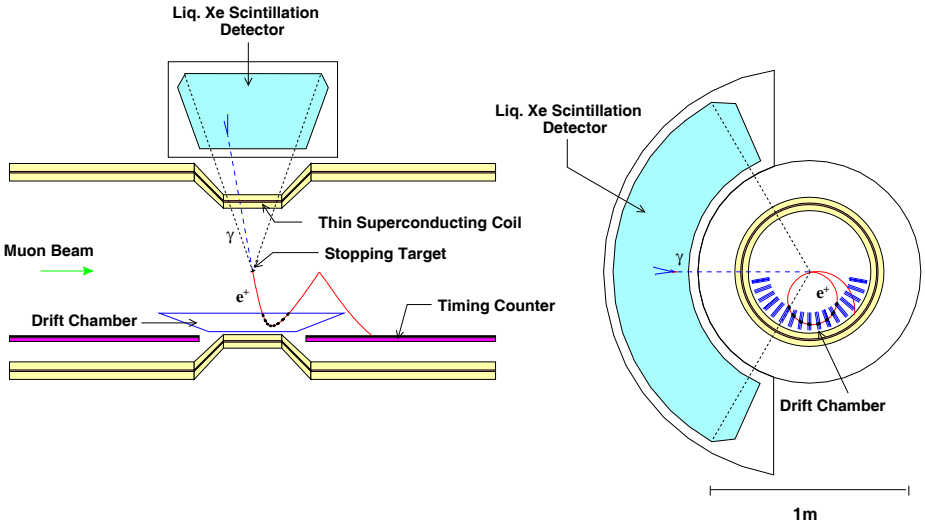

Fig. 1. – Schematic drawing of the MEG detector.

The two major sources of background are the radiative muon decay (RMD) $\mu^+ \to e^+\nu_e\bar{\nu}_\mu\gamma$ and the accidental coincidences between a high-energy positron from the normal muon decay $\mu^+ \to e^+\nu_e\bar{\nu}_\mu$ (Michel decay) and a high-energy photon from sources such as RMD, positron annihilation-in-flight or bremsstrahlung. Both types of background can mimic a signal event by having an almost back-to-back photon and positron. It can be shown [4], taking into account the muon rate as well as the acceptances and resolutions, that the accidental contribution, which scales quadratically with the muon rate, dominates.

Hence the keys to suppress such backgrounds lie in having a continuous muon beam, a good-quality beam transport system and precision detectors with excellent spatial, temporal and energy resolutions. The design of the MEG experiment has been inspired by these arguments.

3. – The detector

A schematic view of the detector is shown in fig. 1.

The MEG experiment [5] is operated at the Paul Scherrer Institut (PSI) in Switzerland, on the πE5 beam line. The positive muon beam of 28 MeV/c momentum, with intensity up to $10^8\,\mu$/s in a ~ 0.5 cm radius spot, is brought to stop in a thin partially depolarizing polyethylene target after passing a stage in which most of the contaminating positrons are eliminated.

Positrons originating from muon decay are analyzed in the COBRA (COnstant-Bending-RAdius) spectrometer consisting of a superconducting magnet with a gradient magnetic field, a tracking system of low-mass drift chambers and two fast-scintillator timing-counter arrays.

The gradient magnetic field in the spectrometer, ranging from 1.27 Tesla at the centre to 0.49 Tesla at either end, is shaped so that monochromatic e^+s from the target follow trajectories with an almost constant projected bending radius, independent of their emission angle over a wide angular range. Furthermore the sweeping capability of

the non-uniform magnetic field reduces the persistence of low longitudinal momentum e^+s in the tracking volume. Both features greatly reduce the accidental pile-up of the Michel positrons, decrease the pattern recognition complexity and enhance the system efficiency.

The drift chamber system (DCH) consists of 16 radially aligned modules, spaced at 10.5° intervals and placed at equal distance from the target. Each drift chamber module contains two staggered layers of anode wire planes each of nine drift cells. The two layers are separated and also enclosed by 12.5 μm thick cathode foils with a Vernier pattern structure. The chambers are operated with a helium:ethane (50:50) gas mixture. The DCH system thickness along the positron trajectory is only $2.0 \times 10^{-3}\, X_0$ and the design momentum resolution for signal e^+s results in 0.4 MeV/c FWHM.

Positron timing information originates from two scintillator timing-counter arrays (TC), placed at each end of the spectrometer. Each array consists of 15 BC404 plastic scintillator bars, with 128 orthogonally placed BCF-20 scintillating fibres. Each bar is read out at both ends by fine-mesh photomultiplier tubes, while the fibres are viewed by avalanche photo-diodes. The e^+ emission time is measured with resolution of 0.1 ns FWHM, while the impact point on the TCs, given by the fibers, provides directional information on the positron for triggering purposes.

The photon detector is a 900 litre homogeneous volume of liquid xenon (LXe) that subtends a solid-angle acceptance of $\sim 10\%$. It uses scintillation light to measure the total energy released by the γ-ray as well as the position and time of its first interaction. In total, 846 photomultiplier tubes (PMTs), internally mounted on all surfaces and submerged in the xenon, are used. The advantages of using liquid xenon are the fast response, the large light yield and the short radiation length. Stringent control of contaminants is necessary since the vacuum ultra-violet (VUV) scintillation light is easily absorbed by water and oxygen even at sub-ppm levels. The xenon is therefore circulated in liquid phase through a series of purification cartridges, and in gas phase through a heated getter. The expected energy, timing and position resolutions on signal photons are, respectively, 4.5%, 0.1 ns and 5 mm, expressed in FWHM.

The electronics signals generated by LXe and TC photomultipliers are actively split and go to both the trigger and the waveform digitizer systems, while DCH signals are directly sent to the latter.

The waveform digitizers are based on the multi-GHz Domino Ring Sampler chip (DRS [6]), which can sample ten analog input channels into 1024 sampling cells each at speeds of up to 4.5 GHz. The sampling speed for the drift chamber signals is 500 MHz, while that of the PMT signals from the photon detector and timing counters is 1.6 GHz. This strategy gives maximum flexibility, allowing various read-out schemes, such as zero suppression, on an event-by-event basis for various trigger types. The system achieves an excellent pile-up recognition, together with superior timing and amplitude resolutions, compared to conventional schemes.

The trigger is based on fast information from the two detectors using PMTs: the liquid-xenon photon detector and the positron timing counters. It makes use of a subset of the kinematic observables from μ-decay at rest, requiring an energy deposit in the photon detector in an interval containing 52.8 MeV, a time coincident positron hit on the timing counters and a rough collinearity of the two particles, through a look-up table. The decay kinematics is reconstructed by electronics boards arranged in a triple layer tree-structure. The signal digitization is executed by means of a 100 MHz, 10-bit flash analog-to-digital converters. A pre-scaled, multi-trigger event scheme is used for data-taking allowing calibration, background and signal events to be read-out together. The

typical event signal rate was 5 Hz, and the total DAQ rate was 6.5 Hz, with an average livetime of $\sim 84\%$.

The trigger and the digitizers systems are contained in nine VME crates, individually read out by front-end computers. The nine event fragments are sent over a Gigabit Ethernet link to a central event building computer that provides data storage.

4. – The run 2008

We operated the apparatus for the $\mu^+ \to e^+\gamma$ search from September to December 2008. In this period $\sim 10^{14}$ muons were stop in the target at a stop rate of $3 \times 10^7\,\mu$/s.

During the data-taking period the light yield of the photon detector was continuously increasing due to the purification of the liquid xenon being performed in parallel with the event acquisition. The absolute Xenon light yield increased by $\sim 45\%$. Furthermore, an increasing number of drift chambers were affected by frequent high-voltage trips. Over the data-taking period this caused a reduction of the positron detection efficiency by a factor of three.

The increase of xenon light yield was carefully monitored with the various calibration tools, described in the next section, and it is taken into account in the determination of the energy scale. The trigger thresholds were also accordingly adjusted to guarantee an uniform efficiency and a constant acquisition rate.

The drift chamber efficiency drop reduced the experiment sensitivity to the signal. We are developing a normalization scheme which depends only on the ratio of the signal positron efficiency over that of the normal muon decay positron. This scheme is therefore independent of a difficult determination of the absolute DCH efficiency.

5. – Monitoring and calibrations

The number of background events entering the signal region can vary in case of time dependence of the detector efficiencies or resolutions. It is therefore necessary to have a continuous and reliable monitoring system of all the experimental resolutions involved in the determination of the signal region.

During the normal data taking, on a daily basis, light from variable intensity LEDs was used to measure the LXe PMT gain, while α events of 5.5 MeV from point like sources deposited on thin wires [7] were used to measure the PMT quantum efficiencies and the liquid xenon optical properties.

Three times per week the muon stopping target was removed, an extendable beam pipe places a $Li_2B_4O_7$ target at the centre of the detector and protons were shut on the target by a dedicated CW-accelerator placed downstream of the experiment. Photons of $E_\gamma = 17.67$ MeV from $^7\mathrm{Li}(p,\gamma)^8\mathrm{Be}$ allowed the monitoring of the LXe detector energy scale, while coincident γ's of $E_\gamma = 4.4, 11.6$ MeV from $^{11}\mathrm{B}(p,\gamma)^{12}\mathrm{C}$, detected simultaneously by the TC and the LXe, allow the determination of time offsets.

Once a week an entire day of radiative muon decay (RMD) acquisition at reduced beam intensity was performed, with the trigger requirements relaxed to include non back-to-back positron-photon events in a wider energy range.

Two runs of pion charge-exchange reaction ($\pi^- p \to \pi^0 n \to \gamma\gamma n$) were conducted, one at the beginning and one at the end of the data acquisition period. Pion capture at rest on hydrogen produces photons with energy $54.9 < E_\gamma < 83.0$ MeV. By detecting one of these photons with the LXe detector and the other at 180° by means of a set of NaI crystals, two mono-energetic calibration lines at the extremes of the energy spectrum are

obtained. These enable measurement of the energy scale and uniformity. Dalitz decays ($\pi^0 \to \gamma e^+ e^-$) were also collected by using a photon-positron coincidence trigger, and used to study the detector time synchronization and resolution.

The combined use of all these methods enables the investigation of possible systematic variations of the apparatus.

6. – Analysis procedure and radiative muon decay signal

The number of signal events will be determined by means of a maximum-likelihood fit of the physical observables: E_γ, E_{e^+}, $\Delta t_{\gamma e^+}$ and $\Delta\Theta_{\gamma e^+}$. In order to prevent any bias in the definition of the probability density functions (PDF) the events falling in a observable window around the signal region, often called "blinding-box", are written to a separate and protected data stream. The analysis parameters and the background are optimized on the events outside the "blinding-box".

The RMD events are the second background source of the experiment. The precise estimation of the PDFs for these events is of great importance because the kinematical observables are correlated. Special runs at reduced μ-stop rate were taken to clearly identify the RMD signal in a wide observables region, well extended beyond the "blinding-box". The small number of collected RMD events, ~ 400, evaluated with the detector efficiencies and acceptance, is in agreement within 20% the published measurement [8].

7. – Expected final sensitivity and perspectives

The accidental background, which turns out to be the dominant component, contributes with $\approx 3 \times 10^{-14}$ events per muon decay, for the running muon stop rate of $R_\mu = 3 \times 10^7\ \mu$/s.

With this R_μ stop rate, the design detector resolutions and a total running time of $\sim 3 \times 10^7$s, the single event sensitivity (SES) of MEG results $\sim 5 \times 10^{-14}$. The sensitivity can be converted into 90% confidence level upper limit of $\sim 1.2 \times 10^{-13}$, in case of no signal observed.

As already mentioned, we are progressing in the comprehension of the detector systematics and we are exploiting the large amount of calibration data to improve the reconstruction algorithms. The MEG Collaboration is planning to complete the analysis of the data taken in the first three months of detector running by summer 2009.

The light yield of the liquid-xenon detector was constantly increasing and, during the winter 2009 shutdown, the xenon was completely evaporated and purified. The light yield is therefore expected to be totally recovered for the next running period. The drift chamber detector were disassembled and a weak point on a printed circuit board, possible cause of the high-voltage trips, was identified and fixed. The run 2009, with improved detectors, is scheduled to start in August for a running period equivalent to the one of 2008.

REFERENCES

[1] Brooks M. L. *et al.*, *Phys. Rev. Lett.*, **83** (1999) 1521.
[2] Barbieri R. *et al.*, *Nucl. Phys. B*, **445** (1995) 215.
[3] Hisano J. *et al.*, *Phys. Rev. B*, **391** (1997) 341.
[4] Kuno Y. and Okada Y., *Rev. Mod. Phys.*, **73** (2001) 151.

[5] Baldini A., Mori T. *et al.*, *The MEG experiment: search for the $\mu \to e\gamma$ decay at PSI*, available at `http://meg.psi.ch/docs`.
[6] Ritt S., *Nucl. Instrum. Methods A*, **518** (2004) 470.
[7] Baldini A. *et al.*, *Nucl. Instrum. Methods A*, **565** (2006) 589.
[8] Crittenden R. R. *et al.*, *Phys. Rev.*, **121** (1961) 1823.

IL NUOVO CIMENTO Vol. 32 C, N. 5-6 Settembre-Dicembre
DOI 10.1393/ncc/i2010-10555-7

Colloquia: LaThuile09

Rare decays and CP violation at B-factories

Y. Unno

Hanyang University - Seoul, South Korea

(ricevuto il 10 Novembre 2009; pubblicato online il 25 Gennaio 2010)

Summary. — Recent results on rare B decays from the two B-factories, Belle and BABAR, are presented. The Wilson Coefficients in $B \to K^{(*)}l^+l^-$ and polarization puzzle in charmless $B \to VV$ decays are addressed.

PACS 13.25.Hw – Hadronic decays of bottom mesons.
PACS 13.20.He – Leptonic, semi-leptonic and radiative decays of bottom mesons.
PACS 11.30.Er – Charge conjugation, parity, time reversal, and other discrete symmetries.

1. – Introduction

Two B-factories, Belle at KEKB and BABAR at PEP-II, have observed CP violation in B meson decays and proved the correctness of KM mechanism which is included in the Standard Model (SM). On the other hand, some results which differ from the SM expectation are also observed. The direction of the B-factories has been modified to search for a hint of new physics beyond the SM. The study of rare B decays allows a thorough test of the SM. At the same time, it plays significant role to search for contributions from new physics. Belle and BABAR have collected integrated luminosity of more than $800\,\mathrm{fb}^{-1}$ and $500\,\mathrm{fb}^{-1}$, respectively, and the combined one has exceeded $1.4\,\mathrm{ab}^{-1}$. From the large data samples, Belle and BABAR have analyzed up to $657\mathrm{M}B\overline{B}$ and $465\mathrm{M}B\overline{B}$ events, respectively. In this report, the recent results on a study of rare B decays; Wilson coefficients in $B \to K^{(*)}l^+l^-$, and polarization puzzle in charmless $B \to VV$, $\rho^0 K^{*0}$, $K^{*0}K^{*+}$, and ωK^*, including PV and VT decays, from the B-factories are presented.

2. – Wilson coefficients from $B \to K^{(*)}ll$

In the SM, the decays $B \to K^{(*)}l^+l^-$, where l represents either an electron or a muon, arise from flavor-changing neutral current processes that are forbidden at tree level, and proceed through either a Z/γ penguin or W^+W^- box diagrams. The amplitudes can be expressed with the effective Wilson coefficients, C_7, C_9, and C_{10}, for the electromagnetic penguin, the vector, and the axial-vector electroweak contributions, respectively. A contribution of new physics can enter the penguin and box diagrams by modifying

TABLE I. – *Isospin asymmetry in low-q^2 region.*

Mode	Belle($q^2 < 8.68\,\mathrm{GeV}^2/c^4$)	BABAR ($q^2 < 7.02\,\mathrm{GeV}^2/c^4$)
Kl^+l^-	$-0.31^{+0.17}_{-0.14} \pm 0.05$ (1.75σ)	$-1.43^{+0.56}_{-0.85} \pm 0.05$ (2.7σ)
$K^*l^+l^-$	$-0.29 \pm 0.16 \pm 0.03$ (1.40σ)	$-0.56^{+0.17}_{-0.15} \pm 0.03$ (3.2σ)
$K^{(*)}l^+l^-$	$-0.30^{+0.12}_{-0.11} \pm 0.04$ (2.24σ)	$-0.64^{+0.15}_{-0.14} \pm .03$ (3.9σ)

the Wilson coefficients at the same order as the SM. In this modes, there are many observables experimentally; branching fraction, isospin asymmetry, lepton flavor ratio, CP asymmetry, and lepton forward-backward asymmetry, so hints of new physics and variety models which predict such effects can be examined from various perspectives. Those have been studied by Belle and BABAR using 657M$B\overline{B}$ and 384M$B\overline{B}$ data samples, respectively [1-3].

The results of branching fraction measurements by Belle are $\mathcal{B}(K^*l^+l^-) = (10.7^{+1.1}_{-1.0} \pm 0.9) \times 10^{-7}$ and $\mathcal{B}(Kl^+l^-) = (4.8^{+0.5}_{-0.4} \pm 0.3) \times 10^{-7}$, and obtained CP asymmetries, which are expected to be very small in the SM, are $\mathcal{A}_{CP}(K^*l^+l^-) = -0.10 \pm 0.10 \pm 0.01$ and $\mathcal{A}_{CP}(Kl^+l^-) = 0.04 \pm 0.10 \pm 0.02$. The results are consistent with measurements by BABAR [2].

The lepton flavor ratios, defined as $R_{K^{(*)}} = \mathcal{B}(K^{(*)}\mu^+\mu^-)/\mathcal{B}(K^{(*)}e^+e^-)$, are expected to be 1.0 and 0.75 for R_K and R_{K^*} in the SM, respectively. R_K is sensitive to the size of the photon pole, and R_{K^*} is sensitive to neutral SUSY Higgs if $\tan\beta$ is large. The consistent results with the SM expectations are measured to be $R_{K^*} = 0.83 \pm 0.17 \pm 0.05(0.96^{+0.44}_{-0.34} \pm 0.05)$ and $R_K = 1.03 \pm 0.19 \pm 0.06(1.37^{+0.53}_{-0.40} \pm 0.09)$ by Belle(BABAR).

Isospin asymmetry $A_I^{K(*)} \equiv [(\tau_{B^+})/(\tau_{B^0}) \times \mathcal{B}(K^{(*)0}l^+l^-) - \mathcal{B}(K^{(*)\pm}l^+l^-)]/[(\tau_{B^+})/(\tau_{B^0}) \times \mathcal{B}(K^{(*)0}l^+l^-) + \mathcal{B}(K^{(*)\pm}l^+l^-)]$ is expected to be $(+6\% - 13\%)$ as $q^2 = m_{ll}^2 \to 0\,\mathrm{GeV}^2/c^4$ in the SM. Both Belle and BABAR found no significant isospin asymmetries in the high-q^2 regions. However, as shown in table I, BABAR found an evidence for large negative asymmetries in the low-q^2 region. Although Belle results are consistent with null asymmetries, those are in agreement with measurements by BABAR and also indicating large negative asymmetries.

Measurements of angular distributions as a function of q^2 are of particular interest because new physics contribution depends on q^2 due to the fact that $K^*l^+l^-$ is a three-body decay proceeding via three different processes, whose relative contributions vary as a function of q^2. The fraction of longitudinal polarization F_L at low q^2 is sensitive to effects from left-handed currents with complex phases different from the SM, or effects from right-handed currents in the photon penguin amplitude. The sign and magnitude of lepton forward-backward asymmetry can be modified significantly if new physics contributes. Results of F_L and A_{FB} measurements as a function of q^2 are shown in fig. 1, together with the SM predictions and sign flipped coefficients cases. The measured A_{FB} by both Belle and BABAR tend to be shifted toward the positive side from the SM expectation at all q^2 regions, and looks like wrong sign C_7 is favored.

3. – Polarization puzzle in $B \to VV$ (with PV and VT)

Results of small longitudinal polarization fraction $f_L \sim 0.5$ in charmless hadronic B decays to vector-vector final states, $B \to \phi K^*$, reported by both Belle and BABAR

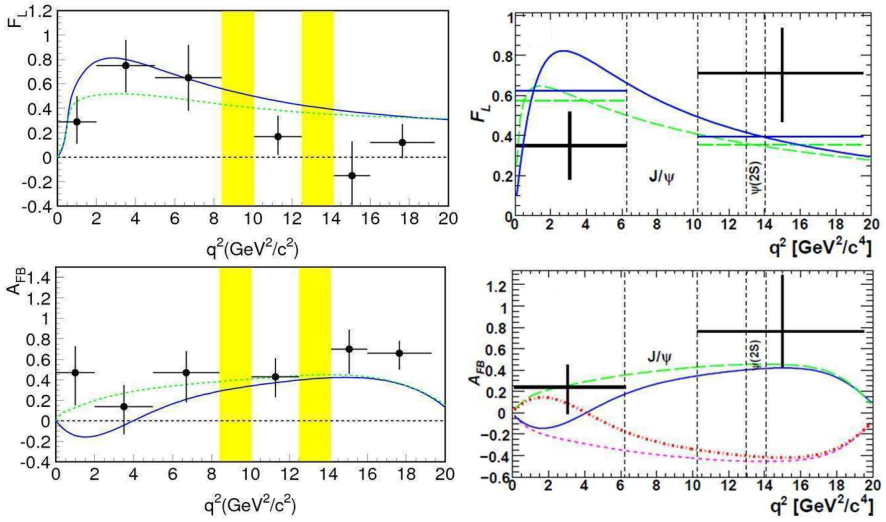

Fig. 1. – Results of F_L (top) and $A_{\rm FB}$ (bottom) measurements as a function of q^2 for the decay $B \to K^* l^+ l^-$ for Belle (left) and BABAR (right). SM predictions are shown as a solid curve together with sign flipped Wilson coefficients cases; $C_7 = -C_7^{\rm SM}$ (long dash), $C_9 C_{10} = -C_9^{\rm SM} C_{10}^{\rm SM}$ (short dash), and $C_7 = -C_7^{\rm SM}$, $C_9 C_{10} = -C_9^{\rm SM} C_{10}^{\rm SM}$ (dash-dot).

came as surprising observations [4,5]. A large f_L is predicted for both tree- and penguin-dominated $B \to VV$ decays in the SM. In fact, the large f_L in tree-dominated decays $B \to \rho\rho$ and $B^+ \to \omega\rho^+$ have been confirmed. In order to resolve the polarization puzzle, several theoretical attempts have been made within or beyond the SM. For the improved understanding on the puzzle, measurements of branching fraction and f_L for other modes dominated by penguin processes play a very important role.

3˙1. $B^0 \to \rho^0 K^{*0}$ *by Belle.* – The decay $B^0 \to \rho^0 K^{*0}$ proceeds via dominant penguin loop and Cabibbo-suppressed tree processes. First observation of this mode using 232M$B\overline{B}$ together with $B^0 \to f^0 K^{*0}$ observation was reported by BABAR [6]. The measured branching fractions are $\mathcal{B}(\rho^0 K^{*0}) = (5.6 \pm 0.9 \pm 1.3) \times 10^{-6}$ with 5.3σ and $\mathcal{B}(f^0 K^{*0}) = (2.6 \pm 0.6 \pm 0.9) \times 10^{-6}$ with 5.0σ, and small f_L in $\rho^0 K^{*0}$ decay is measured to be $0.57 \pm 0.09 \pm 0.08$, which disagree with the SM prediction. Belle has also searched for $\rho^0 K^{*0}$ with 657M$B\overline{B}$ [7] and the results including $f^0 K^{*0}$ and non-resonance decays are summarized in table II. Figure 2 shows projection plots on fitted variables. Belle found neither $\rho^0 K^{*0}$ nor $f^0 K^{*0}$, and set 2σ and 1σ lower upper limits than the branching fractions measured by BABAR. On the other hand, non-resonance decays, $\rho^0 K^+ \pi^-$, $f_0(980) K^+ \pi^-$, and $\pi^+ \pi^- K^{*0}$, are observed with 5.0, 3.5, and 4.5σ significances, respectively.

3˙2. $B^+ \to \overline{K}^{0*} K^{*+}$ *by BABAR, and* $B^+ \to \overline{K}^{0*} K^+$ *by Belle.* – The decay $B^+ \to \overline{K}^{0*} K^{*+}$ occurs through $b \to d$ penguin process same as $B^0 \to \overline{K}^{0*} K^{*0}$ decay. Its branching fraction is expected to be of the same order as $\overline{K}^{0*} K^{*0}$. $B^0 \to \overline{K}^{0*} K^{*0}$ has been already observed by BABAR [8], and the measured branching fraction is $(1.28^{+0.35}_{-0.30} \pm 0.11) \times 10^{-6}$ and large f_L is measured to be $0.80^{+0.10}_{-0.12} \pm 0.06$. BABAR has performed a search for $\overline{K}^{0*} K^{*+}$ using 467M$B\overline{B}$, and found the evidence [9]. The obtained branching

TABLE II. – *Branching fraction measurements of* $\rho^0 K^{*0}$.

Mode	$\mathcal{B}(\times 10^{-6})$	$\mathcal{B}_{\rm UL}(\times 10^{-6})$	$\mathcal{S}(\sigma)$
$\rho^0 K^{*0}$	$2.1^{+0.8+0.9}_{-0.7-0.5}$	< 3.4	2.7
$f_0(980)K^{*0}$	$1.4^{+0.6+0.6}_{-0.5-0.4}$	< 2.2	2.5
$\rho^0 K^+\pi^-$	$2.8 \pm 0.5 \pm 0.5$	–	5.0
$f_0(980)K^+\pi^-$	$1.4 \pm 0.4^{+0.3}_{-0.4}$	–	3.5
$\pi^+\pi^- K^{*0}$	$4.5^{+1.1+0.9}_{-1.0-1.6}$	–	4.5
$\pi^+\pi^- K^+\pi^-$	$-0.1^{+1.2+1.4}_{-1.1-0.8}$	< 2.1	0.0

fraction and f_L are $\mathcal{B} = (1.2 \pm 0.5 \pm 0.1) \times 10^{-6}$ with 3.7σ, and $f_L = 0.75^{+0.16}_{-0.26} \pm 0.03$, which are in agreement with $\overline{K}^{0*}K^{*0}$ results and the SM prediction, but different from f_L in $b \to s$ penguin dominant modes. Similar decay, $B^+ \to \overline{K}^{0*}K^+$, was searched by Belle based on 657M$B\overline{B}$. This PV decay also proceeds through $b \to d$ penguin process. Belle found the first evidence with 4.4σ, and the resulting branching fraction is $(0.68 \pm 0.16 \pm 0.10) \times 10^{-6}$.

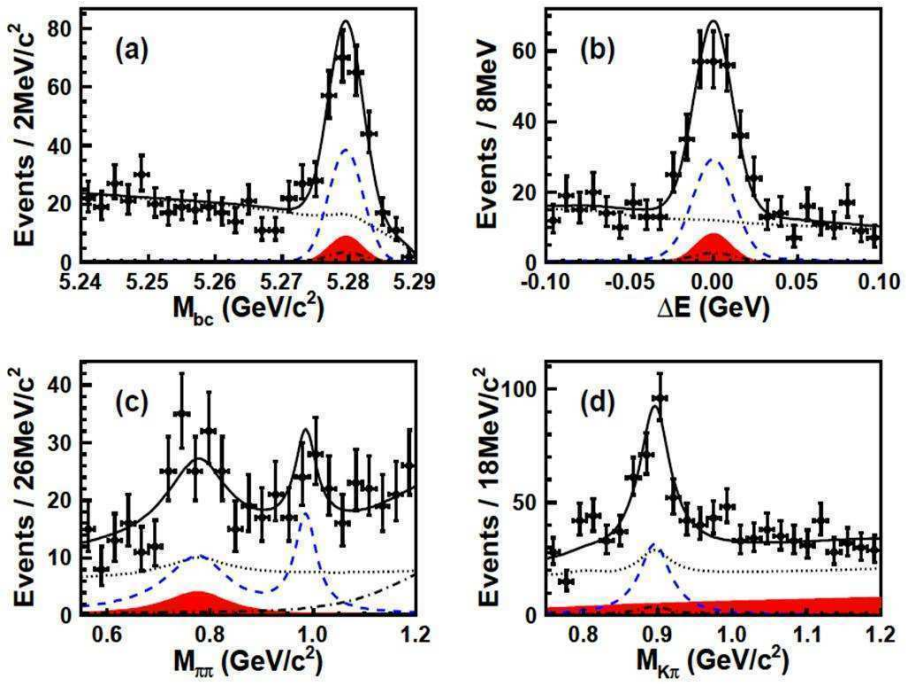

Fig. 2. – Projection plots of fitted results onto (a) M_{bc}, (b) ΔE, (c) $M_{\pi\pi}$, and (d) $M_{K\pi}$. The curves are for the $\rho^0 K^+\pi^-$ (solid-shaded), sum of $\rho^0 K^{*0}$ and $f_0 K^{*0}$ (dashed), $f_2(1270)K^{*0}$ and the sum of feed-down modes (dot-dashed), the sum of the backgrounds (dotted), and the total (solid).

TABLE III. – *Measurements of* $\mathcal{B}$, f_L, *and* $\mathcal{A}_{\rm CP}$ *for* ωK^*, $\omega\rho$, *and* ωf_0.

Mode	$\mathcal{B}$ ($\times 10^{-6}$) (U.L.)	$\mathcal{S}(\sigma)$	f_L	$\mathcal{A}_{CP}$
$\omega K^*(982)^0$	$2.2 \pm 0.6 \pm 0.2$	4.1	$0.72 \pm 0.14 \pm 0.02$	$+0.45 \pm 0.25 \pm 0.02$
$\omega K^*(982)^+$	$2.4 \pm 1.0 \pm 0.2 (< 7.4)$	2.5	$0.41 \pm 0.18 \pm 0.05$	$+0.29 \pm 0.35 \pm 0.02$
$\omega K_0^*(1430)^0$	$18.4 \pm 1.8 \pm 1.7$	9.8	–	$-0.07 \pm 0.09 \pm 0.02$
$\omega K_0^*(1430)^+$	$27.5 \pm 3.0 \pm 2.6$	9.2	–	$-0.10 \pm 0.09 \pm 0.02$
$\omega K_2^*(1430)^0$	$10.1 \pm 2.0 \pm 1.1$	5.0	$0.45 \pm 0.12 \pm 0.02$	$-0.37 \pm 0.17 \pm 0.02$
$\omega K_2^*(1430)^+$	$21.5 \pm 3.6 \pm 2.4$	6.1	$0.56 \pm 0.10 \pm 0.04$	$+0.14 \pm 0.15 \pm 0.02$
$\omega\rho^+$	$15.9 \pm 1.6 \pm 1.4$	9.8	$0.90 \pm 0.05 \pm 0.03$	$-0.20 \pm 0.09 \pm 0.02$
$\omega\rho^0$	$0.8 \pm 0.5 \pm 0.2 (< 1.6)$	1.6	–	–
ωf_0	$1.0 \pm 0.3 \pm 0.1 (< 1.5)$	4.5	–	–

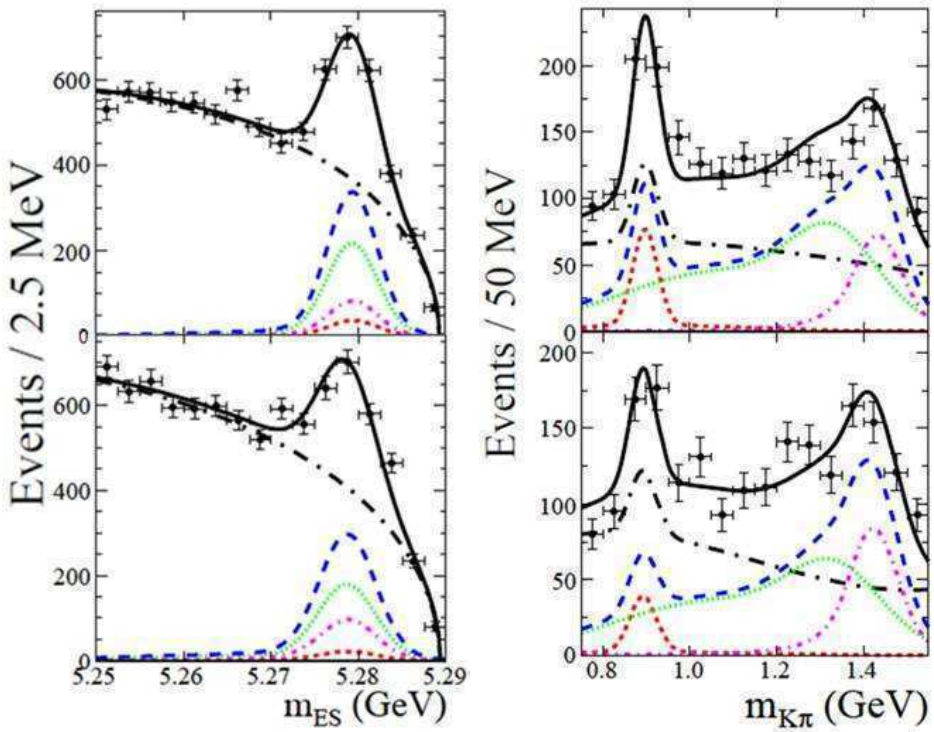

Fig. 3. – Projection plots onto m_{ES} (left) and $m_{K\pi}$ (right) for ωK^{*0} (top) and ωK^{*+} (bottom). The solid curve is the fit function, the long-dashed-dotted curve is the total background, and the dashed curve is the total signal contribution. The short-dashed line is $\omega K^*(892)$, the dotted line is $\omega(K\pi)_0$, and the dot-dashed line is $\omega K_2^*(1430)$.

3˙3. $B \to \omega K^*$ *by BABAR.* – $b \to s$ penguin dominant decay $B^0 \to \omega K^*(982)^0$ was found by Belle for the first time [10], and small f_L was measured to be $0.56 \pm 0.29^{+0.18}_{-0.08}$. Using 467M$B\overline{B}$ data sample, BABAR has also studied $B^0 \to \omega K^*(982)^0$ as well as $\omega K^*(982)^+$, $\omega K_0^*(1430)^{0/+}$, $\omega K_2^*(1430)^{0/+}$, and $\omega\rho^{0/+}$ [11]. The results of branching fraction, f_L, and CP asymmetry measurements are summarized in table III. Projection plots onto fitted variables are shown in fig. 3. $B^0 \to \omega K^*(982)^0$ is found with 4.1σ. The measured f_L agrees with the SM expectation, but it is also consistent with small f_L result measured by Belle. Small f_L in $\omega K^*(982)^+$ is seen although the yield significance is 2.5σ. All of $\omega K_0^*(1430)^{0/+}$ and $\omega K_2^*(1430)^{0/+}$ have been observed with significantly large branching fractions, which are one order larger than $\omega K^*(982)^{0/+}$ decays. Small f_L of both $\omega K^*(982)^{0/+}$ are measured. An interesting feature in the above f_L results is that f_L values between $B \to VV$ and VT are consistent, in contrast to those in $B \to \phi K^*$. BABAR found large f_L in $B \to VT$ decays, $\phi K_2^*(1430)^{0/+}$ [12,13], which are distinct from small f_L results in $B \to VV$ decays, $\phi K^*(982)^{0/+}$. It looks the situation on polarization puzzle extended to the decay to excited final state particles has became increasingly more complex and intringuing.

4. – Conclusions

Recent results of $B \to K^{(*)}l^+l^-$, and charmless $B \to PV, VV$, and VT decays from the two B-factories are presented. Some of results show clear discrepancies from the SM expectations, but more statistics is needed to clarify if the effects come from new physics or not. This would be solved by upgraded B-factories and LHCb, however it is still very important to analyze all possible decays related to the polarization puzzle, which are yet to be studied, with current data sample of two B-factories.

REFERENCES

[1] Adachi I. *et al.* (Belle Collaboration), arXiv:hep-ex/0810.0335.
[2] Aubert B. *et al.* (*BABAR* Collaboration), arXiv:hep-ex/0807.4119.
[3] Aubert B. *et al.* (*BABAR* Collaboration), arXiv:hep-ex/0804.4412.
[4] Adachi I. *et al.* (Belle Collaboration), *Phys. Rev. Lett.*, **94** (2005) 221804.
[5] Aubert B. *et al.* (*BABAR* Collaboration), *Phys. Rev. D*, **78** (2008) 092008.
[6] Aubert B. *et al.* (*BABAR* Collaboration), *Phys. Rev. Lett.*, **97** (2006) 201801.
[7] Adachi I. *et al.* (Belle Collaboration), arXiv:hep-ex/0905.0763.
[8] Aubert B. *et al.* (*BABAR* Collaboration), *Phys. Rev. Lett.*, **100** (2008) 081801.
[9] Aubert B. *et al.* (*BABAR* Collaboration), arXiv:hep-ex/0901.1223.
[10] Adachi I. *et al.* (Belle Collaboration), *Phys. Rev. Lett.*, **101** (2008) 231801.
[11] Aubert B. *et al.* (*BABAR* Collaboration), arXiv:hep-ex/0901.3703.
[12] Aubert B. *et al.* (*BABAR* Collaboration), *Phys. Rev. Lett.*, **99** (2007) 201802.
[13] Aubert B. *et al.* (*BABAR* Collaboration), *Phys. Rev. Lett.*, **101** (2008) 161801.

IL NUOVO CIMENTO Vol. 32 C, N. 5-6 Settembre-Dicembre 2009
DOI 10.1393/ncc/i2010-10546-8

Colloquia: LaThuile09

Heavy-flavor physics at CLEO-c

P. U. E. Onyisi for the CLEO Collaboration
Enrico Fermi Institute, University of Chicago - Chicago, IL 60637, USA

(ricevuto il 10 Novembre 2009; pubblicato online il 20 Gennaio 2010)

Summary. — The CLEO-c experiment, running at charm threshold, has measured many charmed meson properties. Here I summarize results on leptonic and semileptonic decays of D mesons, as well as measurements hadronic decay strong phases that are relevant to the extraction of the CKM angle γ from B decays.

PACS 12.15.Hh – Determination of Kobayashi-Maskawa matrix elements.
PACS 13.20.Fc – Leptonic, semileptonic, and radiative decays of charmed mesons.
PACS 13.25.Ft – Hadronic decays of charmed mesons.

1. – Introduction

Studies of the interactions of matter with the electroweak symmetry breaking sector of the Standard Model have been very fruitful. The interactions of quark mass eigenstates with the weak force—a structure inherited from the Yukawa couplings of the quarks with the Higgs field—must satisfy specific relationships in the Standard Model, and violations of those would signal physics beyond the SM. The non-observation of such effects to date places stringent limits on the form of such scenarios.

All quarks except the top quark are only observed when confined inside hadrons, which is a regime where QCD is non-perturbative. Relating observable hadron decays to "short-distance" weak dynamics requires precision understanding of the strong force. Lattice QCD offers the prospect of a systematically improvable method of calculating hadronic properties from first principles. In the past decade theoretical and technological improvements (in particular the handling of virtual quark-antiquark pairs, the so-called "unquenched" calculations) have allowed the lattice to deliver predictions that are in many cases very precise, have no tunable parameters, and reliably estimate systematic uncertainties. Before application of these results to extract electroweak parameters in the B system, it is desirable to test them elsewhere, for example in charm.

The CLEO-c experiment at the CESR-c electron-positron collider collected large data samples in the charm threshold energy region. Coupled with a well-understood detector, these samples enable tests of lattice predictions for charm hadron decays, as well as studies of many other topics. Here I will discuss measurements of the meson decay

constants f_D and f_{D_s} and branching fractions and form factors for the semileptonic decays $D^{0,+} \to (K,\pi)e^+\nu_e$. In addition, I will discuss studies of D_s semileptonic decays, as well as studies of strong force-induced decay phases that are relevant for interferometry in the B system.

2. – Detector and data samples

The CLEO-c detector was a symmetric general purpose detector at the CESR-c e^+e^- collider. The experiment is described in detail elsewhere [1]. The relevant datasets for the following analyses were collected at center of mass energies of approximately 3.77 GeV (the peak of the $\psi(3770)$ resonance) and 4.17 GeV. The former dataset is used for D^0 and D^+ analyses, and the latter for D_s physics.

At 3.77 GeV the only allowed open charm final states are $D^0\overline{D}^0$ and D^+D^-; at 4.17 GeV the only allowed states involving a D_s meson are $D_s^+D_s^-$ and $D_s^{\pm}D_s^{*\mp}$. This enables the powerful tagging technique pioneered by Mark III [2] which uses the presence of a fully reconstructed D meson which decays to a tag mode to indicate the existence of its antiparticle. This is the basis of the technique for measuring absolute branching fractions used in the analyses discussed below:

$$\mathcal{B}(D \to X) = \frac{N(\overline{D} \to \text{tag}, D \to X)}{N(\overline{D} \to \text{tag})} \frac{\epsilon(\overline{D} \to \text{tag})}{\epsilon(\overline{D} \to \text{tag}, D \to X)}\,, \tag{1}$$

where the ϵ are the respective efficiencies. There are other benefits to tagging: full reconstruction of the visible particles of an event allows a neutrino to be inferred; the removal of the particles constituting a tag strongly reduces the combinatorics (and hence backgrounds) of the rest of the event; and a judicious choice of D^0 tags allows the exploitation of quantum correlations of the initial state to measure phases.

3. – Leptonic decays and decay constants

The decays $X^+ \to \ell^+\nu$ involve a hadronic current (which can be parametrized by the single scalar "decay constant" f_X) and a leptonic current, which is well understood in the electroweak model. Consequently the branching fraction for such a decay can be written as

$$\mathcal{B}(X^+ \to \ell^+\nu) = f_X^2|V|^2\frac{G_F^2}{8\pi}m_X m_\ell^2\left(1-\frac{m_\ell^2}{m_X^2}\right)^2\,, \tag{2}$$

where V is the relevant element of the CKM matrix connecting the valence quarks of X (for D^+ and D_s^+ this is V_{cd} and V_{cs}, respectively). Experiment can measure the quantity $f_X^2|V|^2$; knowing the decay constant, we can obtain the CKM element, and vice versa.

In a naive quantum-mechanical picture, the decay constant can be thought of as a measure of the wave function of the meson at zero separation between the quarks. This means it is relevant for processes where the relevant length scales are much smaller than the hadron size, such as the loop diagrams for B_d^0 and B_s^0 mixing. The mass difference between $B_{(s)}$ eigenstates is proportional to $f_{B_{(s)}}^2$; as this is our primary source of information on V_{td}, reducing theoretical uncertainty is critical.

The measurements are discussed below.

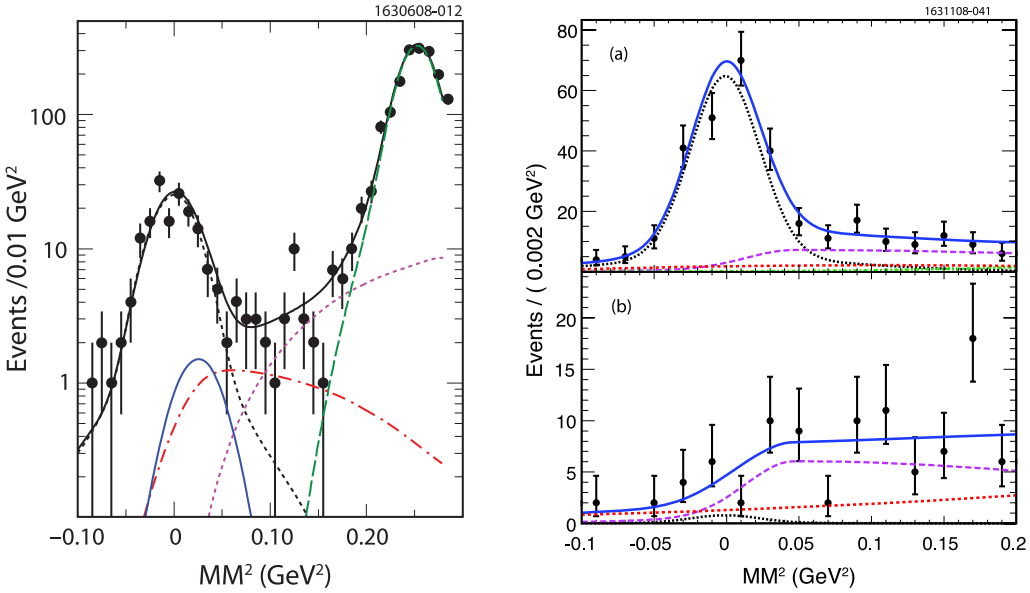

Fig. 1. – (Colour on-line) Left: distribution of MM^2 for $D^+ \to \mu^+\nu$ candidate events. The black solid line is a fit to the spectrum summing the following components: $D^+ \to \mu^+\nu$ signal (dotted black line peaking at zero); $D^+ \to \pi^+\pi^0$ (solid blue); $D^+ \to \tau^+\nu$ (dot-dashed red); $D^+ \to \overline{K}^0\pi^+$ (dashed green); and other three-body decays (dotted purple line rising towards the right of the plot). Right: Distribution of MM^2 for (a) $D_s^+ \to \mu^+\nu$ and (b) $D_s^+ \to \tau^+\nu \to \pi^+\bar{\nu}\nu$ candidate events. The blue solid line is a fit to the spectrum summing the following components: $D_s^+ \to \mu^+\nu$ signal (dotted black line peaking at zero); $D_s^+ \to \tau^+\nu$ (long-dashed purple); other D_s^+ decays (dot-dashed green); and non-D_s^+ decays (dashed red).

3˙1. $D^+ \to \mu^+\nu$. – This analysis [3] uses the full 818 pb^{-1} of 3.77 GeV data. One of six hadronic D^- decays is reconstructed as a tag([1]) which sets the initial number of D^- decays. Exactly one track is allowed aside from those composing the track; this is taken as the muon candidate, and must have deposited less than 300 MeV in the electromagnetic calorimeter and not have been considered a viable kaon candidate by the particle identification algorithm. If the event has extra calorimeter energy, it is vetoed, to eliminate one prong hadronic D^+ decays with π^0s. The four-vectors of the initial state, tag, and muon candidate are then combined to form the missing mass squared $MM^2 \equiv (p_0 - p_{D^-} - p_{\mu^+})^2$. This peaks at zero (the neutrino mass squared) for signal events, as shown in fig. 1. A fit is performed to the spectrum including the signal and various background components. Some $D^+ \to \tau^+\nu$ events are expected to leak into this plot, but the number is too low to fit for explicitly and that component is fixed relative to the $D^+ \to \mu^+\nu$ contribution according to the SM expectation for the ratio.

3˙2. $D_s^+ \to \mu^+\nu$, $\tau^+\nu$ ($\tau^+ \to \pi^+\bar{\nu}$). – This measurement [4] proceeds similarly to the $D^+ \to \mu^+\nu$ analysis. The full 600 pb^{-1} dataset at 4.17 GeV is used. At this energy the dominant D_s^+ production mode is $e^+e^- \to D_s^\pm D_s^{*\mp}$; the $D_s^{*\mp}$ then decays to $D_s^\mp\gamma$ (94.2%)

([1]) Charge conjugate reactions are implied.

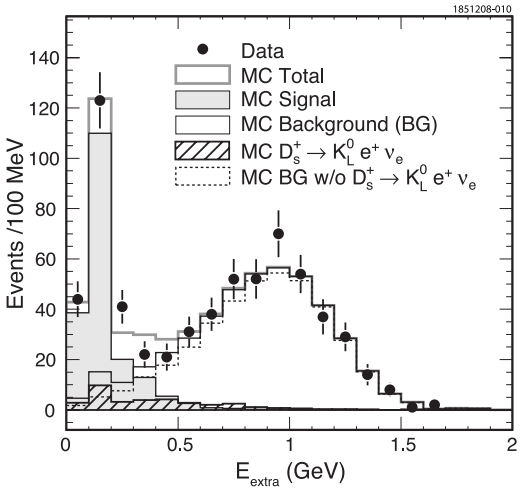

Fig. 2. – Distribution of extra calorimeter energy for $D_s^+ \to \tau^+\nu \to e^+\bar{\nu}\nu\nu$ candidate events. The signal region is 0–400 MeV. The signal shape is the lightly shaded histogram peaking just above zero. The total expected background is the open histogram. The primary background to the measurement, $D_s^+ \to K_L^0 e^+\nu$, is the hatched histogram.

or $D_s^{\mp}\pi^0$ (5.8%) [5]. Thus, compared to the D^+ case, there is an extra particle that must be considered when forming the missing mass squared. Only the photon transition is considered in this analysis.

Nine hadronic D_s^- tag modes are used to obtain the parent sample of events. One extra track is allowed, as well as a transition photon candidate; additional calorimeter energy is vetoed. The extra track is required to be either muon-like (less than 300 MeV deposited in the calorimeter) or pion-like (more than 300 MeV deposited, but track is not an electron candidate). A kinematic fit is performed which uses multiple constraints to improve the MM^2 resolution.

The distribution of the MM^2 is shown in fig. 1.

3˙3. $D_s^+ \to \tau^+\nu$ ($\tau^+ \to e^+\nu\bar{\nu}$). – This measurement [6] uses a different technique from the previously discussed decay constant measurements. In the D^+ case, the missing mass squared variable serves to separate the signal $D^+ \to \mu^+\nu$ from, in particular, K_L^0 backgrounds. For the D^+ the signal is Cabibbo-suppressed and the background (*e.g.*, $D^+ \to K_L^0\pi^+$) is Cabibbo-favored. In the D_s^+ case this is largely reversed. Reconstructing a D_s^+ tag and an electron and imposing an additional track veto selects the signal decay as well as semileptonic decays with neutral hadrons, but critically most of these result in additional photons. Requiring only small amounts of additional calorimeter energy strongly discriminates for the signal, as shown in fig. 2; the main remaining background is the Cabibbo-suppressed $D_s^+ \to K_L^0 e^+\nu$.

3˙4. *Results and combination.* – The results of the leptonic branching fraction measurements and corresponding decay constants are shown in table I. The values of input parameters used to obtain these values are listed in the relevant papers [3, 4, 6].

TABLE I. – *CLEO-c measurements of D^+ and D_s^+ leptonic decay branching fractions and decay constants, compared to lattice QCD predictions from the HPQCD and UKQCD Collaborations* [7].

	CLEO-c result	Lattice QCD
$\mathcal{B}(D^+ \to \mu^+\nu)$	$(3.82 \pm 0.32 \pm 0.09) \times 10^{-4}$	
$\mathcal{B}(D_s^+ \to \mu^+\nu)$	$(5.65 \pm 0.45 \pm 0.17) \times 10^{-3}$	
$\mathcal{B}(D_s^+ \to \tau^+\nu)$ (from $\tau^+ \to \pi^+\bar{\nu}$)	$(6.42 \pm 0.81 \pm 0.18) \times 19^{-2}$	
$\mathcal{B}(D_s^+ \to \tau^+\nu)$ (from $\tau^+ \to e^+\nu\bar{\nu}$)	$(5.30 \pm 0.47 \pm 0.22) \times 10^{-2}$	
f_{D^+}	$205.8 \pm 8.5 \pm 2.5\,\text{MeV}$	$207 \pm 4\,\text{MeV}$
$f_{D_s^+}$ (combined)	$259.5 \pm 6.6 \pm 3.1\,\text{MeV}$	$241 \pm 3\,\text{MeV}$
$f_{D_s^+}/f_{D^+}$	$1.26 \pm 0.06 \pm 0.02$	1.162 ± 0.009

4. – Exclusive semileptonic decays

Exclusive semileptonic decays have a more involved parametrization than leptonic decays, as they involve at least three particles in the final state. The partial width for the decay $X \to X'\ell\nu$, where X and X' are pseudoscalars, can be written as

$$\frac{\mathrm{d}\Gamma(X \to X'\ell\nu)}{\mathrm{d}q^2} = \frac{G_F^2}{24\pi^3}\left[f_+^{X\to X'}(q^2)|V|\right]^2 p_{X'}^3 \tag{3}$$

in the limit where the charged lepton mass is negligible. In eq. (3), q^2 is the invariant mass squared of the $\ell\nu$ system, $|V|$ is the relevant CKM matrix element for the weak transition, and $f_+^{X\to X'}$ is a form factor encapsulating the hadronic physics. As in the leptonic decay case, input for $|V|$ or f_+ allows determination of the other.

4·1. *D^0 and D^+ decays.* – Two separate studies of $D \to (K,\pi)e^+\nu$ were performed on $281\,\text{pb}^{-1}$ of 3.77 GeV data. The "tagged" analysis [8] reconstructs hadronic decays of one D in the event to establish the base sample. A hadron ($K^\pm$, $\pi^\pm$, K_S^0, π^0) and an electron candidate are then selected, and the missing energy E_{miss} and momentum $\vec{p}_{\text{miss}}$ are determined. From these the variable $U \equiv E_{\text{miss}} - |\vec{p}_{\text{miss}}|$ is computed, which for correctly reconstructed events with neutrinos is approximately zero. The "neutrino reconstruction" analysis [9] uses the near-hermeticity of the detector to attempt to reconstruct all visible particles in an event; if the missing four momentum is consistent with the neutrino mass, it is considered a neutrino candidate, and an attempt is made to combine it with electron and kaon or pion candidates to make a $D \to (K,\pi)e\nu$ candidate. In this case the D candidates are discriminated from background by looking at the variables $\Delta E \equiv E_D - E_{\text{beam}}$ and $M_{\text{bc}} \equiv \sqrt{E_{\text{beam}}^2 - |\vec{p}_D|^2}$. Figure 3 shows the signals for both analyses.

The yields as a function of q^2 are used to derive measurements of the form factors. These are fit to several parametrizations: the simple pole model assuming D_s^*/D^* dominance, the "modified pole" model [10], and a series expansion [11]. All fits describe the data reasonably as long as all parameters are allowed to float; however, for example, the implied D_s^*/D^* pole masses in the pole models are many standard deviations from the physical values. Reasonable agreement on the form factor shape and normalization

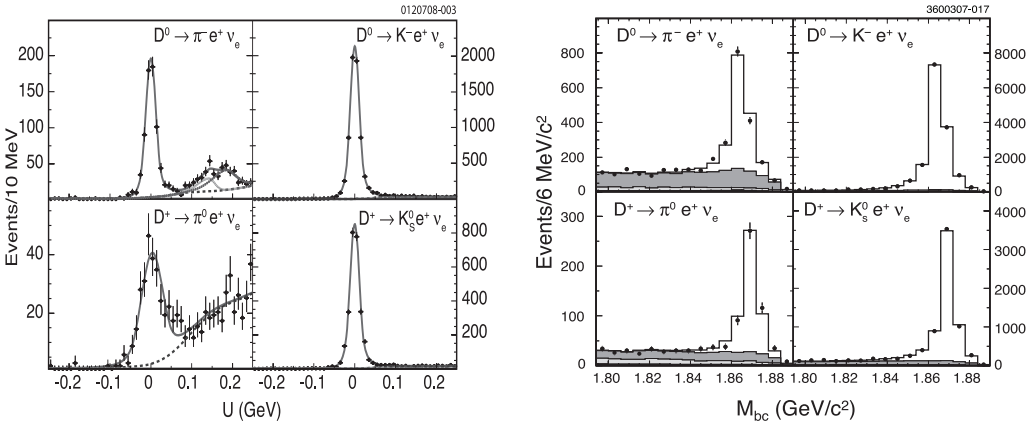

Fig. 3. – Signals for D semileptonic decays in $281\,\mathrm{pb}^{-1}$ of data. Left: distribution of $U \equiv E_{\mathrm{miss}} - |\vec{p}_{\mathrm{miss}}|$ in tagged analysis. Right: distribution of M_{bc} in neutrino reconstruction analysis.

is found with a lattice QCD prediction from the FNAL, MILC, and HPQCD Collaborations [12]. Using lattice predictions for $|f_+(0)|$, values for $|V_{cd}|$ and $|V_{cs}|$ are also obtained, which are limited by lattice uncertainties.

4·2. *D_s^+ decays.* – Using $310\,\mathrm{pb}^{-1}$ of data, CLEO-c has made the first absolute measurement of the semileptonic decay branching fractions $\mathcal{B}(D_s^+ \to Xe^+\nu)$ where $X \in (\phi, \eta, \eta', K^0, K^{*0}, f_0 \to \pi^+\pi^-)$ [13]. In contrast to previous measurements these are not ratios to a hadronic decay of the D_s^+. In addition this is the first observation of the Cabibbo-suppressed modes $K^0e^+\nu$ and $K^{*0}e^+\nu$. The η and η' branching fractions provide useful information on the $\eta - \eta'$ mixing angle and glueball component [14].

5. – Strong phases for γ/ϕ_3 measurements

Of the three angles of the unitarity triangle, γ has the largest uncertainties on its direct measurement. A clean measurement of γ from tree decays can be made by exploiting interference between the decays $b \to c\bar{u}s$ and $b \to u\bar{c}s$. These correspond to decays $\overline{B} \to DK$ and $\overline{B} \to \overline{D}K$; since D^0 and $\overline{D}^0$ can decay to common final states, the interference can be observed. Such final states include $K^-\pi^+$ (interference between Cabibbo-favored and doubly-Cabibbo-suppressed decays) [15] and $K^0_S\pi^+\pi^-$ (Cabibbo favored in both cases, but populating different parts of phase space) [16]. The total observed interference depends on D decay dynamics—specifically phases between D and $\overline{D}$ decays to the same final state that are induced by the strong force. Because B-factories observe definite flavor in D^0 decays (as they tag the soft pion in $D^{*+} \to D^0\pi^+$), they cannot directly observe these phases. In the case of decays to common three-body final states, the phases can be estimated by using models for the resonant substructure of the decays, but this leaves a residual model uncertainty.

Production of $D^0\overline{D}^0$ pairs at threshold provides unique access to the phase information. The initial state is strongly constrained ($J^{PC} = 1^{--}$) and so the decays of the two D mesons are correlated. One obvious correlation is flavor-antiflavor (in the absence of mixing); a less obvious one is CP correlation: if one D decays to a CP eigenstate (for example K^-K^+), the other must decay to a state of opposite CP. This projects out

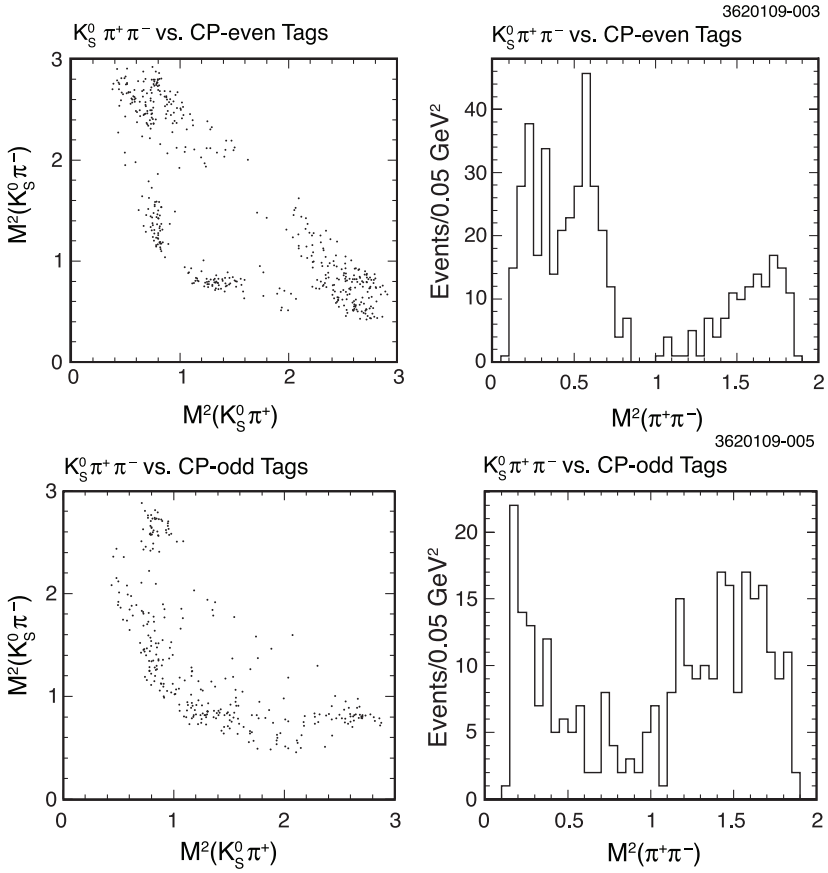

Fig. 4. – Effects of CP correlation on the Dalitz plot of the decay $D^0 \to K^0_S\pi^+\pi^-$. The $K^0_S\rho$ component, clearly visible when $K^0_S\pi^+\pi^-$ recoils against a CP-even tag, disappears opposite a CP-odd tag.

a linear sum of the D^0 and $\overline{D}^0$ flavor eigenstates, which then interfere. Comparing the rates and dynamics of the same decay when it happens opposite flavor and CP eigenstates directly probes the strong phases in D^0 decays without model systematics. The dramatic effect of these correlations is shown in fig. 4.

Here I briefly summarize CLEO-c results relevant to γ measurements. These results are statistically limited by the number of reconstructed CP eigenstate decays.

5˙1. *Strong phase between $D^0 \to K^-\pi^+$ and $\overline{D}^0 \to K^-\pi^+$.* – The relative phase δ between the decays $D^0 \to K^-\pi^+$ and $\overline{D}^0 \to K^-\pi^+$ is relevant for the γ measurement method of ref. [15]. It also relates the D^0 mixing parameters y and y'. The differences in the effective branching fraction for $K^-\pi^+$ decay opposite CP-even and -odd eigenstates, semileptonic decays (which unambiguously determine the charge of the decaying charm quark), and $K^+\pi^-$ are sensitive to δ and in principle to D^0 mixing parameters as well. With $281\,\text{pb}^{-1}$ of data, CLEO-c has made the first measurement of $\cos\delta$, finding it to be $1.03^{+0.31}_{-0.17} \pm 0.06$ [17].

5˙2. *Effective strong phases in multibody decays.* – The γ measurement method using $K^-\pi^+$ decays can be extended to other decays with larger branching fractions [18]. In this case the relative phase depends on the decay kinematics, and the Cabibbo-favored and doubly-Cabibbo-suppressed decays will not have complete overlap over the phase space. These effects can be subsumed in an effective average phase and a "coherence factor" which reflects the dilution of total interference relative to the expectation for a simple two-body decay. CLEO-c has measured these for the $D^0 \to K^-\pi^+\pi^0$ and $K^-\pi^+\pi^+\pi^-$ decays, observing significant coherence in the former [19].

5˙3. *Phase space-dependent measurements.* – One can proceed beyond the averaging approximation above and obtain relative D^0–$\overline{D}^0$ phases as a function of decay kinematics by observing how CP tagging affects Dalitz plots. CLEO-c has performed this measurement for the $K^0_{S,L}\pi^+\pi^-$ decay [20] and work is underway for the $K^0_{S,L}K^-K^+$ mode. Figure 4 shows the effect of the CP correlations on the $D^0 \to K^0_S\pi^+\pi^-$ Dalitz plot. Up to small effects $K^0_L\pi^+\pi^-$ is expected to have a CP structure opposite that of $K^0_S\pi^+\pi^-$, and similarly for $K^0_LK^-K^+$; CLEO-c is able to reconstruct K^0_L candidates based on missing energy and momentum, so these decays can add to the measurement statistics for the phases although the K^0_S modes are the ones relevant for B factory measurements.

5˙4. *Impact on γ measurement.* – The impact of CLEO-c results on future analyses enabled by the large dataset expected from LHCb has been studied. The $D^0 \to K^0_S\pi^+\pi^-$ analysis is expected to reduce the current 7–9° model uncertainties from BaBar and Belle measurements [21] to around 2° [20, 22]. The $K^-\pi^+$ and multibody coherence factor measurements are projected to improve the $10\,\text{fb}^{-1}$ precision of LHCb in $B \to DK$ by 8–35% (depending on unknown B decay parameters) to 2.2–3.5° [23].

* * *

The author wishes to thank J. Libby, C. S. Park, and P. Naik for helpful discussions. This work was partly supported by a Fermi Fellowship from the University of Chicago.

REFERENCES

[1] Kubota Y. *et al.*, *Nucl. Instrum. Methods Phys. Res. A*, **320** (1992) 66; Peterson D. *et al.*, *Nucl. Instrum. Methods Phys. Res. A*, **478** (2002) 142; Artuso M. *et al.*, *Nucl. Instrum. Methods Phys. Res. A*, **554** (2005) 147.
[2] Baltrusaitis R. M. *et al.*, *Phys. Rev. Lett.*, **56** (1986) 2140; Adler J. *et al.*, *Phys. Rev. Lett.*, **60** (1988) 89.
[3] Eisenstein B. I. *et al.*, *Phys. Rev. D*, **78** (2008) 052003.
[4] Alexander J. P. *et al.*, *Phys. Rev. D*, **79** (2009) 052001.
[5] Amsler C. *et al.*, *Phys. Lett. B*, **667** (2008) 1 and 2009 partial update for 2010 edition.
[6] Onyisi P. U. E. *et al.*, *Phys. Rev. D*, **79** (2009) 052002.
[7] Follana E. *et al.*, *Phys. Rev. Lett.*, **100** (2008) 062002.
[8] Ge J. Y. *et al.*, *Phys. Rev. D*, **79** (2009) 052010.
[9] Cronin-Hennessy D. *et al.*, *Phys. Rev. Lett.*, **100** (2008) 251802; Dobbs S. *et al.*, *Phys. Rev. D*, **77** (2008) 112005.
[10] Becirevic D. and Kaidalov A. B., *Phys. Lett. B*, **478** (2000) 417.
[11] Becher T. and Hill R. J., *Phys. Lett. B*, **633** (2006) 61.
[12] Aubin C. *et al.*, *Phys. Rev. Lett.*, **94** (2005) 011601.
[13] Yelton J. *et al.*, *Phys. Rev. D*, **80** (2009) 052007.

[14] Anisovich V. V., Bugg D. V., Melikhov D. I. and Nikonov V. A., *Phys. Lett. B*, **404** (1997) 166.
[15] Atwood D., Dunietz I. and Soni A., *Phys. Rev. Lett.*, **78** (1997) 3257.
[16] Giri A. *et al.*, *Phys. Rev. D*, **68** (2003) 054018; Bondar A. and Poluektov A., *Eur. Phys. J. C*, **47** (2006) 347.
[17] Rosner J. L. *et al.*, *Phys. Rev. Lett.*, **100** (2008) 221801.
[18] Atwood D. and Soni A., *Phys. Rev. D*, **68** (2003) 033003.
[19] Lowrey N. *et al.*, *Phys. Rev. D*, **80** (2009) 031105.
[20] Briere R. A. *et al.*, *Phys. Rev. D*, **80** (2009) 032002.
[21] Aubert B. *et al.*, *Phys. Rev. D*, **78** (2008) 034023; Abe K. *et al.*, arxiv:0803.3375 (2008).
[22] Libby J., CERN-LHCb-2007-141 (2007), unpublished.
[23] Akiba K. *et al.*, CERN-LHCb-2008-031 (2008), unpublished.

IL NUOVO CIMENTO Vol. 32 C, N. 5-6 Settembre-Dicembre 2009
DOI 10.1393/ncc/i2010-10557-5

Colloquia: LaThuile09

LFV and EDMs in SUSY with flavour symmetries

A. Masiero

Dipartimento di Fisica "G. Galilei", Università di Padova and INFN Sezione di Padova - Padova, Italy

(ricevuto il 10 Novembre 2009; pubblicato online il 28 Gennaio 2010)

Summary. — After more than four decades of impressive and frustrating theoretical and experimental efforts to reveal signals of the presence of TeV new physics through its effects in CP-conserving and CP-violating flavour-changing neutral-current processes, the main response seems to lie in an effective flavour blindness of the new physics at the electroweak scale (Minimal Flavour Violation). This perspective keeps still open the door for main surprises in the sector of lepton flavor violation. In this talk I focus on an alternative road where both the flavour puzzle within the Standard Model (*i.e.*, a rationale for the smallness of Yukawa couplings and fermion mixings) and the flavour problem of TeV new physics are simultaneously tackled in a supersymmetric extension of the Standard Model where the flavour structure is dictated by a (spontaneously broken) flavour or horizontal symmetry.

PACS 11.30.Hv – Flavor symmetries.
PACS 12.10.-g – Unified field theories and models.
PACS 12.60.Jv – Supersymmetric models.
PACS 13.35.Bv – Decays of muons.

1. – General status of flavour in our search for new physics

At least 40 years of efforts (and successes) in probing Flavor-Changing Neutral-Current (FCNC) phenomena have lead to the following conclusion: the Cabibbo-Kobayashi-Maskawa (CKM) flavour structure of the Standard Model (SM) represents the main bulk of flavour and (flavour-violating) CP violation in the hadronic sector at least down to distances of the order of $(100\,\mathrm{GeV})^{-1}$. I think that, first of all, the relevance of this result should not be underestimated: this understanding represents a major breakthrough in our knowledge of the fundamental properties of Nature. As for the leptonic sector, the SM brilliantly succeeds to highly suppress charged lepton flavour violations (LFV) linking such suppression to the smallness of neutrino masses.

Unfortunately, the giant progress in our knowledge of flavour was not matched by a major breakthrough in our search for New Physics (NP) signals in rare FCNC and CPV processes. To be sure, we now know much more on the relation between the flavour

structure and TeV NP, namely such low-energy NP should be flavour blind (*i.e.* the only flavour source would be given by the SM Yukawa couplings—the so-called MFV, Minimal Flavour Violation, assumption), or, if it possesses new flavour sources in addition to the SM Yukawa couplings, they should contribute to FCNC processes by no more than 10–20% of what the SM contributes. In both cases, it is clear that the TeV NP should be far from the generic case where it introduces new sources of flavour by its own without any specific suppression characteristic of the SM. Indeed, quite the opposite has to occur: the NP should enjoy a very stringent "flavour protection", either a total one forbidding any new source of flavour connected to the presence of NP (MFV framework) or, in any case, a very efficient suppression of the NP intrinsic FCNC contributions. As for the latter situation, this could obviously arise if the NP instead of being at the TeV scale should appear at a multi-TeV scale, but, in that case, the fine-tuning needed to ensure the correct energy scale for the electroweak breaking would become more and more severe. Alternatively, as usual in particle physics, the concept of "protection" immediately recalls the concept of "symmetry", with the possibility of a slightly broken symmetry to guarantee an adequate suppression of the FCNC NP contributions.

Before tackling this latter issue of the "symmetry protection" with a specific example, let me comment on the other possibility to reconcile TeV NP and FCNC suppression, namely the MFV case. From the theoretical point of view, it is not so simple to obtain a purely MFV situation. For instance, if the TeV NP is represented by a supersymmetric (SUSY) extension of the SM, then, in the case of supergravity (SUGRA), MFV is more an exception than a viable solution: indeed, barring the case of a purely dilaton-mediated SUGRA breaking (which seems hardly achievable, anyway), in all other cases where moduli take part in the process of SUGRA breaking we expect the scalar fermion masses not to be flavour universal, hence inducing a new source of flavour in FCNC SUSY contributions. On the other hand, if other mechanisms are adopted for SUSY breaking, for instance gauge (GMSB)—or anomaly (AMSB)—mediation, then strict MFV can be enforced. If MFV is present, then the chances to observe NP signals in hadronic FCNC processes become quite slim. There are possible exceptions to this grim scenario: for instance, in the case where two Higgs doublets are present, the rate of the process $B_s \to \mu^+\mu^-$ can be extraordinarily enhanced given the very large dependence of the process on the ratio of the two Higgs VEVs (the so-called $\tan\beta$ parameter). Alternatively, one can still try to search for departures from the SM expectations in hadronic FCNC processes, but to have concrete hopes to see something significant one has to go to Super-Flavour machines where accuracies at the percent level may be achieved (at the same time, one has to improve our theoretical accuracy reaching again the percent level, in particular in the calculation of the hadronic matrix elements).

In the case of MFV, the situation appears much more promising when we consider the leptonic sector, more specifically lepton flavour violation (LFV) in the charged lepton sector ($\mu \to e\gamma$, $\mu - e$ conversion in nuclei, $\tau \to \mu\gamma$, etc.). Here two facts play a crucial role and both are related to neutrinos: i) we have to provide a mass to neutrinos, hence we have to extend the particle spectrum of the SM, with the possible introduction of new flavour sources (for instance, new Yukawa couplings related to Yukawa terms where left- and right- handed neutrinos are put into communication); ii) we witness a large LFV in the neutrino sector—neutrino oscillations—with the possibility that such flavour changes may have implications in other sectors of the theory.

The links between the issues of TeV NP and FCNC on one side and neutrino flavour properties and implications on the other side have been since long exploited. More than twenty years ago, Francesca Borzumati and myself pointed out that in supergrav-

ities where neutrinos acquire a mass through the see-saw mechanism, even if the SUSY breaking entails universal sfermion masses, it is possible to (largely) misalign slepton and lepton mass matrices thanks to the influence of the neutrino Yukawa couplings in the running of the slepton masses from the scale at which the soft scalar masses appear down to the right-handed neutrino mass scale(s) [1]. In the 20 years elapsed from that work much (theoretical and experimental) progress has been made and with the new running or upcoming experiments in LFV we are certainly covering very interesting areas of parameters space in several TeV NP cases (see, for instance, the recent review by Junji Hisano [2] and the references quoted therein).

As for the above point ii), the relevance of the large neutrino mixings in other sectors of the theory appears in a striking way when we consider grand-unified theories (GUTs) in the context of SUGRA extensions of the SM. In those frameworks it can happen that the large LFV present in the neutrino sector can be "transferred" to some hadronic sector, typically the masses of the right-handed scalar quarks during their running down to the scale of the right-handed neutrino masses. I take this opportunity to remind here the work in this field of a collaborator of mine, Darwin Chang [3], an enthusiastic researcher in looking for NP signals, who has prematurely left us. The potentialities for NP FCNC contributions in SUGRA GUTs have been thoroughly investigated in a couple of recent papers, in particular emphasizing the intriguing possibility to constrain hadronic (leptonic) FCNC SUSY contributions making use of FCNC leptonic (hadronic) processes [4].

Coming back to the possibility that a symmetry may be the source of the "flavour protection" to solve the NP flavour problem, I am going to briefly report here on a recent work on this issue in collaboration with Lorenzo Calibbi, Joel Jones, Jae-hyeon Park, Werner Porod and Oscar Vives [5].

We were driven by the idea that the SM flavour puzzle (namely, the search for a rationale for fermion masses and mixings) and the NP flavour problem could find a simultaneous answer once the flavour properties of the SM and of the NP beyond it could emerge from a "flavour symmetry". In other words, once we have a theory of flavour this should be able to simultaneously account for the smallness of (some) Yukawa couplings and mixing angles in the SM as well as for the smallness of the FCNC contributions where NP particles run in the loops. The key for such solution can be an enlargement of the SM and NP symmetries with the presence of a flavour or horizontal symmetry. In the limit of exact flavour symmetry we would have a complete degeneracy of three fermion families together with their scalar partners in a SUSY extension of the SM. The (spontaneous) breaking of such symmetry originates the hierarchical structure in fermion families as we observe it as well as it gives rise to a specific pattern of non-universality in the masses of sfermions belonging to different generations.

We consider an $SU(3)$ flavour model. Under the $SU(3)$ flavor symmetry, the three generations of SM fields, both $SU(2)_L$-doublets and singlets, are triplets $\mathbf{3}$ and the Higgs fields are singlets. As flavons, we have θ_3, θ_{23} (anti-triplets $\bar{\mathbf{3}}$), $\bar{\theta}_3$ and $\bar{\theta}_{23}$ (triplets $\mathbf{3}$). The full superpotential is determined by $SU(3)$, and several global symmetries which forbid unwanted terms that would spoil the observed structure of the Yukawa couplings. Using an appropriately chosen set of charges [5], the leading terms in the superpotential are

$$W_{\mathrm{Y}} = H\psi_i\psi_j^c \left[\theta_3^i\theta_3^j + \theta_{23}^i\theta_{23}^j\Sigma + \left(\epsilon^{ikl}\overline{\theta}_{23,k}\overline{\theta}_{3,l}\theta_{23}^j + \epsilon^{jkl}\overline{\theta}_{23,k}\overline{\theta}_{3,l}\theta_{23}^i\right)\left(\theta_{23}\overline{\theta}_3\right) + \epsilon^{ijl}\overline{\theta}_{23,l}\left(\theta_{23}\overline{\theta}_3\right)^2 + \epsilon^{ijl}\overline{\theta}_{3,l}\left(\theta_{23}\overline{\theta}_3\right)\left(\theta_{23}\overline{\theta}_{23}\right) + \dots\right], \tag{1}$$

where the flavon fields have been normalized to the corresponding mediator mass, which means that all the flavon fields in this equation should be understood as θ_i/M_f. The field Σ is a Georgi-Jarlskog field that gets a vev in the $B-L$ direction, distinguishing leptons and quarks. Furthermore, this model is embedded in a $SO(10)$ grand-unified structure at high scales, which allow us to relate quark and lepton (including neutrino) Yukawa couplings. However, the $SU(2)_R$ subgroup of $SO(10)$ must be broken as we need different mediator masses for the up and down sector, and θ_3 and $\overline{\theta}_3$ are $\mathbf{3}\oplus\mathbf{1}$ representations of $SU(2)_R$ which is broken by their vev's [6-8].

The flavon fields get the following vev's:

$$\langle\theta_3\rangle = \begin{pmatrix}0\\0\\1\end{pmatrix}\otimes\begin{pmatrix}a_3^u & 0\\ 0 & a_3^d\, e^{i\chi}\end{pmatrix};\qquad \langle\bar{\theta}_3\rangle = \begin{pmatrix}0\\0\\1\end{pmatrix}\otimes\begin{pmatrix}a_3^u\, e^{i\alpha_u} & 0\\ 0 & a_3^d\, e^{i\alpha_d}\end{pmatrix};$$
$$\langle\theta_{23}\rangle = \begin{pmatrix}0\\ b_{23}\\ b_{23}\, e^{i\beta_3}\end{pmatrix};\qquad \langle\bar{\theta}_{23}\rangle = \begin{pmatrix}0\\ b_{23}\, e^{i\beta_2'}\\ b_{23}\, e^{i(\beta_2'-\beta_3)}\end{pmatrix}; \tag{2}$$

where we require the following relations:

$$\left(\frac{a_3^u}{M_u}\right)^2 = y_t,\quad \left(\frac{a_3^d}{M_d}\right)^2 = y_b,\quad \frac{b_{23}}{M_u} = \varepsilon,\quad \frac{b_{23}}{M_d} = \bar{\varepsilon}, \tag{3}$$

where $\bar{\varepsilon}\simeq 0.15$, $\varepsilon\simeq 0.05$. These relations are valid at the flavour breaking scale, that we take as the GUT scale in the numerical evaluation.

It is straightforward to see that this superpotential reproduces correctly the required Yukawa structure,

$$Y_d \propto \begin{pmatrix}0 & x_{12}^d\,\bar{\varepsilon}^3 & x_{13}^d\,\bar{\varepsilon}^3\\ x_{12}^d\,\bar{\varepsilon}^3 & \bar{\varepsilon}^2 & x_{23}^d\,\bar{\varepsilon}^2\\ x_{13}^d\,\bar{\varepsilon}^3 & x_{23}^d\,\bar{\varepsilon}^2 & 1\end{pmatrix},\qquad Y_u \propto \begin{pmatrix}0 & x_{12}^u\,\varepsilon^3 & x_{13}^u\,\varepsilon^3\\ x_{12}^u\,\varepsilon^3 & \varepsilon^2 & x_{23}^u\,\varepsilon^2\\ x_{13}^u\,\varepsilon^3 & x_{23}^u\,\varepsilon^2 & 1\end{pmatrix}, \tag{4}$$

where x_{ij}^a are $O(1)$ coefficients fixed by the observed values of fermion masses and mixings.

We can now turn to the soft breaking terms. A universal, flavour diagonal mass term will always be allowed. Moreover, in a SUSY theory, the same messenger fields as in the Yukawas will couple the flavons to the scalar fields in the soft terms. Thus, the ε and $\bar{\varepsilon}$ parameters still act as expansion parameters, and represent important corrections to the soft terms.

Clearly any coupling involving a flavon field and its Hermitian conjugate (*i.e.* $\theta_3^{i\dagger}\theta_3^j$) is invariant under the flavour symmetry. From this we can deduce that the soft mass terms get a minimum structure determined uniquely by the flavon content of the model and their vev's. This minimum structure is obtained from the following effective terms:

$$(M_f^2)_i^j = m_0^2\Big(\delta_i^j + \Big[\theta_{3i}^\dagger\theta_3^j + \overline{\theta}_{3,i}\overline{\theta}_3^{\dagger\,j} + \theta_{23i}^\dagger\theta_{23}^j + \overline{\theta}_{23,i}\overline{\theta}_{23}^{\dagger\ j}\Big] + \left(\epsilon_{ikl}\theta_3^k\theta_{23}^l\right)\left(\epsilon^{jmn}\theta_{3m}^\dagger\theta_{23n}^\dagger\right) + \left(\epsilon_{ikl}\overline{\theta}_3^{\dagger\,k}\overline{\theta}_{23}^{\dagger\ l}\right)\left(\epsilon^{jmn}\overline{\theta}_{3,m}\overline{\theta}_{23,n}\right) + \dots\Big). \tag{5}$$

One can find a choice of global charges that reproduces the correct Yukawa structure and does not allow other terms at leading order in the Kähler potential (soft masses).

In the squark sector, after rephasing the fields such that the CKM matrix elements V_{ud}, V_{us}, V_{cb} and V_{tb} are real, the soft masses in the SCKM basis are

$$\left(M^2_{\tilde{u}^c_R}\right)^T = \begin{pmatrix} 1+\varepsilon^2\, y_t & -\varepsilon^3\, e^{i\omega'} & -\varepsilon^3\, e^{i(\omega'-2\chi)} \\ -\varepsilon^3\, e^{-i\omega'} & 1+\varepsilon^2 & \varepsilon^2\, e^{-2i\chi} \\ -\varepsilon^3\, e^{-i(\omega'-2\chi)} & \varepsilon^2\, e^{2i\chi} & 1+y_t \end{pmatrix} m_0^2, \tag{6a}$$

$$\left(M^2_{\tilde{d}^c_R}\right)^T = \begin{pmatrix} 1+\bar{\varepsilon}^2\, y_b & -\bar{\varepsilon}^3\, e^{i\omega_{us}} & -\bar{\varepsilon}^3\, e^{i\omega_{us}} \\ -\bar{\varepsilon}^3\, e^{-i\omega_{us}} & 1+\bar{\varepsilon}^2 & \bar{\varepsilon}^2 \\ -\bar{\varepsilon}^3\, e^{-i\omega_{us}} & \bar{\varepsilon}^2 & 1+y_b \end{pmatrix} m_0^2, \tag{6b}$$

$$M^2_{\tilde{Q}} = \begin{pmatrix} 1+\varepsilon^2\, y_t & -\varepsilon^2\bar{\varepsilon}\, e^{i\omega_{us}} & -\bar{\varepsilon}^3\, y_t e^{i\omega_{us}} \\ -\varepsilon^2\bar{\varepsilon}\, e^{-i\omega_{us}} & 1+\varepsilon^2 & \bar{\varepsilon}^2\, y_t \\ -\bar{\varepsilon}^3\, y_t e^{-i\omega_{us}} & \bar{\varepsilon}^2\, y_t & 1+y_t \end{pmatrix} m_0^2, \tag{6c}$$

where $M^2_{\tilde{Q}}$ is in the basis where Y_d is diagonal. The phases ω_{us}, ω', and δ_i can be found in ref. [5]. The structure of $M^2_{\tilde{Q}}$ in the basis where Y_u is diagonal is similar to $M^2_{\tilde{u}^c_R}$. We have omitted $O(1)$ constants in front of each term, and subdominant terms which can have other phases as β_3 and χ. The slepton soft masses have the same structure, but can be numerically different, since they have a different vev for the Georgi-Jarlskog field $\langle\Sigma_e\rangle = 3\langle\Sigma_d\rangle$.

Although eq. (5) is the minimal structure (RVV1) present for all possible models, it is possible to build other symmetry-dependent soft-mass structures for particular choices of the global symmetries and charges. The observed structure in the Yukawa couplings does not fix completely the introduced global charges and it is possible to add new invariant combinations of flavon fields to the Kähler potential without modifying the Yukawas. The first example of these new combinations of flavon fields in the Kähler is achieved by allowing a $\theta^i_3\bar{\theta}^j_{23}$ term (RVV2). A second possibility is to allow a $(\epsilon^{ikl}\theta^k_3\theta^l_{23})\theta^j_3$ term (RVV3) in the Kähler. The required charges for each of these two possibilities can be found in ref. [5]. The structure of the Yukawa couplings in the superpotential remains unchanged. This is due to the fact that the superpotential is a holomorphic function of the fields while the Kähler is only a real function.

The trilinear couplings follow the same symmetries as the Yukawas. Thus, they have the same flavon structure in RVV1, RVV2 and RVV3. Although they have the same structure, they do not have the same $O(1)$ constants, which means that the rotation into the SCKM basis does not diagonalize them.

In the quark sector, the misalignment of the Y_u and Y_d matrices gives sizeable contributions to the LL and LR sectors. In the lepton sector with RH neutrinos, the same happens due to the misalignment of Y_ν and Y_e [1, 9, 10]. The Y_ν contribution is highly model dependent.

Flavour models based on $SU(3)$ give rise to potentially large rates of LFV processes, such that positive signals of LFV can be found in the currently running or near-future experiments, at least for SUSY masses within the reach of the LHC [11]. The presence of large mixing among flavours relies on the features of the above $SU(3)$ model: the presence of nonuniversal scalar masses already at the scale where the SUSY breaking terms appear, and the fact that the trilinear A_f matrices are in general not aligned with the corresponding Yukawa matrices. Let us start considering the case $A_0 = 0$, where

TABLE I. – *Order of magnitude of LFV mass insertions, for the three models.*

	$\lvert(\delta^e_{LL})_{12}\rvert$	$\lvert(\delta^e_{LL})_{13}\rvert$	$\lvert(\delta^e_{LL})_{23}\rvert$	$\lvert(\delta^e_{RR})_{12}\rvert$	$\lvert(\delta^e_{RR})_{13}\rvert$	$\lvert(\delta^e_{RR})_{23}\rvert$
RVV1	$\frac{1}{3}\varepsilon^2\bar{\varepsilon}$	$y_t\bar{\varepsilon}^3$	$3y_t\bar{\varepsilon}^2$	$\frac{1}{3}\bar{\varepsilon}^3$	$\frac{1}{3}\bar{\varepsilon}^3$	$\bar{\varepsilon}^2$
RVV2	$\frac{1}{3}\varepsilon^2\bar{\varepsilon}$	$\frac{1}{3}\sqrt{y_t}\varepsilon\bar{\varepsilon}$	$\sqrt{y_t}\varepsilon$	$\frac{1}{3}\bar{\varepsilon}^3$	$\frac{1}{3}\sqrt{y_b}\bar{\varepsilon}^2$	$\sqrt{y_b}\bar{\varepsilon}$
RVV3	$3y_t\varepsilon\bar{\varepsilon}^2$	$y_t\varepsilon$	$3y_t\bar{\varepsilon}^2$	$\frac{1}{3}\bar{\varepsilon}^3$	$y_b\bar{\varepsilon}$	$\bar{\varepsilon}^2$

the latter effect is strongly reduced so that, in terms of mass insertions, $\mathrm{BR}(l_i \to l_j\gamma)$ mainly depends on $|(\delta^e_{LL})_{ij}|^2$ and $|(\delta^e_{RR})_{ij}|^2$. Looking at the structure of the slepton soft mass matrices in the three versions of the model (table I), we see that RVV1 and RVV2 are expected to give similar predictions for $\mathrm{BR}(\mu \to e\gamma)$ and $\mathrm{BR}(\tau \to \mu\gamma)$. In the case of RVV3, the prediction for $\mathrm{BR}(\tau \to \mu\gamma)$ will be also similar to the previous two cases, while we expect $\mathrm{BR}(\mu \to e\gamma)$ to be strongly enhanced. For RVV3, the LL mass insertion is larger by a factor $9\, y_t\, \bar{\varepsilon}/\varepsilon = \mathcal{O}(10)$ with respect to RVV1 and RVV2, and the $\mathrm{BR}(\mu \to e\gamma)$ is consequently increased by two orders of magnitude.

To summarize, let us compare the expectations for the different LFV processes. In the case $A_0 = 0$, considering for simplicity only the contribution from δ^e_{LL}, we have

$$\frac{\mathrm{BR}(\tau \to e\,\gamma)}{\mathrm{BR}(\mu \to e\,\gamma)} \approx \left(\frac{m_\tau}{m_\mu}\right)^5 \frac{\Gamma_\mu}{\Gamma_\tau} \frac{(\delta^e_{\mathrm{LL}})^2_{13}}{(\delta^e_{\mathrm{LL}})^2_{12}} \approx \mathcal{O}(1)\,(\mathrm{RVV1}, \mathrm{RVV2}, \mathrm{RVV3}), \tag{7}$$

$$\frac{\mathrm{BR}(\tau \to \mu\,\gamma)}{\mathrm{BR}(\mu \to e\,\gamma)} \approx \left(\frac{m_\tau}{m_\mu}\right)^5 \frac{\Gamma_\mu}{\Gamma_\tau} \frac{(\delta^e_{\mathrm{LL}})^2_{23}}{(\delta^e_{\mathrm{LL}})^2_{12}} \approx \mathcal{O}(10^3)\,(\mathrm{RVV1}, 2), \mathcal{O}(10)\,(\mathrm{RVV3}), \tag{8}$$

where Γ_μ (Γ_τ) is the μ (τ) full width. Given the fact that the upper bound on $\mathrm{BR}(\tau \to e\,\gamma)$ is 4 orders of magnitude higher than that on $\mathrm{BR}(\mu \to e\,\gamma)$, we see that $\mathrm{BR}(\tau \to e\gamma)$ is not able to constrain the parameter space better than $\mathrm{BR}(\mu \to e\gamma)$ in none of the three models. On the other hand, we expect from eq. (8) that the present constraints given by $\mu \to e\gamma$ and $\tau \to \mu\gamma$, that differ by three orders of magnitude, are comparable for RVV1 and RVV2, while $\mu \to e\gamma$ should give the strongest constraint in the case of RVV3.

In the case $A_0 \neq 0$, generally large δ^e_{LR} insertions arise as a consequence of the misalignment between A_f and the corresponding Yukawa matrix Y_f. In this case, the neutralino contribution to $\mathrm{BR}(\mu \to e\gamma)$ gets strongly enhanced [11] and the present (or future) bound requires heavier SUSY masses to be fulfilled, specially in the region where the gaugino mass is much larger than the common sfermion mass. Nevertheless, we expect this effect to be visible only in the case of RVV1 and RVV2, while for RVV3 the very large $(\delta^e_{LL})_{12}$ should still give the dominant contribution.

For the numerical analysis for the LFV decays, we fix the unknown $O(1)$ parameters to random values. The presently allowed region on the m_0-$M_{1/2}$ plane is approximately $(m_0, M_{1/2}) \gtrsim (700, 300)\,\mathrm{GeV}$. In the case of RVV3, $\mu \to e\gamma$ already gives a strong constraint, $(m_0, M_{1/2}) \gtrsim (1400, 800)\,\mathrm{GeV}$, which is much more stringent than the one provided by $\tau \to \mu\gamma$. As a consequence, for SUSY masses lying within the LHC reach, RVV3 results already rather disfavoured, while RVV1 and RVV2 are not strongly constrained. Considering the sensitivity expected at the MEG experiment for $\mathrm{BR}(\mu \to e\gamma)$, $\mathcal{O}(10^{-13})$, we see that also RVV1 and RVV2 will be tested in most of the parameter space accessible to the LHC, while RVV3 will be completely probed well beyond the LHC reach.

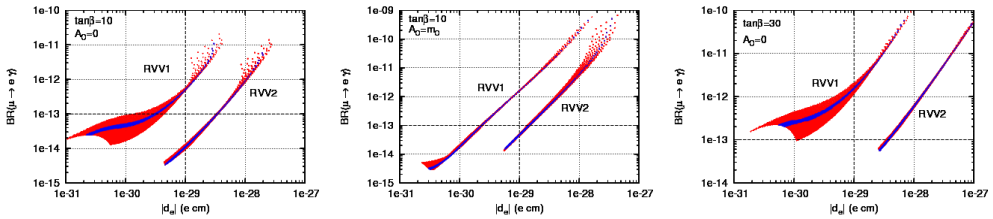

Fig. 1. – (Colour on-line) BR($\mu \to e\gamma$) *vs.* $|d_e|$ for different scenarios. See the text for details.

Moreover, in case of larger values of $\tan\beta$ (*e.g.*, $\tan\beta = 30$), since BR($\mu \to e\gamma$) $\propto \tan^2\beta$, MEG will be able to test all the parameter space accessible to the LHC also for RVV1 and RVV2.

As RVV3 is heavily constrained by LFV, in the following we shall exclude it from our analysis, and concentrate exclusively on RVV1 and RVV2.

The EDMs of fermions, such as the electron and the neutron, are highly suppressed in the SM, and thus they are excellent observables where to look for CP-violation in new physics.

The electron EDM was studied in ref. [11] within the context of RVV1. In these models CP is spontaneously broken in the flavour sector. Therefore, the phases in the μ parameter and diagonal A_f terms are highly suppressed and can be neglected. In such a case, the imaginary parts required for EDMs only appear from flavour-changing mass insertions.

Electron EDM predictions are large enough to be probed at future EDM experiments. For relatively light SUSY masses we obtain $d_e \sim 10^{-29}\, e\,\mathrm{cm}^{-1}$ and $d_e \sim 10^{-28}\, e\,\mathrm{cm}^{-1}$, for RVV1 and RVV2, respectively. The latter predicts a value of d_e about one order of magnitude larger than the former for any particular value of m_0 and $M_{1/2}$ due to the larger ε suppresion. This means that by reaching $d_e \sim 10^{-29}\, e\,\mathrm{cm}^{-1}$ one could probe a much larger part of the evaluated parameter space, with $m_0 \lesssim 1500\,\mathrm{GeV}$, $M_{1/2} \lesssim 2000\,\mathrm{GeV}$. In particular, for RVV2, observation of SUSY at the LHC and solving the ϵ_K tension [12] would force d_e to be larger than $10^{-29}\, e\,\mathrm{cm}^{-1}$. However, we have to take into account that these values will vary by factors $O(1)$ because of the unknown $O(1)$ coefficients to the different MIs.

If we require in addition that the $(g-2)_\mu$ discrepancy between SM and data is explained by SUSY, we are restricted in a region of rather light SUSY masses, where most of the observables are expected to be close to the present experimental bounds.

In fig. 1, we compare the discovery potential of the two most promising leptonic observables, $\mu \to e\gamma$ and the electron EDM. The correlation of BR($\mu \to e\gamma$) *vs.* $|d_e|$ is plotted for both RVV1 and RVV2, in the case $\tan\beta = 10$, $A_0 = 0$ (left), $\tan\beta = 10$, $A_0 = 1$ (center) and $\tan\beta = 30$, $A_0 = 0$ (right). We study the mass range: $0 < m_0 < 2.5\,\mathrm{TeV}$, $0 < M_{1/2} < 1.5\,\mathrm{TeV}$. In the figures, only the "ϵ_K-favoured" region with negative $(\delta^d_{RR})_{12}$ has been plotted with blue and red colours corresponding to two different implementations of the constraint of having SUSY contributions to account for the "SM-deficit" in reproducing the correct ϵ_K value [12]. The horizontal line corresponds to the final sensitivity of MEG, the vertical line to the sensitivity on $|d_e|$ of the running Yale-PdO experiment. We see that, for RVV1, $\mu \to e\gamma$ should be able to constrain the parameter space more strongly than eEDM, while for RVV2 it is $|d_e|$ the most sensitive

observable (except for the large $\tan\beta$ case). These features could be useful in the future, in order to discriminate among different models and, more in general, shed light on the structure of mixings and phases in the slepton mass matrix.

* * *

The main content of this contribution is based on a work done in collaboration with L. Calibbi, J. Jones Pérez, J.-h. Park, W. Porod, and O. Vives. I wish to warmly thank the Organizers of this edition of Les Rencontres de Physique de la Vallée d'Aoste for their effort and success in creating the nice and stimulating atmosphere which has constantly been the characteristic mark of this series of meetings.

REFERENCES

[1] Borzumati F. and Masiero A., *Phys. Rev. Lett.*, **57** (1986) 961.
[2] Hisano J., arXiv:0807.0149 [hep-ph].
[3] Darwin Chang, Masiero A. and Murayama H., *Phys. Rev. D*, **67** (2003) 075013.
[4] Ciuchini M., Masiero A., Paradisi P., Silvestrini L., Vempati S. and Vives O., *Nucl. Phys. B*, **783** (2007) 112.
[5] Calibbi L., Jones-Perez J., Masiero A., Park J. h., Porod W. and Vives O., arXiv:0907.4069 [hep-ph].
[6] Ross G. G. and Velasco-Sevilla L., *Nucl. Phys. B*, **653** (2003) 3 [arXiv:hep-ph/0208218].
[7] King S. F. and Ross G. G., *Phys. Lett. B*, **574** (2003) 239 [arxiv:hep-ph/0307190].
[8] Ross G. G., Velasco-Sevilla L. and Vives O., *Nucl. Phys. B*, **692** (2004) 50 [arXiv:hep-ph/0401064].
[9] Casas J. A. and Ibarra A., *Nucl. Phys. B*, **618** (2001) 171 [arXiv:hep-ph/0103065].
[10] Masiero A., Vempati S. K. and Vives O., *Nucl. Phys. B*, **649** (2003) 189 [arXiv:hep-ph/0209303].
[11] Calibbi L., Jones-Perez J. and Vives O., *Phys. Rev. D*, **78** (2008) 075007 [arXiv:0804.4620 [hep-ph]].
[12] Buras A. J. and Guadagnoli D., *Phys. Rev. D*, **78** (2008) 033005 [arXiv:0805.3887 [hep-ph]].

SESSION VI - ELECTROWEAK AND TOP PHYSICS

IL NUOVO CIMENTO Vol. 32 C, N. 5-6 Settembre-Dicembre 2009
DOI 10.1393/ncc/i2010-10535-y

Colloquia: LaThuile09

Electroweak measurements from the Tevatron

E. Halkiadakis on behalf of the CDF and DØ Collaborations
Rutgers, The State University of New Jersey - Piscataway, NJ, USA

(ricevuto il 10 Novembre 2009; pubblicato online il 18 Gennaio 2010)

Summary. — I review the status of electroweak measurements including W and Z bosons produced at the Tevatron. I describe measurements of the W-boson mass, the W production charge asymmetry, diboson production and limits on anomalous trilinear gauge couplings. These analyses use integrated luminosities ranging from $200\,\mathrm{pb}^{-1}$ to $3.6\,\mathrm{fb}^{-1}$ of data collected by the CDF and DØ Run-II detectors at the Fermilab Tevatron.

PACS 12.15.Ji – Applications of electroweak models to specific processes.
PACS 13.85.Qk – Inclusive production with identified leptons, photons, or other nonhadronic particles.
PACS 14.70.Fm – W bosons.

1. – Introduction

The Fermilab Tevatron is a p-$\bar{p}$ collider at a center-of-mass energy of 1.96 TeV and produces W and Z bosons via q-$\bar{q}$ annihilation at a high rate. Electroweak measurements with W and Z bosons provide us with high-precision tests of the Standard Model (SM) as well as indirect knowledge about the Higgs boson and possible new physics.

In this report, I summarize recent electroweak measurements from the CDF and DØ experiments at the Tevatron using data with integrated luminosities ranging from $200\,\mathrm{pb}^{-1}$ to $3.6\,\mathrm{fb}^{-1}$. First, I focus on the high-precision measurements of the W-boson mass and the W production charge asymmetry. Additionally, I present measurements of diboson production which include a first measurement at the Tevatron of $Z\gamma$ in the purely neutral final state and the observation of ZZ production. I also report a summary of limits on anomalous trilinear gauge couplings.

2. – Single-boson production

2˙1. *Precision measurement of the W-boson mass.* – The W-boson mass, m_W, is a fundamental parameter of the SM and its precision measurement is a primary goal of the Tevatron physics program. Together with the mass of the top quark, a precise measurement of m_W is the key to our understanding of the electroweak interaction, in

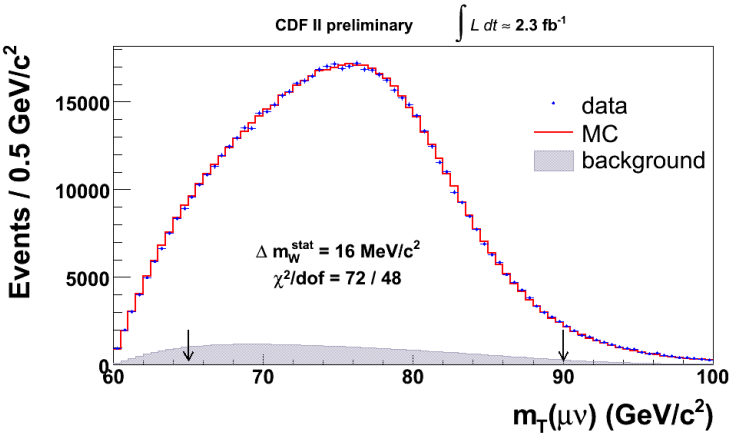

Fig. 1. – The transverse mass distribution of $W \to \mu\nu$ decays from CDF with $2.3\,\mathrm{fb}^{-1}$ of data.

particular the mechanism for electroweak symmetry breaking. In other words, reducing the uncertainty on the measurement of m_W allows us to further constrain the Higgs boson mass.

At the Tevatron, m_W is measured using leptonic W decays and is extracted from a template fit to the transverse mass (m_T), transverse momentum of the lepton (p_T^ℓ) and the transverse missing energy ($\not\!\!E_{\mathrm{T}}$) distributions. A fast Monte Carlo simulation is used to model the lineshape of the template distributions, accounting for the complex detector acceptance and resolution effects. We constrain and evaluate our level of understanding of these important detector and physics effects which determine the precision of the measurement of m_W. Examples of these effects, which are rigorously modeled and studied, include the tracker momentum scale and resolution, the calorimeter energy scale and resolution, the intrinsic W-boson transverse momentum and the proton parton distribution functions (PDFs).

Using $200\,\mathrm{pb}^{-1}$ of Tevatron Run-II data which contains a sample of 63964 $W \to e\nu$ decays and 51128 $W \to \mu\nu$ decays the CDF Collaboration measures $m_W = 80413 \pm 34(\mathrm{stat.}) \pm 34(\mathrm{syst.})\,\mathrm{MeV}/c^2$, with a total measurement uncertainty of $48\,\mathrm{MeV}/c^2$ [1]. Combining this measurement with measurements of m_W from Run I of the Tevatron and LEP with uncertainties of $59\,\mathrm{MeV}/c^2$ and $33\,\mathrm{MeV}/c^2$, respectively, give a current world average of $m_W = 80399 \pm 25\,\mathrm{MeV}/c^2$. Additionally, using a dataset corresponding to $1\,\mathrm{fb}^{-1}$ of data, with 499830 $W \to e\nu$ decays the DØ Collaboration recently presented a preliminary measurement of $m_W = 80401 \pm 21(\mathrm{stat.}) \pm 38(\mathrm{syst.})\,\mathrm{MeV}/c^2 = 80401 \pm 43\,\mathrm{MeV}/c^2$, the most precise to date.

Many of the systematic uncertainties in these measurements are limited by the statistics of the control samples used to understand the detector and physics effects and can be improved with an analysis of the larger datasets in hand. Additionally, improvements in the detector model and the production and decay model (for example, by including the input from updated PDF fits) are likely to further reduce the overall systematic uncertainty on future measurements of m_W. CDF has begun analyzing a data sample with an integrated luminosity of $2.3\,\mathrm{fb}^{-1}$, as can be seen in fig. 1. Studies in progress confirm that many of the systematic uncertainties scale with luminosity as expected and we look forward to an updated m_W measurement with a precision better than the current world average of $25\,\mathrm{MeV}/c^2$.

2˙2. *W production charge asymmetry.* – At the Fermilab Tevatron, $W^+(W^-)$ bosons are created primarily by the interaction of u (d) quarks from the proton and $\bar{d}$ ($\bar{u}$) quarks from the anti-proton. Since u-quarks carry, on average, a higher fraction of the proton's momentum than d-quarks, the W^+ tends to be boosted along the proton beam direction and the W^- tends to be boosted along the anti-proton direction. The difference between the W^+ and W^- rapidity distributions results in a charge asymmetry,

$$A(y_W) = \frac{\mathrm{d}\sigma^+/\mathrm{d}y_W - \mathrm{d}\sigma^-/\mathrm{d}y_W}{\mathrm{d}\sigma^+/\mathrm{d}y_W + \mathrm{d}\sigma^-/\mathrm{d}y_W}\,, \tag{1}$$

where y_W is the W-boson rapidity and $\mathrm{d}\sigma^{\pm}/\mathrm{d}y_W$ is the differential cross-section for W^+ or W^- boson production. The PDFs describing the internal structure of the proton are constrained by measuring $A(y_W)$. Improvements in PDF uncertainties will reduce the total uncertainties on many important measurements, such as the measurement of the W-boson mass described in the previous section.

Traditionally, the W charge asymmetry measurements at the Tevatron have been made as a function of the pseudorapidity η of the leptons from decays of $W \to l\nu_l$ ($l = e, \mu$) since the W decay involves a neutrino whose longitudinal momentum is not determined experimentally. A recent measurement of the lepton charge asymmetry from DØ uses $W \to e\nu$ decays in $750\,\mathrm{pb}^{-1}$ [2]. As shown in fig. 2, the asymmetry is measured in two bins of electron E_T, $25 < E_T < 35\,\mathrm{GeV}$ and $E_T > 35\,\mathrm{GeV}$, since for a given η the two E_T regions probe different ranges of y_W. For higher E_T, the electron direction is closer to the W direction and gives an improved sensitivity to the PDFs. The data are compared to a next-to-leading-order (NLO) perturbative QCD calculation [3,4] with NLO PDFs from CTEQ6.6 [5] and MRST04 [6]. Figure 2 shows that the measured charge asymmetries tend to be lower than the theoretical predictions for high-η electrons.

Since the lepton charge asymmetry is a convolution of the W production charge asymmetry and the $V - A$ asymmetry from W decays these two asymmetries tend to cancel at large pseudorapidities ($|\eta| < 2.0$). This convolution weakens and complicates the constraint on the proton PDFs. In an analysis by CDF, the complication is resolved by using additional information in the lepton E_T and the $\not\!\!E_{\mathrm{T}}$ on an event-by-event basis to measure the asymmetry as a function of the $|y_W|$ instead of the lepton $|\eta|$. Using this new analysis technique [7] CDF presents the first direct measurement of the W production charge asymmetry, which uses $W \to e\nu$ decays and $1\,\mathrm{fb}^{-1}$ of data [8] and is shown in fig. 3. Also shown are the predictions of a NNLO QCD calculation [9] using the MRST 2006 NNLO PDF sets [6] and a NLO QCD calculation using the CTEQ6.1 NLO PDF sets [5], which are in agreement with the measured asymmetry.

These precision measurements of the W charge asymmetry from the Tevatron experiments are testing the accuracy of our knowledge of the proton structure and once included are expected to improve the precision of the global PDFs fits.

3. – Diboson production

The production of dibosons at the Tevatron has similar topologies to beyond the SM searches and therefore contribute as a background to possible new physics, such as in the searches for the Higgs or supersymmetry. Therefore, by making measurements of diboson processes we can test for deviations from SM predictions. These tests can be performed with measurements of the diboson production cross-sections as well as with measurements of triple gauge couplings (TGCs). Couplings between gauge bosons are the

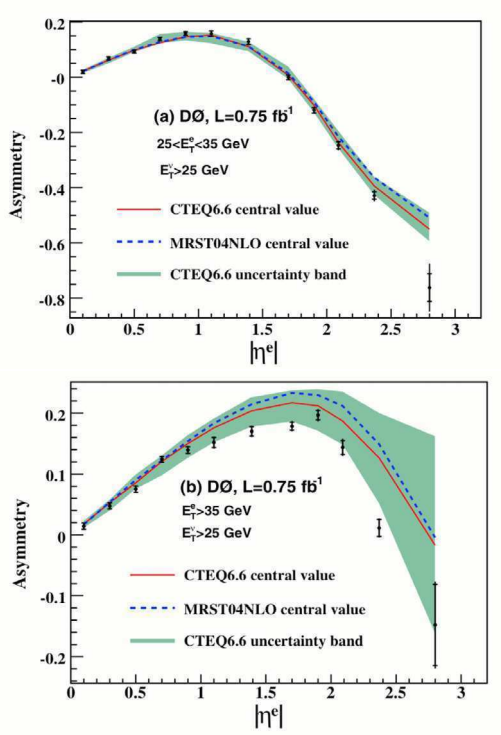

Fig. 2. – The measured electron charge asymmetry distribution from DØ in two electron E_T bins: $25 < E_T < 35\,\text{GeV}$ (left) and $E_T > 35\,\text{GeV}$ (right).

least well-known quantities in the electroweak sector and various SM extensions predict large values of TGCs. The SM allows couplings which involve two W-bosons and either a γ or a Z boson, however, there are no couplings which include only combinations of γ and Z bosons. Measurements of TGCs at the Tevatron are important as they are complementary to the measurements from LEP, exploring a higher $\sqrt{s}$ and different combinations of couplings. What I focus on in this report are the $Z\gamma$ and ZZ processes which probe the $ZZ\gamma$, $Z\gamma\gamma$ and ZZZ couplings and are not permitted in the SM at leading order. A general parameterization is used to describe these anomalous couplings in terms of CP-violating and CP-conserving parameters and are also described by a form factor, with the parameter Λ being the new physics scale responsible for conserving unitarity.

3˙1. *$Z\gamma$ production.* – The SM prediction of $Z\gamma$ production is via two tree-level diagrams: initial-state radiation (ISR) and final-state radiation (FSR). The SM cross-section for $Z\gamma$ is very small and due to infrared divergences it depends on the energy threshold of the photon, E_T^γ.

The channels involving two charged leptons (ℓ = e or μ), $ee\gamma$ and $\mu\mu\gamma$, have been extensively studied at Tevatron. Both CDF and DØ apply similar event selection requiring two isolated high-p_T leptons, a photon with $E_T^\gamma > 7\,\text{GeV}$ and a separation requirement between the photon and the leptons of $\Delta R_{\ell\gamma} > 0.7$. The invariant mass of the two leptons is also required to be $M_{\ell\ell} > 40\,\text{GeV}/c^2$ for CDF and $M_{\ell\ell} > 30\,\text{GeV}/c^2$ for DØ.

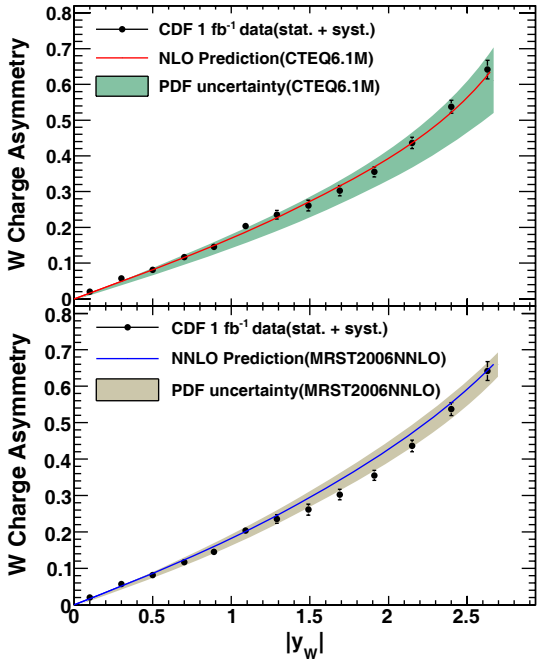

Fig. 3. – The measured W production charge asymmetry from CDF and theoretical predictions from (top) NLO CTEQ6.1 and (bottom) NNLO MRST2006, with their associated PDF uncertainties.

Additionally, CDF separates the ISR from the FSR events by looking at different $M_{\ell\ell\gamma}$ regions; ISR is defined as $M_{\ell\ell\gamma} > 100\,\mathrm{GeV}/c^2$ and FSR is defined as $M_{\ell\ell\gamma} < 100\,\mathrm{GeV}/c^2$. Table I summarizes the cross-section times branching ratio measurements from both CDF and DØ, showing good agreement compared to the NLO prediction [11].

DØ has recently observed with a 5.1σ significance the purely neutral final state of $Z\gamma \to \nu\nu\gamma$ with $3.6\,\mathrm{fb}^{-1}$ of data for the first time at the Tevatron. This is a very challenging analysis. It has a higher acceptance and a higher branching ratio to $\nu\nu$ than to $\ell\ell$ and is also interesting since it is produced uniquely via ISR. The events are selected by making strict requirements of $E_T^\gamma > 90\,\mathrm{GeV}$ and $\not\!\!E_\mathrm{T} > 70\,\mathrm{GeV}$. To suppress backgrounds, events are selected with no jets, and no high-p_T tracks. Additionally,

TABLE I. – *Summary of measured $Z\gamma$ cross-sections from the Tevatron experiments compared to the theoretical predictions.*

Channel	Experiment ($\int \mathcal{L}$)	Measured $\sigma \times$ BR (pb)	NLO Prediction (pb)
$Z\gamma \to \ell\ell\gamma$	DØ ($1\,\mathrm{fb}^{-1}$) [10]	4.96 ± 0.42 (stat.+syst.)	4.7 ± 0.2 [11]
	CDF, ISR (1.1–$2.0\,\mathrm{fb}^{-1}$)	1.2 ± 0.2 (stat.+syst.)	1.2 ± 0.1 [11]
	CDF, FSR (1.1–$2.0\,\mathrm{fb}^{-1}$)	3.4 ± 0.3 (stat.+syst.)	3.3 ± 0.3 [11]
$Z\gamma \to \nu\nu\gamma$	DØ ($3.6\,\mathrm{fb}^{-1}$) [12]	0.032 ± 0.009 (stat.+syst.)	0.039 ± 0.004 [11]

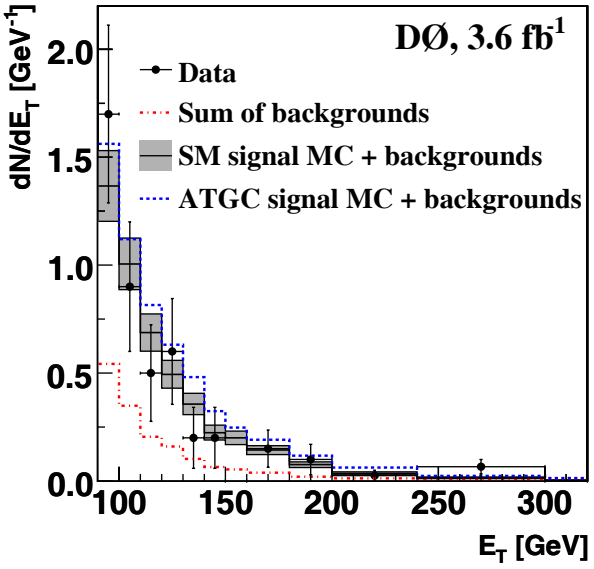

Fig. 4. – The E_T^γ distribution from $Z\gamma \to \nu\nu\gamma$ events analyzed by DØ and used to place limits on anomalous TGCs.

there is a challenging non-collision background coming from cosmic ray muons or beam halo muons which undergo bremsstrahlung radiation. This background is removed by requiring that the photon points back to the primary vertex of the event. The measured cross-section times branching ratio for this process is shown in table I and is in agreement with the SM prediction.

The photon E_T^γ spectra in these processes are used to probe anomalous TGCs, an example of which is shown in fig. 4 from the DØ analysis of $Z\gamma \to \nu\nu\gamma$ events. This figure shows the consistency with the SM prediction and also shows the effect on the shape of the E_T^γ spectrum assuming anomalous couplings near the current bounds. Both CDF and DØ have used the samples described above to set limits at the 95% confidence level (CL) on anomalous $ZZ\gamma$ and $Z\gamma\gamma$ couplings. The CDF results are based upon the $Z\gamma \to \ell\ell\gamma$ channel and were calculated using a scale of $\Lambda = 1.2\,\text{TeV}$ and the limits on the CP-conserving parameters are $|h_{30}^Z| < 0.083$, $|h_{30}^\gamma| < 0.084$, and $|h_{40}^{\gamma,Z}| < 0.0047$. The DØ results combine both the charged and neutral $Z\gamma$ channels and use a scale factor of $\Lambda = 1.5\,\text{TeV}$, giving combined limits of $|h_{30}^{\gamma,Z}| < 0.033$ and $|h_{40}^{\gamma,Z}| < 0.0017$ [10, 12], representing the best limits from the Tevatron to date. The results are similar for the CP odd couplings.

3·2. *ZZ production.* – The ZZ production at the Tevatron is expected to be very small, with a NLO prediction of $1.4 \pm 0.1\,\text{pb}$ [13]. The two experimentally viable modes are: 1) when both Z's decay to charged leptons ($\ell\ell\ell\ell$) and 2) when one Z decays to charged leptons and the other to two neutrinos ($\ell\ell\nu\nu$). Although the $\ell\ell\ell\ell$ channel has a small branching ratio of $\sim 0.5\%$, the contribution from backgrounds is small. The $\ell\ell\nu\nu$ has a roughly six times larger branching ratio of $\sim 3\%$, but suffers from larger backgrounds.

TABLE II. – *Summary of ZZ observed and expected significance results from the Tevatron.*

Experiment ($\int \mathcal{L}$)	Channel:	$\ell\ell\nu\nu$	$\ell\ell\ell\ell$	Combined
CDF ($1.9\,\text{fb}^{-1}$) [14]	P-value	0.12	1.1×10^{-5}	5.1×10^{-6}
	Obs. Sig.	1.2σ	4.2σ	4.4σ
	Exp. Sig.			50% chance of 5σ
DØ (1.0–$2.7\,\text{fb}^{-1}$) [15-17]	P-value	0.42×10^{-2}	4.3×10^{-8}	6.2×10^{-9}
	Obs. Sig.	2.6σ	5.3σ	5.7σ
	Exp. Sig.	2.0σ	3.7σ	5.2σ

The analysis strategy from both CDF and DØ is to consider a combination of both of these final states. Last year, CDF made a first measurement of ZZ production using $1.9\,\text{fb}^{-1}$ of data, observing an excess of events with a probability of 5.1×10^{-6} to be due to the expected background. This corresponds to a significance of 4.4 standard deviations (σ), just shy of a 5σ observation (the expected significance for 5σ being 50%). The CDF measured cross-section is $\sigma(p\bar{p} \to ZZ) = 1.4^{+0.7}_{-0.6}$ (stat. + syst.) pb. More recently DØ using $1.7\,\text{fb}^{-1}$ of data in the $\ell\ell\ell\ell$ channel passed the 5σ threshold for observation. Combining this result with the $\ell\ell\nu\nu$ final state with $2.7\,\text{fb}^{-1}$ and a previous $\ell\ell\ell\ell$ analysis with $1\,\text{fb}^{-1}$ of data yields a significance of 5.7σ and a combined cross-section of $\sigma(p\bar{p} \to ZZ) = 1.60 \pm 0.65$ (stat. + syst.) pb. Figure 5 shows the $M_{\ell\ell}$ and $M_{\ell\ell\ell\ell}$ invariant-mass distributions in the $\ell\ell\ell\ell$ channels for CDF and DØ, respectively. A summary of the observed and expected significance results for ZZ production from the Tevatron is shown in table II. Both experiments measure cross-sections for ZZ production consistent with the SM prediction.

Since neither experiment observes an excess of events beyond what is predicted in the SM, they are able to place 95% CL limits on ZZ CP-violating and -conserving anomalous couplings parameters. DØ uses $1.0\,\text{fb}^{-1}$ of data in the $\ell\ell\ell\ell$ channel to set these limits by comparing the number of observed candidate events to the predicted background plus expected signal assuming anomalous trilinear couplings. The DØ results use a scale factor of $\Lambda = 1.2\,\text{TeV}$ with limits of $|f_4^\gamma| < 0.26$, $-0.30 < f_5^\gamma < 0.28$, $|f_4^Z| < 0.28$, $-0.31 < f_5^Z < 0.29$ [16]. CDF's limits are set with an analysis of $1.9\,\text{fb}^{-1}$ of data in the $\ell\ell$jj channel and uses the di-jet invariant mass distribution in the high $p_T^Z > 210\,\text{GeV}/c$ region. The CDF limits also use a scale factor of $\Lambda = 1.2\,\text{TeV}$ and are $|f_4^\gamma| < 0.10$, $|f_5^\gamma| < 0.11$, $|f_4^Z| < 0.12$, $-0.13 < f_5^Z < 0.12$.

4. – Conclusions

With the increasingly large datasets the Tevatron experiments, CDF and DØ, continue to probe our understanding of electroweak production with new sensitivity. Precision W-boson mass measurements continue to further test the SM and help provide new indirect limits on the Higgs mass. Recent precision measurements of the W charge asymmetry is testing the accuracy of our knowledge of the proton structure. We are now measuring diboson production and couplings with greater and greater precision. ZZ

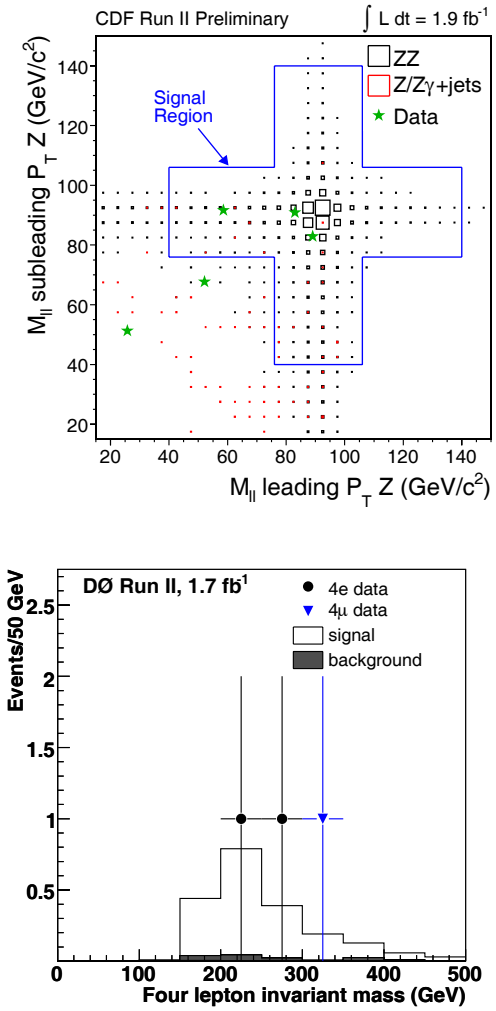

Fig. 5. – Top: the invariant masses of the two lepton pairs ($M_{\ell\ell}$) plotted against each other in the $ZZ \to \ell\ell\ell\ell$ channel from CDF with 1.9 fb^{-1} of data. Bottom: the four-lepton invariant-mass ($M_{\ell\ell\ell\ell}$) distribution in the $ZZ \to \ell\ell\ell\ell$ channel from DØ with 1.7 fb^{-1} of data.

production has now been observed and the first observation of $Z\gamma$ production in the purely neutral final state has been made at the Tevatron. New limits have been set on anomalous couplings for $ZZZ/ZZ\gamma/Z\gamma\gamma$ production.

* * *

I would like to thank the CDF and DØ Collaborations, in particular those whose hard work went into the results presented here, as well as the conference organizers for hosting an excellent conference.

REFERENCES

[1] Aaltonen T. *et al.*, *Phys. Rev. Lett.*, **99** (2007) 151801; *Phys. Rev. D*, **77** (2008) 112001.
[2] Abazov V. M. *et al.*, *Phys. Rev. Lett.*, **101** (2008) 211801.
[3] Balazs C. and Yuan C. P., *Phys. Rev. D*, **56** (1997) 5558.
[4] Barberio E. and Was Z., *Comput. Phys. Commun.*, **79** (1994) 291; PHOTOS version 2.0 is used.
[5] Nadolsky P. M. *et al.*, *Phys. Rev. D*, **78** (2008) 013004; Stump D. *et al.*, *JHEP*, **10** (2003) 046.
[6] Martin A. D., Roberts R. G., Stirling W. J. and Thorne R. S., *Phys. Lett. B*, **604** (2004) 61; hep-ph/0706.0459.
[7] Bodek A., Chung Y., Halkiadakis E., Han B. and McFarland K., *Phys. Rev. D*, **77** (2008) 111301(R).
[8] Aaltonen T. *et al.*, *Phys. Rev. Lett.*, **102** (2009) 181801.
[9] Anastasiou C., Dixon L., Melnikov K. and Petriello F., *Phys. Rev. D*, **69** (2004) 094008.
[10] Abazov V. M. *et al.*, *Phys. Lett. B*, **653** (2007) 378.
[11] Baur U., Han T. and Ohnemus J., *Phys. Rev. D*, **57** (1998) 2823.
[12] Abazov V. M. *et al.*, *Phys. Rev. Lett.*, **102** (2009) 201802.
[13] Campbell J. and Ellis R., *Phys. Rev. D*, **60** (1999) 113006.
[14] Aaltonen T. *et al.*, *Phys. Rev. Lett.*, **100** (2008) 201801.
[15] Abazov V. M. *et al.*, *Phys. Rev. Lett.*, **101** (2008) 171803.
[16] Abazov V. M. *et al.*, *Phys. Rev. Lett.*, **100** (2008) 131801.
[17] Abazov V. M. *et al.*, *Phys. Rev. D*, **78** (2008) 072002.

IL NUOVO CIMENTO Vol. 32 C, N. 5-6 Settembre-Dicembre 2009
DOI 10.1393/ncc/i2010-10547-7

Colloquia: LaThuile09

Precision determination of the top quark mass

L. Brigliadori on behalf of CDF and D0 Collaborations
Università di Bologna and INFN, Sezione di Bologna - Bologna, Italy

(ricevuto il 10 Novembre 2009; pubblicato online il 20 Gennaio 2010)

Summary. — The mass of the top quark is a fundamental parameter of the Standard Model and its measurement allows both to verify the consistency of the model predictions and to set constraints on possible, still unobserved physics. In this paper we present a selected review of the most recent or relevant results obtained by the CDF and D0 Collaborations using up to about $3.6\,\mathrm{fb}^{-1}$ of proton-antiproton collisions at $\sqrt{s} \simeq 1.96\,\mathrm{TeV}$ produced at the Tevatron collider.

PACS 14.65.Ha – Top quarks.
PACS 12.15.Ff – Quark and lepton masses and mixing.

1. – Introduction

The first observation of the top quark by the CDF and D0 experiments at the Fermilab Tevatron collider in 1995 [1, 2] was somehow expected because, in the framework of the Standard Model (SM), a weak isospin partner of the bottom quark, previously observed in 1977, is necessary. However, since its early measurement, the large value of the top quark mass (M_{top}) represented a really striking property of this particle, giving to the top a special role within the SM and suggesting also possible links to new physics. In fact, apart being itself a fundamental parameter of the SM, M_{top} is by far the largest mass among the ones of the observed fermions, and this makes the top quark contribution to higher-order corrections to many electroweak observables dominant. Therefore M_{top} plays a central role in checking the consistency of theoretical predictions of the SM. The radiative corrections apply also to the W-boson propagator, and therefore to the W mass, M_W, so that, as this also depends logaritmically on the mass of the hypothesized Higgs boson, precise measurements of M_W and M_{top} allow to set indirect constraints on the unpredicted value of the mass of this fundamental, but still unobserved particle of the SM. Moreover, possible contributions due to some unknown physics might also be constrained. Finally, the present value of M_{top} makes the Yukawa coupling to the Higgs field of $\mathcal{O}(1)$ and this could indicate a special role of the top quark in the mechanism of electroweak symmetry breaking.

All the reasons listed above make the accurate knowledge of M_{top} a really important issue and push the CDF and D0 Collaborations to measure the top quark mass in all

possible topologies related to $t\bar{t}$ events production. Improvements of the results are obviously due to the increasing statistics, but also to innovative techniques used in the analyses.

2. – Top quark production, decay and signatures

At the Tevatron collider bunches of protons and antiprotons are brought into collision with a center-of-mass energy, $\sqrt{s}$, equal to 1.96 TeV. Data are collected by the multipurpose CDF and D0 detectors [3, 4] which have currently recorded on tape an integrated luminosity of about $6\,\text{fb}^{-1}$ each, even if the most updated analyses reported here use only up to $3.6\,\text{fb}^{-1}$. The goal for the end of Tevatron Run II is to collect up to $8\,\text{fb}^{-1}$ per experiment.

At this energy top quarks are predominantly produced in $t\bar{t}$ pairs by $q\bar{q}$ annihilation ($\sim 85\%$ of the times) or gluon-gluon fusion ($\sim 15\%$). In the SM framework they decay to a W boson and a b-quark with a branching ratio (BR) very close to 100% and, because of their large mass, this happens before any hadronization effect can take place. This implies that informations concerning the top quark can be obtained directly from its decay products. The different final states and signatures of $t\bar{t}$ events are defined by the subsequent decays of the W^+ and W^- bosons and their usual classification is as follows:

– *Di-lepton channel*, where both the W's decay to a charged lepton and a neutrino $t\bar{t} \to W^+ b\, W^- \bar{b} \to (l^+\nu) b\, (l^-\bar{\nu})\bar{b}$. This represents about 9% of the $t\bar{t}$ events.

– *Lepton + jets channel*, with one of the W's decaying to leptons while the other one to hadrons, *e.g.*, $t\bar{t} \to W^+ b\, W^- \bar{b} \to (l^+\nu) b\, (q_1\bar{q}_2)\bar{b}$, and a total BR of 45%.

– *All-hadronic channel* (or all-jets channel), where both the W's decay to quarks. This final state has a BR of 46%.

The current theoretical predictions for the $t\bar{t}$ ("signal") production cross-section at $\sqrt{s} = 1.96\,\text{TeV}$ are in the range 6.7–8.0 pb for $M_{\text{top}} = 172\,\text{GeV}/c^2$ (1) [5] so that one pair of top quarks is produced out of about 10^{10} inelastic $p\bar{p}$ collisions. This makes the measure of top quark properties a really challenging task, requiring tools and selection techniques exploiting at the best the peculiar features of the signal. In particular, these include algorithms for the efficient identification of high transverse momentum (p_T) charged leptons coming from W decay and for the reconstruction of hadronic jets by an appropriate clustering of energy depositions in the calorimeters. Identification of jets generated by b-quarks ("b-tagging") is fundamental in reducing the presence of background events and also the combinatoric problem related to possible jet-to-quark assignments, and is provided by vertex detectors allowing reconstruction of secondary vertices related to the decay of b-hadrons. In measuring M_{top}, the reconstruction of the kinematics of the event, and therefore of the energies of quarks and leptons in the final state is crucial. The estimate of the parton energy requires an accurate knowledge of the correction to be applied to the measured jet energy, because of the instrumental effects as well as the definition of jet clustering algorithms. The uncertainty on this factor (called Jet Energy Scale, JES) is currently of order 2–3% and represents the largest source of systematic uncertainty in most of M_{top} measurements.

(1) This range of values takes into account the uncertainties and is calculated for CTEQ6.6 parton distribution functions.

3. – M_{top} measurement techniques

Apart from the peculiarities of each individual measurement and with a few exceptions, two main techniques are used by the CDF and D0 Collaborations to extract the value of M_{top} from a sample of selected events: the *Matrix Element Method* (ME) and the *Template Method* (TMT).

In the ME, the probability that an event, where a set $\vec{y}$ of variables is measured, come from pair production of top quarks with mass M_{top} or from a background process is defined by considering a possible kinematics $\vec{x}$ at parton level, evaluating its leading order differential cross-section $\mathrm{d}\sigma(\vec{x})$, which includes the calculation of the matrix element for the process, and multiplying it by the "transfer function" $\mathcal{W}(\vec{y}, \vec{x})$, representing the probability that the set of *observed* variables $\vec{y}$ corresponds to the parton level kinematics $\vec{x}$, taking into account the detector effects and the event reconstruction. This function obviously strictly depends on JES too. Integration over possible initial and final states as well as a sum over assignments of observed jets to the partons and solutions for undetected neutrinos momenta are then performed.

In the TMT, a set of n event observables, $\vec{y}$, sensitive to M_{top} is reconstructed and the event probability is simply defined by the distributions *expected* for these variables. These distributions, called "templates" are built from simulated background and $t\bar{t}$ events with various input values of M_{top} for the signal.

In both methods a likelihood for the total sample, written as the product of individual event probabilities, is then usually maximized as a function of M_{top} to extract its value as the one which gives the largest probability to observe the selected set of events.

The power of the ME comes from exploiting a lot of information from the reconstructed event, while its main disadvantage is represented by the intensive usage of computing resources required by the numerical integrations. On the contrary the TMT is computationally much less problematic, but has also a reduced statistical power as, usually, no more than one or two event observables are used to build the templates. Both the methods strictly depend on reliable Monte Carlo event generation and simulation of detector effects. Before the technique is applied to real data, results are usually calibrated by large sets of simulated experiments corresponding to known true values of the variables to be measured.

An important feature of most recent analyses in the lepton + jets and all-hadronic channels is that, in reconstructing the event kinematics, the four-momenta of jets assigned to the W-boson decaying hadronically can be used to constrain the JES, as their invariant mass must equal, within the uncertainties, the well-known mass of the W. This can be exploited through the dependence of the transfer function on JES in the ME and introducing some kind of reconstructed W mass among the templates in the TMT, so that the likelihood can be maximized as a function of M_{top} and JES simultaneously, providing the *in situ* calibration of the latter variable. This technique makes the largest part of the JES uncertainty a component of the statistical uncertainty on M_{top}, therefore scaling down with the increasing of collected luminosity.

4. – Measurements in the di-lepton channel

The fully leptonic channel provides the candidate samples with the best signal-to-background ratio (S/B) because of the presence of two energetic, high-p_T leptons and the b-jets. Moreover the combinatoric problem in assigning jets to partons is small. Unfortunately it suffers of a small BR (about 5% if only channels including electron

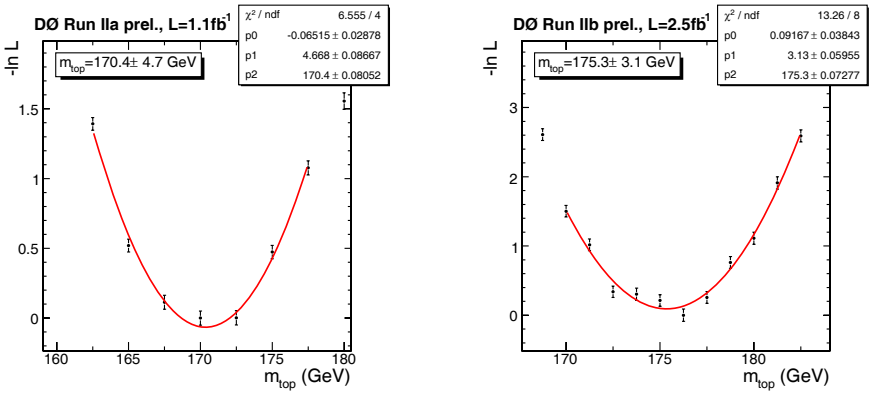

Fig. 1. – Uncalibrated ME likelihood evaluated by D0 analysis [6] in the di-lepton channel on data from two different periods. The minima of the curves denote the measured $M_{\rm top}$ before any calibration.

and/or muons from direct W's decays are considered as usual). The kinematics of the events is underconstrained because the reconstructed transverse missing energy, $\not\!\!E_T$, results from two undetected neutrinos so that assumptions and integrations are needed on unmeasured quantities.

Typical event selections, both in CDF and D0 analyses, require two identified oppositely charged leptons (e or μ) with large E_T ($E_{T,\,l} \geq 15\,\text{GeV}$), at least two energetic hadronic jets ($E_{T,\,\text{jet}} \geq 20\,\text{GeV}$), and a large amount of missing transverse energy ($\not\!\!E_T \geq 25\,\text{GeV}$). Further topological variables may also be used for additional cuts. The S/B can reach a value of about 10 when also b-tagging is required, where the main backgrounds are represented by di-boson events (ZZ, WW, WZ), Drell-Yan process and $W+$jets events where one of the jet is misidentified as a lepton.

The most updated result in this channel comes from the D0 experiment [6] and is obtained by a ME analysis performed in the channel including both an electron and a muon. Apart from direct decays of the W's to $e\nu$ or $\mu\nu$, also the possibility that this final state arise from $W \to \tau\nu_\tau \to (l\nu_l)\nu_\tau$, $l = e,\,\mu$, is considered, so that the total BR is about 3.2% and the dominant background contribution is the $Z+$jets production with the decay chain $Z \to \tau\tau \to (e\nu_e\nu_\tau)(\mu\nu_\mu\nu_\tau)$. In a data sample corresponding to a total of $3.6\,\text{fb}^{-1}$, 154 candidates are selected with an expectation of about 118 $t\bar{t}$ and 23 background events. Figure 1 shows the likelihood function of $M_{\rm top}$ in two samples from different periods. The calibrated measurement yields $M_{\rm top} = 174.8 \pm 3.3\,(\text{stat.}) \pm 2.6\,(\text{syst.})\,\text{GeV}/c^2$, with a relative precision $\delta M_{\rm top}/M_{\rm top} \approx 2.4\%$.

The ME result has been also combined with two TMT analyses using different algorithms to build the templates (the "Neutrino Weighting Algorithm" (NWA) and the "Matrix Weighting Method") and applied to about $1\,\text{fb}^{-1}$ of data [7]. These analyses include a wider cathegory of di-lepton final states, with specific event selections, and templates are defined starting from event weights evaluated by the agreement between possible solutions of the underconstrained kinematics and the observed event topology. The result obtained in [7] is $M_{\rm top} = 174.7 \pm 4.4\,(\text{stat.}) \pm 2.0\,(\text{syst.})\,\text{GeV}/c^2$, while the combination with [6] yields $M_{\rm top} = 174.7 \pm 2.9\,(\text{stat.}) \pm 2.4\,(\text{syst.})\,\text{GeV}/c^2$ with a relative precision $\approx 2.2\%$.

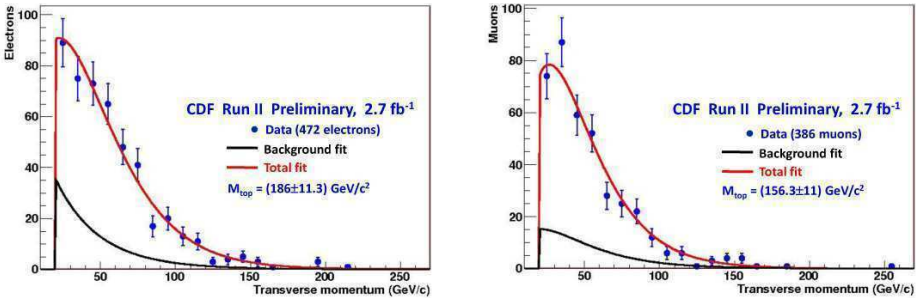

Fig. 2. – Fits of lepton p_T templates to the data in the electron (left) and muon (right) channels in the CDF analysis [10]. The separate results are then combined.

5. – Measurements in the lepton + jets channel

The final state including one charged lepton and jets (among which two are b-quark jets), is considered the "golden channel" as it concerns the measurements of top quark properties, including its mass. In fact it offers the best compromise between the purity of selected samples, reflected in S/B values up to 10 depending on the b-tag requirements, and the available statistics because of its BR of about 45% (30% if only electrons and muon channels are included). This allows both the Tevatron experiments to achieve the best results in this channel.

In particular the best results for M_{top} come from ME analyses [8, 9]. These are based on data samples typically selected by requiring that an event contains an energetic lepton (e or μ), four energetic jets ($E_{T,\text{jet}} \geq 20\,\text{GeV}$) and a good amount of missing energy ($\not\!\!E_T \geq 20\,\text{GeV}$). Moreover, to further reduce the background, at least one of the four jets must be tagged as a b jet. The main background sources are represented by $W+$jets events and multijet QCD events where one of the jet is misidentified as a lepton.

The CDF analysis [8] considers a data sample corresponding to $3.2\,\text{fb}^{-1}$, where 578 candidates are selected with an expected background of 134.1 ± 32.0 events. Here only the event probability for the $t\bar{t}$ process is explicitly calculated for each event and the average contribution of background events is subtracted to obtain a signal-only likelihood. After the calibration the latter is evaluated on the data sample and maximized to obtain $M_{\text{top}} = 172.1 \pm 0.9\,(\text{stat.}) \pm 1.1\,(\text{syst.})\,\text{GeV}/c^2$. The analysis from D0 [9] is applied to a total of $3.6\,\text{fb}^{-1}$ of data and 835 events are selected. The background probability is explicitly calculated by the matrix element of the dominant $W+$ jets process. The measurement yields $M_{\text{top}} = 173.7 \pm 0.8\,(\text{stat.}) \pm 1.6\,(\text{syst.})\,\text{GeV}/c^2$. Both results include the *in situ* calibration of the JES and represent the best individual measurements from each experiment, achieving a relative precision of $\approx 1\%$ on the top quark mass.

In the same channel, a TMT analysis has been recently performed by the CDF experiment using $2.7\,\text{fb}^{-1}$ of data [10]. The variable used to build the templates is the transverse momentum of the lepton (electron or muon) identified in the event, so that interesting features of this analysis are that no event reconstruction is required and the uncertainty due to the JES is negligible because hadronic jets are not directly considered. Fitting the templates to distributions obtained by 472 and 382 events selected in the electron and muon channels respectively and then combining the results a value of $M_{\text{top}} = 172.1 \pm 7.9\,(\text{stat.}) \pm 3.0\,(\text{syst.})\,\text{GeV}/c^2$ is obtained, with $\delta M_{\text{top}}/M_{\text{top}} \approx 4.9\%$. Figure 2 shows results of fits to the data.

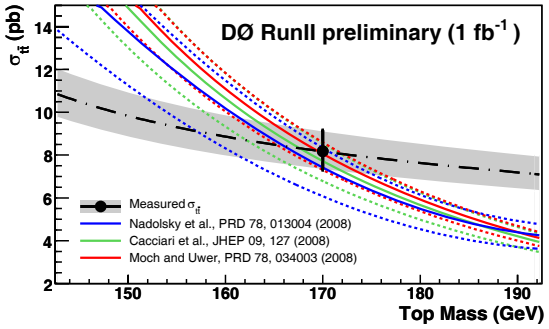

Fig. 3. – Parametrizations of measured and predicted $t\bar{t}$ cross-section, including uncertainties, as a function of the top quark mass, as presented in [12].

6. – Other measurements in the di-lepton and lepton + jets channels

Other interesting results have been recently obtained by the two collaborations exploiting simultaneously information from the di-lepton and lepton+jets channels. A CDF TMT analysis [11] performed with $3.2\,\mathrm{fb}^{-1}$ uses more variables to build two-dimensional templates. In particular, in the lepton + jets channel a top mass, m_t^{rec} is reconstructed for each event by a χ^2 fit constraining the event kinematics to the $t\bar{t}$ topology, while a second variable m_{jj}, related for signal events to the mass of the W boson, is used to have a constraint on the JES, allowing the *in situ* calibration. In the di-lepton channel two variables sensitive to M_{top} are used: m_{T2}, defined by reconstructed tranverse masses of the top quarks in the event, and m_t^{NWA}, defined by applying the NWA previously quoted. A simultaneous fit of templates to the observed distributions provides therefore *in situ* calibration of the JES also for events in the di-lepton channel and gives $M_{\mathrm{top}} = 171.7^{+1.4}_{-1.5}\,(\mathrm{stat.}) \pm 1.1\,(\mathrm{syst.})\,\mathrm{GeV}/c^2$.

A different method is applied by the D0 Collaboration [12]. In fact D0 measures M_{top} comparing a measurement of the $t\bar{t}$ production cross-section on $1\,\mathrm{fb}^{-1}$ of data to various theoretical predictions, including [5]. The cross-section values and their uncertainty are parametrized as a function of M_{top}, obtaining curves $\sigma^{\mathrm{obs}}(M_{\mathrm{top}}) \pm \delta\sigma^{\mathrm{obs}}(M_{\mathrm{top}})$ and $\sigma^{\mathrm{theo}}(M_{\mathrm{top}}) \pm \delta\sigma^{\mathrm{theo}}(M_{\mathrm{top}})$, as shown in fig. 3.

A likelihood including Gaussian terms both for the observed and theoretical cross-sections is maximized with respect to the unknown "true" values $\sigma_{t\bar{t}}$ and M_{top}. This yields, considering, *e.g.*, the calculation from Moch and Uwer in [5], $M_{\mathrm{top}} = 169.1^{+5.9}_{-5.2}\,\mathrm{GeV}/c^2$, but all the results are in a good agreement with the current World Average top quark mass from direct measurements [13]. This method provides complementary information, with different sensitivity to systematic uncertainties, with respect to the direct measurements and therefore represents also a consistency check.

7. – Measurements in the all-hadronic channel

The all-hadronic channel has the advantages of a large BR of about 46%, and of a fully reconstructed kinematics because ideally no particle from the $t\bar{t}$ system escapes the detector. The major downside is the huge background from QCD multijet production which dominates the signal by three orders of magnitude even after the application of

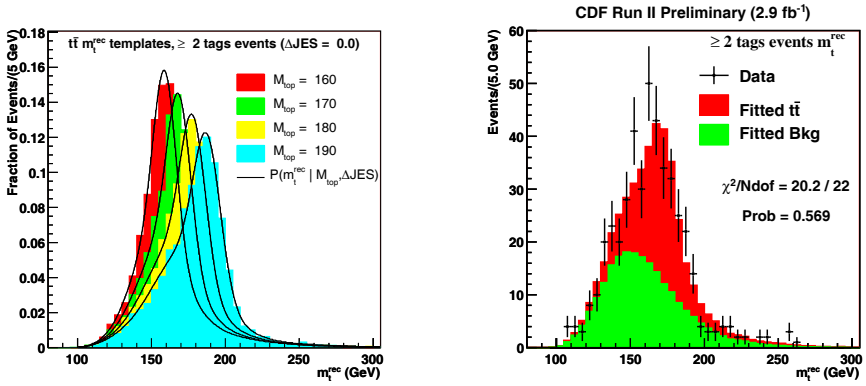

Fig. 4. – Left: examples of signal templates used in the CDF $M_{\rm top}$ measurement in the all-hadronic channel. Sensitivity to input $M_{\rm top}$ is apparent. Right: $m_t^{\rm rec}$ distribution as observed in the data sample with at least 2 b-tagged jets is plotted together with the fitted templates.

specific triggers. Therefore accurate kinematic selections and b-tag requirements are necessary to obtain samples such that $S/B \approx \mathcal{O}(1)$. The former usually require that no energetic lepton is identified in an event, the presence of a large number of jets (≥ 6) and a small amount of missing energy.

The most recent and precise measurement of $M_{\rm top}$ in this channel has been obtained by the CDF experiment by a TMT analysis on $2.9\,{\rm fb}^{-1}$ of data [14]. Beyond preselection cuts, a neural net, including both kinematical and jet shape variables, is exploited to select candidate events together with the requirement of at least one b-tagged jet. Kinematic fits are then performed to reconstruct, for each event a "top mass" $m_t^{\rm rec}$ and a "W mass" $m_W^{\rm rec}$, and distributions of these variables are then used as templates to be fitted to the data in order to obtain the $M_{\rm top}$ measurement with simultaneous JES calibration. Examples of $t\bar{t}$ signal templates are shown on the left of fig. 4. A total of 3452 events with exactly one tagged jet and 441 with at least two tagged jets are selected, with an expected background of 2785 ± 83 and 201 ± 29 events respectively, and the calibrated likelihood fit yields $M_{\rm top} = 174.8 \pm 1.7\,({\rm stat.}) \pm 1.9\,({\rm syst.})\,{\rm GeV}/c^2$ corresponding to $\delta M_{\rm top}/M_{\rm top} \approx 1.5\%$. Observed data and fitted templates are shown on the right of fig. 4.

8. – Systematic uncertainties

Given the increasing data collection and the improvements in the selection techniques, the most precise measurements of $M_{\rm top}$ at the Tevatron are now limited by the systematic uncertainties. The *in situ* calibration allows to reduce greatly the uncertainty due to the knowledge of the JES, which partially becomes statistical, but its purely systematic component still represents the dominant contribution for most of the analyses and for the World Average [13]. Other important sources are primarily related to Monte Carlo generation (*e.g.*, initial- and final-state gluon radiation, hadronization model, parametrization of parton density functions). The CDF and D0 Collaborations are performing a joint effort to define a common way to evaluate the systematics, to improve the knowledge of important effects, to avoid possible overlaps and double counting, but also to study possible sources neglected so far. As an example, uncertainty coming from modeling of color reconnection effects has been introduced in the most recent analyses presented here.

9. – Tevatron combination

CDF and D0 combine their best results from each channel both internally (*i.e.* within each experiment separately) [15] and in a joint number representing the World Average for the value of M_{top} [13]. In such combinations correlations among uncertainties for different results are properly taken into account. As it concerns the World Average, the updated value, including many of the results reported here, is $M_{\text{top}} = 173.1 \pm 0.6\,(\text{stat.}) \pm 1.1\,(\text{syst.})\,\text{GeV}/c^2 = 173.1 \pm 1.3\,\text{GeV}/c^2$ with a χ^2/d.o.f. probability of 79%, denoting a good agreement among all measurements. The relative precision is $\approx 0.75\%$. The values from the different channels are also calculated obtaining $M_{\text{top}}^{\text{di-l}} = 171.4 \pm 2.7\,\text{GeV}/c^2$, $M_{\text{top}}^{\text{l+jets}} = 172.7 \pm 1.3\,\text{GeV}/c^2$, $M_{\text{top}}^{\text{all-had}} = 175.1 \pm 2.6\,\text{GeV}/c^2$. Also these results show a good agreement to each other.

10. – Conclusions

The CDF and D0 Collaborations have both conducted a robust set of analyses performed in order to better and better measure the value of the top quark mass, a fundamental parameter of the Standard Model. Well established techniques are applied to candidates in all channels corresponding to different $t\bar{t}$ final states. Results from individual channels and experiments are combined to obtain the best estimate of M_{top}, whose updated value is $M_{\text{top}} = 173.1 \pm 1.3\,\text{GeV}/c^2$. The precision of this measure (about 0.75%) is already limited by systematic uncertainties, and the two collaborations are working together to reach a common, complete and reliable evaluation of all the effects. Considering that the most updated analyses are now using about half of the final statistic of Tevatron Run II, the precision on M_{top} could reach the 1 GeV level before the collider final shutdown.

REFERENCES

[1] Abe F. *et al.* (CDF Collaboration), *Phys. Rev. Lett.*, **74** (1995) 2626.
[2] Abachi S. *et al.* (D0 Collaboration), *Phys. Rev. Lett.*, **74** (1995) 2632.
[3] Acosta D. *et al.* (CDF Collaboration), *Phys. Rev. D*, **71** (2005) 032001.
[4] Abazov V. M. *et al.* (D0 Collaboration), *Nucl. Instrum. Methods A*, **565** (2006) 463.
[5] Cacciari M. *et al.*, *JHEP*, **127** (2008) 0809; Kidonakis N. and Vogt R., *Phys. Rev. D*, **78** (2008) 074005; Moch S. and Uwer P., *Nucl. Phys. Proc. Suppl.*, **183** (2008) 75.
[6] D0 Collaboration, public notes 5897 (March 2009) and 5743 (July 2008).
[7] Abazov V. M. *et al.* (D0 Collaboration), *Phys. Rev. D*, **80** (2009) 092006.
[8] CDF Collaboration, public note 9692 (February 2009).
[9] D0 Collaboration, public notes 5877 (March 2009) and 5750 (July 2008).
[10] CDF Collaboration, public note 9683 (February 2009).
[11] CDF Collaboration, public note 9679 (March 2009).
[12] Abazov V. M. *et al.* (D0 Collaboration), *Phys. Rev.D*, **80** (2009) 071102.
[13] CDF and D0 Collaborations, FERMILAB-TM-2427-E (2009), CDF public note 9717 (March 2009), DØ public note 5899 (March 2009), arXiv:0903.2503.
[14] CDF Collaboration, public note 9694 (February 2009).
[15] CDF Collaboration, public note 9714 (March 2009), D0 Collaboration, public note 5900 (March 2009).

IL NUOVO CIMENTO Vol. 32 C, N. 5-6 Settembre-Dicembre 2009
DOI 10.1393/ncc/i2010-10521-5

Colloquia: LaThuile09

Top quark properties and cross-section

D. Wicke for the CDF and D0 Collaborations

Johannes Gutenberg Universität Mainz - Staudingerweg 7, 55099 Mainz, Germany
Bergische Universität Wuppertal - Gaußstr. 20, 42097 Wuppertal, Germany

(ricevuto il 10 Novembre 2009; pubblicato online l'8 Gennaio 2010)

Summary. — The CDF and D0 experiments have performed measurements of production and decay properties of the top quark with an unprecedented precision. This talk gives an overview of top quark properties and cross-section measurements performed with top quark pair events in proton anti-proton collision at 1.96 TeV with a luminosity of up to $3.6\,\mathrm{fb}^{-1}$.

PACS 14.65.Ha – Top quarks.

1. – Introduction

Since the top quark was discovered by CDF and D0 at the Tevatron in 1995 [1,2] the number of top events available for experimental studies has been increased by more than an order of magnitude. Tevatron now delivered a luminosity of more than $6\,\mathrm{fb}^{-1}$ up to half of which has been analysed for top quark analyses in CDF and D0. These data are, amongst other studies, investigated to verify the production and decay properties of top quarks as expected by the Standard Model (SM).

In the SM top quark pair production at the Tevatron is expected to be dominated by quark anti-quark annihilation with a contribution of only 15% from the gluon fusion processes. The predicted cross-section depends on the top quark mass. The top quark decays to nearly 100% to a W-boson and a b-quark. The decay channels of top quark pairs are thus fully specified through the W-boson decay modes. Dileptonic decays including electrons and muons allow for the highest purity, but suffer from the low branching fraction of about 10%. The semileptonic decays are considered as the golden channel due to a sizable branching fraction combined with the possibility to reach a reasonable signal to background ratio. The all-hadronic decay channel has the largest cross-section, but due to the absence of leptons it suffers from a huge background due to multijet production. Channels including τ leptons are kept separately due to the difficulties in their identification.

In the following first some new results on the top quark pair production cross-section are described. Then selected measurements of top quark decay properties and the possible presence of particles beyond the SM are discussed. The final section presents a possible admixture of particles beyond the SM in the samples usually considered a top quark events. The top quark mass which is the only free parameter in the top quark sector of the SM and the observation of single top quark production are discussed separately [3,4].

2. – Top pair production cross-section

The total cross-section of top pair production has been computed in perturbation theory using various approximations [5-9]. For a top quark (pole) mass of 175 GeV Moch and Uwer [8] find $\sigma_{t\bar{t}} = 6.90^{+0.46}_{-0.64}$ pb, based on the CTEQ6.6 [10] PDF. Experimentally it is important to measure this value in various decay channels. In addition some measurements are done requiring identified b-jets while others avoid b-jet identification and rely on topological selections. Most analysis use sideband data to evaluate the normalisation of the important background contributions. In the lepton plus jets channel the precision is already dominated by systematic uncertainties.

A sizable contribution of the systematic uncertainties of these measurements stems from the luminosity determination. To overcome this limitation CDF has measured the ratio of top quark pair production to the Z-boson production cross-sections [11, 12]. In 2.7 and 2.8 fb^{-1} of data CDF finds $\sigma_{Z\to\ell\ell}/\sigma_{t\bar{t}} = 35.7 \pm 3.8$ and $\sigma_{Z\to\ell\ell}/\sigma_{t\bar{t}} = 36.5 \pm 2.9$ for the analysis using b jet identification and the topological analysis, respectively. These results are converted to top pair production cross-sections using the theoretical prediction for Z-boson production. The theoretical uncertainty induced by this step is much smaller than the luminosity uncertainties and thus yield results with an uncertainty comparable to the theoretical uncertainty:

$$(1)\quad \begin{aligned} &\sigma_{t\bar{t}} = 7.0 \pm 0.4_{(\text{stat})} \pm 0.6_{(\text{syst})} \pm 0.1_{(\text{theory})}\ \text{pb}, && \text{using } b \text{ jet identification},\\ &\sigma_{t\bar{t}} = 6.9 \pm 0.4_{(\text{stat})} \pm 0.4_{(\text{syst})} \pm 0.14_{(\text{theory})}\ \text{pb}, && \text{using topological selection}. \end{aligned}$$

DØ has recently extended the list of cross-section results measuring the cross-section in a final state with one τ-lepton plus another lepton [13,14]. Hadronic decay of τ-leptons are identified with neural networks for three different decay modes: single charged pion, single charged pion associated with neutral pions and three charged pions associated with neutral pions. Events are selected requiring one τ-lepton identified in one of the above hadronic decay modes, one isolated electron or muon, missing transverse energy and at least two jets, one of which is required to be identified as b-jet. Background from W+jets is normalised to data before selecting events with identified b-jets, multijet background is estimated from events with same sign leptons. The cross-section measured from opposite-sign leptons in 2.2 fb^{-1} of DØ has a systematic uncertainty with important contributions from the background estimation and from limited statistics of the simulation:

$$(2)\qquad \sigma_{t\bar{t}} = 7.32^{+1.34}_{-1.24\,(\text{stat})}{}^{+1.20}_{-1.06\,(\text{syst})} \pm 0.45_{(\text{lumi})}\ \text{pb}.$$

Figure 1 shows a summary of the cross-section measurements performed by CDF and DØ. The two recent results discussed above agree well with the other channels and all channels agree with the theoretical cross-section predicted within the SM.

2˙1. *Limits on charged Higgs.* – The presence on beyond the SM particles may alter the branching fractions of the various top quark pair decay channels. This would alter the deduced cross-section depending on the decay channel. DØ used the cross-sections measured in the semileptonic, the dileptonic and the tau+electron/muon channel to search of a possible contributions of charged Higgs bosons in top quark decays [15, 16]. DØ considered all correlations between the various systematic uncertainties of these measurements and sets limits on $\sigma_{t\bar{t}}\mathcal{B}(t \to H^+)$ for a leptophobic and a tauonic scenario

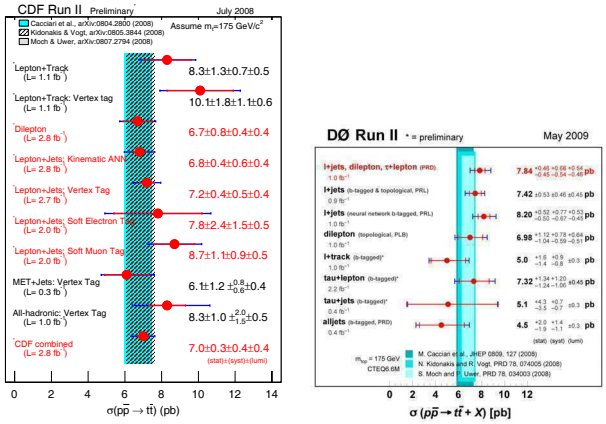

Fig. 1. – Summary of top quark cross-section results for various analysis channels.

for the charged-Higgs decay. These limits can be transfered to exclusion areas in the plane of $\tan\beta$ *vs.* charged-Higgs mass, as seen in fig. 2 (left).

CDF has searched for charged Higgs bosons in the top quark decay using kinematic differences of the two event types in lepton plus jets events. Comparing templates of the dijet invariant mass distribution yields an improved sensitivity at high-charged-Higgs masses, but is less sensitive for charged-Higgs masses near the W-boson mass. The obtained limits are shown in fig. 2 (right).

3. – Top quark decay properties

3˙1. *W helicity.* – The spin structure of the top quark decay is accessible by measuring the W-boson helicity. The SM expects about 70% longitudinally and 30% left-handed polarised W-bosons. Longitudinal polarised W bosons preferably emit the charged leptons orthogonal to the b-quark. Left-handed W bosons prefer the charged lepton to be emitted along the direction of the b-quark, while right-handed W-bosons prefer the charged boson to be opposite to the direction of the b-quark. Both Tevatron experiments mea-

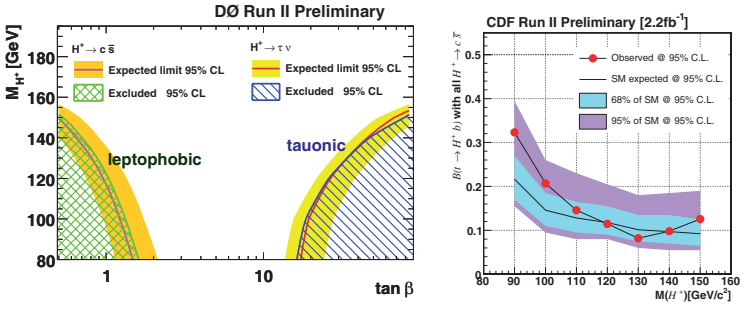

Fig. 2. – (Colour online) Left: exclusion limits derived in leading order for the $\tan\beta$ *vs.* $M_{H^\pm}$ plane in the Minimal Supersymmetric SM [15]. Right: CDF observed limits on $\mathcal{B}(t \to H^+ b)$ from 2.2 fb^{-1} data (red dots) compared with the expected limit in the standard model (black line) [17].

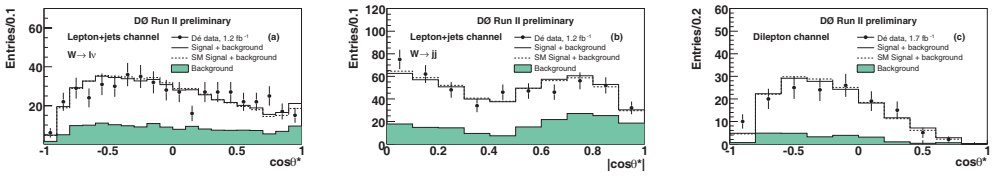

Fig. 3. – W decay angle distributions as measured in 1.2–1.7 fb^{-1} of DØ Run-IIb data. The left and middle show the leptonic decay and the hadronic in the lepton+jet events, respectively. The right plot shows the distribution obtained from dilepton events. The shaded area represents the background contribution [19].

sure cosine of the angle between the b-quark and the charged lepton in the W-boson rest-frame. CDF measures $\cos\theta^*$ from the lepton plus jet events [18] in 1.9 fb^{-1}. DØ uses lepton plus jets and dilepton events using 2.2–2.7 fb^{-1} [19], see fig. 3. The expectations for the left-handed, the right-handed and the longitudinal fractions are compared to the observed data to simultaneously fit the left-handed and the longitudinal fractions:

$$\begin{aligned} \text{D0:} \quad & f_0 = 0.49 \pm 0.14 \quad \text{and} \quad f_+ = +0.11 \pm 0.08, \\ \text{CDF:} \quad & f_0 = 0.66 \pm 0.16 \quad \text{and} \quad f_+ = -0.03 \pm 0.07. \end{aligned} \tag{3}$$

The W helicity measurement is sensitive to anomalous couplings in the Wtb vertex. In general this vertex can contain vector and tensor couplings in left- and right-handed variations. DØ has combined the above measurement of the W helicity with a search for anomalous coupling in single top quark events [20, 21]. The single top quark analysis uses boosted decision trees trained with various anomalous coupling scenarios. The single top quark and the top quark pair events are simultaneously compared to templates that describe the SM coupling and one anomalous coupling at a time. All three scenarios show good agreement with a pure SM coupling as shown in fig. 4.

4. – New physics in top quark like signatures

In the SM top quark pair production does not show any resonances. However, unknown heavy resonances decaying to top pairs may add a resonant part to the SM production mechanism. Resonant production is possible for massive Z-like bosons in extended gauge theories [22], Kaluza-Klein states of the gluon or Z-boson [23, 24], ax-

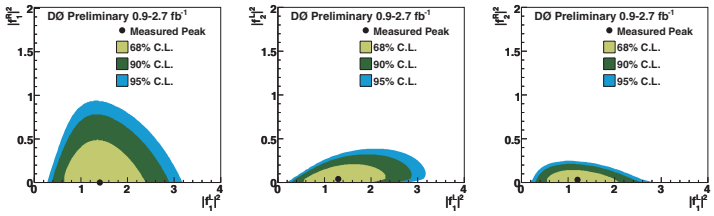

Fig. 4. – Allowed 68%, 90% and 95% CL regions for SM Wtb coupling, f_1^L with anomalous right-handed vector coupling, f_1^R (left) and with anomalous left- and right-handed tensor couplings, $f_1^{L/R}$ (middle and right) [20, 21].

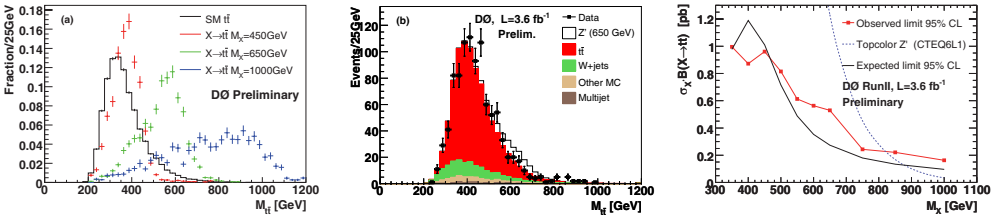

Fig. 5. – Left: shape of SM top pair production (black line) compared to resonant production through a narrow resonance at three different resonance masses. Middle: expected and observed $t\bar{t}$ invariant-mass distribution for the $\ell + 4$ or more jets channels, with at least one identified b-jet. Superimposed as white area is the expected signal for a Topcolor-assisted Technicolor Z'-boson with $M_{Z'} = 650\,\text{GeV}$. Right: limits on $\sigma_X \mathcal{B}(X \to t\bar{t})$ obtained in $3.6\,\text{fb}^{-1}$ [28-30].

igluons [25], Topcolor [26,27], and other theories beyond the SM. Independent of the exact model, such resonant production could be visible in the reconstructed $t\bar{t}$ invariant mass.

4˙1. *Top quark pair invariant-mass distribution.* – DØ investigated the invariant-mass distribution of top pairs in up to $3.6\,\text{fb}^{-1}$ of ℓ+jets events [28-30]. Signal simulation is created for various resonance masses between 350 and 1000 GeV. The width of the resonances was chosen to be 1.2% of their mass, which is much smaller than the detector resolution. The top pair invariant mass, $M_{t\bar{t}}$, is reconstructed directly from the reconstructed physics objects. A constraint kinematic fit is not applied. Instead the momentum of the neutrino is reconstructed from the transverse missing energy, $\not\!\!E_T$, which is identified with the transverse momentum of the neutrino and by solving $M_W^2 = (p_\ell + p_\nu)^2$ for the z-component of the neutrino momentum. p_ℓ and p_ν are the four-momenta of the lepton and the neutrino, respectively. Figure 5 shows the expected shapes of SM and resonant production (left) and the expected and observed invariant mass distribution for the $\ell + 4$ or more jet channel. As the data agrees with the SM expectations, limits on the possible contribution of resonant production $\sigma_X \mathcal{B}(X \to t\bar{t})$ are set. The benchmark model of Topcolor assisted Technicolor can be excluded for Z' masses of $M_{Z'} < 820\,\text{GeV}$.

Recent CDF results unfold the distribution invariant top quark pair mass and measure the differential cross-section in semileptonic events [31]. The invariant mass of the top pairs is reconstructed from the four-momenta of the four leading jets in p_T, the four-momentum of the lepton and the missing transverse energy. The z-component of the neutrino is not reconstructed but used as if it was zero [32]. To obtain the differential cross-section from the background-subtracted distribution of observed $M_{t\bar{t}}$ values, acceptance effects and smearing effects from the reconstruction need to be corrected for. The required acceptance correction is computed from signal simulation with PYTHIA. Correction factors to correct for differences between data and Monte Carlo observed in control samples are applied for the lepton identification and b-jet identification rates. The distortions of the reconstructed distribution are unfolded using the singular value decomposition of the response matrix that is obtained from simulations. The differential cross-section obtained in $2.7\,\text{fb}^{-1}$ of data using the semileptonic decay mode is shown in fig. 6 [31]. The consistency with the Standard Model expectation is computed using Anderson-Darling statistics [33]. The observed p-value is 0.28, showing good agreement with the Standard Model. Finding no evidence for physics beyond the Standard Model limits on gravitons in a Randall-Sundrum model [35] decaying to top quarks are set using the CL_s method. The first resonance is assumed to have a mass of 600 GeV. The

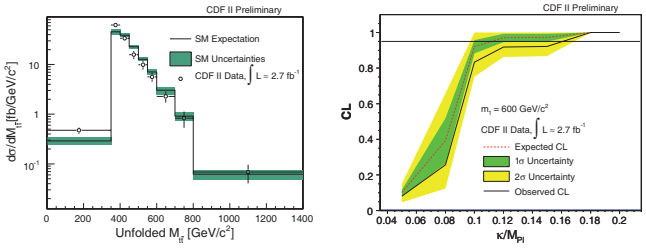

Fig. 6. – Left: differential top pair production cross-section measured by CDF in $2.7\,\mathrm{fb}^{-1}$ of data using the semileptonic decay mode. Indicated are the total uncertainties for each bin, excluding the overall luminosity uncertainty of 6%. Right: expected and observed limit on κ/M_{Pl} in a RS model [31, 34].

Anderson-Darling statistics is used as test statistics in the CL_s method. For the ratio of the warping parameter over the Planck mass CDF finds $\kappa/M_{\mathrm{Pl}} < 0.16$ at 95% CL, see fig. 6 (right).

4˙2. *Stop quark admixture.* – Particles beyond the SM may hide in the samples usually considered to be top quarks. One such candidate is the top quarks supersymmetric partner, the stop quark. The stop decay modes to neutralino and top quark, $\tilde{\chi}_1^0 t$, or through chargino and b-quark, $\tilde{\chi}_1^{\pm} b$, both yield neutralino, b-quark and W-boson, $\tilde{\chi}_1^0 bW$. The neutralino is the lightest supersymmetric particle in many models and is stable if R-parity in conserved. Then it escapes the detector and the experimental signature of stop pair production differs from that of top pair production only by the additional contribution to the missing transverse energy from the neutralino. Production of $\tilde{t}_1\bar{\tilde{t}}_1$ is simulated for various combinations of stop and chargino masses, $m_{\tilde{t}_1}, m_{\tilde{\chi}_1^{\pm}}$.

DØ has performed a search for the top quarks supersymmetric partners in $0.9\,\mathrm{fb}^{-1}$ of semileptonic events [36, 37]. For the sake of this analysis the stop mass was chosen to be less or equal to the top mass. The neutralino mass $m_{\tilde{\chi}_1^0} = 50\,\mathrm{GeV}$ was chosen to be close to the experimental limit. Stop quark signal events are distinguished from SM top quark events using a likelihood discriminant obtained from simulation. The most sensitive observable in this likelihood is the top quark mass reconstructed assuming a SM top quark pair event. Limits are set on the cross-section of various masses of the stop and the chargino, see fig. 7 (left). The sensitivity is not sufficient to exclude MSSM parameter values.

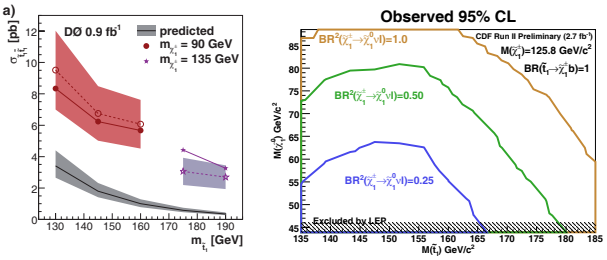

Fig. 7. – Left: limits on stop quark production in semileptonic events obtained in $1\,\mathrm{fb}^{-1}$ by DØ for an example parameter set [37]. Right: exclusions in the stop mass *vs.* neutralino mass plane of the MSSM obtained with $2.7\,\mathrm{fb}^{-1}$ of CDF data [38].

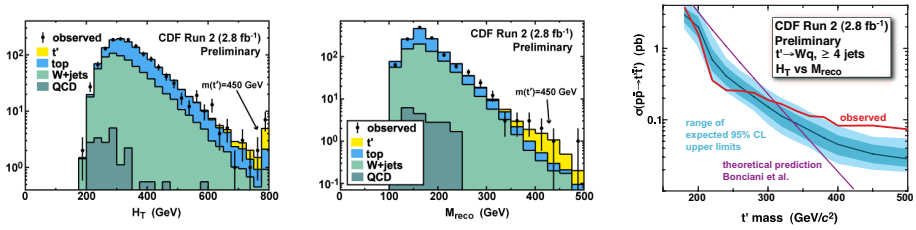

Fig. 8. – Expected and observed distribution of H_T and $m_{t^{(\prime)}}$ (left and middle). Resulting limits on the allowed cross-section of a $t^{(\prime)}$ production (right) [38].

CDF has used the dilepton channel to search for stop quark admixture in $2.7\,\mathrm{fb}^{-1}$ [38]. To distinguish the stop quark events from the SM to quark events, the stop mass is reconstructed using neutrino weighting technique. It is possible to exclude some portion in the stop mass *vs.* neutralino mass plane of the MSSM parameter space as shown in fig. 7 (right).

4˙3. *Fourth-generation u-type quark, t'.* – Another particle that may hide in the top quark samples is a fourth-generation quark, t'. CDF has searched for such a contribution in up to $2.8\,\mathrm{fb}^{-1}$ [39, 38]. In semileptonic events t' quarks are distinguished from SM t-quarks using the scalar sum of transverse momenta, H_T, and the $t^{(\prime)}$ mass reconstructed in a kinematic fit. The observed data are compared to the expectations for the SM and an additional contribution for a t'-quark assuming various t'-quark masses. The observed limits on possible cross-section for such a t'-quark production fall behind the expected ones for $m_{t'} > 300\,\mathrm{GeV}$. They allow to exclude t' masses of less than 311 GeV, c.f. fig. 8.

5. – Conclusions

The increasing Tevatron luminosity allows to measure the top quark cross-section and properties with improved precision. This note only describes a small fraction of all measurements. The Tevatron experiments measure the full spectrum of top quark properties to check the production, the decay and inherent properties of the top quark against the SM expectation. So far no evidence for new physics has been found.

REFERENCES

[1] Abe F. *et al.* (CDF Collaboration), *Phys. Rev. Lett.*, **74** (1995) 2626.
[2] Abachi S. *et al.* (DØ Collaboration), *Phys. Rev. Lett.*, **74** (1995) 2632.
[3] Brigliadori L., *Precision determination of the top mass*, these proceedings.
[4] y Garzon G. O., *First obsrevation of single top quark production*, these proceedings.
[5] Kidonakis N. and Vogt R., *Phys. Rev. D*, **68** (2003) 114014.
[6] Cacciari M. *et al.*, *JHEP*, **09** (2008) 127.
[7] Moch S. and Uwer P., *Phys. Rev. D*, **78** (2008) 034003.
[8] Moch S. and Uwer P., *Nucl. Phys. Proc. Suppl.*, **183** (2008) 75.
[9] Kidonakis N. and Vogt R., *Phys. Rev. D*, **78** (2008) 074005.
[10] Pumplin J. *et al.*, *JHEP*, **07** (2002) 012.
[11] CDF Collaboration, *Measurement of the ratio of the top pair cross section with the z boson cross section*, CDF Note 9616 (Nov. 2008).

[12] CDF Collaboration, *Measurement of the $t\bar{t}$ Cross Section in the Lepton Plus Jets Channel Using Neural Networks in $2.8\,fb^{-1}$ of CDF data. Including: Ratio of $t\bar{t}$ to Z Cross Sections*, CDF Note 9474 (Dec. 2008).
[13] Abazov V. M. *et al.* (D0 Collaboration), *Measurement of $t\bar{t}$ production cross section in the lepton + tau + b-jet(s) + $\not\!\!E_T$ channel using $1.2\,fb^{-1}$ of Run IIb data*, D0 Note 5607 Conf (2008).
[14] Abazov V. M. *et al.* (D0 Collaboration), *Phys. Lett. B*, **679** (2009) 177.
[15] The DØ Collaboration, *A search for charge Higgs bosons in $t\bar{t}$ events*, DØ Note 5715-CONF (July 2008).
[16] Abazov V. M. *et al.* (D0 Collaboration), *Combination and interpretations of $t\bar{t}$ cross section measurements with the D0 detector*, ArXiv:0903.5525 (2009).
[17] CDF Collaboration, *A search for charged Higgs in lepton + jets $t\bar{t}$ events using $2.2\,fb^{-1}$ of CDF data*, CDF Note 9322 (May 2008).
[18] Aaltonen T. *et al.* (CDF Collaboration), *Phys. Lett. B*, **674** (2009) 160.
[19] The DØ Collaboration, *Model-independent measurement of the W boson helicity in top quark decays at DØ*, DØ Note 5722-CONF (July 2008).
[20] Abazov V. M. *et al.* (D0 Collaboration), *Phys. Rev. Lett.*, **102** (2009) 092002.
[21] Abazov V. M. *et al.* (D0 Collaboration), *Measurement of anoumalous top quark couplings at D0*, D0 Note 5838 Conf (2009).
[22] Leike A., *Phys. Rep.*, **317** (1999) 143.
[23] Lillie B., Randall L. and Wang L.-T., *JHEP*, **09** (2007) 074.
[24] Rizzo T. G., *Phys. Rev. D*, **61** (2000) 055005.
[25] Sehgal L. M. and Wanninger M., *Phys. Lett. B*, **200** (1988) 211.
[26] Hill C. T. and Parke S. J., *Phys. Rev. D*, **49** (1994) 4454.
[27] Harris R. M., Hill C. T. and Parke S. J., *Cross section for topcolor $Z'(t)$ decaying to $t\bar{t}$*, ArXiv:hep-ph/9911288 (1999).
[28] Abazov V. M. *et al.* (D0 Collaboration), *Phys. Lett. B*, **668** (2008) 98.
[29] Abazov V. M. *et al.* (D0 Collaboration), *Search for $t\bar{t}$ resonances in the lepton+jets final state in $p\bar{p}$ collisions at $\sqrt{s} = 1.96\,TeV$*, D0 Note 5600 Conf (2008).
[30] Abazov V. M. *et al.* (D0 Collaboration), *Search for $t\bar{t}$ resonances in the lepton+jets final state in $p\bar{p}$ collisions at $\sqrt{s} = 1.96\,TeV$*, D0 Note 5882 Conf (2009).
[31] Aaltonen T. *et al.* (CDF Collaboration), *First Measurement of the $t\bar{t}$ Differential Cross Section $d\sigma/dM_{t\bar{t}}$ in $p\bar{p}$ Collisions at $\sqrt{s} = 1.96\,TeV$*, ArXiv:0903.2850 (2009).
[32] CDF Collaboration, *Measurement of the $t\bar{t}$ differential cross section,* $\mathrm{d}\sigma/\mathrm{d}M_{t\bar{t}}$ *in $2.7\,fb^{-1}$ of data*, public analysis webpage `http://www-cdf.fnal.gov/physics/new/top/2008/tprop/dXs_27fb/webpage/dXs27fb_Public.htm` (Nov. 2008).
[33] Anderson T. W. and Darling D. A., *Ann. Math. Statist.*, **23-2** (1952) 193.
[34] CDF Collaboration, *Measurement of the $t\bar{t}$ differential cross section,* $\mathrm{d}\sigma/\mathrm{d}M_{t\bar{t}}$ *in $2.7\,fb^{-1}$ of CDF-II data*, CDF Note 9602 (Nov. 2008).
[35] Randall L. and Sundrum R., *Phys. Rev. Lett.*, **83** (1999) 3370.
[36] Abazov V. M. *et al.* (D0 Collaboration), *Search for scalar top admixture in the $t\bar{t}$ lepton+jets final state at $\sqrt{s} = 1.96\,TeV$ in $1\,fb^{-1}$ of DØ data*, D0 Note 5438 Conf (2007).
[37] Abazov V. M. *et al.* (D0 Collaboration), *Phys. Lett. B*, **674** (2009) 4.
[38] CDF Collaboration, *Search for heavy top $t' \to Wqs$ in lepton plus jets events*, CDF Conf. Note 9446 (July 2008).
[39] Aaltonen T. *et al.* (CDF Collaboration), *Phys. Rev. Lett.*, **100** (2008) 161803.

IL NUOVO CIMENTO Vol. 32 C, N. 5-6 Settembre-Dicembre 2009
DOI 10.1393/ncc/i2010-10549-5

Colloquia: LaThuile09

First observation of single-top-quark production

G. Otero y Garzón on behalf of the DØ and CDF Collaborations

Universidad de Buenos Aires - Buenos Aires, Argentina
Fermi National Accelerator Laboratory - Batavia IL, USA

(ricevuto il 10 Novembre 2009; pubblicato online il 20 Gennaio 2010)

Summary. — This paper reports the first observation of the electroweak production of single top quarks in $p\bar{p}$ collisions at a center-of-mass energy of 1.96 TeV based on $2.3\,\mathrm{fb}^{-1}$ and $3.2\,\mathrm{fb}^{-1}$ of data collected by the DØ and CDF detectors, respectively, at the Fermilab Tevatron Collider. Using various multivariate techniques to separete the small signal from the large backgrounds, both experiments obtained a significance of the observed data of 5.0 standard deviations. DØ measures $\sigma(p\bar{p} \to tb + X, tqb + X) = 3.94 \pm 0.88\,\mathrm{pb}$ and CDF measures $2.3^{+0.6}_{-0.5}\,\mathrm{pb}$. The CKM matrix element that couples the top and the bottom quarks is also measured. DØ reports $|V_{tb}| > 0.78$ at 95% CL when $f_L^1 = 1$ and $|V_{tb} f_L^1| = 1.02 \pm 0.12$. CDF measures $|V_{tb}| = 0.91 \pm 0.11(\mathrm{stat+syst}) \pm 0.07(\mathrm{theory})$ and sets the limit $|V_{tb}| > 0.71$ at 95% CL.

PACS 14.65.Ha – Top quarks.
PACS 12.15.Ji – Applications of electroweak models to specific processes.
PACS 13.85.Qk – Inclusive production with identified leptons, photons, or other nonhadronic particles.
PACS 12.15.Hh – Determination of Kobayashi-Maskawa matrix elements.

1. – Introduction

At hadron colliders, top quarks can be produced in pairs via the strong interaction or singly via the electroweak interaction [1]. Top quarks were first observed via pair production at the Fermilab Tevatron Collider in 1995 [2, 3]. Since then, pair production has been used to make precise measurements of several top quark properties.

The Standard Model (SM) predicts the production of top quarks via the electroweak force (single top production). This mechanism serves as a probe of the Wtb interaction [4, 5] and its production cross-section provides a direct measurement of the CKM matrix element that mixes the top and the bottom quarks without assuming three quark generations [6]. However, measuring the single top production cross-section is difficult because of its small rate and the large backgrounds.

At Tevatron energies, top quarks can be produced singly through s-channel (also called tb) or t-channel (also named tqb) exchange of a virtual W-boson as shown in

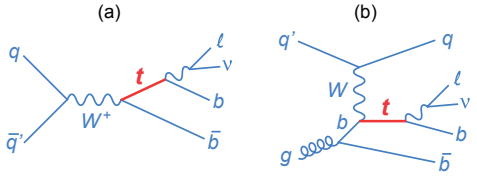

Fig. 1. – Representative Feynman diagrams for (a) s-channel single-top-quark production and (b) t-channel production, showing the top-quark decays of interest.

fig. 1. The sum of the predicted cross-sections of these two processes is 3.5 ± 0.2 pb for $m_t = 170$ GeV [7] and 2.9 ± 0.3 pb for $m_t = 175$ GeV [8].

Both the DØ and CDF Collaborations have published evidence for single-top-quark production at significance levels 3.6 [9, 10] and 3.7 [11] standard deviations, respectively [9-11]. This paper reports significant updates to the previous measurements including larger data samples and new analysis techniques achieving signal significance levels above 5 standard deviations, thus conclusively observing electroweak production of single top quarks. Most definitions and abreviations are defined in the corresponding letters [12, 13].

2. – General analysis strategy

The measurements focus on the final state containing one high transverse momentum (p_T) lepton (electron or muon) not near a jet (isolated), large missing transverse energy ($\not\!\!E_T$) indicative of the passage of a neutrino ν, a b-quark jet from the decay of the top quark ($t \to Wb \to l\nu b$), and possibly another b-jet and a light jet as indicated in fig. 1. In the case of the DØ analysis the data were collected using a logical OR of many trigger conditions and several offline selection criteria, including b-jet identification requirements have been loosened with the net resulf of an 18% increase in signal acceptance compared to the evidence publication [10]. The CDF analysis is based on updates to the published evidence report [11] and the adition of three new multivariate analyses and a new analysis that makes use of a sample that is orthogonal to the event selection described above that adds about 30% to the signal acceptance.

The analyses consider the following backgrounds: W-boson production in association with jets, top quark pair ($t\bar{t}$) production with decay into lepton+jets and dilepton final states (when a lepton in not reconstructed) and multijet production, where a jet is misreconstructed as an electron or a heavy-flavor quark decays into a muon that passes the isolation criteria. Z + jets and diboson processes form minor additional background components.

Because the single-top cross-section is very small compared to the competing backgrounds, a simple cut-based counting experiment is not sufficient to verify the presence of the signal. Because of this, the first step is to apply the loosest event selection possible to maximize the signal acceptance. After the event selection, the expected signal is typically smaller than the uncertainty on the background. Thus, the main strategy implemented by both collaborations is to use sophisticated multivariate techniques to extract the small signal from the overwhelming backgrounds. Each such multivariate technique constructs a powerful discriminant variable that is proportional to the probability of an event to be signal. The discriminant distribution is used as input to the cross-section measurement.

TABLE I. – *Number of expected and observed events in* $2.3\,\mathrm{fb}^{-1}$ *of DØ data for all analysis channels combined. The uncertainties include both statistical and systematic components.*

Source	2 jets	3 jets	4 jets
Signal	139 ± 18	63 ± 10	21 ± 5
W + jets	1829 ± 161	637 ± 61	180 ± 18
Z + jets and dibosons	229 ± 38	85 ± 17	27 ± 7
$t\bar{t}$	222 ± 35	436 ± 66	484 ± 71
Multijets	196 ± 50	73 ± 17	30 ± 6
Total prediction	2615 ± 192	1294 ± 107	742 ± 80
Data	2579	1216	724

Several validation tests are conducted by studying the discriminant output distributions in background enriched control samples.

The single-top-quark production cross-section is measured from the discriminant output distributions using a Bayesian binned likelihood technique [14]. The statistical and all systematic uncertainties and their correlations are considered in these calculations.

3. – DØ analysis

The DØ analysis considers events with two, three, or four jets (which allows for additional jets from initial-state and final-state radiation), reconstructed using a cone algorithm in the (η, ϕ)-space, where η is the rapidity and ϕ is the azimuthal angle, and the cone radius is 0.5 [10]. The highest-p_T (leading) jet must have $p_T > 25\,\mathrm{GeV}$, and subsequent jets have $p_T > 15\,\mathrm{GeV}$; all jets have pseudorapidity $|\eta| < 3.4$. The selection requires $20 < \not\!\!E_T < 200\,\mathrm{GeV}$ for events with two jets and $25 < \not\!\!E_T < 200\,\mathrm{GeV}$ for events with three or four jets. Events must contain only one isolated electron with $p_T > 15\,\mathrm{GeV}$ and $|\eta| < 1.1$ ($p_T > 20\,\mathrm{GeV}$ for three- or four-jet events), or one isolated muon with $p_T > 15\,\mathrm{GeV}$ and $|\eta| < 2.0$. The background from multijets events is kept to $\approx 5\%$ by requiring high total transverse energy and by demanding that the $\not\!\!E_T$ is not along the direction of the lepton or the leading jet.

Table I shows the event yields, separated by jet multiplicity. The acceptances are $(3.7 \pm 0.5)\%$ for the s-channel and $(2.5 \pm 0.3)\%$ for the t-channel, expressed as percentages of the inclusive single top quark production cross-section in each channel.

Systematic uncertainties arise from each correction factor or function applied to the background and signal models. Most affect only the normalization, but three corrections modify the shapes of the distributions; these are the jet energy scale corrections, the tag-rate functions, and the reweighting of the distributions in W + jets events. The largest uncertainties come from the jet energy scale, the tag-rate functions, and the correction for jet-flavor composition in W + jets events, with smaller contributions from the integrated luminosity, jet energy resolution, initial-state and final-state radiation, b-jet fragmentation, $t\bar{t}$ cross-section, lepton efficiency corrections, and MC statistics. All other contributions have a smaller effect. The total uncertainty on the background is (8 to 16)% depending on the analysis channel. After event selection, single-top-quark events are expected to constitute (3 to 9)% of the data sample.

DØ perfomed three independent analyses based on boosted decision trees (BDT) [15], Bayesian neural networks (BNN) [16], and the matrix element (ME) method [17]. The application of these techniques is described in [9, 10]. The analyses presented here differ

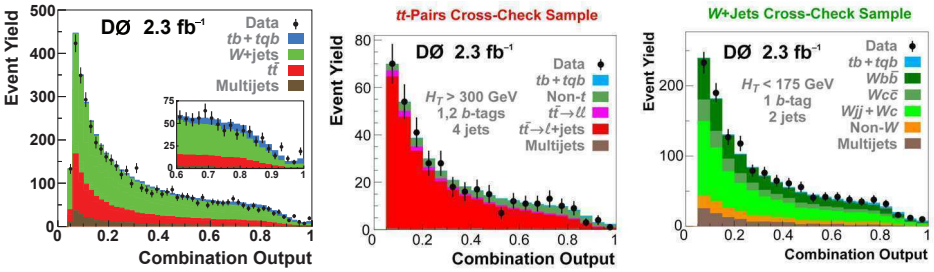

Fig. 2. – Distribution of the DØ discriminant output for the combined analysis (left). Cross check of the discriminant output in signal-depleted and background-enriched samples: $t\bar{t}$ (center) and W + jets (right).

from previous implementations in the choice of input variables and some detailed tuning of each technique.

The BDT analysis has re-optimized the input variables into a common set of 64 variables for all analysis channels. The BNN analysis uses the RuleFitJF algorithm [18] to select the most sensitive of these variables, then combines 18 to 28 of them into a single separate discriminant for each channel. The ME analysis uses only two-jet and three-jet events, divided into a (W + jets)-dominated set and a $t\bar{t}$-dominated set. It includes matrix elements for more background sources to improve background rejection.

Each analysis uses the same data and background model and has the same sources of systematic uncertainty. The analyses are tested using ensembles of pseudodatasets created from background and signal at different cross-sections to confirm linear behavior and thus an unbiased cross-section measurement. The analyses are also checked extensively before b-tagging is applied, and using two control regions of the data, one dominated by W + jets and the other by $t\bar{t}$ backgrounds. These studies confirm that backgrounds are well modeled across the full range of the discriminant output.

The cross-section is determined using the same Bayesian approach as in previous analyses [9, 10]. This involves forming a binned likelihood as a product over all bins and channels, evaluated separately for each multivariate discriminant. The central value of the cross-section is defined by the position of the peak in the posterior density, and the 68% interval about the peak is taken as the uncertainty on the measurement. Systematic uncertainties, including all correlations, are reflected in this posterior interval.

The three multivariate techniques use the same data sample but are not completely correlated. Their combination therefore leads to increased sensitivity and a more precise measurement of the cross-section. The three discriminant outputs are used as inputs to a second set of Bayesian neural networks, and obtain the combined cross-section and its signal significance from the new discriminant output. The resulting expected significance is 4.5 standard deviations. Figure 2 illustrates the importance of the signal when comparing data to prediction and also the behaviour of the discriminant output in background-dominated samples.

The measured cross-section is $\sigma(p\bar{p} \to tb + X, tqb + X) = 3.94 \pm 0.88\,\text{pb}$. The measurement has a p-value of 2.5×10^{-7}, corresponding to a significance of 5.0 standard deviations. Figure 3 shows the results of all DØ analyses and the ensemble test performed to measure the observed significance of the combined analysis.

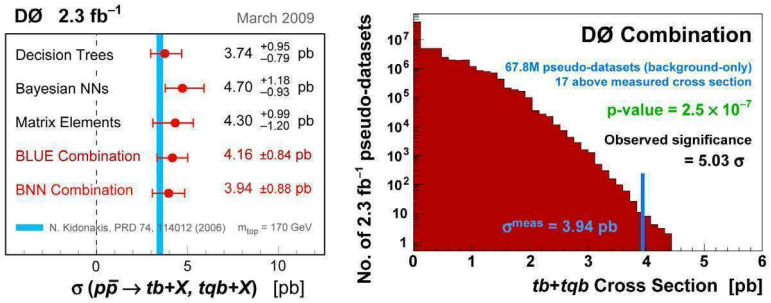

Fig. 3. – DØ cross-section measurements summary (left). Cross-section distribution from background-only ensembles with full systematics included for the DØ combined analysis (right).

The cross-section measurement is used to determine the Bayesian posterior for $|V_{tb}|^2$ in the interval $[0, 1]$ and a limit of $|V_{tb}| > 0.78$ at 95% CL is extracted within the SM. When the upper constraint is removed, $|V_{tb} \times f_1^L| = 1.07 \pm 0.12$ is measured, where f_1^L is the strength of the left-handed W_{tb} coupling.

4. – CDF analysis

The CDF collaboration updated the published [11] likelihood function (LF), matrix element (ME), and neural network (NN) analyses with an additional 1 fb^{-1} of integrated luminosity with their methods unchanged. In addition, three new analyses are added: a boosted decision tree (BDT), a likelihood function optimized for s-channel single-top production (LFS), and a neural-network–based analysis of events with $\not\!\!E_T$ and jets (MJ). The BDT and LFS analyses use events that overlap with the LF, ME, and NN analyses, while the MJ analysis uses an orthogonal event selection that adds about 30% to the signal acceptance.

The LF, ME, NN, BDT, and LFS analyses use lepton + jets events as described in the DØ analysis. The MJ analysis is designed to select events with $\not\!\!E_T$ and jets and to veto events selected by the lepton + jets analyses. It accepts events in which the W-boson decays into τ-leptons and those in which the electron or muon fails the lepton identification criteria. The MJ analysis uses a dataset of 2.1 fb^{-1} of integrated luminosity and selects events that have $\not\!\!E_T > 50$ GeV and two jets with $|\eta| < 2$, at least one of which has $|\eta| < 0.9$. Events must have one jet with transverse energy E_T greater than 35 GeV, and a second jet with E_T greater than 25 GeV. The angular separation between the two jets is required to exceed 1. Events with four or more jets with $E_T > 15$ GeV in $|\eta| < 2.4$ are rejected in order to reduce the multijet (QCD) and $t\bar{t}$ backgrounds and at least one jet is required to originate from a B-hadron. The observed and expected event counts for the all the analyses are given in table II.

After event selection, the samples are dominated by background and multivariate techniques are used to further discriminate the signal. The LF, ME, and NN discriminants are described in detail in [11]. The BDT discriminant uses over 20 input variables. Some of the most sensitive are the neural-network jet-flavor separator, the invariant mass of the $l\nu b$ system $M_{l\nu b}$ and the total scalar sum of transverse energy in the event H_T. The LFS discriminant uses projective likelihood functions [19] to combine the separation power of several variables and is optimized to be sensitive to the s-channel process. The

TABLE II. – *Background composition and predicted number of single-top events in* $3.2\,\text{fb}^{-1}$ *of CDF Run-II data for the* $l + \not\!\!E_T +$ *jets samples (LF, ME, NN, and BDT analyses), and* $2.1\,\text{fb}^{-1}$ *of data for the* $\not\!\!E_T +$ *jets sample (MJ analysis).*

Source	$l + \not\!\!E_T +$ jets	$\not\!\!E_T +$ jets
s-channel signal	77 ± 11	30 ± 4
t-channel signal	114 ± 17	35 ± 6
$W +$ HF	1551 ± 472	304 ± 116
$t\bar{t}$	686 ± 99	185 ± 30
$Z +$ jets	52 ± 8	129 ± 54
Diboson	118 ± 12	42 ± 7
QCD+mistags	778 ± 104	679 ± 28
Total prediction	3377 ± 505	1404 ± 172
Observed	3315	1411

dominant backgrounds are $Wb\bar{b}$ and $t\bar{t}$ production. A kinematic fitter is used to find the most likely resolution of two ambiguities: the z-component of the neutrino momentum and the b-jet that most likely came from the top quark decay. In addition to the outputs of the kinematic fitter, other important inputs to the likelihood are the invariant mass of the two b-tagged jets, the transverse momentum of the $b\bar{b}$ system, the leading jet transverse momentum, H_T, and $\not\!\!E_T$.

The MJ discriminant uses a neural network to combine information from several input variables. The most important variables are the invariant mass of the $\not\!\!E_T$ and the second leading jet, the scalar sum of the jet energies, the $\not\!\!E_T$, and the azimuthal angle between the $\not\!\!E_T$ and the jets.

The LF, ME, NN, BDT, and LFS channels are combined using a super-discriminant (SD) technique similar to that which was applied in [11]. The SD method uses a neural network trained with neuro-evolution [20] to separate the signal from the background taking as inputs the discriminant outputs of the five analyses for each event. With the super-discriminant analysis the sensitivity improves by 13% over the best individual analysis. A simultaneous fit is performed over the two exclusive channels, MJ and SD, to obtain the final combined results. The modeling of the distributions of each input variable and the discriminant outputs are checked in data control samples depleted in

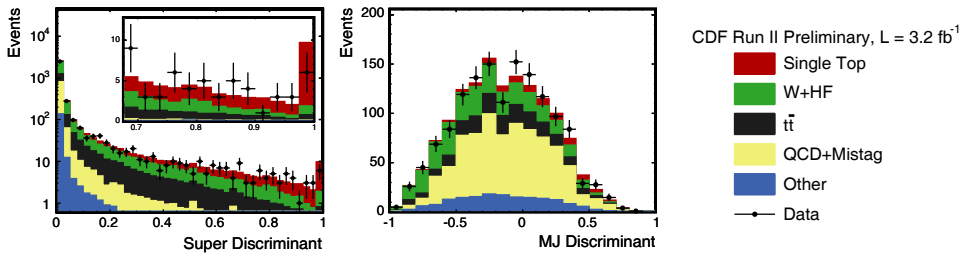

Fig. 4. – CDF's discriminant distributions for the SD (left) and MJ (right) analyses.

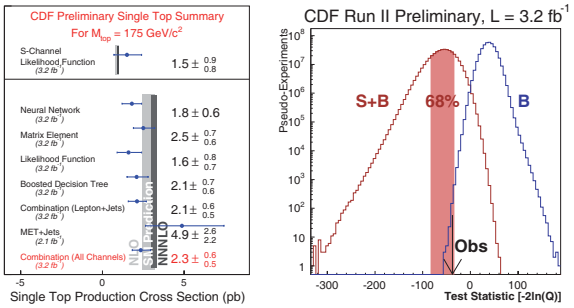

Fig. 5. – CDF's cross-section measurements summary (left). Distribution of the likelihood ratio test statistic $-2\ln Q$ (right).

signal. These are the lepton + b-tagged four-jet sample, which is enriched in $t\bar{t}$ events, and the two- and three-jet samples in which there is no b-tagged jet. The latter has high statistics and is enriched in W + jets and QCD events with kinematics similar to the b-tagged signal samples. The distributions of the SD and MJ discriminants shown in fig. 4 are used to extract the measured cross-section and the signal significance.

The cross-sections are measured using a Bayesian binned likelihood assuming a flat prior in the cross-section in the same way as the DØ analysis. The significance is calculated as a p-value: the probability, assuming single-top-quark production is absent, that $-2\ln Q = -2\ln(p(\text{data}|s+b)/p(\text{data}|b))$ is less than that observed in the data. Figure 5 shows all cross-section measurements and the distributions of $-2\ln Q$ in pseudoexperiments that assume SM single top (S + B) and also those that assume single-top production is absent (B), along with the value observed in data. The p-value is converted into a number of standard deviations using the integral of one side of a Gaussian function. All sources of systematic uncertainty are included and correlations between normalization and discriminant shape changes are considered. Uncertainties in the jet energy scale, b-tagging efficiencies, lepton identification and trigger efficiencies, the amount of initial- and final-state radiation, PDFs, factorization and renormalization scale, and background modeling have been explored and incorporated in all individual analyses and the combination.

The measured p-value is 3.1×10^{-7}, corresponding to a signal significance of 5.0 standard deviations. The sensitivity is defined to be the median expected significance and is in excess of 5.9 standard deviations. The most probable value of the combined s- and t-channels cross-sections is $2.3^{+0.6}_{-0.5}$ pb assuming a top quark mass of 175 GeV/c^2. The cross-section measurement is used to determine that $|V_{tb}| = 0.91 \pm 0.11(\text{stat}+\text{syst}) \pm 0.07(\text{theory})$ and the limit $|V_{tb}| > 0.71$ at 95% CL assuming a flat prior in $|V_{tb}|^2$ from 0 to 1.

5. – Conclusions

The DØ and CDF Collaborations reported the first observation of electroweak production of single top quarks in $p\bar{p}$ collisions at $\sqrt{s} = 1.96$ TeV using 2.3 and 3.2 fb^{-1} of Tevatron data, respectivelly. The results are in agreement with the Standard Model prediction and the measured signal corresponds to an excess over the predicted backgrounds with significances of 5.0 standard deviations. The results provide the most precise direct measurements of the amplitude of the CKM matrix element V_{tb}.

* * *

The author wishes to thank the conference organizers for a very interesting meeting, and members of the single-top working groups from the CDF and DØ Collaborations as well as the Fermilab staff and the techinical staffs of the participating institutions for their vital contributions.

REFERENCES

[1] Willenbrock S. and Dicus D., *Phys. Rev. D*, **34** (1986) 155.
[2] Abe F. *et al.* (The CDF Collaboration), *Phys. Rev. Lett.*, **74** (1995) 2626.
[3] Abachi S. *et al.* (The DØ Collaboration), *Phys. Rev. Lett.*, **74** (1995) 2632.
[4] Heinsion A. *et al.*, *Phys. Rev. D*, **56** (1997) 3114.
[5] Abazov V. *et al.* (The DØ Collaboration), *Phys. Rev. Lett.*, **101** (2008) 221801.
[6] Jikia G. *et al.*, *Phys. Lett. B*, **295** (1992) 136.
[7] Kidonakis N., *Phys. Rev. D*, **74** (2006) 114012.
[8] Sullivan Z., *Phys. Rev. D*, **70** (2004) 114012.
[9] Abazov V. *et al.* (The DØ Collaboration), *Phys. Rev. Lett.*, **98** (2007) 181802.
[10] Abazov V. *et al.* (The DØ Collaboration), *Phys. Rev. D*, **78** (2008) 012005.
[11] Aaltonen T. *et al.* (The CDF Collaboration), *Phys. Rev. Lett.*, **101** (2008) 252001.
[12] Abazov V. *et al.* (The DØ Collaboration), *Phys. Rev. Lett.*, **103** (2009) 092001, arXiv:0903.0850.
[13] Aaltonen T. *et al.* (The CDF Collaboration), *Phys. Rev. Lett.*, **103** (2009) 092002, arXiv:0903.0885.
[14] Bertram I. *et al.*, Fermilab-TM-2104 (2000).
[15] Breiman L. *et al.*, *Classification and Regression Trees* (Wadsworth, Standford) 1984.
[16] Neil R., *Bayesian Learning for Neural Networks* (Springer-Verlag, New York) 1996.
[17] Abazov V. *et al.* (The DØ Collaboration), *Nature*, **429** (2004) 638.
[18] Friedman J. *et al.*, *Ann. Appl. Stat.*, **2** (2005) 094027.
[19] Ackerstaff K. *et al.* (The OPAL Collaboration), *Eur. Phys. J. C*, **1** (1998) 425.
[20] Stanley K. *et al.*, *Evolutionary Computation*, **10** (2002) 99.

SESSION VII - HIGGS SEARCHES

Artur Apresyan	Searches for a low-mass Higgs boson at the Tevatron
Herbert Greenlee	Search for high-mass Standard Model Higgs at the Tevatron
Glen Cowan	Discovery potential for the Standard Model Higgs at ATLAS
Swagato Banerjee	Search for a light Higgs boson at BaBar
Fulvio Piccinini	$H \to b\bar{b}$ in VBF at the LHC with an extra central photon
Jean-Marie Frère	Can colliders disprove leptogenesis?

IL NUOVO CIMENTO Vol. 32 C, N. 5-6 Settembre-Dicembre 2009
DOI 10.1393/ncc/i2010-10534-0

Colloquia: LaThuile09

Searches for a low-mass Higgs boson at the Tevatron

A. Apresyan on behalf of the CDF and D0 Collaborations
Purdue University - West Lafayette, IN 47907, USA

(ricevuto il 10 Novembre 2009; pubblicato online il 18 Gennaio 2010)

Summary. — This proceeding presents an overview of recent experimental searches for the standard model Higgs boson. These searches are based on data collected by the CDF and the D0 experiments operating at the Fermilab Tevatron proton-antiproton collider with $\sqrt{s} = 1.96\,\text{TeV}$. We focus on searches that are sensitive to a low-mass Higgs boson production with $m_H \lesssim 140\,\text{GeV}/c^2$. Using up to $4.2\,\text{fb}^{-1}$ of data, both CDF and D0 find no evidence for Higgs boson production, and set 95% confidence level upper limits on Higgs boson production cross-section times branching ratio.

PACS 13.85.Rm – Limits on production of particles.
PACS 14.80.Bn – Standard-model Higgs bosons.

1. – Introduction

The Higgs boson is the last particle of the standard model (SM) of particle physics which remains to be discovered. The existence of the Higgs boson is expected to be the direct physical manifestation of the mechanism that provides mass to fundamental particles [1]. While the Higgs mechanism is successful in generating masses of particles in the SM, a direct observation of the Higgs boson would be necessary to confirm the predictions of the SM. The mass of the Higgs boson is related to the vacuum expectation value v of the neutral Higgs field by $m_H = \sqrt{2\lambda}v$. Since the Higgs self-coupling parameter, λ, is not specified by the SM, the Higgs boson mass is an unknown quantity.

Direct searches at LEP have excluded the Higgs boson with a mass below $114\,\text{GeV}/c^2$ at 95% confidence level (CL) [2]. Global fits to the precision electroweak measurements using data collected at the LEP, SLD and Tevatron allow one to indirectly constrain the Higgs boson mass to values below $163\,\text{GeV}/c^2$ at 95% CL [3]. Including the direct limit from LEP raises this upper limit to $191\,\text{GeV}/c^2$. These numbers indicate that the Higgs boson is expected to have a relatively low mass and could be in the reach of the Tevatron experiments. Therefore, the search for the Higgs boson is one of the most active areas of research at the Tevatron.

2. – Higgs boson production at the Tevatron

The Tevatron is a $p\bar{p}$ collider that operates at a center of mass energy of $\sqrt{s} = 1.96\,\text{TeV}$. The two general-purpose experiments, CDF and D0, each collected a data sample corresponding to an integrated luminosity of about $5\,\text{fb}^{-1}$. In this paper we review the results that are based on datasets of up to $4.2\,\text{fb}^{-1}$.

A variety of processes can lead to the production of Higgs bosons at the Tevatron, including gluon fusion (the highest production cross-section), associated production with W or Z bosons and vector boson fusion. The searches for the Higgs boson are largely driven by possible decays of the Higgs boson and the ease of triggering on its decay products. Since the coupling of the Higgs boson to massive particles depends on their masses, the most frequent decays of the Higgs boson are to the heaviest particles.

If the mass of the Higgs boson is just above the LEP limit, *i.e.* $m_H > 114\,\text{GeV}/c^2$, then it predominantly decays to $b\bar{b}$. The cross-section of QCD production of quarks at hadron colliders is several orders of magnitude higher than $gg \to H$. Therefore, in the range of $100\,\text{GeV}/c^2 < m_H < 135\,\text{GeV}/c^2$ the $gg \to H$ production mode is overwhelmed by a large, essentially irreducible background from QCD multi-jet production. In the case of associated vector boson production, the decay products of the W or Z boson provide additional handles to reduce the amount of the backgrounds, and these are the production channels that yield the most sensitive results in the low-mass searches.

Various search channels are optimized for a particular final state, depending on the production mechanism and the decays of the produced particles. The results of individual analyses are combined to increase the overall sensitivity of the Tevatron searches. Both CDF and D0 Collaborations search for the Higgs boson in several complementary production channels that individually are not very sensitive to the Higgs boson, but help to increase the Tevatron sensitivity in the combination.

3. – Low-mass Higgs boson at the Tevatron

The first step in the Higgs boson searches is to identify, reconstruct and store events using triggering systems. Excellent trigger performance is crucial in order to maintain high efficiency for potential Higgs boson candidates while rejecting the majority of the unwanted events. The CDF and D0 experiments employ three level trigger systems that allow high efficiency in triggering on charged leptons and jets, the imbalance in energy in the plane transverse to the beam ($\not\!\!E_{\text{T}}$) or photons. The leptonic decays of the W and Z bosons in $\ell\nu b\bar{b}$ and $\ell^+\ell^- b\bar{b}$ channels are primarily detected using the high-p_T electron and muon triggers. These triggers generally detect electrons using the electromagnetic calorimeter, while muons are detected by matching tracks found in a central tracker with hits in scintillation counters and drift chambers surrounding the calorimeters. The charged-lepton identification efficiency is mainly governed by the geometrical acceptance, resulting in muon coverage up to $|\eta| < 1.5$ at CDF and $|\eta| < 2.0$ at D0. The searches in channels with no charged leptons in the final state, such as $\nu\bar{\nu}b\bar{b}$, rely on triggers that require a presence of large $\not\!\!E_{\text{T}}$ and jets. Additionally, the sample collected with the $\not\!\!E_{\text{T}}$ + jets trigger helps to recover events where the charged lepton is not identified by the dedicated triggers and leaves a signature of apparent missing transverse energy. Dedicated τ lepton triggers are used to identify the hadronic decays of taus, which search for narrow jets that are matched to a small number of charged tracks. Photons are identified by requiring isolated electromagnetic objects, without a matching track compatible with the cluster energy.

Sophisticated algorithms can be applied offline, after the events are stored, to increase the purity or increase the reconstruction efficiency of physics objects of interest. Efficient identification of jets originating from b quarks plays a crucial role in searches for a low-mass Higgs boson. The key element to distinguish the Higgs boson signal from background events is the invariant mass of the $b\bar{b}$ system, which for signal has a sharp peak around the Higgs boson mass, while the backgrounds have smoother distributions. Therefore, improvements in jet energy resolution are crucial for Higgs boson searches in low mass. Since the b-quark decays through a weak force, the lifetime of b-hadrons is long enough to move a considerable distance before decaying to lighter hadrons, typically travelling a few millimeters away from the primary vertex. Reconstruction of the decay products of the b-hadron allows one to look for the trajectories of the decay products that have a large impact parameter and identify b-jets ("b tagging"). Various algorithms are used by the CDF and D0 Collaborations, in order to maximize the b tagging efficiency.

As a last step of the Higgs boson searches, the observed data is compared to the predictions of the signal and backgrounds models. In searches for rare processes at hadron colliders, such as Higgs boson production, the traditional method of a counting experiment does not provide sufficient sensitivity. A better sensitivity can be achieved by a fit to a kinematic distribution that distinguishes the signal process events from backgrounds. The resonance in the dijet invariant-mass spectrum yields the most striking feature of the low-mass Higgs boson signal events, and searches at LEP and Tevatron have been performed by scanning this spectrum. Additional kinematic and topological features of the signal process can provide further discrimination from backgrounds, increasing the sensitivity of the search. These additional features can be combined into a single discriminating variable using multivariate techniques, such as artificial neural networks (NN), boosted decision trees (BDT) or matrix element techniques (ME). Validation of the techniques is performed in dedicated control samples, as well as by performing the measurements of well-known physics processes, *e.g.*, the measurement of the top pair production cross-section at CDF [4] or the evidence of of WW/WZ production with lepton + jets final states at D0 [5].

4. – Low-mass Higgs boson searches at the Tevatron

In the following sections we review the current state of the various Higgs searches at CDF and D0.

4·1. $ZH \to \ell^+\ell^- b\bar{b}$. – This decay mode provides the cleanest experimental signature, since the SM processes rarely produce a similar final state. Additionally, it is possible to fully reconstruct both Z and Higgs bosons, allowing to further constrain the backgrounds. Traditionally the decays of a Z-boson to a pair of electrons or muons are considered, since the τ identification at hadron colliders is more challenging. Due to the low branching fraction ($\mathrm{Br}(Z \to l^+l^-) \sim 0.07$ for e, μ combined) the number of expected signal events in this channel is relatively low, with an expectation of around 1 event per fb^{-1} (if $m_H = 115\,\mathrm{GeV}/c^2$) after the analysis cuts. Therefore, the main challenges in this channel are to increase the b tagging and lepton identification efficiencies.

In order to increase the signal acceptance, the CDF and D0 experiments analyse events where both b-jets are tagged with a high-efficiency and low-purity tag ("loose" tagging). Additionally, events where only one jet is b tagged with a lower-efficiency but higher-purity tag ("tight" tagging) are also analyzed to increase the overall sensitivity. The CDF and D0 experiments also use several categories of leptons which are identified

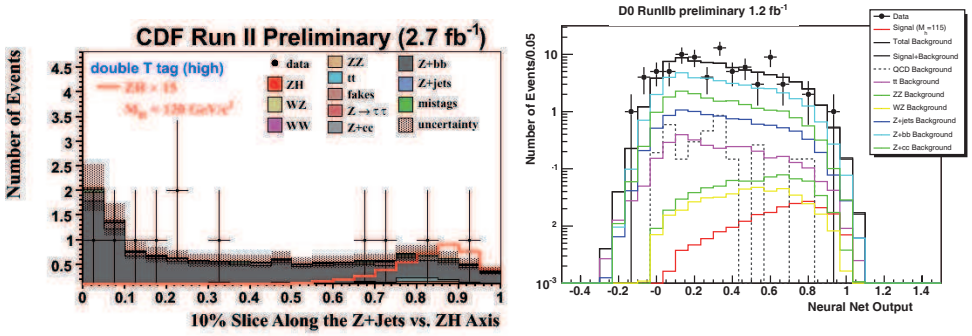

Fig. 1. – Discriminant output distributions used in $ZH \to \ell^+\ell^- b\bar{b}$ searches. Left: a slice of the 2D NN used in the CDF analysis; right: the NN discriminant used at the D0 experiment.

with looser cuts on the information from the lepton detectors. The CDF analysis also uses forward electrons and electrons that are identified based only on calorimeter information.

The CDF analysis exploits the fact that any imbalance of calorimeter energy in the transverse plane is mainly caused by downward fluctuations in the jet energies. By assigning the event $\not\!\!E_{\mathrm{T}}$ to the jets in the event allows to improve the jet energy measurements and improve the dijet invariant-mass resolution. A dedicated neural network is developed for this analysis, which corrects the energy of the dijet system by assigning the $\not\!\!E_{\mathrm{T}}$ to the jets according to the topology of the event.

Both CDF and D0 experiments employ multivariate techniques to further increase the reach of the Higgs boson searches in this channel. Two approaches are used at CDF: one using a two-dimensional NN and another one using ME technique. The D0 experiment uses the output of the BDT discriminant to scan for the presence of the Higgs boson in the muon channel, and the output of a NN discriminant for the electron channel. Figure 1 shows the outputs of the discriminant distributions from CDF and D0.

After analyzing up to $2.7\,\mathrm{fb}^{-1}$ at CDF and $2.3\,\mathrm{fb}^{-1}$ at D0, the observed data agrees well with the background model both at CDF and D0. The 95% CL upper limits on the Higgs boson cross-section are therefore derived. The analyses set an observed (expected) limit of 7.1 (9.9) $\times$ SM in the NN analysis at CDF and 11 (12.3) $\times$ SM in the D0 analysis, assuming $m_H = 115\,\mathrm{GeV}/c^2$ mass.

4·2. $WH \to \ell\nu b\bar{b}$. – Due to the higher production cross-section compared to Z associated production, and a higher branching fraction ($\mathrm{Br}(W^\pm \to l^\pm\nu) \sim 0.22$ for e, μ combined), this final state provides one of the most sensitive channels for Higgs boson searches. The expected number of Higgs boson events in this channel is around 3–4 per fb^{-1} (if $m_H = 115\,\mathrm{GeV}/c^2$) after the analysis cuts. Similar to $ZH \to \ell^+\ell^- b\bar{b}$ channel, final states with electrons or muons are traditionally considered, although recently the D0 Collaboration added a dedicated search for $WH \to \tau\nu b\bar{b}$.

Efficient lepton identification and b tagging are required in this analysis, in order to enhance the sensitivity of the search. Both experiments have achieved increased signal acceptance by extending the lepton identification algorithms. The D0 analysis increases signal acceptance with muon events from any triggers, achieving close to 100% efficiency of muon detection (single muons, muon + jets, topological triggers). Both CDF and D0 Collaborations extend their lepton coverage by accepting events with forward-going

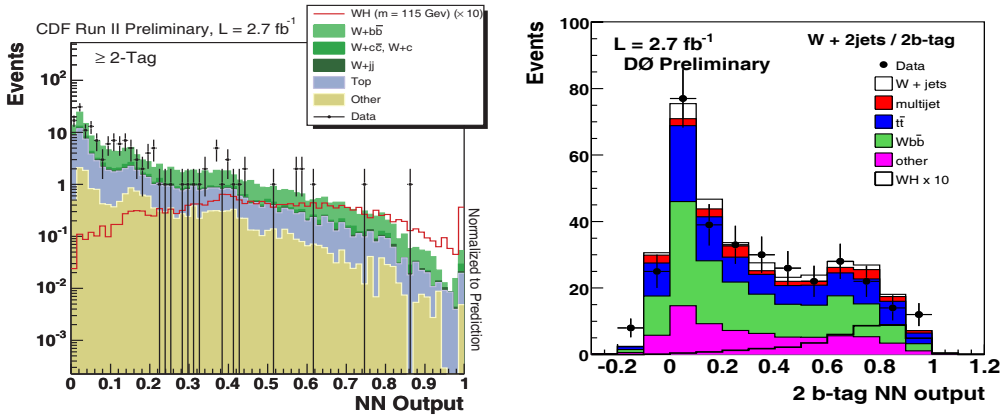

Fig. 2. – Discriminant output distributions used in $WH \to \ell\nu b\bar{b}$ searches. Left: the output of the CDF combined discriminant and right: the output of the NN discriminant used at the D0.

electrons. The CDF Collaboration extends its lepton detector coverage using leptons collected by the $\not\!\!E_{\mathrm{T}}$+jets triggers, which allows to recover leptons that were not identified at the trigger level. These include muons that went through the regions of the CDF detector that are not covered by the muon detectors, but can be identified using the tracking information, or the corresponding muon detectors are not part of the trigger system.

Additional sensitivity is achieved by the CDF Collaboration by incorporating neural network based jet energy corrections and by including events with only one b-tagged jet. The D0 analysis has recently added events with 3 jets in the final state, which further increase the signal acceptance. Both CDF and D0 use multivariate techniques in this channel as the final discriminant. Two approaches are used at CDF: one using a NN and another one using BDT with ME technique. The results of these two analysis are combined at the end. The D0 experiment uses the output of the NN+ME technique. Figure 2 shows the outputs of the discriminant distributions from CDF and D0.

After analyzing $2.7\,\mathrm{fb}^{-1}$ at CDF and D0, the observed data agrees well with the background model both at CDF and D0. The 95% CL upper limits on the Higgs boson cross-section are therefore derived. The analyses set an observed (expected) limit of 5.6 (4.8) × SM in the CDF combined analysis and 6.7 (6.4) × SM in the D0 analysis, assuming $m_H = 115\,\mathrm{GeV}/c^2$ mass.

4˙3. $VH \to \not\!\!E_{\mathrm{T}} + b\bar{b}$. – The main feature of this channel is the presence of a large energy imbalance in the transverse plane ($\not\!\!E_{\mathrm{T}}$) and the absence of identified charged leptons from the decays of the vector bosons. The $\not\!\!E_{\mathrm{T}}$ in the events originates either from the $Z \to \nu\nu$ decays or from $W^{\pm} \to l^{\pm}\nu$ when the charged lepton escapes detection. As a result, the effective production cross-section increases, but the lack of charged leptons weakens the constraints on the backgrounds. The expected number of Higgs boson events in this channel is around 3–4 per fb^{-1} (if $m_H = 115\,\mathrm{GeV}/c^2$) after analysis cuts.

This channel has an advantage of large number of expected Higgs boson signal events, as described above. However, due to the final-event signature, it suffers from contribution from many background sources, the most prominent of which is the QCD multi-jet production with a presence of fake $\not\!\!E_{\mathrm{T}}$ originating from mismeasurement of jet energies.

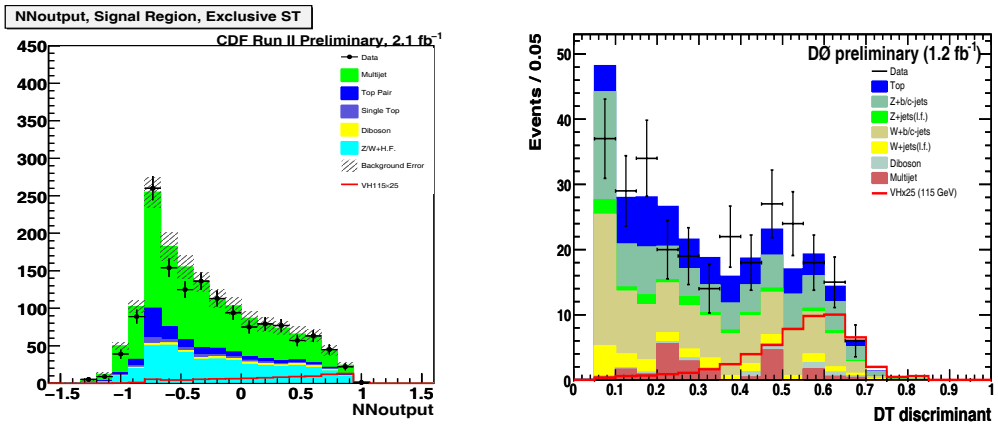

Fig. 3. – Discriminant output distributions used in $VH \to \not\!\!E_{\mathrm{T}} + b\bar{b}$ searches. Left: the output of the CDF discriminant NN distribution and right: the output of the BDT discriminant used at the D0.

Critical issues for this analysis are to achieve a high signal-to-background ratio and to accurately model the multi-jet production.

Both CDF and D0 experiments reduce the number of fake $\not\!\!E_{\mathrm{T}}$ events by comparing the missing energy measured by the calorimeter and the tracker. A dedicated neural network was developed at CDF to drastically reduce the multijet background, by combining several calorimeter and tracker based variables. Data driven techniques are used by both experiments to estimate the contribution of the remaining multijet events. Similar to other searches, also in this channel the CDF analysis includes events where only one of the jets is b-tagged, adding around 10% to the overall sensitivity.

Additional sensitivity is achieved by the CDF Collaboration by incorporating track-based jet energy corrections. CDF and D0 also include events with three jets in the final state, which allows to accept signal events where the third jet is produced either from radiation from initial- or final-state partons or when an e or τ from the W boson decay is reconstructed as a jet. As a final discriminant at CDF the output distribution of a NN is used, while the D0 analysis uses BDT. Figure 3 shows the outputs of the discriminant distributions from CDF and D0.

The CDF and D0 Collaborations have analyzed $2.1\,\mathrm{fb}^{-1}$ of data, and the observed data agrees well with the background model. The analyses set an observed (expected) limit of 6.9 (5.6) $\times$ SM in the CDF analysis and 7.5 (8.4) $\times$ SM in the D0 analysis, assuming $m_H = 115\,\mathrm{GeV}/c^2$ mass.

4˙4. *Higgs boson searches in complementary channels.* – Both collaborations perform searches in several channels, which by themselves are not very sensitive, but nevertheless help to increase the combined sensitivity of the Tevatron searches. Some of these channels, such as those involving $H \to \tau\tau$ or $H \to \gamma\gamma$, are also interesting due to the LHC potential.

The D0 Collaboration performs a search for Higgs bosons decaying to two photons. The critical issue in this search is to reduce the background of QCD jets that are misidentified as photons. Analyzing $4.2\,\mathrm{fb}^{-1}$ of data and scanning the spectrum of diphoton mass for signal excess, the D0 Collaboration was able to set an upper expected limit of

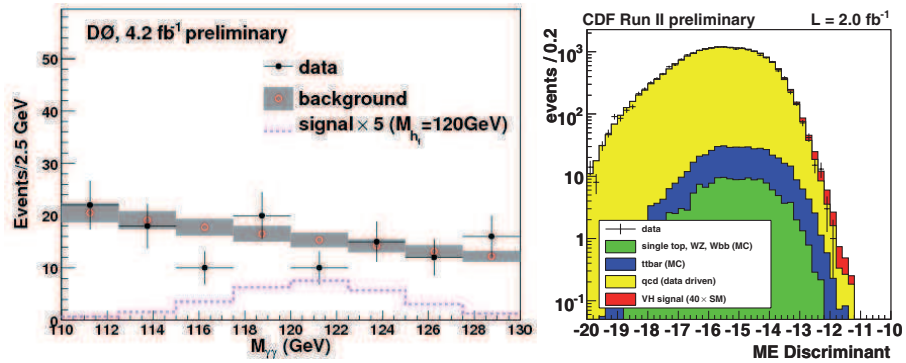

Fig. 4. – Discriminant output distributions used in complementary searches. Left: the diphoton mass in $H \to \gamma\gamma$ (D0); right: the output of the ME discriminant in $VH \to qqb\bar{b}$ (CDF).

$18.5 \times$ SM. CDF performs a search in $H \to \gamma\gamma + 2$ jets channel, which has contributions from various Higgs boson production modes: WH/ZH, vector boson fusion and gluon fusion. Using NN as a final discriminant the sensitivity of $30.5 \times$ SM was obtained. A dedicated search for $WH \to \tau\nu b\bar{b}$ performed at D0 achieves a sensitivity of $42.1 \times$ SM. The all hadronic mode of the associated Higgs boson production is probed at CDF with the search in $VH \to qqb\bar{b}$ final state. The all hadronic sample provides a very high signal yield, however the background from QCD multijet background is very large. A data driven background model was developed to describe the overwhelming background from QCD multi-jets, and the analysis achieved the sensitivity of around $37 \times$ SM using ME discriminant. Higgs boson production in association with top quarks is explored by the D0 Collaboration. While the cross-section of this process is very small at the Tevatron, it is interesting because it may allow us to study the top Yukawa coupling. The limit obtained by the D0 Collaboration by looking at the scalar sum of the transverse momenta of the 4 or 5 leading jets using $2.1\,\text{fb}^{-1}$ of data allowed to achieve the sensitivity around $45 \times$ SM. Figure 4 shows the outputs of the discriminant distributions in $H \to \gamma\gamma$ from D0 and $VH \to qqb\bar{b}$ from CDF.

5. – CDF and D0 combined results

The results from various, statistically independent, analyses are combined and then the results from the CDF and D0 experiments are also combined, in order to maximize the experimental reach of the Tevatron. This allows to increase the sensitivity of searches at the Tevatron by doubling the amount of analyzed data. At the time of this meeting the most recent result of the Tevatron combination were not yet finalized. We show the results of combining the results within the CDF and D0 experiments.

Both CDF and D0 Collaborations compute the upper limits including systematic uncertainties. These include the rate uncertainties (*e.g.*, uncertainties on cross-sections for backgrounds and signal) and uncertainties that can affect the shape of the discriminant distributions. The systematic uncertainties are included as nuisance parameters in the calculations. The CDF Collaboration uses a Bayesian technique and the D0 Collaboration uses a CLs technique to perform the combination. The combination of the results from CDF Collaboration sets an upper limit of 3.8 (3.2 expected) $\times$ SM. The combination of D0 results sets an upper limit of 5.3 (4.6 expected) $\times$ SM. The distributions of

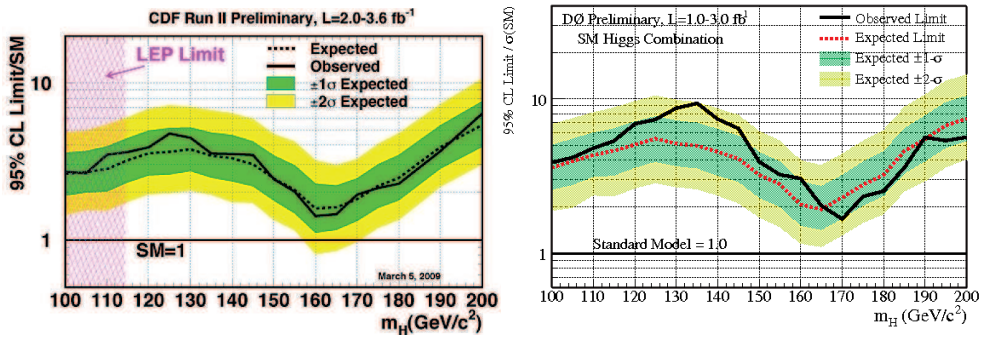

Fig. 5. – (Colour on-line) The CDF (left) and D0 (right) combined 95% CL upper limits as a function of the Higgs boson mass between 100 and 200 GeV/c^2. Solid black: observed limit/SM; dashed black: median expected limit/SM. Colored bands: ± 1, 2 σ distributions around median expected limit.

the upper limits obtained by the CDF and D0 Collaborations are shown in fig. 5. The combined Tevatron expected cross-section limit for a Higgs mass of 115 GeV/c^2 should fall below three times the SM prediction.

6. – Conclusions

The most recent results of the low-mass Higgs boson searches at Tevatron were presented. While the searches in this mass regime are not yet sensitive to the SM Higgs boson production cross-sections, numerous improvements in the analysis techniques were developed over the last year [6, 7], leading to the increase of the Tevatron sensitivity at rate which is much higher than that expected from the larger accumulated dataset alone. With the additional data that will be accumulated by the Tevatron experiments, and a steady rate of improvements, the prospects of the Higgs boson searches at the CDF and D0 are very promising.

REFERENCES

[1] Higgs P. W., *Phys. Rev. Lett.*, **13** (1964) 508.
[2] ALEPH, DELPHI, L3 and OPAL Collaborations, *Phys. Lett. B*, **565** (2003) 61.
[3] LEP electroweak working group web page `http://lepewwg.web.cern.ch/LEPEWWG/`, arXiv:hep-ph/0809.4566; the Tevatron electroweak working group web page `http://tevewwg.fnal.gov/`, arXiv:hep-ex/0612034v2, and references therein.
[4] CDF Collaboration, CDF public note, 9474 (2008).
[5] D0 Collaboration, *Phys. Rev. Lett.*, **102** (2009) 161801.
[6] `http://www-cdf.fnal.gov/physics/new/hdg/hdg.html`.
[7] `http://www-d0.fnal.gov/Run2Physics/WWW/results/higgs.htm`.

IL NUOVO CIMENTO Vol. 32 C, N. 5-6 Settembre-Dicembre 2009
DOI 10.1393/ncc/i2010-10530-4

Colloquia: LaThuile09

Search for high-mass Standard Model Higgs at the Tevatron

H. Greenlee for the CDF and D0 Collaborations
Fermi National Accelerator Laboratory - Batavia, IL, USA

(ricevuto il 10 Novembre 2009; pubblicato online il 18 Gennaio 2010)

Summary. — In this paper, we present results on searches for Standard Model Higgs boson production in the channels $H \to WW \to \ell^+\ell^-$, $WH \to WWW \to \ell^\pm\ell^\pm$, and $H \to \gamma\gamma$. No evidence for the Higgs boson is observed, and we set upper bounds on Higgs boson production. Taking into account Standard Model predictions for Higgs boson production and decay, the existence of the Standard Model Higgs boson is excluded at 95% CL for $m_H = 170\,\text{GeV}$.

PACS 14.80.Bn – Standard-model Higgs bosons.

The Standard Model of elementary-particle physics with three generations of quarks and leptons is very successful at explaining phenomena associated with strong, weak, and electromagnetic interactions. In addition to the observed fermions and gauge bosons, the consistency of the Standard Model requires the existence of a "Higgs sector" containing one or more scalar fields to regulate the ultraviolet behavior of the theory. In the simplest case, there is one Higgs doublet, which leads to a single physical scalar particle, which is the "Standard Model Higgs boson". The mass of the Higgs boson is not predicted by the theory. However, once the mass of the Higgs boson is specified, there are no other free parameters, and all interactions of the Higgs boson are determined.

Experimental constraints on the Higgs boson mass come from direct searches at LEP [1], which put a lower limit on the Higgs boson mass of 114.4 GeV, and from precision electroweak measurements that are sensitive to the effects of higher-order corrections involving virtual Higgs particles [2]. The latter predict a Higgs boson mass of $m_H = 84^{+34}_{-26}\,\text{GeV}$, or $m_H < 154\,\text{GeV}$ at 95% CL.

1. – Experiments and data samples

The results presented in this paper are based on data collected as part of Tevatron collider Run II, which began in April 2002 and is still continuing, in which protons and antiprotons collide at $\sqrt{s} = 1.96\,\text{TeV}$. Data from from both Tevatron experiments, CDF and D0, are included. The combined Higgs boson results shown here are from the "summer 2008" Tevatron Higgs combination [3], although some individual channels have been updated since then. A typical integrated luminosity for channels included in the

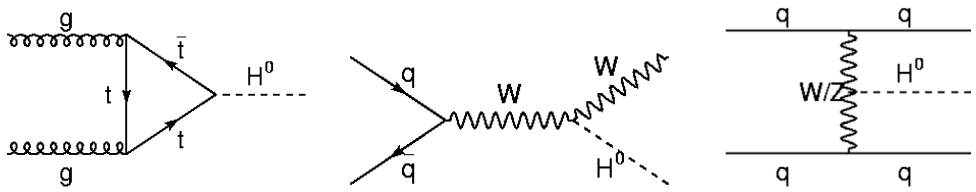

Fig. 1. – Higgs boson production mechanisms gluon fusion (left), associated production (center), and vector boson fusion (right).

summer 2008 combination is about $3.0\,\mathrm{fb}^{-1}$, although some channels may be higher or lower.

2. – Higgs boson phenomenology

At the Tevatron, there are three experimentally important mechanisms of Higgs boson production, which are gluon fusion, vector boson associated production, and vector boson fusion (fig. 1). The dominant decay modes of the Higgs boson are $H \to b\bar{b}$ for $m_H < 135\,\mathrm{GeV}$ and $H \to WW$ for $m_H > 135\,\mathrm{GeV}$. Other decay modes are much smaller than one of these decays at all Higgs masses, but may be experimentally significant nonetheless due to smaller backgrounds.

The combination of Higgs boson production and decay determines the complete experimental signature. Various signatures have been determined to be viable methods of searching for the Standard Model Higgs boson at the Tevatron. The two most important signatures are $VH \to \ell\ell' b\bar{b}$ for low Higgs boson masses ($m_H < 135\,\mathrm{GeV}$), and $H \to WW \to \ell\ell'\nu\nu'$ (opposite-sign dilepton) for high Higgs boson masses ($m_H > 135\,\mathrm{GeV}$). In this paper, we are concerned with the latter, plus two additional signatures $WH \to WWW \to \ell^{\pm}\ell^{\pm} + X$ (like-sign dilepton) and $H \to \gamma\gamma$.

3. – $H \to WW$

The most sensitive channel for Higgs boson searches is the high-mass region at the Tevatron is the opposite-sign dilepton channel $H \to WW \to \ell\ell$, with maximum sensitivity around $m_H = 160\,\mathrm{GeV}$. The experimental signature is two high-p_T, isolated, opposite-sign leptons ($\ell = e$ or μ) and missing transverse energy. There are three subchannels corresponding to $\ell\ell = ee$, $e\mu$, and $\mu\mu$. The major backgrounds are diboson (WW, WZ, ZZ), $Z \to \ell\ell$, $Z \to \tau\tau$, and fake lepton backgrounds from $W + \gamma$/jets and QCD multijets.

The WW diboson background is a fundamental physics background, and one of the largest backgrounds. The most sensitive variable for distinguishing Higgs boson signal from the WW diboson background is the dilepton azimuthal opening angle $\Delta\phi_{\ell\ell}$. In the case of Higgs boson signal, the two charged leptons tend to be emitted in the same direction (small $\Delta\phi_{\ell\ell}$) due to spin correlation, whereas in the case of diboson (and other) background, the two charged leptons tend to be emitted back-to-back ($\Delta\phi_{\ell\ell}$ close to π). The dilepton opening angle is not the only variable that is useful for distinguishing signal from background, however. Therefore, both experiments have used multivariate techniques, including neural networks (NN), boosted decision trees (BDT) and matrix element (ME) to get the best possible sensitivity.

TABLE I. – *Preselection cuts for $H \to WW$.*

		ee	$e\mu$	$\mu\mu$
CDF	Leptons	$p_{T1} > 20\,\text{GeV}$, $p_{T2} > 10\,\text{GeV}$, $m_{\ell\ell} > 16\,\text{GeV}$		
	$\not\!\!E_{T\text{spec}}$ (GeV)	> 25	> 15	> 25
D0	Leptons	$p_{T\mu} > 10\,\text{GeV}$, $p_{Te} > 15\,\text{GeV}$, $m_{\ell\ell} > 15\,\text{GeV}$		
	$\not\!\!E_T$ (GeV)	> 20	> 20	> 20
	$\not\!\!E_T^{\text{scaled}}$	> 7	> 6	> 5
	M_T^{min} (GeV)	> 20	> 30	> 20
	$\Delta\phi_{\ell\ell}$	< 2.0	< 2.0	< 2.5

3˙1. *CDF $H \to WW$ analysis.* – The CDF result for the $H \to WW$ channel has been updated since the summer 2008 Higgs combination with a new result based on an integrated luminosity of $3.6\,\text{fb}^{-1}$ [4]. The preselection cuts are shown in table I. The preselection makes use of a modified missing E_T variable called $\not\!\!E_{T\text{spec}}$, which is the ordinary $\not\!\!E_T$ multiplied by the sine of $\Delta\phi$ from the $\not\!\!E_T$ vector to the nearest charged lepton or jet (if $\Delta\phi < \pi/2$).

Additional analysis after the preselection stage is based on neural networks (NN). Separate NNs are used for 0, 1, and 2 or more jets. The 0-jet subsample uses a 5-variable NN. The 1- and 2-or-more-jet subsamples use an 8-variable NN. Additionally, the 0- and 1-jet subsamples are further subdivided high– and low–signal-to-background subsamples based on the quality of the lepton identification. This subdivision is motivated by the fact that different backgrounds are important in these cases. Distributions of the NN output are shown in figs. 2–4.

The Higgs boson cross-section times branching ratio is obtained from a simultaneous likelihood fit of all five NN distributions. The 95% CL upper limit on Higgs boson production relative to the SM prediciton is shown in fig. 5.

3˙2. *D0 $H \to WW$ analysis.* – The D0 result for the $H \to WW$ channel is based on an integrated luminosity of $3.0\,\text{fb}^{-1}$ [5]. The variables used for preselection include $\not\!\!E_T^{\text{scaled}}$, which is an approximation of the missing E_T significance, M_T^{min} which is the minimal transverse mass of either charged lepton and the missing E_T, and the charged lepton azimuthal opening angle $\Delta\phi_{\ell\ell}$ as described at the beginning of this section. Subsequent

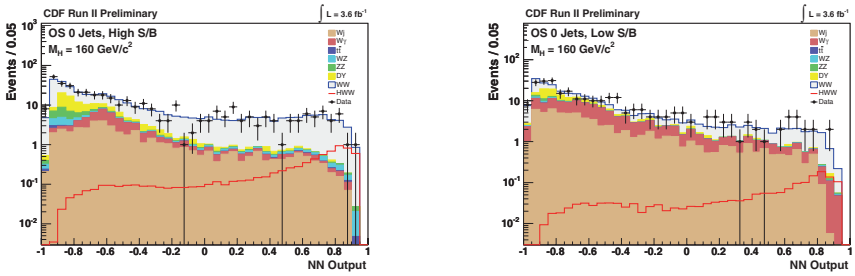

Fig. 2. – CDF $H \to WW + 0$ jets NN distributions for high-(S/B) (left) and low-(S/B) (right) lepton identification.

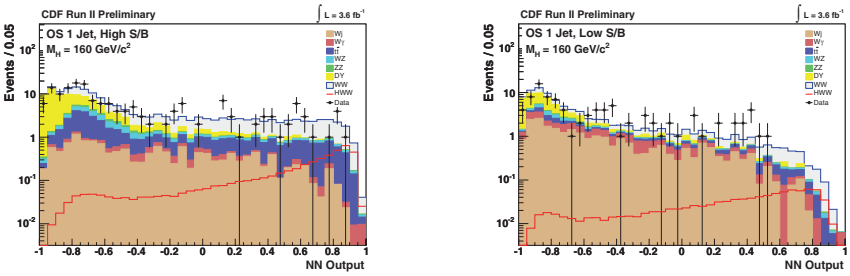

Fig. 3. – CDF $H \to WW + 1$ jets NN distributions for high-(S/B) (left) and low-(S/B) (right) lepton identification.

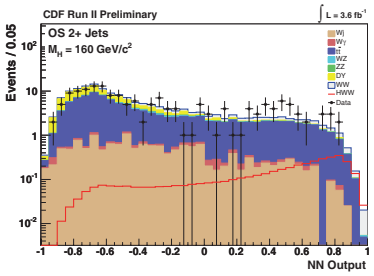

Fig. 4. – CDF $H \to WW + 2$ jets NN distributions.

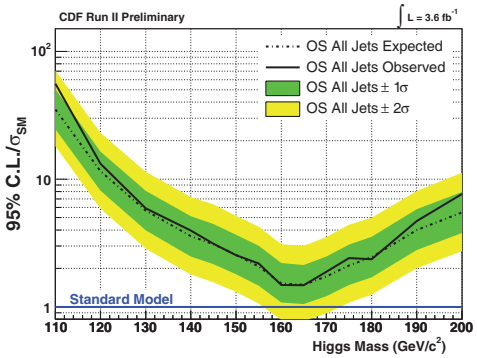

Fig. 5. – CDF $H \to WW$ upper limit on Higgs boson production relative to SM prediction.

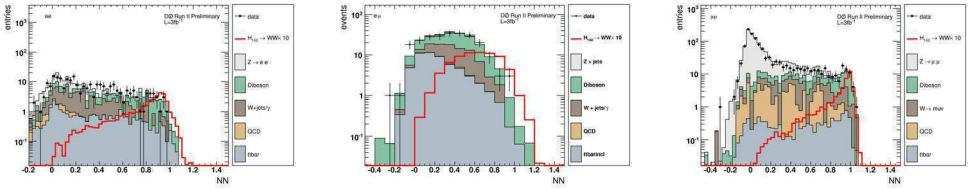

Fig. 6. – D0 $H \to WW$ NN distribution for ee (left), $e\mu$ (center), $\mu\mu$ (right).

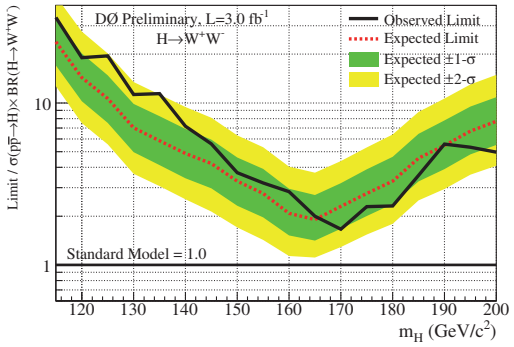

Fig. 7. – D0 $H \to WW$ upper limit on Higgs boson production relative to SM prediction.

analysis is based on a 14-variable neural network. The NN output for the three subchannels is shown in fig. 6. The observed NN distribution is consistent with background. The 95% CL upper limit on Higgs boson production relative to the SM predicion is shown in fig. 7.

4. – $WH \to WWW$

The second channel we are considering in this paper is $WH \to WWW \to \ell^{\pm}\ell^{\pm} + X$. The signature is two like-sign leptons ($\ell = e$ or μ). The cross-section time branching ratio is smaller than the $H \to WW$ channel, but the background is also lower. Physics background comes from diboson production (WZ and ZZ), but instrumental backgrounds (charge flips and fake leptons) are dominant.

4·1. *CDF $WH \to WWW$.* – The CDF result for the $WH \to WWW$ channel has been updated since the summer 2008 Higgs combination with a new result based on an integrated luminosity of $3.6\,\text{fb}^{-1}$ [6]. Preselection cuts for this channel are two like-sign leptons (e or μ) with $p_T > 20\,\text{GeV}$. Subsequent analysis is based on a 13-variable neural network. The measured Higgs boson $\sigma \times BR$ is based on a likelihood fit of the NN distribution. No excess events above background are observed. The NN distribution and 95% CL upper limits on Higgs boson production are shown in fig. 8.

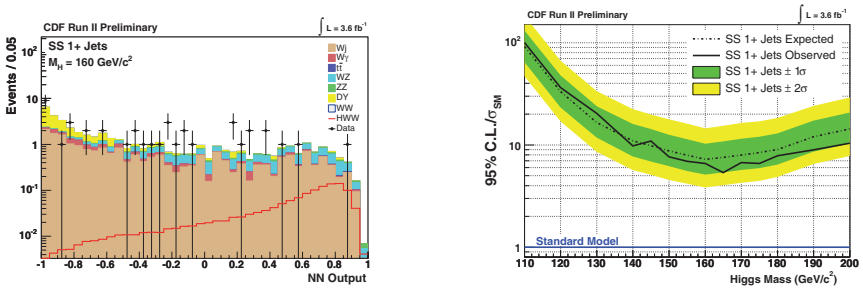

Fig. 8. – CDF $WH \to WWW$ NN distribution (left) and 95% CL upper limit on Higgs boson production relative to SM prediction (right).

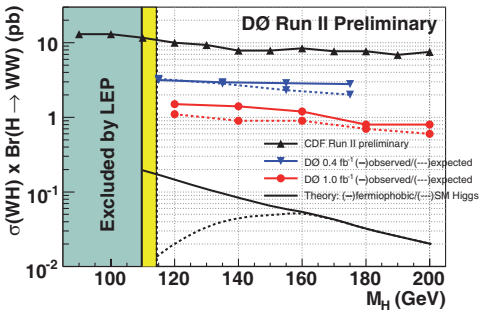

Fig. 9. – D0 $WH \to WWW$ 95% CL upper limit on Higgs boson production.

4˙2. *D0 $WH \to WWW$.* – The D0 result for the $WH \to WWW$ channel is based on an integrated luminosity of 1.1 fb^{-1} [7]. Preselection cuts are two like-sign leptons (e or μ) with $p_T > 15$ GeV. Higgs production is measured using a 2-dimensional multivariate likelihood fit. No excess above background is observed. The 95% CL upper limit on Higgs production is shown in fig. 9.

4˙3. *Tevatron high-mass Higgs combined limit.* – The results shown in this section are from the summer 2008 Tevatron high-mass Higgs combination [3], which includes results from the $H \to WW$ (opposite-sign dilepton) and $WH \to WWW$ (like-sign dilepton) channels from both experiments, taking into account correlated systematic errors. The result of this combination is often displayed as a log-likelihood ratio (LLR), defined as

$$LLR(m_H) = -2 \ln \frac{P(\text{data}|m_H)}{P(\text{data}|\text{Null})}, \tag{1}$$

where P(data|hypothesis) is the probability of obtaining a particular experimental outcome ("data") assuming a given hypothesis. Figure 10 shows $LLR(m_H)$ and the 95% CL upper limit on Higgs boson production relative to the SM prediction. By way of interpretation, the maximum expected sensitivity occurs when the LLR corresponding to the null hypothesis (black dashed line) has the maximum separation from the LLR corresponding to the Higgs mass hypothesis (red dashed-dotted line). The maximum

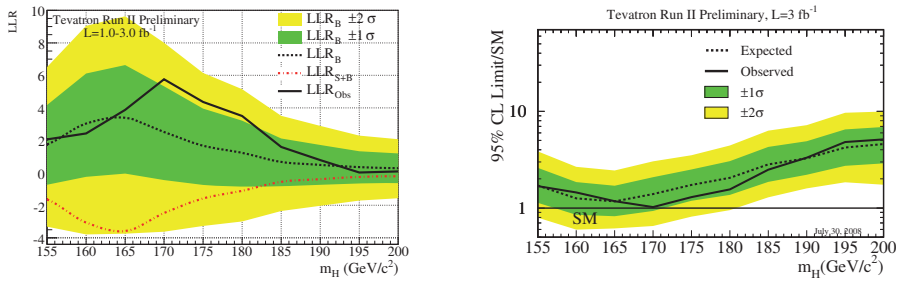

Fig. 10. – (Colour on-line) $LLR(m_H)$ (left) and 95% CL upper limit on Higgs production relative to SM prediction (right).

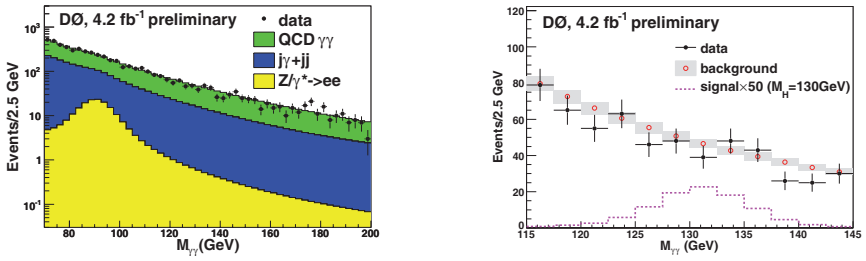

Fig. 11. – D0 $H \to \gamma\gamma$ diphoton invariant-mass distributions.

actual sensitivity occurs when the LLR corresponding to the observed data (black solid line) has the maximum separation from the LLR corresponding to the Higgs mass hypothesis (red dashed-dotted line). The latter occurs at $m_H = 170\,\text{GeV}$, and in fact m_H is excluded at 95% CL. The LLR is calculated at 5 GeV intervals, and m_H is the only excluded point.

5. – $H \to \gamma\gamma$

The Higgs boson decay $H \to \gamma\gamma$ has a fairly small branching ration (maximum about 0.2%), but it is still interesting for several reasons. The branching ratio for $H \to \gamma\gamma$ is maximum in the intermediate mass range $m_H \sim 120$–$130\,\text{GeV}$, where the sensitivity of the dilepton and associated production modes is weakest. Additionally, the $H \to \gamma\gamma$ channel can have enhanced importance in several non-SM scenarios, including the four-generation and fermiphobic Higgs scenarios (although the limites presented here only directly apply to the SM case).

The signature for the $H \to \gamma\gamma$ channel is two high-p_T isolated photons forming a narrow invariant mass peak at the Higgs boson mass. An important and fundamental physics background is nonresonant QCD $\gamma\gamma$ production. There are also instrumental backgrounds jets faking photons (QCD γ + jet and dijet) and electrons faking photons (Z and Drell-Yan ee production).

5˙1. *D0 $H \to \gamma\gamma$.* – D0 has a new SM $H \to \gamma\gamma$ result based on an integrated luminosity of $4.2\,\text{fb}^{-1}$ [8]. Event selection requires two photons with tight photon identification,

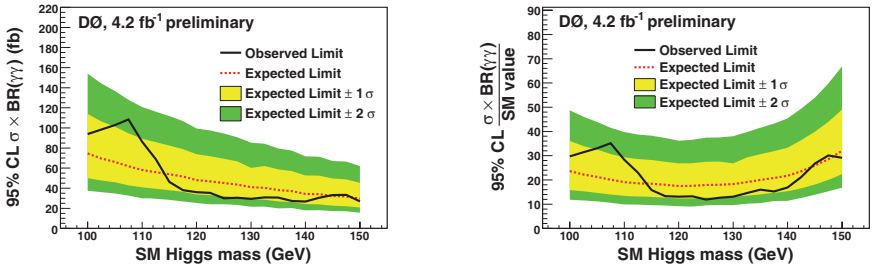

Fig. 12. – D0 $H \to \gamma\gamma$ 95% CL upper limit on Higgs boson production shown as absolute $\sigma \times BR$ (left) and relative to SM prediction (right).

with $E_T > 25\,\text{GeV}$ and pseudorapidity $|\eta| < 1.1$. The invariant mass spectrum of $\gamma\gamma$ events is shown in fig. 11 for the different background contributions (left) and comparing background and the expected signal for a particular Higgs boson mass (right). The observed events are consistent with the expected background. The Higgs boson $\sigma \times BR$ is measured as a function of m_H using the expected Higgs boson lineshape (fig. 11 right). The 95% CL upper limit on Higgs boson production is shown in fig. 12.

6. – Conclusions

Results have been presented from the CDF and D0 experiments for the Higgs boson channels $H \to WW$, $WH \to WWW$ and $H \to \gamma\gamma$. Combined results from the first two channels (the Tevatron summer 2008 high-mass Higgs combination) have been presented which exclude SM Higgs boson production at $m_H = 170\,\text{GeV}$.

* * *

We thank the staffs at Fermilab and collaborating institutions, and acknowledge support from the DOE and NSF (USA); CEA and CNRS/IN2P3 (France); FASI, Rosatom and RFBR (Russia); CNPq, FAPERJ, FAPESP and FUNDUNESP (Brazil); DAE and DST (India); Colciencias (Colombia); CONACyT (Mexico); KRF and KOSEF (Korea); CONICET and UBACyT (Argentina); FOM (The Netherlands); STFC and the Royal Society (United Kingdom); MSMT and GACR (Czech Republic); CRC Program, CFI, NSERC and WestGrid Project (Canada); BMBF and DFG (Germany); SFI (Ireland); The Swedish Research Council (Sweden); CAS and CNSF (China); and the Alexander von Humboldt Foundation (Germany).

REFERENCES

[1] Barate R. *et al.*, *Phys. Lett. B*, **565** (2003) 61.
[2] LEP Electroweak Working Group, arXiv:0712.0929 [hep-ex] and `http://lepewwg.web.cern.ch/LEPEWWG/`.
[3] Tevatron New Phenomena & Higgs Working Group, arXiv:0808.0534v1 [hep-ex] and `http://tevnphwg.fnal.gov/`.
[4] CDF Collaboration, CDF Note 9764.
[5] D0 Collaboration, D0 Note 5757-CONF.
[6] CDF Collaboration, CDF Note 9764.
[7] D0 Collaboration, D0 Note 5485-CONF.
[8] D0 Collaboration, D0 Note 5858-CONF.

IL NUOVO CIMENTO Vol. 32 C, N. 5-6 Settembre-Dicembre 2009
DOI 10.1393/ncc/i2010-10540-2

Colloquia: LaThuile09

Discovery potential for the Standard Model Higgs at ATLAS

G. Cowan on behalf of the ATLAS Collaboration
Physics Department, Royal Holloway, University of London - Egham, Surrey TW20 0EX, UK

(ricevuto il 10 Novembre 2009; pubblicato online il 18 Gennaio 2010)

Summary. — The potential of the ATLAS experiment to discover or exclude the Standard Model Higgs boson is reviewed. Several important decay channels are considered, and more will be included in the future. The statistical treatment used here to combine the channels relies on a large sample approximation that is expected to be valid for an integrated luminosity of at least $2\,\mathrm{fb}^{-1}$. Results are presented for the expected statistical significance of discovery and expected exclusion limits.

PACS 14.80.Bn – Standard model Higgs bosons.

1. – Introduction

The search for the Higgs boson is one of the primary physics goals of the Large Hadron Collider. The LHC will provide colliding proton beams with a design centre-of-mass energy of 14 TeV and a luminosity of $10^{34}\,\mathrm{cm}^{-2}\,\mathrm{s}^{-1}$, after an initial phase at lower CM energy planned for 2009/10. Here we review the prospects for discovery or exclusion of the Standard Model Higgs boson by the ATLAS detector, considering the period of 14 TeV running with a data sample achievable within the first several years (up to $30\,\mathrm{fb}^{-1}$).

The ability to discover and study the Standard Model Higgs boson over a wide range of masses was an important design criterion of the ATLAS detector. This has led to a detector with excellent tracking and calorimetry as well as lepton identification over a wide angular range. Details on the ATLAS experiment can be found in ref. [1].

Standard Model Higgs boson production and decay are reviewed briefly in sect. **2**. The present study uses the decay modes $\mathrm{H} \to \mathrm{ZZ}^{(*)} \to 4l$ ($l = \mathrm{e}, \mu$), $\mathrm{H} \to \tau^+\tau^-$, $\mathrm{H} \to \gamma\gamma$ and $\mathrm{H} \to \mathrm{W}^+\mathrm{W}^- \to e\nu\mu\nu$. Including additional decay channels, *e.g.*, $\mathrm{H} \to \mathrm{W}^+\mathrm{W}^-$ with the W-bosons decaying to $e\nu e\nu$ or $\mu\nu\mu\nu$, will improve the sensitivity beyond what is reported here. The searches based on individual channels are described in sect. **3**.

Section **4** describes the statistical combination of the channels into a single statement of discovery significance or exclusion limits. The approach taken here uses the profile likelihood ratio, where effects of systematic uncertainties are incorporated by use of appropriate nuisance parameters. Results are shown in sect. **5**; more information can be found in ref. [2]. These studies represent updates of previous investigations reported in ref. [3].

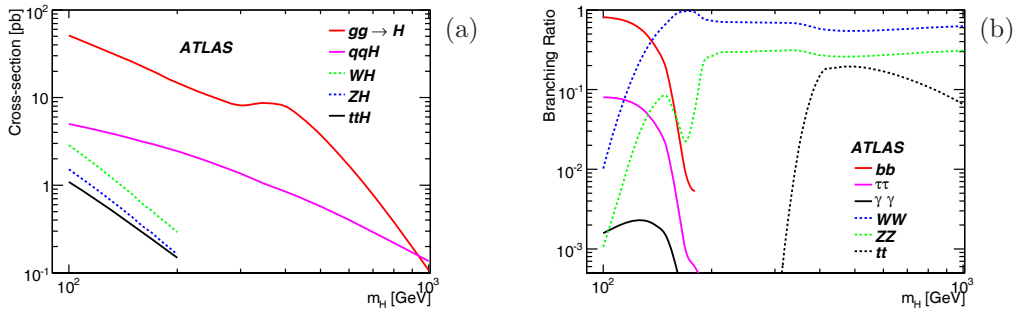

Fig. 1. – (a) The production cross-sections and (b) branching ratios for decays to several important final states for the Standard Model Higgs boson as a function of its mass (from ref. [2]).

2. – Properties of the Standard Model Higgs boson

The cross-section for production of a Standard Model Higgs in pp collisions is shown in fig. 1(a) as a function of the Higgs mass for several production modes. Gluon fusion has by far the largest cross-section for the relevant mass range. The Vector Boson Fusion (VBF, *i.e.* $qq \to qq\mathrm{H}$) cross-section is lower by an order of magnitude, but these events are characterized by two jets separated by a large-rapidity gap with no hadronic activity in the central region, and this helps distinguish them from background events. The cross-sections for a Higgs produced with a vector boson or heavy quark pair are much smaller and therefore in the present study we focus on gluon fusion and VBF production.

The branching ratios for different Higgs decay modes depend strongly on its mass m_{H}, as can be seen in fig. 1(b). The decay $\mathrm{H} \to b\bar{b}$ dominates at low mass, but the resulting b-jets are swamped by the QCD background. Although the branching ratio for $\mathrm{H} \to \gamma\gamma$ is only around 2×10^{-3} in the low-mass range, the signature of these events is distinctive and the mode is important for discovery. The rate for $\mathrm{H} \to \tau^+\tau^-$ lies between that of $\gamma\gamma$ and $b\bar{b}$ for low mass, and this mode is also important for low m_{H} despite the difficulties in reconstructing tau-leptons. At higher m_{H} the decay $\mathrm{H} \to \mathrm{W}^+\mathrm{W}^-$ grows in importance, dominating for m_{H} near $2M_{\mathrm{W}}$. Although the branching ratio for ZZ stays a factor of two below that of WW even above its kinematic threshold of $2M_{\mathrm{Z}}$, it quickly becomes the dominant channel in terms of discovery potential because of its clear signature when both Z-bosons decay to electron or muon pairs.

3. – Overview of Higgs channels studied

3·1. $\mathrm{H} \to \mathrm{ZZ}^{(*)} \to 4l$ ($l = \mathrm{e}, \mu$). – The decay channel $\mathrm{H} \to \mathrm{ZZ}^{(*)} \to 4l$, where here l indicates either an electron or muon, is effective in the Higgs search for masses in the range $130 < m_{\mathrm{H}} < 1000\,\mathrm{GeV}$, with the exception of the small gap around $m_{\mathrm{H}} \approx 2M_{\mathrm{W}}$ where the dominant decay $\mathrm{H} \to \mathrm{W}^+\mathrm{W}^-$ suppresses all other modes.

Successful reconstruction of a Higgs boson in this mode requires excellent lepton efficiency, since four of them must be found. At least one of the Z bosons is required to be on shell, which suppresses $t\bar{t}$ background. The remaining dominant background is from continuum $\mathrm{ZZ}^{(*)}$ production, the level of which is fitted from the sidebands of the four-lepton mass distribution. The expected shape of this distribution for $m_{\mathrm{H}} = 130\,\mathrm{GeV}$ is shown in fig. 2(a), which is normalized to an integrated luminosity of $30\,\mathrm{fb}^{-1}$.

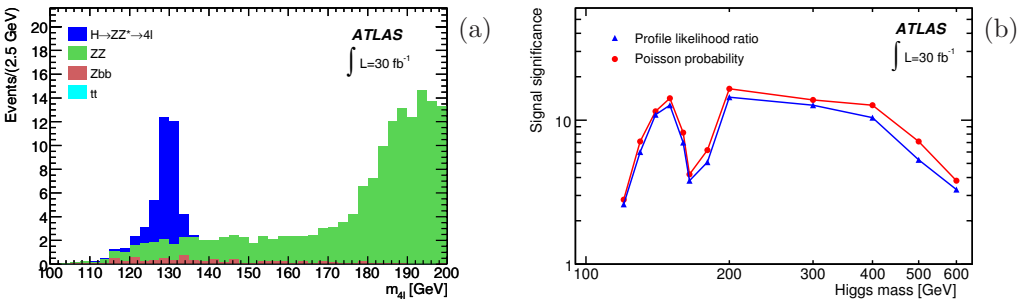

Fig. 2. – (a) The four-lepton invariant-mass distribution expected for an integrated luminosity of $30\,\mathrm{fb}^{-1}$. (b) The expected signal significance *versus* Higgs mass for the $\mathrm{H} \to \mathrm{ZZ}^{(*)} \to 4l$ channel based on $30\,\mathrm{fb}^{-1}$.

Figure 2(b) shows the expected discovery significance (number of standard deviations) based on this mode alone for an integrated luminosity of $30\,\mathrm{fb}^{-1}$, and it is well above the 5σ discovery threshold for a broad mass range. The upper points in the plot show the significance based on counting events in a mass window around the Higgs mass being tested, without consideration of the systematic uncertainty in the background shape of the four-lepton mass distribution. The lower points (triangles) includes this systematic uncertainty by modeling the shape with a sufficiently flexible parametric function that is fitted to the data.

3˙2. $\mathrm{H} \to \tau^+\tau^-$. – The decay $\mathrm{H} \to \tau^+\tau^-$ is investigated for the case where the Higgs is produced together with two forward jets (VBF production). Events are considered where either both taus decay to e or μ (the ll-channel) or where one decays to leptons and the other to hadrons (lh-channel). In both cases one has missing neutrinos, and thus the invariant mass of the visible decay products does not give the Higgs mass. However, as the tau-leptons typically have very high momenta compared to the tau mass, their decay products are highly boosted and almost collinear with the direction of the taus. Using this approximation and by measuring the missing transverse energy in the event, one can reconstruct the invariant mass of the $\tau^+\tau^-$ system.

The expected $\tau^+\tau^-$ mass distribution is shown in fig. 3(a), which is scaled to an integrated luminosity of $30\,\mathrm{fb}^{-1}$. The dominant background is from events with two jets plus a Z which decays to $\tau^+\tau^-$, resulting in the large peak at M_Z. This background is estimated by selecting events with two jets plus a Z decaying to either $\mu^+\mu^-$ or $\mathrm{e}^+\mathrm{e}^-$. The leptons are then replaced with simulated tau-decays. The uncertainty in the background related to the jet production is thus measured directly from data.

The expected significance (number of standard deviations) for $\mathrm{H} \to \tau^+\tau^-$ alone is shown in fig. 3(b) as a function of the Higgs mass for an integrated luminosity of $30\,\mathrm{fb}^{-1}$. Although the lh-channel gives the most sensitivity, the ll-channel also makes an important contribution and thus both are used in the combined search.

3˙3. $H \to \gamma\gamma$. – The decay $H \to \gamma\gamma$ is comparatively rare with a branching ratio around 2×10^{-3} for $110 < m_\mathrm{H} < 140\,\mathrm{GeV}$. Nevertheless, the events are sufficiently distinct from the background to make this channel important for the discovery of a Higgs boson in this mass range. Although backgrounds from direct photons as well as

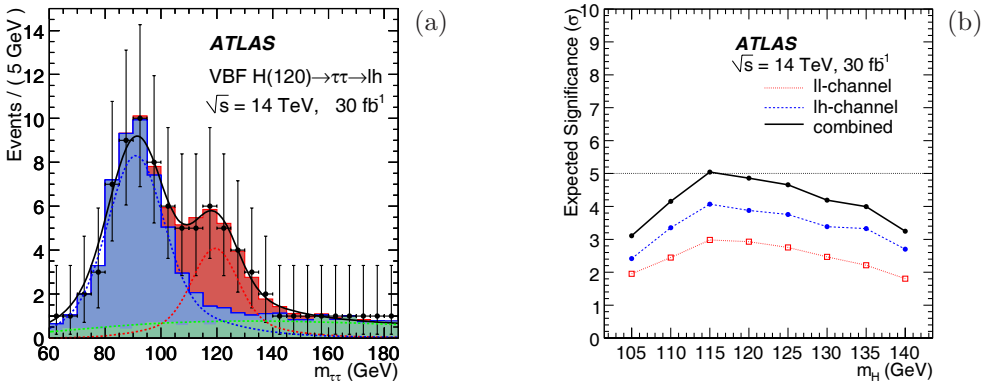

Fig. 3. – (a) The di-tau invariant-mass distribution expected for an integrated luminosity of $30\,\mathrm{fb}^{-1}$. The error bars shown are to indicate the level of statistical fluctuation one would expect in such a sample. (b) The expected signal significance *versus* Higgs mass for the $\mathrm{H} \to \tau^+\tau^-$ channel based on $30\,\mathrm{fb}^{-1}$.

neutral pions from hadronic jets are difficult to predict in absolute terms, they can be assumed to give a smooth diphoton mass distribution, and thus can be measured directly from the sidebands around the Higgs signal peak. An example is shown in fig. 4(a).

The expected signal significance from the $\gamma\gamma$ channel is shown as a function of m_{H} in fig. 4(b). This is shown for fixed m_{H} and also for the case where m_{H} is regarded as a free parameter, which accounts for the so-called "look-elsewhere effect" (see sect. **4**). For purposes of the combination done here, the fixed-mass result based on the inclusive analysis is used, which only uses the diphoton mass in a one-dimensional fit. Exclusive analyses where a photon pair is found with 0, 1, or 2 jets have also been carried out, and in this case, the diphoton mass and other kinematic variables are used in a multivariate analysis. The combination of exclusive analyses is found to have the highest sensitivity, and it is planned to use this instead of the inclusive analysis at a later stage.

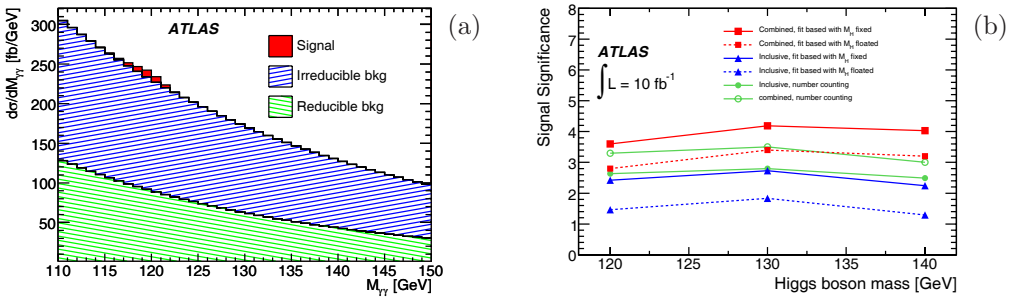

Fig. 4. – (a) The di-photon invariant-mass distribution $\mathrm{d}\sigma/\mathrm{d}M_{\gamma\gamma}$ in fb/GeV. The irreducible background refers to pairs of prompt photons; the reducible background is the case where one or both photons are faked by hadronic jets containing a high-energy π^0. (b) The expected signal significance *versus* Higgs mass for the $\mathrm{H} \to \gamma\gamma$ channel based on $10\,\mathrm{fb}^{-1}$.

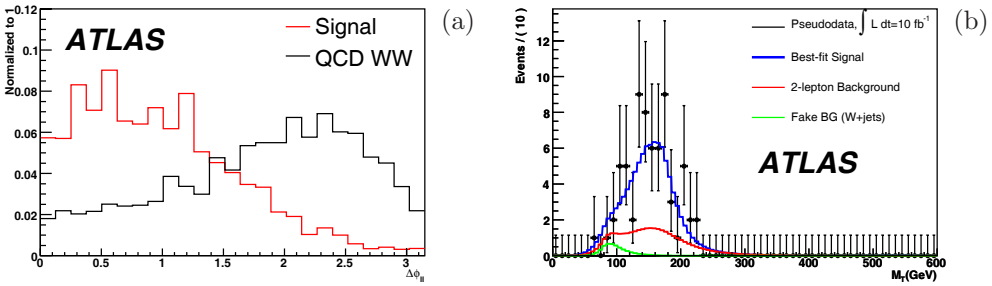

Fig. 5. – (a) The expected distributions of $\Delta\phi_{ll}$ for signal and background for the W^+W^- channel with no hard jets (normalized to unit area). (b) The transverse mass distribution expected for the W^+W^- channel with two hard jets for an integrated luminosity of $10\,\mathrm{fb}^{-1}$. Both plots assume a true Higgs mass of 170 GeV.

3˙4. $H \to W^+W^- \to e\nu\mu\nu$. – The decay channel $H \to W^+W^-$ is most important for the Higgs mass range from somewhat below $2M_W$, where its branching ratio becomes dominant, up to about $2M_Z$, above which the ZZ mode takes over as the most significant. The analysis of this mode includes two separate searches: one where a W^+W^- pair is found with no additional high-p_T hadron jets, where the Higgs signal would come primarily from gluon fusion, and the other where one finds two additional hard jets, which is sensitive to VBF production. In both cases, the W pairs are found using only the decay channel $e\nu\mu\nu$. Other possibilities, *e.g.*, $e\nu e\nu$, $\mu\nu\mu\nu$ and $l\nu qq$, are under study and will be included later.

Because of the missing neutrinos in the W decays, one is unable to reconstruct the Higgs candidate's mass. Instead, an effective variable for separating signal from background is the transverse mass, defined by

$$m_T = \sqrt{(E_{T,\mathrm{miss}} + E_{T,ll})^2 - (\vec{p}_{T,\mathrm{miss}} + \vec{p}_{T,ll})^2}, \tag{1}$$

where $E_{T,ll} = \sqrt{p^2_{T,ll} + m^2_{ll}}$ and $E_{T,\mathrm{miss}} = \sqrt{p^2_{T,\mathrm{miss}} + m^2_{ll}}$. Another important variable is $\Delta\phi_{ll}$, the opening angle between the two leptons in the transverse plane. The distribution of $\Delta\phi_{ll}$ is enhanced at low angles for Higgs events, which results from the spins of the two W bosons being antiparallel. The distributions of the transverse mass and $\Delta\phi_{ll}$ for signal and background are shown in fig. 5.

The main background for the W^+W^- channel with no hard jets is from continuum WW events. The Higgs search for this channel uses the transverse mass, the p_T of the WW system, and the angle $\Delta\phi_{ll}$. For the two-jet analysis the main background comes from $t\bar{t}$ events. Here events are selected in a range of the angular variables $\Delta\phi_{ll}$ and the rapidity $\Delta\eta_{ll}$, and then the distributions of the transverse mass and a neural network based on jet activity are used in a simultaneous fit. Further details on the sensitivity achievable with the WW channel alone can be found in ref. [2].

4. – Statistical combination of channels

To obtain the maximum discovery sensitivity for the Higgs boson one wishes to exploit all of information available from each channel. Here this is done using a statistical

formalism based on the *profile likelihood ratio*. Other approaches, for example, methods similar to those used at LEP [4] or Bayesian methods, are also being considered.

Here we report the discovery significance based on a search for a Higgs boson of a fixed mass m_{H}. If one tests a large range of mass values, however, then there is an increased probability that a fluctuation will lead to an apparent signal for some mass in the range considered (the so-called "look-elsewhere-effect"). This can be taken into account either by regarding m_{H} as a free parameter in the search or by adjusting the fixed-mass result with a correction factor derived from Monte Carlo. These corrections are not considered for the combined result here, although both the fixed and floating-mass approaches have been studied for several of the channels individually (see ref. [2]).

For the analysis of a given channel one measures for each event a set of kinematic variables such as the invariant mass of the Higgs candidate. Here we describe the procedure for a binned analysis, but the extension to the unbinned case is straightforward. The number of entries found in bin i of a kinematic variable is a number n_i assumed to follow a Poisson distribution with an expectation value $E[n_i] = \mu s_i + b_i$, where s_i is the expected number of signal events assuming a Standard Model Higgs and b_i is the expected number of background events, here taken to mean the prediction of the Standard Model without real Higgs production. The quantity μ is a global strength parameter common to all channels designed such that $\mu = 0$ is the background-only hypothesis and $\mu = 1$ corresponds to a Standard Model Higgs.

The expected number of signal and background events in a bin of a kinematic variable x can be written as

$$s_i = s_{\mathrm{tot}} \int_{\mathrm{bin}\, i} f_s(x; \vec{\theta}_s)\, \mathrm{d}x, \tag{2}$$

$$b_i = b_{\mathrm{tot}} \int_{\mathrm{bin}\, i} f_b(x; \vec{\theta}_b)\, \mathrm{d}x, \tag{3}$$

where b_{tot} is the total background and $\vec{\theta}_s$ and $\vec{\theta}_b$ represent shape parameters needed to describe the distributions of x for the signal and background, respectively. These quantities, collectively referred to as $\boldsymbol{\theta}$, are treated as nuisance parameters, and μ is thus the only parameter of interest.

The single-channel likelihood can be written as the product of Poisson terms for the number of entries in each bin. Some channels also use subsidiary measurements of distributions that provide information on the background rate and possibly also shape. The numbers of entries in the bins of these distribution are also included in the likelihood as independent Poisson variables. The i-th decay channel is thus described by a likelihood function $L_i(\mu; \vec{\theta}_i)$, and since the data samples for each channel are disjoint, the full likelihood can be written as a product over the channels: $L(\mu, \boldsymbol{\theta}) = \prod_i L_i(\mu; \vec{\theta}_i)$. Here the vector $\boldsymbol{\theta}$ represents all of the parameters of the problem except the single parameter of interest μ, which is assumed to be common to all channels.

To test a hypothesized value of the strength parameter μ one constructs the profile likelihood ratio

$$\lambda(\mu) = \frac{L(\mu, \hat{\hat{\boldsymbol{\theta}}})}{L(\hat{\mu}, \hat{\boldsymbol{\theta}})}\,. \tag{4}$$

Here $\hat{\mu}$ and $\hat{\boldsymbol{\theta}}$ in the denominator indicate the values of the parameters that maximize the likelihood, and $\hat{\hat{\boldsymbol{\theta}}}$ in the numerator maximizes the likelihood for the specified value

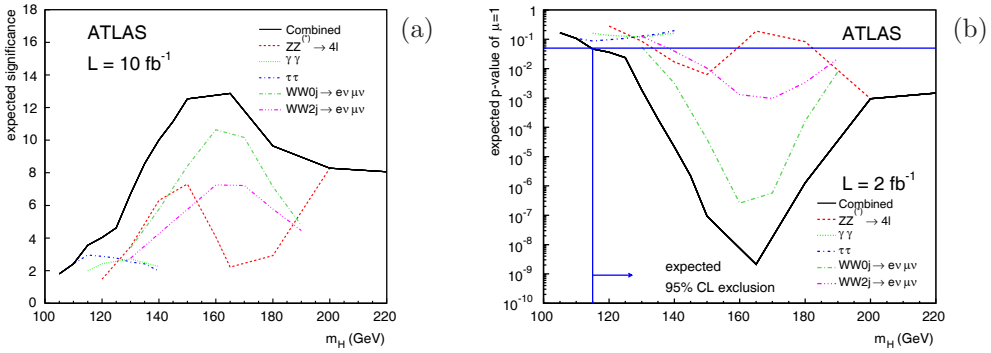

Fig. 6. – (a) The median discovery significance and (b) the median p-value of the Standard Model Higgs hypothesis *versus* the Higgs boson mass m_{H} based on the combination of all channels considered here for an integrated luminosity of $10\,\mathrm{fb}^{-1}$.

of μ. If the data are in good agreement with the hypothesized μ, then one will find $\hat{\mu}$ close to μ and $\lambda(\mu)$ close to one.

For purposes of establishing discovery, we define $q_\mu = -2\ln\lambda(\mu)$, and one is specifically interested in excluding the case $\mu = 0$. For setting upper limits on μ, it is more appropriate to define $q_\mu = -2\ln\lambda(\mu)$ for $\hat{\mu} < \mu$ and zero otherwise; further discussion can be found in ref. [2].

For both discovery and upper limits, larger values of q_μ indicate that the data are in increasing disagreement with the hypothesized μ. The level of disagreement is quantified by giving the p-value, which is the probability, assuming μ, to see data with equal or less compatibility with μ, *i.e.*, it is the integral of $f(q_\mu|\mu)$ from the observed value $q_{\mu,\mathrm{obs}}$ to infinity. This is usually converted to an equivalent significance, Z, defined as the number of standard deviations of a Gaussian variable giving an upper-tail area equal to p, *i.e.*, $Z = \Phi^{-1}(1-p)$ where Φ is the Standard Gaussian cumulative distribution.

Thus to find the p-value one requires the distribution, assuming data generated with a given value μ, of the statistic q_μ. For a sufficiently large data sample this can be related to a chi-square distribution for one degree of freedom. In this case the relation between the observed value of q_μ and the significance Z is simply $Z = \sqrt{q_\mu}$ (this holds for both discovery and upper limits). From Monte Carlo studies described in ref. [2] it was found that this approximation should be valid for an integrated luminosity of at least $2\,\mathrm{fb}^{-1}$.

5. – Results

By "discovery" of the Higgs boson here one means rejecting the $\mu = 0$ hypothesis using the statistic q_0 with a high significance, usually taken to mean $Z \geq 5$. Naturally one would still need to investigate further properties of the observed signal before one could establish whether it really is a Standard Model Higgs boson. To characterize the sensitivity of the experiment, we give the median discovery significance (Z value based on a test of $\mu = 0$) where the median corresponds to a Standard Model Higgs signal. This is shown in fig. 6(a) as a function of the hypothesized Higgs mass for an integrated luminosity of $10\,\mathrm{fb}^{-1}$.

To quantify the expected limits one expects to set if the Higgs signal is absent, we compute the p-value of the $\mu = 1$ hypothesis, where the median corresponds to data generated with no signal present. This is shown in fig. 6(b) for the individual channels and for the combination. Values of m_{H} for which the combined p-value is less than 0.05 are regarded as excluded at 95% CL. For $2\,\mathrm{fb}^{-1}$, one expects to exclude m_{H} down to 115 GeV, essentially closing the gap with the 114.4 GeV lower limit set by LEP [4].

6. – Conclusions

Several decay channels of the Standard Model Higgs boson have been studied and their combined sensitivity for discovery and limits has been investigated. Future inclusion of additional channels, such as the $\mu\nu\mu\nu$, $e\nu e\nu$ and $l\nu qq$ decays for the $\mathrm{H} \to \mathrm{W}^+\mathrm{W}^-$ mode, and use of combined exclusive channels for the $\mathrm{H} \to \gamma\gamma$ mode, will lead to greater sensitivity.

The statistical procedure for combination is based on the profile likelihood ratio, which accounts for systematic uncertainties by use of sufficiently flexible parametric models. Other statistical approaches, such as those used at LEP and Bayesian methods, are also under study.

The median discovery significance under assumption of a Standard Model Higgs signal and the median upper limits assuming data with no Higgs signal have been shown. These results use approximations expected to be valid for a data sample of at least $2\,\mathrm{fb}^{-1}$; below this the results are expected to be conservative. For an integrated luminosity of $2\,\mathrm{fb}^{-1}$, we expect discovery at 5σ or more for $143 < m_{\mathrm{H}} < 179\,\mathrm{GeV}$, and if the Higgs signal is absent, the expected upper limit on m_{H} at 95% CL is 115 GeV.

* * *

I would like thank the conference organisers for a very stimulating and enjoyable meeting. I am also indebted to numerous ATLAS colleagues for their kind help in preparing this contribution, especially E. Gross, A. Nisati, K. Assamagan, B. Quayle, Y. Fang and R. Gonçalo.

REFERENCES

[1] Aad G. *et al.* (The ATLAS Collaboration), *J. Instrum.*, **3** (2008) S08003.
[2] Aad G. *et al.* (The ATLAS Collaboration), *Expected Performance of the ATLAS Experiment: Detector, Trigger and Physics*, arXiv:0901.0512, CERN-OPEN-2008-20 (2008).
[3] The ATLAS Collaboration, *Detector and physics performance technical design report*, CERN/LHCC99-15 (1999).
[4] Abbiendi G. *et al.* (The ALEPH, DELPHI, OPAL and L3 Collaborations), *Phys. Lett. B*, **565** (2003) 61, arXiv:hep-ex/0306033.

IL NUOVO CIMENTO Vol. 32 C, N. 5-6 Settembre-Dicembre 2009
DOI 10.1393/ncc/i2010-10542-0

Colloquia: LaThuile09

Search for a light Higgs boson at BaBar

S. Banerjee on behalf of the BaBar Collaboration
University of Victoria - P.O. Box 3055, Victoria, BC, Canada V8W 3P6

(ricevuto il 10 Novembre 2009; pubblicato online il 20 Gennaio 2010)

Summary. — We search for evidence of a light Higgs boson (A^0) in the radiative decays of the narrow $\Upsilon(3S)$ resonance: $\Upsilon(3S) \to \gamma A^0$, where $A^0 \to$ invisible or $A^0 \to \mu^+\mu^-$. Such an object appears in extensions of the Standard Model, where a light *CP*-odd Higgs boson naturally couples strongly to *b*-quarks. We find no evidence for such processes in a sample of 122×10^6 $\Upsilon(3S)$ decays collected by the BaBar Collaboration at the PEP-II B-factory, and set 90% CL upper limits on the product of the branching fractions $\mathcal{B}(\Upsilon(3S) \to \gamma A^0) \times \mathcal{B}(A^0 \to \text{invisible})$ at $(0.7-31) \times 10^{-6}$ in the mass range $m_{A^0} \leq 7.8\,\text{GeV}$, and on the product $\mathcal{B}(\Upsilon(3S) \to \gamma A^0) \times \mathcal{B}(A^0 \to \mu^+\mu^-)$ at $(0.25\text{–}5.2) \times 10^{-6}$ in the mass range $0.212 \leq m_{A^0} \leq 9.3\,\text{GeV}$. We also set a limit on the dimuon branching fraction of the recently discovered η_b-meson $\mathcal{B}(\eta_b \to \mu^+\mu^-) < 0.8\%$ at 90% CL. The results are preliminary.

PACS 12.60.Fr – Extensions of electroweak Higgs sector.
PACS 14.80.Cp – Non-standard-model Higgs bosons.
PACS 13.66.Fg – Gauge and Higgs boson production in e^-e^+ interactions.

1. – Introduction

The concept of mass is one of the most intuitive ideas in physics since it is present in everyday human experience. Yet the fundamental nature of mass remains one of the greatest mysteries in physics. The Higgs mechanism is a theoretically appealing way to account for the different masses of elementary particles [1]. The Higgs mechanism implies the existence of at least one new particle called the Higgs boson, which is the only Standard Model (SM) [2] particle yet to be observed. If it is found, its discovery will have a profound effect on our fundamental understanding of matter. A single Standard Model Higgs boson is required to be heavy, with the mass constrained by direct searches to $m_H > 114.4\,\text{GeV}$ [3] and $m_H \neq 170\,\text{GeV}$ [4], and by precision electroweak measurements to $m_H = 129^{+74}_{-49}\,\text{GeV}$ [5].

The Standard Model and the simplest electroweak symmetry-breaking scenario suffer from quadratic divergences in the radiative corrections to the mass parameter of the Higgs potential. Several theories beyond the Standard Model that regulate these divergences have been proposed. Supersymmetry [6] is one such model; however, in its simplest

form (the Minimal Supersymmetric Standard Model, MSSM) questions of parameter fine-tuning and "naturalness" of the Higgs mass scale remain.

Theoretical efforts to solve unattractive features of MSSM often result in models that introduce additional Higgs fields, with one of them naturally light. For instance, the Next-to-Minimal Supersymmetric Standard Model (NMSSM) [7] introduces a singlet Higgs field. A linear combination of this singlet state with a member of the electroweak doublet produces a *CP*-odd Higgs state A^0 whose mass is not required to be large. Direct searches typically constrain m_{A^0} to be below $2m_b$ [8] making it accessible to decays of Υ-resonances. An ideal place to search for such *CP*-odd Higgs would be $\Upsilon \to \gamma A^0$, as originally proposed by Wilczek [9]. A study of the NMSSM parameter space [10] predicts the branching fraction to this final state to be as high as 10^{-4}.

Other new-physics models, motivated by astrophysical observations, predict similar light states. One recent example [11] proposes a light axion-like pseudoscalar boson a decaying predominantly to leptons and predicts the branching fraction $\mathcal{B}(\Upsilon \to \gamma\, a)$ to be between 10^{-6} and 10^{-5} [11]. Empirical motivation for a light Higgs search comes from the HyperCP experiment [12]. HyperCP observed three anomalous events in the $\Sigma \to p\mu^+\mu^-$ final state, that have been interpreted as a light scalar with mass of 214.3 MeV decaying into a pair of muons [13]. The large datasets available at *BABAR* allow us to place stringent constraints on such models.

If a light scalar A^0 exists, the pattern of its decays would depend on its mass. In dark-matter–inspired scenarios, $A^0 \to$ invisible decays could be dominant. For low masses $m_{A^0} < 2m_\tau$, relevant for the axion [11] and HyperCP [12] interpretations, the dominant decay mode should be $A^0 \to \mu^+\mu^-$. Significantly above the tau-pair threshold, $A^0 \to \tau^+\tau^-$ would dominate, and the hadronic decays may also be significant.

Preliminary results from search for invisible Higgs decays are described in ref. [14]. This analysis [15] searches for the radiative production of Higgs in $\Upsilon(3S)$ decays, which subsequently decays into muons:

$$\Upsilon(3S) \to \gamma A^0; \qquad A^0 \to \mu^+\mu^-.$$

The current best limit on the branching fraction $\mathcal{B}(\Upsilon \to \gamma A^0)$ with $A^0 \to \mu^+\mu^-$ comes from a measurement by the CLEO Collaboration on $\Upsilon(1S)$ [16]. The quoted limits on $\mathcal{B}(\Upsilon(1S) \to \gamma A^0) \times \mathcal{B}(A^0 \to \mu^+\mu^-)$ are in the range (1–20) $\times\, 10^{-6}$ for $m_{A^0} < 3.6\,\mathrm{GeV}$. There are currently no competitive measurements at the higher-mass Υ resonances or for the values of m_{A^0} above the $\tau\tau$ threshold.

In the following, we describe a search for a resonance in the dimuon invariant-mass distribution for fully reconstructed final state $\Upsilon(3S) \to \gamma(\mu^+\mu^-)$. We assume that the decay width of the resonance is negligibly small compared to experimental resolution, as expected [11, 17] for m_{A^0} sufficiently far from the mass of the η_b [18]. We also assume that the resonance is a scalar (or pseudo-scalar) particle; while significance of any peak does not depend on this assumption, the signal efficiency and, therefore, the extracted branching fractions are computed for a spin-0 particle. In addition, following the recent discovery of the η_b meson in $\Upsilon(3S)$ decays [18], we look for the leptonic decay of the η_b through the chain $\Upsilon(3S) \to \gamma\eta_b$, $\eta_b \to \mu^+\mu^-$. If the recently discovered state is the conventional quark-antiquark η_b-meson, its leptonic width is expected to be negligible. Thus, setting a limit on the dimuon branching fraction sheds some light on the nature of the recently discovered state. We assume $\Gamma(\eta_b) = 10\,\mathrm{MeV}$, which is expected in most theoretical models and is consistent with *BABAR* results [18].

2. – The *BABAR* detector and dataset

We search for two-body transitions $\Upsilon(3S) \to \gamma A^0$, followed by the decay $A^0 \to$ invisible [14] or $A^0 \to \mu^+\mu^-$ [15] in a sample of $(121.8 \pm 1.2) \times 10^6$ $\Upsilon(3S)$ decays collected with the *BABAR* detector at the PEP-II asymmetric-energy e^+e^- collider at the Stanford Linear Accelerator Center. The data were collected at the nominal center-of-mass (CM) energy $E_{\rm cm} = 10.355\,\text{GeV}$. The CM frame was boosted relative to the detector approximately along the detector's magnetic field axis by $\beta_z = 0.469$.

We use a sample of $78.5\,\text{fb}^{-1}$ accumulated on $\Upsilon(4S)$-resonance ($\Upsilon(4S)$ sample) for studies of the continuum backgrounds; since $\Upsilon(4S)$ is three orders of magnitude broader than $\Upsilon(3S)$, the branching fraction $\Upsilon(4S) \to \gamma A^0$ is expected to be negligible. For characterization of the background events and selection optimization we also use a sample of $2.4\,\text{fb}^{-1}$ collected 30 MeV below the $\Upsilon(3S)$ resonance.

The *BABAR* detector is described in detail elsewhere [19]. We use the `GEANT4` [20] software to simulate interactions of particles traversing the *BABAR* detector, taking into account the varying detector conditions and beam backgrounds.

3. – Event selection for $A^0 \to \mu^+\mu^-$ decays

We select events with exactly two oppositely charged tracks and a single energetic photon with a CM energy $E^*_\gamma \geq 0.5\,\text{GeV}$. We allow other photons to be present in the event as long as their CM energies are below 0.5 GeV. We assign a muon mass hypothesis to the two tracks (henceforth referred to as muon candidates), and require that they form a geometric vertex with the $\chi^2_{\rm vtx} < 20$ (for 1 degree of freedom), displaced transversely by at most 2 cm from the nominal location of the e^+e^- interaction region. We perform a kinematic fit to the $\Upsilon(3S)$ candidate formed from the two muon candidates and the energetic photon, constraining the CM energy of the $\Upsilon(3S)$ candidate, within the beam energy spread, to the total beam energy $\sqrt{s}$. We also assume that the $\Upsilon(3S)$ candidate originates from the interaction region. The kinematic fit improves the invariant mass resolution of the muon pair. We place a requirement on the kinematic fit $\chi^2_{\Upsilon(3S)} < 39$ (for 6 degrees of freedom), which corresponds to the probability to reject good kinematic fits of less than 10^{-6}. The kinematic fit χ^2, together with a requirement that the total mass of the $\Upsilon(3S)$ candidate is within 2 GeV of $\sqrt{s}$, suppresses background events with more than two muons and a photon in the final state, such as cascade decays $\Upsilon(3S) \to \gamma\chi_b(2P) \to \gamma\gamma\Upsilon(1S) \to \gamma\gamma\mu^+\mu^-$ etc. We further require that the momentum of the dimuon candidate A^0 and the photon direction are back-to-back in the CM frame to within 0.07 radians, and select events in which the cosine of the angle between the muon direction and A^0 direction in the center of mass of A^0 is less than 0.88. We reject events in which neither muon candidate is positively identified in the muon chamber.

The kinematic selection described above is highly efficient for signal events. After the selection, the backgrounds are dominated by two types of QED processes: "continuum" $e^+e^- \to \gamma\mu^+\mu^-$ events in which a photon is emitted in the initial or final state, and the initial-state radiation (ISR) production of the vector mesons J/ψ, $\psi(2S)$, and $\Upsilon(1S)$, which subsequently decay into muon pairs. In order to suppress contributions from ISR-produced $\rho^0 \to \pi^+\pi^-$ and $\phi \to K^+K^-$ final states in which a pion or a kaon is misidentified as a muon or decays (*e.g.*, through $K^+ \to \mu^+\nu_\mu$), we require that both muons are positively identified when we look for A^0 candidates in the range $m_{A^0} < 1.05\,\text{GeV}$. Finally, when selecting candidate events in the η_b mass region $m_{\mu\mu} \sim 9.39\,\text{GeV}$, we require that no secondary photon above a CM energy of $E^*_2 = 0.08\,\text{GeV}$ is present in

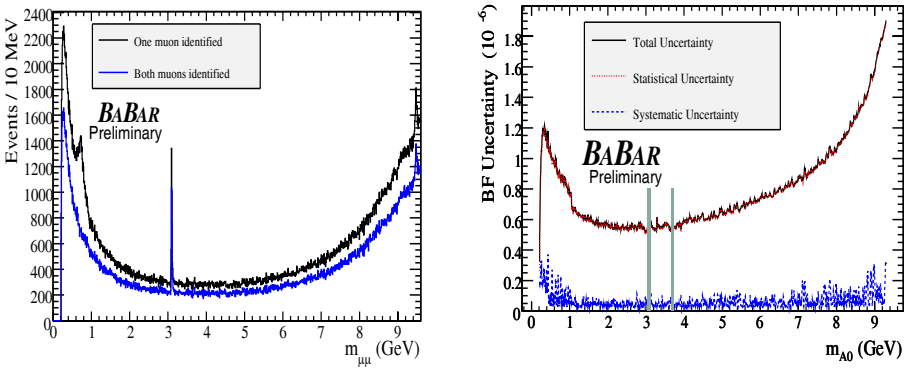

Fig. 1. – (Colour online) Distribution of the dimuon invariant mass $m_{\mu^+\mu^-}$ in the $\Upsilon(3S)$ data is shown on the left. Statistical and systematic uncertainty on the product of branching fractions $\mathcal{B}(\Upsilon(3S) \to \gamma A^0) \times \mathcal{B}(A^0 \to \mu^+\mu^-)$ are shown on the right as a function of m_{A^0}, extracted from the fits to the $\Upsilon(3S)$ data. Statistical errors are shown as red dot-dashed line, systematic uncertainties are shown as blue dotted line, and the total uncertainty, computed as a quadrature sum of statistical and systematic errors, is the solid black line. The shaded areas show the regions around the J/ψ and $\psi(2S)$ resonances excluded from the search.

the event; this requirement suppresses decay chains $\Upsilon(3S) \to \gamma_2\chi_b(2S) \to \gamma_1\gamma_2\Upsilon(1S)$, in which the photon γ_2 has a typical CM energy of 100 MeV.

We use Monte Carlo samples generated at 20 values of m_{A^0} over a broad range $0.212 < m_{A^0} \leq 9.5\,\text{GeV}$ of possible A^0 masses to measure selection efficiency for the signal events. The efficiency varies between 24 and 44%, depending on the dimuon invariant mass.

4. – Extraction of signal yields for $A^0 \to \mu^+\mu^-$ decays

The invariant-mass spectrum for the selected candidates in the $\Upsilon(3S)$ dataset is shown in fig. 1 (left). We extract the yield of signal events as a function of the assumed mass m_{A^0} in the interval $0.212 \leq m_{A^0} \leq 9.3\,\text{GeV}$ by performing a series of unbinned extended maximum-likelihood fits to the distribution of the "reduced mass"

$$m_R = \sqrt{m^2_{\mu\mu} - 4m^2_\mu}. \tag{1}$$

The choice of this variable is motivated by the distribution of the *continuum background* from $e^+e^- \to \gamma\mu^+\mu^-$, which is a smooth function of m_R across the entire range of interest, in particular, the region near the kinematic threshold $m_{\mu\mu} \approx 2m_\mu$ ($m_R \approx 0$). Each fit is performed over a small range of m_R around the value expected for a particular m_{A^0}. We use the $\Upsilon(4S)$ sample to determine the probability density functions (PDFs) for the continuum background in each fit window, which agree within statistical uncertainties with Monte Carlo simulations. We use a threshold (hyperbolic) function to describe the background below $m_R < 0.23\,\text{GeV}$; its parameters are fixed to the values determined from the fits to the $\Upsilon(4S)$ dataset. Elsewhere the background is well described in each limited m_R range by a first-order ($m_R < 9.3\,\text{GeV}$) or second-order ($m_R > 9.3\,\text{GeV}$) polynomial.

The signal PDF is described by a sum of two Crystal Ball functions [21] with tail parameters on either side of the maximum. The signal PDFs are centered around the expected values of $m_R = \sqrt{m_{A^0}^2 - 4m_\mu^2}$ and have the typical resolution of 2–10 MeV, which increases monotonically with m_{A^0}. We determine the PDF as a function of m_{A^0} using a set of high-statistics simulated samples of signal events, and we interpolate PDF parameters and signal efficiency values linearly between simulated points. We determine the uncertainty in the PDF parameters by comparing the distributions of the simulated and reconstructed $e^+e^- \to \gamma_{\rm ISR} J/\psi$, $J/\psi \to \mu^+\mu^-$ events.

Known resonances, such as J/ψ, $\psi(2S)$, and $\Upsilon(1S)$, are present in our sample in specific intervals of m_R, and constitute *peaking background*. We include these contributions in the fit where appropriate, and describe the shape of the resonances using the same functional form as for the signal, a sum of two Crystal Ball functions, with parameters determined from the dedicated MC samples. We do not search for A^0 signal in the immediate vicinity of J/ψ and $\psi(2S)$, ignoring the region of $\approx \pm 40$ MeV around J/ψ (approximately $\pm 5\sigma$) and $\approx \pm 25$ MeV ($\approx \pm 3\sigma$) around $\psi(2S)$.

For each assumed value of m_{A^0}, we perform a likelihood fit to the m_R distribution under the following conditions:

- $0.212 \le m_{A^0} < 0.5$ GeV: we use a fixed interval $0.01 < m_R < 0.55$ GeV. The fits are done in 2 MeV steps in m_{A^0}. We use a threshold function to describe the combinatorial background PDF below $m_R < 0.23$ GeV, and constrain it to the shape determined from the large $\Upsilon(4S)$ dataset. For $m_R > 0.23$ GeV, we describe the background by a first-order Chebyshev polynomial and float its shape, while requiring continuity at $m_R = 0.23$ GeV. Signal and background yields are free parameters in the fit.
- $0.5 \le m_{A^0} < 1.05$ GeV: we use sliding intervals $\mu - 0.2 < m_R < \mu + 0.1$ GeV (where μ is the mean of the signal distribution of m_R). We perform fits in 3 MeV steps in m_{A^0}. First-order polynomial coefficient of the background PDF, signal and background yields are free parameters in the fit.
- $1.05 \le m_{A^0} < 2.9$ GeV: we use sliding intervals $\mu - 0.2 < m_R < \mu + 0.1$ GeV and perform fits in 5 MeV steps in m_{A^0}. First-order polynomial coefficient of the background PDF, signal and background yields are free parameters in the fit.
- $2.9 \le m_{A^0} \le 3.055$ GeV and $3.135 \le m_{A^0} \le 3.395$ GeV: we use a fixed interval $2.7 < m_R < 3.5$ GeV; 5 MeV steps in m_{A^0}. First-order polynomial coefficient of the background PDF, signal, J/ψ, and background yields are free parameters in the fit.
- $3.4 \le m_{A^0} < 3.55$ GeV: we use sliding intervals $\mu - 0.2 < m_R < \mu + 0.1$ GeV and perform fits in 5 MeV steps in m_{A^0}. First-order polynomial coefficient of the background PDF, signal and background yields are free parameters in the fit.
- $3.55 \le m_{A^0} \le 3.66$ GeV and $3.71 \le m_{A^0} < 4.0$ GeV: we use fixed interval $3.35 < m_R < 4.1$ GeV; 5 MeV steps in m_{A^0}. First-order polynomial coefficient of the background PDF, signal, $\psi(2S)$, and background yields are free parameters in the fit.
- $4.0 \le m_{A^0} < 9.3$ GeV: we use sliding intervals $\mu - 0.2 < m_R < \mu + 0.1$ GeV; 5 MeV steps in m_{A^0}. First-order polynomial coefficient of the background PDF, signal and background yields are free parameters in the fit.

– η_b region ($m_{\eta_b} = 9.390\,\text{GeV}$): we use a fixed interval $9.2 < m_R < 9.6\,\text{GeV}$. We constrain the contribution from $e^+e^- \to \gamma_{\text{ISR}}\Upsilon(1S)$ to the expectation from the $\Upsilon(4S)$ dataset (436 ± 50 events). Background PDF shape (second-order Chebyshev polynomial), yields of $\Upsilon(3S) \to \gamma\chi_b(2P) \to \gamma\gamma\Upsilon(1S)$, signal $\Upsilon(3S) \to \gamma\eta_b$ events, and background yields are free parameters in the fit.

The step sizes in each interval correspond approximately to the resolution in m_{A^0}.

5. – Systematic uncertainties for $A^0 \to \mu^+\mu^-$

The largest systematic uncertainty in $\mathcal{B}(\Upsilon(3S) \to \gamma A^0)$ comes from the measurement of the selection efficiency. We compare the overall selection efficiency between the data and the Monte Carlo simulation by measuring the absolute cross-section $\mathrm{d}\sigma/\mathrm{d}m_R$ for the radiative QED process $e^+e^- \to \gamma\mu^+\mu^-$ over the broad kinematic range $0 < m_R \leq 9.6\,\text{GeV}$, using a sample of $2.4\,\text{fb}^{-1}$ collected 30 GeV below the $\Upsilon(3S)$. We use the ratio of measured to expected cross-sections to correct the signal selection efficiency as a function of m_{A^0}. This correction reaches up to 20% at low values of m_{A^0}. We use half of the applied correction, or its statistical uncertainty of 2%, whichever is larger, as the systematic uncertainty on the signal efficiency. This uncertainty accounts for effects of selection efficiency, reconstruction efficiency (for both charged tracks and the photon), trigger efficiency, and the uncertainty in estimating the integrated luminosity. We find the largest difference between the data and Monte Carlo simulation in modeling of muon identification efficiency.

We determine the uncertainty in the signal and peaking background PDFs by comparing the data and simulated distributions of $e^+e^- \to \gamma_{\text{ISR}}J/\psi$ events. We correct for the observed 24% difference (5.3 MeV in the simulations *versus* 6.6 MeV in the data) in the width of the m_R distribution for these events, and use half of the correction to estimate the systematic uncertainty on the signal yield. This is the dominant systematic uncertainty on the signal yield for $m_{A^0} > 0.4\,\text{GeV}$. Likewise, we find that changes in the tail parameters of the Crystal Ball PDF describing the J/ψ peak lead to variations in event yield of less than 1%. We use this estimate as a systematic error in the signal yield due to uncertainty in tail parameters.

We find excellent agreement in the shape of the continuum background distributions for $m_R < 0.23\,\text{GeV}$ between $\Upsilon(3S)$ and $\Upsilon(4S)$ data. We determine the PDF in the fits to $\Upsilon(4S)$ data, and propagate their uncertainties to the $\Upsilon(3S)$ data, where these contributions do not exceed $\sigma(\mathcal{B}) = 0.3 \times 10^{-6}$. For the higher masses $m_R > 0.23\,\text{GeV}$, the background PDF parameters are floated in the likelihood fit.

We test for possible bias in the fitted value of the signal yield with a large ensemble of pseudo-experiments. For each experiment, we generate a sample of background events according to the number and the PDF observed in the data, and add a pre-determined number of signal events from fully reconstructed signal Monte Carlo samples. The bias is consistent with zero for all values of m_{A^0}, and we assign a branching fraction uncertainty of $\sigma(\mathcal{B}) = 0.02 \times 10^{-6}$ at all values of m_{A^0} to cover the statistical variations in the results of the test.

The uncertainties in PDF parameters of both signal and background and the bias uncertainty affect the signal yield (and therefore significance of any peak); signal efficiency uncertainty does not. The effect of the systematic uncertainties on the signal yield is generally small. The statistical and systematic uncertainties on the branching fraction $\mathcal{B}(\Upsilon(3S) \to \gamma A^0)$ as a function of m_{A^0} are shown in fig. 1 (right).

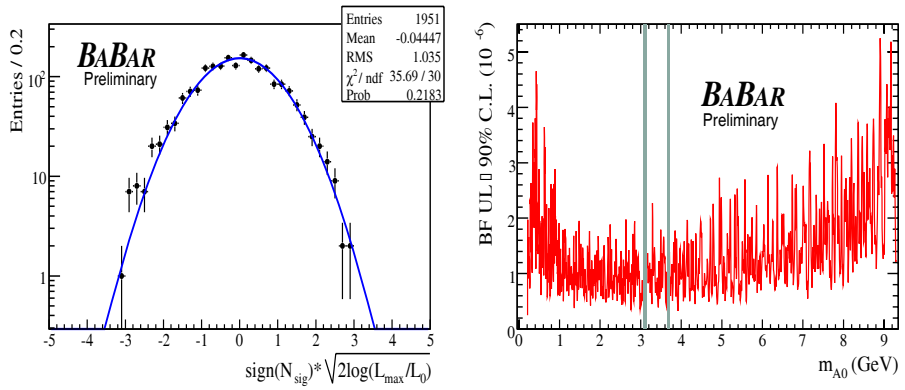

Fig. 2. – (Colour online) Distribution of the likelihood ratio variable $\mathcal{S}$ with additive systematic uncertainties included for the fits to the $\Upsilon(3S)$ dataset, overlayed with a blue curve showing the Gaussian fit with fixed $\mu = 0$ and $\sigma = 1$, is shown on the left. Upper limits on the product of branching fractions $\mathcal{B}(\Upsilon(3S) \to \gamma A^0) \times \mathcal{B}(A^0 \to \mu^+\mu^-)$ as a function of m_{A^0} from the fits to $\Upsilon(3S)$ data are shown on the right. The shaded areas show the regions around the J/ψ and $\psi(2S)$ resonances excluded from the search.

6. – Results for $A^0 \to \mu^+\mu^-$

For a small number of fits in the scan over the $\Upsilon(3S)$ dataset, we observe local likelihood ratio values $\mathcal{S}$ of about 3σ. The most significant peak is at $m_{A^0} = 4.940 \pm 0.003\,\text{GeV}$ (likelihood ratio value $\mathcal{S} = 3.0$, including systematics; $\mathcal{B} = (1.9 \pm 0.7 \pm 0.1) \times 10^{-6}$). The second most-significant peak is at $m_{A^0} = 0.426 \pm 0.001\,\text{GeV}$ (likelihood ratio value $\mathcal{S} = 2.9$, including systematics; $\mathcal{B} = (3.1 \pm 1.1 \pm 0.3) \times 10^{-6}$). The peak at $m_{A^0} = 4.940\,\text{GeV}$ is theoretically disfavored (since it is significantly above the τ threshold), while the peak at $m_{A^0} = 0.426\,\text{GeV}$ is in the range predicted by the axion model [11]. However, since our scans have $\mathcal{O}(2000)$ m_{A^0} points, we should expect several statistical fluctuations at the level of $\mathcal{S} \approx 3$, even for a null signal hypothesis. At least 80% of our pseudo-experiments contain a fluctuation with $\mathcal{S} = 3\sigma$ or more. Taking this into account, we conclude that neither of the above-mentioned peaks are significant.

Since we do not observe a significant excess of events above the background in the range $0.212 < m_{A^0} \leq 9.3\,\text{GeV}$, we set upper limits on the branching fraction $\mathcal{B}(\Upsilon(3S) \to \gamma A^0) \times \mathcal{B}(A^0 \to \mu^+\mu^-)$. We add statistical and systematic uncertainties (which include the additive errors on the signal yield and multiplicative uncertainties on the signal efficiency and the number of recorded $\Upsilon(3S)$ decays) in quadrature. The 90% CL Bayesian upper limits, computed with a uniform prior and assuming a Gaussian likelihood function, are shown in fig. 2 (right), as a function of mass m_{A^0}. The limits fluctuate depending on the central value of the signal yield returned by a particular fit, and range from 0.25×10^{-6} to 5.2×10^{-6}.

We do not observe any significant signal at the HyperCP mass, $m_{A^0} = 0.214\,\text{GeV}$. We find $\mathcal{B}(\Upsilon(3S) \to \gamma A^0(214)) = (0.12^{+0.43}_{-0.41} \pm 0.17) \times 10^{-6}$, and set an upper limit $\mathcal{B}(\Upsilon(3S) \to \gamma A^0(214)) < 0.8 \times 10^{-6}$ at 90% CL.

From a fit to the η_b region, we find $\mathcal{B}(\Upsilon(3S) \to \gamma\eta_b) \times \mathcal{B}(\eta_b \to \mu^+\mu^-) = (0.2 \pm 3.0 \pm 0.9) \times 10^{-6}$, consistent with zero. Taking into account the *BABAR* measurement

of $\mathcal{B}(\Upsilon(3S) \to \gamma\eta_b) = (4.8 \pm 0.5 \pm 1.2) \times 10^{-4}$, we can derive $\mathcal{B}(\eta_b \to \mu^+\mu^-) = (0.0 \pm 0.6 \pm 0.2)\%$, or an upper limit $\mathcal{B}(\eta_b \to \mu^+\mu^-) < 0.8\%$ at 90% CL. This is consistent with expectations from the quark model. All results above are preliminary.

The limits we set [15] are more stringent than those recently reported by the CLEO Collaboration [16]. Our limits rule out much of the parameter space allowed by the light Higgs [10] and axion [11] models.

7. – Conclusions

We find no evidence for light Higgs boson in a sample of 122×10^6 $\Upsilon(3S)$ decays collected by the *BABAR* Collaboration at the PEP-II B-factory, and set 90% CL upper limits on the product of the branching fractions $\mathcal{B}(\Upsilon(3S) \to \gamma A^0) \times \mathcal{B}(A^0 \to \text{invisible})$ at $(0.7 - 31) \times 10^{-6}$ in the mass range $m_{A^0} \leq 7.8\,\text{GeV}$ [14] and on the product $\mathcal{B}(\Upsilon(3S) \to \gamma A^0) \times \mathcal{B}(A^0 \to \mu^+\mu^-)$ at $(0.25 - 5.2) \times 10^{-6}$ in the mass range $0.212 \leq m_{A^0} \leq 9.3\,\text{GeV}$ [15]. We also set a limit on the dimuon branching fraction of the recently discovered η_b meson $\mathcal{B}(\eta_b \to \mu^+\mu^-) < 0.8\%$ at 90% CL [15]. The results are preliminary.

REFERENCES

[1] Higgs P. W., *Phys. Rev. Lett.*, **13** (1964) 508.
[2] Weinberg S., *Phys. Rev. Lett.*, **19** (1967) 1264; Salam A., *Elementary Particle Theory*, edited by Svartholm N. (Almquist and Wiksells, Stockholm) 1969, p. 367; Glashow S. L., Iliopoulos J. and Maiani L., *Phys. Rev. D*, **2** (1970) 1285.
[3] LEP Working Group for Higgs boson searches, Barate R. *et al.*, *Phys. Lett. B*, **565** (2003) 61.
[4] Herndon M., rapporteur talk at ICHEP '08, arXiv:0810.3705 [hep-ex] (2008).
[5] LEP-SLC Electroweak Working Group, *Phys. Rep.*, **427** (2006) 257.
[6] Wess J. and Zumino B., *Nucl. Phys. B*, **70** (1974) 39.
[7] Dermisek R. and Gunion J. F., *Phys. Rev. Lett.*, **95** (2005) 041801.
[8] Dermisek R. and Gunion J. F., *Phys. Rev. D*, **73** (2006) 111701.
[9] Wilczek F., *Phys. Rev. Lett.*, **39** (1977) 1304.
[10] Dermisek R., Gunion J. F. and McElrath B., *Phys. Rev. D*, **76** (2007) 051105.
[11] Nomura Y. and Thaler J., preprint arXiv:0810.5397 [hep-ph] (2008).
[12] Park H. *et al.* (HyperCP Collaboration), *Phys. Rev. Lett.*, **94** (2005) 021801.
[13] He X. G., Tandean J. and Valencia G., *Phys. Rev. Lett.*, **98** (2007) 081802.
[14] Aubert B. *et al.* (*BABAR* Collaboration), arXiv:0808.0017 [hep-ex].
[15] Aubert B. *et al.* (*BABAR* Collaboration), arXiv:0902.2176 [hep-ex].
[16] Love W. *et al.* (CLEO Collaboration), *Phys. Rev. Lett.*, **101** (2008) 151802.
[17] Fullana E. and Sanchis-Lozano M. A., *Phys. Lett. B*, **653** (2007) 67.
[18] Aubert B. *et al.* (*BABAR* Collaboration), *Phys. Rev. Lett.*, **101** (2008) 071801.
[19] Aubert B. *et al.* (*BABAR* Collaboration), *Nucl. Instrum. Methods Phys. Res. A*, **479** (2002) 1.
[20] Agostinelli S. *et al.* (GEANT4 Collaboration), *Nucl. Instrum. Methods Phys. Res. A*, **506** (2003) 250.
[21] Oreglia M. J., Ph.D Thesis, report SLAC-236 (1980), Appendix D; Gaiser J. E., Ph.D Thesis, report SLAC-255 (1982), Appendix F; Skwarnicki T., Ph.D Thesis, report DESY F31-86-02(1986), Appendix E.

IL NUOVO CIMENTO Vol. 32 C, N. 5-6 Settembre-Dicembre 2009
DOI 10.1393/ncc/i2010-10533-1

Colloquia: LaThuile09

$H \to b\bar{b}$ in VBF at the LHC with an extra central photon(*)

F. Piccinini
INFN, Sezione di Pavia - v. A. Bassi 6, I-27100 Pavia, Italy

(ricevuto il 10 Novembre 2009; pubblicato online il 18 Gennaio 2010)

Summary. — The LHC potential for a measurement of the Higgs boson coupling to the b-quark in the standard model is not well established yet. We show that requiring a large-transverse-momentum photon in the light Higgs boson production via vector-boson fusion (with subsequent $H \to b\bar{b}$ decay) could provide a further handle on the $Hb\bar{b}$ coupling determination, and on the measurement of the HWW coupling as well.

PACS 12.15.-y – Electroweak interactions.
PACS 12.15.Ji – Applications of electroweak models to specific processes.

1. – Introduction

Once the Higgs boson is discovered at the LHC, it will be crucial to test its properties, and check how well they fit in the standard model (SM) framework. Higgs boson couplings to vector bosons, heavy quarks and heavy leptons can in principle be measured by combining informations on different production and decay channels [1].

A measurement of the Higgs boson coupling to b quarks seems presently quite challenging. On the one hand, the SM Higgs production channel $b\bar{b} \to H$ is overwhelmed by the main production process $gg \to H$ at the LHC [2]. On the other hand, processes involving the $Hb\bar{b}$ coupling via the Higgs decay $H \to b\bar{b}$ (for $m_H \lesssim 140\,\text{GeV}$) seem at the moment hard to manage, due to the large b (and, more generally, jet) background expected from pure QCD processes. The $H \to b\bar{b}$ decay in the Higgs production via vector-boson fusion (VBF) has been studied in [3]. It gives rise to four-jet final states, out of which two jets should be b-tagged. Although the VBF final states have quite distinctive kinematical features (*i.e.*, two forward jets with a typical transverse momentum of order M_W plus a resonant b-jet pair produced centrally), different sources of QCD backgrounds and hadronic effects presently make the relevance of this channel for a $Hb\bar{b}$ coupling determination difficult to assess. For instance, triggering on $b\bar{b}jj$ final states must confront

(*) Based on work done in collaboration with Emidio Gabrielli, Fabio Maltoni, Barbara Mele, Mauro Moretti and Roberto Pittau.

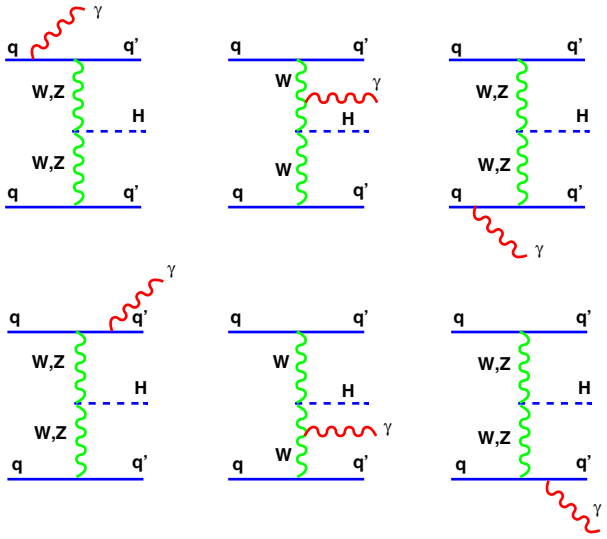

Fig. 1. – Tree-level t-channel Feynman diagrams for H production via $pp \to H\,\gamma\,jj$.

with the corresponding large QCD four-jet trigger rate. The $Ht\bar{t}$ associated production, where the Higgs boson is radiated by a top-quark pair, with subsequent $H \to b\bar{b}$ decay, could also provide a $Hb\bar{b}$ coupling measurement. Nevertheless, the recent inclusion of more reliable QCD background estimate and detector simulation in the corresponding signal analysis [4] have lowered the expectations on the potential of this channel.

Here we report on a further process that could help in determining the $Hb\bar{b}$ coupling, that was recently studied in [5] (where more details can be found). We consider the Higgs boson production in VBF in association with a large-transverse-momentum photon (*i.e.*, $p_{\mathrm{T}} \gtrsim 20\,\mathrm{GeV}$) emitted centrally (*i.e.*, with pseudorapidity $|\eta_\gamma| < 2.5$)

$$pp \to H\,\gamma\,jj + X \to b\bar{b}\,\gamma\,jj + X, \tag{1}$$

where H decays to $b\bar{b}$, and, at the parton level, the final QCD partons are identified with the corresponding jets j. Disregarding the resonant contribution to the process coming from the $WH\gamma$, $ZH\gamma$ production, the dominant Feynman diagrams are the ones involving VBF (as shown in fig. 1, where the Higgs decay to $b\bar{b}$ is not shown). Final states $b\bar{b}\,\gamma\,jj$ arising from photon radiation off one of the two b-quarks arising from the Higgs boson decay (via $pp \to H(\to b\bar{b}\,\gamma)\,jj$) fall outside the experimental $m_{b\bar{b}}$ resolution window around the m_H, due to the requirement of a large-p_{T} photon.

2. – Benefits from the central photon

Adding a central photon to the $pp \to H(\to b\bar{b})\;jj$ final state, despite a further e.m. fine-structure constant α that depletes production rates, gives a number of benefits [5]:

– first of all, the presence of an additional high-p_{T} photon can improve the triggering efficiencies for multi-jet final states, such as those needed to select $pp \to H(\to b\bar{b})\;jj$ events;

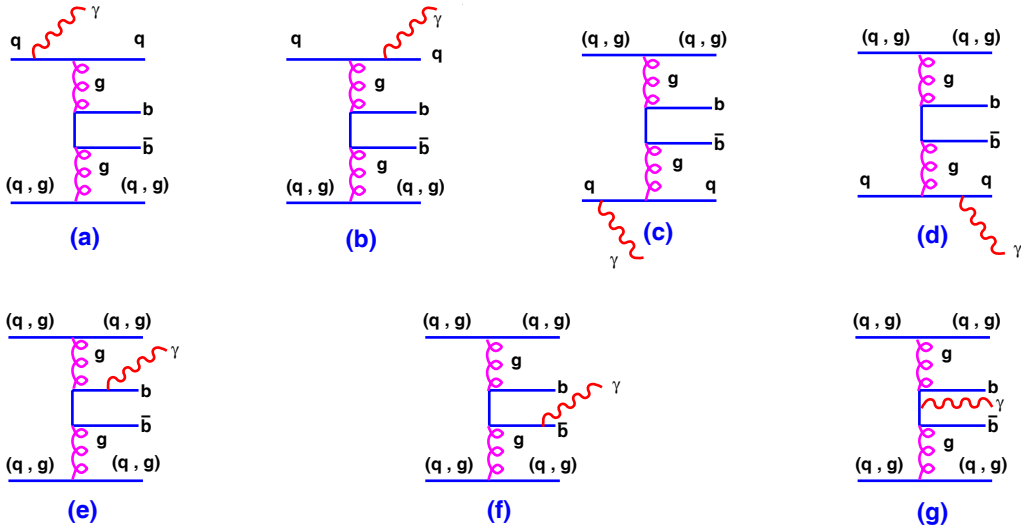

Fig. 2. – Representative classes of Feynman diagrams contributing, at parton level, to the background process $pp \to b\bar{b}\,\gamma\,jj$. Here q and g stand for a light quark (u, d, s) and gluons, respectively.

– there is a large gluonic component entering the partonic processes giving rise to the QCD backgrounds to the $b\bar{b}\,\gamma\,jj$ final state, as shown in fig. 2; as a consequence, the QCD backgrounds are in general much less *active* in radiating a large-p_{T} photon with respect to the VBF signal;

– further dynamical *coherence* effects dramatically suppress the radiation of a photon in the irreducible QCD background to $b\bar{b}\,\gamma\,jj$, when the photon is central (*i.e.* emitted outside the typical radiation cone around the initial/final quark legs, for quarks scattered in the t-channel);

– a similar *coherence* effect depletes the HZZ amplitudes (involving neutral currents) with the respect to the HWW ones (involving charged currents) in fig. 1, increasing the relative sensitivity to the HWW coupling in the radiative channel; then, a measurement of the $b\bar{b}\,\gamma\,jj$ rate could lead to a combined determination of the Higgs boson couplings to b quarks and W vector bosons, with less contamination from the HZZ coupling uncertainties;

– the requirement of a central photon strongly reduces the background arising from alternative Higgs boson production processes, such as the one coming from the virtual gluon fusion $g^*g^* \to H$ diagrams, with a photon radiated off any external quark leg.

In the following, we will elaborate on a few of the previous items.

3. – Production rates: signal *versus* background

In table I, the cross-sections for the signal and irreducible background for the process in eq. (1) are shown for three values of the Higgs boson mass, as independently obtained by the Monte Carlo event generators ALPGEN [6], and MadEvent [7], with the choice of

TABLE I. – *Cross-sections for the signal and the irreducible background for the optimized event selection, as defined in eq.* (2)*. The signal and irreducible background production rates for the plain VBF process are also shown, with the same event selection.*

m_H	120 GeV	130 GeV	140 GeV
$\sigma[H(\to b\bar{b})\gamma jj]$	3.6 fb	2.9 fb	2.0 fb
$\sigma[b\bar{b}\gamma jj]$	33 fb	38 fb	40 fb
$\sigma[H(\to b\bar{b})jj]$	320 fb	255 fb	168 fb
$\sigma[b\bar{b}jj]$	103 pb	102 pb	98 pb

parameters described in [5]. The following event selection, that optimizes the significance $S/\sqrt{B}$, has been applied:

$$
\begin{array}{lll}
p_{\mathrm{T}}^{j1,b1} \geq 60\,\mathrm{GeV}, & p_{\mathrm{T}}^{j2,b2} \geq 30\,\mathrm{GeV}, & p_{\mathrm{T}}^{\gamma} \geq 20\,\mathrm{GeV}, \\
\Delta R_{ik} \geq 0.7, & |\eta_\gamma| \leq 2.5, & |\eta_b| \leq 2.5, \\
|\eta_j| \leq 5, & m_{jj} > 800\,\mathrm{GeV}, & m_H(1-10\%) \leq m_{b\bar{b}} \leq m_H(1+10\%), \\
|\Delta\eta_{jj}| > 4, & m_{\gamma H} \geq 160\,\mathrm{GeV}, & \Delta R_{\gamma b/\gamma j} \geq 1.2,
\end{array}
\tag{2}
$$

where ik is any pair of partons in the final state, and $\Delta R_{ik} = \sqrt{\Delta^2\eta_{ik} + \Delta^2\phi_{ik}}$, with η the pseudorapidity and ϕ the azimuthal angle. For comparison, cross-sections and irreducible background for the plain VBF process are also shown.

The above optimized event selection has been obtained by generating events according to the basic event selection

$$
\begin{array}{lll}
p_{\mathrm{T}}^{j} \geq 30\,\mathrm{GeV}, & p_{\mathrm{T}}^{b} \geq 30\,\mathrm{GeV}, & \Delta R_{ik} \geq 0.7, \\
|\eta_\gamma| \leq 2.5, & |\eta_b| \leq 2.5, & |\eta_j| \leq 5, \\
m_{jj} > 400\,\mathrm{GeV}, & m_H(1-10\%) \leq m_{b\bar{b}} \leq m_H(1+10\%), & \\
p_{\mathrm{T}}^{\gamma} \geq 20\,\mathrm{GeV}, & &
\end{array}
\tag{3}
$$

and maximizing the significance on the differential distributions

$$
\frac{\mathrm{d}\sigma}{\mathrm{d}m_{jj}}, \qquad \frac{\mathrm{d}\sigma}{\mathrm{d}p_{\mathrm{T}}^{j1}}, \qquad \frac{\mathrm{d}\sigma}{\mathrm{d}p_{\mathrm{T}}^{b1}}, \qquad \frac{\mathrm{d}\sigma}{\mathrm{d}m_{\gamma H}}, \qquad \frac{\mathrm{d}\sigma}{|\Delta\eta_{jj}|},
$$

where $j1$ and $b1$ denote the leading p_{T} light jet and b-jet, respectively, and $m_{\gamma H}$ is the invariant mass of the $\gamma b\bar{b}$ system.

In case the usual pattern of QED corrections held, the request of a further hard photon would keep the relative weight of signal and background unchanged with respect to the $pp \to H\,jj$ case. Indeed, the rates for $pp \to H\,\gamma\,jj$ and its background would be related to a $\mathcal{O}(\alpha)$ rescaling of the rates for the $H\,jj$ signal and its background, respectively, keeping the S/B ratio approximately stable. On the other hand, both the $H\,\gamma\,jj$ signal and its background statistics would decrease according to the rescaling factor $\mathcal{O}(\alpha)$. Consequently, if $(S/\sqrt{B})|_{H(\gamma)\,jj}$ is the signal significance for the VBF process (with) without a central photon, the signal significance for $pp \to H\,\gamma\,jj$ would fall down as $(S/\sqrt{B})|_{H\gamma\,jj} \sim \sqrt{\alpha}\,(S/\sqrt{B})|_{H\,jj} \lesssim 1/10\,(S/\sqrt{B})|_{H\,jj}$ with respect to the basic VBF

TABLE II. – *Statistical significances with the optimized event selection as defined in eq.* (2)*, for an integrated luminosity of* $100\,\mathrm{fb}^{-1}$*. The value* $\epsilon_b = 60\%$ *for the b-tagging efficiency and a Higgs boson event reduction by* $\epsilon_{b\bar{b}} \simeq 70\%$*, due to the finite* ($\pm 10\%$) $b\bar{b}$ *mass resolution, are assumed. Jet-tagging efficiency and photon identification efficiency are set to 100%. Only the irreducible background is included in B.*

m_H	120 GeV	130 GeV	140 GeV
$S/\sqrt{B}\vert_{H\gamma jj}$	2.6	2.0	1.3
$S/\sqrt{B}\vert_{H jj}$	3.5	2.8	1.9

process. This would question the usefulness of considering the $H\,\gamma\,jj$ variant of the $H\,jj$ process, apart from the expected improvement in the triggering efficiency of the detectors due to the lower background rates.

In table I, one can see that the QED naive expectations do not necessarily apply when restricted regions of phase space are considered (as discussed in detail in [5]). We see that the naive QED rescaling fails for the main background processes $pp \to b\bar{b}\,(\gamma)\,jj$, whose rate drops by about a factor 3000 after requiring a central photon, due to destructive interference (*coherence*) effects discussed in [5]. Since, on the other hand, the signal cross-section roughly follows the naive QED rescaling $\sigma_\gamma \sim \sigma/100$, the requirement of a central photon gives rise to a dramatic increase (by more than one order of magnitude) in the S/B ratio. Indeed, in table II, comparable statistical significances for the signal with and without a photon are obtained, for an integrated luminosity of $100\,\mathrm{fb}^{-1}$.

In order to have a sensible estimate of the achievable S/B ratio and statistical significance at parton level, we computed in [5] with ALPGEN the cross-sections, assuming $m_H = 120\,\mathrm{GeV}$ and with the optimized event selection of eq. (2), for three main potentially dangerous processes([1]):

- $pp \to \gamma + 4$ jets, where two among the light jets are fake tagged as b-jets;
- $pp \to b\bar{b} + 3$ jets, where one of the light jets is misidentified as a photon;
- $pp \to 5$ jets, where one of the light jets is misidentified as a photon, and two light jets are fake tagged as b-jets.

The cross-sections quoted in table III should then be multiplied by the appropriate efficiencies: $\epsilon^2_{\mathrm{fake}}$ for $pp \to \gamma + 4$ jets, $\epsilon^2_b \epsilon_{\gamma j}$ for $pp \to b\bar{b} + 3$ jets and $3\,\epsilon^2_{\mathrm{fake}}\,\epsilon_{\gamma j}$ for $pp \to 5$ jets, where ϵ_{fake} is the efficiency of mistagging a light jet as a b-jet, and $\epsilon_{\gamma j}$ is the rejection factor of a jet against a photon. Assuming $\epsilon_{\mathrm{fake}} = 1\%$ and $\epsilon_{\gamma j} = 1/5000$([2]), one can see that the reducible backgrounds do not perturbe dramatically the significancies of table II.

Apart from enhancing the S/B ratio, coherence effects in $pp \to H(\to b\bar{b})\gamma\,jj$ remarkably curb the relative contribution of the $ZZ \to H$ boson fusion diagrams with respect to the $WW \to H$ ones. In order to prove this last statement, we selected, among all possible subprocesses contributing to $pp \to H\,(\gamma)\,jj$, a first set of subprocesses (named N) mediated only by the ZZ fusion, namely $qq \to H(\gamma)qq$ (in particular, we summed up cross-sections for $q = (u, d, s, c, \bar{u}, \bar{d}, \bar{s}, \bar{c})$), and a second set of subprocesses (named C)

([1]) We estimated that the process $p\bar{p} \to c\bar{c}\gamma jj$, where the c-quarks are both mistagged as b-quarks, (assuming $\epsilon_c = 10\%$) can be safely neglected.
([2]) This is the value quoted in [8], see also [9].

TABLE III. – *Cross-sections for reducible background channels, for the optimized event selection* (2). *The value* $m_H = 120\,\text{GeV}$ *is assumed.*

Process	$p_{\text{T}}^{\gamma} \geq 20\,\text{GeV}$
$\sigma(pp \to \gamma + 4j)$	2.27(2) pb
$\sigma(pp \to b\bar{b} + 3j)$	61.1(3) pb
$\sigma(pp \to 5j)$	2.40(1) nb

mediated only by the WW fusion (in this case, we summed up the 8 cross-sections of the type $u\bar{c} \to H(\gamma)\, d\bar{s}$). Calling $\sigma^{(N,C)}$ the cross-sections for the two latter sets, we computed the following ratios among the radiative and the non-radiative processes at the LHC:

$$\frac{\sigma^{(N)}(H\gamma\, jj)}{\sigma^{(N)}(H\, jj)} = 0.0016, \qquad \frac{\sigma^{(C)}(H\gamma\, jj)}{\sigma^{(C)}(H\, jj)} = 0.013,$$

where we applied the cuts $p_{\text{T}}^{\gamma} \geq 20\,\text{GeV}$, $|\eta_{\gamma}| \leq 2.5$, and $\Delta R_{j\gamma} \geq 0.7$, assuming $m_H = 120\,\text{GeV}$. It is then clear that the radiation is suppressed in the presence of the HZZ vertex.

Thanks to the above feature, the $H(\to b\bar{b})\gamma\, jj$ production at the LHC can have a role not only in the determination of the Hbb coupling, but also for a cleaner determination of the HWW coupling.

The analysis presented above does not include parton shower effects. The latter are expected to further differentiate the signal and background final-state topology and composition. A preliminary analysis of showering and central-jet veto effects points to an improvement of $S/\sqrt{B}$ by about a factor two [5]. The inclusion of complete showering, hadronization, and detector simulations will be needed to establish the actual potential of the process $pp \to H(\to b\bar{b})\gamma\, jj$.

* * *

I wish to thank G. CHIARELLI, M. GRECO and G. ISIDORI and for their kind invitation. Pleasant and fruitful collaboration with E. GABRIELLI, F. MALTONI, B. MELE, M. MORETTI and R. PITTAU is acknowledged.

REFERENCES

[1] See, for instance, REINA L., arXiv:hep-ph/0512377.
[2] HAHN T., HEINEMEYER S., MALTONI F., WEIGLEIN G. and WILLENBROCK S., arXiv:hep-ph/0607308.
[3] MANGANO M. L., MORETTI M., PICCININI F., PITTAU R. and POLOSA A. D., *Phys. Lett. B*, **556** (2003) 50 [arXiv:hep-ph/0210261].
[4] CUCCIARELLI S. *et al.*, CERN-CMS-NOTE-2006-119.
[5] GABRIELLI E., MALTONI F., MELE B., MORETTI M., PICCININI F. and PITTAU R., *Nucl. Phys. B*, **781** (2007) 64 [arXiv:hep-ph/0702119].
[6] MANGANO M. L., MORETTI M., PICCININI F., PITTAU R. and POLOSA A. D., *JHEP*, **0307** (2003) 001 [arXiv:hep-ph/0206293].
[7] MALTONI F. and STELZER T., *JHEP*, **0302** (2003) 027 [arXiv:hep-ph/0208156].
[8] ESCALIER M., DERUE F., FAYARD L., KADO M., LAFORGE B., REIFEN C. and UNAL G., ATL-PHYS-PUB-2005-018.
[9] PIERI M., ARMOURT K. and BRANSON J. G., CERN-CMS-Note-2006-007.

IL NUOVO CIMENTO Vol. 32 C, N. 5-6 Settembre-Dicembre 2009
DOI 10.1393/ncc/i2010-10526-0

Colloquia: LaThuile09

Can colliders disprove leptogenesis?

J-M. Frère
Physique Théorique, Université Libre de Bruxelles - Bruxelles, Belgium

(ricevuto il 10 Novembre 2009; pubblicato online il 15 Gennaio 2010)

Summary. — While leptogenesis is a very solid but hard to check contender for the generation of the observed excess of baryons over anti-baryons in the Universe, we show that the observation of gauge bosons associated with right-handed currents at present or future colliders would suffice to disprove its most canonical mechanism.

PACS 12.60.Cn – Extensions of electroweak gauge sector.
PACS 11.30.Fs – Global symmetries (*e.g.*, baryon number, lepton number).
PACS 98.80.-k – Cosmology.

1. – Introduction

This short article will outline a suggestion, not really for testing leptogenesis in general terms, but rather to disprove it, should some gauge bosons coupled to the right-handed fermions (we will call them generically "Right-Handed W's" or W_R) be discovered at current or future colliders.

We begin by a quick recapitulation of the leptogenesis scheme, insisting on its attractiveness, its robustness, but also on the difficulty to submit it to experimental verification. We will later insist on the fact that extended gauge symmetries are the natural framework for leptogenesis, and show that the discovery of right-handed W's would invalidate the "canonical" leptogenesis mechanism.

Full details of this latter analysis can be found in our common work with Thomas Hambye and Gilles Vertongen [1], where a more complete bibliography is also provided.

2. – Why leptogenesis?

The current excess of baryons (in fact we do not know about matter in general, since we cannot count the cosmic background neutrinos) over anti-baryons is one of the big observational evidences calling for explanation. A first suggestion came from Grand-Unified theories, more specifically $SU(5)$, but quickly met with an objection related to the late evolution of the Universe. Anomalies and the resultant non-conservation of B and L, when operative at the electroweak transition could indeed destroy a previously

generated baryon asymmetry on the simple condition that it be consistent with $B-L=0$, which is precisely the case in $SU(5)$.

The obvious answers are to use this late occasion either as a new source of B generation (electroweak baryogenesis), or as a way to mutate a previously generated asymmetry into the observed B number: in this latter case, it is necessary that the previous asymmetry satisfy $B-L\neq 0$.

As is now well known, the first possibility, despite its elegance, fails in the Standard Model alone, for lack both of sufficient CP violation, and of the out-of-equilibrium component which requires a first-order phase transition. This can be fixed in more extended models (additional singlets, supersymmetry), but the scheme keeps requiring new CP violation, and depends very heavily on the poorly controlled dynamics of the B and L violation at the phase transition.

The choice solution therefore has become leptogenesis [2]. In its canonical form, it is closely associated to the see-saw mechanism, where heavy right-handed neutrinos coupled by Yukawas to the left-handed ones, are used to generate the very small observed masses. The large Majorana mass of the neutrinos provides the necessary L violation, the small Yukawa couplings provide the out-of-equilibrium decays, in such a way that a very robust L asymmetry is generated at high temperature. At the electroweak phase transition, a fraction of this L is converted into a baryonic asymmetry. One of the big advantages is that this conversion process operates by reaching some equilibrium between B and L components, and is fairly independent of the precise dynamics of the B violation at the (slow) electroweak phase transition.

The difficulty to prove leptogenesis resides precisely in its sturdiness, and its quite generic character. Even if the main elements appearing in the calculation of the leptonic (and later baryonic) asymmetry are the same as those governing the (accessible) light neutrino masses, they intervene in completely different combinations, so that low-energy data are not constraining for the process.

In this paper, we will show that, even if leptogenesis is difficult to establish, and fairly resilient as a mechanism, it could still be excluded if W_R particles are observed at colliders.

3. – Orders of magnitude

Let us take as a starting point the mass terms for the heavy right-handed neutrinos N, and their Yukawa couplings to the light ones, namely

$$\mathcal{L}_{\text{mass}} = -\overline{L}\,\widetilde{H}\,\lambda_\nu^\dagger\,N - \frac{1}{2}\,\overline{N}\,m_N\,N^c + \text{h.c.}, \tag{1}$$

where λ is a matrix in generation space, H is the Brout-Englert-Higgs doublet (possibly part of a larger grand-unified multiplet), L are the light left-handed fermions.

Since we are just interested here in orders of magnitude, we will use in this paragraph λ as a single number, assuming (wrongly) that all Yukawa couplings are of similar size. We want now to express the conditions (the values of λ) that provide the correct order of magnitude for light neutrino masses, for the out-of-equilibrium decay of the heavy N, and for sufficient CP violation.

CP violation is provided by the interference of tree-level and one loop diagrams, all controlled by λ. Unless there is a special enhancement, we may thus expect the amount of CP violation to be of order λ^4, while the direct decays are of order λ^2. The proportion

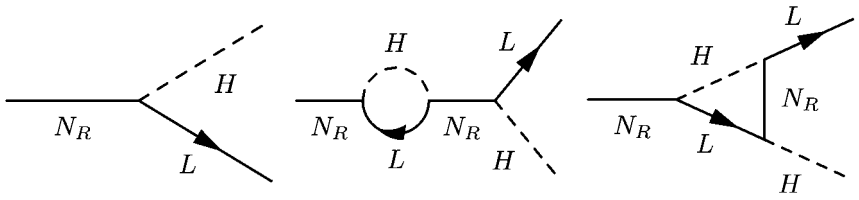

Fig. 1. – N decay and CP violation.

of CP violating decay for each heavy N is thus expected to be of order λ^2 (see fig. 1). Since other effects tend to dilute the baryogenesis effect, this amount of CP asymmetry must exceed the wanted early universe asymmetry, namely $\epsilon > 10^{-8}$.

The out-of-equilibrium condition states that the decay rate must be slower than the Universe expansion at the time of decoupling (that is, roughly at temperature $T \approx m_N$). Here g^* is the effective number of degrees of freedom at that time

$$\begin{aligned} &\Gamma \simeq \lambda^2 m, \\ &\Gamma \ll H, \\ &H = \sqrt{g^*} T^2/(10^{19}\,\mathrm{GeV}). \end{aligned} \tag{2}$$

We group in table I the various constraints on λ and m_N, adding the request to get reasonable light neutrino masses (say, of order 0.01 eV), through the see-saw formula $m_\nu = \lambda^2 v 2/M$, where $v \approx 100\,\mathrm{GeV}$ is the electroweak symmetry breaking.

As seen clearly from this table, the leptogenesis mechanism is fairly resilient over a wide range of λ, m_N, but tuning becomes needed for low values of these parameters. Such tuning can take place either through adjusting the individual elements of the Yukawa coupling matrix λ, or a considerable enhancement can be found by making the self-energy diagram nearly resonant. This is obviously another kind of tuning, which requests the heavy neutrinos N_1, N_2, ... to be nearly degenerate. If the mass splitting is of order λ^2, the CP violation asymmetry can then be considerable. Arguably, very low-energy leptogenesis could then take place [3].

TABLE I. – *Bounds on m_N (in GeV) for various λ, assuming a light neutrino mass of order* 0.01 eV.

λ	Light neutrino mass $m_N \sim$ (GeV)	Out-of-equilibrium decay $m_N >$ (GeV)	Enough CP violation
10^{-5}	10^7	10^8	needs tuning
10^{-4}	10^9	10^{10}	bordeline
10^{-3}	10^{11}	10^{12}	yes
10^{-2}	10^{13}	10^{14}	yes
10^{-1}	10^{15}	10^{16}	yes
1	10^{17}	10^{18}	yes

4. – Improving or falsifying leptogenesis

As announced, the main point of this note is to stress that, even if it is extremely difficult to establish leptogenesis, it could at least be falsified. In particular, we contend that the observation at present or future colliders (that is in practice in the TeV range) of W_R's would make the canonical form of leptogenesis (the case outlined above, with the lepton number carried by neutrinos) untenable.

The possible observation of a W_R will of course be justification enough for its consideration! Still, a few words of motivation for such a particle may be useful, and may help put back in context the whole leptogenesis approach.

In my view indeed, introducing singlet fermions like the N's of *ad hoc* mass (quite separate from the electroweak and grand-unification scales) and Yukawa couplings, if done outside a broader context, is mainly a reparametrization of an effective Lagrangian, and involves no less fine tuning than putting by hand the small parameters this construction replaces. The situation is entirely different if such new particles are related to a wider (for instance, gauge) structure, in which case a much more compelling picture emerges.

Without being specific about the wider gauge structure (one may think of $SO(10)$, E6, or broader schemes), some generators and their associated gauge bosons will typically involve $l_R - \nu_R$ (or in the present notation $l_R - N$) transitions. They will also presumably couple to the right-handed quark structure. For this reason, we consider specifically the case of W_R. Other effects may be associated with the other members of the extended structure, notably extra Z's, or scalars, but we expect (at least in the case of canonical leptogenesis considered here) that they will usually play in the same direction.

Including the W_R sector was of course already considered, notably in [4] and [5]. In both cases, the study was involved with very heavy extra gauge bosons, and the way they would affect leptogenesis and low-energy implications. The most obvious result, as shown in [4] is that the presence of W_R will introduce new, CP-conserving decay channels, potentially large, and lead to an extra dilution of the generated lepton asymmetry, up to the point that the case $M_{W_R} < m_N$ is virtually excluded. This is however by far not the only effect. Further reduction of leptogenesis is associated to diffusion processes, but quite interestingly, the opposite effect may also arise.

As shown indeed in [5], the presence of W_R may play a determinant role when the N population has been destroyed through inflation and needs to be rebuilt. If, as sometimes assumed, the N do not couple directly to the reheating process, small Yukawa couplings (associated to particularly light neutrinos) would in fact preclude the rebuilding of a sufficient population. In that case, the presence of right-handed gauge interactions saves the day, and destroys the possible lower limits on neutrino masses which could be induced.

5. – The main effects

We start thus by including the new interaction term

$$\mathcal{L}_{W_R} = \frac{g}{\sqrt{2}} W_R^\mu \left(\bar{u}_R \gamma_\mu d_R + \bar{N} \gamma_\mu \, l_R \right) . \tag{3}$$

The most evident effect is on the decay channels. Since these are CP-conserving, they introduce a dilution of the asymmetry $\epsilon^{(0)}$ generated in the standard case:

$$\epsilon = \frac{\Gamma_N^{(l)} - \overline{\Gamma}_N^{(l)}}{\Gamma_{\rm tot}^{(l)} + \Gamma_{\rm tot}^{(W_R)}} \equiv \epsilon^{(0)} \frac{\Gamma_{\rm tot}^{(l)}}{\Gamma_{\rm tot}^{(l)} + \Gamma_{\rm tot}^{(W_R)}} . \tag{4}$$

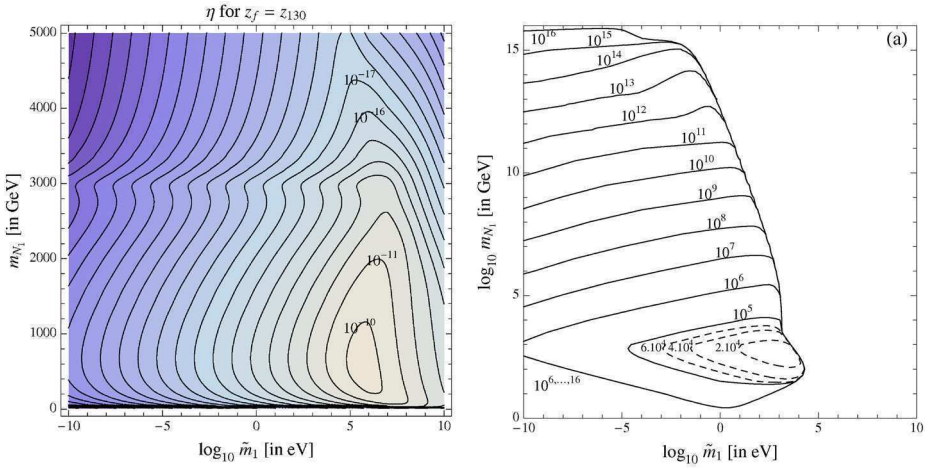

Fig. 2. – Main results: the panel on the left gives for $M_{W_R} = 3\,\text{TeV}$ the efficiencies reached as a function of m_N and $\tilde{m}_1 = v^2 \lambda_\nu^\dagger \lambda_{\nu 11}/m_N$ (z_f refers to the scale at which the decoupling of the sphaleron conversion mechanism is assumed). The panel on the right gives the lower limit acceptable for the W_R mass (in GeV) assuming a maximal leptonic asymmetry due to CP violation ($\epsilon = 1$).

We denote the abundances $Y_i \equiv n_i/s$, $Y_{\mathcal{B}} \equiv Y_B - Y_{\bar{B}}$, $Y_{\mathcal{L}} \equiv Y_L - Y_{\bar{L}}$, where n_i the comoving number density of the species "i", "eq" refering to the equilibrium number density, and s the comoving entropy density. In a now standard notation,

$$Y_{\mathcal{B}} = Y_{\mathcal{L}}\, r_{\mathcal{L}\to\mathcal{B}} = \varepsilon_N\, \eta\, Y_N^{\text{eq}}(T \gg m_N)\, r_{\mathcal{L}\to\mathcal{B}}, \tag{5}$$

where $r_{\mathcal{L}\to\mathcal{B}}$ is the conversion rate of lepton to baryon number at the electroweak phase transition, and η is referred to as the efficiency, and involves all the effects of evolution of the lepton number under the Boltzmann equations.

To facilitate the discussion, we will now slightly depart from the usual conventions, and will include the above-mentioned dilution effect (that is, the factor $\frac{\Gamma_{\text{tot}}^{(l)}}{\Gamma_{\text{tot}}^{(l)}+\Gamma_{\text{tot}}^{(W_R)}}$ appearting in eq. (4)) in the expression of the efficiency η. Using this convention, $\epsilon \to \epsilon^0$.

We now set to examine if the dilutions effects due to a light W_R are sufficient to make canonical leptogenesis impossible. For this purpose, we can, in the above convention, replace ϵ by the largest possible value. While both degenerate and non-degenerate cases are considered in [1], we will consider here the least favorable situation (for our purpose of disproving the mechanism), namely $\epsilon = 1$ (thus allowing for resonance enhancement).

A very important effect arises from the scatterings. Indeed, the W_R have the important property of interacting with gauge strength with the right-handed quarks in the thermal plasma. This keeps them in thermal equilibrium, but also enhances the effect of the scatterings, since the "relic" N particles interact through W_R with normally abundant quarks and light leptons (at the difference of the case where the relic particles must annihilate mutually).

The results are most easily read from fig. 2, where we give (in the rightmost panel), the lower bound on M_{W_R} compatible with leptogenesis. The values, given in GeV are clearly out of reach of the currently operating or planned colliders (we find a lower bound

of 18 TeV in the present case). As an example, we also list (in the leftmost panel) the actual efficiencies (which would also be the lepton number generated, in case $\epsilon = 1$) for $M_{W_R} = 3\,\text{TeV}$, a value reachable at the LHC (remember that a leptonic excess of at least 10^{-8} must be generated to accommodate the currently observed matter asymmetry).

The above considerations put some new urgency to the quest at colliders for W_R bosons, or possibly even light N. In particular, the search [6] should be extended to include the situation where the N is heavier than the W_R, a case where the exclusion of leptogenesis is even more severe.

* * *

This work was performed in collaboration with Thomas Hambye and Gilles Vertongen, with support from IISN and Belgian Science Policy (PAI VI/11)

REFERENCES

[1] Frere J. M., Hambye T. and Vertongen G., *JHEP*, **0901** (2009) 051.
[2] Fukugita M. and Yanagida T., *Phys. Lett. B*, **174** (1986) 45; for recent reviews see, *e.g.*, Strumia A., Davidson S., Nardi E. and Nir Y., arXiv:0802.2962 [hep-ph].
[3] Covi L., Roulet E. and Vissani F., *Phys. Lett. B*, **384** (1996) 169, Pilaftsis A., *Phys. Rev. D*, **56** (1997) 5431, Flanz M., Paschos E. A. and Sarkar U., *Phys. Lett. B*, **345** (1995) 248; **382** (1996) 447 (Erratum).
[4] Carlier S., Frere J. M. and Ling F. S., *Phys. Rev. D*, **60** (1999) 096003 [arXiv:hep-ph/9903300]; Ma E., Sarkar S. and Sarkar U., *Phys. Lett. B*, **458** (1999) 73.
[5] Cosme N., *JHEP*, **0408** (2004) 027 [arXiv:hep-ph/0403209].
[6] Bayatian G. L. *et al.* (CMS Collaboration), *CMS physics: Technical design report*, CERN/LHCC 2006-021; Buescher V., Carena M. S., Dobrescu B. A., Mrenna S., Rainwater D. and Schmitt M., arXiv:hep-ph/0608322.

SESSION VIII - SEARCHING FOR NEW PHYSICS

Miguel Vidal	Search for SUSY at the Tevatron
Henning Flaecher	Search for supersymmetry in di-jet events with novel data-driven background estimation
Yongdok Ri	Searches for New Physics at HERA
Claudia Gemme	Status of the ATLAS detector and its readiness for early BSM Physics
Fabio Happacher	Study of multi-muon events at CDF
Alex Pomarol	Non-supersymmetric extensions of the SM

IL NUOVO CIMENTO Vol. 32 C, N. 5-6 Settembre-Dicembre 2009
DOI 10.1393/ncc/i2010-10551-y

Colloquia: LaThuile09

Search for SUSY at the Tevatron

M. Vidal

CIEMAT - E-28040, Madrid, Spain

(ricevuto il 10 Novembre 2009; pubblicato online il 20 Gennaio 2010)

Summary. — This report presents the most recent results on supersymetry searches in $p\bar{p}$ collisions at $\sqrt{s} = 1.96\,\text{TeV}$, in events with large missing transverse energy, leptons, photons, and multiple jets in the final state using data collected by the D0 and CDF Run-II detectors at Tevatron. No evidence of new physics is found and exclusions limits in several scenarios are extracted.

PACS 14.80.Ly – Supersymmetric partners of known particles.
PACS 12.60.Jv – Supersymmetric models.

1. – Introduction

Supersymmetry (SUSY) [1] is regarded as one of the most compelling theories to describe physics at arbitrarily high energies beyond the Standard Model (SM). In SUSY, a new spin-based symmetry turns a bosonic state into a fermionic state—and vice versa—postulating the existence of a superpartner for each of the known fundamental particles, with spin differing by 1/2 unit. The phenomenology is determined by the breaking mechanism of the symmetry and several constraints are assumed to reduce the vast SUSY parameter space. In mSUGRA [2], one of the most extensively studied models, symmetry breaking is achieved via gravitational interactions and only five parameters determine the low-energy phenomenology from the scale of Grand Unification (GUT). If R-parity([1]) is conserved, SUSY particles have to be produced in pairs and ultimately decay into the lightest supersymmetric particle (LSP), usually identified as the lightest neutralino $\tilde{\chi}_1^0$, which constitutes a valid candidate for cold dark matter because it is colorless and neutral. Due to these properties the LSP escapes detection and it is identified as a large imbalance in transverse momentum historically called missing transverse energy ($\not\!\!E_T$).

([1]) $R_P = (-1)^{3(B-L)+2S}$, where B is the baryon number, L is the lepton number, and S is the spin.

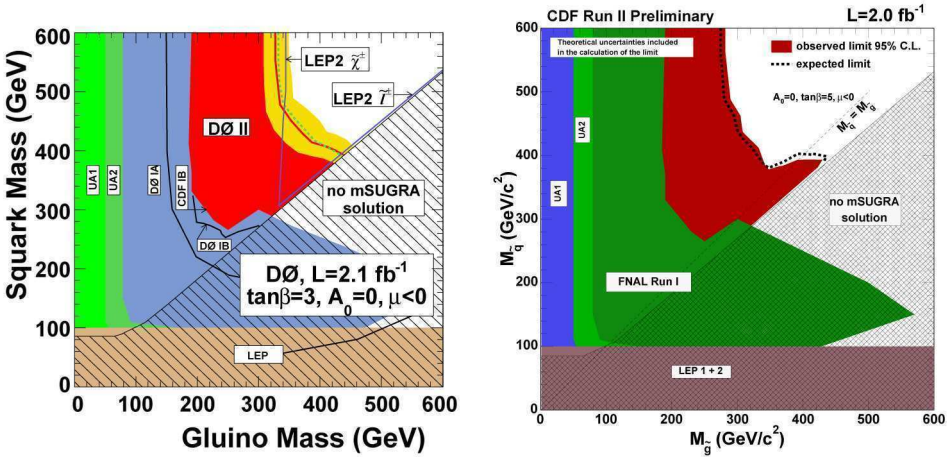

Fig. 1. – Exclusion limit at 95% CL in the squark-gluino mass plane by D0 (left) and CDF (right) experiments with 2.1 fb^{-1} and 2.0 fb^{-1} of data, respectively. Previous exclusion limits are also reported.

2. – Searches for SUSY particles

The experiments at Tevatron are performing searches for SUSY particles in low and high $\tan\beta$ scenarios. Squarks and gluino, sbottom, stop, and chargino+netralino searches are described in this section.

2˙1. *Inclusive search for squark and gluino production.* – Squarks and gluinos are searched for in events with large $\not\!\!E_T$ and multiple jets in the final state. An R-parity conserved mSUGRA scenario is assumed, with the common soft trilinear SUSY breaking parameters $A_0 = 0$, the sign of the higgsino mass term $\mu < -1$, and the ratio of the Higgs vacuum expectation values at the electroweak scale $\tan\beta = 5$. The gluino-squark mass plane is scanned via variations of the parameters m_0 and $m_{1/2}$, common scalar and gaugino mass at the GUT scale, respectively. Light-flavor squark masses are considered degenerate, while 2-to-2 processes involving stop ($\tilde{t}$) and sbottom ($\tilde{b}$) production are excluded to avoid strong theoretical dependence on the mixing in the third generation. Depending on the relative masses of $\tilde{q}$ and $\tilde{g}$, different event topologies are expected. If squarks are significantly lighter than gluinos, $\tilde{q}\tilde{q}$ production is enhanced, and since the squark tends to decay according to $\tilde{q} \to q\tilde{\chi}_1^0$, a dijet topology is favoured, along with large $\not\!\!E_T$ due to the two neutralinos in the final state. If gluinos are lighter than squarks, $\tilde{g}\tilde{g}$ process dominates and the gluino decay via $\tilde{g} \to q\bar{q}\tilde{\chi}_1^0$ yields topologies containing a large number of jets (≥ 4) and moderate $\not\!\!E_T$. For $m_{\tilde{g}} \approx m_{\tilde{q}}$, a topology with at least three jets in the final state is expected to be dominant. Three different analyses are carried out, requiring at least 2, 3 or 4 jets in the final state, respectively.

No significant deviation from SM predictions is found in the analysis performed by the D0 [3] and CDF [4] Collaborations. The results are translated into 95% CL upper limits on the cross-section for squark and gluino production in different regions of the squark-gluino mass plane (fig. 1), using a Bayesian approach and including statistical and systematic uncertainties.

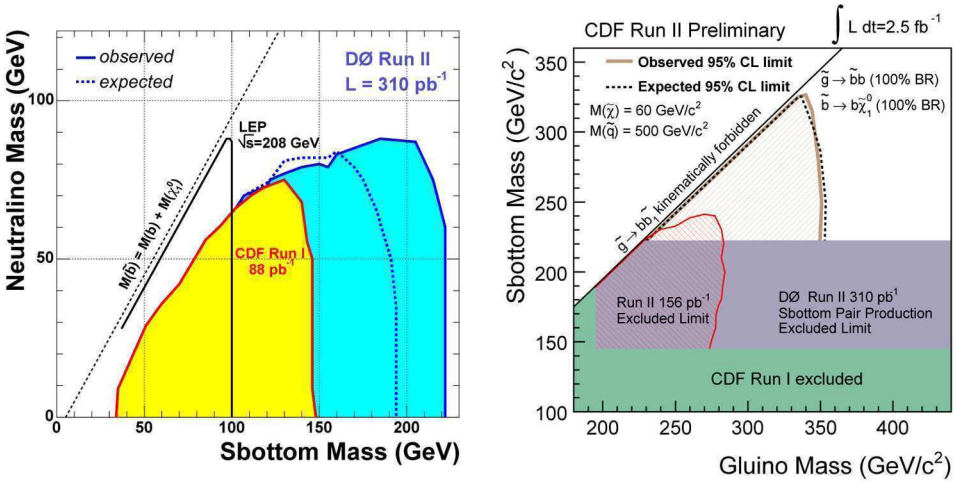

Fig. 2. – Exclusion limits at 95% CL in the neutralino-sbottom mass plane (left) for direct $\tilde{b}$ production and in the sbottom-gluino mass plane (right) for $\tilde{b}$ production through $\tilde{g}$ decays.

2˙2. *Sbottom searches.* – If $\tan\beta$ is large, then there can be a large mass splitting in the scalar bottom sector, yielding a mass to the lightest state ($\tilde{b}$) in the reach of the Tevatron center-of-mass energy. Assuming R-parity conservation the only particle lighter than the $\tilde{b}$ is the LSP.

At Tevatron, two different searches for sbottom are performed depending on its production mechanism. Direct $\tilde{b}$ production with the subsequent sbottom decay to a b-quark and the lightest neutralino ($\tilde{\chi}^0$), leads to the main signature for $\tilde{b}$ detection which includes two b-jets and $\not\!\!E_T$. The other one is the $\tilde{b}$ production through gluino ($\tilde{g}$) decays. Under the assumption that mass of the $\tilde{g}$ is smaller than mass of the $\tilde{q}$, but larger than mass of the $\tilde{b}$, the gluino pair production, $p\bar{p} \to \tilde{g}\tilde{g}$, is one of the dominant SUSY processes. After production the gluino decays to $\tilde{g} \to b\tilde{b}$ with the subsequent sbottom decay to a b-quark and $\tilde{\chi}^0$, $\tilde{b} \to b\tilde{\chi}^0$.

Although involving more particles and constraints in the SUSY spectrum, this last approach is stronly motivated by the fact that the gluino pair production cross-section is large ($\sigma(g\tilde{g}) \sim 10 \times \sigma(b\tilde{b})$) compared to direct sbottom pair production of similar mass.

Since both analyses have b-jets in the final state, applying a b-tagging algorithm is a mandatory tool to enhance the sensitivity by reducing backgrounds. The B-hadrons in jets coming from b-quark fragmentation have an average flight path of about 500 microns, yielding secondary vertices relative to the interaction point (primary vertex). The tagging algorithms are optimized to find these sencondary vertices using different approaches in each experiment.

The search for direct $\tilde{b}$ production [5] is performed by the D0 Collaboration using $310\,\mathrm{pb}^{-1}$ of data while the search for $\tilde{b}$ production through $\tilde{g}$ decays [6] is performed by the CDF Collaboration using $2.5\,\mathrm{fb}^{-1}$ of data. In both analyses the results are in good agreement with the SM prediction and no hints of sbottom have been found. They were used to extract exclusion limits for the cross-section of the described process. Figure 2 shows the exclusion limits at 95% CL in the neutralino-sbottom mass plane for direct $\tilde{b}$ production and in the sbottom-gluino mass plane for $\tilde{b}$ production through $\tilde{g}$ decays.

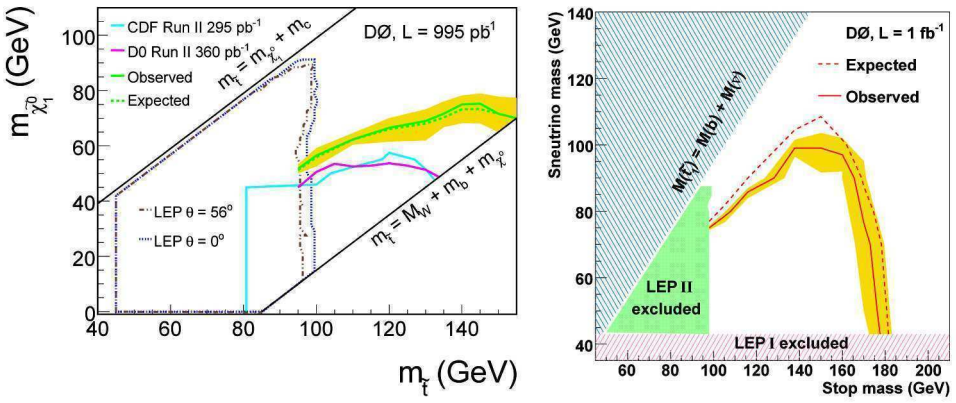

Fig. 3. – Exclusion limits at 95% CL in the neutralino-stop mass plane (left) for stop decaying into charm+neutralino at D0, and in the sneutrino-stop mass plane (right) for stop decaying into bottom+lepton+sneutrino at D0. Stop mass (right) for the stop decaying into bottom+neutralino+lepton+neutrino at CDF.

2˙3. *Stop searches.* – Due to the large mass of the top quark, the mass splitting between the two stop quarks states $(\tilde{t}_1, \tilde{t}_2)$ may be large, allowing $\tilde{t}_1$ to possibly be the lightest squark, and possible even lighter than the top quark.

Three different seaches for $\tilde{t}_1$ particles are performed at Tevatron depending on their dacay mode.

The first scenario is accessible in the range $m_{\tilde{t}_1} < m_b + m_{\tilde{\chi}^+}$ and $m_{\tilde{t}_1} < m_W + m_b + m_{\tilde{\chi}^0}$. The dominant $\tilde{t}_1$ decay mode in this model is the flavor-changing process $\tilde{t}_1 \to c\tilde{\chi}^0$, which is typically assumed to occur with 100% branching fraction. The $\tilde{t}_1 \to t\tilde{\chi}^0$ decay is kinematically forbidden over the $\tilde{t}_1$ mass range currently accessible at Tevatron, and the tree level four-body decays $\tilde{t}_1 \to bff'\tilde{\chi}^0$ can be neglected. In this particular case the experimental signature consists of two c-jets and $\not\!\!E_T$ from the undetected $\tilde{\chi}^0$ [7].

In the second scenario we assume that $\mathrm{BR}(\tilde{t}_1 \to bl\tilde{\nu}) = 1$, where $\tilde{\nu}$ is the scalar neutrino (sneutrino). Among possible stop decays, this final state is one of the most attractive from the experimental point of view; in addition to a b-quark, it benefits from the presence of a lepton with high transverse momentum with respect to the beam axis. The sneutrino is either the LSP or decays invisibly: $\tilde{\nu} \to \nu\tilde{\chi}^0$ or $\nu\tilde{G}$, where the lightest neutralino, $\tilde{\chi}^0$, or the gravitino, $\tilde{G}$, is the LSP. The signal topology consists of two isolated leptons, $\not\!\!E_T$, coming mainly from undetected sneutrinos, and jets [8].

The third scenario happens when $\tilde{t}_1 \to b\tilde{\chi}^+ \to b\tilde{\chi}^0 l\nu$ assuming a 100% branching ratio of the stop squark into a b-quark and chargino, and allowing for the chargino to decay through a variety of channels to the dilepton decay mode. These stop events produce signatures similar to those of SM top quark decays, and could potentially be hiding in the top samples of the Tevatron data.

No significant deviation from the SM prediction was observed in any of the previous searches, the results were used to extract exclusion limits for the cross-section of the described process. Figure 3 shows the exclusion limits at 95% CL in the neutralino-stop mass plane for stop decaying into charm+neutralino, the exclusion limits at 95% CL in the sneutrino-stop mass plane for stop decaying into $\tilde{b}l\tilde{\nu}$. The stop invariant mass for the stop decaying into $b\tilde{\chi}^0 l\nu$ is shown in fig. 4.

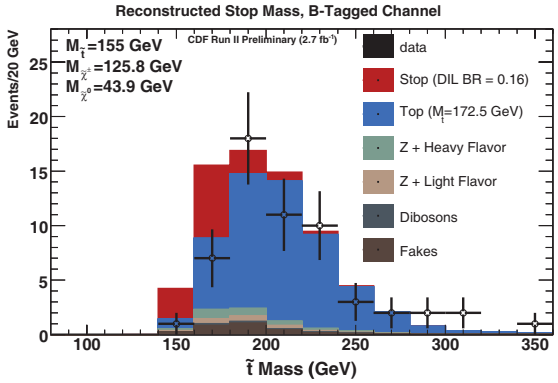

Fig. 4. – Stop mass for the stop decaying into $b\tilde{\chi}^0 l\nu$ at CDF.

2˙4. *Chargino+neutralino in the trilepton final state.* – In $p\bar{p}$ collisions, charginos and neutralinos can be produced in pairs via an off-shell W-boson or the exchange of squarks. They decay into fermions and the lightest neutralino $\tilde{\chi}_1^0$, which is assumed to be the LSP and to escape undetected. The analysis shown describes the search for $p\bar{p} \to \tilde{\chi}_1^{\pm}\tilde{\chi}_2^0$ in purely leptonic decay modes in final states with $\not\!\!E_T$ and three charged leptons (e, μ or τ). This signature of three leptons can be particularly challenging in regions of parameter space where lepton momenta are very soft due to small mass differences of the SUSY particles. The analyses performed by D0 [9] are based on data corresponding to an integrated luminosity of $2.3\,\mathrm{fb}^{-1}$, with the exception of the analysis using identified hadronic τ lepton decays, which is based on $1\,\mathrm{fb}^{-1}$ of data.

The final state with three leptons plus $\not\!\!E_T$ is a very clean signature at hadron colliders, however the huge amount of backgrounds, from jets faking leptons, Drell-Yan and electroweak bosons production, makes the search challenging.

The analysis combines five separate final states depending on the final lepton combination: ee lepton, $\mu\mu$ l, $e\mu$ l, $\tau\mu$ l, and $\mu\tau\tau$, where l is any other kind of lepton. The invariant mass of the dimuon system is shown in fig. 5 for the $\mu\mu$ lepton channel.

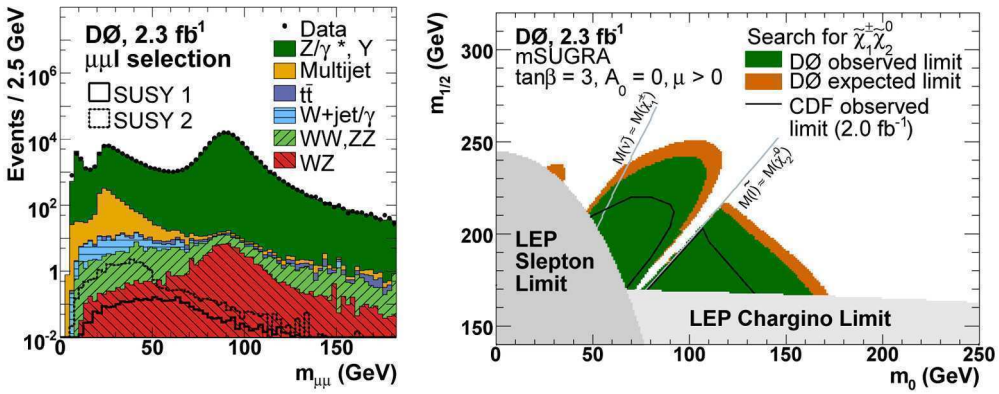

Fig. 5. – Invariant mass (left) of the dimuon sistem in the $\mu\mu$ lepton channel. Exclusion limit at 95% CL in the $(m_{1/2}, m_0)$-plane (right).

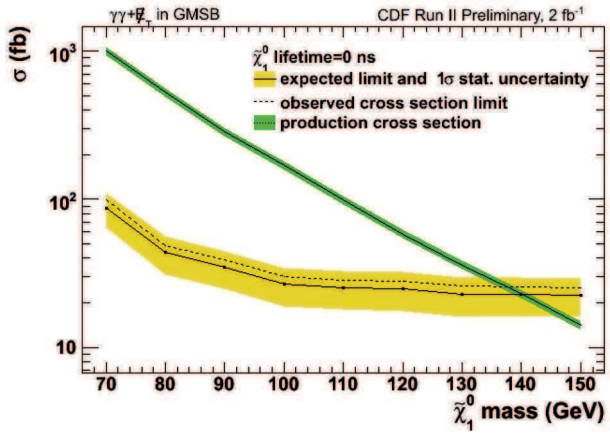

Fig. 6. – Exclusion limit at 95% CL in terms of cross-section as a function of the neutralino mass at a lifetime of 0 ns.

No evidence for a signal is observed, and upper limits on the product of production cross-section and leptonic branching fraction have been set. Within the mSUGRA model with $\tan\beta = 3$, $A_0 = 0$, and $\mu > 0$, this result translates into excluded regions in the $m_{1/2}$-m_0 plane as is shown in fig. 5, that significantly extend beyond previously existing limits from direct searches for supersymmetric particles.

3. – Searches with photons

An example of a theory that would produce these high-energy photon events is gauge-mediated supersymmetry breaking (GMSB) with $\tilde{\chi}_1^0 \to \gamma\tilde{G}$ where the $\tilde{\chi}_1^0$ is the lightest neutralino and the next-to-lightest supersymmetric particle (NLSP) and $\tilde{G}$, a gravitino as the LSP. At the Tevatron gaugino pair-production dominates and the decays produce $\tilde{\chi}_1^0$'s in association with jets, with each $\tilde{\chi}_1^0$ decaying into a $\tilde{G}$, giving rise to $\not\!\!E_T$, and a photon. Depending on how many of the two $\tilde{G}$'s decay inside the detector, due to their large decay length, the event has the signature $\gamma\gamma + \not\!\!E_T$ or $\gamma + \not\!\!E_T$ with one or more additional jets.

Using 2.0 fb^{-1} of CDF data, one event is found which is consistent with the background estimate of 0.62 ± 0.29 events from the SM expectations. A limit on GMSB models with a $\tilde{\chi}_1^0$ mass reach of 138 GeV/c^2 at a $\tilde{\chi}_1^0$ lifetime of 0 ns is set as is shown in fig. 6.

4. – Searches for MSSM Higgs

One of the outstanding questions in modern particle physics is the dynamics of electroweak (EW) symmetry breaking and the origin of particle masses. In the SM, EW symmetry is spontaneously broken through the Higgs mechanism, by the introduction of a doublet of self-interacting complex scalar fields with non-zero vacuum expectation values. The physical manifestation of this scenario is the existence of a massive scalar Higgs boson $h_{\rm SM}$. Theoretical difficulties related to divergent radiative corrections to the $h_{\rm SM}$ mass have natural solution in SUSY models and, in this context, the MSSM is

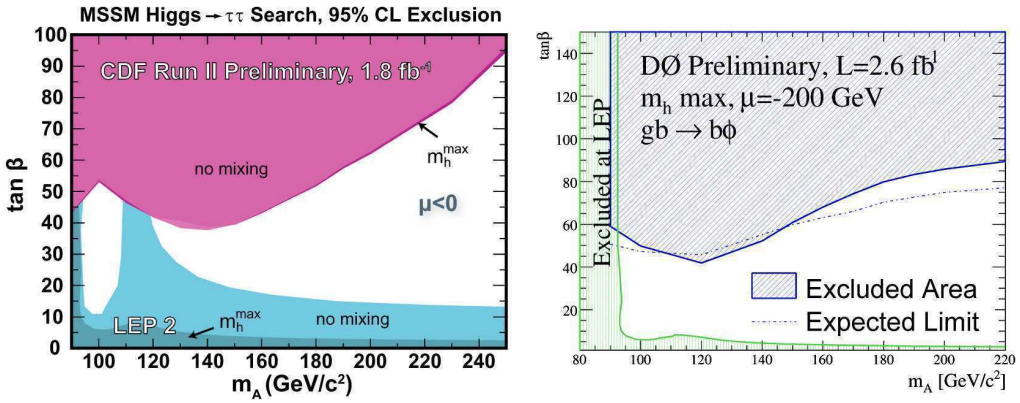

Fig. 7. – Exclusion limits at 95% CL in the $(\tan\beta, m_A)$-plane for the $\phi \to \tau\tau$ (left), and $\phi \to b\bar{b}$ (right) analyses.

the simplest realistic SUSY theory. It requires two Higgs doublets resulting in a Higgs sector with two charged and three neutral scalar bosons. Assuming CP-invariance, one of the neutral bosons (A) is CP-odd, and the other two (h, H) are CP-even. The usual notation uses h (H) for the lighter (heavier) CP-even neutral Higgs boson, and ϕ to denote any of h, H, A. At tree level, the MSSM Higgs bosons are described by two free parameters, chosen to be the mass of A (m_A), and $\tan\beta = v_2/v_1$, where v_2, v_1 are the vacuum expectation values of the neutral Higgs fields that couple to up-type and down-type fermions, respectively. The Yukawa couplings of A to down-type fermions (such as the b quark and τ) are enhanced by a factor of $\tan\beta$ relative to the SM. For large $\tan\beta$ one of the CP-even bosons is nearly mass-degenerate with A and has similar couplings. There are two dominant production mechanisms of neutral MSSM Higgs bosons at hadronic colliders: gluon fusion and $b\bar{b}$ fusion. The leading decay modes of A and the corresponding mass-degenerate CP-even Higgs boson are $\phi \to b\bar{b}$ ($\sim 90\%$) and $\phi \to \tau\tau$ ($\sim 10\%$). Despite the smaller branching fractions, Higgs searches in the ditau channel have advantages because they do not suffer from the large di-jet and multi-jet backgrounds as $\phi \to b\bar{b}$. The LEP experiments have excluded $m_A \leq 93\,\mathrm{GeV}/c^2$, and higher-mass A for small $\tan\beta$. Searches at hadron colliders are complementary, providing sensitivity in the large $\tan\beta$ region.

At Tevatron, both Collaborations D0 and CDF perform searches for $b\phi \to bb\bar{b}$ and $\phi \to \tau\tau$. One more channel: $b\phi \to \tau\tau$ complements previous searches and it is performed by D0 Collaboration. Since no significant deviation from the SM prediction was observed in any of the performed analyses the results were used to extract exclusion limits in the $(\tan\beta, m_A)$-plane as shows fig. 7.

5. – Conclusions

The most recent results on searches for SUSY at the Tevatron in events with large missing transverse energy, leptons, photons and multiple jets in the final state have been presented. No evidence of New Physics has been found yet and stringent exclusion limits have been extracted for the production of particles predicted in supersymetric extension of the SM, especially for squarks, gluinos, charginos, neutralinos, and higgses. With

more than $4\,\mathrm{fb}^{-1}$ of data already collected, CDF and D0 Collaborations could reveal hints of New Physics, or place more severe limits on the SUSY parameter space before the start-up of the LHC.

REFERENCES

[1] Wess J. and Zumino B., *Nucl. Phys. B*, **70** (1974) 39.
[2] Chamseddine A. H., Arnowitt R. and Nath P., *Phys. Rev. Lett.*, **49** (1982) 970.
[3] Abazov V. *et al.*, *Phys. Lett. B*, **660** (2008) 449.
[4] Aaltonen T. *et al.*, *Phys. Rev. Lett.*, **102** (2009) 121801.
[5] Abazov V. M. *et al.*, *Phys. Rev. Lett.*, **97** (2006) 171806.
[6] Aaltonen T. *et al.*, hep-ex/0903.2618.
[7] Abazov V. M. *et al.*, *Phys. Lett. B*, **665** (2008) 1.
[8] Abazov V. M. *et al.*, *Phys. Lett. B*, **675** (2009) 289.
[9] Abazov V. *et al.*, hep-ex/0901.0646.

IL NUOVO CIMENTO Vol. 32 C, N. 5-6 Settembre-Dicembre 2009
DOI 10.1393/ncc/i2010-10553-9

Colloquia: LaThuile09

Search for supersymmetry in di-jet events with novel data-driven background estimation

H. U. Flaecher on behalf of the CMS Collaboration
PH Department, CERN - CH-1211 Geneva 23, Switzerland

(ricevuto il 10 Novembre 2009; pubblicato online il 25 Gennaio 2010)

Summary. — We present a search for supersymmetry (SUSY) in di-jet events with the CMS detector at the LHC. Our study is focused on a SUSY parameter space where squarks are pair produced and both directly decay to a quark and neutralino with the latter escaping the detector, thus leaving a missing energy signature. Although the background from QCD di-jet events is overwhelming, the particular kinematics of the SUSY events allow to define powerful discriminating variables which enable a clear separation of signal and QCD events. Therefore, the only important SM background left for this search is the invisible decay of the Z boson accompanied with two jets in the final state. This background can be estimated by utilizing a novel approach using gamma+jet events thus enabling a possible discovery of SUSY in the di-jet system with the early physics data.

PACS 11.30.Pb – Supersymmetry.
PACS 12.38.-t – Quantum chromodynamics.

1. – Introduction

We present a search strategy for a possible discovery of supersymmetric (SUSY) signatures at the LHC using di-jet events following a recently proposed new approach [1]. It is based on the assumption that squarks are pair-produced and subsequently decay directly to a quark and the χ_1^0, the lightest stable particle (LSP). This approach is most promising for regions in SUSY parameter space where squarks have large branching fractions to decay directly to the LSP. This configuration in turn requires the gluino to be heavier than the squarks, thus avoiding cascade decays of squarks via the gluino. Therefore the event topology under investigation consists of two high-p_{T} jets and two invisible neutralinos which lead to a missing energy signature. The main background processes for this topology are QCD di-jet events and Z + jet events where the Z decays into two neutrinos. It is however possible to define kinematic variables that can discriminate between signal and background without relying on the missing energy measurement from the calorimeters. The presented analysis [2] is an extension to the existing SUSY searches within CMS which so far have focused on missing E_{T} signatures with at least three jets and/or involving charged leptons [3].

2. – Di-jet search using the kinematic variable $\alpha_{(\mathrm{T})}$

2˙1. *Event selection.* – The results presented here are carried out assuming an integrated luminosity of $1\,\mathrm{fb}^{-1}$ collected at a LHC centre-of-mass energy of 14 TeV. The Monte Carlo samples considered consist of QCD processes generated using `PYTHIA` [4], including minimum bias and high-energy jet data. Further backgrounds are $\mathrm{t\bar{t}}$ + jets, W + jets, and Z + jets events (excluding $\mathrm{Z} \to \nu\nu$), all simulated using `ALPGEN` [5] and Z + jets events with $\mathrm{Z} \to \nu\nu$, generated with `PYTHIA`. In addition, single top, γ + jets and $\mathrm{b\bar{b}}$ + jets background samples were investigated which, however, only play a negligible role in the presented search. Possible SUSY signal yields are estimated using the CMS low-mass mSuGra points LM1–LM4 [3].

We select events that pass a two-jet trigger where the Level 1 trigger conditions are either one jet with E_T greater than 150 GeV or two jets with E_T greater than 70 GeV. At the High Level Trigger this cut is raised to two jets with each E_T greater than 150 GeV. For calorimeter jet clustering, the corrected iterative cone algorithm with $R = 0.5$ is used and two jets with $p_\mathrm{T} > 50\,\mathrm{GeV}$ and the electromagnetic fraction $F_\mathrm{em} < 0.9$ are required. Based on the two leading jets two additional variables are defined: HT as the scalar sum of the two leading jet p_T's, $\mathrm{HT} = p_\mathrm{T}^{\mathrm{j1}} + p_\mathrm{T}^{\mathrm{j2}}$ and missing p_T (MHT) of the event calculated as $\vec{\mathrm{MHT}} = -(\vec{p}_\mathrm{T}^{\,\mathrm{j1}} + \vec{p}_\mathrm{T}^{\,\mathrm{j2}})$. In order to select clean di-jet events, any event where either an isolated electron or muon with momentum $p_\mathrm{T} > 10\,\mathrm{GeV}$ was identified is vetoed. Furthermore, events with any additional jets with $p_\mathrm{T} > 50\,\mathrm{GeV}$, which also includes jets from hadronic τ decays, are also vetoed. To protect against significant mismeasurements of jet energies, events where the missing p_T based on the two-jet system points into the same direction as one of the first three jets, are rejected by requiring $\Delta\phi(\mathrm{jet}, \mathrm{MHT}) < 0.3\,\mathrm{rad}$. This definition of missing E_T based on the two jet momenta should also be robust against fake signals and noise in the calorimeters. In addition to the selection criteria above, the leading jet must be within pseudo-rapidity $|\eta| < 2.5$.

2˙2. *Event kinematics.* – As mentioned in the previous section the di-jet trigger requires already two (uncorrected) jets with $p_\mathrm{T} > 150\,\mathrm{GeV}$ each, which implies $\mathrm{HT} > 300\,\mathrm{GeV}$. For signal events, two high-p_T jets come directly from a squark decay with typical mass of the order of 500 GeV. Therefore, to make the analysis cuts more restrictive than the trigger and to further reduce background contributions it is required that HT exceeds 500 GeV. Even after requiring two high-p_T jets, sizeable background contributions from a number of processes remain, the most important of which are

- QCD di-jet events due to their (overwhelmingly) large cross-section and sizeable uncertainties in higher-oder corrections, in particular production of extra jets due to gluon emission;
- $\mathrm{Z} \to \nu\nu$ events which present an irreducible background as the invisible Z decay leads to real missing E_T;
- W + jets events, with $\mathrm{W} \to \tau\nu$ followed by a hadronic τ decay which is wrongly identified as a jet.

It is however possible to define kinematic variables to disentangle QCD events and signal-like events with real missing E_T. In well-measured QCD di-jet events, transverse momentum conservation requires the p_T of the two jets to be of equal magnitude and back-to-back in the plane transverse to the beam. In contrast, in signal-like events the two squarks decay independently of each other and therefore the resulting jet p_T's can

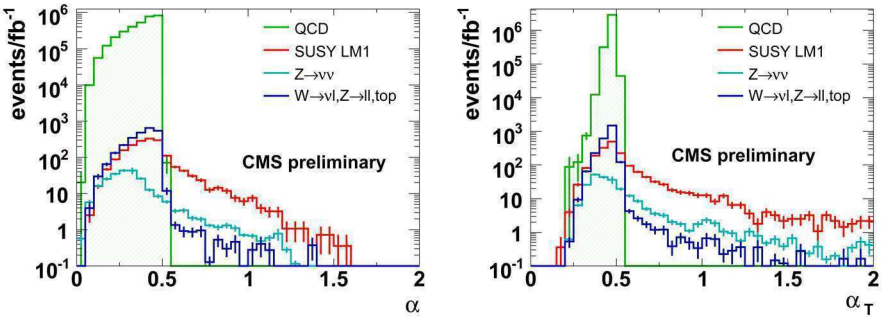

Fig. 1. – Distribution of α and α_{T} after all other selection cuts have been applied.

be of different magnitude and their ϕ values (largely) uncorrelated. In ref. [1], a new variable α was suggested which exploits the requirement of back-to-back jets of equal magnitude for QCD events:

(1)
$$\alpha = E_{\mathrm{T}}^{\mathrm{j2}}/M_{\mathrm{j1,j2}}, \text{ which for massless particles is equal to } \alpha = \frac{E_{\mathrm{T}}^{\mathrm{j2}}}{\sqrt{2E^{\mathrm{j1}}E^{\mathrm{j2}}(1-\cos\Theta)}},$$

where Θ is the angle between the two jets. As can be seen from eq. (1), α can at most have a value of 0.5 for well-measured QCD events. In addition, as the E_{T} of the second energetic jet enters in the numerator, uncertainties introduced through energy mis-measurements partly cancel out in α. (If one of the two jet energies is mis-measured by a large amount, the order of the two jets is reversed.) A modified version of this variable is also explored in which the transverse mass of the two jets is used instead of the invariant mass:

(2)
$$\alpha_{\mathrm{T}} = E_{\mathrm{T}}^{\mathrm{j2}}/M_{\mathrm{T_{j1,j2}}} = \frac{E_{\mathrm{T}}^{\mathrm{j2}}}{\sqrt{2E_{\mathrm{T}}^{\mathrm{j1}}E_{\mathrm{T}}^{\mathrm{j2}}(1-\cos\Delta\phi)}} = \frac{\sqrt{E_{\mathrm{T}}^{\mathrm{j2}}/E_{\mathrm{T}}^{\mathrm{j1}}}}{\sqrt{2(1-\cos\Delta\phi)}},$$

where $\Delta\phi$ is the difference in azimuthal between the two jets. For well-measured QCD di-jet events, α_{T} is exactly 0.5. The α and α_{T} distributions are shown in fig. 1 for the different background processes and exemplary for LM1.

While the present selection is safe with respect to the effects of hard extra gluon radiation by rejecting events with extra jets with $p_{\mathrm{T}} > 50\,\mathrm{GeV}$, multiple soft gluon emission might still noticeably affect the $\Delta\phi$ distribution. It is therefore safer to use α and α_{T} in the event selection as these variables also reject events where the p_{T} of the two jets is not balanced, in addition to being sensitive to the $\Delta\phi$ between the two jets. Compared with $\Delta\phi$, α and α_{T} have the additional benefit that they are more effective in rejecting $\mathrm{Z} \to \nu\nu$ events. In the following α and α_{T}, shown in fig. 1 are used in the event selection. Both variables are highly correlated to $\Delta\phi$, *i.e.* an additional cut on $\Delta\phi$, has a negligible effect. To account for finite jet energy and ϕ resolution as well as missed jets with $p_{\mathrm{T}} < 50\,\mathrm{GeV}$ it is required that α (α_{T}) exceeds 0.55.

2˙3. *Expected event yields from simulations.* – After the selection criteria described above are applied, the event yields listed in table I are obtained for background events

TABLE I. – *Numbers of expected events after each selection cut for background samples (QCD, $t\bar{t}$, W, Z + jets, and $Z \to \nu\nu$) and LM1 signal point. The final numbers of events selected are shown after a cut on α or alternatively α_T and $\Delta\phi_{j1,j2}$.*

Selection cut	QCD	$t\bar{t}$, W, Z	$Z \to \nu\nu$	LM1
Trigger	1.1×10^8	147892	1807	25772
Preselection	3.4×10^7	9820	878	2408
$HT > 500\,\text{GeV}$	3.2×10^6	2404	243	1784
$\alpha > 0.55$	0	7.2	19.7	227.6
$\alpha_T > 0.55$	0	19.9	58.2	439.6
$\Delta\phi_{j1,j2} < 2\pi/3$	0	18.7	57.2	432.4

and the LM1 signal point. All the numbers correspond to an integrated luminosity of $1\,\text{fb}^{-1}$. Both α and α_T are very effective in reducing the backgrounds, particularly from QCD di-jet events but also for electroweak processes. When α_T is used instead of α, the signal yield for the LM1 point is almost doubled. The dominant background from $Z \to \nu\nu$ however rises by about a factor three while the background from $t\bar{t}$, W, and Z decays doubles as well. It is therefore proposed to study both variables with real data as the signal-to-background ratio differs in the two cases. Nevertheless, in each case signal-over-background ratios larger than five are expected.

Beside the mSuGra point LM1, the event yields for the low-mass SUSY points LM2–LM4 were studied. We find signal yields of 132 events for LM2, 138 events for LM3 and 195 events for LM4, where the selection on α_T was used. Accordingly a signal-over-background ratio in excess of 2 can be achieved for LM4 while for LM2 and LM3, the signal would still dominate over the expected background.

2˙4. *Jet-energy scale and resolution uncertainties.* – The systematic uncertainties due to miscalibration and mismeasurement of jets were estimated by applying the following systematic variations:

– a Gaussian smearing of the transverse jet momenta of 10% and a Gaussian smearing of the azimuthal angle ϕ by 0.1 rad;

– a scaling of the jet energy scale by ±5%;

– a scaling of the jet energy scale in the forward direction ($|\eta| > 1.4$) by ±3%.

It was found that the Gaussian smearing only has a small effect ($\sim 3\%$) on the selected signal and background events. The upward scaling of the transverse momenta of the jets effectively relaxes the HT cut and hence more events pass the selection. Conversely, the reduced momentum therefore leads to fewer events. The largest deviation is a 12% reduction in both, the signal and background efficiencies, leaving the signal-over-background ratio largely unchanged. The miscalibration applied for the jet energy scale in the forward regions has a negligible effect. Overall the signal-to-background ratio remains stable under varying conditions and the background from QCD remains small in all scenarios.

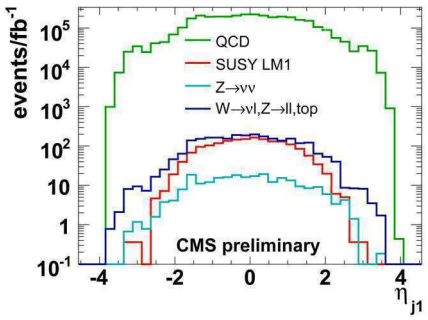

Fig. 2. – Distribution of η for QCD, $t\bar{t}$, W, Z, and SUSY LM1 events. Shown is the expected number of events for a luminosity of 1 fb^{-1}, after all selection cuts except the cut on α_T and $|\eta_{j1}|$.

3. – Data-driven background estimation

In the following we outline data-driven methods for background estimation for jets + missing energy searches. The main emphasis is on an approach where signal enhanced and depleted regions in phase space are defined and the combination of all backgrounds can be estimated simultaneously. In addition, we discuss how the dominant remaining background from $Z \to \nu\nu$ events can be estimated by using a data control sample of photon + jets events.

3˙1. *Background estimation using the η dependence of α_T via the matrix method.* – The idea of the matrix method is to find two variables, $\mathcal{V}_1$ and $\mathcal{V}_2$, which are uncorrelated for background events and for which in the 2-d plane three quadrants exists that are signal depleted and one that is signal enriched, *i.e.* each variable has a signal-enriched and a signal-depleted region. In this case it is possible to determine the amount of background events directly from the data. The two variables in question for the present analysis are the pseudo-rapidity $|\eta|$ of the leading jet and α_T. As can be seen from fig. 2, the leading jet from a SUSY event is on average more central than those from the background processes, QCD, $t\bar{t}$, W, Z + jets and $Z \to \nu\nu$. Therefore, the forward regions with $|\eta| > 2.5$ are considered as signal depleted. Similarly, the region formed by $\alpha_T > 0.55$ is signal enriched while that with $\alpha_T < 0.55$ is signal depleted.

The variable $R^i_{\alpha_T} = N_{\alpha_T>0.55}/N_{\alpha_T<0.55}$ is defined as the ratio of events with $\alpha_T > 0.55$ to those with $\alpha_T < 0.55$ for a given bin i in $|\eta|$. For the method outlined above to be applicable this ratio needs to be constant. While in real data it will not be possible to distinguish the different background processes on an event-by-event basis, Monte Carlo simulation shows that R_{α_T} is, to a good approximation, constant for all the relevant individual background contributions. It is therefore legitimate to combine all the backgrounds and to determine the sum of all backgrounds with the help of the matrix method. In fig. 3, R_{α_T} is shown for all backgrounds combined and as expected the "combined R_{α_T}" is flat as a function of $|\eta|$. In addition, R_{α_T} is shown for the case of a LM1 signal present in the data.

To estimate the number of background events in the $|\eta| < 2.5$ regions, $N_{\text{pred}}(|\eta|)$, R_{α_T} needs to be multiplied with the number of events with $\alpha_T < 0.55$, $N_{\text{bkgd}}(|\eta|)$, in the corresponding $|\eta|$ bin: $N_{\text{pred}}(|\eta|) = R_{\alpha_T} \cdot N_{\text{bkgd}}(|\eta|)$.

Figure 4 shows the numbers of background events predicted and measured in the different η regions after all selection cuts. In the absence of a signal, the background

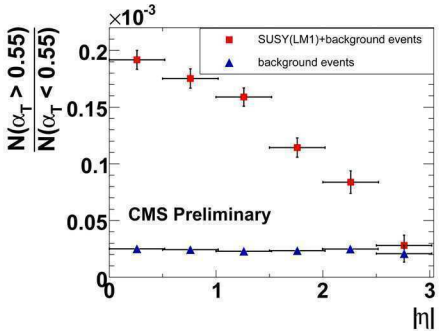

Fig. 3. – (Colour on-line) R_{α_T} as a function of $|\eta|$ of the leading jet after all selection cuts except the cut on α_T, and $|\eta|$, shown for background events only (blue triangles) and for a mixture of background and SUSY LM1 events (red squares).

can be predicted within the simulated statistical precision. In fig. 4, the total number of signal-plus-background events is also compared to the number of predicted background events. The presence of a SUSY signal leads to a slight overestimate of the background. Despite the large statistical uncertainty on the background prediction, a clear signal is still visible. The stability of the presented matrix method was verified against the systematic variations discussed in subsect. **2**˙4.

The validity of this method can be estimated directly from data. To do so, the selection cuts are loosened until the signal contribution becomes negligible compared to the backgrounds. Then R_{α_T} should be independent of $|\eta|$. Figure 5 shows R_{α_T} for a mix of SUSY LM1 and background events for several different HT cuts. For relatively low requirements on HT, R_{α_T} stays approximately constant while for stricter requirements on HT, R_{α_T} is falling off with larger values of $|\eta|$. This study presents an elementary check that will need to be carried out once real collision data are available.

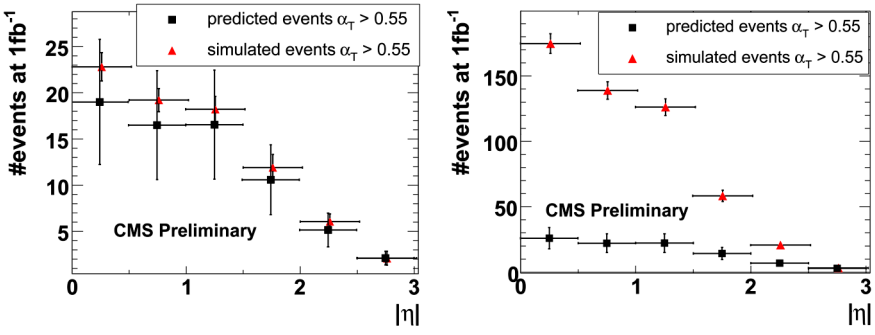

Fig. 4. – (Colour on-line) Comparison of the number of predicted and simulated (measured) events for a luminosity of $1\,\mathrm{fb}^{-1}$ with $\alpha_T > 0.55$. Left: background events only. The black squares indicate the number of predicted events, the number of simulated events is shown as red triangles. Right: background + SUSY LM1 signal. The black squares indicate the number of predicted background events, the total number of observed events is shown as red triangles.

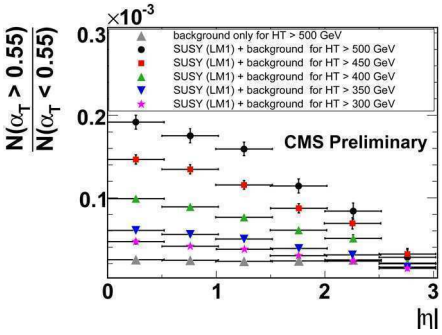

Fig. 5. – R_{α_T} as a function of $|\eta|$ for different HT cuts.

4. – Estimation of $Z \to \nu\nu$ missing energy spectrum from photon + jets events

In the following we present an alternative to the standard approach of using $Z \to \mu\mu$ events for estimation of the background contribution from $Z \to \nu\nu$ events in jets + missing energy searches. We will instead use a sample containing a high-p_T photon produced with high-p_T jets that has larger statistics. The missing energy (MET) spectrum is obtained by removing the identified photon and correcting for residual differences between these events and invisible Z events. Similarly, a sample of W + jets events could be used [6].

The differential production cross-sections for W, Z or photon plus exactly two additional partons, including all contributing subprocesses as evaluated by MadGraph [7], are shown in fig. 6. The production of W bosons is higher by a factor of three at high p_T, as expected, while photon production is within 20% of Z production. The γ-to-Z ratio levels out at a value that is simply predicted by the differences in the couplings of Z's *versus* photons to up-like and down-like quarks. Above $\sim 150\,\text{GeV}$ boson p_T these ratios depend mostly on the electroweak characteristics of the events. Stated another way, the

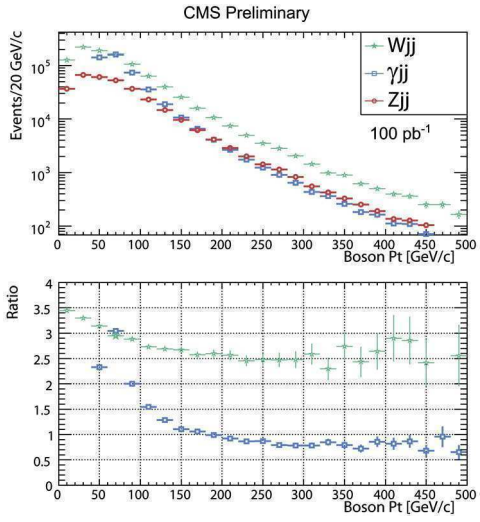

Fig. 6. – Top: differential event yield as a function of boson p_T, for the processes pp → boson + 2 partons (boson = W, γ, or Z) at generator level for $100\,\text{pb}^{-1}$ integrated luminosity. Bottom: ratios of the yields of W relative to Z and γ relative to Z.

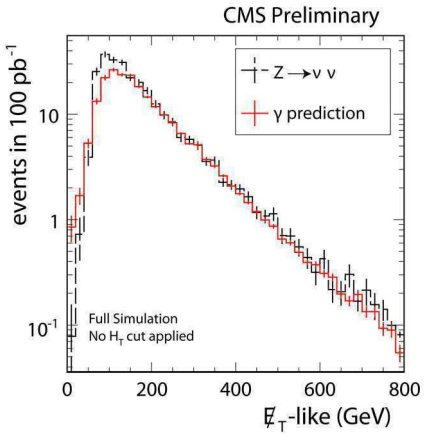

Fig. 7. – Comparison of MET from Z $\to \nu\nu$ events and the "MET-like" quantity from photon + jets events after all corrections.

hadronic parts of these events are not easily predicted, but to good approximation do not depend upon whether the boson is a Z, W, or photon. The ratios are thus relatively robust to variations in selection criteria, such as number and transverse energies of jets. In the absence of large contributions to these samples from new physics, they have the potential to be suitable for predicting the MET spectrum for invisible Z's at high p_{T}.

The Monte Carlo samples used do not take into account theoretical uncertainties such as Q^2 scale variations, and contributions from uncertainties in parton distribution functions. Initial studies indicate that the former can affect the relative normalization of photon+jets to Z+jets events at the $\sim 10\%$ level, while the latter have much smaller impact. The difference due to collinear photon production is expected to be mitigated by isolation requirements. In general there is also a difference in the η distribution of photons relative to that of Z bosons, as a result of different phase space factors for massive Z bosons *versus* massless on-shell photons, and to a lesser extent, due to the different vector and axial couplings. However, at sufficiently high p_{T} the bosons tend to be found in the central region, which significantly mitigates the difference.

Once the photon p_{T} spectrum is measured for events passing the event selection criteria (in this case three jets within $|\eta| < 3$ and with uncorrected $p_{\mathrm{T}} > 180\,\mathrm{GeV}$, $> 110\,\mathrm{GeV}$ and $> 30\,\mathrm{GeV}$, respectively, and an isolated photon with $p_{\mathrm{T}} > 100\,\mathrm{GeV}$), the transverse component of the vector sum of photon E_{T} and event calorimeter MET is computed, and this "MET-like" quantity is corrected for the photon isolation efficiency and the Z $\to \nu\nu$ branching ratio. Taking into account residual differences associated with couplings to quarks, a final correction was calculated via the ratio of Z plus three parton to photon plus three parton generator level events obtained with ALPGEN [5]. The ratio is flat at high E_{T} as expected. The resulting spectrum is found to be in excellent agreement with that of the invisible Z events in the MET region above 200 GeV as seen in fig. 7. For this exercise, all the corrections were evaluated and applied in the barrel and endcap separately. For $100\,\mathrm{pb}^{-1}$, the contribution of Z $\to \nu\nu$ events to the MET $> 200\,\mathrm{GeV}$ region can be estimated with a statistical uncertainty of order 10% while systematic uncertainties obtained via data-driven techniques are expected to be roughly 20%. A more detailed description of how to use photon + jets but and W + jets events to determine the background contribution from Z $\to \nu\nu$ events can be found in [6].

5. – Conclusions

A prospective search for a low-mass SUSY signature with di-jet events has been carried out. In this study two new kinematic variables, α and α_{T} were explored which are very powerful in suppressing the several orders of magnitude larger background from QCD di-jet events without making explicit use of a calorimeter-based missing E_{T} measurement. With the discrimination power of α (α_{T}), several SUSY benchmark points can be discovered with a data sample smaller than $1\,\mathrm{fb}^{-1}$, for which signal-over-background ratios of up to 6 are achieved. Over the past few months the α_{T} method has been further developed and extended to multi-jet events [8]. Furthermore two independent data-driven techniques have been developed for background estimation. By defining signal-depleted and -enriched regions in the leading jet η it was shown that a matrix method can be used to predict the total number of background events in the central η region with $\alpha_{\mathrm{T}} > 0.55$. In an alternative approach that can be used as a cross-check it was demonstrated how to use photon + jets event to determine the dominant $\mathrm{Z} \to \nu\nu$ background.

REFERENCES

[1] Randall L. and Tucker-Smith D., *Phys. Rev. Lett.*, **101** (2008) 221803.
[2] The CMS Collaboration, *CMS Physics Analysis Summary*, CMS PAS SUS-08-005.
[3] Bayatian G. L. *et al.* (The CMS Collaboration), *J. Phys. G*, **34** (2007) 995.
[4] Sjostrand T. *et al.*, *Comput. Phys. Commun.*, **135** (2001) 238.
[5] Mangano M. L., Moretti M., Piccinini F., Pittau R. and Polosa A. D., *JHEP*, **07** (2003) 001.
[6] The CMS Collaboration, *CMS Physics Analysis Summary*, CMS PAS SUS-08-002.
[7] Alwall J. *et al.*, *JHEP*, **0709** (2007) 028.
[8] The CMS Collaboration, *CMS Physics Analysis Summary*, CMS PAS SUS-09-001.

IL NUOVO CIMENTO Vol. 32 C, N. 5-6 Settembre-Dicembre 2009
DOI 10.1393/ncc/i2010-10548-6

Colloquia: LaThuile09

Searches for New Physics at HERA

Y. D. Ri(*) on behalf of the H1 and ZEUS Collaborations
Institute of Particle and Nuclear Studies, KEK - Tsukuba-shi, Japan

(ricevuto il 10 Novembre 2009; pubblicato online il 20 Gennaio 2010)

Summary. — Recent results from searches for new physics at HERA are presented. HERA finished 16 years of successful data taking and both the H1 and ZEUS Collaborations are finalizing analyses based on the full HERA datasets. Possible new phenomena were probed, like quark substructure, new interactions between electrons and quarks and excited states of fermions. The data are also used to investigate rare final states like multi-lepton events at high transverse momentum and events with isolated leptons and missing transverse momentum. A model-independent search for deviations from the standard model in a multitude of event topologies is also presented.

PACS 12.60.-i – Models beyond the standard model.

1. – Introduction

The world's only *ep* collider, HERA, collided an electron or positron beam of 27.5 GeV with a proton beam of 920 GeV (820 GeV until 1997) and yielded the center-of-mass energy of $\sqrt{s} = 318\,\text{GeV}$. The kinematic range of deep inelastic scattering (DIS) measurements was extended by two orders of magnitude in the negative four-momentum transfer squared, Q^2, and the *eq* interaction has been probed at very small distance of about one-thousandth proton size, *i.e.* $\sim 10^{-3}$ fm. Measurements in this domain allow searches for beyond standard model (BSM) phenomena at characteristic mass scales in the TeV range predominantly in the t-channel, which is complementary to s-channel LEP and TeVatron searches.

HERA operation started on summer 1992 and ceased in June 2007. In the 16 years of successful data taking, H1 and ZEUS Collaborations collected data samples with integrated luminosities of $\sim 0.5\,\text{fb}^{-1}$ for each experiment. In this paper, recent results of the BSM searches at HERA from H1 and ZEUS Collaborations utilizing full data sets are presented for model-dependent and -independent searches.

(*) Now at Yamanaka Group, Physics Department, Osaka University, Japan.

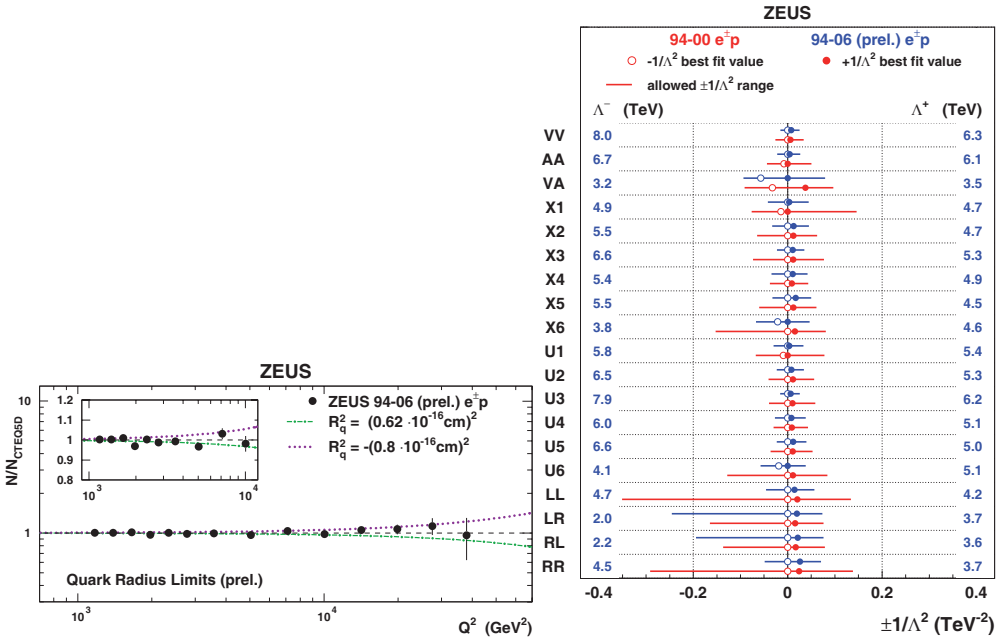

Fig. 1. – Left: measured cross-section as a function of Q^2 normalized to the SM predictions using ZEUS e^+p and e^-p combined data obtained in 1994-2006 running. The results are compared with 95% CL exclusion limits on R_q. The inset shows the comparison in the $Q^2 < 10^4\,\mathrm{GeV}^2$ region with linear scale. Right: confidence intervals of $\pm 1/\lambda^2$ at 95% CL for considered CI models. The numbers at the right (left) margin are the corresponding lower limits on the Λ for positive (negative) couplings and the filled (open) circles correspond to the best-fit values for positive (negative) couplings.

2. – Model-dependent search

2˙1. *Limit on the quark radius.* – From ep collisions of incident e beam energy of $\sim 200\,\mathrm{MeV}$ on fixed proton in 1956, the proton was found to be not a point-like particle and its root-mean-square radii of charge and magnetic moment were measured. Since HERA serves as a giant electron-microscope, analogous search for quark substructure was performed.

If the quark charge is distributed over finite spatial size, R_q, the measured DIS cross-section deviates from the SM as

$$\frac{\mathrm{d}\sigma}{\mathrm{d}Q^2} = \left(\frac{\mathrm{d}\sigma}{\mathrm{d}Q^2}\right)_{\mathrm{SM}} \left(1 - \frac{R_q^2}{6}\right)^2, \tag{1}$$

where the electron is assumed to be point-like. As shown in fig. 1 (left), no deviation was found up to the highest Q^2 region, accessible at HERA. The H1 and ZEUS Collaborations set limits on R_q as

$$\text{ZEUS:} R_q < 0.62 \times 10^{-3}\,\mathrm{fm}, \tag{2}$$

$$\text{H1:} R_q < 0.74 \times 10^{-3}\,\mathrm{fm}. \tag{3}$$

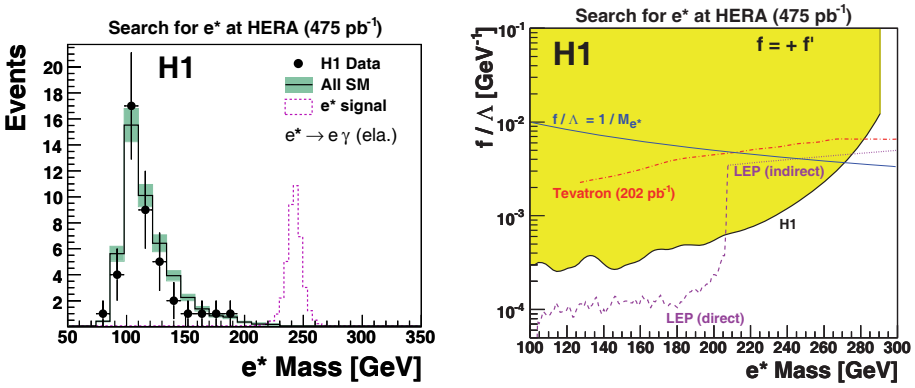

Fig. 2. – Left: invariant mass distribution of the $e^\star$ candidates in the elastic search channel. Data points are compared with the SM prediction drawn as histogram. The band of the SM shows the quadrature sum of model uncertainties and experimental systematic errors. The dashed line represents the reconstructed $e^\star$ distribution of $M_{e^\star} = 240\,\text{GeV}$ with an arbitrary normalisation. Right: mass-dependent exclusion limit on the coupling f/Λ at 95% CL with the assumption $f = +f'$. Limits obtained at LEP and TeVatron are overlaid for comparison. The curve $f/\Lambda = 1/M_{e^\star}$ is also indicated.

2˙2. *Search for the contact interactions.* – Searches of deviations from the SM at high Q^2 can be performed with a more general approach. New interactions between e and q at the energy scale higher than the center-of-mass energy may interfere with the SM processes and modify the cross-section as a function of Q^2. Such physics processes are modeled as an effective four-fermion contact interaction (CI) in their low-energy limit, in analyogy to Fermi's weak-interaction theory.

The amplitudes describing CI interactions are proportional to the ratio of a coupling strength (g) and an energy scale of new physics (Λ) as $\pm g^2/\Lambda^2$. The convention $g^2 = 4\pi$ is adopted here. Various models with different chiral structure of the CI were considered to take into account distinct interference effects with the SM processes.

Both H1 and ZEUS Collaborations used their DIS data at high Q^2 to search for the CI and found that the data agree well with the SM within statistical errors. Thus, limits were derived for each considered model as

(4) ZEUS 1994–2006 data: $\Lambda > 2.0$–$8.0\,\text{TeV}$,

(5) H1 1994–2000 data: $\Lambda > 1.6$–$5.5\,\text{TeV}$.

Figure 1 (right) shows the result from ZEUS at 95% CL for models with different chiral structure. By including high-statistics data taken after 2000, results are clearly improved.

2˙3. *Searches for excited fermions.* – An attractive explanation of three-family structure and mass hierarchy of fermions are provided by models assuming that quark and leptons are built from more fundamental particles. In such models, fermions can be excited to a higher-mass scale and decay into the stable state via the emission of gauge bosons such as γ, Z and W. Thus, the search strategy is to reconstruct the invariant mass of fermion and boson.

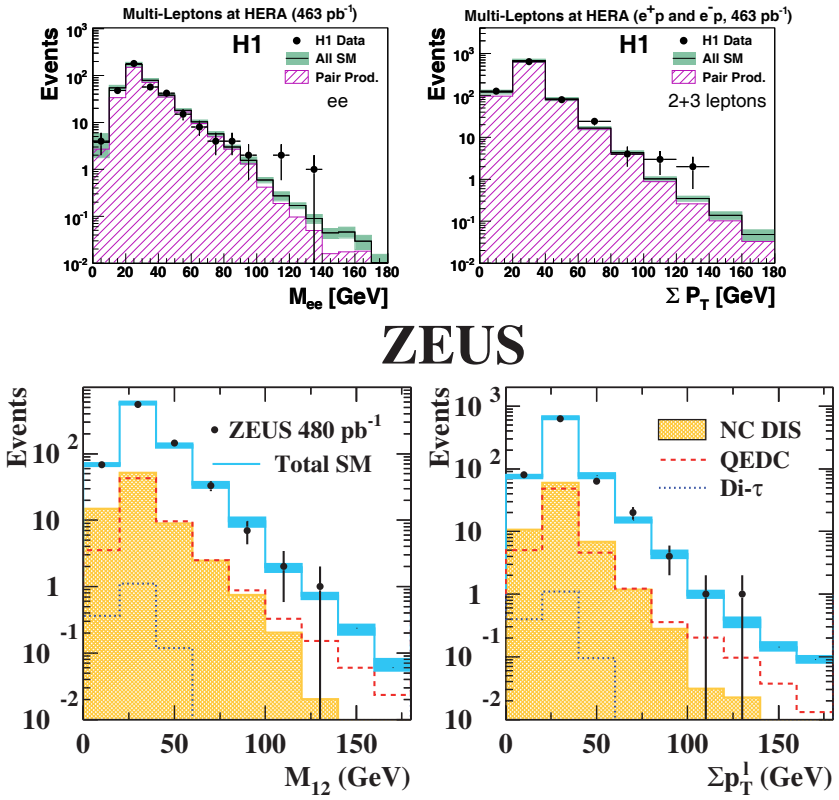

Fig. 3. – The results of multi-lepton search performed by the H1 (upper plots) and ZEUS (bottom plots) Collaborations. Left: invariant mass distribution of ee (combined e and μ) channel(s) from H1 (ZEUS) experiment. Right: scalar sum of the transverse momentum for combined e and μ channels. Data points are compared with the SM expectation shown as histograms.

H1 searched for excited fermions in the following decay channels: $q^\star \to q\gamma, qZ, q'W$; $e^\star \to e\gamma, eZ, \nu W$ using full data set of $\sim 0.5\,\mathrm{fb}^{-1}$; and $\nu^\star \to \nu\gamma, \nu Z, eW$ using electron data of $\sim 0.2\,\mathrm{fb}^{-1}$([1]); where subsequent hadronic or leptonic decays of W and Z are considered [1].

Figure 2 (left) shows, as an example, the invariant mass distribution of the $e^\star$ candidates in the elastic search channel. Including also other decay channels, observed distributions were in agreement with the SM expectation and no evidence for a resonance was found. Therefore, limits were set based on gauge mediated model in which the production cross sections depend on coupling constants, f, f' and f_s associated to the gauge groups $SU(2)$, $U(1)$ and $SU(3)$, respectively, and the compositeness scale, Λ. Once the relationships between the couplings are fixed, the decay branching ratios to different gauge bosons are determined and the cross-section depends only on the ratio f/Λ for given invariant mass of excited fermion.

([1]) Since electron data have a much higher sensitivity than positron data for the $\nu^\star$ search.

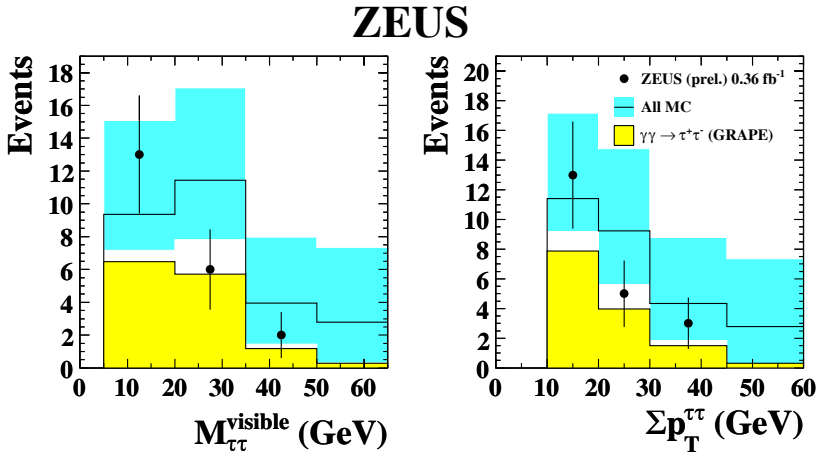

Fig. 4. – Distributions of the visible invariant mass and the scalar sum of the transverse momentum of di-τ from ZEUS experiment. Data points are compared with the SM expectation as given by the histogram in which uncertainty is represented as error bands.

Figure 2 (right) shows, as an example, the upper limit on the f/Λ as a function of the excited fermion mass for $e^\star$. The HERA limits show unique sensitivity in the high-mass region beyond the LEP center-of-mass energy. With the conventional assumption $f/\Lambda = 1/M_{f^\star}$, masses of excited fermions are excluded below 252 GeV for $q^\star$, 272 GeV for $e^\star$ and 213 GeV for $\nu^\star$ at 95% CL. For the $q^\star$ search, the limits on f/Λ are derived under the assumptions of $f = f'$ and $f_s = 0$ where the latter condition yields results complementary to searches at the TeVatron using $f_s \neq 0$.

3. – Model-independent search

Signature based searches for any deviations from the SM were performed in various topologies. This approach does not rely on any *a priori* definition of new physics and thus provides another way to find possible BSM phenomena complementary to searches presented above.

3˙1. *Multi-lepton events.* – Multi-lepton events at HERA are produced mainly in the Bethe-Heitler reaction $\gamma\gamma \to l^+l^-$ where the photons are radiated from the initial q and e. Such events are sensitive to the BSM phenomena, because the SM cross-section is low at high transverse momenta, where new physics is expected to show up.

Both the H1 and ZEUS Collaborations have finished the search for e and μ channels using their full data set of $\sim 0.5\,\text{fb}^{-1}$ [2]. Two-lepton and three-lepton topologies: ee, $e\mu$, $\mu\mu$, eee and $e\mu\mu$, were considered. The three-lepton events included the scattered electron detected in the central detector. Figure 3 (left) shows the invariant mass distribution for ee channel from H1 (upper plot) and combined e and μ channels from ZEUS (bottom plot). Figure 3 (right) shows the scalar sum of the transverse momentum for the combined e and μ channels from H1 (upper plot) and ZEUS (bottom plot). Agreement with the SM was found up to the high-mass region $M > 100\,\text{GeV}$. A combination of H1 and ZEUS results is ongoing.

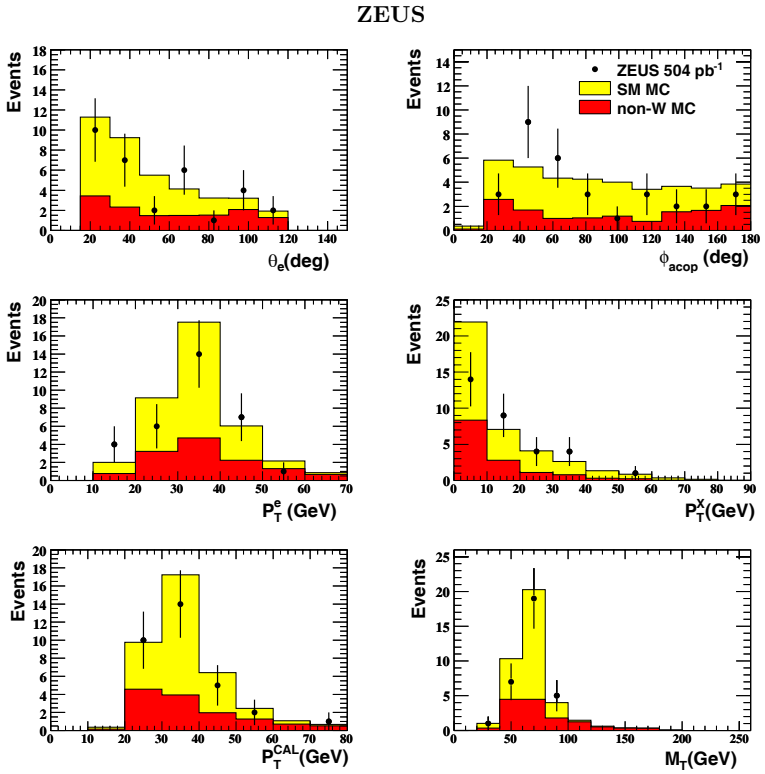

Fig. 5. – Distributions of the isolated e events from ZEUS. Shown are the polar angle of e (θ_e), the acoplanarity angle between e and hadronic particles ($\phi_{\rm acop}$), the p_T of e (p_T^e), the p_T of hadronic particles (p_T^X), the missing transverse momentum measured by the calorimeter ($p_T^{\rm CAL}$), and the transverse mass for W bosons (M_T). The data points are compared with the SM expectation represented as histograms in which all SM processes and non-W production processes are shown separately.

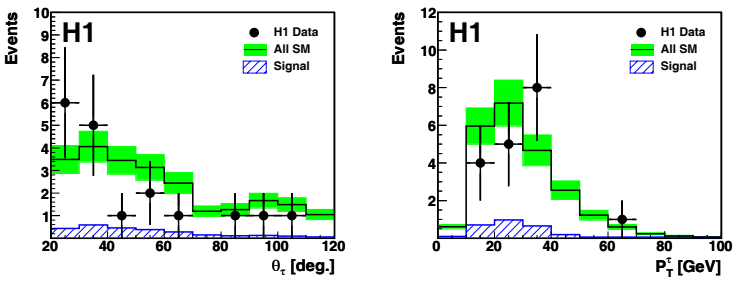

Fig. 6. – Distributions of the isolated τ events from H1. Shown are the polar angle and the p_T of the τ-jet candidates. The data points are compared with the SM expectation represented as histograms with total uncertainty shown as the shaded band.

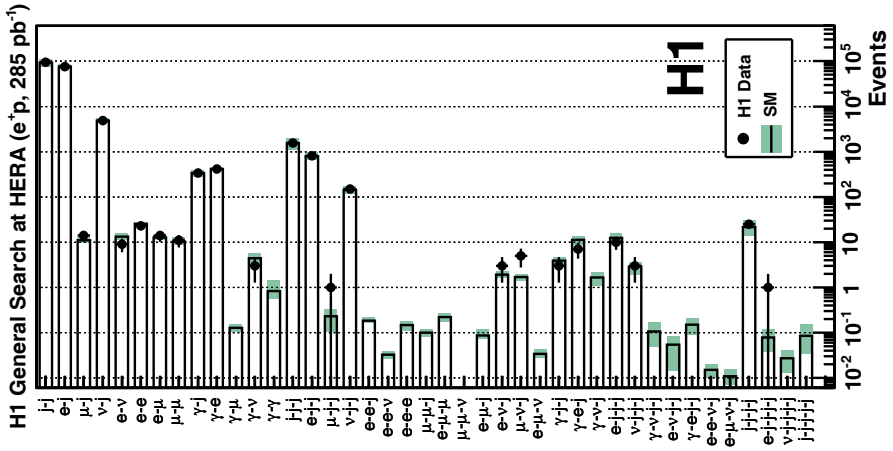

Fig. 7. – Event yield comparison between observed data events and the SM expectation for each considered event topologies for e^+p collisions. The error bands on the SM predictions represent quadrature sum of model uncertainties and experimental systematic errors.

ZEUS also performed a search for events containing two high transverse momentum τ using $0.36\,\mathrm{fb}^{-1}$. Since the branching fraction of τ leptons to hadronic particles is greater than 60%, the hadronic decay channel was used to reconstruct the τ lepton. It is a challenging analysis to discriminate hadron jets produced by τ from huge backgrounds of other QCD induced jets. Properties of hadron τ jets, *i.e.* low mass, low multiplicity and pencil-like jet, were utilized. Figure 4 shows the visible invariant mass distribution and the scalar p_T sum of di-τ for selected events. A total of 21 data events were selected with a 48% purity while $27.3^{+5.8}_{-5.2}$ SM events were expected. Thus, consistent results with the SM were obtained.

3˙2. *Events with isolated lepton and missing transverse momentum.* – Events with isolated e or μ and missing p_T are studied by H1 and ZEUS experiments using their full $e^{\pm}p$ data sets [3]. Within the SM, such types of events are very rare and mainly originate from the single W boson production.

Figure 5 shows several distributions for e channel from ZEUS. The data were well described by the SM predictions. The same agreement was observed for the μ channel. Results obtained by H1 also show agreement with the SM.

Since no significant deviation from the SM was found, the total single W production cross section has been measured by each ZEUS and H1 experiment as

$$\text{ZEUS:}\quad 0.89^{+0.25}_{-0.22}(\text{stat.}) \pm 0.10(\text{sys.})\text{pb}, \tag{6}$$

$$\text{H1:}\quad 1.14 \pm 0.25(\text{stat.}) \pm 0.14(\text{sys.})\text{pb}, \tag{7}$$

in agreement with the SM prediction of $1.3 \pm 0.2\,\mathrm{pb}$.

In addition, H1 also performed the τ channel which complements the analysis of the e and μ channels to test lepton universality as predicted by the SM. The τ lepton was identified in the hadronic decay mode. Figure 6 shows the distributions of the τ-jet candidates for the polar angle and the p_T. 18 data events were observed in agreement with the SM expectation of 23.2 ± 3.8.

3˙3. *General search.* – A general search for events containing high-p_T objects such as: e, μ, j (jet), γ or ν, in the final state, was performed by H1 using full $e^{\pm}p$ data sets [4]. Events with at least two objects with $p_T > 20\,\text{GeV}$ were selected. According to the number and types of objects, the selected events were classified into mutually exclusive channels.

Data events were observed in 27 different final states and events containing up to 5 high-p_T objects were found. Event yields were compared between data and the SM expectation for each topology, as shown in fig. 7 for e^+p collisions. To search for regions with deviations from the SM, kinematical distributions of the invariant mass and the scalar sum of p_T were systematically investigated. In addition, angular distributions and energy sharing among reconstructed object were studied. A good agreement with the SM was found for all topologies under study. Therefore, the measurement demonstrated a good understanding of high-p_T SM phenomena observed at HERA.

4. – Conclusions and prospects

HERA finished 16 years of successful data taking and about $1\,\text{fb}^{-1}$ of data were taken by H1 and ZEUS Collaborations. These data provides a unique and complementary sensitivity to new physics compared to other collider experiments. In this paper, recent results from searches for new physics at HERA were presented for model-dependent and -independent analyses. A good agreement with the SM has been confirmed.

Searches at HERA are being finalized for each H1 and ZEUS experiment using full data sets, and to gain higher sensitivity, the combination of results by two experiments is also ongoing.

REFERENCES

[1] Aaron F. D. *et al.* (H1 Collaboration), *Phys. Lett. B*, **663** (2008) 382; **666** (2008) 131; **678** (2009) 335.
[2] Aaron F. D. *et al.* (H1 Collaboration), *Phys. Lett. B*, **668** (2008) 268; Chekanov S. *et al.* (ZEUS Collaboration), *Phys. Lett. B*, **672** (2009) 106.
[3] Aaron F. D. *et al.* (H1 Collaboration), *Eur. Phys. J. C*, **64** (2009) 251.
[4] Aaron F. D. *et al.* (H1 Collaboration), *Phys. Lett. B*, **674** (2009) 257.

IL NUOVO CIMENTO Vol. 32 C, N. 5-6 Settembre-Dicembre 2009
DOI 10.1393/ncc/i2010-10523-3

Colloquia: LaThuile09

Status of the ATLAS detector and its readiness for early BSM Physics

C. Gemme on behalf of the ATLAS Collaboration
INFN, Sezione di Genova - Genova, Italy

(ricevuto il 10 Novembre 2009; pubblicato online il 15 Gennaio 2010)

Summary. — The general status of the ATLAS experiment at the LHC is reviewed. Particular emphasis is given to the results from the *in situ* commissioning of the detector using calibration and cosmics data taking. The commissioning period has prepared ATLAS for the first beam injection in September 2008. Some results from the beam experience will be described. Finally, given the present knowledge of the detector performance, the readiness of the detector for early studies of Physics beyond the Standard Model will be discussed.

PACS 29.40.Gx – Tracking and position-sensitive detectors.
PACS 29.40.Vj – Calorimeters.

1. – Introduction

The Large Hadron Collider (LHC) at CERN will soon start its activity with unprecedent high energy and luminosity: bunches of 10^{11} protons will collide with a frequency of 25 ns to provide 14 TeV proton-proton collisions at a design luminosity of $10^{34}\,\mathrm{cm}^{-2}\,\mathrm{s}^{-1}$. ATLAS is one of the general-purpose detectors built to probe the interactions of protons. The high interaction rates, radiation flux, particle multiplicities and energies, as well as precision measurements required for successful physics studies have set important constraints on its design. A detailed and complete description of the detector as installed in the cavern can be found in [1].

The tracker (or ID, Inner Detector) is immersed in a 2 T solenoidal field. Because of the expected high track density at nominal luminosity, and in order to achieve excellent vertex and momentum measurements, the central tracker consists of two parts: high-resolution semiconductor Pixel and microstrip (SCT, or SemiConductor Tracker) detectors in the inner part and a Transition Radiation Tracker (TRT), made of straw tubes, in the outer part of the tracking volume.

Calorimeters cover the range $|\eta| < 4.9$, using different techniques suited to the wildly varying requirements of the physics processes of interest and of the radiation environment over this large η-range. High-granularity liquid-argon (LAr) electromagnetic sampling

calorimeters, with excellent performance in terms of energy and position resolution, surround the tracker and cover the pseudorapidity range $|\eta| < 3.2$. The hadronic calorimetry in the range $|\eta| < 1.7$ is provided by a scintillator-tile calorimeter (Tile). In the end-caps ($|\eta| > 1.5$), LAr technology is also used for the hadronic calorimeters. The LAr forward calorimeters provide both electromagnetic and hadronic energy measurements and extend the pseudorapidity coverage to $|\eta| = 4.9$.

The calorimeters are surrounded by the muon spectrometer. The air-core toroid system, with a long barrel and two inserted end-cap magnets, generates a strong bending power in a large volume (1.5 to 5.5 Tm for $|\eta| < 1.4$ and 1 to 7.5 Tm in the region $1.6 < |\eta| < 2.7$) within a light and open structure. Multiple scattering is minimized and excellent muon momentum resolution is achieved with three layers of high-precision tracking chambers. Trigger chambers with a time resolution of 1.5–4 ns complete the functionality of the muon spectrometer.

The Level-1 trigger system uses a subset of the detector information coming from the muon spectrometer and the calorimeters to reject uninteresting events, reducing the data rate to ≈ 75 kHz (limited by the bandwidth of the readout system, which is upgradeable to 100 kHz). Two subsequent levels of trigger using more accurate information coming from the full detector reduce the final data taking to ≈ 200 Hz from the initial 40 MHz rate.

The complete operation of the ATLAS detector has been exercised during several periods of combined cosmics data-taking. They allow for basic detector studies like noise measurements, identification of hot or dead channels and malfunctioning services. Additionally, the trajectories of cosmic-ray particles can be used to align the many components of the detector and to time-in all subdetectors.

The subdetectors' readiness for beam in autumn 2008 will be summarized in the following sections to illustrate the success of the commissioning period, while sect. **5** illustrates the results obtained during the circulation of single beam in September 2008. Finally, sect. **6** describes examples of potential early discoveries in physics beyond the Standard Model with an integrated luminosity of $\approx 200\,\mathrm{pb}^{-1}$, expected to be collected in the first year of operation.

2. – Installation and commissioning of the Inner Detector

The Inner Detector installation started in August 2006 with the SCT and TRT barrels and was completed with the Pixel detector in June 2007.

However, waiting for the complete connection of services (including cables and pipes for the cooling system), the very fist commissioning of the Pixel and SCT detectors started in April 2008. The evaporative cooling plant suffered a major failure of its compressors at the beginning of May 2008 and its repair and cleaning were then in the critical path for the closure of the full detector. In early August 2008 a successful bake-out of the beam pipe was however possible, the latter being particularly critical because it requires the evaporative cooling system fully operational to protect the Pixel layers from overheating. In spite of the little time left, the ID was ready for beams in September, with 96% of the Pixel modules, 99% of the barrel and 97% of the end-cap SCT modules and 98% of the TRT.

After the LHC incident, a very intense commissioning period started with the purpose of calibrating the detector. In autumn, the ID was included in a long combined data-taking period, collecting 7.6 million tracks.

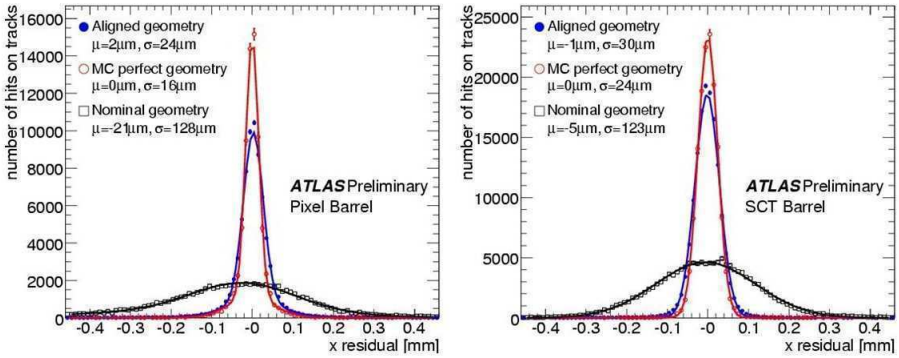

Fig. 1. – Residual distribution in x, the precision coordinate, integrated over all hits-on-tracks in the Pixel (left) and SCT (right) barrel before alignment and using a preliminary aligned geometry. As a comparison, prediction by Monte Carlo study with perfect detector alignment is shown. The residual is defined as the measured hit position minus the expected hit position from the track extrapolation. Tracks are selected to have $p_{\mathrm{T}} > 2\,\mathrm{GeV}$ and to go through the Pixel innermost layer.

One of the most important commissioning goals with the cosmics data is the alignment of the detector in order to achieve the designed tracking accuracy. Alignment is performed in steps of increasing number of degrees of freedom: subdetectors with respect to each other first, then layers, then individual modules. The distribution of residuals from straight track fitting for the barrel region of the Pixel and SCT subsystems before and after alignment is shown in fig. 1. The obtained alignment accuracy is close to the expected performance predicted by the Monte Carlo study with perfect detector alignment. Residual resolutions indicate remaining misalignment of $O(10\,\mu\mathrm{m})$.

3. – Installation and commissioning of the calorimeters

The LAr and Tile calorimeters have undergone a very long period of commissioning in ATLAS with cosmics since 2006, when the installation of the detectors was completed. After the detector closure in summer 2008, the LAr calorimeters had only 0.02% of isolated dead channels, plus some 0.8% of dead read-out channels, including one missing (out of eight) hadronic end-cap low-voltage power supplies which failed after closure of the detector. The Tile calorimeter operated with 0.2% isolated dead cells and 2 out of 256 sectors off due to power supply problems. The performance of the Lar and Tile calorimeters in terms of energy response, noise and timing has been extensively studied and calibration was performed.

4. – Installation and commissioning of the muon spectrometer

In the fall of 2008, the status of the muon spectrometer was the following: less than 1% precision chambers with a problem, and more than 99% of the alignment system working. For the trigger chambers all TGC were working, and three of the 16 RPC sectors were still under final timing adjustments.

The primary performance goal for the muon spectrometer is to obtain a standalone transverse-momentum resolution of approximately 10% for 1 TeV tracks, which translates

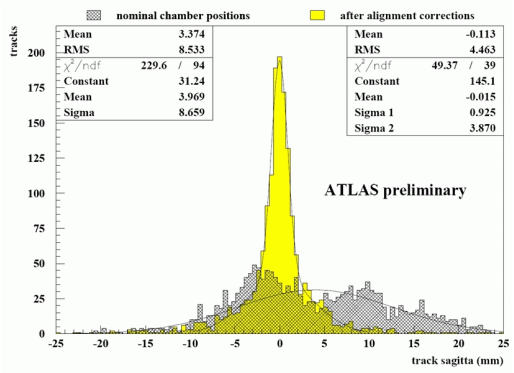

Fig. 2. – (Colour online) "Track" sagittas (the distance in the precision coordinate of the EM segment from the line joining the EI-EO segments) before (gray) and after (yellow) applying alignment corrections determined by the optical alignment of the end-caps. The "after alignment corrections" yellow histogram has a mean value compatible with zero, and a width of 1.5 mm, compatible with the expected multiple-scattering width, thus proving that the optical alignment can provide the required accuracy on the chambers alignment.

into a sagitta along the z (beam) axis of about 500 μm to be measured with a resolution of $\approx 50\,\mu$m. As the single chamber resolution is $\approx 40\,\mu$m, the precision on the relative position of chambers must be $\approx 40\,\mu$m. To achieve this accuracy on the chambers position, an optical alignment system of 12 thousand sensors tracks any displacement with great precision and provides an initial absolute precision. Figure 2 shows that the achieved accuracy is close to the required one in the end-caps, that had a better starting point thanks to a survey done during commissioning period. For the barrel, on the other hand, the present accuracy is still poor ($\approx 200\,\mu$m in large barrel sectors, ≈ 1 mm in small barrel sectors) and track alignment will be needed to get more precise initial alignment constants.

5. – Operation with circulating beam

The circulation of a single-beam in September 2008 has allowed for additional detector performance tests, mainly timing and energy calibration. The first beam passed through ATLAS on September 10^{th} during the official LHC start-up day. Then, during several days, proton bunches containing $2{\cdot}10^9$ protons of 450 GeV energy were being injected into the LHC ring and circulated without acceleration. ATLAS was running with the Pixel detector and SCT barrel off; SCT end-caps, forward calorimeters and muon chambers at reduced HV for safety reasons.

Two types of events were recorded: *beam-splash* events illuminating the full detector and generated by proton collisions with the collimators, located 140 m upstream from ATLAS, closed for this purpose; *beam-halo* events with circulating beams, typically with lower-energy deposition depending on beam conditions.

Events were triggered by the Minimum Bias Trigger Scintillators (MBTS), placed on the front face of the end-cap calorimeter cryostats and by the beam pick-up detectors (BPTX) positioned in the beam pipe 175 m upstream of the interaction point. Other ATLAS Level-1 trigger components were active but not used to select events.

In *beam-splash* events many particles hit the entire detector at the same time. Therefore it is possible to check and eventually correct the time calibration in the full detector

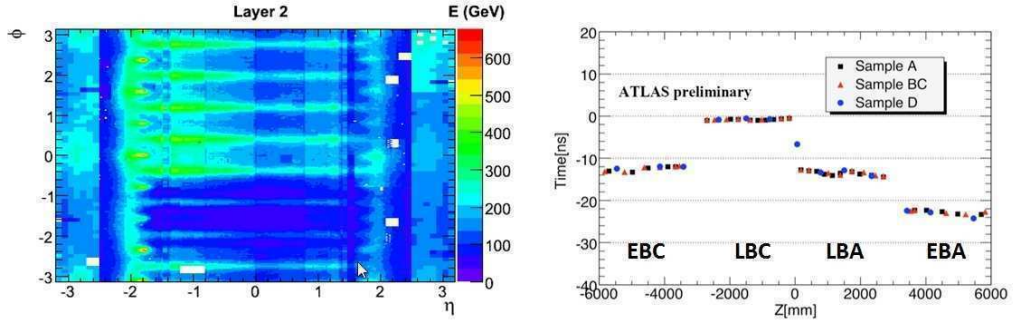

Fig. 3. – (Colour online) On the left, the 2-dimensional plot presents, for layer 2 of the LAr Calorimeter, the accumulated energy per cell over 100 *beam-splash* events (Beam 2, incoming from negative η). To select the signal, only cells with $E > 5$*noise are summed. Zones without signal correspond to problematic channels which have been masked using the database. On the right plot, timing of TileCal signals recorded with single beam data on Sept. 10, 2008 (Beam 2, incoming from negative z). The average time over all cells with the same ϕ (azimuth) coordinate is shown as a function of the z-coordinate (along beam axis), for all three radial samplings (represented with different colors). Timing corrections based on laser data and ToF assuming tracks parallel to the z-axis have been applied. The visible discontinuities at $z = 0$, ± 3000 mm are due to the uncorrected time differences between the four TileCal partitions.

with very few events and to time-in the ATLAS trigger systems. Figure 3 (left) shows the energy deposition in the LAr calorimeter in *beam-splash* events: the 8-fold structure in ϕ due to the end-cap toroid material in front of calorimeters, for particles coming from outside the detector, as well as a lower response at the bottom of the detector ($\phi = -\pi/2$), due to additional material (mainly detector support structure) are clearly visible. Moreover a reduced flux, and correspondingly reduced energy deposition, is seen along the beam direction (η).

Muon energy deposition from *beam-halo* events has been used to check timing in the Tile calorimeter. Figure 3 (right) shows the timing of signals in the detector after the time-of-flight correction. Once these corrections have been applied, time dispersion in each partition is ≈ 2 ns with a residual offset (to be fixed) between partitions within 1 BC. This demonstrates that the time equalization performed with laser calibration data was extremely accurate.

6. – Readiness for BSM physics

During the LHC run in 2009/2010, it is expected that the integrated luminosity will be $\approx 200\,\mathrm{pb}^{-1}$ [2, 3]. The data collected will be initially extremely useful for the purpose of improving trigger performance, timing, alignment and in general, the detector performance [4]. In this perspective, Standard Model benchmark signals will be used not only as a measurement by itself but also to understand the detector complexity. A window on an energy scale never reached before will be opened and a search for deviations from Standard Model predictions will potentially allow observation of extraordinary new physics signatures.

In the following paragraphs, two examples of BSM measurements are reported. They represent certainly a small fraction of the measurements that will be possible. They have

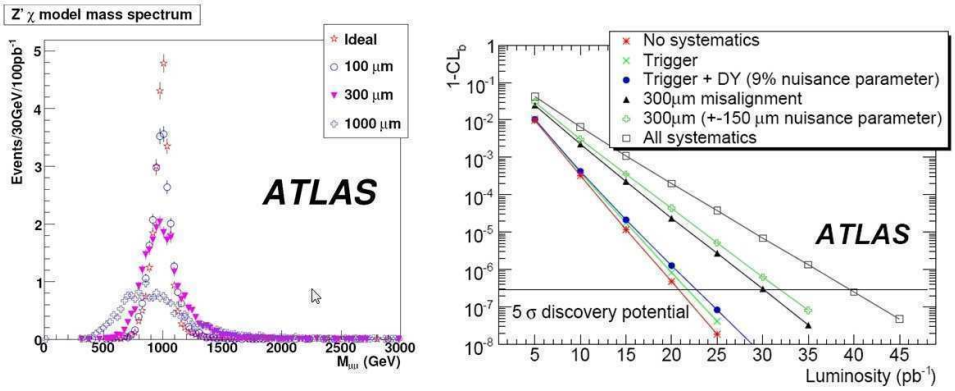

Fig. 4. – Left: reconstructed invariant mass of the Z'_χ model for different misalignment scenarios and an integrated luminosity of $100\,\mathrm{pb}^{-1}$. In the ideal case the position of the chambers in the muon spectrometer is known to be about $40\,\mu$m. Right: results of 1-CL$_b$ for $m = 1\,\mathrm{TeV}$ Z'_χ bosons. The horizontal line indicates the 1-CL$_b$ value corresponding to 5σ discovery.

been chosen because they are relatively less sensitive to the large detector performance uncertainties expected in the first period of data-taking([1]).

6˙1. *Dilepton resonances at high mass*. – New heavy states forming a resonance decaying into opposite sign dileptons are predicted in many extensions of the Standard Model. Due to the simplicity of the final state, the dilepton channel is considered a potential discovery channel with early ATLAS data [4]. The strictest direct limits on the existence of heavy neutral particles come from direct searches at the Tevatron; the highest excluded mass is currently almost 1 TeV. The LHC with a center-of-mass energy of 14 TeV should ultimately increase the search reach for new heavy particles to the 5–6 TeV range.

In the first year of data taking, even with a small integrated luminosity and a not perfectly aligned detector, discovery of new particles with mass of $\approx 1\,\mathrm{TeV}$ will still be possible: Figure 4 shows the necessary integrated luminosity needed to discover a resonance at 1 TeV mass in the dimuon channel. Since at large p_T an important contribution to the muon momentum resolution comes from the alignment of the muon spectrometer, the effect of different misalignment scenarios is also reported in the plots. Misalignment leads to a broadening of the peak (left) and a larger luminosity will be needed to achieve the 5σ discovery (right). However the amount of integrated luminosity needed for discovery ranges from 20 to $40\,\mathrm{pb}^{-1}$.

6˙2. *SUSY*. – SUperSYmmetry (SUSY) is one of the favoured theories for physics beyond the Standard Model. The basic prediction of SUSY is the existence, for each Standard Model particle, of a corresponding superpartner, with spin differing by half a unit. In order for the theory to conserve baryonic and leptonic quantum numbers, a new multiplicative quantum number, R-parity, is introduced. The consequences of

([1]) All the plots shown assume a center-of-mass energy of 14 TeV. However in 2009/2010 run, LHC will not exceed a center-of-mass energy of 10 TeV. Moving from 14 TeV to 10 TeV requires about twice as much data for equivalent sensitivity.

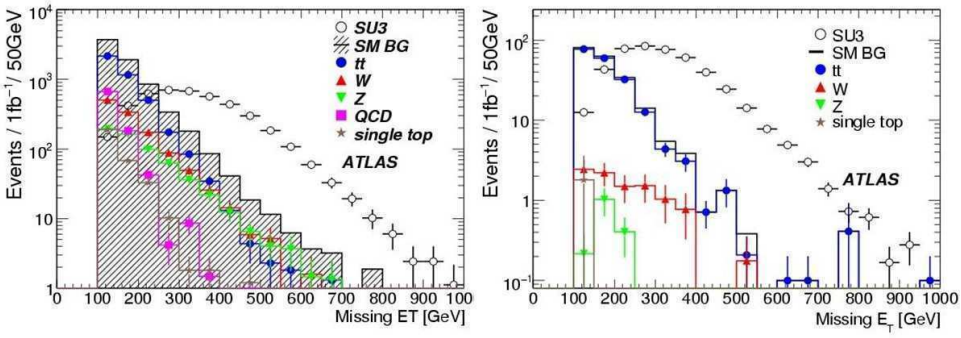

Fig. 5. – (Color online) $E_{\mathrm{T}}^{\mathrm{miss}}$ for the background processes and for a SUSY benchmark model ($SU3$) in the zero-lepton mode (left) and in the one-lepton mode (right) for an integrated luminosity of $1\,\mathrm{fb}^{-1}$. Events are selecting by requiring at least four high-energy jets, $E_{\mathrm{T}}^{\mathrm{miss}} > 100\,\mathrm{GeV}$ and zero or one, respectively, isolated lepton. The black circles show the SUSY signal. The hatched histogram shows the sum of all Standard Model backgrounds; also shown in different colours are the various components of the background.

R-parity conservation are that supersymmetric particles must be produced in pairs and that at the end of their decay chain, the lightest SUSY particle (LSP), stable and weakly interacting, will remain. Therefore, events from R-parity conserving SUSY models are generally characterized by the presence of many hard jets, and sometimes leptons, coming from the decay cascade down to the LSP, as well as a large amount of missing transverse energy ($E_{\mathrm{T}}^{\mathrm{miss}}$) due to the LSP which will escape direct detection in the ATLAS volume.

Figure 5 shows the $E_{\mathrm{T}}^{\mathrm{miss}}$ distribution for events passing the selection criteria in the two inclusive channels with one-lepton or zero-lepton requirement. The one-lepton search mode is expected to play a major role in the SUSY search, especially at the beginning, since the requirement of an isolated lepton will be effective in suppressing QCD background. However the zero-lepton mode has the best estimated 5σ reach.

Even if the signal is enhanced with respect to background, it will clearly be crucial to understand the Standard Model background and the detector effects on the tails of the $E_{\mathrm{T}}^{\mathrm{miss}}$ distribution. In real data there will be sources of fake $E_{\mathrm{T}}^{\mathrm{miss}}$ which are not fully modeled in MC simulations such as, for example, the mis-modeling of material distributions and instrumental failures. As the details of these fake $E_{\mathrm{T}}^{\mathrm{miss}}$ sources are understood with time, analysis techniques will be developed to minimize their associated effect on the backgrounds while maintaining high selection efficiencies for signals with genuine missing energy. While it is difficult to predict in advance the exact sources of mis-modeled fake $E_{\mathrm{T}}^{\mathrm{miss}}$, it is nevertheless possible to simulate hardware failures in the Monte Carlo samples and evaluate their effects. An example is a study based on samples with simulated dead regions of the calorimeter. Figure 6 (left) shows the large $E_{\mathrm{T}}^{\mathrm{miss}}$ tails seen when holes in calorimeter coverage have been introduced. The EM Fraction Method suppresses events with large fake $E_{\mathrm{T}}^{\mathrm{miss}}$ by finding the closest calorimeter jet to the $E_{\mathrm{T}}^{\mathrm{miss}}$ direction vector and looking at its EM fraction (ratio between the electromagnetic energy and the sum of electromagnetic and hadronic energy). Figure 6 (right) shows the EM fraction distributions: small EM fractions are due to a dead LAr EM calorimeter crate, whereas large EM fractions are due to a dead hadron calorimeter crate. The fake $E_{\mathrm{T}}^{\mathrm{miss}}$ can be partially suppressed by requiring the EM fraction to be in a window from 0.40 to 0.96.

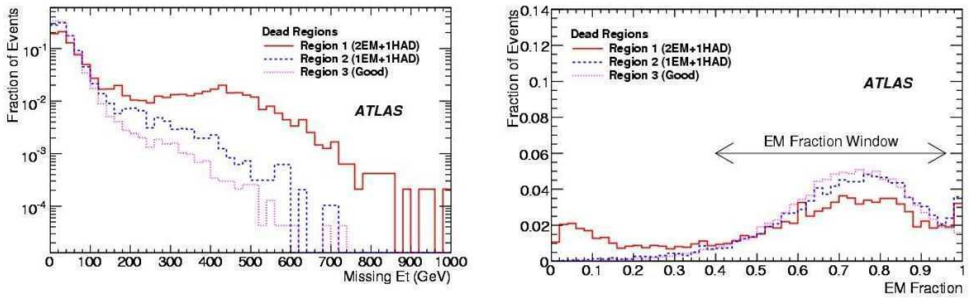

Fig. 6. – $E_{\mathrm{T}}^{\mathrm{miss}}$ (left) and EM fraction (right) in a high-p_T ($560 < p_T < 1120\,\mathrm{GeV}$) g+jet MC sample with killed cells. Based on the location of these hardware failures the calorimeter is divided into three regions of fake $E_{\mathrm{T}}^{\mathrm{miss}}$: Region 1 with EM endcap and hadronic endcap problems, Region 2 with EM barrel problems and Region 3 with no problems.

Even if SUSY particles searches require a good knowledge of the detector performance, a mass reach of $\approx 400\,\mathrm{GeV}$ should be possible with less than $100\,\mathrm{pb}^{-1}$ of good data, even at a center-of-mass energy of 10 TeV. This would compete with the actual limit of 400 GeV obtained by Tevatron experiments. Running at lower energy ($< 8\,\mathrm{TeV}$) would suppress considerably the sensitivity.

7. – Conclusions

The installation of the ATLAS detector has been completed in 2008. It was ready for the first beam injection, thanks to the commissioning effort performed with the use of cosmics data. A few percent of the subdetector channels were not operational and, when possible, they are being repaired. During the long winter 2009 shutdown, problems and weaknesses that have been identified will be fixed. As the plan is to run during 2009/2010 for an extremely long run of almost ten months, this preparation has to be very thorough, considering that access and possible maintenance will be limited during that time. In order to be ready for collisions and for measurement of SM and possibly new physics, global commissioning of the ATLAS detector will restart with cosmics data taking, with all subdetectors turned on, two months before the beam injection.

REFERENCES

[1] Aad G. *et al.* (ATLAS Collaboration), *JINST*, **3** (2008) S08003.
[2] Myers S. and Zimmermann F., *LHC Performance Workshop, Chamonix 2009* (CERN-ATS) 2009-001, pp. 318-323.
[3] Ferro-Luzzi M., *LHC Performance Workshop, Chamonix 2009* (CERN-ATS) 2009-001, pp. 273-281.
[4] Aad G. *et al.* (ATLAS Collaboration), *Expected Performance of the ATLAS Experiment, Detector, Trigger and Physics*, CERN-OPEN-2008-020, Geneva, 2008.

IL NUOVO CIMENTO Vol. 32 C, N. 5-6 Settembre-Dicembre 2009
DOI 10.1393/ncc/i2010-10552-x

Colloquia: LaThuile09

Study of multi-muon events at CDF

F. Happacher on behalf of the CDF Collaboration
Laboratori Nazionali di Frascati dell'INFN - Frascati, Italy

(ricevuto il 10 Novembre 2009; pubblicato online il 20 Gennaio 2010)

Summary. — We report the observation of anomalous multimuon events produced at the Fermilab Tevatron collider and recorded by the CDF II detector. In a data set acquired with a dedicated dimuon trigger and corresponding to an integrated luminosity of $2100\,\mathrm{pb}^{-1}$, we isolate a sample of events in which the identified muons have extremely large impact parameters. Within these events, the muon multiplicity is also anomalously large. We are unable to explain these events through standard model processes in conjunction with our current understanding of the CDF II detector, trigger and event reconstruction. In addition to describing the analysis, we explore a conjecture of new physics that is manifestly suggested by the topology and kinematical properties of these events.

PACS 13.85.-t – Hadron-induced high- and super-high-energy interactions (energy $> 10\,\mathrm{GeV}$).
PACS 14.65.Fy – Bottom quarks.
PACS 14.80.-j – Other particles (including hypothetical).

This study reports the observation of an anomalous muon production in $p\bar{p}$ interactions at $\sqrt{s} = 1.96\,\mathrm{TeV}$. The analysis was motivated by the presence of several inconsistencies that affect or affected the $b\bar{b}$ production at the Tevatron: a) the ratio of the observed $b\bar{b}$ correlated production cross-section to the exact next-to-leading-order (NLO) QCD prediction [1] is 1.15 ± 0.21 when b quarks are selected via secondary vertex identification, whereas this ratio is found to be significantly larger than two when identifying b-quarks through their semileptonic decays [2]; b) sequential semileptonic decays of single b-quarks are supposedly the main source of dileptons with invariant mass smaller than that of a b-quark, but the observed invariant mass spectrum is not well modeled by the standard model (SM) simulation of this process [3]; and c) the value of $\bar{\chi}$, the average time-integrated mixing probability of b flavored hadrons derived from the ratio of muon pairs from b and $\bar{b}$ quarks semileptonic decays with opposite- and same-sign charge, is measured at hadron colliders to be larger than that measured by the LEP experiments [4, 5].

This analysis extends a recent study [6] by the CDF Collaboration which has used a dimuon data sample to measure the correlated $\sigma_{b\to\mu,\bar{b}\to\mu}$ cross-section. After briefly describing that study, it is shown that varying the dimuon selection criteria isolates

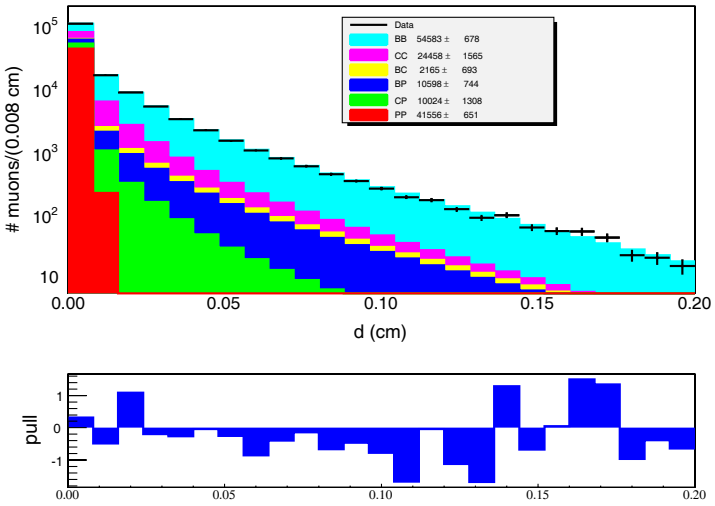

Fig. 1. – Impact parameter distribution of muons contributed by different physics processes.

a sizable, but unexpected background that contains muons with an anomalous impact parameter([1]) distribution. Further investigation shows that a smaller fraction of these events also has anomalously large track and muon multiplicities. We are unable to account for the size and properties of these events in terms of known SM processes, even in conjunction with possible detector mismeasurement effects, and we offer a conjecture of new physics that models this contribution.

The CDF II detector [7] consists of a magnetic spectrometer, based on a 96-layer drift chamber, surrounded by electromagnetic and hadron calorimeters and muon detectors. Precision impact parameter and vertex determinations are provided by a trio of tracking devices collectively referred to in this paper as the "SVX". The SVX is composed of eight layers of silicon microstrip detectors ranging in radius from 1.5 to 28 cm in the pseudorapidity region $|\eta| < 1$.

The study presented here, which is further detailed in ref. [8], uses the same data and Monte-Carlo–simulated samples, and the same analysis methods described in ref. [6]. We use events containing two central ($|\eta| < 0.7$) muons, each with transverse momentum $p_T \geq 3\,\mathrm{GeV}/c$, and with invariant mass larger than $5\,\mathrm{GeV}/c^2$. In ref. [6], the value of $\sigma_{b\to\mu,\bar{b}\to\mu}$ is determined by fitting the impact parameter distribution of these primary muons with the expected shapes from all known sources. To ensure an accurate impact parameter determination, ref. [6] uses a subset of dimuon events in which each muon track is reconstructed in the SVX with hits in the two inner layers and in at least four of the inner six layers. The data are nicely described by a fit with contributions from the following QCD processes: semileptonic heavy flavor decays, prompt quarkonia decays, Drell-Yan production, and instrumental backgrounds from hadrons mimicking the muon signal. Using the fit result, shown in fig. 1, ref. [6] reports $\sigma_{b\to\mu,\bar{b}\to\mu} = 1549 \pm 133\,\mathrm{pb}$ for muons with $p_T \geq 3\,\mathrm{GeV}/c$ and $|\eta| \leq 0.7$.

That result is in good agreement with theoretical expectations as well as with analo-

([1]) The impact parameter is defined as the distance of closest approach of a track to the primary event vertex in the transverse plane with respect to the beamline.

gous measurements that identify b-quarks via secondary vertex identification [9,10]. However, it is also substantially smaller than previous measurements of this cross-section [11, 12], and raises some concern about the composition of the initial dimuon sample prior to the SVX requirements. The tight SVX requirements used in ref. [6] select events in which both muons arise from parent particles that have decayed within a distance of $\simeq 1.5$ cm from the $p\bar{p}$ interaction primary vertex in the plane transverse to the beam line. Using Monte-Carlo–generated samples of events that are passed through the CDF detector simulation, we estimate that approximately 96% of the dimuon events contributed by known QCD processes satisfy this latter condition. Since the events selected in [6] are well described by known QCD processes, we can independently estimate the efficiency of the tight SVX requirements. Using control samples of data from various sources and the sample composition determined by the fit to the muon impact parameter distribution, we estimate that $(24.4 \pm 0.2)\%$ of the initial sample should survive the SVX tight requirements, whereas only $(19.30 \pm 0.04)\%$ actually do. This suggests the presence of an unexpected background that has been suppressed when making the tight SVX requirements. The size of this unexpected dimuon source can be determined by subtracting from the total number of dimuon events, prior to any SVX requirements, the expected contribution from the known QCD sources, which is estimated as the number of events surviving the tight SVX requirements divided by the efficiency of that selection. In a data set corresponding to an integrated luminosity of $742\,\mathrm{pb}^{-1}$, 143743 dimuon events survive the tight SVX cuts. After dividing by the 24.4% efficiency, 589111 ± 4829 QCD events are expected in the initial dimuon sample, whereas 743006 are observed. The difference, 153895 ± 4829 events, is comparable in magnitude to the expected dimuon contribution from $b\bar{b}$ production, 221564 ± 11615. This estimate assumes the unexpected source of dimuon events is completely rejected by the tight SVX requirements.

More typically CDF analyses use a less stringent set of SVX criteria and only require tracks to have hits in at least three of the eight SVX layers. This standard SVX selection accepts muons from parent particles with decay lengths as long as 10.6 cm. Applying the standard SVX selection reduces the estimated size of the unknown dimuon source by a factor of two, whereas 88% of the known QCD contribution is expected to survive.

Table I summarizes these estimates of the size of this unexpected source of dimuons, which will also be referred to as the ghost contribution, for various sets of SVX requirements. In this table and throughout this paper the expected contribution from known QCD sources, referred to as QCD contribution, will be estimated from the sample of dimuons surviving the tight SVX requirements and properly accounting for the relevant SVX efficiencies using the sample composition from the fits of ref. [6]. We choose to proceed in this way since the tight SVX sample provides a well-understood sample [6]. The ghost contribution will always be estimated from the total number of events observed in the data after subtracting the expected QCD contribution. We also give the event yields separately for the subset of events in which the dimuons have opposite-sign (OS) and same-sign (SS) charge. The ratio of OS to SS dimuons is approximately 2:1 for QCD processes but is approximately 1:1 for the ghost contribution. At this stage it is worth commenting further on the set of inconsistencies mentioned above. The general observation is that the measured $\sigma_{b\to\mu,\bar{b}\to\mu}$ increases as the SVX requirements are made looser and is almost a factor of two larger than that measured in [6] when no SVX requirements are made [12]. As mentioned above, the magnitude of the ghost contribution is comparable to the $b\bar{b}$ contribution when no SVX selection is made and in combination would account for the measurement reported in [12]. Similarly, for the standard SVX criteria, the magnitude of the ghost contribution, when added to the expected $b\bar{b}$ contri-

TABLE I. – *Number of events that pass different SVX requirements. Dimuons are also split into pairs with opposite* (OS) *and same* (SS) *sign charge.*

Type	No SVX	Tight SVX	Standard SVX
Total	743006	143743	590970
Total OS		98218	392020
Total SS		45525	198950
QCD	589111 ± 4829	143743	518417 ± 7264
QCD OS		98218	354228 ± 4963
QCD SS		45525	164188 ± 2301
Ghost	153895 ± 4829	0	72553 ± 7264
Ghost OS		0	37792 ± 4963
Ghost SS		0	34762 ± 2301

bution of 194976 ± 10221 events, coincides with the cross-section measurement reported in [11] and the $\bar{\chi}$ value reported in [4] since these measurements use similar sets of silicon criteria. Moreover, as demonstrated in [8], when applying the tight SVX criteria to initial muons, the invariant mass spectrum of combinations of an initial muon with an additional accompanying muon is well described by known QCD sources and is dominated by sequential semileptonic heavy flavor decays. In contrast, without any SVX requirement the invariant mass spectrum cannot be modeled with the SM simulation and the inconsistencies at low invariant mass reported in [3] are reproduced. Thus, this unknown source of dimuon events seems to offer a plausible resolution to these long-standing inconsistencies related to $b\bar{b}$ production and decay. The remainder of this paper is dedicated to a further exploration of these events.

The general nature of the anomalous events can be characterized by four main features. The impact parameter distribution of the initial muon pair cannot be readily understood in terms of known SM processes. In small angular cones around the initial muons the rate of additional muons is significantly higher than that expected from SM processes. The invariant mass of the initial and additional muons looks different from that expected from sequential semileptonic decays of hadrons with heavy flavor. The impact parameter distribution of the additional muons has the same anomalous behavior as the initial muons. We will discuss each of these features in turn.

As shown in fig. 2, muons due to ghost events have an impact parameter distribution that is completely different from that of muons due to QCD events.

A number of potential background sources have been evaluated. The one expected to contribute significantly arises from in-flight-decays of pions and kaons. Based upon a generic QCD simulation, we predict a contribution of 57000 events [8], 44% and 8% of which pass the standard and tight SVX selection, respectively. The uncertainty of this prediction is difficult to assess, but, as shown by the insert in fig. 2, in-flight decays alone cannot account for the shape of the muon impact parameter distribution in ghost events. A minor contribution of K^0_S and hyperon decays in which the punchthrough of a hadronic prong mimics a muons signal has been also investigated [8]. Secondary interactions in the tracking volume are also possible candidates, and more difficult to quantify. The possibility of instrumental effects, trigger and reconstruction biases have been investigated in detail in ref. [8]. For example, we have verified the soundness of

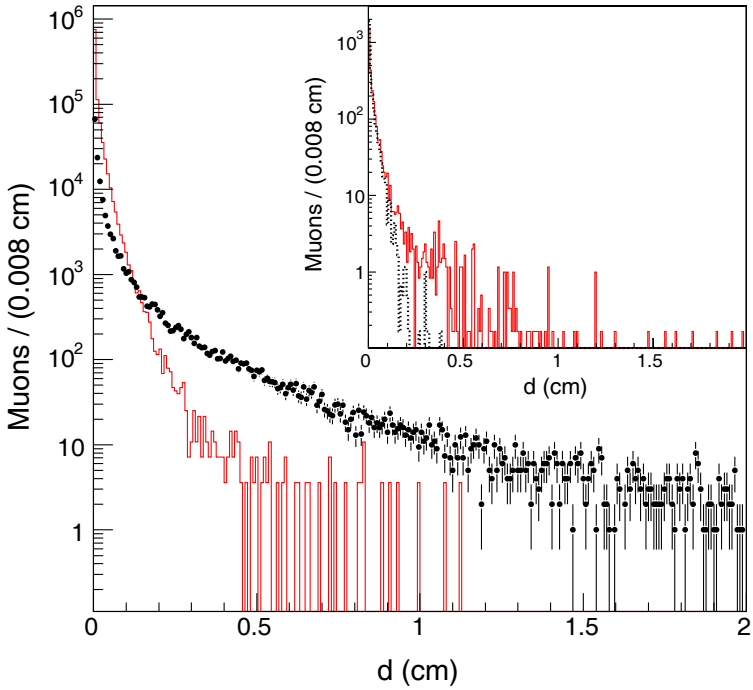

Fig. 2. – Impact parameter distribution of muons contributed by ghost (•) and QCD (histogram) events. Muon tracks are selected with standard SVX requirements. The detector resolution is $\simeq 30\,\mu$m, whereas bins are $80\,\mu$m wide. In the insert, we show the distribution of (histogram) simulated muons that pass the same analysis selection as the data and arise from the in-flight-decays of pions and kaons produced in a QCD heavy flavor simulation. The dashed histogram shows the impact parameter of the parent hadrons.

large impact parameter tracks by measuring the lifetime of K^0_S decays reconstructed in the same data set used for this analysis. As shown in We search QCD and ghost events that contain a pair of initial muons that pass our analysis selection (without any SVX requirement) for additional muons with $p_T \geq 2\,\mathrm{GeV}/c$ and $|\eta| \leq 1.1$. We have the following motivations: a) events acquired because of in-flight decays or secondary interactions are not expected to contain an appreciable number of additional muons; b) QCD events that might appear in the ghost sample because of not-yet-understood detector malfunctions should not contain more additional leptons than QCD events with well reconstructed initial dimuons; and c) we want to investigate if the anomaly reported in ref. [3] is also related to the presence of the unexpected background. According to the simulation [8], additional muons arise from sequential decays of single b hadrons. In addition, one expects a contribution due to hadrons mimicking the muon signal. In the data, 9.7% of the dimuon events contain an additional muon (71835 out of 743006 events). The contribution of events without heavy flavor, such as all possible conventional sources of ghost events mentioned above, is depressed by the request of an additional muon. For example, in events containing an $\Upsilon(1S)$ or K^0_S candidate, that are included in the dimuon sample, the probability of finding an additional muon is $(0.90 \pm 0.01)\%$ and

$(1.7 \pm 0.8)\%$, respectively. However, the efficiency of the tight SVX selection in dimuon events that contain additional muons drops from 0.1930 ± 0.0004 to 0.166 ± 0.001. This simple observation anticipates that a fraction of ghost events contains more additional muons than QCD data.

This paragraph summarizes a detailed study of the rate and kinematic properties of events that contain at least three muons reported in ref. [8]. This study uses a data set of larger integrated luminosity that corresponds to 1131090 ± 9271 QCD and 295481 ± 9271 ghost events. Reference [8] shows that the rate and kinematics of three-muon combinations are correctly modeled by the QCD simulation only if the two initial muons are selected with the tight SVX requirement. Muon pairs due to b sequential decays peak at small invariant masses and small opening angles. The distributions of analogous pairs in the unexpected background have a quite similar behaviour. However, combinations of initial and additional muons in ghost events have a smaller opening angle and a smaller invariant mass than those from sequential b decays [8]. Therefore, the study of ghost events is further restricted to muons and tracks contained in a cone of angle $\theta \leq 36.8^\circ$ ($\cos\theta \geq 0.8$) around the direction of each initial muon. As reported in ref. [8], less than half of the OS and SS muon combinations in ghost events can be accounted for by fake muons, and ghost events are shown to contain a fraction of additional real muons (9.4%) that is four times larger than that of QCD events (2.1%). Reference [8] investigates at length the possibility that the predicted rate of fake muons is underestimated. The fraction of additional real muons in QCD and ghost events is verified by selecting additional muons with $p_T \geq 3\,\mathrm{GeV}/c$ and $|\eta| \leq 0.7$. In this case, because of the larger number of interaction lengths traversed by hadronic tracks, the fake rate is negligible [6]. This study, in which the muon detector acceptance is reduced by a factor of five, shows that the rate of such additional muons is $(0.40 \pm 0.01)\%$ in QCD and $(1.64 \pm 0.08)\%$ in ghost events.

Figure 3 shows the two-dimensional distribution of the impact parameter of an initial muon *versus* that of all additional muons in a $\cos\theta \geq 0.8$ cone around its direction. The impact parameter distribution of the additional muons is found to be as anomalous as that of primary muons. However, the impact parameters of the additional and initial muons are weakly correlated (the correlation factor is $\rho_{d_{0p}d_{0s}} = 0.03$).

For comparison, fig. 4 shows that the impact parameter distribution of additional muons in QCD events is not anomalous at all.

Taken as a whole, it is difficult to reconcile the rate and characteristics of these anomalous events with expectations from known SM sources. Although one can never rule out the possibility that these data could be at least partially explained by detector effects not presently understood, in the following we present additional properties of the ghost sample along with a phenomenological conjecture of new physics that is based on the characteristics of the ghost events. This conjecture is possibly one of many, but yields a number of additional predictions that are successfully tested with the data.

Figure 5 (a) shows the distribution of the number of muons found in a $\cos\theta \geq 0.8$ cone around a primary muon in ghost events. In the plot, an additional muon increases the multiplicity by 1 when of opposite and by 10 when of same sign charge as the initial muon.

Leaving aside the case in which no additional muons are found, an increase of one unit in the muon multiplicity corresponds in average to a population decrease of approximately a factor of seven. This factor is very close to the inverse of the $\tau \to \mu$ branching fraction (0.174) multiplied by the 83% efficiency of the muon detector, and makes it hard to resist the interpretation that these muons arise from τ decays with a kinematic acceptance

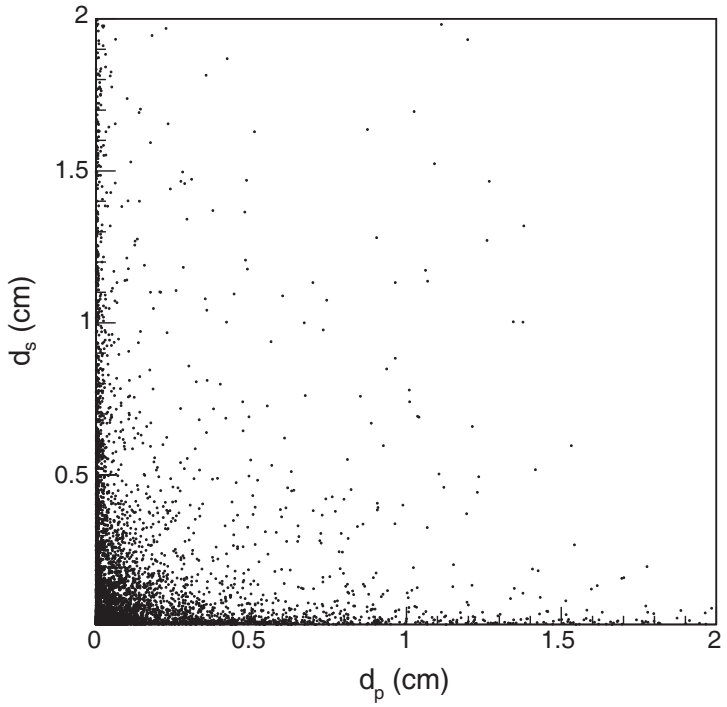

Fig. 3. – Two-dimensional distribution of the impact parameter of an initial muon, d_{0p}, *versus* that, d_{0s}, of additional muons in ghost events. Muons are selected with standard SVX requirements.

close to unity. The multiplicity distribution corrected for the fake muon contribution [8] is shown in fig. 5 (b). The fake contribution is evaluated on a track-by-track basis using the probability that pions from D^0-mesons from B-hadron decays mimic a muon signal. Unfortunately, the multiplicity distribution of muons and tracks contained in a 36.8° cone around the direction of such D^0-mesons does not have the high multiplicity tail of ghost events. In the D^0 control sample, we do not observe any dependence of the fake rate on the track and muon multiplicity, but we also cannot rule out a drastic increase of the fake probability per track in events with multiplicities much larger than those of QCD standard processes. A study based on higher quality muons [8] does not show any evidence of that being the case. We use Monte Carlo pseudoexperiments to model the shape of this multiplicity distribution. The pseudoexperiments generate 4 $\tau^+ + 4\ \tau^-$ leptons, decay them to muons with a 17.4% probability, and identify them with the 83% efficiency of the muon detector. The pseudoexperiment result is shown in fig. 5 (b). The pseudoexperiment distribution is normalized to the integral of the data for multiplicity bins higher than 10, but also models data with smaller multiplicities.

The comparison of the muon multiplicity distribution in ghost events with the toy-simulation suggests that approximately 13200 events contain 8 τ leptons inside a $\cos\theta \geq 0.8$ cone. One possible interpretation is that they are 8-τ decays of objects h_1 relatively light with respect to the transverse momentum with which they are produced. If the interpretation is correct, one also expects that 36.8° cones corresponding to de-

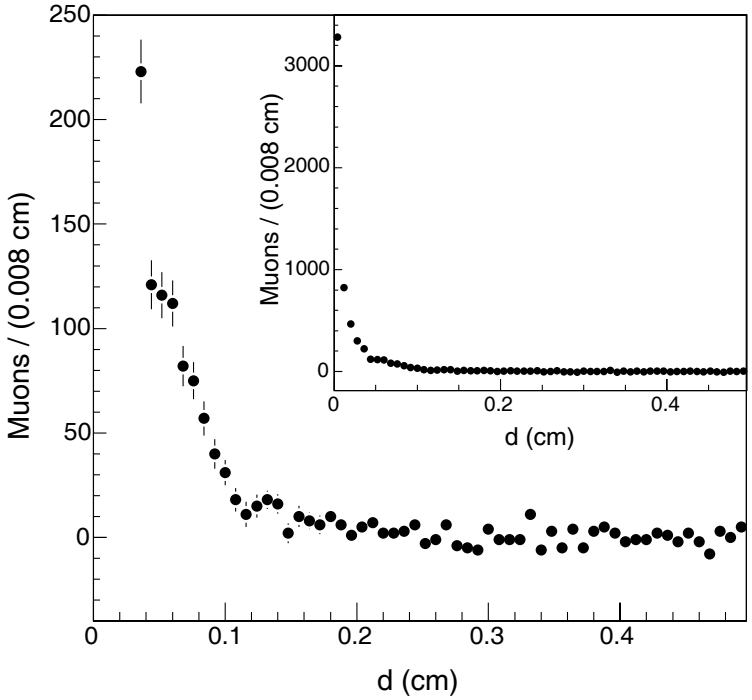

Fig. 4. – Exploded impact parameter distribution of additional muons in QCD events. The entire distribution is shown in the insert. Muons are selected without any SVX requirements.

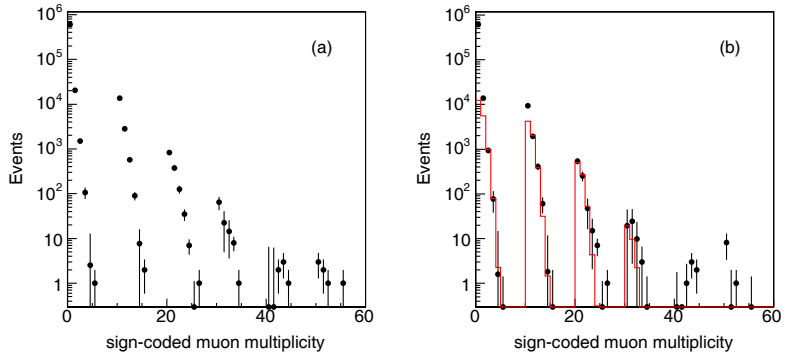

Fig. 5. – Multiplicity distribution of additional muons found in a $\cos\theta \geq 0.8$ cone around the direction of a primary muon before (a) and after (b) correcting for the fake muon contribution. An additional muon increases the multiplicity by 1 when it has opposite and by 10 when it has same sign charge as the initial muon. The solid line is the prediction of the toy-simulation of a decay into eight τ-leptons (see text).

cays of h_1 states with large transverse momentum contain approximately 9.5 tracks with $p_T \geq 2\,\mathrm{GeV}/c$. In order to account for the detector response, we compare the data to simulated decays of h_1 states with large transverse momentum that for convenience were generated by using the fictitious process $p\bar{p} \to H \to h_1 h_1$, where H is a scalar particle, $m_H = 115\,\mathrm{GeV}/c^2$, and $m_{h_1} = 15\,\mathrm{GeV}/c^2$ [8]. The QCD contribution is minimized by the request of at least three muons in a 36.8° cone. The asymptotic value of the average track multiplicity in the data brings support to the conjecture of a $h_1 \to 8\tau$ decay initially suggested by the muon multiplicity distribution.

In conclusion, we report the observation of anomalous muon production in $p\bar{p}$ collisions at $\sqrt{s} = 1.96\,\mathrm{TeV}$. This unknown source of dimuon events seems to offer a plausible resolution to long-standing inconsistencies related to $b\bar{b}$ production and decay. We offer a phenomenological conjecture of new physics based on the anomalous characteristics of these events. The conjecture is intended to provide a basis for a possible theoretical model if the observed anomalies will continue to remain unexplained in terms of SM processes in conjunction with not yet understood detector effects.

REFERENCES

[1] Mangano M. L., Nason P. and Ridolfi G., *Nucl. Phys. B*, **373** (1992) 295.
[2] Happacher F. *et al.*, *Phys. Rev. D*, **73** (2006) 014026; Happacher F., *Status of the Observed and Predicted $b\bar{b}$ Cross Section at the Tevatron*, `www-conf.kek.jp/dis06/doc/WG5/hfl20-happacher.ps`, to appear in the *Proceedings of DIS 2006, Tsukuba, Japan*.
[3] Apollinari G. *et al.*, *Phys. Rev. D*, **72** (2005) 072002.
[4] Acosta D. *et al.*, *Phys. Rev. D*, **69** (2004) 012002.
[5] Yao W.-M. *et al.*, *J. Phys. G*, **33** (2006) 1.
[6] Aaltonen T. *et al.*, *Phys. Rev. D*, **77** (2008) 072004.
[7] Acosta D. *et al.*, *Phys. Rev. D*, **71** (2005) 032001; Blair R. *et al.*, Fermilab Report No. FERMILAB-Pub-96/390-E (1996); Hill C. S. *et al.*, *Nucl. Instrum. Methods Phys. Res. A*, **530** (2004) 1; Cabrera S. *et al.*, *Nucl. Instrum. Methods Phys. Res. A*, **494** (2002) 416; Ashmansas W. *et al.*, *Nucl. Instrum. Methods Phys. Res. A*, **518** (2004) 532.
[8] Aaltonen T. *et al.*, *Observation of anomalous multi-muon events produced in $p\bar{p}$ interactions at $\sqrt{s} = 1.96$ TeV*, arXiv:0810.5357[hep-ex].
[9] Acosta D. *et al.*, *Phys. Rev. D*, **69** (2004) 072004.
[10] Shears T., *Charm and Beauty Production at the Tevatron*, *Proceedings of the International Europhysics Conference on High Energy Physics, PoS (HEP2005)*, 072 (2005).
[11] Abe F. *et al.*, *Phys. Rev. D*, **55** (1997) 2546.
[12] Abbott B. *et al.*, *Phys. Lett. B*, **487** (2000) 264.

IL NUOVO CIMENTO Vol. 32 C, N. 5-6 Settembre-Dicembre 2009
DOI 10.1393/ncc/i2010-10545-9

Colloquia: LaThuile09

Non-supersymmetric extensions of the SM

A. Pomarol

Departament de Física and IFAE, Universitat Autònoma de Barcelona - 08193 Bellaterra Barcelona, Spain

(ricevuto il 10 Novembre 2009; pubblicato online il 20 Gennaio 2010)

Summary. — We discuss the implications of having the Higgs particle arising as a composite pseudo-Goldstone boson, either from a new strong interacting sector at the TeV, or from the 5th-component of a gauge field in extra dimensional models.

PACS 12.60.-i – Models beyond the standard model.

1. – Introduction

In most people's mind the Minimal Supersymmetric Standard Model (MSSM) is the ideal (and, sometimes, unique) candidate for physics beyond the SM, becoming, in recent times, the new orthodoxy. The MSSM gained its present status after LEP1, where electroweak precision tests (EWPT) of the SM left behind its main competitors such as Technicolor models. A manifestation of this strong feelings towards supersymmetric theories, that arose around the end of the nineties, can be found in Veneziano's summary talk at the SUSY 98 conference in Paris: "To conclude, the score on precision tests puts the MSSM first, with the SM itself a close second. Technicolour theories appear to lag far behind and ... there is not much else in the race."

But after LEP1, it came LEP2 and Tevatron II and those expectations for finding supersymmetric states or, at least, the light MSSM Higgs at energies $\sim 100\,\mathrm{GeV}$, were not met. At present we can claim that almost any MSSM model must be tuned at the 1–10% in order to pass all the experimental constraints.

Due to this new situation the obvious question is, in the words of Veneciano, is there something else in the "race"? In the last 10 years several new solutions to the hierarchy problem have been proposed: Large extra dimensions, Randall-Sundrum models, ... In this talk I will review the only one that, I think, can provide some clues on the origin of electroweak symmetry breaking: the idea that the Higgs arises as a Pseudo-Goldstone Boson (PGB) of a new sector. This scenario is clearly inspired by QCD where one observes that the (pseudo) scalar states, *e.g.*, the pions, are the lightest particles. We understand the reason for this: the pions are Goldstone states arising from the chiral symmetry breaking $SU(2)_L \times SU(2)_R \to SU(2)_V$ of QCD. This symmetry, however,

is explicitly broken by the gauging of electromagnetism and the quark masses, giving to the pions a mass around 100 MeV, smaller than the masses of the other resonances $m_\rho \sim 1\,\text{GeV}$. In other words, the pion mass is protected by the global chiral symmetry under which the pion fields shift, and, for this reason, is smaller than the QCD mass gap.

Could we have a similar scenario in which the Higgs arises as a PGB [1]? This could work in the following way [2]. Let us assume that at the TeV we have a new strong sector whose global symmetry-breaking pattern, induced by the condensation of some composite scalar operator, is $SO(5) \to SO(4)$. This implies that the Goldstone spectrum corresponds to a unique weak-doublet, the Higgs. Two bonus come automatically from this idea. First, the electroweak interactions and the SM fermion couplings to the Higgs must explicitly break the global $SO(5)$-symmetry that protects the Higgs mass. Correspondingly, a Higgs potential will be induced at the one-loop level. The heaviness of the top plays here an important role. Since fermionic loops give negative contributions to the Higgs mass, a vacuum expectation value (VEV) will be induced for the Higgs, breaking the electroweak symmetry (EWSB). Therefore, this scenario predicts inevitably EWSB, as observed in nature. Second, the VEV of the Higgs will be of the order of the decay constant of the PGB, f, that can be smaller than the mass of the other resonances of the model. For $f \sim 500\,\text{GeV}$, that is roughly the lowest value allowed by EWPT [2], one obtains that the lightest resonance has a mass around 2 TeV, out of the reach of past colliders (*e.g.*, LEP and Tevatron). This could explain the absence of new states at any collider before the LHC. Finally, the physical Higgs mass arises in these models at the one-loop level and therefore is predicted to be around 100–200 GeV.

2. – Unraveling the composite nature of the Higgs

If the Higgs arises as a PGB from a strongly interacting sector, we expect it will show properties of a composite particle. In an ideal collider we could easily differentiate between an elementary and a composite Higgs, in the same way as we do with pions: we probe them with photons at large virtual momentum q^2; if the electromagnetic form factor stays (almost) constant for large q^2, we claim to see an elementary state; if it drops to zero, we claim we have a composite state. Although the Higgs does not couple at tree-level to photons, we could probe it with the reaction $Wh \to Wh$ where the large q^2 must go from the incoming W to the ingoing h. If we could measure this cross-section at very high energies, we could easily determine the nature of the Higgs. Nevertheless, in a real collider (LHC) we cannot probe the Higgs form factor at sufficiently high energies to see whether it goes or not to zero. We must look therefore for other signatures of compositeness.

We can get again some inspiration from QCD. We know that at small q^2, the form factor of the pion goes approximately as $F(q^2) \sim 1 - q^2/m_\rho^2$, so deviations from 1 arise suppressed by the mass of the lowest QCD resonance, $m_\rho \sim 1\,\text{GeV}$. Nevertheless, we have other types of pion interactions that are not suppressed by m_ρ but by f, the decay constant of the pion. For example, the amplitude of $\pi\pi \to \pi\pi$ grows with the energy as E^2/f^2. For $f \sim 100\,\text{MeV}$, this process seems to be enhanced by a factor 10 as compare to deviations on the gauge form factors.

For a composite PGB Higgs we also expect this kind of behavior arising from the low-energy operator $\mathcal{O}_H \equiv (\partial_\mu (H^\dagger H))^2/f^2$ where H is the Higgs doublet [3]. This, however, does not seem to be very useful since a $hh \to hh$ process is not at the reach of the LHC. Nevertheless, there is, as we said, an important difference between the Higgs and the pions; the Higgs is expected to get a VEV and therefore the operator

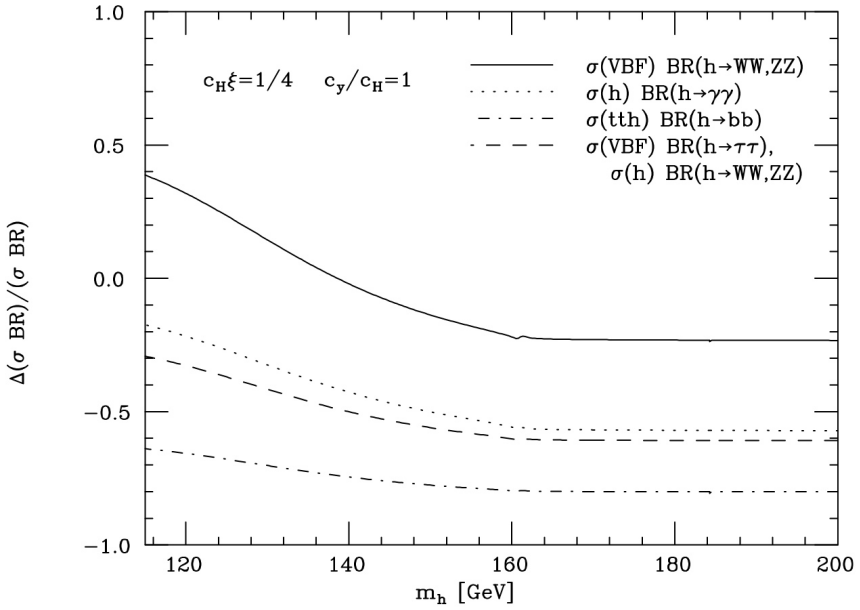

Fig. 1. – Deviations from the SM predictions of Higgs production cross-sections and decay branching ratios expected in composite Higgs models. See [3] for details.

$\mathcal{O}_H$ gives a modification to the Higgs propagator $\xi(\partial_\mu h)^2$ where $\xi = \langle H\rangle^2/f^2$. This has several important implications. First, this Higgs will not completely unitarize the WW interaction, and therefore this is expected to grow at high energies $\mathcal{M}(WW \to WW) \sim E^2/f^2$. Secondly, the Higgs partial widths will be modified (see fig. 1).

Can this be seen at the LHC? Clearly, this is going to be difficult. For $f > 500\,\text{GeV}$, we have $\xi < 0.2$; this suppression, although small, makes already very difficult to see the composite nature of the Higgs at the LHC. First studies show that with about 300/fb of integrated luminosity, it is possible to measure Higgs production rate times branching ratio in different channels with only a 20–40% precision [4]. For the WW interaction, the signal of Higgsless models, that corresponds to $\xi = 1$, can be only measured with a 30–50% accuracy for 200/fb.

3. – Models for Higgs as PGB

There could be other indirect signals of Higgs compositeness. For example, in QCD, the pions are accompanied by a rich hadronic spectrum. Therefore, we could try to measure the heavy states accompanying the Higgs. What are the expected masses and quantum numbers of these states? It is very difficult to answer this question. As in QCD, it is very difficult to calculate the spectrum in strongly interacting theories. This has been the main reason that has discouraged particle physicist to pursue this kind of models since they were proposed in the 80's.

The situation, however, has changed in the last years. The AdS/CFT correspondence [5] has afforded a new tool to calculate within strongly interacting theories. The most important feature that emerges from this correspondence is that strongly coupled

gauge theories in the limit in which the number of colors, N_c, and the 'tHooft coupling, $g^2 N_c$, are both large, can be described by weakly coupled theories living in extra dimensions.

This has boosted the studies of 5D models with the Higgs as PGB. The simplest version of these models is a five-dimensional gauge theory compactified by two 4D boundaries, the UV-boundary and IR-boundary, and with the following symmetry pattern [2]:

$$\begin{aligned} &\text{UV-boundary:} && SU(2)_L \otimes U(1)_Y \otimes SU(3)_c, \\ &\text{5D Bulk:} && SO(5) \otimes U(1)_X \otimes SU(3)_c, \\ &\text{IR-boundary:} && O(4) \otimes U(1)_X \otimes SU(3)_c, \end{aligned}$$

where $Y = T_R^3 + X$, with T_R^3 being the 3rd component generator of one of the two $SU(2)$ inside the $SO(5)$. This is the minimal scenario that accomplishes three things: it delivers a PGB being a **2** of $SU(2)_L$, the Higgs, it has a custodial $SU(2)_V$ symmetry after EWSB (up to UV-boundary terms), and it contains the SM gauge group. The SM fermions are embedded into 5D Dirac spinors which live in the bulk and belong to the **5** representation of $SO(5)$. By an appropriate determination of the bulk and boundary masses we can obtain a realistic theory of fermion masses. In AdS_5 small fermion masses can be naturally obtained since the Higgs is localized towards the IR-boundary. Therefore small Yukawas can be obtained for the 1st and 2nd family by localizing the zero-mode fermions towards the UV-boundary and then having a small overlapping with the Higgs. The most interesting features of the heavy spectrum that come out of this model is the following: We have a light Higgs, with a mass around 110–180 GeV; there are fermionic resonances in the $\mathbf{2_{1/6}}$ and $\mathbf{2_{7/6}}$ representations of the SM with masses ranging around 500–1500 GeV; vector resonances appear around 2–3 TeV, while spin 2 states are much heavier, around 4 TeV.

Another different approach towards models with PGB Higgs that has been pursued in the last years comes with the name of "Little Higgs" (LH) [6]. The idea is to generate a Higgs quartic coupling at the one-loop level, but engineer a model such that the Higgs mass-term appears only at the two-loop level. If so, the EW scale will be two loops below the strongly interacting scale, that can be then around 100 TeV. To accomplish this, however, new states must be introduced in the theory around the TeV (heavy vector bosons and color fermions). Present fully realistic models realizing this idea are, however, too complicated to be described here.

3˙1. *LHC phenomenology.* – In most of the models in which the Higgs appears as a PGB we have extra W and Z resonances, W' and Z', with masses around the TeV. In 5D models these states mostly decay to tops, Higgs or W_{long} and Z_{long}, while for LH models they decay to leptons. LHC will be able to reach them if they are not heavier than ~ 2 TeV.

In 5D models we also have gluonic resonances, g'. They decay mostly into a pair of tops, and could be reached at the LHC if their masses are not higher than ~ 4 TeV. Also color fermionic resonances are present in all PGB models. In LH there is, for example, a resonance of the t_R-quark, t'_R, that decays mostly to Wb. Nevertheless extradimensional models predict the existence of extra exotic color states. In particular, a colored fermion with electromagnetic charge of 5/3 is the most distinctive signal of 5D composite Higgs models.

4. – Conclusion

There is light beyond supersymmetry. The idea presented here of composite PGB Higgs is not only theoretically well motivated, but, at present, we can find models realizing this idea in a realistic and predictive way. Most importantly, they give clear signals for the LHC worthy to fully explore.

* * *

I would like to thank the organizers for their kind invitation to this conference.

REFERENCES

[1] See, for example, Kaplan D. B. and Georgi H., *Phys. Lett. B*, **136** (1984) 183.
[2] Agashe K., Contino R. and Pomarol A., *Nucl. Phys. B*, **719** (2005) 165; Contino R., Da Rold L. and Pomarol A., *Phys. Rev. D*, **75** (2007) 055014.
[3] Giudice G. F., Grojean C., Pomarol A. and Rattazzi R., *JHEP*, **0706** (2007) 045.
[4] Duhrssen M., The determination of the Higgs boson couplings to fermions and bosons, ATL-PHYS-2003-030.
[5] Maldacena J. M., *Adv. Theor. Math. Phys.*, **2** (1998) 231 (*Int. J. Theor. Phys.*, **38** (1999) 1113) [arXiv:hep-th/9711200]; Gubser S. S., Klebanov I. R. and Polyakov A. M., *Phys. Lett. B*, **428** (1998) 105 [arXiv:hep-th/9802109]; Witten E., *Adv. Theor. Math. Phys.*, **2** (1998) 253 [arXiv:hep-th/9802150].
[6] Arkani-Hamed N., Cohen A. G. and Georgi H., *Phys. Lett. B*, **513** (2001) 232; Arkani-Hamed N., Cohen A. G., Katz E., Nelson A. E., Gregoire T. and Wacker J. G., *JHEP*, **0208** (2002) 021; Arkani-Hamed N., Cohen A. G., Katz E. and Nelson A. E., *JHEP*, **0207** (2002) 034.

SESSION IX - PHYSICS AND SOCIETY

IL NUOVO CIMENTO Vol. 32 C, N. 5-6 Settembre-Dicembre 2009
DOI 10.1393/ncc/i2010-10556-6

Colloquia: LaThuile09

The energy challenge of a post-fossil world: Seasonal energy storage

C. Forsberg

Massachusetts Institute of Technology - Cambridge, MA, USA

(ricevuto il 10 Novembre 2009; pubblicato online il 28 Gennaio 2010)

Summary. — Fossil fuels are an energy source and an energy storage system. The demand for electricity and heat varies daily, weekly, and seasonally with seasonal variations often varying by a factor of two or more. The variable demand is met by fossil fuels because 1) fossil fuels are inexpensive to store in coal piles, oil tanks, and underground natural gas storage facilities and 2) the capital cost of the equipment to burn fossil fuels and convert the energy to heat or electricity is small relative to the cost of the fossil fuels. Concerns about climate change may limit the conventional use of fossil fuels. The alternative low-carbon energy production systems (nuclear, fossil fuels with carbon dioxide sequestration, wind, and solar) are capital-intensive energy sources with low operating costs. To obtain favorable economics, these technologies must operate at full capacity; but, their output does not match energy demand. We have energy alternatives to fossil fuels but no replacements for the energy storage capabilities of fossil fuels. Proposed strategies and technologies to address the grand storage challenge (including seasonal storage of electricity) are described. The options suggest a nuclear-renewables future to address seasonal energy storage needs in a low-carbon world.

PACS 89.30.Gg – Nuclear fission power.
PACS 88.20.gc – Fischer-Tropsch (F-T) liquids (hydrocarbons).
PACS 88.30.em – Electrolytic hydrogen.

1. – Introduction

Les Rencontres de Physique de la Vallée d'Aoste addresses the challenges in particle physics. There are equal challenges for world energy policies that in the next several decades will likely be driven by two factors: the end of inexpensive oil and limits on the traditional uses of fossil fuels because of concerns about climate change. It is usually assumed that the primary energy challenge is to replace fossil fuels as an energy source; however, an equal or greater challenge may be to replace the storage functions of fossil fuels. This paper examines energy storage in the context of electricity and transportation.

2. – The storage challenge

Electricity demand varies daily, weekly, and seasonally. At higher latitudes, there is also a 3-day cycle associated with weather patterns. Parallel to the electricity demand, the demand for heating and cooling has similar cycles. On a different time cycle are the variable energy demands by the transport sector. Today the burning of fossil fuels is the primary technology to match energy production with fluctuating energy demand. Fossil fuels are used for variable electricity, heat, and motive production because 1) they are inexpensive to store until needed and 2) the equipment for conversion of fossil fuels to useful energy has relatively low capital costs.

The use of fossil fuels to meet variable energy demands may be limited in the future because of concerns about climate change. In the United States, the Obama administration's goal in the United States is to reduce greenhouse gas emissions by 80% by 2050. Such goals imply eliminating fossil emissions from almost all major sources.

Greenhouse gas emissions can be reduced from fossil plants by sequestering the carbon dioxide underground [1]; however, such fossil power plants are likely to be uneconomic for variable production of electricity or heat because of their high capital costs and the technical difficulties in operating such plants with variable output. It is not practical to collect and sequester carbon dioxide from small users of fossil fuels—such as for heating homes and commercial buildings. To avoid these greenhouse gas releases, there will likely be increased use of electricity for building heating and cooling. This implies larger seasonal swings in electricity demand. In the transport sector [2], the likely introduction of plug-in hybrid vehicles will partly replace gasoline and diesel fuel with electricity; however, the demand for transport is higher in the summer implying growing seasonal variations in electricity demand.

The primary low-carbon electricity systems for the future are nuclear, hydro, wind, geothermal, solar, and fossil fuels with carbon-dioxide sequestration. All of these technologies have high capital costs (when delivered capacity is factored in) and low operating costs; thus, it is essential to operate them at their full capacities to minimize increases in electricity costs.

If capital-intensive electrical generating technologies are not operated at full capacity, there will be large increases in the cost of electricity. This can be seen by example. A recent study [3] evaluated the cost of electricity from new nuclear, coal, and natural gas plants in the United States. Using the same financial rules([1]), the respective levelized electricity costs were 6.6, 6.2, and 6.5 ¢/kWh. The capital cost component of the electricity costs were respectively 72, 45, and 15%.

Today, natural gas is used for variable electricity production. If a natural gas plant operates half the time *versus* all the time to match production with demand, it has little impact on the cost of electricity because only 15% of the cost is associated with the initial plant construction. The rest of the cost is associated with fuel and operations. In contrast, for nuclear power plants (and capital-intensive renewable power plants), most of the cost of electricity is associated with paying for the plant. If the plant operates half the time, the costs of electricity will be almost doubled because the capital cost remains

([1]) Without federal loan guarantees, it is assumed that the first few new nuclear plants in the U.S. will pay a higher cost of capital than for other types of generating plants. This financial risk premium would increase the electricity costs to 8.4 ¢/kWh. Such a risk premium would not exist for latter plants.

fixed while the production is cut in half. Operating capital-intensive electric generating technologies at anything but full capacity results in high electricity costs.

Concerns about climate change will likely impose restrictions on carbon dioxide releases from burning fossil fuels. If a $\$25/tCO_2$ tax is imposed to avoid carbon dioxide releases to the atmosphere, the respective electricity costs from new coal and natural plants increase 8.3 and 7.4 ¢/kWh. Restrictions on greenhouse gas emissions have significant impacts on the costs of electricity from fossil fuels.

No single low-carbon electricity source or combination of electricity sources comes close to matching the variable electricity demand. The mismatch between production and demand requires rethinking of our electrical systems if conventional fossil fuel use is limited. There are four options to address the mismatch between electricity production and demand in a low-carbon world.

- Operate capital-intensive energy production systems at part load at times of low power demand. This is an expensive option—particularly for renewables such as wind where there is often a seasonal mismatch between peak production and demand.

- Chose energy sources to match energy demand. If storage and part-load operation of power generation equipment is expensive, costs can be reduced by choosing the combination of energy production technologies whose outputs most closely match energy demand to minimize partial-load operation of capital-intensive power plants and minimize energy storage needs.

- Develop energy storage technologies. Many technologies exist to store energy for a few days (pumped hydro, batteries, thermal storage systems) but there is only one non-fossil seasonal energy storage technology—large-scale hydroelectricity. For most of the world there is insufficient hydro to meet storage needs.

- Develop new energy markets that can consume excess energy when available from capital-intensive energy production sources.

A candidate strategy to address the seasonal energy storage challenge is described herein (fig. 1) that uses new seasonal storage technologies and new markets for off-peak power. Such a strategy combines nuclear and renewable energy sources to maximize utilization of high-capital-cost energy production technologies.

3. – Seasonal storage of electricity

In a low-carbon world of high-capital-cost, low-operating-cost nuclear, wind, and solar plants, electrical generating facilities should operate at their maximum output to minimize costs. This requires gigawatt-year electricity storage capacities if excess electricity production in the spring and fall are to meet peak electricity demands in the winter and summer. One set of options uses hydrogen as the storage media [4, 5] and is potentially deployable within a decade. An example of such a system is the Hydrogen Intermediate and Peak Electrical System (HIPES) for variable electricity demand on a daily, weekly, and seasonal basis. It consists of three major components.

Hydrogen production. Hydrogen is produced from water with the by-product production of oxygen. The commercial low-carbon hydrogen production option today is electrolysis where the energy input is in the form of electricity. The midterm option is

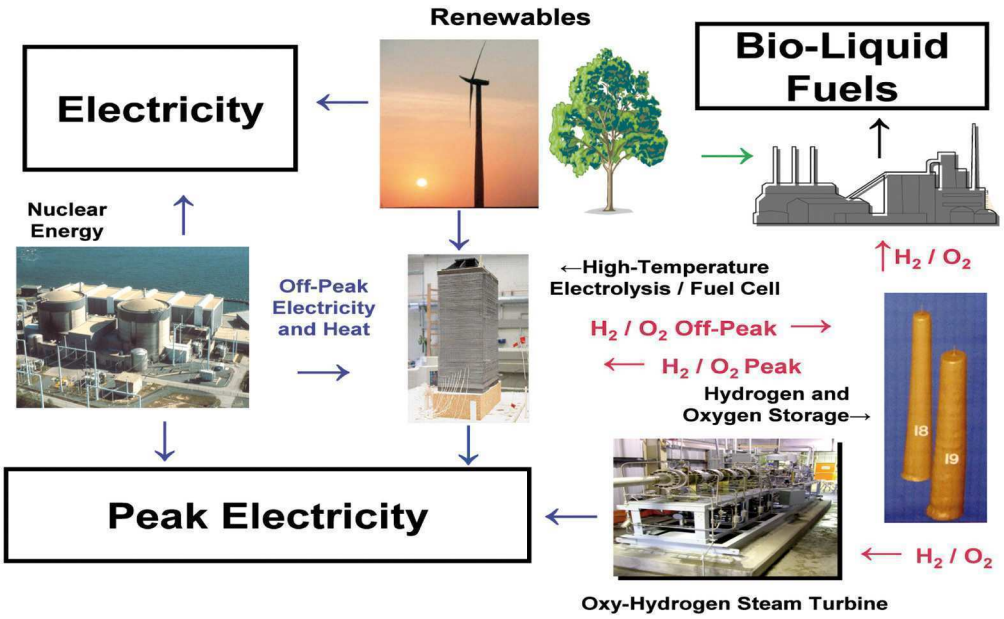

Fig. 1. – Example system to replace the fossil fuel storage functions.

high-temperature electrolysis (HTE) where heat, electricity, and water produce hydrogen and oxygen. HTE has potentially lower costs than traditional electrolysis because lower-cost heat partly substitutes for more expensive electricity. The HTE energy sources would be nuclear reactors that supply heat and electricity and renewable systems that could provide electricity. The hydrogen production efficiency with a light-water reactor using HTE is projected to be close to the production efficiency for electricity [5,6]. Hydrogen production would be at times of low electrical demand to maximize utilization of capital-intensive electric generating technologies.

Hydrogen and oxygen storage. Underground storage facilities would be used for the low-cost storage of hydrogen and oxygen on a daily, weekly, or seasonal basis. Unlike electricity, hydrogen can be stored inexpensively for days, weeks, or months in large underground facilities using the same technology developed to store natural gas. In the United States, approximately 400 underground storage facilities store at high pressure a third of a year's production of natural gas in the fall before the winter heating season.

A limited number of such hydrogen storage facilities now exist in Europe and the United States to support the chemical and refining industries. *Hydrogen is today the only non-fossil energy storage media for which the commercial technology exists to store energy on a scale sufficiently large to cover seasonal variations in electricity demand.* There have been studies on bulk oxygen storage; but, this technology has not been commercialized.

Hydrogen-to-electricity conversion. There are multiple technologies to convert hydrogen and oxygen to electricity. The leading midterm technologies are fuel cells and oxy-hydrogen steam turbines because of their potentially high efficiencies and low capital costs compared to traditional natural-gas-fired combined-cycle plants used today for peak power production. The two technologies have complimentary capabilities.

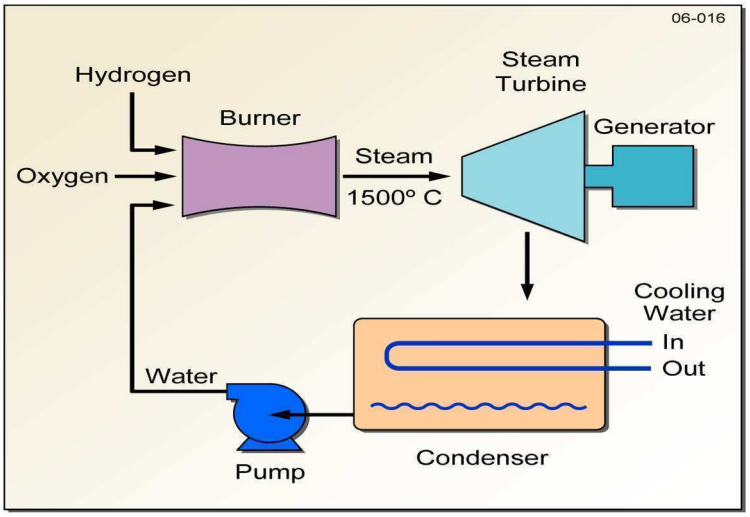

Fig. 2. – Oxy-hydrogen steam cycle.

Solid-oxide high-temperature fuel cells are being developed for electricity production. For peak power applications within HIPES, this technology has a unique advantage because a solid-oxide high-temperature fuel cell operated in reverse is a HTE system producing hydrogen. By using the same piece of equipment for both electricity and hydrogen production, the system capital costs are minimized. The fuel cell/HTE combination would allow the utility operator to vary electricity output from the nuclear station to the electrical grid from zero (all energy to HTE for hydrogen and oxygen production) to $\sim$ 170% of base-load electrical production (electricity to grid from the reactor and fuel cells). Wider variations in electricity output are possible if renewables are used to provide electricity to the HTE system with the nuclear reactor used to provide primarily heat at times of low electricity demand.

Siemens is developing a fuel cell/turbine combination that uses hydrogen and air with a projected efficiency of about 70%. This variant would avoid the need for oxygen storage. Alternatively, if oxygen is stored, the fuel cell size is reduced relative to a fuel cell operating on air because the oxygen electrode determines fuel-cell performance. A fuel cell operated on oxygen will have two to four times the output of a fuel cell operated on air.

The other peak-power technology is the oxy-hydrogen steam cycle (fig. 2). Hydrogen, oxygen, and water are fed directly to a burner to produce high-pressure, high-temperature steam. The resultant steam is fed directly to an aero-derived high temperature turbine that drives an electric generator. With actively cooled blades, it is expected that peak steam temperatures at the inlet of the first turbines can approach 1500 °C. The projected heat-to-electricity efficiency for advanced turbines approaches $\sim$ 70%, starting with compressed oxygen and hydrogen from the storage facilities.

The technology is based on ongoing development of an advanced natural-gas electric plant that uses oxygen rather than air [7] by Clean Energy Systems, Inc. Combustors with outputs of $\sim$ 20 MW(t) are being tested. With a feed of natural gas and oxygen, a mixture of steam and carbon dioxide is created. After this mixture passes through the

turbine to the condenser, the steam is condensed and the carbon dioxide is available for 1) injection into oil fields to increase the recovery of oil and/or 2) sequestration.

This peak power technology has one unique characteristic. Based on what we know today, the capital costs [4] are significantly less than traditional natural-gas-fired gas turbines or any other available peak power technology. The system does not require compression of air as in traditional gas turbines or have the boilers to produce steam. Consequently, there are large incentives to develop such a peak electricity technology to provide the backup for renewables where power production can drop quickly. The technical constraint is that the system requires large-scale hydrogen and oxygen storage to enable the direct production of steam.

4. – Transportation

Oil provides about 35% of the world's energy demand and is the fuel of choice for the transport sector because it's an easy to store energy source. In a low-carbon world, oil consumption must be dramatically reduced. Existing technologies such as electrification of trains and near-term technologies such as plug-in hybrid vehicles may reduce oil demand in half. However, the transport sector needs a transportable fuel.

Liquid hydrocarbon fuels excel as transport fuels because they are an excellent energy storage system [2]. The primary options for low-carbon liquid fuels are fuels from biomass. Carbon dioxide is removed from the air and converted into biomass. The biomass is converted into liquid fuels and the fuels are burnt in vehicles with return of the carbon dioxide to the atmosphere. This is an attractive concept; however, *it is limited by the availability of world biomass production*. The contribution of biomass to liquid fuels production depends upon how efficiently we convert biomass to liquid fuels.

We have the technology today to convert any carbon source to liquid fuels. However, the less the carbon source looks like diesel fuel or gasoline, the more energy is required for the conversion process. For example [8], the energy input in refining to convert oil into diesel fuel is 15 to 20% of the energy value of the crude oil. If the starting material is coal, the energy consumption inside the coal liquefaction plant exceeds the energy value of the diesel fuel that is produced.

Available data indicate that U.S. biomass resources are about typical of the world as a whole; thus, U.S. biomass data will be used herein in understanding the liquid fuels potential of different biomass processing options in terms of liquid-fuels production. The United States [9] could produce about 1.3 billion dry tons of biomass feedstock per year for conversion to liquid fuels without major cost or availability impacts on the production of food or fiber. Except for the grains, most of the biomass resources are cellulosic biomass that can not be used as food for humans.

The energy value [2,10] of the 1.3 billion tons of dry biomass per year that is available in the United States depends upon the form in which it is used.

- *Burn biomass*. The energy content of the biomass, if burnt, would be equal to burning 9.8 million barrels of diesel fuel per day.
- *Fuel ethanol*. If the biomass were converted to fuel ethanol, the energy value of the ethanol would be equal to about 4.7 million barrels of diesel fuel per day. This scenario assumes that some of the biomass is converted into ethanol and that the remainder of the biomass provides the energy for the biomass-to-ethanol conversion processes. Like the conversion of heavy oils and coal to liquid fuels, biomass requires significant energy inputs for production of high-quality liquid fuels.

– *Diesel fuel*. If all of the carbon in the biomass were converted to diesel fuel, 12.4 million barrels of diesel fuel could be produced per day. This assumes that non-biomass energy sources provide the needed energy to operate the biomass-to-fuel plants and to produce the hydrogen needed for the conversion process.

For the United States, liquid fuels from biomass could potentially meet the nation's need for liquid transport fuels, but only if the biomass is used as a feedstock and not as the energy source to operate the biomass-to-liquid-fuels conversion plants. The same principle is applicable worldwide. Today nuclear energy is the only low-carbon energy source that can provide the heat and hydrogen under the conditions that are required by a bio-refinery (steady state operation).

Most of the energy input is in the form of hydrogen. In this context, the integration of the electric sector with the fuels production sector could provide the source of hydrogen. Excess electricity at times of low energy demand could be converted to hydrogen, that hydrogen can be stored, and the hydrogen can be used for liquid fuels production. In effect, excess electricity is converted into "storable" liquid fuels while fully utilizing all electricity generation capabilities.

5. – Conclusions

Fossil fuels serve two functions: an energy source and an energy storage media. While much attention has been given to alternative energy sources, little attention has been given to replacing the energy storage functions of fossil fuels. While there are multiple technologies for short-term storage of energy, there are very few options today to address seasonal energy storage requirements. From the limited work that has been done, several preliminary conclusions can be reached.

There are significant technical and economic incentives to create nuclear-renewable hybrid energy systems. Biomass liquid fuels production requires outside heat and hydrogen sources if sufficient biomass liquid fuels are to be produced to replace conventional oil in our transport system. In the electricity sector, the large scale use of renewables requires large-scale seasonal energy storage systems with gigawatt-year capacities. Hydrogen is a leading candidate for this energy storage role. The most efficient methods to make hydrogen from water require both electricity and heat. The storage, handling, and production technologies are intrinsically large-scale technologies. These characteristics imply a natural coupling between nuclear energy, hydrogen production [11], and seasonal energy storage systems.

The most important role for renewables will likely be biofuels production. Peak electricity systems that include seasonal storage would enable renewables to become large-scale electricity sources—beyond the current limits of 10 to 15% of electricity production. Our ability to develop energy storage systems, particularly seasonal energy storage, may determine the total energy system architecture and the difficulty of developing an economic low-carbon energy world.

REFERENCES

[1] Massachusetts Institute of Technology, *The Future of Coal: Options for a Carbon-Constrained World* (Cambridge, MA) 2007.
[2] Forsberg C. W., *Int. J. Hydrogen Energy*, **34** (2009) 4227.

[3] Du Y. and Parsons J. E., *Update on the Cost of Nuclear Power*, 09-004 MIT Center for Energy and Environmental Policy Research (2009).
[4] Forsberg C. W., *Nucl. Technol.*, **166** (2009) 18.
[5] Forsberg C. and Kazimi M., *4th Information Exchange Meeting on Nuclear Production of Hydrogen, 14-16 April 2009, Chicago*, Nuclear Energy Agency, `http://mit.edu/canes/pdfs/nes-10.pdf`.
[6] O'Brien J. E. *et al.*, *Analysis of Commercial-Scale Implementation of HTE to Oil Sands Recovery*, DOE Milestone Report, NHI Program, Idaho National Laboratory, Idaho Falls (September 15, 2006).
[7] Anderson R. E. *et al.*, *Proceedings of ASME Turbo Expo 2008: Power for Land, Sea and Air, GT2008, June 9-13, Berlin, Germany.*
[8] Marano J. J. and Ciferno J. P., *Life-Cycle Greenhouse-Gas Emissions Inventory for Fischer-Tropsch Fuels, Energy and Environmental Solutions*, U.S. Department of Energy National Energy Technology Laboratory, Pittsburgh, PA (2001).
[9] Perlack R. D. *et al.*, *Biomass as Feedstock for a Bioenergy and Bioproducts Industry: The Technical Feasibility of a Billion-Ton Annual Supply*, DOE/GO-102995-2135, U.S. Department of Energy, Washington, D.C. (2005).
[10] Ragausk A. J. *et al.*, *Science*, **311** (2006) 484.
[11] Forsberg C. W., *Nucl. Technol.*, **166** (2009) 3.

SESSION X - PERSPECTIVES

IL NUOVO CIMENTO Vol. 32 C, N. 5-6 Settembre-Dicembre 2009
DOI 10.1393/ncc/i2010-10554-8

Colloquia: LaThuile09

The Super$B$ project

M. Rama
INFN, Laboratori Nazionali di Frascati - Via E. Fermi 40, I-00044 Frascati, Italy

(ricevuto il 10 Novembre 2009; pubblicato online il 25 Gennaio 2010)

Summary. — Super$B$ is a next generation asymmetric e^+e^- flavor factory with a baseline luminosity of $10^{36}\,\mathrm{cm}^{-2}\,\mathrm{s}^{-1}$, 50–100 times the peak luminosity of existing B-factories. The physics motivation is presented and the complementarity with the LHC is discussed. The conceptual design of the detector is also briefly described.

PACS 12.15.Hh – Determination of Kobayashi-Maskawa matrix elements.
PACS 13.25.Hw – Decays of bottom mesons.
PACS 14.40.Nd – Bottom mesons.

1. – The role of a super flavor factory in the LHC era

Super$B$ is a next generation asymmetric e^+e^- flavor factory with very high peak luminosity ($\mathcal{L} = 10^{36}\,\mathrm{cm}^{-2}\,\mathrm{s}^{-1}$) proposed to be built in the Rome area. The main purpose of the experiment is to search for evidence of physics beyond the Standard Model (SM) and investigate its nature.

The search for new physics (NP) is the main goal of elementary particle physics in the next decade. The search is encouraged by the expectation that the NP mass scale is around 1 TeV, thus directly accessible to the Large Hadron Collider (LHC) at CERN. In this context, it is important to clarify the role of a Super$B$ factory by considering two scenarios depending on whether or not evidence of NP is actually found at the LHC.

If direct evidence of NP is found at the LHC, Super$B$ will help determining the flavor structure of NP by constraining its couplings, mixing angles and masses through the measurement of rare decays whose amplitudes are mediated by loops in the SM, or through the observation of lepton flavor violating processes. The flavor physics observables measured at a Super Flavor Factory provide a set of independent constraints complementary to those measured at high-p_T processes. It is important to stress that to reconstruct the NP Lagrangian both are required.

If instead the LHC does not discover NP particles, then Super$B$ will allow to explore mass scales up to 10 TeV or beyond (depending on the models). In this case the NP Lagrangian cannot be fully determined, but a NP discovery at Super$B$ would provide a solid indication that the NP mass scale is likely to be within one order of magnitude away from the LHC scale.

TABLE I. – *Golden modes in different New Physics scenarios. An "X" indicates the golden channel of a given scenario. An "O" marks modes which are not the "golden" one of a given scenario but can still display a measurable deviation from the Standard Model. The label CKM denotes golden modes which require the high-precision determination of the CKM parameters achievable at Super$B$.*

	H^+ high $\tan\beta$	Minimal FV	Non-minimal FV	NP Z-penguins	Right-handed currents
$\mathcal{B}(B \to X_s\gamma)$		X	O		O
$A_{CP}(B \to X_s\gamma)$			X		O
$\mathcal{B}(B \to \tau\nu)$	X-CKM				
$\mathcal{B}(B \to X_s l^+ l^-)$			O	O	O
$\mathcal{B}(B \to K\nu\overline{\nu})$			O	X	
$S(K_S\pi^0\gamma)$					X
β			X-CKM		O

One may ask how the Super$B$ program compares with the flavor physics potential of LHCb. The striking outcome of the comparison is that even in this case the complementarity is large. For example, rare decay modes with one or more neutrinos in the final state such as $B^+ \to l^+\nu$ and $B^+ \to K^{(*)+}\nu\bar{\nu}$, inclusive analyses of processes such as $b \to s\gamma$ and $b \to sl^+l^-$ or measurements of the CKM matrix elements $|V_{ub}|$ and $|V_{cb}|$ are unique to Super$B$, where the environment of the e^+e^- collider is clean and relatively simple compared to the events at the hadronic machine [1]. Some examples will be given in sect. **2**. On the other hand, for example, the large boost of the B hadrons produced at LHCb allows time-dependent studies of the oscillations of B_s mesons, which are not possible at a Super$B$.

It is important to stress that Super$B$ will also provide huge samples of charm hadron and τ lepton pairs (2.0×10^{10} and 1.4×10^{10} per year, respectively, at the nominal luminosity), enabling powerful studies of NP effects in the up-type quark and lepton sectors with unprecedented precision. Moreover, the machine is being designed to run in a wide range of center-of-mass (CM) energies, down to the τ threshold and up to the $\Upsilon(5S)$ mass, thus enriching further the physics program.

To reach the goals of Super$B$ in terms of sensitivity, a data sample of about two orders of magnitude larger than the ones accumulated by the current B-factories BaBar ($0.53\,\mathrm{ab}^{-1}$) and Belle ($0.95\,\mathrm{ab}^{-1}$) is needed. A collider baseline luminosity of $10^{36}\,\mathrm{cm}^{-2}\,\mathrm{s}^{-1}$ would allow to collect $15\,\mathrm{ab}^{-1}$ per year ($1\,\mathrm{y} = 1.5 \times 10^7\,\mathrm{s}$) corresponding to a data sample of more than 80 billion $B\bar{B}$ pairs in five years of running at the $\Upsilon(4S)$ CM energy.

2. – The physics case of Super$B$

In this section a short selection of measurements which are part of the Super$B$ physics program are discussed. The reader is referred to refs. [2, 3] for an extensive discussion of the physics reach of the experiment.

TABLE II. – *Comparison of current experimental sensitivities with those expected at SuperB (75 ab^{-1}). Only a small selection of observables is shown. Quoted sensitivities are relative uncertainties if given as a percentage, and absolute uncertainties otherwise. For more details, see refs.* [2, 5, 1].

Mode	Sensitivity	
	Current	Expected (75 ab^{-1})
$\mathcal{B}(B \to X_s\gamma)$	7%	3%
$A_{CP}(B \to X_s\gamma)$	0.037	0.004–0.005
$\mathcal{B}(B^+ \to \tau^+\nu)$	30%	3–4%
$\mathcal{B}(B^+ \to \mu^+\nu)$	not measured	5–6%
$\mathcal{B}(B \to X_s l^+ l^-)$	23%	4–6%
$A_{\rm FB}(B \to X_s l^+ l^-)_{s_0}$	not measured	4–6%
$\mathcal{B}(B \to K\nu\overline{\nu})$	not measured	16–20%
$S(K^0_S\pi^0\gamma)$	0.24	0.02–0.03

2˙1. *Rare B decays.* – One of the strengths of the physics program of Super$B$ is the large number of decays where the SM uncertainty is small and which can display a measurable deviation from the SM in one or more NP scenarios. A large fraction of these "golden" channels are rare B decays where NP particles enter the leading loops. A selection of golden modes in different NP scenarios is reported in table I. The list of observables in the table is not complete, as well as the number of NP scenarios considered. Table II reports the comparison of the experimental sensitivity today and with 75 ab^{-1}, showing that in most cases Super$B$ is able to measure the observables with a few percent accuracy. As already mentioned in the previous section these decays are very difficult or impossible to reconstruct at the LHC. Even at the clean environment of Super$B$ the selection is experimentally challenging and to suppress backgrounds to an acceptable level the recoil technique is often necessary, in which the other B in the $B\bar{B}$ event is reconstructed in either a semileptonic or hadronic decay.

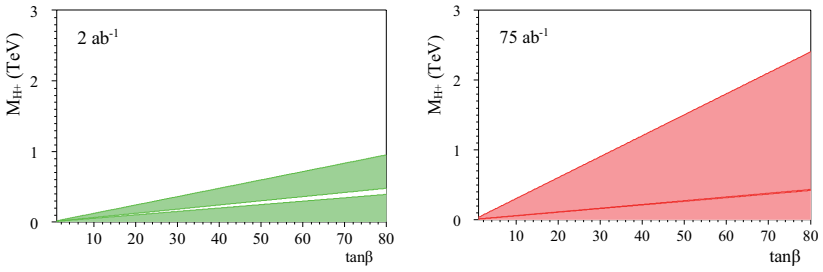

Fig. 1. – Exclusion regions in the $m(H^+)$-$\tan\beta$ plane arising from the combinations of the measurement of $\mathcal{B}(B \to \tau\nu)$ and $\mathcal{B}(B \to \mu\nu)$ using 2 ab^{-1} (left) and 75 ab^{-1} (right). We assume that the result is consistent with the Standard Model.

TABLE III. – *Uncertainties of the CKM parameters obtained from the Standard Model fit using the experimental and theoretical information available today (left) and at the time of SuperB with a dataset of* $50\,\mathrm{ab}^{-1}$ *(right).*

Parameter	SM fit today	SM fit at Super$B$
$\overline{\rho}$	0.163 ± 0.028	± 0.0028
$\overline{\eta}$	0.344 ± 0.016	± 0.0024
α (°)	92.7 ± 4.2	± 0.45
β (°)	22.2 ± 0.9	± 0.17
γ (°)	64.6 ± 4.2	± 0.38

As an example of process sensitive to NP we consider the decays $B \to l\nu$ with $l = \tau, \mu$, whose rates are strongly affected by a charged Higgs in a scenario with large $\tan\beta$. For example, in the two Higgs doublet model the effect of the charged Higgs is that the branching fraction is scaled by a factor $(1 - \tan^2\beta(M_B^2/M_{H^+}^2))^2$ [4], where M_{H^+} is the mass of the Higgs boson. Figure 1 gives the exclusion regions in the M_{H^+}-$\tan\beta$ plane from a measurement of $\mathcal{B}(B \to l\nu)$ with $2\,\mathrm{ab}^{-1}$ and $75\,\mathrm{ab}^{-1}$, assuming that the result is consistent with the SM. In scenarios with large $\tan\beta$, for example $\tan\beta \sim 50$, Super$B$ can push the lower bound on M_{H^+} from the hundreds of GeV region up to almost 2 TeV.

2˙2. *Time-dependent CP asymmetry in penguin-dominated modes.* – New Physics can be probed in mixing-induced CP violation of processes dominated by $b \to s$ penguin loops. In the SM the time-dependent CP asymmetry of these decays should measure $\sin 2\beta$([1]) up to small corrections, *i.e.* $\Delta S \equiv \sin 2\beta|_{b\to s} - \sin 2\beta \simeq 0$. However, NP particles in the loops can cause measurable deviations from the SM prediction. The potential of this approach depends on the accuracy of the SM prediction for ΔS and on the experimental uncertainty on $\sin 2\beta|_{b\to s}$ for the individual channels. The decays where the expected deviation ΔS and the associated theoretical uncertainty are the smallest are $\eta' K^0$, ϕK^0 and $K_S K_S K_S$, making them the theoretically cleanest probes of NP. At present it appears that the reconstruction of these modes at a hadronic machine is at least challenging [1].

The current experimental errors are still large compared to the theoretical uncertainties, and no significant deviations from the SM predictions are observed. By extrapolating the current measurements of a wide range of channels, one concludes that a data sample of at least $50\,\mathrm{ab}^{-1}$ is necessary to reduce the experimental errors on ΔS to the level of 0.01–0.03, close to the current theory precisions of the cleanest modes. Therefore at a super$B$-factory these processes will be sensitive probes of NP.

2˙3. *Precise measurement of the CKM parameters.* – Super$B$ can dramatically improve our knowledge of the CKM matrix thanks to the possibility of performing a wide range of measurements which constrain its elements. Table III compares the errors of the CKM parameters obtained from the SM fit using the experimental and theoretical information available today and at a Super$B$, showing that the uncertainties would be reduced by a factor 10. The current constraints in the $\bar{\rho}$-$\bar{\eta}$ plane are reported in the left plot of

([1]) Modulo a sign depending on the CP content of the final state.

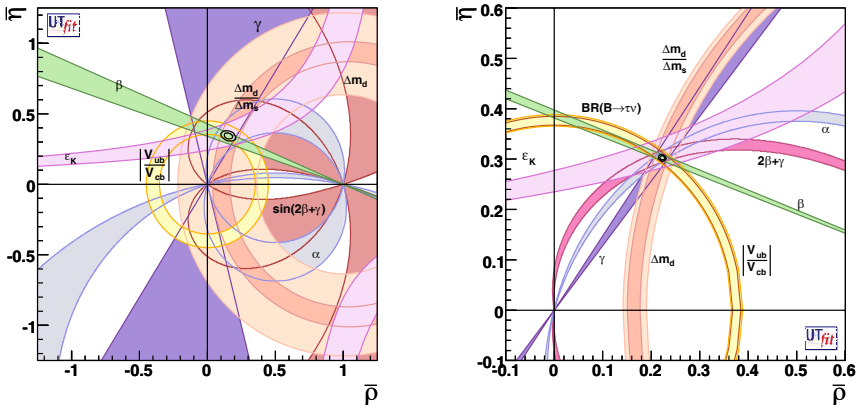

Fig. 2. – Allowed regions corresponding to 95% probability for $\bar{\rho}$ and $\bar{\eta}$ selected by different constraints, assuming present central values and errors (left) or a scenario with perfect agreement among the measurements and with the errors expected at a Super$B$ (right).

fig. 2, while the right plot shows the impressive improvement expected with a dataset of $50\,\mathrm{ab}^{-1}$ in a scenario where there is perfect agreement with the SM predictions. A precise knowledge of the CKM matrix is important per se, but it is also a powerful tool to spot inconsistencies in the SM and evidence of NP. Several measurements used for the determination of $\bar{\rho}, \bar{\eta}$ can in fact be affected by the presence of NP, revealing itself as an inconsistency in the $\bar{\rho}$-$\bar{\eta}$ plane.

2˙4. *Lepton flavor violation in τ decays.* – Super$B$ will be able to explore a significant portion of the parameter space in many NP scenarios by searching for lepton flavor violation (LFV) in transitions between the third and first or second lepton generations, complementing studies in the muon sector such as the search for $\mu \to e\gamma$ being performed by the MEG experiment [6]. Compared to the potential of the current B-factories considered together, with a data sample of $75\,\mathrm{ab}^{-1}$ Super$B$ can increase the sensitivity by more than a factor 7 in the worst hypothesis of background-dominated analyses even assuming no improvement in the analysis techniques. For analyses which are background-free the sensitivity is at least 50 times better. Moreover, the baseline Super$B$ machine design incorporates the polarization of the electron beam (up to 85%), which will produce polarized τ leptons. The polarization can be exploited either to improve the background-signal separation, or to better determine the features of the LFV interaction once it is observed. Table IV summarizes the sensitivities for various LFV decays together with the current world average upper limits [7]. In a number of NP models the branching ratios of flavor-violating τ decays can be enhanced up to $\mathcal{O}(10^{-8})$, just below the current B-factories reach and beyond the possibility of LHC [8] but well above the reach of Super$B$. Other sensitive probes of NP include tests of lepton flavor universality and the search of CP violation in τ decays.

2˙5. *Charm physics.* – Super$B$ can operate as a charm factory at both the CM energy of the $\Upsilon(4S)$ and of the $\Psi(3770)$, where the quantum correlations in the coherent production of $D^0\bar{D}^0$ can be exploited [3]. The charm production cross-section at the $\Upsilon(4S)$ CM energy is comparable to the $B\bar{B}$ cross-section, $\sigma(e^+e^- \to c\bar{c}) \sim 1.3\,\mathrm{nb}$. On the other

TABLE IV. – *Expected 90% CL upper limits on representative LFV τ lepton decays with* $75\,\mathrm{ab}^{-1}$ *and current world average upper limits.*

Process	Sensitivity at Super$B$	Current limit
$\mathcal{B}(\tau \to \mu\gamma)$	2×10^{-9}	4.5×10^{-8}
$\mathcal{B}(\tau \to e\gamma)$	2×10^{-9}	1.1×10^{-7}
$\mathcal{B}(\tau \to \mu\mu\mu)$	2×10^{-10}	3.2×10^{-8}
$\mathcal{B}(\tau \to eee)$	2×10^{-10}	3.6×10^{-8}
$\mathcal{B}(\tau \to \mu\eta)$	4×10^{-10}	6.5×10^{-8}
$\mathcal{B}(\tau \to e\eta)$	6×10^{-10}	9.2×10^{-8}
$\mathcal{B}(\tau \to eK_S^0)$	2×10^{-10}	3.3×10^{-8}
$\mathcal{B}(\tau \to \mu K_S^0)$	2×10^{-10}	4.0×10^{-8}

hand, the luminosity at production threshold is smaller by a factor of ten with respect to the baseline value, but it is partially compensated by a cross-section about three times larger. The recent observation of the D^0-$\bar{D}^0$ mixing opens a unique window to the search of CP violation in the charm sector, whose observation would provide a strong hint of physics beyond the SM. The program also includes the search of CP violation in time-independent measurements and the study of rare and forbidden charm decays, as well as precise measurements of CKM parameters.

3. – The detector

To reach the required luminosity of $10^{36}\,\mathrm{cm}^{-2}\,\mathrm{s}^{-1}$ Super$B$ exploits a new collision scheme which is based on a small collision area, very small β_y^* at the interaction point, large Piwinsky angle and the "crab waist" scheme [2, 9, 10]. This novel approach has several advantages, most notably the fact that the very large improvement in luminosity is achieved with beam currents and wall plug power similar to those of the current B-factories, and with limited background rates. In the current layout the accelerator consists of 4 GeV/7 GeV positron/electron beams, corresponding to a CM boost $\beta\gamma \sim 0.28$ in the lab frame (half the value in BaBar).

The Super$B$ detector concept is based on the BaBar design [11] with some modifications required to deal with the reduced boost and higher event rates. A number of components of the SLAC B-factory can be reused, resulting in a significant reduction of costs. This includes parts of the PEP-II accelerator complex, the super-conducting solenoid, the CsI(Tl) crystals of the barrel electromagnetic calorimeter (EMC) and the quartz bars of the Cherenkov particle identification system (DIRC).

In the remainder of this section a short description of the detector under development is provided, focussing on a few aspects where Super$B$ differs from BaBar.

The tracking system is composed of a silicon vertex detector (SVT) surrounded by the drift chamber (DCH). To maintain sufficient Δt resolution for time-dependent CP violation measurements with the reduced Super$B$ boost, the vertex resolution is improved by reducing the radius of the innermost layer of SVT (layer-0) down to about 1.5 cm, which is the lower limit allowed by the background rates according to preliminary simulation studies. Two main options are being considered for the layer-0, CMOS monolithic active pixels thin sensors [12] or hybrid pixels detectors [13], while the outer silicon layers are

made of microstrips silicon sensors. The starting point for the DCH layout is the BaBar drift chamber, though the design optimization process may eventually end up in a quite different device. Anticipated improvements include a lighter, carbon-fiber, mechanical structure and faster readout electronics. The hadron particle identification system is placed just outside the DCH and will make use of the radiator quartz bars of the BaBar DIRC, with the old PMTs replaced by fast pixelated PMTs and the imaging region reduced in size to control the background rates. The EMC can re-use the barrel portion of the BaBar barrel EMC, made of 5760 CsI(Tl) crystals. This fact is very important because the barrel EMC is the most expensive element of the detector. In contrast, the CsI(Tl) crystals of the forward endcap will be replaced with L(Y)SO crystals, which are suitable for their excellent radiation hardness, fast decay time, small Molière radius and relatively high light yield. The outermost detector system is the Instrumented Flux Return for the detection of muons and neutral hadrons. The Resistive Plate Chambers and Limited Streamer Tubes used in BaBar will be replaced by extruded scintillator bars *à la* MINOS [14]. The amount and distribution of the absorber (iron or brass) will be optimized.

Two additional systems are being considered to possibly improve the performance of the detector: a forward particle identification device placed between the DCH and the forward endcap EMC, and a backward EMC calorimeter. Two candidates for the PID system are being compared, an aerogel radiator RICH and a time-of-flight system using a sheet of fused silica radiator [2]. The main purpose of the backward EMC would be to reject background events by detecting extra energy in that region, and therefore the energy resolution is not a critical parameter. A relatively simple device made of lead plates and scintillating strips may be adequate.

A Technical Design Report of the project is in preparation and is expected to be completed within two years.

4. – Conclusions

Super$B$ is a next generation asymmetric energy e^+e^- flavor factory operating mainly at the $\Upsilon(4S)$ CM energy but with the possibility to run in a wide range of energies, from the $\tau\tau$ threshold up to the $\Upsilon(5S)$. The main goal of the experiment is to search for evidence of physics beyond the Standard Model in the decays of heavy quarks and leptons, and to constrain its parameters. Super$B$ and the LHC are largely complementary in their effort to observe NP effects. In five years at the baseline luminosity of $10^{36}\,\mathrm{cm}^{-2}\,\mathrm{s}^{-1}$ Super$B$ can collect $75\,\mathrm{ab}^{-1}$, which correspond to about 8×10^{10} $B\bar{B}$ pairs, 5×10^{10} τ lepton pairs and 1×10^{11} $c\bar{c}$ pairs. This dataset allows to explore and test the flavor sector of the Standard Model with unprecedented precision. The project has entered the TDR phase which is expected to last two years.

* * *

The author would like to thank the conference organizers for the opportunity to give this talk, and the Super$B$ community.

REFERENCES

[1] Browder T. *et al.*, arXiv:0802.3201.
[2] Bona M. *et al.*, arXiv:0709.0451.

[3] Hitlin D. *et al.*, arXiv:0810.1312v2.
[4] Hou W. S., *Phys. Rev. D*, **48** (1993) 2342.
[5] Browder T. *et al.*, *JHEP*, **0802** (2008) 110 [arXiv:0710.3799].
[6] Grassi M., *Nucl. Phys. Proc. Suppl.*, **149** (2005) 369.
[7] Amsler C. *et al.* (Particle Data Group), *Phys. Lett. B*, **667** (2008) 1 and 2009 partial update for the 2010 edition.
[8] Biasini M. and Santinelli R., CMS NOTE 2002/037; Mazumdar K., *Czech. J. Phys. A*, **54** (2004) 291.
[9] Raimondi P. *et al.*, physics/0702033.
[10] Raimondi P., these proceedings.
[11] Aubert B. *et al.*, *Nucl. Instrum. Methods Phys. Res. A*, **479** (2002) 1.
[12] Rizzo G. *et al.*, *Nucl. Instrum. Methods Phys. Res. A*, **565** (2006) 195.
[13] For a similar concept see, for example, Kluge A. *et al.*, *Nucl. Instrum. Methods Phys. Res. A*, **582** (2007) 728.
[14] Ambats I. *et al.*, NUMI-L-337, FERMILAB-DESIGN-1998-02 (1998).

PARTICIPANTS

Abbiendi Giovanni	INFN-Sezione di Bologna	Italy
Altarelli Guido	Università di Roma Tre and CERN, Geneva	Switzerland
Antinori Federico	INFN-Sezione di Padova and CERN, Geneva	Switzerland
Antonelli Antonella	INFN-LNF Frascati (RM)	Italy
Antonelli Mario	INFN-LNF Frascati (RM)	Italy
Apresyan Artur	Purdue University, West Lafayette, IN	USA
Arnowitt Richard	Texas A&M University, College Station, TX	USA
Babichev Eugeny	APC Laboratory, Paris	France
Bagliesi Giuseppe	Università di Pisa	Italy
Banerjee Swagato	University of Victoria	Canada
Baroncelli Antonio	Università di Roma Tre	Italy
Begel Michael	Brookhaven National Laboratory, Upton, NY	USA
Bellettini Giorgio	Università di Pisa	Italy
Bernieri Enrico	INFN-Sezione di Roma Tre	Italy
Bilokon Halina	INFN-LNF Frascati (RM)	Italy
Borissov Guennadi	Lancaster University	UK
Bozzi Concezio	INFN-Sezione di Ferrara	Italy
Braibant Sylvie	Università di Bologna	Italy
Brigliadori Luca	Università di Bologna	Italy
Bucci Francesca	Università di Firenze	Italy
Cacciari Matteo	LPTHE Paris	France
Capone Antonio	Università La Sapienza, Roma	Italy
Chavez Carlos	University of Liverpool	UK
Cheatham Sue	Lancaster University	UK
Chen Andrew	INAF-IASF Milano	Italy
Chiarella Vitaliano	INFN-LNF Frascati (RM)	Italy
Chiarelli Giorgio	INFN-Sezione di Pisa	Italy
Cowan Glen	Royal Holloway, University of London	UK
De Angelis Alessandro	Università di Trieste	Italy
De Rujula Alvaro	CERN, Geneva	Switzerland
Del Duca Vittorio	INFN-LNF, Frascati (RM)	Italy
Dell'Agnello Simone	INFN-LNF Frascati (RM)	Italy
Devenish Nicholas	University of Sussex, Falmer	UK
Di Capua Francesco	INFN-Sezione di Napoli	Italy
Djouadi Abdelhak	Université Paris-Sud, Orsay	France
Dokuchaev Vyacheslav	Russian Academy of Sciences, Moscow	Russia
Dolgov Alexander	INFN, Università di Ferrara and ITEP, Moscow	Russia

Eigen Gerald	University of Bergen	Norway
Ermolaev Boris	Ioffe Physico-Technical Institute, St. Petersburg	Russia
Evans Lyn	CERN, Geneva	Switzerland
Fantechi Riccardo	Università di Pisa	Italy
Fargion Daniele	INFN and Università La Sapienza, Roma	Italy
Filippini Jeffrey	California Institute of Technology, Pasadena, CA	USA
Flaecher Henning	CERN, Geneva	Switzerland
Forsberg Charles	MIT, Cambridge, MA	USA
Frère Jean-Marie	Physique Théorique, ULB, Brussels	Belgium
Gambino Paolo	Università di Torino	Italy
Gardi Einan	University of Edinburgh	UK
Gastaldi Ugo	INFN-LNL, Legnaro (PD)	Italy
Gemme Claudia	Università di Genova	Italy
Gervino Gianpiero	Università di Torino	Italy
Giacomelli Paolo	INFN-Sezione di Bologna	Italy
Giglietto Nicola	Università di Bari	Italy
Giovannella Simona	INFN-LNF Frascati (RM)	Italy
Giunti Carlo	INFN-Sezione di Torino	Italy
Grassi Marco	INFN-Sezione di Pisa	Italy
Greco Mario	Università di Roma Tre	Italy
Greenlee Herbert	Fermilab, Batavia, IL	USA
Halkiadakis Eva	Rutgers University, Piscataway, NJ	USA
Happacher Fabio	INFN-LNF Frascati (RM)	Italy
Hartnell Jeffrey	University of Sussex, Brighton	UK
Hautmann Francesco	University of Oxford	UK
Heeger Karsten	University of Wisconsin, Madison, WI	USA
Hiraide Katsuki	Kyoto University	Japan
Hoang Andre	MPI Munich	Germany
Holtkamp Norbert	ITER Organization, St. Paul lez Durance	France
Hung P. Q.	University of Virginia, Charlottesville, VA	USA
Incagli Marco	Università di Pisa	Italy
Iodice Mauro	INFN-Sezione di Roma Tre	Italy
Isidori Gino	INFN-LNF Frascati (RM)	Italy
Jonckheere Alan	Fermilab, Batavia, IL	USA
Karagiorgi Georgia	MIT, Cambridge, MA	USA
Kašpar Jan	Institute of Physics of the ASCR, Praha	Czech Republic
Konigsberg Jacobo	University of Florida, Gainesville, FL	USA
Konikowska Dominika	Institute of Theoretical Physics, University of Warsaw	Poland
Lami Stefano	INFN-Sezione di Pisa	Italy
Leone Sandra	Università di Pisa	Italy
Lhenry-Yvon Isabelle	Institut de Physique Nucléaire d'Orsay	France
Maccarrone Giovanni	INFN-LNF Frascati (RM)	Italy
Magnea Lorenzo	Università di Torino	Italy
Mariotti Mosè	Università di Padova	Italy
Masiero Antonio	Università di Padova	Italy
Masso Eduard	Universitat Autónoma de Barcelona	Spain
Mateev Matey	University of Sofia	Bulgaria
Miscetti Stefano	INFN-LNF Frascati (RM)	Italy
Mizuk Roman	ITEP, Moscow	Russia

Moggi Niccolò	Università di Bologna	Italy
Mussa Roberto	INFN-Sezione di Torino	Italy
Novikov Victor	ITEP, Moscow	Russia
Onyisi Peter	University of Chicago, IL	USA
Otero y Garzón Gustavo	University of Buenos Aires	Argentina
Palla Fabrizio	Università di Pisa	Italy
Pepe Altarelli Monica	CERN, Geneva	Switzerland
Peruzzi Ida	INFN-LNF Frascati (RM)	Italy
Piccinini Fulvio	Università di Pavia	Italy
Piccolo Marcello	INFN-LNF Frascati (RM)	Italy
Pomarol Alex	Universitat Autónoma de Barcelona	Spain
Raimondi Pantaleo	INFN-LNF Frascati (RM)	Italy
Rama Matteo	INFN-LNF Frascati (RM)	Italy
Ri Yongdok	KEK, Tsukuba	Japan
Rozen Yoram	Technion, Haifa	Israel
Schmidt Andreas	CDF, KIT, Karlsruhe	Germany
Sciolla Gabriella	MIT, Cambridge, MA	USA
Spagnolo Paolo	Università di Pisa	Italy
Sparvoli Roberta	Università Tor Vergata, Roma	Italy
Studenikin Alexander	Moscow State University	Russia
Tenchini Roberto	Università di Pisa	Italy
Toms Konstantin	University of New Mexico, NM	USA
Traynor Daniel	Queen Mary, University of London	UK
Trinchero Gian Carlo	INAF-IFSI, Torino	Italy
Turini Nicola	Università di Siena	Italy
Unno Yuuji	Hanyang University, Tsukuba-shi	Japan
Venturi Andrea	Università di Pisa	Italy
Vidal Miguel	CIEMAT, Madrid	Spain
Weiner Neal	New York University, NY	USA
Wicke Daniel	Bergische Universität Wuppertal	Germany
Zanetti Marco	CERN, Geneva	Switzerland
Zavatarelli Sandra	Università di Genova	Italy

FRASCATI PHYSICS SERIES VOLUMES

Volume I
Heavy Quarks at Fixed Target
Eds.: S. Bianco and F.L. Fabbri
Frascati, May 31–June 2, 1993
ISBN—88–86409–00–1

Volume II – Special Issue
Les Rencontres de Physique de la Vallée d'Aoste – Results and Perspectives in Particle Physics
Ed.: M. Greco
La Thuile, Aosta Valley, March 5 –11, 1995
ISBN—88–86409–03–6

Volume III
Heavy Quarks at Fixed Target
Ed.: B. Cox
University of Virginia, Charlottesville
October 7–10, 1994, 11
ISBN—88–86409–04–4

Volume IV
Workshop on Physics and Detectors for DAΦNE
Eds.: R. Baldini, F. Bossi, G. Capon, G. Pancheri
Frascati, April 4–7, 1995
ISBN—88–86409–05–2

Volume V – Special Issue
Les Rencontres de Physique de la Vallée d'Aoste – Results and Perspectives in Particle Physics
Ed.: M. Greco
La Thuile, Aosta Valley, March 3–9, 1996
ISBN—88–86409–07–9

Volume VI
Calorimetry in High Energy Physics
Eds.: A. Antonelli, S. Bianco, A. Calcaterra, F.L. Fabbri
Frascati, June 8–14, 1996
ISBN—88–86409–10–9

Volume VII
Heavy Quarks at Fixed Target
Ed.: L. Kőpke
Rhinefels Castle, St. Goar, October 3–6, 1996
ISBN—88–86409–11–7

Volume VIII
ADONE a milestone on the particle way
Ed.: V. Valente 1997
ISBN—88–86409–12–5

Volume IX – Special Issue
Les Rencontres de Physique de la Vallée d'Aoste – Results and Perspectives in Particle Physics
Ed.: M. Greco
La Thuile, Aosta Valley, March 2–8, 1997
ISBN–88–86409–13–3

Volume X
Advanced ICFA Beam Dynamics
Workshop on Beam Dynamics Issue for e^+e^- Factories
Eds.: L. Palumbo, G. Vignola
Frascati, October 20–25, 1997
ISBN—88–86409–14–1

Volume XI
Proceedings of the XVIII International Conference on Physics in Collision
Eds.: S. Bianco, A. Calcaterra, P. De Simone, F. L. Fabbri
Frascati, June 17–19, 1998
ISBN—88–86409–15–X

Volume XII – Special Issue
Les Rencontres de Physique de la Vallée d'Aoste – Results and Perspectives in Particle Physics
Ed.: M. Greco
La Thuile, Aosta Valley, March 1–7, 1998
ISBN—88–86409–16–8

Volume XIII
Bruno Touschek and the Birth of thee^+e^-
Ed.: G. Isidori
Frascati, 16 November, 1998
ISBN—88–86409–17–6

Volume XIV – Special Issue
Les Rencontres de Physique de la Vallée d'Aoste – Results and Perspectives in Particle Physics
Ed.: M. Greco
La Thuile, Aosta Valley, February 28–March 6, 1999
ISBN—88–86409–18–4

Volume XV
Workshop on Hadron Spectroscopy
Eds.: T. Bressani, A. Feliciello, A. Filippi
Frascati, March 8 2 1999
ISBN—88–86409–19–2

Volume XVI
Physics and Detectors for DAΦNE
Eds.: S. Bianco, F. Bossi, G. Capon, F.L. Fabbri,
P. Gianotti, G. Isidori, F. Murtas
Frascati, November 16 –19, 1999
ISBN—88–86409–21–4

Volume XVII – Special Issue
Les Rencontres de Physique de la Vallée d'Aoste –
Results and Perspectives in Particle Physics
Ed.: M. Greco
La Thuile, Aosta Valley, February 27 March 4, 2000
ISBN—88–86409–23–0

Volume XVIII
LNF Spring School
Ed.: G. Pancheri
Frascati, 15–20 May, 2000
ISBN—88–86409–24–9

Volume XIX
XX Physics in Collision
Ed.: G. Barreira
Lisbon June 29–July1st. 2000
ISBN—88–86409–25–7

Volume XX
Heavy Quarks at Fixed Target
Eds.: I. Bediaga, J. Miranda, A. Reis
Rio de Janeiro, Brasil, October 9–12, 2000
ISBN—88–86409–26–5

Volume XXI
IX International Conference on Calorimetry in
High Energy Physics
Eds.: B. Aubert, J. Colas, P. Nédélec, L. Poggioli
Annecy Le Vieux Cedex, France, October 9–14, 2000
ISBN—88–86409–27–3

Volume XXII – Special Issue
Les Rencontres de Physique de la Vallée d'Aoste – Results and Perspectives in Particle Physics
Ed.: M. Greco
La Thuile, Aosta Valley, March 4–10, 2001
ISBN—88–86409–28–1

Volume XXIII
XXI Physics in Collision
Ed.: Soo–Bong Kim
Seoul, Korea, June 28 30, 2001
ISBN—88–86409–30–3

Volume XXIV
International School of Space Science – 2001 Course on: Astroparticle and Gamma–ray Physics in Space
Eds.: A. Morselli, P. Picozza
L'Aquila, Italy, August 30 September 7, 2000
ISBN—88–86409–31–1

Volume XXV
TRDs for the 3rd Millennium Workshop on Advanced Transition Radiation Detectors for Accelerator and Space Applications
Eds. N. Giglietto, P. Spinelli
Bari, Italy, September 20–23, 2001
ISBN—88–86409–32–X

Volume XXVI
KAON 2001 International Conference on CP Violation
Eds.: F. Costantini, G. Isidori, M. Sozzi
Pisa Italy, June 12th 17th, 2001
ISBN—88–86409–33–8

Volume XXVII – Special Issue
Les Rencontres de Physique de la Vallée d'Aoste – Results and Perspectives in Particle Physics
Ed.: M. Greco
La Thuile, Aosta Valley, March 3–9, 2002
ISBN—88–86409–34–6

Volume XXVIII
Heavy Quarks at Leptons 2002
Eds.: G. Cataldi, F. Grancagnolo, R. Perrino, S. Spagnolo
Vietri sul mare (Italy), May 27th June 1st, 2002
ISBN—88–86409–35–4

Volume XXIX
Workshop on Radiation Dosimetry: Basic Technologies, Medical Applications, Environmental Applications
Ed.: A. Zanini
Rome, Italy, February 56, 2002
ISBN—88–86409–36–2

Volume XXIX – Suppl.
Workshop on Radiation Dosimetry: Basic Technologies, Medical Applications, Environmental Applications
Ed.: A. Zanini
Rome, Italy, February 56, 2002
ISBN—88–86409–36–2

Volume XXX – Special Issue
Les Rencontres de Physique de la Vallée d'Aoste – Results and Perspectives in Particle Physics
Ed.: M. Greco
La Thuile, Aosta Valley, March 9–15, 2003
ISBN—88–86409–39–9

Volume XXXI
Frontier Science 2002 – Charm, Beauty and CP, First International Workshop on Frontier Science
Eds.: L. Benussi, R. de Sangro, F.L. Fabbri, P. Valente
Frascati, October 6–11, 2002
ISBN—88–86409–37–0

Volume XXXII
19th International Conference on x–ray and Inner–Shell Processes
Eds.: A. Bianconi, A. Marcelli, N.L. Saini
Universitá di Roma La Sapienza June 24–28, 2002
ISBN—88–86409–39–07

Volume XXXIII
Bruno Touschek Memorial Lectures
Ed.: M. Greco, G. Pancheri
Frascati, May 11, 1987
ISBN—88–86409–40–0

Volume XXXIV – Special Issue
Les Rencontres de Physique de la Vallée d'Aoste – Results and Perspectives in Particle Physics
Ed.: M. Greco
La Thuile, Aosta Valley, February 29 – March 6, 2004
ISBN—88–86409–42–7

Volume XXXV
Heavy Quarks And Leptons 2004
Ed.: A. López
San Juan, Puerto Rico, 1–5 June 2004
ISBN—88–86409–43–5

Volume XXXVI
DAΦNE 2004: Physics At Meson Factories
Eds.: F. Anulli, M. Bertani, G. Capon, C. Curceanu–Petrascu,
F.L. Fabbri, S. Miscetti
Frascati, June 7–11, 2004
ISBN—88–86409–53–2

Volume XXXVII
Frontier Science 2004, Physics and Astrophysics in Space
Eds.: A. Morselli, P. Picozza, M. Ricci
Frascati, 14–19 June, 2004
ISBN—88–86409–52–4

Volume XXXVIII
II Workshop Italiano sulla Fisica di ATLAS e CMS
Eds.: Gianpaolo Carlino and Pierluigi Paolucci
Napoli, October 13 – 15, 2004
ISBN—88–86409–44–3

Volume XXXIX – Special Issue
Les Rencontres de Physique de la Vallée d'Aoste –
Results and Perspectives in Particle Physics
Ed.: M. Greco
La Thuile, Aosta Valley, February 27 – March 5, 2005
ISBN—88–86409–45–1

Volume XL
Frontier Science 2005 – New Frontiers in Subnuclear Physics
Eds.: A. Pullia, M. Paganoni
Milano, September 12 - 17, 2005
ISBN—88–86409–46–X

Volume XLI
Discoveries in Flavour Physics at e^+e^- Colliders
Eds.: L. Benussi, S. Bianco, C. Bloise, R. de Sangro, C. Gatti,
G. Isidori, M. Martini, F. Mescia, S. Miscetti
Frascati, February 28th - March 3rd, 2006
ISBN—88–86409–51–6

Volume XLII – Special Issue
Les Rencontres de Physique de la Vallée d'Aoste –
Results and Perspectives in Particle Physics
Ed.: M. Greco
La Thuile, Aosta Valley, March 5 March 11, 2006
ISBN—88–86409–47–8

Volume XLIII – Special Issue
Neutral Kaon Interferometry at A Phi-Factory: from Quantum Mechanics to Quantum Gravity
Ed.: A. Di Domenico
Frascati, March 24th 2006
ISBN 978—88–86409–50–8

Volume XLIV– Special Issue
Les Rencontres de Physique de la Vallée d'Aoste –
Results and Perspectives in Particle Physics
Ed.: M. Greco
La Thuile, Aosta Valley, February 28, 2 March 5, 2007
ISBN 978—88–86409–49–4

Volume XLV *Frontier Science – Science with the New Generation*
High Energy Gamma-ray Experiments
Eds.: A. Lionetto, A. Morselli
Villa Mondragone, Monteporzio, Italy, June 18 -20, 2007
ISBN–978—88–86409–54–0

Volume XLVI
XII International Conference on Hadron Spectroscopy
Eds.: L. Benussi, M. Bertani, S. Bianco, C. Bloise, R. de Sangro, P. de Simone, P. di Nezza, P. Giannotti, S. Giovanella, M.P. Lombardo, S. Pacetti
Laboratori Nazionali di Frascati, October 713, 2007
ISBN—978–88–86409–55–1

Volume XLVII – Special Issue
Les Rencontres de Physique de la Vallée d'Aoste –
Results and Perspectives in Particle Physics
Ed.: M. Greco
La Thuile, Aosta Valley, February 24, 2 March 1^{st}, 2008
ISBN 978–88–86409–56–8

Volume XLVIII
The XIV LNF Spring School "Bruno Touschek" in Nuclear, Subnuclear and Astroparticle Physics
Young Researchers Workshop "Physics Challenges in the LHC Era"
Ed. E. Nardi
Laboratori Nazionali di Frascati, Frascati, May 11th - May 14th, 2009
ISBN 978–88–86409–57-5

Volume XLIX
Workshop on Monte Carlo's, Physics and Simulations at the LHC
Ed. P. Nason
Laboratori Nazionali di Frascati, Frascati, February 27-28, 2006
ISBN 978–88–86409–58-2

FRASCATI PHYSICS SERIES VOLUMES – Italian Collection

Collana: Scienza Aperta Vol. I (2006) - ComunicareFisica2005
Atti 1 Convegno "Comunicare Fisica e altre Scienze",
Frascati, 24-27 Ottobre, 2005
Eds: Franco L. Fabbri, Piero Patteri
ISBN – 88-86-409-48-6

Finito di stampare
nel mese di Febbraio 2010
Compositori Ind. Grafiche - Bologna